



HAL
open science

Caractérisation moléculaire et cellulaire de la réponse du tissu sain à la radiothérapie FLASH

Maxime Dubail

► **To cite this version:**

Maxime Dubail. Caractérisation moléculaire et cellulaire de la réponse du tissu sain à la radiothérapie FLASH. Biologie cellulaire. Université Paris-Saclay, 2025. Français. NNT : 2025UPASL007 . tel-04960675

HAL Id: tel-04960675

<https://theses.hal.science/tel-04960675v1>

Submitted on 21 Feb 2025

HAL is a multi-disciplinary open access archive for the deposit and dissemination of scientific research documents, whether they are published or not. The documents may come from teaching and research institutions in France or abroad, or from public or private research centers.

L'archive ouverte pluridisciplinaire **HAL**, est destinée au dépôt et à la diffusion de documents scientifiques de niveau recherche, publiés ou non, émanant des établissements d'enseignement et de recherche français ou étrangers, des laboratoires publics ou privés.

Molecular and cellular characterization of the response of healthy tissue to FLASH radiotherapy

*Caractérisation moléculaire et cellulaire de la réponse du tissu sain à la
radiothérapie FLASH*

Thèse de doctorat de l'université Paris-Saclay

École doctorale n°582 Cancérologie : Biologie – Médecine – Santé (CBMS)
Spécialité de doctorat : Sciences du cancer
Graduate School : Life Sciences and Health. Référent : Faculté de médecine

Thèse préparée dans l'unité de recherche **Signalisation radiobiologie et cancer**
(**Université Paris-Saclay, Inserm, CNRS**), sous la direction de **Charles FOUILLADE**,
PhD HDR, la co-direction de **Marie DUTREIX**, PhD, HDR.

Thèse soutenue à Paris-Saclay, le 10 février 2025, par

Maxime DUBAIL

Composition du Jury

Membres du jury avec voix délibérative

Boris BARDOT Professor, Université Paris Saclay	Président
Constantinos KOUMENIS Professor, University of Pennsylvania, Perelman School of Medicine	Rapporteur & Examineur
Céline MIRJOLET Principal investigator, Centre Georges-François Leclerc	Rapporteuse & Examinatrice
Stéphanie DESCROIX Professor, Institut Curie	Examinatrice

Title : Molecular and cellular characterization of the response of healthy tissue to FLASH radiotherapy

Keywords : FLASH radiotherapy, lung, PCLS, lung dividing cells, single cell RNA sequencing

Abstract : Radiotherapy is a crucial therapeutic option for approximately 50% of cancer patients, but it can damage surrounding healthy tissues, leading to acute or chronic toxicities. In the lungs, radiation-induced damage manifests as pneumonitis, which can progress to pulmonary fibrosis. FLASH radiotherapy, a new treatment modality that delivers ultra-high dose rates, has been shown to spare healthy tissues while maintaining anti-tumor efficacy, an effect observed in several organs. However, challenges remain before successful clinical implementation, including the need to define optimal irradiation parameters and better understand the underlying mechanisms of FLASH.

In this work, we developed an *ex vivo* PCLS model to study the sparing effect in the acute phase of pulmonary radio-induced injury. Using this model, we demonstrated that FLASH irradiation spares cycling cells in the lung compared to conventional radiotherapy.

We also explored the optimal irradiation parameters to trigger the protective effect, showing that dose rate and pulse dose are crucial factors. Furthermore, we provided the first clinical evidence of a FLASH radiotherapy protective effect on healthy human tissue by developing organotypic slices derived from lung resections.

Finally, using scRNAseq analysis, we identified potential underlying mechanisms, including sparing effects on lipid metabolism in AT2 cells, mitochondrial function preservation in endothelial cells, and preliminary data on different activation pathways for alveolar regeneration in cycling cells via the MIF/Cd74 pathway. Although further validations are underway, these findings support the clinical transition of FLASH and contribute to a better understanding of the underlying mechanisms occurring at the acute phase of pulmonary radio-induced injury.

Titre : Caractérisation moléculaire et cellulaire de la réponse du tissu sain à la radiothérapie FLASH

Mots clés : Radiothérapie FLASH, poumon, cellules en cycle, coupes organotypiques, transcriptomique.

Résumé : La radiothérapie est une option thérapeutique essentielle pour environ 50 % des patients atteints de cancer, mais elle peut endommager les tissus sains environnants, entraînant des toxicités aiguës ou chroniques. Dans le poumon, les dommages induits par les radiations se manifestent par une pneumonie, qui peut évoluer vers une fibrose pulmonaire. La radiothérapie FLASH, une nouvelle modalité de traitement à ultra-hauts débits de dose, a montré qu'elle pouvait épargner les tissus sains tout en maintenant son efficacité antitumorale, effet qui a été observé dans plusieurs organes. Cependant, des défis subsistent avant une transition clinique réussie, notamment la nécessité de définir les paramètres d'irradiation optimaux et de mieux comprendre les mécanismes sous-jacents du FLASH.

Dans ces travaux, nous avons développé d'une part un modèle *ex vivo* de coupes organotypiques de poumons pour étudier l'effet d'épargne du FLASH dans la phase aiguë de réponse aux dommages radio-induits. Ce modèle nous a permis de démontrer que l'irradiation FLASH épargne les cellules en cycle dans le poumon par rapport à la radiothérapie conventionnelle. A l'aide de ce modèle, nous avons également étudié les paramètres d'irradiation optimaux pour déclencher l'effet

de protection, en montrant que le débit de dose et la dose par pulse sont des facteurs cruciaux. Ensuite, nous avons apporté une première preuve clinique d'un effet protecteur de la radiothérapie FLASH sur le tissu sain humain en développant un modèle de coupes organotypiques dérivés de résection pulmonaire.

Enfin, à l'aide d'analyse en cellule unique, nous avons identifié de potentiels mécanismes sous-jacents, notamment une épargne du métabolisme lipidique dans les cellules AT2, des fonctions mitochondriales dans les cellules endothéliales et finalement de premières données concernant des voies d'activation différentielle de la régénération alvéolaire dans les cellules qui cyclent via la voie MIF/Cd74.

Bien que de nouvelles validations restent en cours, l'ensemble de ces travaux supporte la transition clinique du FLASH et aide à une meilleure compréhension de ces mécanismes sous-jacents survenant dans la phase de toxicité aiguë dans le poumon.

Host institution :



Funding :



A tout ceux que j'aime, ceux qui feront toujours partie de ma famille.

To all those I love, those who will always be a part of my family.

“One, remember to look up at the stars and not down at your feet. Two, never give up work. Work gives you meaning and purpose and life is empty without it. Three, if you are lucky enough to find love, remember it is there and don't throw it away”.

Stephen Hawking.

“The important thing is not to stop questioning. Curiosity has its own reason for existing. One cannot help but be in awe when one contemplates the mysteries of eternity, of life, of the marvellous structure of reality. It is enough if one tries to comprehend only a little of this mystery every day”.

Albert Einstein.

ACKNOWLEDGEMENTS

My PhD has been a real personal achievement, and I owe my success to many of you, whether colleagues or family. In this acknowledgment, I would like to express my deep gratitude to all those who have played an important role in the progress of my thesis.

First, I would like to thank my two supervisors on this project, **Dr. Charles Fouillade** and **Dr. Marie Dutreix**.

Charles, as my supervisor, I want to thank you for your dedication to this project. Your feedback was always insightful. Above all, I want to thank you for helping me evolve professionally. Thanks to you, I have learned what the true role of a researcher is, a profession I have long aspired to pursue. Always attentive, you supported my decisions and gave me the autonomy to shape my own vision on my project. For that, you are an outstanding supervisor. I hope that over these four years, I have gone from being a student to a future collaborator for the years to come.

As for **Dr. Marie Dutreix**, I sincerely thank you for your trust and support throughout my PhD. Through your inspiring career and our discussions, you helped me develop a passion for translational research. It has been a real honor to be one of your last PhD students.

I would also like to thank **Dr. Sophie Heinrich**. Although you are not officially listed as a supervisor for my thesis, in my mind, you are. I've learned so much from you. As someone who loves interdisciplinarity in science, you allowed me to rekindle my interest in physics. Thanks to you, I learned a bit about radiation physics, which I greatly enjoyed over these four years. In any case, we couldn't do FLASH without a physicist, and luckily, we have an exceptional one! I will greatly miss our FLASH team office !

I would like to thank the rapporteurs of my PhD jury, **Prof. Constantinos Koumenis** and **Dr. Céline Mirjolet**, for the time they dedicated to evaluating my thesis. I also thank my examiners, **Dr. Stéphanie Descroix**, as well as the president of the jury, **Prof. Boris Bardot**, for kindly accept to participate in my PhD jury.

I would like to express my gratitude to the members of my monitoring committee, **Dr. Fabien Millat** and **Dr. Agnès François** from IRSN. A special mention to **Agnès**, who was one of my first internship supervisors during my second year of undergraduate studies, and surely that is what sparked my interest in radiobiology! I also thank **Dr. Danijela Vignjevic** for being part of this committee, your expertise was invaluable to this project.

Moreover, I would like to thank **unit U1021** at Institut Curie, especially **Sandrine Bourgeois** and **Véronique Piveux**, for ensuring that everything was running smoothly. A huge thank you to **Sophie Leboucher** for her support in histology; the platform is not the same without you and your expertise. I also thank **Marie-Noëlle Soler** and **Laetitia Besse** for training me on almost all the microscopes on the platform. Although this came later in my PhD, a special thank you to **Charlène Lasgi**, head of the cytometry platform and the new single-cell platform at Orsay. You are so kind, and it's always a pleasure to discuss with you. Thank you again for your help with my projects! I hope I still remember how to start the sorter, although I can't promise anything. I also thank **Julio Lopes Sampaio** and **Lydia Boudighaghen** for their help with our lipidomics analysis. Finally, I would also like to thank everyone involved in the animal facility, particularly **Pauline Dubreuil**, with whom I had the chance to work and learn a lot.

I want to thank all the current and past members of **Team Dutreix** and **Team Londono**, with whom I had the great opportunity to work with. A big thank you to our team and unit leader, **José Arturo Londono Vallejo**. I would also like to thank other PhD students who have passed through, like **Dr. Sandra Curras-Alonso**, **Dr. Anouk Sesink**, and **Dr. Juliette Soulier**, as well as those still working to obtain their PhD, like **Hugo Laporte**, **Ayan Mallick**, and **Camilla Giaccaglia**. **Camilla**, it was a great opportunity to work with you at LOA, and I hope I've passed on some of my "biologist" side for the future, we should plan soon the zebrafish experiment in LOA. Of course, I would also like to thank the other members of our somewhat atypical team, as we have very distinct themes of research, including **Pierre-Marie Girard**, **Delphine Javelaud**, and **Nathalie Berthault**. Finally, I would of course like to thank **Dr. Vincent Favaudon**, without whom research on FLASH radiotherapy would not have been possible. Your enthusiasm for research is an example to follow, and I hope I too can still be in the lab at your age ! Thank you all for making our work environment so pleasant, and I wish you all the best for the future.

I would also like to thank the past members of the team, such as **Margaux Becerra** and **Lucie Portier**. **Lucie**, thank you for supervising me during my master's and for instilling in me your experimental rigor. I would also like to thank those with whom I had the pleasure of collaborating on my project, such as **Jessica Bastian**, for your kindness, **Antoine Mavrikios** and **Guillaume Camprodon**, with whom we exchanged ideas between radiation oncologists and radiobiologists!

Tout à fait à part, je voudrais également remercier un chercheur en particulier qui a pu me transmettre sa passion dès mon entrée au lycée. Un immense merci donc au **Dr. Amar Madi**, notre professeur de biotechnologie en STL avec Laura. On se rend compte bien plus tard que certaines personnes ont pu changer votre vie et m'avez permis de faire germer la graine de ma passion pour la recherche et pour cela, je vous serais toujours reconnaissant.

D'un point de vue personnel, je souhaite également remercier les membres de ma famille pour leur soutien sans faille tout au cours de mon parcours et durant ma thèse. Je commence bien sûr par **mes parents**. Merci à tous les deux pour m'avoir soutenu pendant ces longues années d'étude et je conçois bien que m'entendre parler de sciences et théoriser à longueur de temps n'a pas dû toujours être facile. L'avantage c'est que maintenant vous ne pourrez plus vous moquer de moi quand je vous parle d'une de mes théories qui a en fait déjà été démontré 40 ans plus tôt. « Le chercheur du passé » va maintenant pouvoir ajouter sa pierre à l'édifice et c'est en grande partie grâce à vous. Même si les dernières années ont été difficile à certains moments, je suis fier que l'on avance ensemble et je serais à jamais reconnaissant pour votre soutien. La force dont tu as fait preuve m'inspireras toujours Maman !

Il en est de même pour **mes grands-parents** qui ont toujours été attentionné avec moi. Mamie Annette, c'est grâce à toi que j'ai développé ma curiosité, nos sorties au musée et ta passion pour l'histoire m'ont toujours fasciné. Je pense que que Pepère serait fier de moi aujourd'hui pour avoir accompli mes objectifs ! Mamie Martine et Papy Alain, vous m'avez transmis beaucoup de votre caractère et je suis heureux de pouvoir partager avec vous cet accomplissement personnel, merci d'être toujours là pour moi. Merci également **Tata**, Corinne, ma marraine comme tu aimes bien le rappeler, merci à ta gentillesse et pour ton sens de l'hospitalité à Ormoy qui nous permettent de tous nous réunir. Une petite pensée à mon cousin **Arman**, votre expérience au Japon avec **Juliette** nous a tellement inspiré que l'on marche sur vos pas, je te souhaite le meilleur pour la suite, mais n'oublie surtout pas d'être productif. Quand je parle de famille, je veux bien sûr étendre à **mes beaux-parents**, Christelle et Jean-Max, ça fait déjà 11 ans que l'on a pu discuter de nos projets et c'est un plaisir d'accomplir tout ça en votre compagnie. Je pense aussi à **Stéphanie** et **Raphael** ainsi qu'au petit **Camille**, mon neveu, qui je le sens, feras un grand scientifique.

Bien sûr je garde le meilleur pour la fin, je voudrais exprimer mon immense gratitude à **Laura**, ma fiancée. Ma thèse va déjà dépasser les 300 pages donc je ne vais pas non plus être trop exhaustif au risque d'en écrire 100 pages de plus mais tu le sais, notre relation est le moteur de ma réussite. Cela fait déjà 11 ans, au début un peu perdu, je ne savais plus quoi faire et c'est en te rencontrant que j'ai réappris à me fixer des objectifs ambitieux. Depuis que nous sommes ensemble, nous avons rencontré du succès dans tout ce que nous entreprenons. Au-delà de ma thèse, ces dernières années ont été le fruit de nombreux moments gravés dans ma mémoire comme nos chats (Luna et Maya), notre premier chez nous, nos fiançailles. Nous sommes toujours là l'un pour l'autre et je te serais à jamais reconnaissant pour le soutien émotionnel que tu m'apportes au quotidien. Cette thèse n'aurait donc pas vu voir le jour sans toi et maintenant, une nouvelle page se tourne vers notre nouvelle vie au pays du soleil levant.

PUBLICATIONS AND COMMUNICATIONS

Publications

Maxime Dubail, Sophie Heinrich, Lucie Portier, Jessica Bastian, Lucia Giuliano, Lilia Aggar, Nathalie Berthault, José-Arturo Londoño-Vallejo, Marta Vilalta, Gael Boivin, Ricky A. Sharma, Marie Dutreix and Charles Fouillade. **Lung Organotypic Slices Enable Rapid Quantification of Acute Radiotherapy Induced Toxicity**. Cells. doi : [10.3390/cells12202435](https://doi.org/10.3390/cells12202435)

Maxime Dubail, Chloé Lafouasse, Sophie Heinrich, Vincent Favaudon, Arturo Londoño-Vallejo, Marie Dutreix, Delphine Colin, Jean-François Côté, Jérôme Didier, Christelle Pouliquen, Abdelali Benali, Pierre Verrelle, Marine Lefèvre, Nicolas Girard, Agathe Seguin-Givelet, Gilles Créhange, Charles Fouillade. **Potential of FLASH Radiotherapy Uncovered in Human Lung**.

Submitted to *Clinical Cancer Research*.

Juliette Soulier, Sandra Curras-Alonso, **Maxime Dubail**, Hugo Laporte, Ayan Mallick, Chloé Lafouasse, Delphine Colin, Jean-François Côté, Jérôme Didier, Christelle Pouliquen, Abdelali Benali, Marco Alifano, Catherine Durdux, Diane Damotte, Marine Lefèvre, Mylène Bohec, Kim Cao, Gilles Créhange, Pierre Verrelle, Nicolas Girard, Agathe Seguin-Givelet, Arturo Londoño-Vallejo, Charles Fouillade. **Radiotherapy triggers pro-angiogenic signaling in human lung**. BioRxiv. doi: <https://doi.org/10.1101/2024.10.11.617840>

Anouk Sesink, Margaux Becerra, Jia-Ling Ruan, Sophie Leboucher, **Maxime Dubail**, Sophie Heinrich, Wael Jdey, Kristoffer Petersson, Charles Fouillade, Nathalie Berthault, Marie Dutreix, Pierre-Marie Girard. **The AsiDNA™ decoy mimicking DSBs protects the normal tissue from radiation toxicity through a DNA-PK/p53/p21-dependent G1/S arrest**. NAR Cancer. doi: [10.1093/narcan/zcae011](https://doi.org/10.1093/narcan/zcae011)

E. Prades-Sagarra · F. Laarakker · J. Dissy · N.G. Lieuwes · R. Biemans · **M. Dubail** · C. Fouillade · A. Yaromina · L.J. Dubois. **Caffeic Acid Phenethyl Ester (CAPE), a natural polyphenol to increase the therapeutic window for lung adenocarcinomas**. Radiotherapy and Oncology. doi: [10.1016/j.radonc.2023.110021](https://doi.org/10.1016/j.radonc.2023.110021)

Wenxin Li, Chi Zhang, Shuhei Aramaki, Lili Xu, Shogo Tsuge, Takumi Sakamoto, Md. Al Mamun, Ariful Islam, Takamitsu Hayakawa, Yusuke Takanashi, **Maxime Dubail**, Kenta Konishi, Tomohito Sato, Tomoaki Kahyo, Charles Fouillade, Katsumasa Nakamura, and Mitsutoshi Setou. **Lipid Polyunsaturated Fatty Acid Chains in Mouse Kidneys Were Increased within 5 min of a Single High Dose Whole Body Irradiation.** International Journal of Molecular Sciences. DOI: [10.3390/ijms241512439](https://doi.org/10.3390/ijms241512439)

Robin P. Journot, Mathilde Huyghe, Alexandre Barthelemy, Hugo Couto-Moreira, Jakub Sumbal, Marisa M. Faraldo, **Maxime Dubail**, Charles Fouillade, Silvia Fre. **Conserved signals orchestrate self-organization and symmetry breaking of bi-layered epithelia during development and regeneration.** BioRxiv. DOI: [10.1101/2024.07.21.603898](https://doi.org/10.1101/2024.07.21.603898)

Other publications including scRNAseq analysis on AT2 cells and lipidomics, FLASH irradiation optimal parameters, analysis on lung dividing cells and responses to FLASH as well as VHEE collaborative work are ongoing but not submitted at the time of thesis manuscript submission.

Oral communications

- **FRPT24** : FLASH radiotherapy spares mitochondrial function in human healthy lung.
- **FRPT23** : First evidence and transcriptional characterization of the FLASH effect in human lung samples
- **Optimizing imaging and dose response in radiotherapies workshop 2023** : Development of an ex vivo assay enabling rapid quantification of radiotherapy induced toxicities in healthy lung
- **FRPT22** : Studying the FLASH effect at the single cell level
- **SFBR** : Caractérisation de la réponse du poumon sain à la radiothérapie FLASH
- **FRPT21** : New models for FLASH studies

Poster communications

- **Immunorad 2023** : FLASH radiotherapy spares the transcription of a lipid metabolism pattern specific to murine lung AT2 cells
- **ESTRO 2023** : First evidence of a FLASH sparing effect in human healthy lung samples

Other posters and oral communications based on collaborative work or thesis work have also been presented during my thesis by M2 interns or PhD students

Prize

- **Best abstract prize at FRPT23** on - First evidence and transcriptional characterization of the FLASH effect in human lung samples

RESUME

Contexte et objectifs : La radiothérapie est une option thérapeutique essentielle pour environ 50 % des patients atteints de cancer, mais elle peut endommager les tissus sains, entraînant des toxicités aiguës et chroniques. Dans le poumon, ces dommages se manifestent par une pneumonie radio-induite, qui peut évoluer vers une fibrose pulmonaire. La radiothérapie FLASH, une technique d'irradiation à ultra-hauts débits de dose, a montré un effet protecteur sur les tissus sains tout en conservant une efficacité antitumorale. Cependant, avant une transition clinique réussie, des défis demeurent, notamment la définition des paramètres d'irradiation optimaux et une meilleure compréhension des mécanismes biologiques sous-jacents au FLASH. Dans ce projet, nous avons développé un modèle *ex vivo* basé de coupes précises de poumons (PCLS) afin d'étudier l'effet d'épargne du FLASH dans la phase aiguë des dommages radio-induits. À travers ce modèle, nous avons étudié les paramètres d'irradiation optimaux et évalué l'effet du FLASH sur le tissu pulmonaire humain. De plus, nous avons mené des analyses transcriptomiques à l'échelle unicellulaire pour identifier les mécanismes sous-jacents impliqués dans la réponse au FLASH.

Méthodes : Dans un premier temps, nous avons établi un modèle *ex vivo* de PCLS permettant d'évaluer les toxicités aiguës après irradiation FLASH et conventionnelle (CONV-RT). Ce modèle a été utilisé pour déterminer les paramètres optimaux du FLASH et démontrer son effet protecteur sur les cellules en cycle dans le poumon. Nous avons également développé un modèle PCLS dérivé de résections pulmonaires de patients, permettant une première investigation d'un effet protecteur du FLASH sur le tissu sain humain. Dans une deuxième partie, nous avons mené des analyses transcriptomiques en cellule unique (scRNAseq) afin d'explorer les modifications transcriptionnelles post-irradiation sur des compartiments de cellules résidentes pulmonaires. Nous avons étudié la réponse du métabolisme lipidique des cellules alvéolaires de type 2 (AT2), la préservation des fonctions mitochondriales des cellules endothéliales, ainsi que des voies potentielles de régénération alvéolaire impliquant MIF/Cd74 dans les cellules épargnées qui cyclent après irradiation FLASH.

Résultats : Les expériences *ex vivo* ont révélé que le FLASH épargne préférentiellement les cellules en cycle dans le poumon, contrairement à la radiothérapie conventionnelle. Nous avons déterminé que les paramètres optimaux du FLASH nécessitent un débit de dose supérieur à 100 Gy/s, et plus précisément, supérieur à 300 Gy/s. De plus, nous avons montré que la dose par impulsion devait excéder 1 Gy/pulse pour observer un effet protecteur du FLASH dans le modèle PCLS. Chez l'homme, l'utilisation du modèle PCLS-Hu a permis de mettre en évidence un effet protecteur du FLASH sur la division cellulaire dans 94 % des échantillons testés, suggérant une transposabilité de l'effet FLASH aux tissus humains. Les analyses transcriptomiques ont révélé que l'irradiation FLASH limite l'activation des voies inflammatoires impliquées dans le stress oxydatif, comparée à la

radiothérapie conventionnelle. Nous avons observé une préservation du métabolisme lipidique dans les cellules AT2, une réduction des dommages mitochondriaux dans les cellules endothéliales, ainsi qu'une activation différentielle des voies de régénération alvéolaire via MIF/Cd74. Ces résultats suggèrent que l'effet FLASH repose sur une combinaison de mécanismes cellulaires et moléculaires permettant une meilleure préservation du tissu sain.

Conclusion : Grâce au développement du modèle PCLS et à l'étude des réponses transcriptionnelles post-irradiation, nous avons apporté des éléments nouveaux démontrant que le FLASH protège les cellules en cycle et limite les dommages aux tissus sains par plusieurs mécanismes biologiques. Nos résultats confirment que l'optimisation des paramètres d'irradiation est essentielle pour maximiser l'effet protecteur du FLASH et faciliter sa transition vers une application clinique. L'utilisation du modèle PCLS-Hu permet de rapprocher les observations expérimentales d'un potentiel bénéfique thérapeutique chez l'homme. En combinant ces avancées, nous proposons une meilleure compréhension des mécanismes sous-jacents au FLASH, ouvrant la voie à son intégration dans les stratégies de radiothérapie oncologique.

SUMMARY

Background and Objectives : Radiotherapy is a crucial therapeutic option for approximately 50% of cancer patients, but it can damage healthy tissues, leading to acute and chronic toxicities. In the lungs, radiation-induced damage manifests as pneumonitis, which can progress to pulmonary fibrosis. FLASH radiotherapy, a novel ultra-high dose rate irradiation technique, has shown a protective effect on healthy tissues while maintaining anti-tumor efficacy. However, challenges remain before its successful clinical translation, including the need to define optimal irradiation parameters and a better understanding of the biological mechanisms underlying the FLASH effect. In this work, we developed an ex vivo model based on precision-cut lung slices (PCLS) to investigate the protective effects of FLASH radiotherapy in the acute phase of radiation-induced injury. Using this model, we optimized irradiation parameters and assessed the protective effect of FLASH on human lung tissue. Additionally, we performed single-cell transcriptomic analyses to identify the cellular and molecular mechanisms involved in the response to FLASH irradiation.

Methods : In the first part of this study, we established an ex vivo PCLS model to evaluate acute toxicities following FLASH and conventional radiotherapy (CONV-RT). This model was used to determine optimal FLASH irradiation parameters and to demonstrate its protective effect on cycling cells in the lung. We further developed an organotypic human lung slice model (PCLS-Hu) derived from patient lung resections, providing the first clinical evidence of a FLASH-induced protective effect on healthy human tissue. In the second part, we conducted single-cell RNA sequencing (scRNAseq) analysis to investigate transcriptional changes occurring post-irradiation. We explored the role of lipid metabolism preservation in alveolar type 2 (AT2) cells, mitochondrial function maintenance in endothelial cells, and differentially activated pathways involved in alveolar regeneration via the MIF/Cd74 pathway.

Results : Ex vivo experiments demonstrated that FLASH selectively spares cycling cells in the lung, unlike conventional radiotherapy. We identified that optimal FLASH parameters require a dose rate above 100 Gy/s, and more specifically, exceeding 300 Gy/s. Additionally, we showed that a pulse dose greater than 1 Gy/pulse is necessary to trigger a protective effect in the PCLS model. In human lung tissue, the PCLS-Hu model revealed a FLASH-induced protective effect on cell division in 94% of tested samples, suggesting translatability of the FLASH effect to human tissues. Single-cell transcriptomic analyses showed that FLASH irradiation reduces the activation of inflammatory pathways associated with oxidative stress compared to conventional radiotherapy. We observed preservation of lipid metabolism in AT2 cells, reduced mitochondrial damage in endothelial cells, and differentially activated alveolar regeneration pathways via MIF/Cd74. These findings suggest that the FLASH effect relies on a combination of cellular and molecular mechanisms that contribute to better preservation of healthy tissue.

Conclusion : By developing the PCLS model and analyzing transcriptional responses post-irradiation, we provided new evidence that FLASH protects cycling cells and limits radiation-induced damage to healthy tissues through multiple biological mechanisms. Our results confirm that optimizing irradiation parameters is essential to maximize the protective effect of FLASH and facilitate its clinical translation. The use of the PCLS-Hu model bridges the gap between experimental observations and potential therapeutic benefits in humans. By combining these advancements, we propose a deeper understanding of the mechanisms underlying FLASH, paving the way for its integration into oncological radiotherapy strategies.

CONTENTS

Acknowledgements	8
Publications and communications	11
Contents	18
List of figures	20
Abbreviations	23
I- Introduction	26
1. Radiotherapy, cellular response and SoC for cancer patients	26
1.1 Ionizing Radiation.....	27
1.2 Conventional External Beam Radiotherapy (EBRT)	28
1.3 From ionizing radiation interaction to cellular biological response	39
1.4 Improvement of Therapeutic Index of Radiation Therapy	50
2. The lung, a model for investigating radiation-induced toxicities	57
2.1 Structure, function and cell composition of the respiratory system	57
2.2 Radiation induced lung injuries (RILI).....	83
2.3 Modeling radio-induced toxicities.....	102
3. FLASH, a new way to deliver radiation therapy	119
3.1 The FLASH sparing effect in preclinical-murine models. ...	120
3.2 Assessing the antitumoral isoefficacy of FLASH-RT.....	126
3.3 Underlying mechanisms of the FLASH effect	131
3.4 Clinical translation of FLASH radiotherapy	145
II- Hypothesis and main objectives	158
III- Part 1 – Development of an ex vivo model for FLASH studies..	161
1. Modeling the flash effect <i>ex vivo</i>	161
1.1 Introduction	161
1.2 Material and method/Results – Article 1	162
1.3 Conclusion	177
2. Optimal parameters for FLASH-RT in the lung	178
2.1 Introduction	178
2.2 Material and methods.....	179
2.3 Results	182
2.4 Conclusion	191
3. FLASH sparing effect in patients	192
3.1 Introduction	192
3.2 Material and method/Results – Article 2	193
3.3 Additional results – Article 2	213
4. Conclusion part 1 – Key insights from ex vivo PCLS model on FLASH-RT sparing effect in the lung	216

IV- Part 2 – Transcriptional acute and late changes occurring post-FLASH or CONV-RT in mouse lung at the single cell level.....	217
1. Transcriptional characterization of the FLASH sparing effect in mouse whole lung	217
1.1 Introduction	217
1.2 Material and method.....	218
1.3 Results	222
V- Part 3 – Characterization of the FLASH effect in lung dividing cells	245
1. Deciphering the underlying mechanisms of FLASH in dividing cells	245
1.1 Introduction	245
1.2 Material and method.....	246
1.3 Results	250
VI- Discussion	284
1. Pertinence of ex vivo PCLS model for acute radiation injuries.....	285
2. PCLS model help to characterize optimal FLASH irradiation parameters in the lung	286
3. PCLS model to investigate the presence of acute FLASH sparing effect in healthy patient samples.....	288
4. Acute molecular characterization of the FLASH sparing effect in the whole lung and lung cycling cells compartment	289
4.1 FLASH-RT spares lipid metabolism in AT2 cells compared to CONV-RT	289
4.2 Is there a FLASH sparing effect related to mitochondrial function in endothelial cells ?	291
4.3 Characterization and proposed mechanisms of FLASH sparing effect in lung cycling cells	292
VII- Conclusion and perspectives	295
Bibliography	297
Annex 1 – Additional results and papers part 1	339
1. Additional results.....	340
1.1 Complementary studies on radioprotector of healthy lung tissue to radiation	340
1.2 Proof of concept of PCLS-tumor model obtention.....	341
2. The AsiDNA™ decoy mimicking DSBs protects the normal tissue from radiation toxicity through a DNA-PK/p53/p21-dependent G1/S arrest.....	343
3. Caffeic Acid Phenethyl Ester (CAPE), a natural polyphenol to increase the therapeutic window for lung adenocarcinomas	362
Annex 2 – Other co-author contributions	370
1. Radiotherapy triggers pro-angiogenic signaling in human lung ...	370
2. Lipid Polyunsaturated Fatty Acid Chains in Mouse Kidneys Were Increased within 5 min of a Single High Dose Whole Body Irradiation	390

LIST OF FIGURES

Figure 1. External Beam Radiation Therapy (EBRT).....	27
Figure 2. Dose distribution in IMRT for lung cancer.....	29
Figure 3. Cisplatin action mechanism.	30
Figure 4. Mechanisms of action of cetuximab (anti-EGFR monoclonal antibody) and gefinitinib (TKI).....	32
Figure 5. Mechanism of Immune Response with Radio-Immunotherapy.....	35
Figure 6. Stade classification for lung cancer	38
Figure 7. TOPAS-based Monte Carlo simulations of the integrated normalized dose deposited for 6 MV photons, 12 MeV electrons, 150 MeV protons, 320 MeV/n carbon-12 ions, and a 250 MeV VHEE beam.....	39
Figure 8. Diagram illustrating the sequential stages of radiation-induced water radiolysis.....	40
Figure 9. Indirect and direct radiation induced DNA damage.....	42
Figure 10. Nrf2 Keap1 signaling pathway in response to oxidative stress	43
Figure 11. DNA damage responses overview.....	45
Figure 12. DNA damage detection via ATM/ATR and p53 pathway.....	47
Figure 13. Cell cycle checkpoints upon ionizing radiation damages.. ..	48
Figure 14. Scheme for therapeutic Index of radiotherapy.....	50
Figure 15. Scheme illustrating the concepts of target volumes in radiotherapy	52
Figure 16. Multimodal Imaging for hypoxic tumor in Head and Neck Cancer	53
Figure 17. Comparison of Conventional Radiotherapy and Minibeam Radiotherapy (MBRT) distributions	56
Figure 18. Respiratory tract structure.....	58
Figure 19. Cellular Composition of the lower respiratory tract.....	61
Figure 20. Classification of the human airway epithelium.....	63
Figure 21. Analysis of alveolar epithelial cell differentiation and trajectory using scRNA-seq and in vitro assays.....	64
Figure 22. Expression level of Stk11 is associated with the differentiation of ciliated cells in airways	67
Figure 23. Dynamics of AT0 cells and distinct cellular trajectories in the human alveolar epithelium	71
Figure 24. Characterization of alveolar, adventitial, and peribronchial fibroblasts	73
Figure 25. Distinct Capillary Endothelial Cell Types in the Alveolar Network.....	75
Figure 26. Human lung cell atlas umap representation for Immune, Epithelial and Endothelial/Stromal compartment.....	80
Figure 27. Alveolar structure differences between Human and mouse lung.....	82
Figure 28. CT Imaging of Radiation-Induced Changes in Lung.....	85
Figure 29. Histopathology of representative lung sections stained for fibrosis with Masson's trichrome.....	87
Figure 30. Proinflammatory and profibrotic profile of alveolar and interstitial macrophages after fibrogenic doses of IR.....	95
Figure 31. Myofibroblasts contribute to the ECM deposition after IR17Gy.....	97
Figure 32. Characterization of the ECs after radiation injury	101
Figure 33. Differential sensitivity to COPD- and non-COPD PBEC irradiation in ALI culture	104
Figure 34. Characterization of Human Lung Organoids	106
Figure 35. Human Lung Alveolus Chip recapitulates hallmark features of RILI	109
Figure 36. Embedding of Precision-Cut Lung Slices in Engineered Hydrogel Biomaterials Supports Extended Ex Vivo Culture	112
Figure 37. Characterization of PCLS structure and cellular microenvironment.....	114
Figure 38. Various applications of PCLS for modeling COPD, IPF and lung cancer	115
Figure 39. Comparative study on various lung model advantages and drawbacks.	118
Figure 40. First Evidence of the FLASH Effect in vivo	119
Figure 41. FLASH sparing effect on various healthy murine tissues.....	123
Figure 42. Range of FLASH-RT dose modifying factors from preclinical mouse studies per organ.	

.....	125
Figure 43. Non-exhaustive list of tumor types used to demonstrate the isoefficacy of FLASH radiotherapy in murine models.....	127
Figure 44. FLASH and CONV-RT antitumoral immune response	129
Figure 45. FLASH effect is influenced by the tissue's partial pressure of oxygen.....	132
Figure 46. Comparative Analysis of DNA Damage and Repair Dynamics in CONV-RT and FLASH-RT.....	135
Figure 47. Inflammatory Cytokine Response and TGF- β 1 Expression Following FLASH-RT and CONV-RT.....	138
Figure 48. Reverse Electron Flow and the FLASH Effect on Mitochondrial Function	143
Figure 49. Optimal Irradiation Parameters in FLASH Radiotherapy.....	152
Figure 50. Large Mammal Studies of FLASH Radiotherapy.....	155
Figure 51. Ongoing clinical trials for FLASH-RT.....	156
Figure 52. Impact of the mean dose rate on the FLASH protective effect.....	183
Figure 53. Impact of a single pulse FLASH irradiation on healthy tissue sparing effect.	184
Figure 54. Minimal dose per pulse/Number of pulses to trigger a FLASH sparing effect in PCLS.....	185
Figure 55. Importance of temporal structure of FLASH-RT	186
Figure 56. Impact of oxygen concentration on FLASH-RT sparing effect in PCLS.....	188
Figure 57. Conservation of the FLASH sparing effect in previously irradiated lung tissue	190
Figure 58. FLASH-RT reduced activation of electron transport chain system in patient lung samples.....	214
Figure 59. FLASH reduces radio-induced acute inflammation in human lung compared to CONV-RT.....	216
Figure 60. Scheme of experimental protocol for transcriptional analysis using ScRNAseq 24 hours after FLASH or CONV-RT at 13Gy.....	217
Figure 61. Single-cell data visualization of the NI and irradiated lungs.....	223
Figure 62. Lung cell type identification and canonical marker expression	224
Figure 63. Common response 24 hours after FLASH and CONV-RT in the whole lung.....	226
Figure 64. Distribution of lung cells subpopulations upon FLASH or CONV-RT.....	227
Figure 65. FLASH spares lipid metabolism pathway in AT2 cells at 24 hours post-treatment...	229
Figure 66. Experimental setup and relevance of lipidomic analysis for AT2 sorted cells.....	230
Figure 67. Increased level of ceramide is correlated with a common upregulation of ferroptosis related genes following radiation in AT2 cells.....	231
Figure 68. FLASH spares lipid droplet-related lipids level in AT2 cells compared to CONV-RT 24h after irradiation.....	232
Figure 69. Characterization of AT2 cell clusters and Apoe expressions from 24 hours to 5 months post-irradiation.....	233
Figure 70. Dynamic of Apoe expression months following FLASH or CONV-RT.....	234
Figure 71. Dynamic of Plin2 expression months following FLASH or CONV-RT.....	234
Figure 72. Identification of endothelial subpopulations and their distribution across irradiation conditions.....	237
Figure 73. FLASH-RT spares mitochondrial genes expression in endothelial subpopulations..	240
Figure 74. Upregulation of mitochondrial genes after FLASH is maintained across time post-radiation.....	242
Figure 75. Identification of dividing cells in lung dataset.....	244
Figure 76. Experimental setup and protocol for the identification of Mki67+ cells and cell fate analysis.....	250
Figure 77. Gating procedure for FACS analysis with Mki67 Cre ERT2 x R26 mtmG mice.....	251
Figure 78. FLASH spares total Mki67+ cells 24 hours post-radiation but has no impact on Mki67+ cells distribution across lung compartments	252
Figure 79. Preliminary results suggest that FLASH spares all lung dividing cells subpopulations at 24 hours post-radiation.....	253
Figure 80. Monitoring of Mki67+ cells that divided in the lung within 24 hours post-irradiation.	254
Figure 81. Experimental setup and protocol for studying cell division across lung subpopulations after CONV or FLASH-RT.....	255
Figure 82. Selection of antibody panel for microvascular lung subpopulation identification in flow	

cytometry.....	256
Figure 83. Dynamic of whole lung cell division after FLASH or CONV-RT at 13 Gy from 1 to 4 week post-treatment.....	257
Figure 84. Dynamic of immune lung cells division after FLASH or CONV-RT at 13 Gy from 1 to 4-week post-treatment.....	258
Figure 85. Dynamic of epithelial/mesenchymal cells division after FLASH or CONV-RT at 13 Gy from 1 to 4-week post-treatment.....	259
Figure 86. Dynamic of endothelial cells division after FLASH or CONV-RT at 13 Gy from 1 to 4-week post-treatment.....	260
Figure 87. Dynamic of microvascular endothelial cells division after FLASH or CONV-RT at 13 Gy from 1 to 4-week post-treatment.....	261
Figure 88. Sorting of Mki67+ cells for ScRNAseq at a dose of 13 Gy revealed a FLASH sparing effect.....	262
Figure 89. Identification and distribution of Mki67+ cells after CONV or FLASH-RT in lung subpopulations.....	263
Figure 90. Characterization of cell division markers in Mki67 sorted populations across conditions.....	267
Figure 91. CONV-RT induces active endothelial regeneration related genes compared to FLASH-RT.....	268
Figure 92. Endothelial cells exacerbate an inflammatory signature related to immune recruitment after FLASH-RT.....	269
Figure 93. FLASH-RT induces an upregulation of mitochondrial associated OXPHOS chain genes compared to CONV-RT in T cells.....	271
Figure 94. CONV-RT induce an upregulation of TNF α via NFKb related genes in T-cells compared to FLASH-RT.....	272
Figure 95. TNF α via NFKb related genes are commonly upregulated after CONV-RT in various immune cells populations.....	272
Figure 96. Common upregulation of AP-1 transcription factor related genes in immune Mki67 compartment after CONV-RT.....	273
Figure 97. Identification of an inflammatory and AP-1 related cluster of Neutrophils after CONV-RT.....	274
Figure 98. Identification of an inflammatory and AP-1 related cluster of Monocytes after CONV-RT.....	275
Figure 99. Identification of an inflammatory and AP-1 related cluster of AM after CONV-RT....	275
Figure 100. CONV-RT induces an upregulation of Btg1 and Btg2 in various immune Mki67 sorted cell types which is associated with a drop in active dividing T cells.....	277
Figure 101. FLASH-RT induces a specific upregulation of Mif factor and Cd74 receptor in sorted Mki67 T cells.....	278
Figure 102. FLASH-RT induces an upregulation of Cd74 receptor expression in alveolar macrophages.....	279
Figure 103. FLASH-RT induces an upregulation of Cd74 receptor expression in AT2 and AT0 Mki67 sorted cells.....	280
Figure 104. Overview and scheme of proposed differential mechanisms in Mki67 sorted lung cells subpopulations.....	281
Figure 105. Sorting of FLASH, CONV and non-treated crypt Mki67+ cells following radiation for scRNAseq analysis 24 hours post-treatment.....	282
Figure 106. Generation of PCLS-tumor from orthotopic LL2-Luc tumor mouse model.....	342

ABBREVIATIONS

ALI	Air liquid interface
ALK	Anaplastic lymphoma kinase
AM	Alveolar macrophage
ARP	Acute radiation pneumonitis
ATM	Ataxia-telangiectasia mutated
ATR	ATM and Rad3-related
AT0	Alveolar type 0 cells
AT1	Alveolar epithelial type I cells
AT2	Alveolar epithelial type II cells
BASCs	Bronchioalveolar stem cells
BCs	Basal cells
BER	Base excision repair
CDK	Cyclin-dependent kinase
CCRT	Concurrent chemotherapy
CONV	Conventional radiotherapy
COPD	Chronic obstructive pulmonary disease
CT	Computed tomography
CTV	Clinical target volume
DC	Dendritic cells
DEG	Differential expressed gene
DSB	Double strand break
EDU	5-Ethynyl-2'-deoxyuridine
ECM	Extracellular matrix
EGFR	Epidermal growth factor receptor
EndoMT	Endothelial-to-mesenchymal transition
ETC	Electron transport chain
EBRT	External beam radiotherapy
F-PRT	FLASH proton radiotherapy
GSEA	Gene set enrichment analysis
GTV	Gross tumor volume
Gy	Gray
HLCA	Human lung cell atlas
HR	Homologous recombination
ICI	Immune checkpoint inhibitor
IGRT	Image-guided radiotherapy
IM	Interstitial macrophage
IMPT	Intensity modulated proton therapy
IMRT	Intensity-modulated radiotherapy
IOeRT	Intraoperative electron radiation therapy
IR	Ionizing radiation
ITV	Internal tumor volume
LET	Linear energy transfer
LINAC	Electron linear accelerator
LOC	Lung on chip
LR-MSCs	Lung-resident mesenchymal stromal cells
MBRT	Microbeam radiotherapy
MDSCs	Myeloid-derived suppressor cells
MMR	Mismatch repair
MRI	Magnetic resonance imaging
NEB	Neuroepithelial body
NER	Nucleotide excision repair

NHEJ	Non homologous end joining
NK	Natural killer
NSCLC	Non-small cell lung cancer
OAR	Organ at risk
ORR	Objective response rate
OS	Overall survival
PET	Positron emission tomography
PCLS	Precision-cut lung slices
PFS	Progression-free survival
PMCs	Pulmonary mesothelial cells
PNECs	Pulmonary neuroendocrine cells
PRV	Planning risk volume
PTV	Planning target volume
RASCs	Respiratory airway secretory cells
RIPF	Radiation-induced pulmonary fibrosis
RILI	Radiation-induced lung injury
ROS	Reactive oxygen species
RP	Radiation pneumonitis
SBRT	Stereotactic body radiation therapy
SASP	Senescence-associated secretory phenotype
ScRNA-seq	Single cell RNA sequencing
SFRT	Spatially fractionated radiotherapy
SFTPC	Surfactant protein C
S-PRT	Conventional proton therapy
SCLC	Small cell lung cancer
SI	International system
SOC	Standard of care
SOD	Superoxide dismutase
SSB	Single strand break
TAM	Tumor-associated macrophage
TKI	Tyrosine kinase inhibitor
TME	Tumor microenvironment
Treg	Regulatory T cells
VEGF	Vascular Endothelial Growth Factor
VHEE	Very High Energy Electrons
WBI	Whole brain irradiation

CHAPTER I : INTRODUCTION

I- INTRODUCTION

Cancer treatment for patients involves a combination of therapeutic approaches, depending on the tumor, localization, stage, and individual patient characteristics. The goal of these treatment is to kill cancer cells while minimizing damage to healthy tissues. For that purpose, the standard of care (SOC) forms the basis of treatment protocols, most SOC protocols recommend a combination of chemotherapy, radiotherapy, and surgery, each playing a complementary role. These standards are often updated with new methods and drugs that demonstrate additional benefits in clinical trials when combined with actual SOC. Chemotherapy is one of the most widely used cancer treatments. It involves the administration of chemical agents, which work to inhibit cell growth or division. Chemotherapy can be used in a neoadjuvant setting (before surgery or radiotherapy) to shrink tumors or as adjuvant therapy (after surgery or radiotherapy) to eliminate remaining cancer cells. However, due to its impact on normal cells, chemotherapy is often accompanied by significant side effects. Another SOC is surgery, which is known as the most effective modality for removing solid tumors and which is used in approximately 80% of cancer. Surgeons aim to remove the tumor along with surrounding tissue called margins to ensure complete removal. However, for certain tumors located in areas where surgery can't be used, another SOC, radiotherapy, is the primary local treatment option. Radiotherapy is used in over half of all cancer cases and is essential for both curative and palliative applications. It works by using ionizing radiation to destroy the cancer cells, focusing on the tumor while sparing surrounding healthy tissues as much as possible. In this manuscript, radiotherapy will be the central focus. The work will delve into the underlying mechanisms of radiation interactions at the cellular and molecular levels, explore novel radiation modalities such as FLASH radiotherapy that could mitigate radiation-induced normal tissue injuries.

1. RADIOTHERAPY, CELLULAR RESPONSE AND SOC FOR CANCER PATIENTS

Radiotherapy is a major cancer treatment, with more than half of all diagnosed patients receiving ionizing radiation as part of their therapeutic course¹⁻³. In specific cases, such as breast or central nervous system cancers, the use of radiotherapy is over 80%⁴⁻⁶. In the context of non-small cell lung cancer (NSCLC) patients, half will undergo radiotherapy at some point during their treatment⁷. Radiotherapy has a widespread use for a broad range of cancers. It could be used for both curative and palliative purposes. In the following section, we will explore the complexity of ionization events in radiotherapy that involve multidisciplinary approaches from physics, chemistry, and biology.

1.1 Ionizing Radiation

Ionization, in chemistry, refers to a process in which an atom or molecule acquires a positive or negative charge by gaining or losing electrons. It then results in the formation of ions⁸. Ionizing radiation (IR) is a form of high-energy radiation able to ionize atoms or molecules, thus generating ions that can disrupt covalent bonds⁹. Radiotherapy (RT) use ionizing radiation as a treatment to kill tumor cells⁴. To obtain a quantitative measure of the effects of ionizing radiation, the radiation dose, critical for both the efficacy and safety of radiotherapy, has been defined. In the new international system (SI), the dose is measured in Gray (Gy) which correspond to the amount of radiation energy absorbed by one kilogram of tissue¹⁰.

Through generation of ions that disrupt molecular structures, IR can effectively damage the DNA of cancer cells, making it a powerful tool in cancer treatment. To harness this potential, precise measurement of radiation dose is essential to balance treatment efficacy and safety. Building on the principles of IR, Conventional External Beam Radiotherapy (EBRT) applies focused radiation beams from an external source to target tumors with precision (**Figure 1**). In the following section, we will delve into the methodologies and clinical applications of EBRT in modern cancer therapy.

Radiation Therapy

External beam radiation therapy (EBRT)

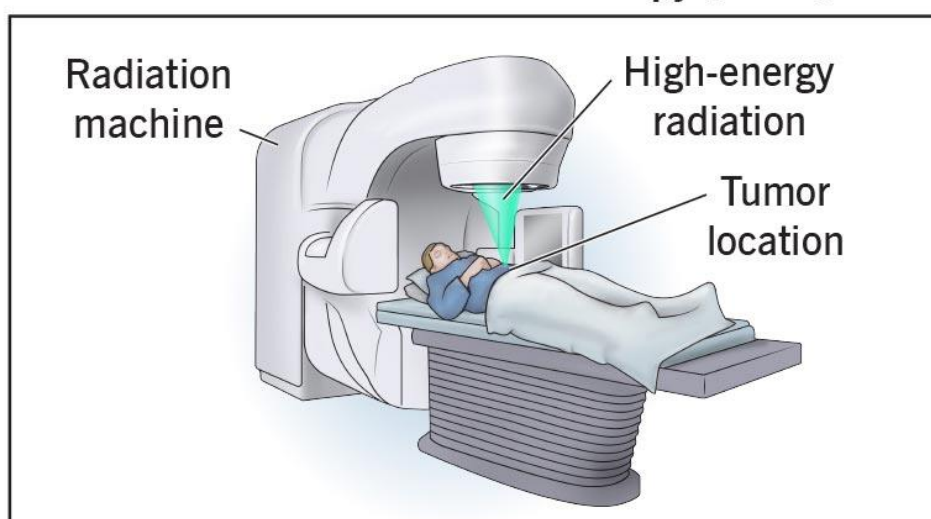


Figure 1. External Beam Radiation Therapy (EBRT). *The patient lies on a treatment table, and a radiation machine directs radiation beams precisely at the tumor location.*

1.2 Conventional External Beam Radiotherapy (EBRT)

EBRT is a commonly used form of radiotherapy in which radiation beams are directed from an external source to the tumor localization (**Figure 1**)¹¹. Unlike brachytherapy, which involves placing radioactive sources near organ presenting tumors, EBRT is non-invasive and enables a better targeting of tumors. EBRT is used in the treatment of various cancers including the lung, breast, prostate, head and neck, and brain tumors. By using complementary imaging techniques such as CT, MRI, or PET scans for treatment planning, EBRT allows for precise localization of the tumor, minimizing radiation exposure to surrounding healthy tissues. EBRT can be employed as a curative or palliative. In the upcoming sections, we will explore the standard protocols for EBRT and their application in clinical practice, including recent advancements that improved its safety and efficacy.

1.2.1 Standard of care radiotherapy protocols

The guidelines for administering EBRT are based on protocols that are constantly updated to ensure both the effectiveness of treatment and the safety of patients¹². The initial step in EBRT is treatment planning, which involves using imaging techniques like CT (computed tomography), MRI (magnetic resonance imaging), or PET (positron emission tomography) scans. These imaging methods enable radiation oncologists to precisely outline the shape, size, and location of the tumor in relation to other vital organs. . Specialized softwares are used to plan the arrangement and intensity of the radiation beams on the tridimensional image of the patient's anatomy, ensuring precise focusing of the radiation to the tumor¹². The process also includes determining the radiation dose to be directed at the tumor, ensuring it is high enough to destroy cancer cells. Dose fractionation is another essential component of standard EBRT protocols. In conventional fractionation scheme, the total radiation dose is divided into smaller doses (fractions) administered daily over several weeks. Typically, each session delivers around 2 Gy per day, five days a week, over a total of 5 to 8 weeks¹³. This approach has been reported to minimize acute side effects by allowing healthy tissue to recover between treatments but also ensuring a more continuous exposure of cancer cells to radiation therapy over weeks¹³. For certain types of cancer, hypofractionation, where fewer, higher doses are administered over a shorter period, may be used to achieve similar to better therapeutic effects on a more convenient schedule, such as 8 to 9 Gy per fraction. Additionally, Intensity-Modulated Radiotherapy (IMRT) is a significant technological advancement that has become a standard part of radiotherapy treatment¹⁴. IMRT allows for the modulation of radiation intensity across the treatment area to conform closely to the tumor's shape, enabling higher

doses to be delivered to the tumor while sparing surrounding normal tissues (**Figure 2**)¹⁴. For small and well-defined tumors, SBRT (Stereotactic Body Radiation Therapy) delivers treatment using a few highly focused beams that converge on the tumor with millimeter-level precision. This approach incorporates advanced image guidance and precise patient immobilization to achieve a steep dose falloff around the target. In clinical practice, EBRT is widely used for various cancers and it's often combined with surgery or chemotherapy, depending on the type and stage of cancer¹².

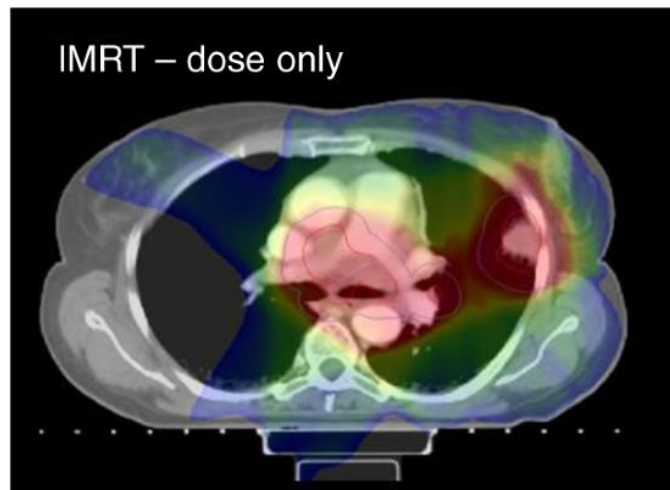


Figure 2. Dose distribution in IMRT for lung cancer. *This figure shows the dose distribution in Intensity-Modulated Radiotherapy (IMRT), computed on a CT scan, for thoracic cancer treatment. The color gradient represents varying radiation intensities, with high-dose regions (red) concentrated on the tumor while minimizing exposure to surrounding healthy tissues such as the lungs and heart¹⁵.*

1.2.2 Treatment combination for radiotherapy

a) Chemoradiotherapy

The combination of EBRT with chemotherapy is commonly used for treatment of cancer for improving the effectiveness of radiotherapy against tumors. Platinum-based drugs like cisplatin and carboplatin are often used in that purpose (**Figure 3**). These drugs make cancer cells more sensitive to radiation via the disruption of DNA repair pathways, making them more susceptible to radiation damages¹². In clinical setting, for example, in the case of NSCLC, concurrent chemoradiotherapy has been proven to enhance local control and survival rates, particularly in advanced localized disease¹⁶. Research indicates that this combination is especially effective when chemotherapy is administered alongside radiotherapy, boosting radiation's ability to induce some irreversible DNA damage and resulting in better cancer free survival^{13,17}.

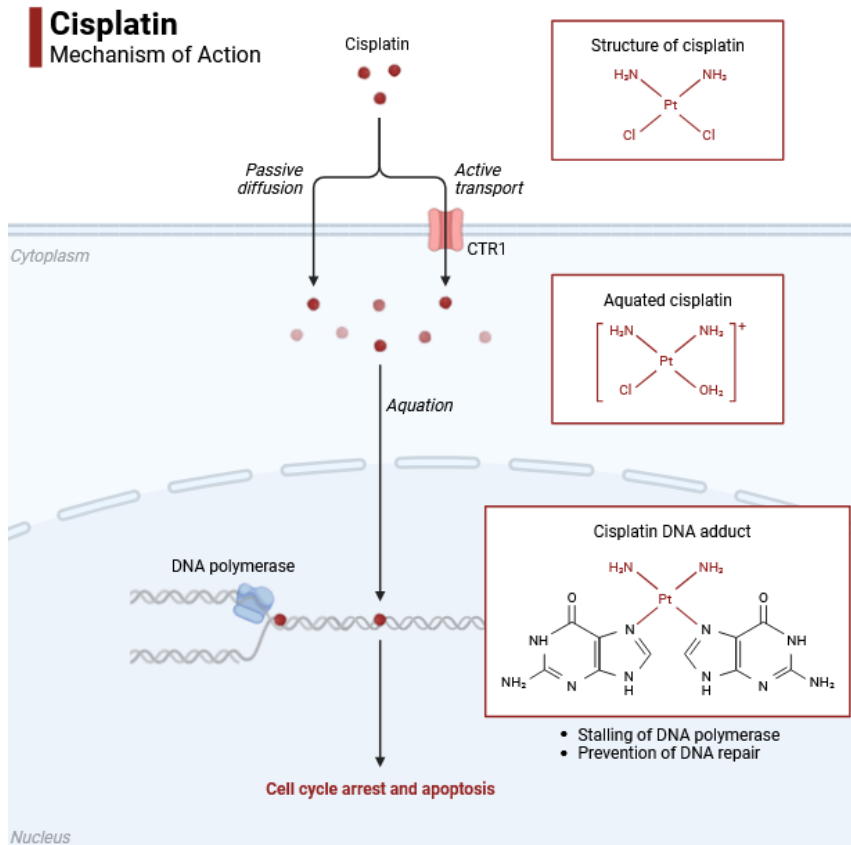


Figure 3. Cisplatin action mechanism. *Cisplatin* can enter the cell via passive diffusion or active transport (facilitated by the copper transporter CTR1). Inside the cell, cisplatin undergoes aquation process, where it becomes activated and gain ability to bind DNA, forming cisplatin-DNA adducts. These adducts prevent DNA replication and repair by stalling DNA polymerase, leading to cell cycle arrest and apoptosis, effectively inhibiting cancer cell proliferation.

b) Targeted therapies, anti-EGFR and Tyrosine kinases inhibitors

In the past few years, targeted therapies have become interesting drugs to use in combination with EBRT. They encompass cetuximab, an anti-EGFR monoclonal antibody, which blocks the epidermal growth factor receptor (EGFR) which is frequently overexpressed in cancer cells. **(Figure 4)**¹⁸. In clinical practice, its use alongside radiation has been reported to enhance outcomes in head and neck cancers¹⁹. For NSCLC, combining targeted therapies with radiotherapy has shown significant improvements in survival rates in clinical trials. For example, the RTOG 0324 trial demonstrated that using cetuximab with chemoradiotherapy for stage IIIA/IIIB NSCLC patients resulted in a 24-month overall survival (OS) which is a notable increase compared to prior standards²⁰. Additionally, a subgroup analysis of the RTOG 0617 phase III trial indicated that patients receiving cetuximab and presenting a high EGFR expression had a median OS of 42 months, compared to 21.2 months in those without cetuximab²¹. In oligometastatic NSCLC, a phase II study that administered SBRT in combination with erlotinib achieved an extended PFS for patients with six or fewer metastatic sites. Furthermore, trials in oligoprogressive NSCLC have shown that adding radiotherapy to targeted therapies can control progression in specific metastasis sites, potentially extending the time before the need to switch treatments²². These results underscore how targeted therapy-radiotherapy combinations is a promising approach in both locally advanced and metastatic NSCLC treatment.

Another instance is the combination of tyrosine kinase inhibitors (TKIs) with radiotherapy, which has displayed potential in treating lung cancers for patients with EGFR mutations **(Figure 4)**. In that case, Gefitinib and erlotinib have been used alongside chemoradiotherapy as both concurrent treatments and maintenance therapies for locally advanced NSCLC. While phase III trials did not show consistent benefits for all patient groups, they did indicate improved progression-free survival (PFS) or overall survival for patients with EGFR amplification or mutations²². Finally, anti-angiogenesis agents targeting VEGF, such as bevacizumab, have also been combined with radiotherapy. For ALK-positive NSCLC, ALK inhibitors have also been tested in phase III trials potentially enhancing response rates and survival outcomes²³. Ongoing research aims to refine combinations of targeted therapies with radiotherapy, which could finally help to increase outcomes for various NSCLC subtypes and progression stages.

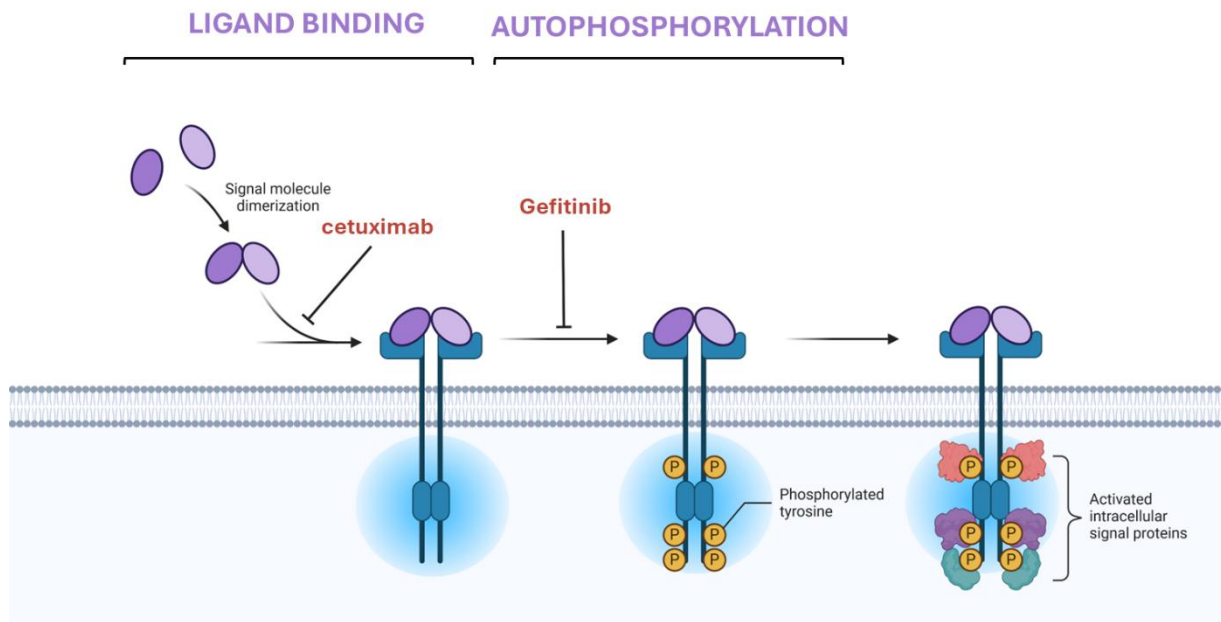


Figure 4. Mechanisms of action of cetuximab (anti-EGFR monoclonal antibody) and gefitinib (TKI). The binding of ligands like EGF or TGF α to EGFR induce receptor autophosphorylation as well as the activation of downstream signaling pathways that control cellular functions such as proliferation, apoptosis, invasion, metastasis, and angiogenesis. Cetuximab, a monoclonal antibody, hinders the attachment of ligands to EGFR, whereas Gefitinib, a TKI can blocks the receptor's autophosphorylation, thereby interrupting subsequent transduction of signal and leading to decreased cell proliferation, enhanced apoptosis, and the inhibition of metastasis and angiogenesis.

c) Immunotherapy

Immune checkpoint inhibitors (ICIs) have recently revolutionized cancer treatment by targeting what is called immune checkpoints such as PD-1, PD-L1, and CTLA-4, that downregulate immune responses, which is exploited by cancer cells to avoid detection by immune cells²⁴. ICI drugs, such as pembrolizumab and nivolumab, are working by blocking these proteins which results in a boost of T-cell activity against cancer cells. ICIs are particularly effective in cancers expressing high level of PD-L1, like some advanced NSCLC. In such cases, pembrolizumab could even be used as a first-line treatment. ICIs are sometimes paired with chemotherapy to further increase immune recognition of tumor cells.

The integration of immunotherapy with radiotherapy represents the most recent progress in cancer treatment. ICIs have been proven to work in conjunction with radiotherapy by boosting the immune system's ability to recognize and eliminate cancer cells (**Figure 5**). Radiotherapy, through its impact on the tumor microenvironment, can elevate the immunogenicity of cancer cells, rendering them more susceptible to immune response. The combination demonstrates effectiveness in treating metastatic cancers such as metastatic melanoma and NSCLC. The combination of EBRT with ICIs has demonstrated enhanced response rates and overall survival in these cases²⁵. Despite RT's immune-stimulating potential, it can also induce immune-suppressive mechanisms within the tumor microenvironment (TME), including recruitment of tumor-associated macrophages (TAMs), regulatory T (Treg) cells, and myeloid-derived suppressor cells (MDSCs). Furthermore, RT can promote the secretion of TGF- β and HIF-1 α , which inhibits DC maturation and lead to RT resistance in endothelial cells. ICIs, by blocking immune checkpoints (such as PD-1 or PD-L1), counteract this immunosuppressive response²⁴. Studies have shown that RT can increase PD-L1 expression in the TME, making tumors more responsive to PD-1/PD-L1 blockade and thereby amplifying the immune system's antitumoral activity. For example, combining RT with PD-1 blockade in mouse models has led to increased infiltration of CD8+ T cells, enhanced antitumor response, and improved local and distant tumor control²⁶.

This innovative approach is currently under active investigation in clinical trials for different cancers. Indeed, numerous trials support the efficacy of combining RT with ICIs. The PACIFIC trial, for example, demonstrated that durvalumab following chemoradiotherapy significantly improved PFS and OS in advanced NSCLC²⁷. Additionally, the phase II study by Theelen et al. investigated stereotactic body radiation therapy (SBRT) followed by pembrolizumab in advanced NSCLC. Results showed that patients in the experimental arm receiving SBRT

before pembrolizumab had improved objective response rates (ORR) at 12 weeks (36% versus 18%), suggesting that RT may sensitize tumors to ICIs by modifying the TME²⁸. Furthermore, a secondary analysis of the KEYNOTE-001 trial indicated longer PFS and OS in patients who had undergone prior radiation. However, several questions remain unanswered, particularly as regards the radiation doses to be used in combination with radiotherapy. There is ongoing research into dose optimization, as high-dose or hypofractionated RT may elicit a more robust immune response. For instance, fractions of 8–10 Gy are thought to be ideal for maximizing the immune response, but doses exceeding 12–18 Gy might activate the exonuclease TREX1, degrading cytosolic DNA and thereby dampening the STING pathway.

Combining RT with ICIs introduces additional challenges related to toxicity, particularly immune-related adverse events (irAEs) such as pneumonitis, dermatitis, and colitis. Clinical trials like NICOLAS and PACIFIC have reported increased pneumonitis rates, though without compromising efficacy. It remains important to balance treatment efficacy with the risk of irAEs, and certain subgroups may require careful monitoring. Additionally, the risk of radiation-induced lymphopenia, which correlates with poorer outcomes, underscores the need for dose and volume optimization, possibly favoring radiotherapy techniques like SBRT and proton therapy to minimize systemic exposure.

Although immunotherapies targeting the PD-1/PD-L1 pathway have transformed the treatment of metastatic cancers, they only benefit a small subset of patients, with response rates often below 20%. This limited efficacy underlines the urgent need for innovative approaches. Current research, like the phase I clinical trial NCT05259319, explores combining PD-1/PD-L1 inhibitors with other agents, such as the anti-TIGIT antibody tiragolumab and SBRT, to enhance immune response²⁹.

In conclusion, immunotherapy, particularly through ICIs targeting pathways such as PD-1, PD-L1, and CTLA-4, has revolutionized the treatment of many cancers. Combining ICIs with RT has shown promising results by creating a synergistic effect, where RT modifies the tumor microenvironment to make cancer cells more susceptible to immune response.

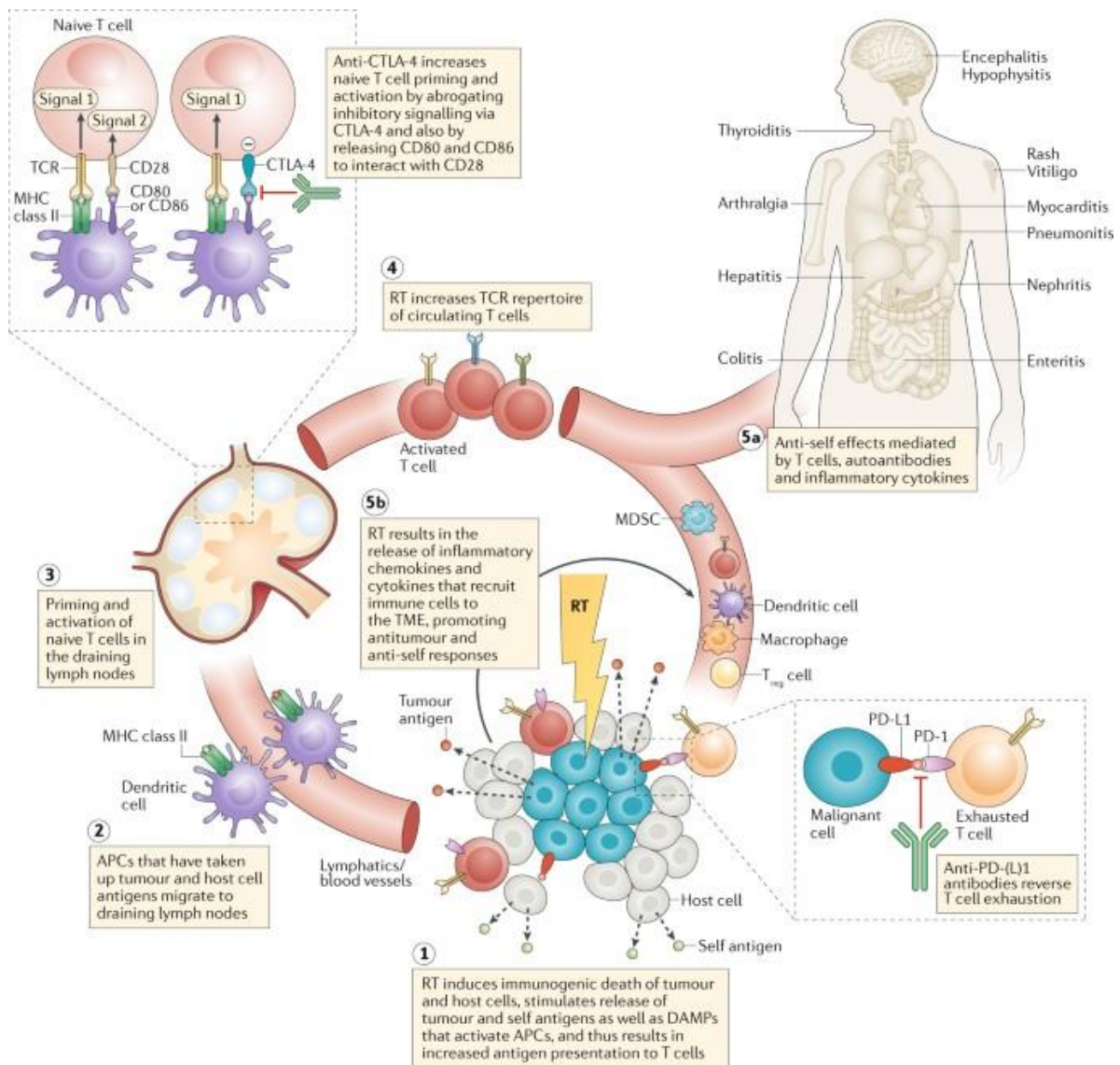


Figure 5. Mechanism of Immune Response with Radio-Immunotherapy. RT increases the presentation of tumor antigens, activating dendritic cells and subsequently T-cells. Immunotherapy, through checkpoint inhibitors like anti-CTLA-4 and anti-PD-1, prevents tumor cells from evading immune detection. The combination of RT and immunotherapy enhances T-cell activity and promotes an immune-mediated attack on the tumor, while potential side effects include inflammation of various organs such as the thyroid, liver, and skin³⁰.

1.2.3 Standard of care for lung cancer patients and challenges

There are two classifications of lung cancer: non-small cell lung cancer (NSCLC) and small cell lung cancer (SCLC). NSCLC comprises approximately 85% of total lung lesions and include adenocarcinoma, squamous cell carcinoma, and large cell carcinoma, whereas SCLC, a more invasive and harmful cancer type, makes up 10-15% of cases³¹. Even with improvements in SOC, the 5-year survival rate for lung cancer remains poor, particularly for patients with advanced stages, including those with metastatic disease. The 5-year survival rate for NSCLC patients is approximately 24% but can increase to 60% for individuals with localized disease if they receive early treatment including surgeries or radiotherapy as a first line³². Lung cancer staging is critical for applying the right SOC and estimating patient prognosis. This classification typically uses the TNM system, which assesses tumor size, lymph node involvement, and the presence of metastases.

Stage I lung cancer is localized within the lung, with no lymph node involvement, tumor size is generally smaller than 3 centimeters (**Figure 6**). Stage I are often treated with surgery or, in some cases, SBRT for patients who are inoperable. Indeed, SBRT is now widely recognized as an optimal treatment for non-operable patients with early-stage NSCLC due to its high precision and effectiveness. Studies have shown that SBRT offers comparable outcomes to surgery, with three-year local control rates reaching up to 98% and overall survival rates ranging from 43% to 95% for these early stage patients³³. This approach ensures that inoperable patients can benefit from a non-invasive and effective cancer treatment.

Stage II lung cancer indicates local advancement, often involving close lymph nodes but without distant spread ((**Figure 6**). Treatment generally includes surgery followed by adjuvant chemotherapy to enhance outcomes. It usually involving cisplatin, is still the preferred treatment for individuals with locally advanced NSCLC. Nevertheless, this method can induce notable toxicities. Indeed, the development of radiation-induced esophagitis, pneumonitis, and myelosuppression is increased using a combination of chemotherapy and radiation²¹. Radiation pneumonitis, especially, continues to be a significant side effect of thoracic radiation treatment, with the potential to cause respiratory failure in some severe instances³⁴.

Stage III lung cancer can be split into stages IIIA and IIIB, it signifies more extensive regional spread and lymph node involvement, often treated with a multimodal approach combining surgery, chemotherapy, and radiation therapy ((**Figure 6**). This stage may now also include immunotherapy as part of the treatment to improve disease control³⁵. In spite of its promise,

the combination of immunotherapy and radiotherapy can lead to immune-related side effects such as colitis, pneumonitis, and hepatitis³⁶.

Lastly, Stage IV represents the most advanced stage, characterized by the presence of metastases to distant organs, such as the brain, bones, or liver ((**Figure 6**). Treatment in Stage IV is palliative, focusing on systemic therapies like chemotherapy, targeted therapies, and immunotherapy, aiming to prolong survival and manage disease symptoms. Indeed, individualized treatments like targeted therapies and immunotherapy have become more prominent³⁷. Specifically designed for patients with mutations, targeted therapies such as gefitinib and erlotinib (known as tyrosine kinase inhibitors or TKIs) provide a personalized treatment option with fewer side effects compared to traditional chemotherapy for those with EGFR or ALK mutations. Each stage underscores the importance of precise, individualized treatment approaches to optimize patient outcomes across the different stages of lung cancer progression.

Despite enhancements in SOC, the outlook for late-stage lung cancer patients is still grim. An additional obstacle in the treatment of lung cancer is tumor resistance processes such as tumor hypoxia which can make it difficult to achieve local control using SOC. Areas of low oxygen in the tumor microenvironment decrease radiation effectiveness because of DNA damage dependence on oxygen. Addressing this, the next section will describe the mechanisms of radiation itself, from its interactions at the atomic level to the cellular responses it triggers.

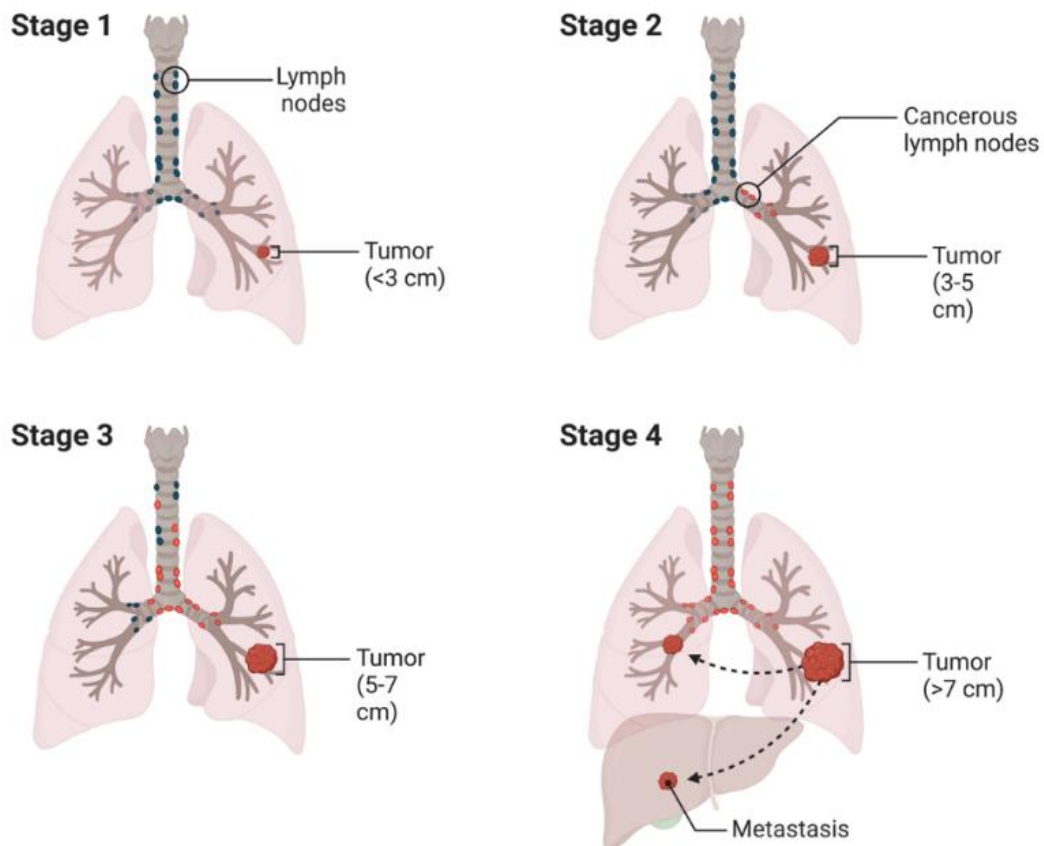


Figure 6. Stade classification for lung cancer. Scheme representing the four stages of lung cancer progression. In Stage 1, the tumor is small (less than 3 cm) and confined to the lung, with no involvement of lymph nodes. By Stage 2, the tumor grows to a size of 3-5 cm, and cancerous cells could spread to nearby lymph nodes. In Stage 3, the tumor continues to enlarge (5-7 cm) and involves more distant lymph nodes within the chest. Finally, Stage 4 marks advanced progression, where the tumor exceeds 7 cm and metastasizes to other organs outside the lung. These stages are essential for guiding treatment decisions and assessing patient prognosis.

1.3 From ionizing radiation interaction to cellular biological response

1.3.1 Physical level : interaction and distribution of energy through matter

When ionizing radiation interacts with matter, it transfers a significant amount of energy to electrons. This is leading to their removal from atomic orbitals. Ionizing radiation can be either electromagnetic or particulate³⁸. On the one hand, electromagnetic radiations are high-energy, massless photons³⁹ that have different origins, such as x-rays and gamma rays. Gamma rays are emitted from the nucleus of an atom during radioactive decay, while x-rays result from the rearrangement of orbital electrons or the interaction of a free electron with an atom. Photon-atom interactions are quite sparse, but the ejected electron, set into motion, has enough kinetic energy to cause a cascade of secondary ionization of other atoms. This is referred as indirect ionization events⁴⁰. In the other hand, particle radiation consists of particles with mass, including positively charged protons, positively charged alpha α particles, negatively charged electrons, positively charged heavy ions, and uncharged neutrons. These charged particles continuously deposit energy along their path, creating direct ionization tracks⁴¹. The absorbed dose, expressed in Gy, is the sum of the energy absorbed locally by the matter through direct and/or indirect ionization events, per unit of mass. The distribution of dose deposition with depth is influenced by the mass, charge, and initial energy of the ionizing radiation (**Figure 7**). To understand the implications of these ionization tracks, it is essential to consider how energy is distributed as these particles move through matter. The amount of energy deposited per unit distance, known as linear energy transfer (LET) is measured in keV/ μm . LET varies depending on the type of particle. For example, electrons typically have a low LET, while alpha particles have a high LET⁴².

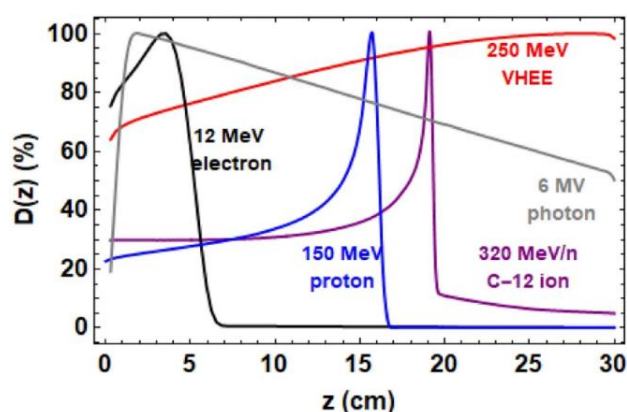


Figure 7. TOPAS-based Monte Carlo simulations of the integrated normalized dose deposited for 6 MV photons, 12 MeV electrons, 150 MeV protons, 320 MeV/n carbon-12 ions, and a 250 MeV VHEE beam⁴².

1.3.2 Chemical level : from radiolysis of water to ROS generation

In biological matter, ionization events primarily result in the radiolysis of water (i.e. the breakdown of water molecules), which induce formation of free radicals (**Figure 8**). When water undergoes radiolysis, it initially produces primary reactive species such as $\text{H}_2\text{O}^\bullet$, H_2O^+ , and electrons (e^-). By reacting, these primary species then give rise to secondary radicals like hydrogen atoms (H^\bullet), hydroxyl radicals (HO^\bullet), hydrogen molecules (H_2), hydronium ions (H_3O^+), and solvated electrons (e^-_{aq}). Further reactions can lead to the formation of tertiary species such as hydrogen peroxide (H_2O_2), hydroxide ions (OH^-), as well as other reactive oxygen species (ROS)^{43,44}. ROS consist of free radicals like superoxide anion radical ($\text{O}_2^{\bullet-}$) and hydroxyl radical (HO^\bullet), as well as non-radical molecules such as hydrogen peroxide (H_2O_2), peroxyxynitrite (ONOO^-), and hypochlorous acid (HOCl). These reactive species can interact with one another, generating new radicals that can react within cellular systems. For example, superoxide dismutase (SOD) converts $\text{O}_2^{\bullet-}$ into hydrogen peroxide, which can then further generate hydroxyl radicals through the Fenton reaction in the presence of iron⁴⁵. These ROS exhibit differences in diffusion rates and lifespans, with some being more stable than others. Hydroxyl radicals ($\bullet\text{OH}$) are particularly significant due to their high reactivity. Indeed, they can affect carbon-based molecules (e.g., lipids, proteins, DNA) and form carbon-centered radicals^{43,44}. These radicals can subsequently react with molecular oxygen, producing peroxy radicals (ROO^\bullet)²⁰. Peroxy radicals, being long-lived, can migrate to different cellular compartments, where they contribute to oxidative damage to biological molecules. This sequence of reactions after water radiolysis is crucial in comprehending radiation-induced cellular damage, particularly the role of ROS in triggering oxidative stress and their contribution to DNA damage, protein oxidation, and lipid peroxidation.

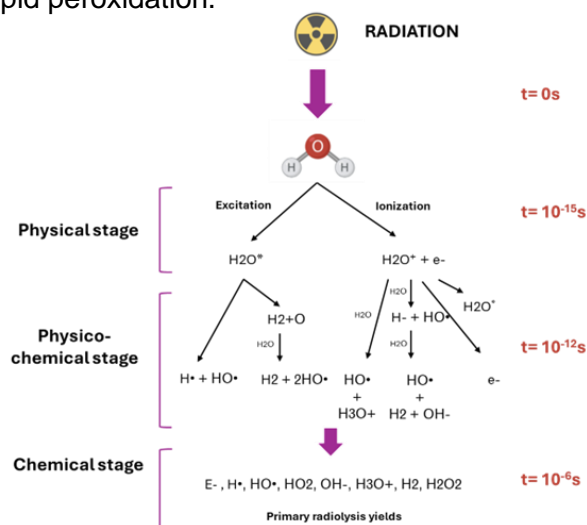


Figure 8. Diagram illustrating the sequential stages of radiation-induced water radiolysis.

1.3.3 Biological response : ROS and biomolecules damage

Radiation-induced oxidative stress can cause both direct and indirect DNA damage (**Figure 9**)⁴⁶. Particularly, ROS can cause indirect DNA damage by interacting with DNA bases or the sugar-phosphate backbone which results in oxidation processes as well as mutations. Hydroxyl radicals are also extremely reactive and can cause significant DNA damage by removing hydrogen atoms from DNA, leading to single-strand breaks (SSBs) generation, double-strand breaks (DSBs), and base modifications. Furthermore, other ROS such as peroxy radicals (ROO●), which have a longer lifespan⁴⁷ and that can travel long distances within cells, can reach and damage nuclear DNA from their origin sites in the cytoplasm. This ability to migrate makes peroxy radicals especially harmful for DNA integrity. In contrast to indirect damage, direct DNA damage occurs when ionizing radiation deposits energy into the DNA molecule during ionization events. Both direct and indirect mechanisms contribute to the creation of complex, clustered DNA damage. High LET radiation is especially effective at causing such cluster damage. This complex DNA damage is challenging for cells to repair and may lead to mutations or cell death processes⁴⁸. Additionally, the so-called bystander effect can amplify radiation-induced damage. This phenomenon occurs when damaged cells communicate their injury to neighboring non-irradiated cells through signaling molecules or gap junctions⁴⁹. If repair mechanisms are overwhelmed, the persistence of this damage can result in genomic instability, aging, and the development of radiation-induced cancer.

Radiation-induced oxidative stress not only harms DNA but also has a serious impact on cellular lipids and proteins integrity. The oxidation of polyunsaturated fatty acids in cellular membranes, initiated by ROS such as hydroxyl radicals (●OH) can lead to lipid peroxidation process, ending by generating lipid radicals and peroxy radicals (ROO●) that can perpetuate further lipid oxidation⁵⁰. This compromises membrane integrity, increases permeability, and disrupts cellular signaling⁵¹. The end products of lipid peroxidation, including malondialdehyde (MDA) and 4-hydroxynonenal (HNE), are toxic and can form adducts with proteins and DNA, increasing cellular dysfunction and oxidative stress⁵². Proteins are also susceptible to oxidative damage as ROS, particularly hydroxyl radicals, can oxidize amino acid side chains, resulting in protein carbonylation, fragmentation, and aggregation⁵³. This oxidative modification can affect protein function (enzymes, receptors, or structural proteins). However, cells have an antioxidant defense system to counteract the effects of ROS on lipids, proteins, and other cellular components, consisting of both enzymatic and non-enzymatic antioxidants, which play an important role in neutralizing ROS.

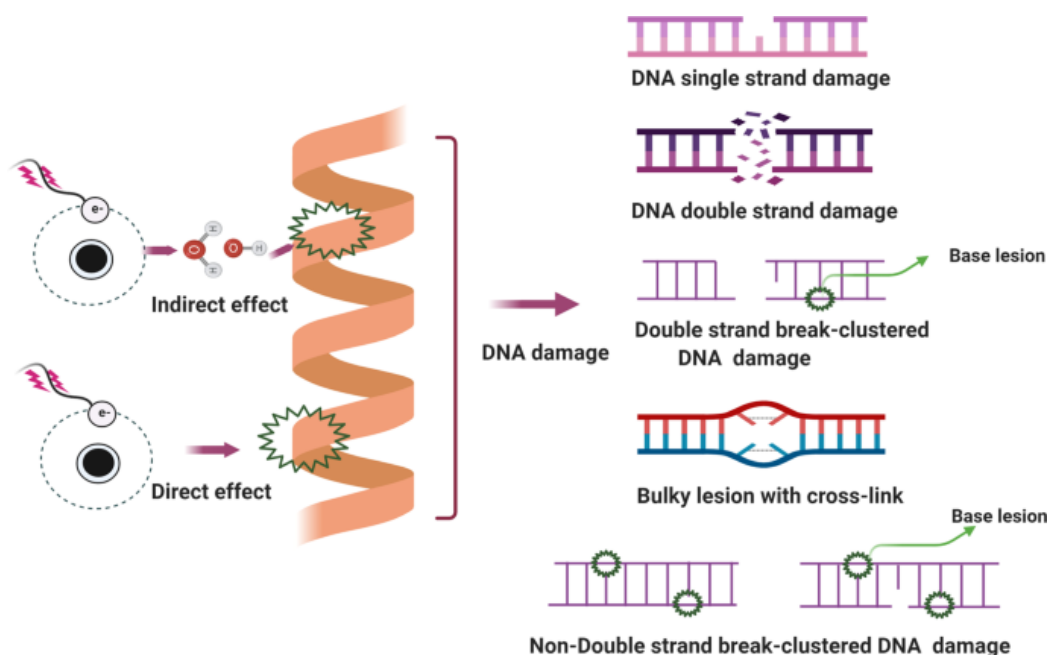


Figure 9. Indirect and direct radiation induced DNA damage. Biorender.

1.3.4 ROS antioxidant detection and defense system

Cells antioxidant defense plays a role in counteracting ROS related damages after radiation. This system comprises enzymatic and non-enzymatic antioxidants that work synergistically to neutralize ROS in cells⁵⁴. Key enzymatic antioxidants include superoxide dismutase (SOD), which can convert superoxide anion ($O_2^{\bullet-}$) into hydrogen peroxide (H_2O_2) and oxygen⁵⁴. Hydrogen peroxide is then detoxified by catalase, which breaks it down into water and oxygen, this occurring in cell peroxisomes. Another enzyme, glutathione peroxidase (GPx), reduces both hydrogen peroxide and lipid hydroperoxides using glutathione as a substrate, which can protect lipids from peroxidation processes⁵⁴.

The system is also supported by non-enzymatic antioxidants, such as vitamins C and E, glutathione, and coenzyme Q10, which scavenge free radicals and repair oxidative damage. Together, these antioxidants create a robust defense network, minimizing oxidative stress. However, when ROS production overwhelms the antioxidant capacity, oxidative stress ensues, contributing to cell damage after radiation.

The detection of ROS and the activation of antioxidant defense mechanisms is regulated via the Nrf2-Keap1 signaling pathway (**Figure 10**)⁵⁴. Nuclear factor erythroid 2-related factor 2 (Nrf2) is a transcription factor that plays a major role in cellular responses to oxidative stress⁵⁵. Under physiologic conditions, Nrf2 is retained in the cytoplasm by its repressor, Keap1 (Kelch-like ECH-associated protein 1), which induce the ubiquitination and degradation of Nrf2, keeping its levels low in cells⁵⁵.

However, in response to oxidative stress, ROS can modify specific cysteine residues on Keap1, causing a conformational change that prevents it from binding to Nrf2⁵⁵. As a result, Nrf2 escapes degradation, accumulates in the cytoplasm, and then translocate to the nucleus⁵⁵. In the nucleus, Nrf2 can bind to antioxidant response elements (AREs) in the promoter regions of various genes that encode for antioxidant proteins and enzymes, such as glutathione peroxidase (GPx), superoxide dismutase (SOD), and catalase⁵⁵. This activation boosts the cell's antioxidant defenses, neutralizing ROS and protecting against oxidative damage (**Figure 10**).

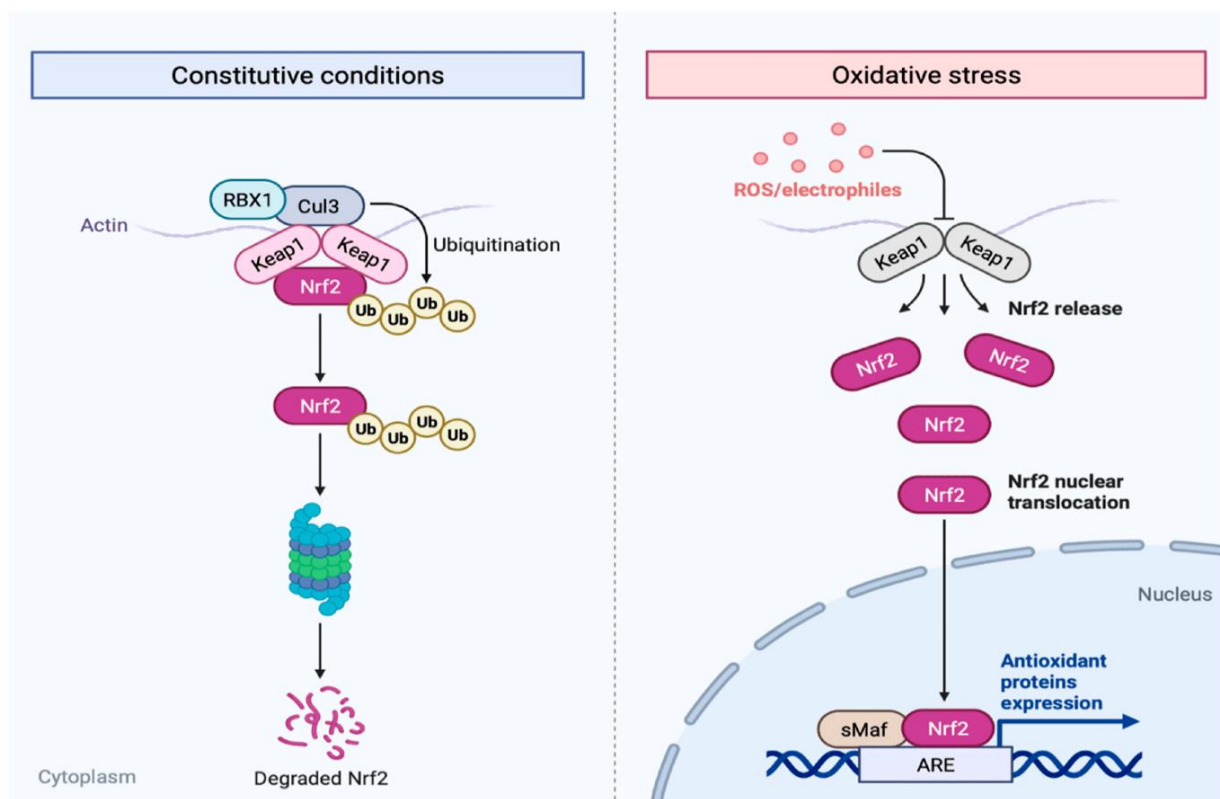


Figure 10. Nrf2 Keap1 signaling pathway in response to oxidative stress. Biorender

1.3.5 DNA damage response in cells

When cells are exposed to radiation, they dispose of various DNA repair mechanisms to prevent the damages caused by ionizing radiation and reactive oxygen species produced during water radiolysis process⁵⁶. These repair pathways maintain the stability of the genetic material by ability to fix both SSBs and DSBs, as well as oxidative damage to DNA bases **(Figure 11)**⁵⁶.

Base Excision Repair (BER) is a pathway that corrects minor lesions such as 8-oxoguanine formation, which is a common result of damage induced by reactive oxygen species⁵⁷. In the BER process, DNA glycosylases identify and remove damaged bases, creating an abasic site⁵⁷. Then, AP endonucleases cut the DNA at this site, allowing DNA polymerase to fill in the gap before DNA ligase seals the repaired DNA strand⁵⁷.

On the other hand, Nucleotide Excision Repair (NER) addresses bulky, helix-distorting lesions and can handle certain types of radiation-induced damage⁵⁸. In this mechanism, a small DNA segment around the lesion is removed, followed by the synthesis of the correct sequence by DNA polymerase and ligation by DNA ligase⁵⁸.

For DSBs, cells depend on two main repair mechanisms which are Non-Homologous End Joining (NHEJ) and Homologous Recombination (HR)⁵⁹. NHEJ is a quick but error-prone repair process that directly reconnects the broken ends of DNA, often resulting in deletions or insertions⁵⁹. In contrast, HR is a error proof but slower process, utilizing a homologous DNA template, typically a sister chromatid, to guide the repair of DSBs⁵⁹. HR is usually active during the S and G2 phases of the cell cycle when a sister chromatid is available⁵⁹.

Lastly, another important repair pathway is Mismatch Repair (MMR), which rectifies replication errors and identifies specific radiation-induced lesions⁶⁰. This pathway is crucial for preserving genetic integrity by preventing mutations during DNA replication⁶⁰.

Despite these mechanisms, some damage may be too severe to repair, causing cells to activate programmed death pathways. These responses are also crucial for preventing the proliferation of cells with damaged DNA.

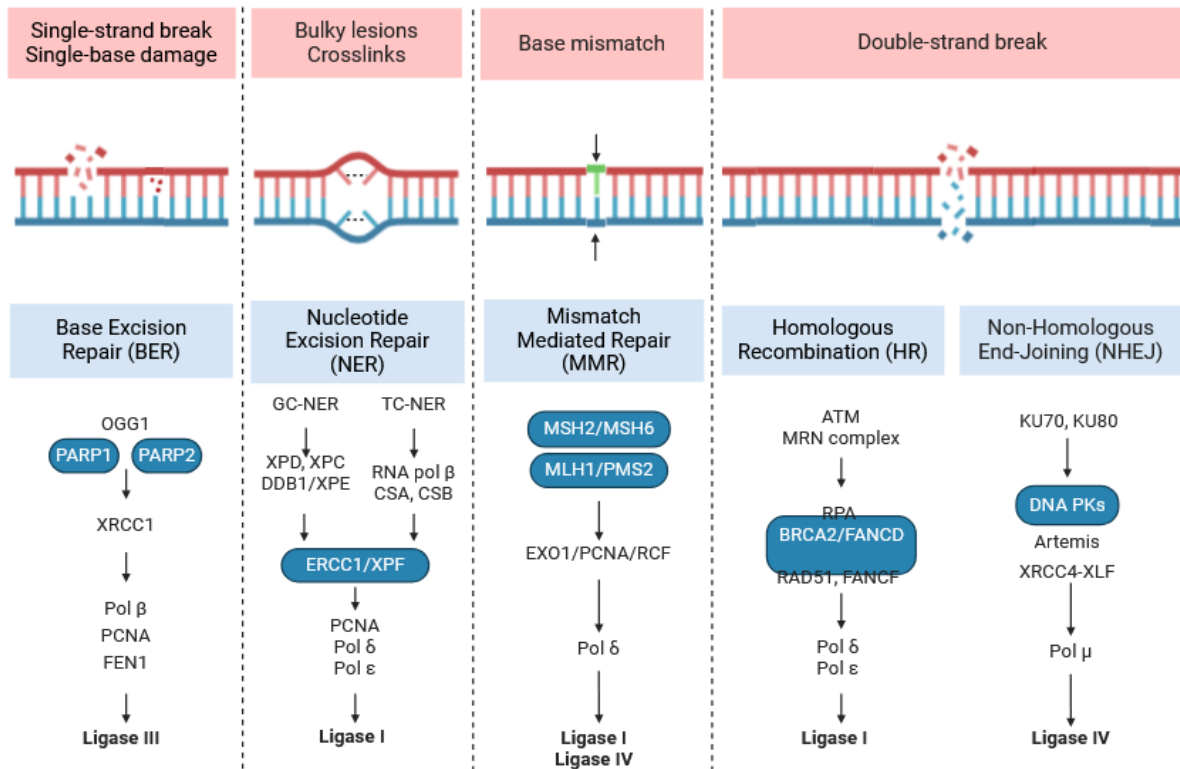


Figure 11. DNA damage responses overview⁶¹. This diagram illustrates the DNA repair pathways activated in response to various types of DNA damage including radiation. For single-strand breaks and single-base damage, the Base Excision Repair (BER) pathway is utilized, involving enzymes like OGG1, PARP1/2, and XRCC1, and completed by Ligase III. For bulky lesions and crosslinks, the Nucleotide Excision Repair (NER) pathway is responsible, with components such as XPD/XPC and ERCC1/XPF, concluding with Ligase I. Mismatch repair (MMR) corrects base mismatches using proteins like MSH2/MSH6 and MLH1/PMS2, also involving Ligase I and IV. Double-strand breaks are addressed by either Homologous Recombination (HR), which includes proteins such as BRCA2/FANCD, or Non-Homologous End-Joining (NHEJ), with key factors like DNA-PKs and Ligase IV. Each pathway targets specific DNA lesions to maintain genomic stability.

1.3.6 DNA damage detection in cells

Detection of DNA damage plays a crucial role in determining how cells respond to ionizing radiation. Two key proteins, ataxia-telangiectasia mutated (ATM) and ATM and Rad3-related (ATR), can detect and signal the presence of these radio-induced DNA damage^{62,63}. ATM is activated by DSBs, which are produced in large numbers by ionizing radiation. When these breaks are detected, the MRN complex (MRE11, RAD50, and NBS1) brings in and activates ATM at the damage site³⁷. Once activated, ATM phosphorylates substrates, including CHK2 and p53, triggering cell cycle arrest at the G1 phase, giving cells time to repair the damage (**Figure 12**)⁶⁴. Conversely, ATR is more sensitive to SSBs and regions of stalled replication forks, which are common when cells face oxidative stress from radiotherapy⁶⁴. ATR phosphorylates and activates CHK1, leading to a halt in the cell cycle in the S and G2 phases, allowing cells to repair the less severe damage before proceeding⁶⁵. Cells with mutated p53 or defective ATM, are more susceptible to radiation and have a lower ability to repair DNA damage, leading to increased cell death in response to radiation damage⁶⁵. However, tumors with highly functional DDR mechanisms can sometimes develop resistance to radiation, requiring the use of radiosensitizers to inhibit proteins like ATM or ATR, thus increasing the treatment's effectiveness⁶⁶. In summary, the detection of DNA damage is essential for coordinating the cellular response to ionizing radiation. Once damage is identified, pathways like ATM and ATR can induce repair mechanisms but also regulate the cell cycle, ensuring that cells stop division until the damage is repaired. In the following section, we will explore how ionizing radiation impacts the cell cycle, disrupting its phases and triggering checkpoints to that are participating in maintaining genomic integrity.

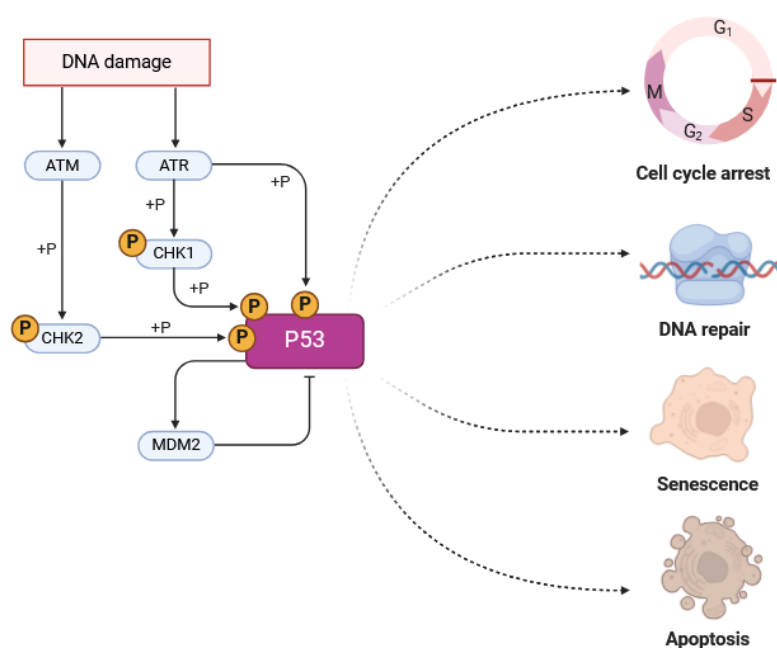


Figure 12. DNA damage detection via ATM/ATR and p53 pathway. Upon DNA damage, the kinases ATM and ATR are activated, leading to phosphorylation of CHK2 and CHK1, respectively. These checkpoint kinases, in turn, phosphorylate p53, stabilizing and activating it. Activated p53 plays a pivotal role in determining cellular fate, which include cell cycle arrest to prevent propagation of damaged DNA, DNA repair to fix the damage, senescence as a permanent cell-cycle arrest, and apoptosis to eliminate severely damaged cells. Additionally, MDM2 is regulated by p53 as part of a feedback loop, controlling p53 activity and stability. This pathway ensures genomic integrity by coordinating the appropriate cellular response to DNA damage. Adapted from Biorender.

1.3.7 Impact of ionizing radiation on cell cycle

The regulation of the cell cycle is disrupted by ionizing radiation through the induction of various types of DNA damage, as discussed in **section 1.3.6**. The cell cycle is a highly regulated process that includes multiple phases (G1, S, G2, and M), each of which is major for ensuring an accurate DNA replication and cell division (**Figure 13**). Upon exposure to ionizing radiation, DNA damage induce signaling pathways that can activate cell cycle checkpoints. These checkpoints provide the cell with time to repair the damage before progressing through the cycle. Notably, at the G1/S, intra-S, and G2/M transitions, these checkpoints work to prevent the proliferation of damaged cells and uphold genomic integrity (**Figure 13**)⁶⁷.

The first defense mechanism activated in response to DNA damage caused by ionizing radiation is the G1/S checkpoint (**Figure 13**). This checkpoint is regulated through the ATM-p53-CHK2 pathway, as described in **section 1.3.6**⁵⁶. The ATM kinase identifies DSBs and phosphorylates p53 tumor suppressor protein, which then triggers the expression of p21 which is an inhibitor of cyclin-dependent kinases (CDKs). This inhibition of CDK activity stops cell cycle progression into the S phase, allowing the cell time to repair DNA lesions. If the damage is too extensive to repair, p53 can induce apoptosis, preventing the spread of cells with damaged genomes⁶⁸. Loss of p53 function, often observed in many cancers, weakens this checkpoint and can result in uncontrolled cell proliferation and tumorigenesis⁶⁹.

Another crucial defense mechanism responding to DNA damage during DNA replication is the intra-S checkpoint. As described, ionizing radiation activates both ATM and ATR kinases, with ATR being particularly sensitive to replication stress and SSBs⁷⁰. By delaying the replication process, the intra-S checkpoint prevent chromosomal aberrations that could arise from replicating damaged DNA.

Finally, the G₂/M checkpoint is essential for preventing cells with damaged DNA from entering mitosis process. CHK1 and CHK2 inhibit the activity of CDC25, a phosphatase responsible for activating CDK1, thereby blocking entry into the M phase until DNA repair is complete⁷¹.

The malfunction of these cell cycle checkpoints, whether caused by mutations in essential regulatory proteins such as p53 or by an excess of DNA damage that surpasses repair mechanisms, may lead to the survival of cells with impaired DNA. Therefore, the reaction of the cell cycle to ionizing radiation plays a crucial role in determining the effectiveness of radiotherapy or the risk of radiation-induced tumor formation.

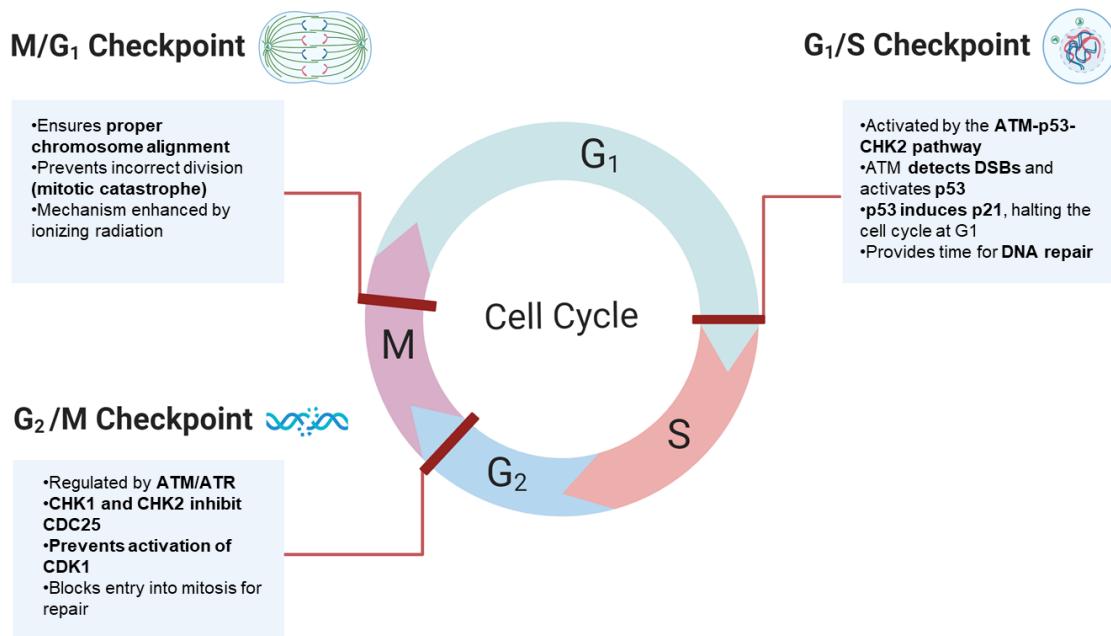


Figure 13. Cell cycle checkpoints upon ionizing radiation damages. The M/G₁ checkpoint ensures proper chromosome alignment to prevent mitotic errors, a mechanism that can be induced by ionizing radiation. The G₁/S checkpoint is activated by the ATM-p53-CHK2 pathway. ATM detects double-strand breaks (DSBs) and activates p53, which induces p21 to halt the cell cycle at G₁, allowing time for DNA repair. Finally, the G₂/M checkpoint is regulated by ATM and ATR, with CHK1 and CHK2 inhibiting CDC25, thus preventing activation of CDK1 and delaying entry into mitosis to facilitate repair. Adapted from Biorender.

1.3.8 P53 and response to radiation

The p53 protein, often termed "guardian of the genome," is major in maintaining cellular integrity under stress, preventing malignant transformations through its ability to regulate cell cycle arrest, DNA repair, apoptosis, and senescence. P53 was considered an oncogene in previous research, such as Donehower et al. in 1992. Then its critical role as a tumor suppressor was clarified, especially given that p53 mutations occur in over 50% of cancers. Its structure comprises five main domains which are the DNA-binding domain, transactivation domain, tetramerization domain, proline-rich region, and regulatory domain. These regions are necessary for its function in transcriptional regulation, allowing it to interact with various cofactors such as MDM2 to activate or repress gene expression in response to DNA damage. Post-translational modifications (PTMs), including phosphorylation, acetylation, and ubiquitination can regulate p53 activity. For instance, phosphorylation at specific sites enhances p53 stability by reducing MDM2-mediated degradation, thus prolonging its active state, which is essential for initiating DNA repair mechanisms or apoptotic cell death.

In response to ionizing radiation, phosphorylation at Ser15 and Ser20 by ATM/ATR and Chk1/Chk2 kinases, respectively, stabilize p53, allowing it to halt the cell cycle via transcriptional activation of p21, facilitating DNA repair and, if necessary, promoting apoptosis through PUMA and BAX induction. p53's role in response to radiation varies by tissue. For example, p53 activation protects endothelial cells against radiation-induced damage which maintains cellular integrity and vascular structure. In the hematopoietic system, p53 mediates cell fate through pathways involving apoptosis and senescence. The loss of its function has been shown to increase sensitivity to radiation-induced toxicity such as it is the case in Fanconi anemia patients⁷². In the gastrointestinal tract, p53 induce early apoptosis in radiosensitive epithelial cells and its absence can then delays apoptosis, leading to mitotic catastrophe rather than programmed cell death. Research has also shown that p53's involvement in intestinal cell dedifferentiation and regeneration is crucial following radiation injury, maintaining cellular homeostasis through its regulation by MDM2.

While its mutation is advantageous for cancer progression, its regulatory capabilities in normal cells make it essential for tissue response under various stress, especially in the context of radiation therapy.

1.4 Improvement of Therapeutic Index of Radiation Therapy

The therapeutic index of radiotherapy, defined as the balance between the radiation dose that can eradicate the tumor and the dose that leads to strong toxicity in surrounding normal tissues, is a critical focus of radiotherapy treatment (**Figure 14**)⁷³. In the context of novel radiotherapy technologies, significant progress has been achieved in balancing tumor control with reducing harmful effect to surrounding healthy tissue. In this part, we will examine different advancements that have improved the therapeutic index of this SOC . We will mainly focus on management of organs at risk (OAR), and recent improvements such as the use of stereotactic body radiation therapy (SBRT), particle therapy, and will later explore the potential of ultra-high dose rate radiation therapy (FLASH-RT).

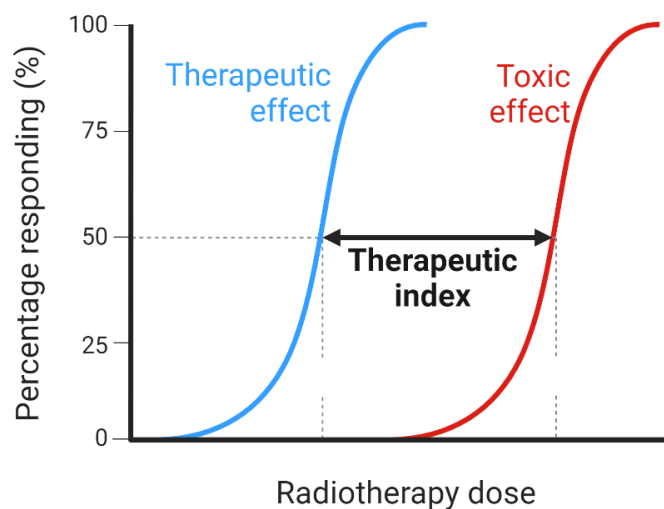


Figure 14. Scheme for therapeutic Index of radiotherapy. *The therapeutic index represents the dose range where tumor control is achieved while minimizing the risk of damage to healthy tissues. The wider the gap between the therapeutic and toxic effects, the more favorable the therapeutic index, enabling effective cancer treatment with reduced side effects.*

1.4.1 Organ at risk

Organ at risk (OAR) are important to plan the radiotherapy treatment, especially in challenging localization such as lung cancer. OARs are healthy tissues or organs near the target tumor that are sensitive to radiation exposure and may experience irreversible damage if exposed to high doses. During the planning of lung cancer treatment, major organs like the heart, lungs, esophagus, and spinal cord must be considered⁷⁴. Sophisticated imaging methods like CT and MRI enable accurate outlining of the tumor and nearby OARs. This stage is important to ensure that the tumor receives a higher dose of radiation while reducing exposure to OARs. In instances NSCLC, the heart and healthy lung tissue face a significant risk of radiation-related toxicity, potentially resulting in complications such as pneumonitis, cardiac issues, or esophageal inflammation⁷⁵. To reduce these risks, IMRT and Image-Guided Radiotherapy (IGRT) allow for more accurate tumor targeting. IMRT allows for adjustment of radiation intensity to shape the dose distribution to protect surrounding OARs, while IGRT utilizes real-time imaging to compensate for tumor displacement due to respiration.

The Gross Tumor Volume (GTV) represents the visible tumor lesion based on imaging, including any detectable tumor mass or lymph node involvement. Surrounding the GTV, the Clinical Target Volume (CTV) accounts for areas where microscopic cancer cells may reside, expanding the treated area to include potential local spread. If breathing or other physiological movements must be considered, Internal Tumor Volume (ITV) accounts for tumor motion. Finally, the Planning Target Volume (PTV) includes an additional margin around CTV or ITV to accommodate setup variability during treatment. These three volumes, GTV, CTV, and PTV are used to ensure that the tumor is consistently targeted with the appropriate radiation dose, even with daily patient shifts or breathing-induced motion⁷⁶ (**Figure 15**) Dose constraints are established for OARs to limit radiation exposure and prevent toxicity. When OAR motion is a factor, a Planning Risk Volume (PRV) is used to account for potential movement. For example, in the case of healthy lungs, typical constraints for conventional fractionation include a Mean Lung Dose < 20 Gy and a V20 (Volume receiving 20 Gy or more) < 30%⁷⁷. This structured approach improves treatment accuracy, helping to maximize tumor control while minimizing the risk of radiation damage to OARs. Thus, incorporating OAR limitations into treatment planning is crucial for improving the therapeutic index.

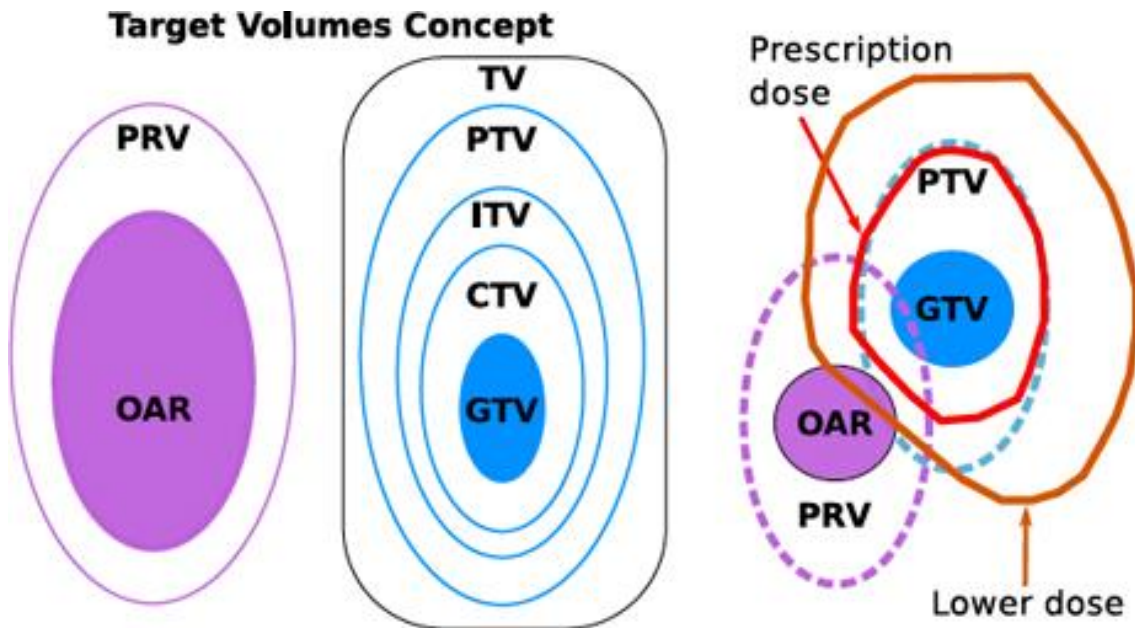


Figure 15. Scheme illustrating the concepts of target volumes in radiotherapy⁷⁶. The Gross Tumor Volume (GTV) represents the visible tumor. Surrounding it, the Clinical Target Volume (CTV) includes areas that may contain microscopic tumor cells. The Planning Target Volume (PTV) adds an additional margin around the CTV to account for patient movement and positioning variations. The diagram also highlights the importance of Organs at Risk (OAR), protected by a Planning Risk Volume (PRV) to avoid high radiation doses, while delivering the prescription dose to the PTV for optimal tumor treatment.

1.4.2 Current limitations to radiation therapeutic index

Even with improved methods, accurately targeting tumors is easier, but protecting surrounding tissues is still a major issue. One major restriction is the discrepancy in the radiation dose needed to kill tumor cells and the dose that leads to side effects on surrounding healthy tissues⁷³. Reaching a high level of tumor control in the local area frequently requires doses that are very close to surpassing the tolerance of surrounding OARs. Furthermore, some tumors may be resistant to radiation due to either hypoxia or mutations in DNA repair pathways¹². Areas with low oxygen levels, known as hypoxic regions, decrease the efficiency of radiation treatment due to oxygen's crucial role in causing DNA damage. To tackle issue like tumor hypoxia, PET scans can be used for evaluating oxygenation levels and helping with dose adjustments⁷⁸ (**Figure 16**). Another restriction comes from the unpredictability's in administering doses and outlining targets, particularly in moving organs such as the lungs.

Breathing can cause movement of the tumor and nearby organs, such as the heart and esophagus, during treatment. While IGRT has increased precision, achieving perfect alignment across multiple treatments is challenging, and any variations can result in either underdosing the tumor or overdosing healthy tissue⁷⁹. Additionally, there remains a concern regarding late radiation side effects. In the lungs, patients might experience pneumonitis or fibrosis several months or years following treatment, causing a significant impact on their quality of life⁷³.

The upcoming parts of this manuscript will discuss radiation-induced damages in the lungs, investigating the clinical outcomes and molecular mechanisms at play. But first, in the next section we will describe recent developments that aim to improve radiation therapy index.

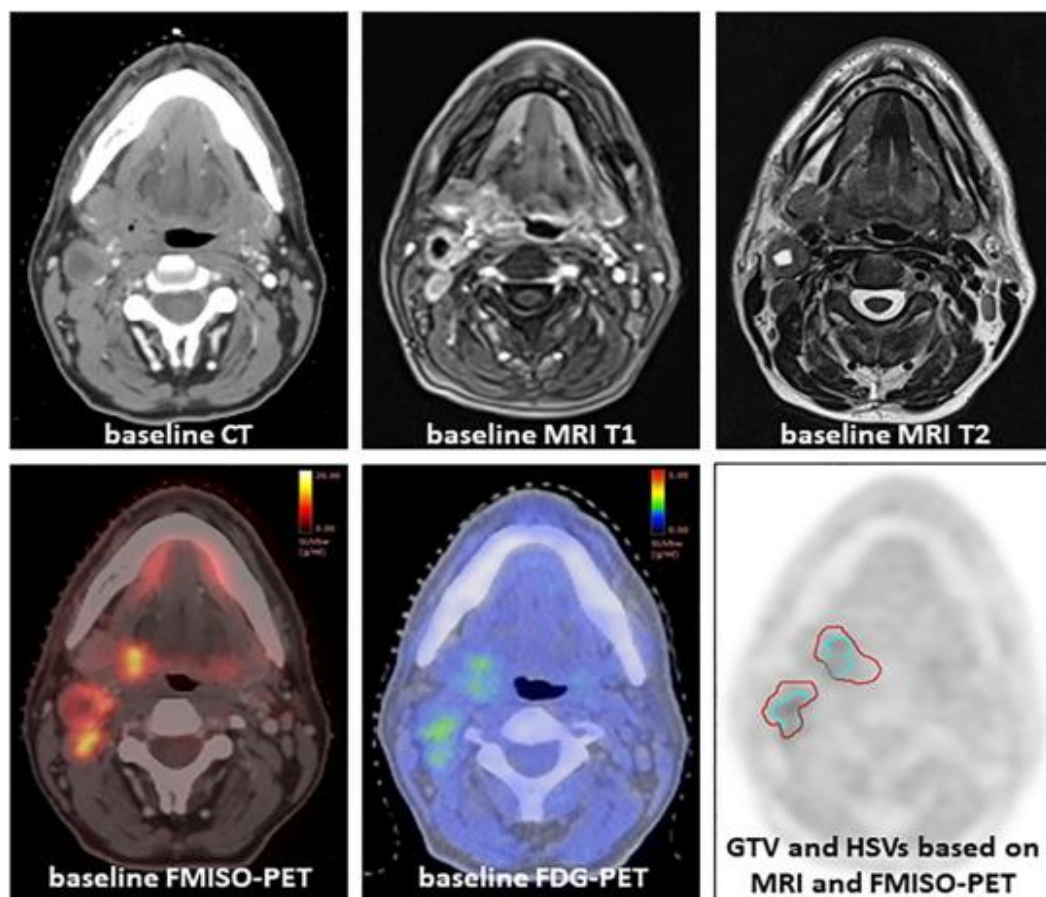


Figure 16. Multimodal Imaging for hypoxic tumor in Head and Neck Cancer. *Baseline imaging of a head and neck tumor using multiple modalities, including CT, MRI (T1, T2), FMISO-PET, and FDG-PET scans. The Gross Tumor Volume (GTV) and hypoxia sub-volumes (HSVs) are delineated based on MRI and FMISO-PET. FMISO-PET highlights hypoxic regions, while FDG-PET identifies areas of increased glucose metabolism, providing critical information for treatment planning.*⁷⁸

1.4.3 *Recent innovations in radiation therapy treatment*

Recent advances in radiation therapy have revolutionized cancer treatment, particularly by enhancing the therapeutic index. Introduced recently in clinical practice, SBRT is a highly precise technique that delivers high-dose radiation in fewer fractions (generally 1 to 5), making it especially effective for some cancer localizations. It involves the use of multiple beams of varying intensity, targeted at the tumor from different angles, concentrating the highest dose of radiation at the tumor site. This is particularly important for tumors located near OARs. By also using advanced imaging technologies such as CT, PET, and MRI, SBRT ensures accurate tumor targeting and reduces radiation exposure to surrounding healthy tissues⁸⁰.

Additionally, the exploration of heavy particle therapies has opened new avenues in radiotherapy treatment. It leads to the development of particle therapy, which encompasses both proton and heavy ion treatments. This approach is based on the physical properties of charged particles to deliver more focused doses of radiation to tumors. Indeed, Proton therapy can target tumors near OARs due to its ability to concentrate radiation at a precise depth, the Bragg peak, which can significantly reduce radiation exposure to tissues beyond the tumor⁸¹. Furthermore, it involves similar beam implementations as photon irradiations including IMRT based Intensity-Modulated Proton Therapy (IMPT). IMPT implements functions identical to those of IMRT. Similarly, heavy ion therapy, which uses ions like carbon, goes a step further by not only targeting tumors with high precision but also offering a potential superior biological effectiveness⁸¹.

Recent research has also extended our understanding of immune responses to proton therapy. While conventional photon-based radiotherapy is known to stimulate immune responses, including modulation of the tumor microenvironment, the immune effects of proton therapy have only recently begun to be elucidated. One pioneering study on Balb/c mice with CT26 colon tumors demonstrated that a single 16.4 Gy dose of proton irradiation stimulated a significant immune response⁸². Analysis at three days post-treatment revealed increased immune-related gene expression, particularly in pathways associated with interferon signaling. These findings open the door to clinical exploration of proton therapy in combination with ICIs. Despite the numerous advantages that proton and heavy ion therapy offer, there are also significant limitations associated. One major challenge lies in the infrastructure that are required. Indeed, particle accelerators used to generate protons, and heavy ions particle therapy are expensive, and often inaccessible in many health centers which limits their widespread use. Additionally, while the precision of dose delivery is beneficial for targeting tumors, it also presents a challenge when the target, such as a lung tumor, moves during

treatment due to breathing or other physiological processes. If not managed correctly, this movement can result in high radiation doses being delivered to nearby healthy tissues, leading to increased toxicity.

Following the advancements brought by SBRT and particle radiotherapy, another innovative approach has emerged, called spatially fractionated radiotherapy (SFRT). Techniques such as minibeam and microbeam radiotherapy (MBRT) represent this concept, where radiation is delivered in distinct, narrow beams that are spatially fractionated. These beams, typically 500-700 μm in diameter, are separated by 1 to 3 mm gaps, leading to a "peaks and valleys" dose distribution across the tumor and nearby tissues. This distribution allows tissue within the peaks to receive the highest radiation dose, while tissue in the valleys is minimally exposed, receiving scattered radiation from surrounding peak regions (**Figure 17**)⁸³. Unlike conventional radiotherapy, which uniformly irradiates the tumor, SFRT has been reported to preserve the healthy tissues located between irradiated zones. This concept has demonstrated promising results, especially in preclinical studies, where animal models showed significantly reduced normal tissue toxicity while maintaining robust tumor control. For instance, animal models exposed to pMBRT displayed a reduction in side effects such as brain damage and enhanced tumor control, compared to standard proton radiotherapy⁸⁴. This approach also benefits from biological mechanisms such as the bystander effect, enhanced vascularization, and even immune system involvement, which contribute to decreased toxicity and better outcomes^{85,86}. However, while these techniques offer exciting possibilities, challenges remain in the clinical application of spatial fractionation. The complexity of geometry in maintaining the peaks and valleys during treatment delivery, particularly with photon beams, has proven to be difficult. To mitigate this, research has shifted toward implementing MBRT with protons, which offers better control over dose distribution and reduces scattering.

In the last introductory chapter of this manuscript, we will explore the potential of ultra-high dose rate radiation therapy (FLASH), another innovative technique that was developed 10 years ago and promised to further revolutionize radiotherapy by delivering radiation at unprecedented speeds. Indeed, it promises to reduce toxicity while maintaining same levels of tumor control. But first, the upcoming section will focus on the lung as a model for studying radiation-induced toxicities as it will be my model organ for experimental studies involving FLASH-RT. Indeed, given the lung's sensitivity and its common involvement in thoracic cancers, it serves as a critical model for evaluating both the therapeutic benefits and possible side effects of advanced radiation techniques.

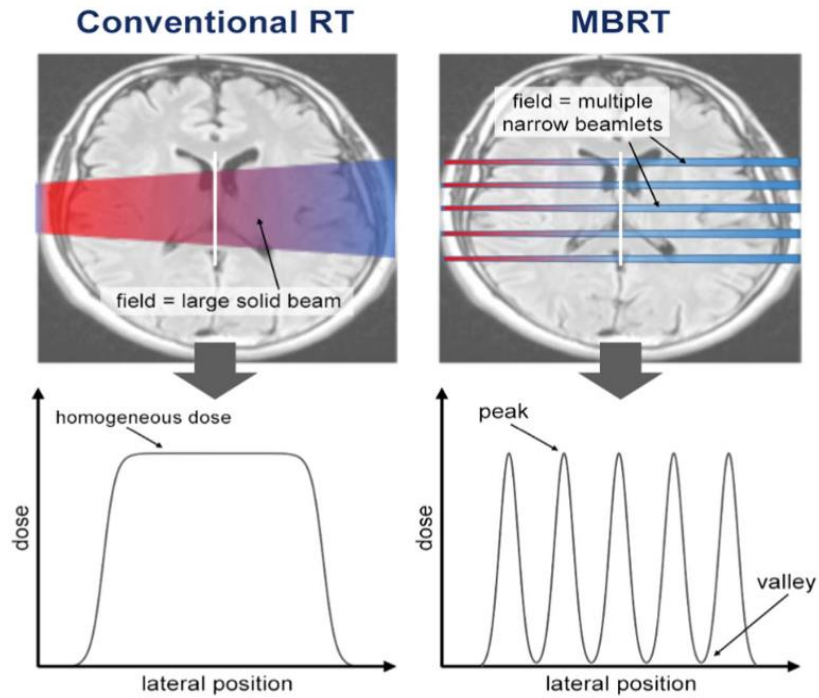


Figure 17. Comparison of Conventional Radiotherapy and Minibeam Radiotherapy (MBRT) distributions. *MBRT employs multiple narrow beamlets, creating a “peak and valley” distribution. The peaks represent areas of high radiation dose targeting the tumor, while the valleys correspond to regions of lower dose exposure, reducing damage to surrounding normal tissues.*⁸⁷

2. THE LUNG, A MODEL FOR INVESTIGATING RADIATION-INDUCED TOXICITIES

As my thesis focused on the underlying mechanisms of FLASH-RT, most of the research I conducted was on the lung which is highly sensitive to radiation-induced damage. In the next section, I will introduce the respiratory system and the lung cellular composition in detail. We will address pulmonary physiology, cellular composition, and how the lung regenerates after injury. With this physiological background established, the next step will be to examine the harmful effects of radiation on the lungs. Here, I will first introduce the concept of the lungs as OARs during radiotherapy treatment before discussing the early toxicities, such as radiation pneumonitis, and late chronic toxicities, including radiation-induced lung fibrosis. This will lead to an exploration of the molecular mechanisms of radiation induced lung injuries (RILI). Finally, in the last section, we will examine various research alternative models used or that could be used to study acute RILI. This will cover murine models but considering the 3Rs in radiation research, it will include the benefits and limitations of cell culture models, organoids, organ on chips and organotypic lung slices.

2.1 Structure, function and cell composition of the respiratory system

The respiratory system is very complex and responsible for pulmonary ventilation as well as the essential gas exchanges (**Figure 18**). This system consists of a series of organs and structures, each playing an important role in ensuring the effective delivery of oxygen to the whole-body tissues but also managing the removal of carbon dioxide which is a metabolic waste product. The respiratory system can be divided into two main parts: the upper and lower respiratory tracts (**Figure 18**). The upper tract function is to conduct air, while the lower tract performs both conducting and respiratory roles. This arrangement facilitates the sterilization, warming, and moistening of the inhaled air before it reaches its ultimate structure of lungs, the alveoli, where gas exchange takes place (**Figure 18**).

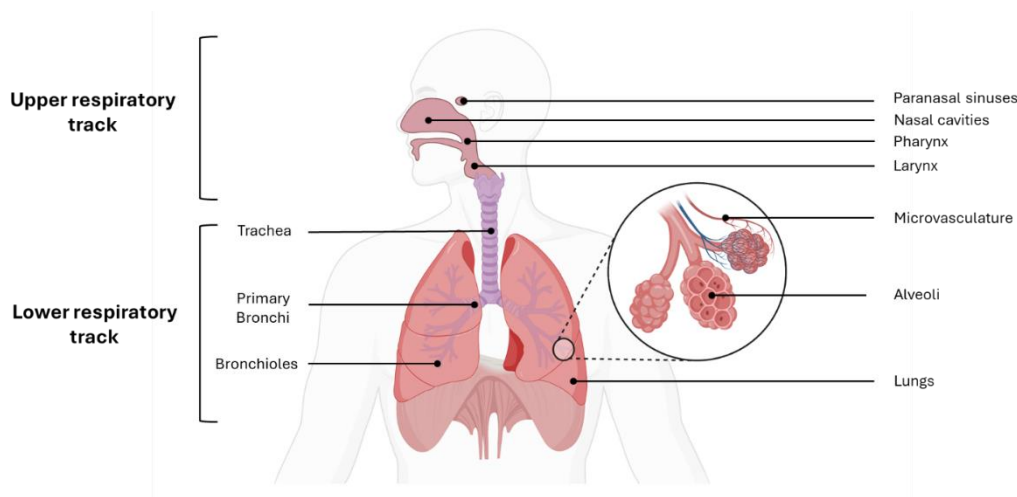


Figure 18. Respiratory tract structure. *The structure of the respiratory system is divided into the upper and lower respiratory tracts. The upper respiratory tract includes paranasal sinuses, nasal cavities, pharynx, and larynx, primarily responsible for air conduction, filtering, and humidification. The lower respiratory tract consists of the trachea, primary bronchi, and bronchioles, leading to the alveoli where gas exchange occurs. A magnified view shows the alveoli and associated microvasculature, highlighting the critical role of alveoli in oxygen-carbon dioxide exchange.*

2.1.1 Upper respiratory tract : functions, structure and physiology

The upper respiratory tract prepares the air before it reaches the more sensitive lower airways. This part of the respiratory system includes the nose, nasal cavities, paranasal sinuses, pharynx, and the part of the larynx above the vocal folds (**Figure 18**). Its main function is to conduct air toward the lower tract, but it also has other functions such as filtering, humidifying, and warming the air, which are essential for protecting lung tissues⁸⁸. Furthermore, these functions help prevent infections and maintain homeostasis, making the upper respiratory tract an important defense system against pathogens and irritants⁸⁸. Dysfunction or injury to the upper tract can lead to increased susceptibility to respiratory infections and inflammation, which could disrupt normal breathing and lung function. We will now describe the various organs and structures that make up the upper respiratory tract, following the path of the air to the alveolar structures.

The nose is the primary entrance for inhaled air and plays a significant role in both olfaction and preparing the air for gas exchanges. The nostrils, which are lined with coarse hairs are a filter, as they are trapping larger particles like dust and pollen⁸⁸. These nostrils lead into the nasal cavity, a large space inside the skull that is involved in breathing and olfaction. The nasal cavity is divided into two chambers by the nasal septum and lined with different types of mucous membranes that help condition the air before it moves deeper into the respiratory system⁸⁸. The nasal cavity is composed of squamous mucosa which is a stratified squamous epithelium that is particularly resistant to physical damage from environmental factors. This respiratory mucosa is composed of a ciliated pseudostratified columnar epithelium⁸⁸. Another component is the olfactory mucosa, lined by a specialized type of pseudostratified columnar epithelium⁸⁹. This region is responsible for the smell sense, and it contains olfactory sensory neurons that detect chemicals and can contribute to taste and smell⁸⁹. Any dysfunction in this region can lead to olfactory disorders, which can impair both smell and taste sensations.

The nasal cavity is surrounded by paranasal sinuses, which include the maxillary, frontal, ethmoidal, and sphenoidal sinuses. These sinuses play roles in humidifying the air⁹⁰. They includes epithelial cells similar to those in the nasal cavity, with ciliated cells and goblet cells playing key roles in mucociliary clearance⁹⁰. These cells help maintain sterility even though the nearby nasal cavity is colonized by microorganisms.

As air moves forward into the respiratory system, it passes through the pharynx which is a muscular tube that serves as a pathway for air and food. The pharynx is divided into three parts which are the nasopharynx (located behind the nasal cavity), the oropharynx (behind the oral cavity), and the laryngopharynx (which leads to both the esophagus and the larynx)⁹¹. The pharynx's ability to handle both food and air is crucial, as it ensures the separation of respiratory and digestive tracts. Any malfunction in the pharynx can result in aspiration, where food or liquids accidentally enter the airway, leading to complications such as pneumonia.

At the lower end of the upper respiratory tract lies the larynx, a cartilaginous structure that houses the vocal cords⁹². It plays a vital role in breathing, sound production and protect the lower airways during swallowing⁹². The larynx contains the epiglottis, a flap of cartilage that covers the trachea during swallowing to prevent food from entering the respiratory system⁹². Damage to or dysfunction of the larynx can lead to voice disorders and breathing difficulties.

2.1.2 Lower respiratory tract : functions, structure and physiology

As air moves through the respiratory system, it enters the lower respiratory tract, also referred to as the respiratory tree which included the lower larynx, trachea, bronchi, bronchioles, and alveoli (**Figure 18**). Its main function is exchange of gases between the external environment and the bloodstream. The structure of the lower respiratory tract is highly specialized, with a complex network of airways designed to maximize the efficiency of this gas exchange⁹³.

The trachea is a tubular structure of about 10 centimeters, extending from the larynx into the thorax⁹⁴. It serves as the main conduit for air between the upper respiratory tract and the lungs⁹⁴. The trachea's structure is reinforced by C-shaped rings of cartilage, which keep the airway open while allowing flexibility for breathing⁹⁴. The posterior part of the trachea is made up of smooth muscle, which can contract to reduce the diameter of the airway during coughing or swallowing, helping to expel foreign objects or prevent aspiration. The trachea's walls are composed of a pseudostratified columnar epithelium, including ciliated cells, goblet cells, and basal cells, all of which play crucial roles in protecting the respiratory system from particles and pathogens⁹⁴.

The trachea then bifurcates into the left and right main bronchi, which enter the lungs and continue to branch into progressively smaller airways⁹³. The primary bronchi are divided into secondary bronchi, which serve the lobes of each lung. In the human lung, there are three lobes in the right lung and two lobes in the left lung. Each secondary bronchus further subdivides into tertiary bronchi, each of which supplies a specific bronchopulmonary segment of the lung. As the bronchi continue to branch into smaller and smaller airways, they become bronchioles, which lack cartilage. The bronchioles are less than one millimeter in diameter and lead to the terminal bronchioles. Beyond the terminal bronchioles are the respiratory bronchioles, which mark the beginning of the respiratory zone where gas exchange occurs. The walls of the bronchioles are composed of a cuboidal epithelium and contain smooth muscles, which can constrict or dilate to regulate airflow. This smooth muscle is controlled by the autonomous nervous system, allowing the bronchioles to adjust the airflow in response to various stimuli.

At the very end of the respiratory tree are the alveoli, tiny sac-like structures where gas exchange takes place (**Figure 18**). The lungs contain over 300 million alveoli, providing an immense surface area for oxygen and carbon dioxide to diffuse. Each alveolus is surrounded by capillaries, allowing oxygen from the air to enter the blood and carbon dioxide from the blood to be expelled into the alveolar space for exhalation⁹³. The walls of the alveoli are made up of two types of cells: alveolar epithelial type I (AT1) cells, which are involved in gas exchange, and alveolar epithelial type II (AT2) cells, which secrete surfactant. Surfactant is a lipid-protein complex that reduces surface tension within the alveoli. It is preventing their collapse during exhalation. Damage to the alveolar membrane composed by this close interaction between endothelial capillary cells and epithelial alveoli cells, can significantly impair lung function, leading to decreased oxygen uptake and difficulty breathing⁹³.

2.1.3 Cellular composition of the human lung and regeneration processes

The adult human lung is a complex organ composed of many specialized cells. These include multiple epithelial cell types that are composing the airways and alveoli, endothelial cells forming the vasculature, smooth muscle cells, fibroblasts preserving lung structure, various immune cells, and other stromal components (**Figure 19**). Together, these cells ensure lung gas exchanges and homeostasis. Over 40 different cell phenotypes have been identified throughout the respiratory tract, from the trachea to the alveolar sacs⁹⁵. This cellular composition is also essential for the lung's ability to respond to environmental challenges and repair processes that occur after injury.

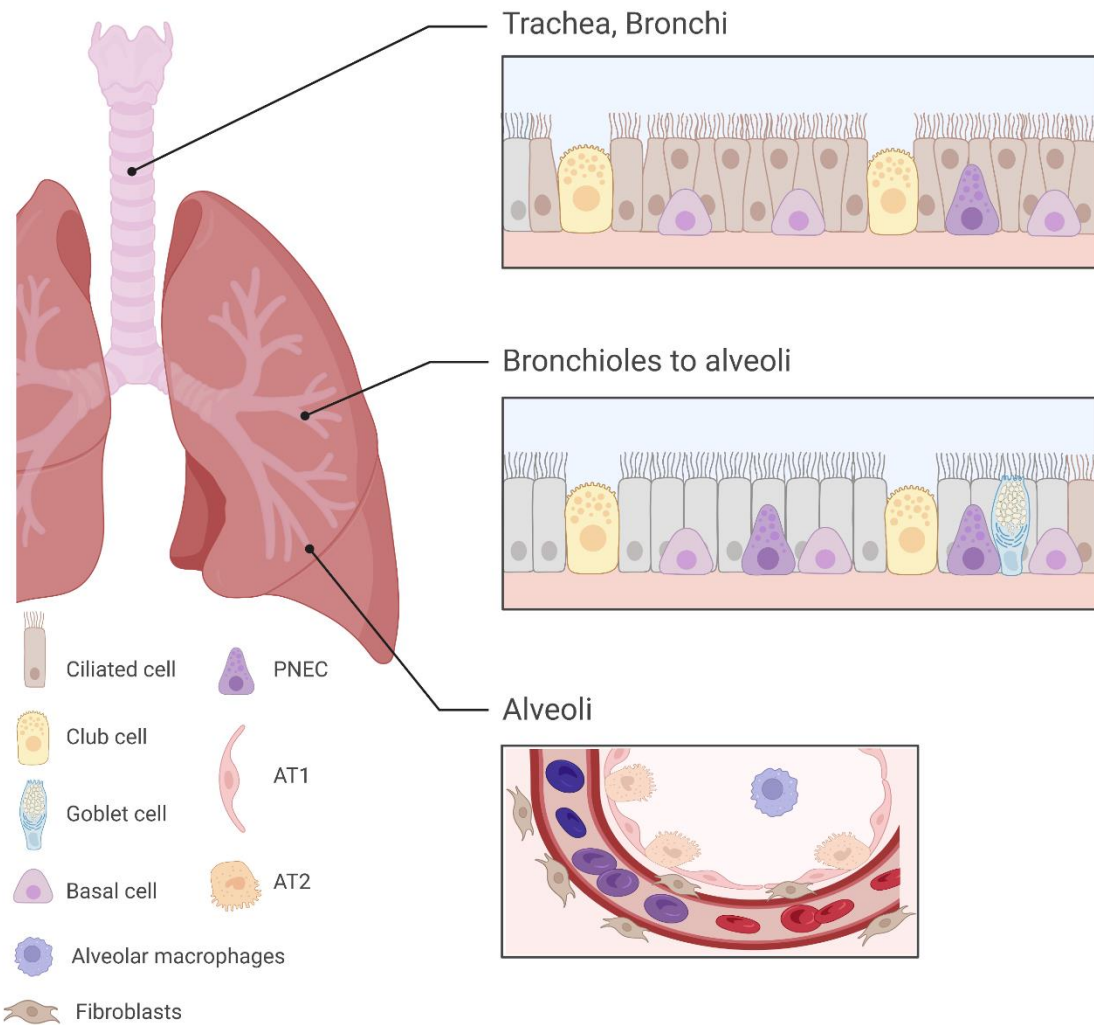


Figure 19. Cellular Composition of the lower respiratory tract. *In the trachea and bronchi, the epithelium consists of ciliated cells, club cells, basal cells, and goblet cells, with PNEC (pulmonary neuroendocrine cells). Moving deeper into the bronchioles, the cellular structure begins to include goblet cells as well. In the alveoli, AT1 and AT2 cells dominate the structure, with AT1 cells facilitating gas exchange, AT2 cells producing surfactants, but also alveolar macrophages and fibroblasts contributing to immune defense and structural integrity, respectively.*

a) Trachea to bronchioles epithelial cells

The respiratory epithelium is a physical barrier to prevent pathogen entry, facilitating mucociliary clearance by trapping inhaled particles in mucus and propelling them out of the airways. It is also involved in cytokines and chemokines secretion which can induce immune responses. Finally, this epithelium is regulating fluid homeostasis by controlling water and ion movement across the epithelial surface. The composition of the respiratory epithelium changes along the respiratory tract, with varying cellular composition from the proximal to distal regions to accommodate functional demands (**Figure 19**)⁹⁶. We will now describe all the cell populations composing the lower respiratory track, from the trachea, via the bronchi and bronchioles, to the functional unit of the lung, the alveoli.

Basal cells (BCs) are a population of multipotent stem cells present at the base of the pseudostratified mucociliary epithelium. They are playing a key role in maintaining the integrity and function of the respiratory epithelium. BCs represents approximately 30% of the pseudostratified airway epithelium⁹⁷. They present a cuboidal shape and are primarily located in the extrapulmonary airways in mice but are also present into smaller intrapulmonary conducting airways in humans⁹⁸. BCs provide structural support by anchoring the columnar epithelium to the basement membrane, thus contributing to the stability of the airway epithelium. In addition to their structural role, BCs act as progenitor cells with the ability to differentiate into various other cell types, including club and ciliated cells. BCs express several key markers, such as TRP63, Keratins KRT5 and KRT14, and CD44, which are involved in their function in both maintaining the airway epithelium and modulating physiological and inflammatory responses through interactions with surrounding neurons, mesenchymal cells, and immune cells. Their regenerative capacity is major for epithelial homeostasis. BCs are able of replacing damaged cells to restore the airway barrier. Moreover, studies have highlighted BC diversity, suggesting that these cells may not form a homogenous pool but rather consist of distinct subpopulations with varying roles in airway maintenance and repair⁹⁹. For instance, a subpopulation of KRT14+ BCs has been identified, which rapidly expands in response to airway injury. This population has been described to primarily contributes to generating more BCs rather than differentiating into other cell types¹⁰⁰. Recent research using single-cell RNA sequencing (scRNA-Seq) have provided further insights into the complexity and heterogeneity of BCs in both human and murine airways. In human lungs, BCs have been classified into multiple subpopulations, including multipotent, proliferating, primed secretory, and activated states, reflecting their functional diversity for homeostasis and response to damages (**Figure 20**)¹⁰¹. Basal cells, as key progenitors in the airway epithelium, give rise to various specialized cells, including club cells, which we will further describe.

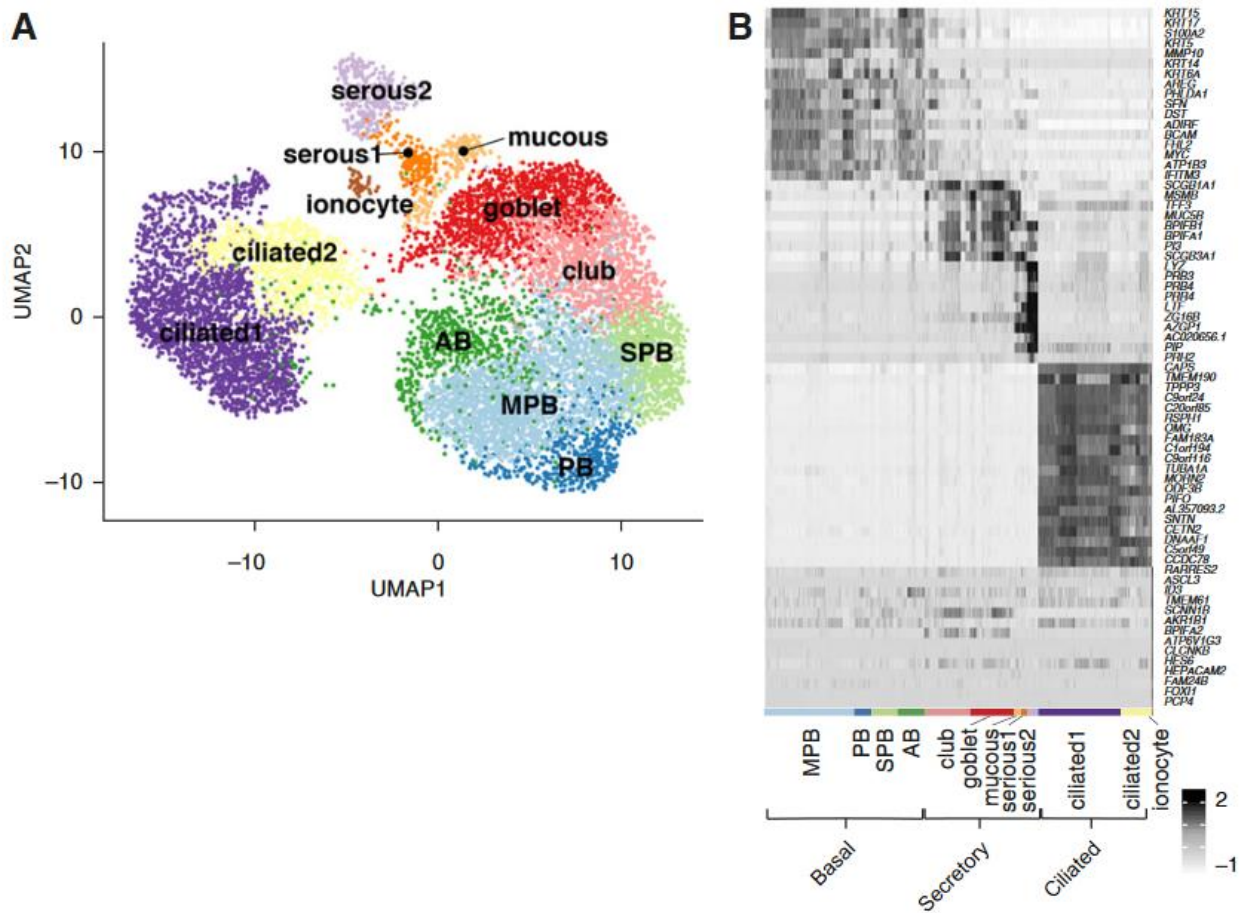


Figure 20. Classification of the human airway epithelium. (A) UMAP clustering of single-cell RNA-sequencing data generated for normal human lung airway epithelium. (B) Expression of differentially expressed genes that distinguish major cell types shown by heatmap with z-score values. Cell subtypes are shown within each major cell type. Adapted for Carraro et al.¹⁰¹

Club cells are critical to the lung's defense and also for repair processes. Predominantly located in the bronchioles, these cells play a protective role by secreting bioactive compounds that shield the bronchiolar epithelium from inhaled toxins and pathogens¹⁰². One of the key proteins secreted by these cells is SCGB1A1 which is part of the secretoglobulin family. SCGB1A1, by suppressing the activity of phospholipase A2 and modulating immune functions, helps to maintain lung homeostasis in the lungs^{103,104}. In addition to their protective functions, club cells are actors of bronchiolar epithelium regeneration, particularly following injury. As progenitor cells, they can differentiate into various other epithelial cells, including ciliated cells. Recent evidence also suggests that a subset of Scgb1a1+ cells can act as progenitor cells for the alveolar epithelium in mice, especially in response to injuries¹⁰⁵. For instance, Kim et al. identified SP-C+Scgb1a1+ bronchioalveolar stem cells (BASCs) in adult mouse lungs, and demonstrate that these cells could differentiate into AT2 cells *in vitro*¹⁰⁶. While data supporting the progenitor function of club cells in humans is less substantial, research has found that between 11% and 44% of proliferating cells in the human airway epithelium express Scgb1a1¹⁰⁷. The presence of a human equivalent to mouse BASCs remains uncertain, though some club cells have been shown to produce phospholipids that are characteristic of AT2 cells¹⁰⁸. Since then, multiple studies have found a population of terminal/respiratory bronchiolar cells marked by SCGB3A2 and AT2 cells markers, including SFTPb, with either low or no expression of mucins MUC5B or MUC5AC, and in some cases, high expression of MHC II genes¹⁰⁹. In a recent study, Basil et al. used trajectory analysis to demonstrate that in human lungs, SCGB3A2+ respiratory airway secretory cells (RASCs) and AT2 cells exist along a pseudo-temporal developmental trajectory, indicating that SCGB3A2+ cells may differentiate into AT2 (**Figure 21**)¹¹⁰. Additionally, these researchers showed that the conversion of SCGB3A2+ cells into AT2 could be triggered by Notch inhibition and Wnt activation¹¹⁰. Although these findings suggest a functional equivalence between this population of distal airway cells and mouse BASCs, they do not conclusively prove the existence of a direct human equivalent. In mice, the maintenance and differentiation of club cells are tightly regulated by the Notch signaling pathway, especially through the interaction of the Notch2 receptor and Jagged ligands¹¹¹. This signaling ensures that club cells can respond appropriately to tissue damage and environmental stressors. Club cells, with their protective and regenerative roles, not only maintain the bronchiolar epithelium but also give rise to other crucial cell types, including ciliated cells, which are essential for mucociliary clearance in the respiratory system.

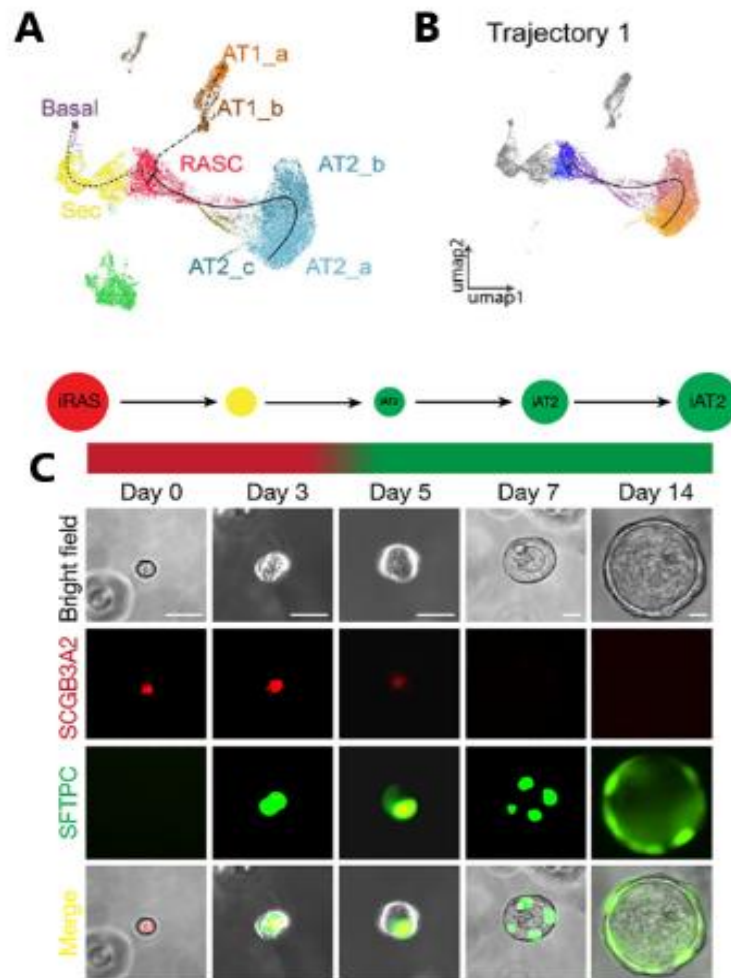


Figure 21. Analysis of alveolar epithelial cell differentiation and trajectory using scRNA-seq and in vitro assays, adapted from Maria C. Basil et al. and time-course images of alveolar epithelial progenitor cells transitioning into mature cell types in culture. (A) UMAP plot depicting clusters of alveolar epithelial cells, including basal, secretory (Sec), and different AT1 and AT2 subsets (e.g., AT1_a, AT1_b, AT2_a, AT2_b, AT2_c). A rare alveolar stem cell (RASC) population is highlighted, representing a transitional state between progenitor and mature cells. (B) Trajectory analysis along UMAP dimensions illustrates the progression pathway from iRAS (induced RASC) through various intermediate stages, ultimately leading to fully differentiated alveolar cell types (iAT2). This model provides insights into cellular plasticity and differentiation processes within the alveolar epithelium. *Bright-field images and immunofluorescence staining show markers SCGB3A2 (red, indicative of progenitor cell stages) and SFTPC (green, surfactant protein expressed in mature AT2 cells) over 14 days. Merged images confirm co-expression and the dynamic transition from progenitor to differentiated cell states.*

Ciliated cells are also component of the airway epithelium, their principal function is to maintain mucociliary clearance. These columnar-shaped cells are resting on the basement membrane. They have an increase prevalence as the airway branches, comprising up to 73% of the small airway epithelium¹¹². Each ciliated cell contains between 200 to 300 cilia on its luminal surface, with cilia measuring approximately 0.2 to 0.3 μm in diameter and ranging from 4 to 7 μm in length, depending on the airway's size¹¹³. In addition to cilia, the apical surface of these cells is also populated with microvilli, contributing to fluid and electrolyte transport across the epithelial barrier¹¹³. The primary function of ciliated cells is to propel the mucus gel to maintain the mucociliary escalator, a crucial defense mechanism in the respiratory system. This is achieved through the highly coordinated beating of cilia, generating wave-like movements that drive mucus loaded with pathogens and particulates out of the respiratory tract. Structurally, ciliated cells are connected by tight junctions and E-cadherin-based adherens junctions, which regulate solute and ion passage across the epithelial barrier while maintaining firm cell-to-cell adhesion¹¹⁴. At their basal pole, these cells are anchored to the airway epithelial basement membrane either directly or through desmosomes that attach to underlying basal cells¹¹⁵. Ciliated cells are terminally differentiated, meaning they cannot self-renew. Instead, they are replenished by basal cells. This process is notably accelerated after injury, such as mechanical damage to the airways, where ciliated cells are replaced within 14 days¹¹⁶. The differentiation of basal cells into ciliated cells is driven by the activation of key transcription factors, including FOXJ1, which is essential for ciliogenesis, and RFX family proteins that contribute to the formation of motile cilia¹¹³. Additionally, structural proteins like TUBB4 form part of the ciliary cytoskeleton, ensuring proper function of these motile organelles¹¹³. It has recently been shown that the tumor suppressor STK11 is required for normal ciliated cell differentiation in airways (**Figure 22**)¹¹⁷. Ciliated cells work in close coordination with goblet cells, as the mucus produced by goblet cells is propelled by the beating of the cilia, ensuring that pathogens and particulates are effectively trapped and cleared from the respiratory tract.

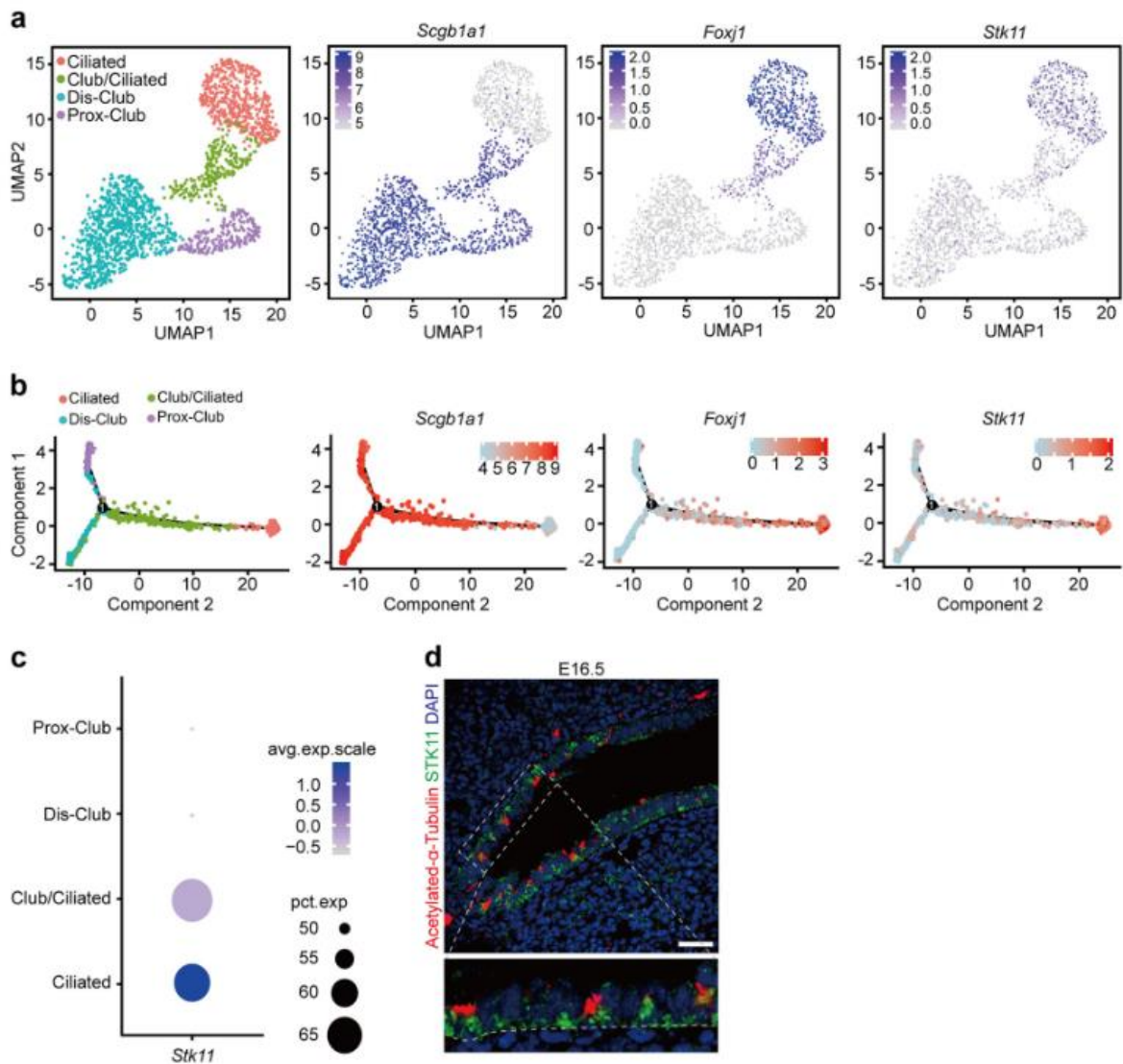


Figure 22. Expression level of *Stk11* is associated with the differentiation of ciliated cells in airways from Chu et al. 2019. (a) The UMAP show the expression of *Scgb1a1*, *Foxj1*, or *Stk11* in airway epithelial cells from adult lungs. (b) The pseudo-time trajectories show that the expression level of *Scgb1a1* decreased during the ciliated cell differentiation process, whereas the expression levels of *Foxj1* and *Stk11* increased during the ciliated cell differentiation process. (c) The dot plot of *Stk11* expression score in different cell types. (d) E16.5 lungs were stained with antibodies against acetylated- α -Tubulin and STK11. Scale bars: 25 μ m

Goblet Cells are secretory cells found in the superficial epithelium of the large airways, their role is to produce and secrete mucus that maintain airway protection. Mucus produced by goblet cells can trap inhaled pathogens, particles, and toxins, which are then cleared from the respiratory tract through the coordinated action of ciliated cells. However, their function can become dysregulated in certain respiratory diseases, leading to excessive mucus production and contributing to airway obstruction. A key transcriptional regulator of goblet cell differentiation is the sterile alpha motif-pointed domain-containing ETS transcription factor (SPDEF)¹¹⁸. It drives goblet cell differentiation by upregulating several key genes, including FOXA3 and the endoplasmic reticulum protein anterior gradient homolog 2. In mouse models, SPDEF deletion leads to a complete deletion of goblet cells in the airway epithelium, underscoring its essential role in maintaining goblet cell populations¹¹⁸. The process of goblet cell mucin secretion involves a complex secretory apparatus. This includes proteins such as the P2Y2 purinergic receptor, myristoylated alanine-rich C-kinase substrate (MARCKS), Munc proteins, and SNARE proteins (soluble N-ethylmaleimide-sensitive factor attachment protein receptors), along with heat shock protein 70 and autophagy proteins¹¹⁸. Together, these components ensure the regulated exocytosis of mucin granules, which are critical for the formation and maintenance of the mucus barrier. Goblet cells, while essential for mucus production and maintaining airway defense, interact with various other epithelial cell types to preserve respiratory function. Pulmonary neuroendocrine cells (PNECs) also play a significant, role in maintaining lung integrity, emphasizing the diverse mechanisms at work in the respiratory epithelium. These specialized sensory cells, complement the functions of secretory and ciliated cells by responding to environmental cues and contributing to airway repair after injury.

PNECs, although comprising less than 1% of the lung epithelium, play essential roles in sensing environmental changes and maintaining lung homeostasis. These rare epithelial cells, found either as solitary entities or grouped in clusters called neuroepithelial bodies (NEBs), are located at airway bifurcations, localizing them to detect changes in the airway environment¹¹⁹. PNECs act as sensory transducers by responding to stimuli such as hypoxia, mechanical forces, and even harmful substances like nicotine. Upon sensing these changes, PNECs release a range of bioactive substances including serotonin, calcitonin gene-related peptide (CGRP), and bombesin. These neuropeptides and neurotransmitters regulate local airway tone and immune responses. PNECs secretion of serotonin in response to low oxygen levels can trigger vasoconstriction in pulmonary arteries, while CGRP act as a vasodilator¹²⁰. Additionally, PNECs express key developmental markers such as ASCL1 and PROX1, which are implicated in their differentiation¹²¹. Beyond their sensory functions, PNECs can have stem cell-like properties, contributing to lung repair following significant injury. Particularly after

damage to the airway epithelium, PNECs can differentiate into various cell types, including club cells and ciliated cells¹²¹. NEBs, which are clusters of PNECs, serve as potential stem cell niches, particularly under conditions of severe injury, playing a pivotal role in epithelial repair.

b) Alveoli epithelial cells

The alveolar space is the site for gas exchange in the lungs, it contains two main types of epithelial cells. The first is AT1 cells and second is AT2 cells. AT1 cells are responsible for the diffusion of oxygen and carbon dioxide between the air and blood, while AT2 cells secrete surfactants to prevent alveolar collapse. Furthermore, they serve as progenitors for both cell types during lung regeneration and in response to lung injuries.

AT1 cells are large and thin cells that cover approximately 95% of the alveolar surface area, despite comprising only a small fraction of the total number of alveolar cells¹²². Their flattened structure is highly specialized for gas exchange, allowing an efficient diffusion of oxygen and carbon dioxide across the alveolar-capillary barrier¹²³. Indeed, their cytoplasm is extremely thin, often only a few hundred nanometers thick, except around the nucleus, where the cell is slightly more prominent. AT1 cells are characterized by the expression of markers such as podoplanin (PDPN), advanced glycosylation end product-specific receptor (AGER), and aquaporin 5 (AQP5), which are essential for their function in maintaining alveolar permeability and fluid transport¹²⁴. They are also involved in forming tight junctions with neighboring cells, creating a continuous barrier that protects the alveoli from pathogens and prevents fluid leakage. Though traditionally considered terminally differentiated, recent research suggests that AT1 cells retain some level of plasticity, particularly in response to lung injury. Studies have identified two subpopulations of AT1 cells based on the expression of insulin-like growth factor-binding protein 2 (Igfbp2) and Hopx. Hopx+Igfbp2- AT1 cells have been shown to transdifferentiate into AT2 cells during alveolar regeneration following injury or pneumonectomy. However, Hopx+Igfbp2+ AT1 cells are terminally differentiated and do not contribute to this regenerative process¹²³.

AT2 is the other subpopulation of epithelial cells present in the alveoli. They were described to produce and secrete pulmonary surfactants which is a lipid-protein complex essential for reducing surface tension in the alveoli, preventing collapse during exhalation. AT2 cells have a cuboidal shape and contain distinctive lamellar bodies that store the pulmonary surfactant. This surfactant consists of 90% lipids and 10% proteins. More precisely, it consists of phospholipids, particularly dipalmitoyl phosphatidylcholine (DPPC), and surfactant proteins (SP-A, SP-B, SP-C, and SP-D)¹²⁵. AT2 cells are also involved in host defense. They express

various immune-related molecules, including Toll-like receptors (TLRs), which help recognize pathogens and initiate immune responses. Through the secretion of chemokines and cytokines, AT2 cells contribute to the recruitment of immune cells in alveoli, such as neutrophils and macrophages.¹²⁵ The two key markers of AT2 cells are surfactant protein C (SFTPC) and lysozyme C-2 (LYZ2).¹²⁵ In addition to surfactant production, AT2 cells, upon injury, act as progenitor cells within the alveoli. They can proliferate and differentiate into AT1 cells. Recent studies identified a transition state during AT2 to AT1 differentiation which is now known as AT0 cells. This newly identified AT0 bridges the gap between AT2 and AT1 cells during repair processes, particularly in response to significant alveolar damage. Alveolar type-0 (AT0) cells represent a newly discovered cell state found in the human distal airways, particularly within terminal and respiratory bronchioles (TRBs). These cells were recently characterized through spatial transcriptomics and single-cell profiling. AT0 cells emerge from AT2 cells during lung repair processes, especially in response to alveolar injury, such as in acute lung injury or pulmonary fibrosis models¹²⁶ (**Figure 23**).

While epithelial cells in the trachea, bronchioles, and alveoli provide a vital barrier and perform essential functions for respiration and defense, mesenchymal cells like lung-resident mesenchymal stromal cells (LR-MSCs) and fibroblasts offer foundational support and structural integrity.

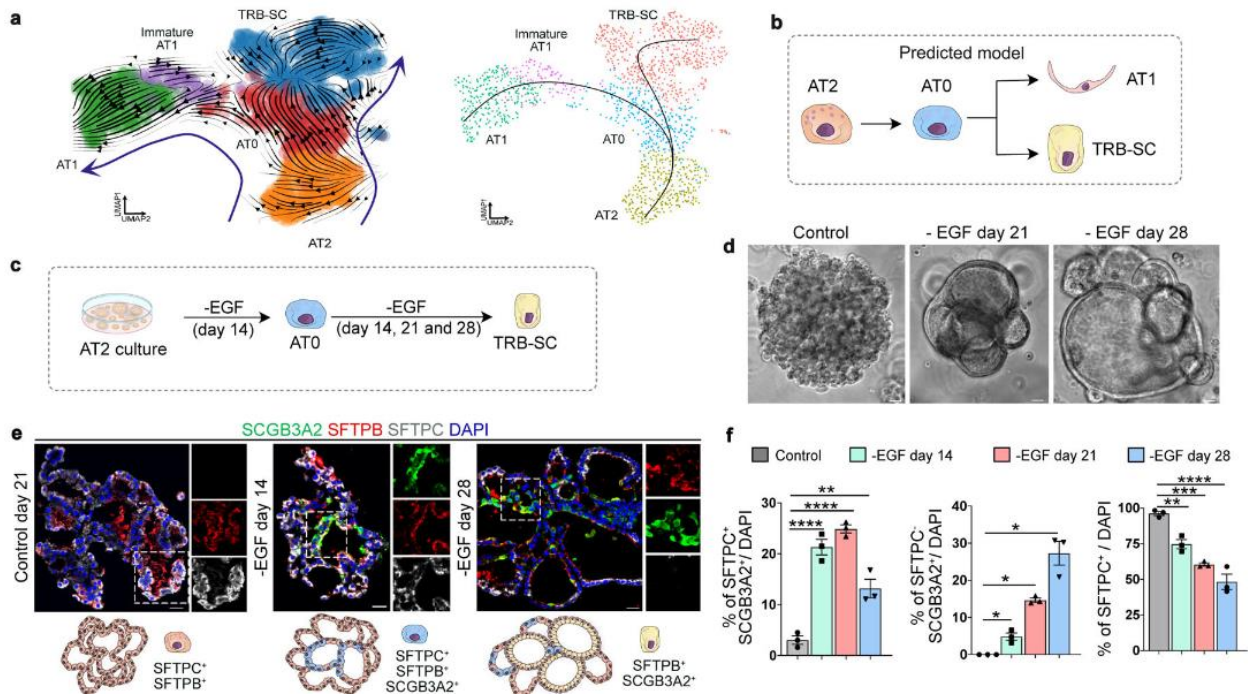


Figure 23. Dynamics of AT0 cells and distinct cellular trajectories in the human alveolar epithelium from Murthy et al. 2022. (A) Using scVelo (left) and Slingshot (right) analysis, researchers identified predicted lineage trajectories among AT2, AT0, immature AT1, AT1, and TRB-SCs in normal adult distal lung, as indicated by arrows. (B-C) A schematic model illustrates these predicted cellular pathways, complemented by a detailed workflow diagram of the experimental process. (D) Representative brightfield images depict organoid morphology, with a scale bar of 500 μm, showing distinct structural characteristics under different conditions. Immunostaining reveals expression patterns for SCGB3A2 (green), SFTPB (red), and SFTPC (grey), with a lower panel schematic highlighting the cellular and morphological variations across different organoid conditions, scale bar 20 μm. Quantitative analysis shows the proportion of SFTPC+ SCGB3A2+ cells, SFTPC- SCGB3A2+ cells, and SFTPC+ cells, with statistical significance marked (**** p < 0.0001, ** p = 0.0016, * p = 0.05) across three experiments (n=3).

c) Mesenchymal lung cells

LR-MSCs are also participating in the regulation of lung homeostasis and their role in lung regeneration and repair. LR-MSCs are defined by the expression of surface markers such as CD73, CD90, and CD105. They are lacking hematopoietic and endothelial markers like CD34 and CD45¹²⁷. Their primary localization is in vascular stem niche near blood vessels within the alveolar interstitium¹²⁸. Their multipotent differentiation potential allows them to differentiate into mesenchymal lineages, including fibroblasts and myofibroblasts which are responsible for the continuous production and remodeling of the extracellular matrix (ECM) in the lung¹²⁹. The primary function of LR-MSCs is to support lung tissue through paracrine signaling and direct cell-to-cell interactions. By releasing growth factors such as hepatocyte growth factor (HGF), keratinocyte growth factor (KGF), and VEGF, LR-MSCs modulate the behavior of surrounding epithelial, endothelial, and immune cells, promoting lung regeneration^{129,130}. Their regenerative capacity is closely linked to their ability to modulate immune responses, including polarizing macrophages toward an anti-inflammatory M2 phenotype and enhancing Tregs¹³⁰. Building on the regenerative influence of LR-MSCs within the lung's vascular stem cell niche, resident fibroblasts further contribute to pulmonary homeostasis and ECM turnover.

Resident fibroblasts are essential for lung structure, positioned in the lung's interstitium near alveolar epithelial cells, they produce ECM¹³¹. This population is heterogeneous, encompassing subtypes distinguished by surface markers, receptor expression, and cytokine profiles¹³². Among fibroblasts, two specialized types are lipofibroblasts and myofibroblasts. Lipofibroblasts (CD140 α +CD34+) accumulate neutral lipids that support AT2 cell function. In contrast, myofibroblasts (CD140 α +CD29+), characterized by α -smooth muscle actin (α -SMA) fibers, participate in wound healing and tissue remodeling¹³³. Lineage tracing studies suggest that various lung stromal cells, including interstitial fibroblasts, lipofibroblasts, pericytes, and mesothelial cells, can differentiate into myofibroblasts¹³¹. Recent studies using scRNA-seq have significantly refined the classification of fibroblast subtypes within the lung, revealing nuanced roles in health and disease. Tsukui et al., for instance, identified specific populations such as mesenchymal alveolar niche cells, which support the alveolar epithelial cells by producing essential ECM components, and myogenic progenitor cells, which possess a potential to differentiate into myofibroblasts under injury or fibrotic conditions. These progenitor cells are critical in maintaining lung structure post-injury and in conditions of fibrotic response. Further work helps to characterized a wider range of mesenchymal populations, identifying distinct subtypes that vary in both functional and structural roles (**Figure 24**)¹³⁴. These subtypes include populations with unique gene expressions related to ECM production,

immune signaling, and growth factor interactions, each potentially modulating fibrotic processes differently, which will be developed later in the manuscript.

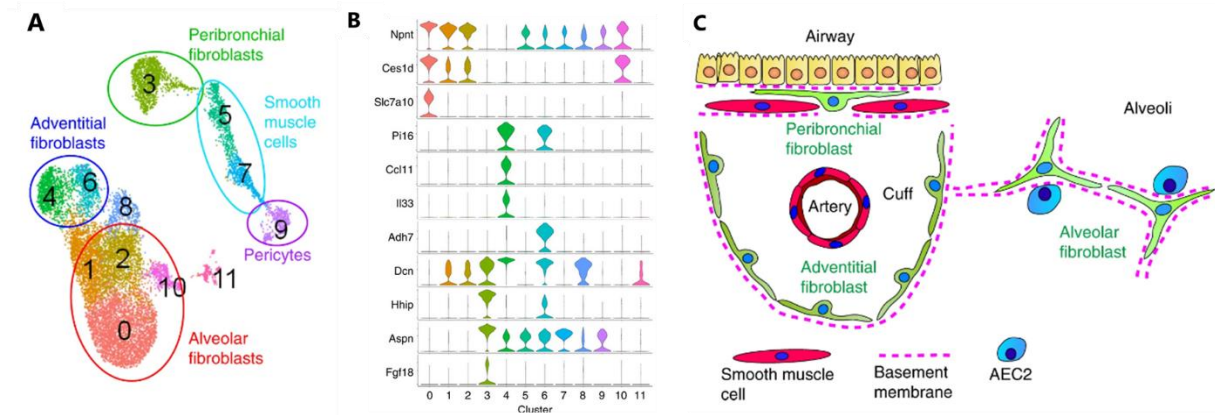


Figure 24. Characterization of alveolar, adventitial, and peribronchial fibroblasts from Tsukui et al 2020. (A) Collagen-producing subpopulations identified are shown on UMAP plot of *Col1a1*⁺ cells. (B) Violin plots showing the expression levels in each cluster of representative marker genes (C) Schematic showing the distinct localization of fibroblast subpopulations.

Pericytes are contractile cells that surround capillaries and venules which contribute to maintain vascular stability. They express markers such as CSPG4, PDGFR- β , α -SMA, and ABCG2, and are involved in the regulation of blood vessel formation¹³⁵. Studies have identified specific populations of pericytes, such as *Foxd1* progenitor-derived pericytes, ABCG2⁺ pericytes, and *Gli1*⁺ pericytes, that proliferate after lung injury and differentiate into myofibroblasts, significantly contributing to fibrosis processes upon injury^{136,137}.

In contrast, mesothelial cells form a monolayer of specialized epithelial cells lining the pleura which is the membrane surrounding the lungs. These cells secrete lubricating serous fluid that reduces friction during lung expansion and contraction. In addition to their structural role, pulmonary mesothelial cells (PMCs) are involved in inflammatory responses and wound repair following pleural injury. Although traditionally considered non-contributory to the lung mesenchyme during normal homeostasis, recent studies suggest that mesothelial cells may undergo epithelial-to-mesenchymal transition (EMT) in response to injury. This process is driven by factors such as TGF- β 1, leading mesothelial cells to lose polarity, migrate into lung parenchyma, and differentiate into myofibroblasts¹³⁸.

d) Endothelial lung cells

The pulmonary endothelium is a monolayer of ECs lining the inner surface of blood vessels in the lung. Structurally, In alveoli, ECs form an interface between the bloodstream and surrounding tissue, essential for gas exchange, nutrient delivery, and waste removal¹³⁹. Additionally, these cells produce various anticoagulant and anti-inflammatory molecules which help to maintain blood fluidity but also support vascular homeostasis. Like this, they prevent clot formation and excessive immune cell infiltration¹³⁹. The pulmonary endothelium is further subdivided into macrovascular and microvascular compartments¹⁴⁰. On the one hand, macrovascular ECs line larger vessels, such as pulmonary arteries and veins, and handle the transport of blood to and from the lungs. On the other hand, the microvascular compartment is composed of capillary endothelial cells which cover vessels within the alveoli sacs, facilitating the exchange of gases between inhaled air and blood¹⁴⁰. ScRNA-seq has revolutionized our understanding of endothelial cell heterogeneity within the pulmonary vasculature, researchers have been able to identify previously unrecognized subpopulations of ECs. Interestingly, two pulmonary capillary EC subtypes have been classified, general capillary endothelial cells (gCap) and aerocytes (aCap), which differ not only in gene expression profiles but also in functional specialization and anatomical localization (**Figure 25**)¹⁴¹.

aCap are highly specialized for gas exchange, forming thin segments of the alveolar capillary network where they are in close contact with AT1 epithelial cells. This proximity allows for efficient oxygen and carbon dioxide exchange across the alveolar membrane. Aerocytes are marked by the expression of apelin (Apln) and other genes associated with gas exchange efficiency and leukocyte trafficking, including EDNRB and SOSTDC1 (**Figure 25**). Their distinct morphology, larger cell bodies with extensive membrane surface area, further supports their role in maintaining the air-blood barrier essential for respiration. Aerocytes are terminally differentiated cells, meaning they do not typically proliferate, even under conditions of lung injury. Instead, they rely on the regenerative input of other EC types.

In contrast, gCap play a versatile role in vascular homeostasis, functioning as progenitor-like cells within the alveolar capillary network. Unlike aerocytes, gCap cells are capable of proliferation. They are marked by the expression of the apelin receptor (Aplnr) and genes related to vasodilator synthesis, such as Nos3 and Ptgis. Their stem-like capabilities of is critical for both the maintenance and repair of the alveolar capillary network ¹⁴¹.

Beyond the identification of aCap and gCap cells, scRNA-seq has also revealed other endothelial subtypes in the lung, including arterial, venous, and lymphatic ECs^{142,143}. Each subtype demonstrates unique molecular signatures that align with their respective physiological functions within the lung. For instance, pulmonary-venous ECs, marked by COL15A1, are localized in the lung parenchyma, while systemic-venous ECs are found in airway and pleural regions. Additionally, distinct lymphatic and arterial ECs maintain tissue fluid balance and blood flow regulation across the pulmonary network. These findings underscore the remarkable complexity of the pulmonary endothelium, where each cell subtype contributes to the overall structural integrity and function of the lung.

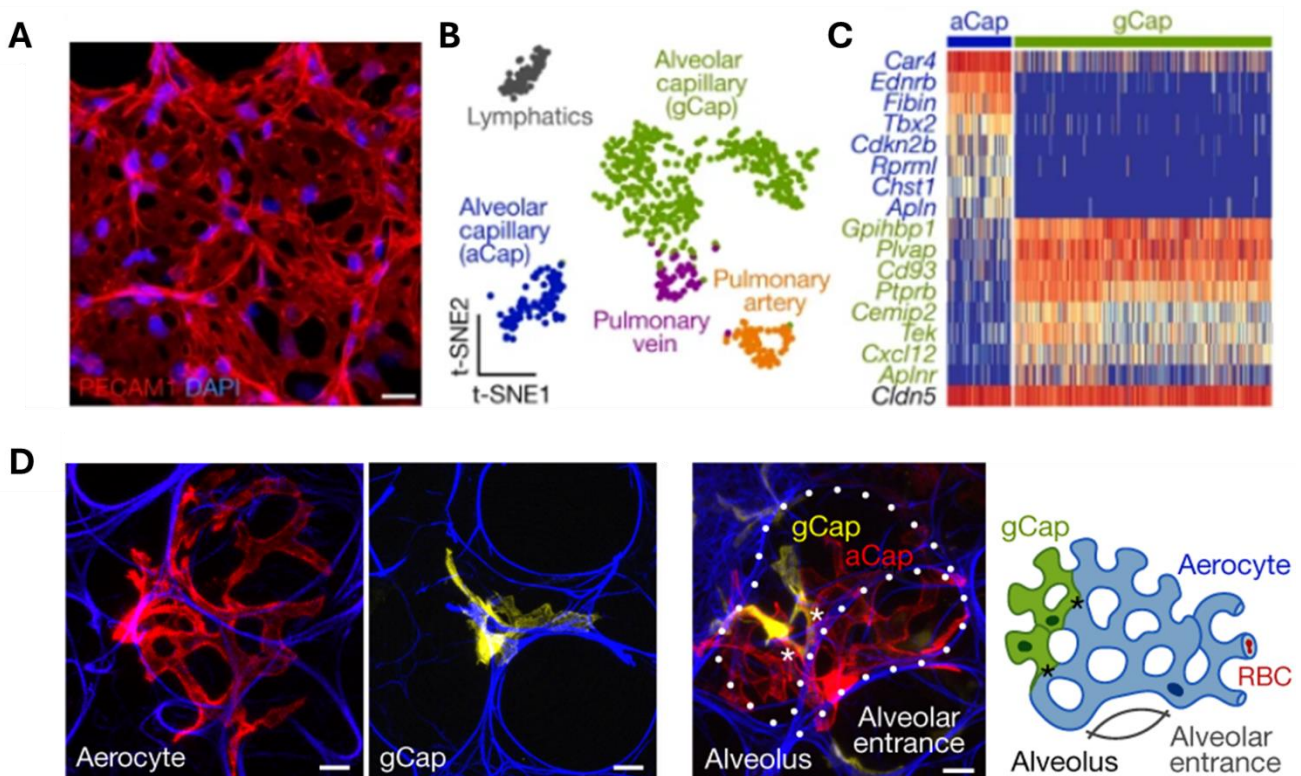


Figure 25. Distinct Capillary Endothelial Cell Types in the Alveolar Network. (A) Alveolar capillaries in adult mouse lung immunostained for PECAM1. (B) t-SNE plot of endothelial cell populations annotated in scRNA-seq data for adult mouse lungs. (C) Heatmap of expression of capillary subset markers and the general endothelial marker *Cldn5* in individual capillary cells. (D) The images on the left show the two main types of capillary endothelial cells in the lung: aerocytes (aCap) in red and general capillary cells (gCap) in yellow. These cells are uniquely positioned within the alveolar structure, with aerocytes located at the alveolar entrance for optimized gas exchange and gCap cells surrounding them for vascular homeostasis and repair functions. Adapted from Gillich et al.¹⁴¹.

Although traditionally considered quiescent, recent studies indicate that ECs can undergo rapid and targeted repair following damage, demonstrating significant plasticity in the lung microenvironment. When the pulmonary endothelium is injured, there are generally two hypothesized mechanisms for its restoration : the proliferation of existing mature ECs and the activation of local endothelial progenitor cells (EPCs). Some researchers suggest that differentiated ECs near the injury site can proliferate to restore the damaged tissue, while others propose that specialized EPCs, possibly existing within the vascular niche, play a primary role in reconstituting the endothelium through differentiation and integration into the vessel walls¹⁴⁴. Additionally, ECs in the lung can modulate the behavior of BASCs¹⁴⁵.

In situations where endothelial homeostasis is compromised, such as in chronic lung diseases, ECs may also transition through endothelial-to-mesenchymal transition (EndoMT), thus acquiring mesenchymal properties. In this transformed state, endothelial cells adopt mesenchymal characteristics. They become elongated in fibroblast-like shape, they show enhanced migratory ability, as well as structural changes in the cytoskeleton and cell junctions. These cells have higher proliferation capabilities, and can secrete increased amounts of ECM components¹⁴⁶. Furthermore, they lose typical endothelial markers like VE-cadherin, VEGF, CD34, and CD31/PECAM-1, while acquiring mesenchymal markers such as S100A4, vimentin, α -SMA, and fibronectin. Key pathways regulating this EndoMT include the TGF- β family, Wnt/ β -catenin, Notch signaling, and various inflammatory cascades, which activate shared transcriptional regulators.

e) Immune cells

Alveolar macrophages (AMs), localized within the alveolar space, are major components of the lung's immune defense system. AMs are uniquely positioned to encounter airborne particles and microorganisms, enabling them to swiftly respond¹⁴⁷. AMs are highly effective at clearing pathogens and cellular debris, which helps to maintain immune homeostasis and prevent inflammation in the lung. In their quiescent state, AMs generally exhibit an anti-inflammatory phenotype, producing regulatory cytokines like transforming growth factor-beta (TGF- β), which supports immune tolerance and prevents unnecessary inflammation in response to innocuous particles (e.g., pollen or dust). With their regulatory role, AMs can rapidly shift to a pro-inflammatory state when infection or tissue damage occurs. In the presence of pathogens, AMs enhance their phagocytic activity and secrete cytokines and chemokines, such as tumor necrosis factor-alpha (TNF- α) and interleukin-6 (IL-6), which recruit and activate additional immune cells to the site of infection. Importantly, AMs exhibit self-renewal capacity, maintaining their population independently of circulating monocytes

under steady-state conditions¹⁴⁷. However, under certain circumstances, like severe infection or inflammation, monocytes from the bloodstream can be recruited to the lung, differentiate into macrophages, and contribute to the AM pool.

Interstitial Macrophages (IMs) reside within the lung parenchyma in contrary to AMs that reside in the alveolar space. Unlike AMs, which primarily act as the first line of defense against inhaled pathogens, IMs are strategically positioned in the connective tissue, where they can manage immune responses and support tissue repair without direct exposure to the external environment¹⁴⁷. They act as a secondary defense layer and are involved in antigen presentation, enabling the activation and regulation of T cells in the lungs. IMs produce various immunoregulatory cytokines, such as interleukin-10 (IL-10), both under normal conditions and in response to inflammatory stimuli, which helps limit excessive immune activation and prevents tissue damage. Recent research has identified heterogeneity among IMs, suggesting distinct subpopulations with specialized functions in the lung tissue¹⁴⁸. For instance, certain subsets characterized by the expression of the mannose receptor (CD206), they have been shown to be involved in tissue repair and fibrosis regulation¹⁴⁹. Others, expressing markers that align with their roles in antigen presentation, such as MHC class II, can drive adaptive immunity by interacting with T cells. IMs also differ from AMs in their origin and renewal mechanisms. While AMs are largely self-sustaining and do not rely on blood monocytes for replenishment, IMs often derive from circulating monocytes, which can migrate into the lung tissue, especially during inflammation¹⁴⁷.

Pulmonary Lymphoid Cells are the components of the adaptive immune system within the lungs, encompassing various cell types that contribute to targeted immune responses and long-term immune memory. The primary lymphoid cells in the lung include T cells, B cells, and natural killer (NK) cells, each playing distinct roles in defense against pathogens. T cells, which are divided into helper (CD4+) and cytotoxic (CD8+) subsets, are activated upon recognition of specific antigens presented by antigen-presenting cells, such as dendritic cells^{147,150}. Helper T cells aid in orchestrating the immune response by releasing cytokines that attract and activate other immune cells, while cytotoxic T cells directly target and eliminate infected or abnormal cells. Notably, a specialized subset of T cells, tissue-resident memory T cells (TRM), resides within the lung tissue, offering rapid, localized responses upon re-exposure to pathogens^{147,150}. TRM cells express unique markers, such as CD69, which enhance their retention within lung tissue, providing a critical advantage in responding quickly to recurrent infections like influenza and respiratory viruses^{147,150}.

B cells is another subset of lymphoid cells, they produce antibodies that neutralize pathogens and facilitate their clearance^{147,150}. These cells are particularly important in chronic respiratory conditions and recurrent infections, as they contribute to immune memory by retaining the ability to quickly produce pathogen-specific antibodies upon re-infection^{147,150}. Some evidence suggests the presence of lung-resident B cells, which remain within lung tissue to provide continuous surveillance and protection^{147,150}. Natural killer (NK) cells, though traditionally considered part of the innate immune system, share functional characteristics with adaptive lymphoid cells^{147,150}. They provide immediate responses to infected or transformed cells without prior sensitization. NK cells can induce apoptosis in target cells through cytotoxic granules containing perforin and granzymes^{147,150}. In the lung, NK cells also produce cytokines like interferon-gamma (IFN- γ), which aids in shaping the adaptive immune response and enhances the activation of macrophages and other immune cells during infections^{147,150}. Together, these pulmonary lymphoid cells form a sophisticated network that ensures efficient immune surveillance and rapid responses to respiratory pathogens, while also maintaining immune tolerance to non-threatening inhaled particles.

Neutrophils are rapidly recruited from the bloodstream to sites of infection or tissue injury in response to inflammatory signals such as cytokines and chemokines, which guide them to the inflamed tissues. In the lungs, neutrophils play a crucial role in combating pathogens by engulfing and destroying bacteria, fungi, and viruses through phagocytosis^{147,150}. They release antimicrobial peptides, proteases, and ROS that help neutralize pathogens^{147,150}. Furthermore, neutrophils can produce extracellular traps (NETs), which are networks of chromatin and antimicrobial proteins that trap and kill microbes in the extracellular environment, providing an additional line of defense against infections. Neutrophils are generally programmed for a short life span, and they undergo apoptosis after fulfilling their immune functions^{147,150}. The timely removal of apoptotic neutrophils by macrophages is essential to limit inflammation; macrophages ingest these neutrophils and subsequently release anti-inflammatory mediators like TGF- β and IL-10, which contribute to the resolution of inflammation and tissue healing^{147,150}.

DCs are antigen-presenting cells (APCs) that play a key role in initiating and regulating immune responses in the lung^{147,150}. They serve as sentinels at the lung's epithelial surface, where they continuously sample the environment for pathogens and other antigens. Upon encountering an invader, dendritic cells capture, process, and present antigen fragments on their surface, which they then use to activate T cells in the lymph nodes. This action bridges the innate and adaptive immune systems, as it triggers a tailored immune response that can efficiently target specific pathogens. Lung DCs are highly heterogeneous and can be broadly

divided into several subtypes, primarily plasmacytoid dendritic cells (pDCs) and conventional myeloid dendritic cells (cDCs), with the latter further classified into CD103+ (cDC1) and CD11b+ (cDC2) subsets^{147,150}. Each DC subtype in the lung has specialized functions. The CD103+ cDC1s, located close to the alveolar epithelium, are essential for generating cytotoxic T-cell responses and are known to produce IL-12, which promotes Th1-type immunity and enhances anti-viral and anti-tumor responses^{147,150}. In contrast, CD11b+ cDC2s, found in the lung interstitium, are involved in Th2-type immune responses, playing a role in conditions like asthma by promoting allergic inflammation^{147,150}. Plasmacytoid DCs, although less common, are critical for anti-viral immunity, as they secrete large amounts of type I interferons in response to viral infections^{147,150}.

f) Conclusion

In summary, the human lung is a complex organ composed of a highly specialized cellular microenvironment that supports its functions of gas exchange, immune defense, and tissue repair. From epithelial cells that line the airways and alveoli to immune cells that safeguard against pathogens, each cell type plays a distinct and interdependent role in maintaining pulmonary homeostasis. The regenerative capacity of certain lung cells, such as basal cells, club cells, and AT2 cells, underscores the lung's ability to repair itself after injury. Additionally, advancements in single-cell RNA sequencing have provided a deeper understanding of cellular heterogeneity, revealing specialized cell subsets with unique functions in lung physiology and immune response.

2.1.4 Revolution of single cell transcriptomic analysis for lung cell identification

The improvement of transcriptomic techniques has profoundly enhanced the study of lung physiology, leading to remarkable insights at the cellular level. By capturing gene expressions at the level of individual cells, scRNA-seq has revealed previously unknown cell types and complex cellular interactions within the lung. One significant finding from scRNA-seq is the identification of ionocytes in the airway epithelium, which play a crucial role in fluid regulation¹⁵¹. Studies validating these findings through RNA FISH (fluorescence in situ hybridization) demonstrate that ionocytes express specific markers, such as Foxi1 and CFTR (cystic fibrosis transmembrane conductance regulator). These cells are maintained by basal progenitor cells. The lung is indeed a highly complex tissue, composed of approximately 40 cell types. Traditional microscopy, which cannot distinguish cells with similar appearances but distinct functions, may under-represent this diversity. Thus, two projects, the human and mouse lung atlases aimed to document cell diversity at a single-cell resolution to reveal a full picture of cellular composition and function^{152–155} (**Figure 26**).

The Human Lung Cell Atlas (HLCA) network maps healthy lung cell types, capturing their molecular profiles, state transitions and serves as a reference for studying disease-associated changes. Studies by Travaglini et al. and Schiller et al. identified 58 cell populations¹⁵³. Travaglini's research showed subpopulations within fibroblasts, such as alveolar and adventitial types, each with unique markers and tissue locations. AT2 cells were also separated into quiescent and Wnt signaling clusters¹⁵². Another major study by Deprez et al. analyzed 77,969 cells from the human respiratory tract across 10 volunteers, revealing cell type variability across different regions. This research clarified the roles of poorly understood cells, such as ionocytes and pulmonary neuroendocrine cells, contributing valuable insights into lung composition¹⁵⁵. Furthermore, Schupp et al. identified new endothelial cell subtypes, showcasing the lung's endothelial heterogeneity and expanding the known markers associated with endothelial cell types¹⁴². These insights continue to improve our understanding of lung biology, guiding both physiological and pathological investigations. Finally, Sikkema et al. introduced a comprehensive, integrated dataset that combines 49 single-cell studies to cover over 2.4 million cells from 486 individuals. By integrating these datasets, the HLCA standardizes cell type annotations and identifies unique cell types, even rare or previously unknown ones.

Transitioning this section, we will now explore the differences between murine and human pulmonary structures and functions. This comparison is essential, as mice are commonly used as models for lung studies. However, significant anatomical, cellular, and physiological differences exist between the two species. Understanding these distinctions will help contextualize findings from murine studies and their relevance to human lung health and disease.

HUMAN LUNG CELL ATLAS

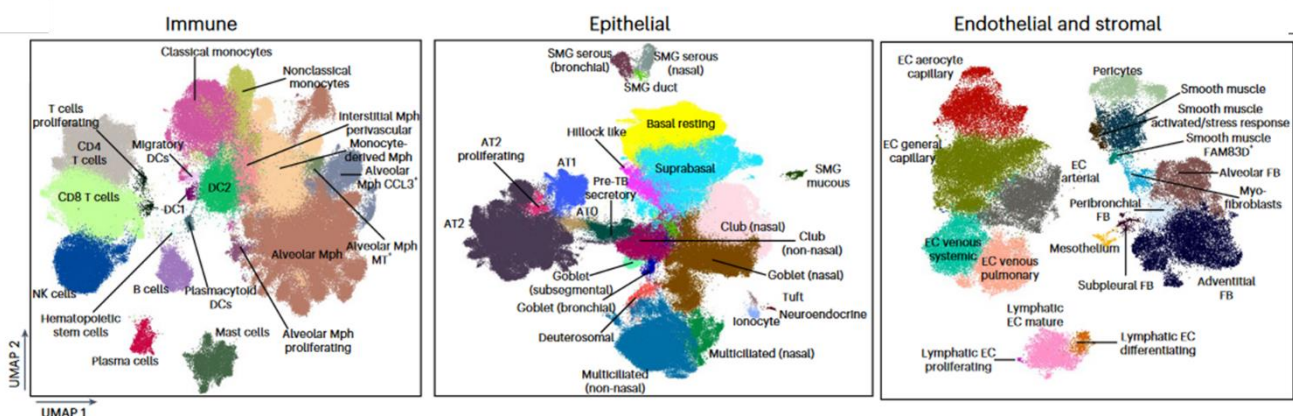


Figure 26. Human lung cell atlas UMAP representation for Immune, Epithelial and Endothelial/Stromal compartment¹⁵⁴.

2.1.5 Murine respiratory system and cell composition

Murine lung model is widely used in research to mimic human respiratory development, function, and diseases, including radiation damage. This is due to notable anatomical, histological, and developmental similarities between mice and human lungs. Despite these parallels, several differences in architecture, tissue components, and cellular composition require careful consideration when translating findings from mice to humans. One major structural difference between mouse and human lungs is the arrangement of lobes. Mice have four lobes in the right lung (superior, middle, inferior, and accessory) and one in the left lung. In contrast, humans possess two lobes in the left lung and three in the right lung. Moreover, human lung lobes are subdivided into distinct segments, which are absent in the mouse lung. The size of alveoli is another crucial distinction, with human alveoli being significantly larger, averaging 200 μm in diameter, compared to the much smaller alveoli in mice, which measure around 40 μm (**Figure 27**).⁹⁶.

The cellular composition of the airway epithelium in mice also varies from that of humans. The mouse trachea and proximal bronchi are composed of a pseudostratified mucociliary epithelium, which consists mainly of non-ciliated epithelial cells and features fewer goblet cells than human lungs. Basal cells, which are a key component in the airway epithelium, are more abundant in the mouse trachea and proximal airways. These basal cells, important for attachment and maintaining airway architecture, express markers such as keratin 5 and keratin 14, like their human counterparts. However, as the airway diameter decreases in mice, the number of basal cells diminishes, and none are present in the terminal bronchioles⁹⁶. In contrast, human airways are richer in goblet cells, and basal cells are found throughout the airways, even in distal sections. This cellular arrangement in humans supports more extensive mucus production, which plays a crucial role in trapping pathogens and particulates. In the mouse lung, club cells are the predominant secretory cell type. These non-ciliated, dome-shaped cells secrete protective proteins and detoxify harmful substances in the airway. They also serve as progenitors for ciliated cells, especially in the bronchioles where basal cells are scarce. Club cells express the marker SCGB1A1, which is critical for lung immunity and repair¹⁵⁶. Goblet cells, which are responsible for mucus secretion, are significantly fewer in mice than in humans. In mice, goblet cells mainly reside in the larger airways, whereas in humans, they are more abundant and distributed throughout both large and small airways. This difference contributes to the variation in mucosal protection and response to irritants between the two species¹⁵⁶. While the basic function of AT1 and AT2 cells is conserved between mice and humans, the regenerative capacity of these cells is a significant area of

interest in both species. In mice, AT2 cells can act as progenitors, regenerating both AT2 and AT1 cells after injury, a process that is also observed in humans, albeit to a different extent due to species-specific variations in lung repair mechanisms. Lung mesenchyme plays an essential role in supporting epithelial function and regeneration in both mice and humans. Mesenchymal cells include various fibroblasts, pericytes, and smooth muscle cells, which provide structural integrity and secrete ECM proteins. In mice, mesenchymal subsets that express the WNT-responsive *Pdgfra* gene are particularly efficient in supporting AT2 cell proliferation and differentiation during lung regeneration¹⁵⁶. Fibroblasts in the mouse lung also contribute to maintaining alveolar architecture by producing ECM components such as collagen and elastin. The ability of these fibroblasts to promote proper alveolar repair and prevent fibrosis is crucial, as dysregulation in this process can lead to diseases like pulmonary fibrosis in both mice and humans¹⁵⁶. The immune cell composition of the mouse lung is similar to that of the human lung, with alveolar macrophages playing a central role in maintaining homeostasis and responding to pathogens¹⁵⁶.

In conclusion, while the mouse lung provides an excellent model for studying many aspects of human lung biology, careful attention must be paid to species-specific differences in cellular composition and tissue architecture. These differences influence how both species respond to injury and repair, making it essential to consider the limitations and translational potential of murine models in lung research.

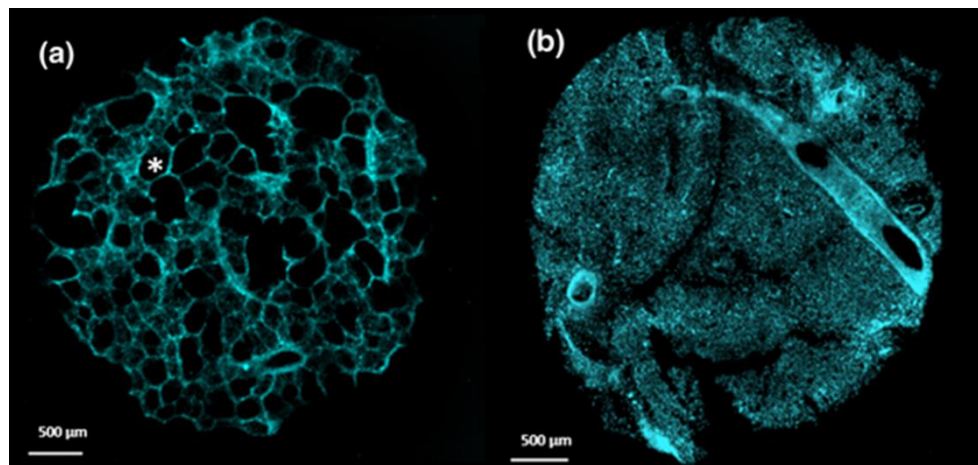


Figure 27. Alveolar structure differences between Human and mouse lungs. *Organotypic lung slices sections illustrate alveolar structures in human (a) and mouse (b) lungs. The images highlight the notable difference in alveolar size and arrangement between the two species¹⁵⁷.*

2.2 Radiation induced lung injuries (RILI)

Radiation therapy often places the surrounding lung parenchyma at significant risk for damage, leading to potential RILI. These injuries are a direct consequence of radiation's impact on the lung's structure and function, posing both acute and long-term risks to patients. Both acute and chronic phases of RILI are characterized by inflammatory processes, cytokine release, and cellular damage^{158,159}.

RILI depends on multiple parameters including patient-specific risk factors as well as treatment parameters such as total radiation dose, fractionation schedule, and treated volume. While advances in radiation delivery such as IMRT and SBRT have allowed for more targeted tumor irradiation, effectively reducing collateral exposure to lung tissue, the risk of RILI persists^{158,159}. As a result, careful constraints are essential, particularly for patients with pre-existing pulmonary conditions, as their compromised lung function predisposes them to more severe RILI outcomes.

This section on RILI will provide a comprehensive understanding of the complications and cellular damage caused by radiation therapy in lung tissue. RILI poses serious implications for treatment, impacting both short-term and long-term lung function and patient quality of life. This section examines various dimensions of RILI, from its manifestation in early-stage toxicity, such as pneumonitis, to the progression into chronic conditions like radiation-induced pulmonary fibrosis (RIPF). Additionally, we will delve into the molecular mechanisms underlying RILI.

2.2.1 Lung, organ at risk

Among thoracic organs, the lungs are the most sensitive OARs during radiotherapy for lung cancer but also for others such as breast cancer. The alveolar-capillary network, responsible for oxygen and carbon dioxide exchange, is especially vulnerable to damage from ionizing radiation. AT1, which form a thin barrier for gas diffusion, are particularly radiation-sensitive, and damage to these cells can trigger a cascade of inflammatory responses, including the activation of AT2 as a repair mechanism. Unfortunately, this process often results in excessive extracellular matrix deposition, contributing to long-term fibrotic changes within the lung. In the acute phase following radiation exposure, approximately 5-20% of patients develop acute radiation pneumonitis (ARP)⁷³. The severity of ARP is influenced by several factors, such as

patient age, smoking history, and baseline lung function. ARP symptoms include cough, shortness of breath, and chest pain, and in severe cases, it can progress to respiratory failure. If ARP fail to resolve, it can transition into a chronic phase marked by RLPF, where the lung tissue undergoes permanent structural remodeling. This fibrotic phase, affecting around 10-17% of patients, manifests symptoms like progressive dyspnea and impaired lung function and may ultimately lead to chronic respiratory insufficiency¹⁵⁸.

RILI development in patients can be influenced by various factors. For example, the higher the dose of radiation is, the greater the patient's risk to develop pneumonitis. Indeed, Metrics such as V20, representing the volume of lung tissue exposed to at least 20 Gy, and mean lung dose (MLD) have been correlated with higher grades of lung toxicity¹⁵⁹. Additionally, fractionation schedules, such as those used in SBRT, can increase the risk, particularly with higher doses per fraction. The combination of radiotherapy with certain chemotherapeutic agents, known for their radiosensitizing properties, also contributes to RILI. Drugs like doxorubicin, taxanes, and cyclophosphamide enhance the radiotherapy effect on lung tissue, while concurrent chemoradiotherapy (CCRT) has been shown to elevate pneumonitis risk¹⁵⁸. Advanced age, especially over 65, is another factor, particularly in patients treated with platinum-taxane regimens^{158,159}. Immunotherapy, specifically immune checkpoint inhibitors targeting PD-1/PD-L1 pathways, has also been associated with pneumonitis as an immune-related adverse event, with combination therapies increasing this risk. Despite the precision offered by modern radiotherapy techniques, balancing effective tumor control with the mitigation of lung toxicity remains challenging. For instance, while proton therapy offers a promising alternative by minimizing off-target effects, it may not eliminate the risk of RILI, especially in patients with large or central tumors near the hilum. As research go forward, a better understanding of the dose-response relationship and molecular mechanisms underlying RILI could offer new strategies for protecting lung tissue and enhancing the therapeutic index of radiotherapy for thoracic cancers.

2.2.2 Early radiation toxicities – pneumonitis

Radiation pneumonitis (RP) is a dose-limiting toxicity observed primarily in patients undergoing thoracic radiotherapy, often presenting clinically within the first 1-3 months post-treatment¹⁵⁹. Histologically, RP is characterized by diffuse alveolar damage, which manifests as a combination of interstitial edema, thickened alveolar septa, and inflammatory cell infiltration. These early changes lead to congestion within the alveolar spaces and thickening of the pulmonary interstitium. Histopathological examination often reveals lymphocytes and

macrophages infiltration, which contribute to a localized inflammatory response¹⁵⁹. This response is also marked by interstitial fibrosis, which, if unresolved, may progress to chronic lung injury or fibrosis over time .Clinically, RP symptoms range from mild to severe and can significantly impact a patient's quality of life. Common symptoms include a persistent dry cough, progressive shortness of breath, and chest discomfort or tightness¹⁵⁸. In severe cases, patients may experience hypoxemia due to compromised alveolar-capillary gas exchange. Radiographically, RP patients may present ground-glass opacities or consolidation, often localized to the radiation field, with imaging features such as patchy, segmental, or lobar opacities seen on CT scans (**Figure 28**). In some cases, pneumonitis extends beyond the radiation field, suggesting a broader immune-mediated response. RP's clinical impact is often more pronounced in patients with pre-existing lung conditions like chronic obstructive pulmonary disease or in those who smoke, as these factors exacerbate the inflammatory response and further compromise pulmonary function. Recognizing RP early and initiating timely treatment, typically with corticosteroids, is a standard of care to manage symptoms and prevent progression to fibrosis.

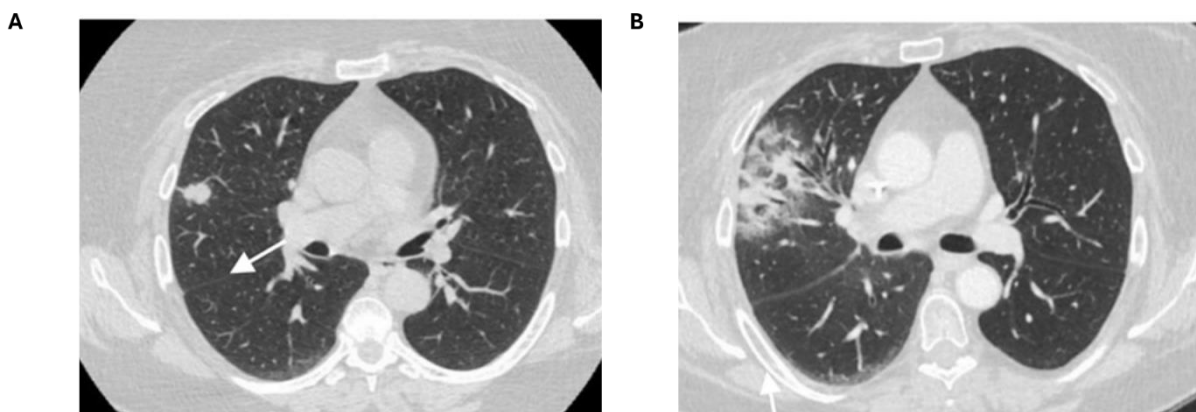


Figure 28. CT Imaging of Radiation-Induced Changes in Lung from Rahi et al. (A) Axial CT chest image showing a well-defined 2 cm nodular lesion in the Right Middle Lobe (RML), indicated by an arrow. (B) Follow-up axial CT chest image 1.5 months after radiation therapy, demonstrating the development of ground-glass opacity in the previously irradiated area.

2.2.3 Late and chronic toxicities – Radio-induced lung fibrosis

RIPF is a severe late complication that typically develops 6 to 24 months after thoracic radiotherapy, following the initial phase of radiation pneumonitis^{158,159}. The early/latent phase is characterized by a decrease in AT1 cells that leads to basement membrane denudation as well as morphologic changes in AT2 cells, interstitial oedema, transudation of the alveoli and capillaries obstruction. Then, the intermediate/acute phase or RP from 1 to 6 months post-treatment is characterized by increase release of proteins in the alveolar space, thickening of the alveolar septa and recruitment of diverse immune cells which causes lung inflammation and alveolar interstitial oedema. AT1 cells undergo necrosis and apoptosis, followed by hyperplasia of AT2 cells, who do not correctly secrete surfactant proteins, resulting in a loss of surface tension and disruption of the alveolar integrity^{158,159}. Finally, the late/fibrotic phase from 6 to 24 months is characterized by loss of capillaries, further decrease in AT1 cells, infiltration of inflammatory cells and accumulation of fibroblasts and myofibroblasts, which overproduce extracellular matrix and collagen that eventually results in the progressive and irreversible development of fibrosis^{158,159}. The loss of epithelial and endothelial cells causes a loss of barrier function and vessel integrity, reducing the density of micro-vessels and oxygen perfusion. In response to profibrotic stimuli, undifferentiated resident lung fibroblasts differentiate into myofibroblasts, who are the main cell type secreting extracellular matrix proteins and collagen (mainly COL1A1 and COL1A2) that can contribute to the development of fibrosis^{158,159}. Myofibroblasts can also derive from circulating fibrocytes from bone marrow¹⁶⁰ and also from AT2 cells through EMT¹⁶². Histologically, RIPF is characterized by dense collagen deposition, architectural distortion, and the replacement of normal alveolar structures with fibrotic tissue, leading to a progressive reduction in lung compliance and gas exchange efficiency (**Figure 29**)^{158,159}.

Clinically, RIPF manifests as chronic dyspnea, persistent dry cough, and reduced exercise tolerance^{158,159}. As fibrosis progresses, patients may experience respiratory insufficiency and hypoxemia, ultimately impacting their quality of life and long-term prognosis^{158,159}. Imaging studies, particularly high-resolution computed tomography (HRCT), reveal hallmark features of fibrosis, such as reticular opacities, traction bronchiectasis, and, in advanced stages, honeycombing^{158,159}. These radiologic patterns are frequently observed within the radiation field but may also extend to adjacent lung regions. In patients with significant pre-existing lung disease, the risk and severity of RIPF are higher, as these conditions exacerbate the fibrotic response. Management of RIPF is challenging, as current treatment options primarily aim at symptom relief rather than reversing fibrosis. Corticosteroids and antifibrotic agents are sometimes employed, though their efficacy in halting fibrosis progression remains limited.

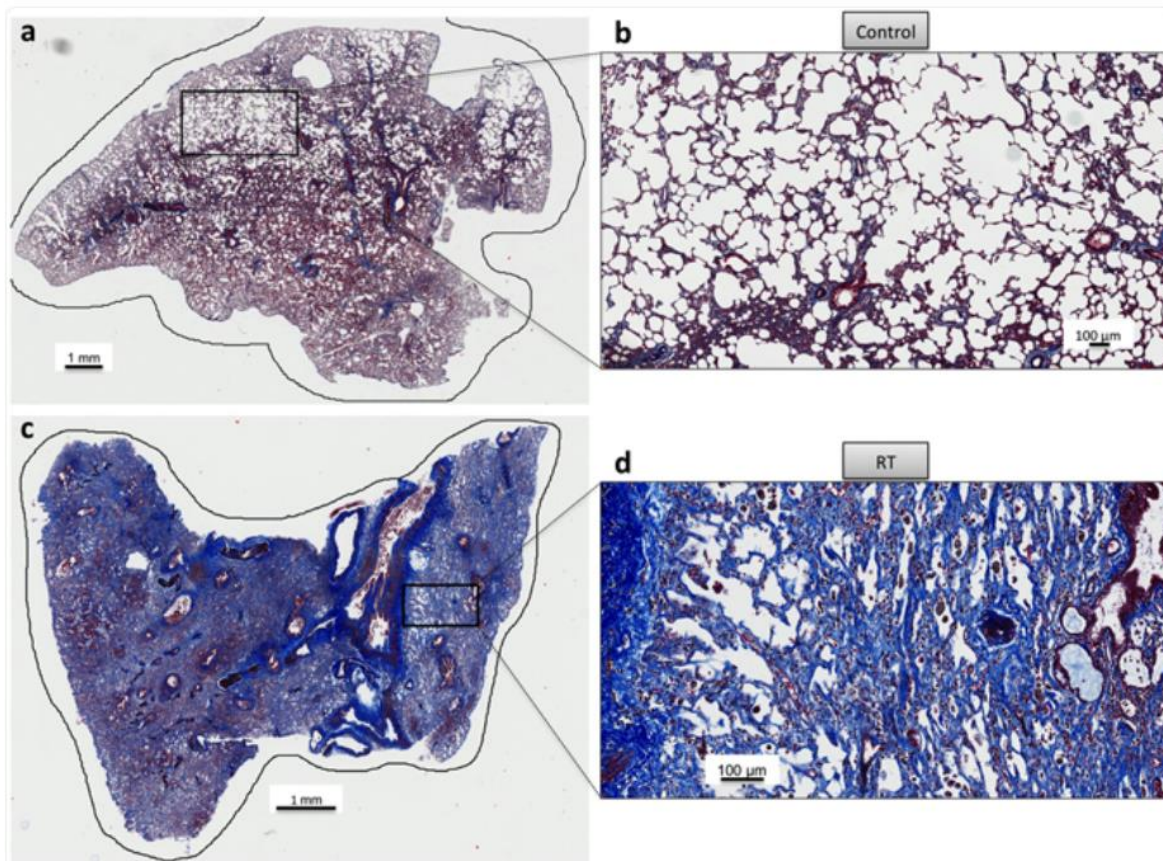


Figure 29. Histopathology of representative lung sections stained for fibrosis with Masson's trichrome from Perez et al.¹⁶¹. (a) Control whole slide. (b) Control zoomed in. (c) RT whole slide. (d) RT zoomed in. Fibrosis appears blue.

2.2.4 Molecular mechanisms of RILI

At first, radiation injury results from two main mechanisms: direct DNA damage and generation of ROS. This injury results in localized inflammation, which ultimately evolves into a fibrotic process characterized by transdifferentiation of fibroblasts into myofibroblasts, collagen and ECM deposition, poor vascularization and, ultimately, scarring. Several cytokines and growth factors serve as mediators in this fibrotic response, which, together with their associated signaling pathways, are the main targets for the existing current therapies¹⁶². It has been hypothesized that RIPF is an epithelial fibroblastic disease, in which IR injures the epithelium and endothelium, leading to the secretion of proinflammatory cytokines and the recruitment of macrophages and lymphocytes to the injured regions¹⁶³. Several studies have also described immune responses during tissue repair after IR playing a main role, together with fibroblast reprogramming and the emergence of a pro-inflammatory senescent environment likely involving complex intercellular communications^{164,165}. In this section, we will discuss the main characteristics of RIPF at the molecular levels.

a) Cytokines and inflammation processes

In addition to the traditional DNA damage and oxidative stress response that may trigger apoptosis in lung cells, RIPF also relies on a strong inflammatory response and cytokine release from the cells exposed to radiation. Cytokines constitute a diverse array of proteins that manage key cellular activities. They function via transmembrane receptors and can trigger autocrine, paracrine, or endocrine signaling pathways. Cytokines can initiate the release of additional cytokines, leading to self-amplification or self-inhibition, which results in various biological processes such as proliferation, differentiation, chemotaxis, fibrogenesis, inflammation, or cell death¹⁶⁶. The generation of cytokines in reaction to radiation depends on both time and radiation dose. Numerous cytokines and chemokines have a strong impact on the progression of radiation-induced pulmonary fibrosis, including Interleukin-1 (IL-1), IL-6, IL-13, platelet-derived growth factor (PDGF), tumor necrosis factor alpha (TNF- α), and transforming growth factor beta (TGF- β). Impairing their release has been demonstrated to slow the advancement of RIPF¹⁶⁷. Specifically, TNF- α and TGF- β are recognized to have the greater influence in the progression of pulmonary fibrosis. Activated macrophages and other immune cells primarily produce TNF- α after being exposed to an injury¹⁶³. This cytokine is recognized as a regulator of different pulmonary inflammatory conditions, including bronchitis, COPD, asthma, or acute lung injury¹⁶⁸. In contrast, TGF- β is a strong pro-fibrotic growth factor involved in inflammation and tissue remodeling processes. This cytokine stimulates Smad proteins, which can control gene expression of various targets by functioning as both transduction proteins and transcription factors. These targets participate in cellular activities including wound healing, cell growth, regulation of the cell cycle, epithelial-mesenchymal transition, programmed cell death, cell differentiation, remodeling of the matrix, immune modulation, and inflammation¹⁶⁷. TGF- β is crucial in the progression of lung fibrosis because it initially encourages the proliferation and differentiation of fibroblasts into myofibroblasts, along with epithelial-to-mesenchymal transition. Additionally, it enhances the synthesis and deposition of collagen, fibronectin, and proteoglycans, while inhibiting the production of collagenase and plasminogen activator, leading to a decrease in tissue elasticity and damage to alveolar spaces. Ultimately, it gathers various inflammatory cells including monocytes and macrophages to the site of inflammation and encourages the release of PDGF, TNF- α , IL-4, IL-6, IL-13.

Inflammation is a major factor in the healing process of wounds caused by ionizing radiation. When cells are damaged they emit DAMP molecules such as extracellular DNA, extracellular ATP, heat shock protein 70, and uric acid. These molecules stimulate cell surface-bound TOLL-like receptors (TLR) 2 and 4. The activation of these cells initiates the sequential

release of various mediators (e.g., pro-IL-1b, pro-IL-18, and type I interferon) that provoke an inflammatory response. This reaction is marked by the swift gathering, expansion, and activation of specific cells like neutrophils, macrophages, or lymphocytes, which invade the injured lung and aid in tissue repair¹⁶³. The inflammatory response involved in wound healing needs to be organized and regulated for the quick restoration of normal tissue architecture and if this response goes to strong and chronic, it may lead to the onset of lung fibrosis¹⁶⁹.

Neutrophils are the initial responders to the damaged area. The movement and activation of neutrophils can trigger inflammation in the respiratory system. To prevent this, activated neutrophils in the inflamed region undergo apoptosis and are removed by activated macrophages, which also encourage apoptosis in other resident cells and consume them¹⁷⁰. Consequently, although a temporary presence of neutrophils may be noted, the primary feature of RILI is the buildup of alveolar and interstitial macrophages, recognized as the key regulators of inflammation and fibrosis¹⁷¹.

Macrophages can be stimulated by classical M1 or alternative M2 ligands to create polarized groups. This activation may result from the direct impact of IR or an indirect influence from the signals arising from cellular injury and the removal of apoptotic cells¹⁷². On one side, classical macrophage M1 activation is initiated by pro-inflammatory cytokines including IFN- γ and TNF- α . M1 macrophages secrete TGF- β , which can modulates the feedback loop to promote the resolution of inflammation and also activates fibroblasts leading to the formation of myofibroblasts that generate ECM to aid repair and, if prolonged, induce fibrosis. Conversely, TGF- β may also be released by profibrotic M2 macrophages, which become activated following their interaction with the anti-inflammatory agents IL-4 and IL-13¹⁷³. In contrast, M2 macrophages perform immunoregulatory functions by releasing IL10 and various other cytokines.

In conclusion, the inflammatory response and cytokine release following radiation exposure play critical roles in the progression of RIPF. Cytokines like TNF- α and TGF- β not only contribute to initial inflammation but also foster fibroblast activation and ECM deposition, which ultimately leads to lung fibrosis . This inflammatory cascade, involving neutrophils, macrophages, and various signaling pathways, underscores the complexity of cellular responses in RILI. The persistent activation of these inflammatory pathways also connects closely to another critical process which is radiation-induced cellular senescence.

b) Radiation induced senescence in the lung

Conversely, radiation can lead to long term damage through the senescence process. Cellular senescence is defined by a lasting and irreversible state in the cell cycle without leading to cell death and is linked to significant cellular restructuring and changes in protein expression and secretion¹⁷⁴. Senescent cells remain metabolically active with modified secretory pathways that eventually lead to the formation of the SASP, which is characterized by an increase in the secretion of inflammatory cytokines, chemokines, immune modulators, growth factors, and proteases. SASP triggered the recruitment of immune cells and fibroblasts, along with angiogenesis, proliferation, and differentiation of stem or progenitor cells¹⁷⁵. Senescent cells are also marked by acidic lysosomal SA- β -Gal activity, signifying increased autophagy and expansion of the lysosomal compartment.

Senescence typically occurs during the G1 phase of the cell cycle. The two key signaling pathways that control cellular senescence are the p53/p21 pathway and the p16 pathway. Following a stress, growth arrest may be initiated by the p53/p21 pathway, through the p16 pathway, or both simultaneously¹⁷⁶. On one side, p53 promotes the production of the cyclin-dependent kinase (CDK) inhibitor p21, which activates retinoblastoma protein pRb by obstructing cyclins D and E. pRb inhibit the factor E2F, thereby preventing cells from progressing into the S phase. Moreover, p16 acts as a CDK inhibitor that blocks CDK4 and CDK6, which activate pRb and suppress E2F, resulting in cell cycle arrest. As stated, senescence can occur via either p53 or p16; however, in the absence of p16, the inactivation of p53 can reverse the early senescence arrest. Nonetheless, reducing p53 levels when p16 is highly expressed cannot reverse the cell cycle arrest, indicating that p16 acts as a backup regulator of p53 essential for senescence maintenance¹⁷⁷. Finally, oxidative stress caused by radiation can activate the mitogen-activated protein kinase (MAPK) p38, resulting in cellular senescence through the induction of p16 expression and/or interactions with p53.

Ionizing radiation is known to effectively induce the emergence of senescence markers, a characteristic that hinders the repair and regeneration of irradiated tissues. Irradiating mice with a sublethal dose showed that senescence markers (DNA damage foci and elevated p16 expression) are expressed long-term, lasting up to 45 weeks, leading to a lasting impairment of tissue function. Certain studies has shown that irradiating the thorax of mice raises the count of senescent cells in the lungs and results in pulmonary fibrosis. It has been shown that stereotactic high dose IR in small lung volume in mice promotes lung injury and long-term senescence in AT2 cells, macrophages and ECs¹⁷⁸. In AT2 cells population, Citrin et al demonstrated that the number of AT2 cells SA- β -gal positive and expressing p21 was higher

in mice exposed to thorax irradiation, and treatment of the mice with an inhibitor of NADPH oxidase (NOX), attenuated radiation-induced senescent AT2 cells and lung fibrosis, suggesting that senescent AT2 cells might contribute to RIPF¹⁷⁹. Treatment of irradiated mice with ABT-263 senolytic drug that selectively kills AT2 senescent cells also demonstrated a senescent cell reduction and a reverse in the pulmonary disease¹⁸⁰. Apart from epithelial cells, some studies have also pointed at the importance of senescent ECs. However, knowledge about the molecular mechanisms of endothelial senescence after radiation-induced lung injury remains still very poorly understood¹⁸¹. *In vitro* studies in microvascular HMVEC-L showed that IR induced long term senescence. Furthermore, they showed persistent p53 activation and mitochondrial dysfunction, characterized by superoxide generation, inhibition of respiratory complex II activity and overexpression of detoxification enzymes. Inhibition of p53 and superoxide generation independently showed that IR-induced senescence in quiescent ECs occurs through mitochondrial respiratory complex II dysfunction and superoxide generation¹⁸².

In summary, radiation-induced senescence plays a pivotal role in the development of RIPF by interrupting cell division and promoting the secretion of inflammatory and fibrogenic factors through the SASP. This prolonged state of senescence not only impacts lung epithelial cells, like AT2 cells, but also endothelial cells, both of which contribute to a persistent pro-fibrotic environment that hampers lung tissue repair and regeneration. However, senescence is only one of several processes involved in the fibrotic response. Another mechanism associated with radiation-induced fibrosis is the transition of epithelial and endothelial cells into mesenchymal-like cells known as EMT and EndoMT. This transition supports ECM buildup and tissue stiffening, which are central to the fibrotic progression in the lungs. In the following section, we will explore the contributions of EMT and EndoMT in RILI.

c) EMT and EndoMT

Throughout fibrosis development, elevated levels of TGF- β promote the EMT of alveolar AT2 cells¹⁸³ and trigger EndoMT in microvascular¹⁸⁴. The key feature of EMT and EndoMT is that AT2 and microvascular ECs lose their polarity and specific markers such as E-cadherin, VE-cadherin, tight junction proteins and begin expressing mesenchymal markers (like vimentin, collagens I and III, α -SMA), which gives them a mesenchymal-like phenotype, migratory ability, and invasiveness, enabling them to migrate to the interstitium¹⁸³. Numerous studies have demonstrated EMT process *in vivo* through lineage tracing studies that tracked the expression of β -galactosidase, which was exclusively expressed in lung epithelial cells. Following the induction of pulmonary fibrosis through thorax irradiation in mice, the emergence of β -galactosidase positive cells showing mesenchymal markers (α -SMA, vimentin, S100A4),

alongside cells co-expressing mesenchymal and AT2 cell markers, indicated that epithelial cells were undergoing EMT^{185,186}. Recent research indicates that AT2 cells experiencing EMT foster a pro-fibrotic microenvironment due to their production of paracrine signals, leading to abnormal interactions that stimulate nearby fibroblasts¹⁸⁷. Various transcription factors, including Snail, slug, twist, ZEB1 (Zinc finger E-box binding-1), and ZEB2 (Zinc finger E-box binding-2) proteins, serve as inducers connecting radiation-induced EMT and fibrosis¹⁸⁸. Although numerous studies indicate that AT2 cells undergo EMT, there is no proof of EMT occurring in AT1 cells population¹⁸⁹.

In endothelial cells, EndoMT has been shown in tissue culture models, where treating capillary ECs with TGF- β leads to the loss of EC markers and the acquisition of fibroblast and myofibroblast markers (e.g., FSP1, α -SMA, DDR2, collagen I, and vimentin)¹⁸³. Irradiated ECs may also experience EndoMT via the Snail/miR-199a-5p axis, facilitating the transformation of fibroblasts into myofibroblasts¹⁹⁰. Additional research has also shown evidence of EndoMT in the vasculature (through TGF β -R1/Smad signaling) during the onset of RIPF, which seems to occur in the initial stage of RIPF, prior to the emergence of EMT in the AT2 cells. Additionally, they note particular EC hypoxic injury in the exposed lung tissue. The suppression of hypoxia-inducible factor 1-alpha (HIF1 α) expression reduced EndoMT and lowered collagen deposition¹⁹¹. A recent study has shown that the removal of vascular endothelial-specific HIF1 α just prior to IR diminished EndoMT and hindered the advancement of RIPF, while an extended deletion before radiation treatment did not. Furthermore, the HIF1 α inhibitor (2-ME) applied by Choi et al. was effective in inhibiting EndoMT and RIPF after irradiation treatment. These findings indicate that altering EC-specific hypoxic injury may prevent EndoMT and the fibrotic reaction to irradiation, highlighting 2-ME treatment as a therapeutic approach to enhance radiation therapy effectiveness by counteracting radiation-induced EndoMT.

In summary, the processes of EMT and EndoMT play essential roles in the progression of RIPF by inducing a transition of epithelial and endothelial cells into mesenchymal-like cells that contribute to fibrosis.

The insights into cytokine-driven inflammation, senescence, and EMT/EndoMT processes illustrate how cellular responses within the lung contribute to the progression of RIPF following radiation exposure. Each of these mechanisms disrupt the balance of cell renewal, repair, and structural integrity within the lung, creating an environment prone to chronic fibrosis. In the next section, we will explore the cellular responses of the various lung subpopulations in RILI.

2.2.5 RILI and cellular response to lung radiation

a) Immune cells response to radiation in the lung

The first inflammatory cell to arrive at the injured site are the neutrophils, whose extravasation and transmigration into tissues is enhanced by the increased expression of intercellular adhesion molecule (ICAM-1) and platelet endothelial cell adhesion molecule (PECAM-1) on the surface of injured endothelial cells. At the site of injury and in the presence of collagen and fibronectin, neutrophils secrete proinflammatory cytokines that maintain the ROS generation and enhance inflammation processes.

In response to IR, lymphocytes can acquire pro-inflammatory (acute phase) or anti-inflammatory and pro-fibrotic phenotypes (chronic phase)¹⁹². When monocytes and lymphocytes arrive, their interaction promotes monocytes differentiation into classically activated pro-inflammatory M1 or alternatively activated anti-inflammatory M2 macrophages. M2 macrophages can secrete PDGF, which promotes neoangiogenesis and fibroblasts migration into the site of injury, as well as TGF- β which is involved in the recruitment of fibroblasts from bone marrow progenitors. TGF- β participate to the differentiation of fibroblasts into myofibroblasts¹⁶². The elimination of TGF- β from M2 macrophages attenuated EMT, suggesting that TGF- β secreting M2 macrophages play a key role in the EMT regulation after IR, thus contributing to RIPF¹⁹³. Moreover, the development of radiation induced pulmonary fibrosis is enhanced by CD73, an enzyme that is found in the surface of various cell populations in the lung and that is upregulated after thorax IR¹⁹⁴. In fact, the loss of this enzyme prevents the accumulation of M2 macrophages and, therefore, the formation of profibrotic organized clusters of macrophages that promote the development of fibrosis. Thus, radiation induced activation of CD73 promotes RIPF by enhancing the formation of alternatively activated profibrotic macrophages clusters¹⁹⁵. ScRNAseq has also helped to decipher the role of the macrophages subpopulation during lung fibrosis development. One of the first groups who analyzed the macrophages from IPF patients revealed the existence of two types of AM. The first group was healthy and one novel population of profibrotic alveolar macrophages was described (CHI3L1+, MARCKS+, IL1RN+, PLA2G7+, MMP9+, SPP1+)¹⁹⁶. This was further confirmed by two publications, which described a profibrotic macrophage population that expresses high levels of SPP1, which play a role in the activation of IPF myofibroblasts during fibrosis^{197,198}. More recently, a population of pro-fibrotic aberrant macrophages (IPFeM Φ) population has been described, which show a hybrid transitional state between AM and IM, with M2-like phenotype¹⁹⁹. However, their involvement in RIPF has not yet been demonstrated.

In a murine model of R1PF, it has been shown that macrophages exhibit distinct pro-inflammatory and pro-fibrotic profiles in response to high-dose fibrogenic radiation²⁰⁰. In interstitial macrophages, a subpopulation showed an increased expression of pro-inflammatory genes, such as *Ccr2* and *Stat1*, especially after fibrogenic dose radiation, suggesting the presence of an M1 pro-inflammatory phenotype (**Figure 30**). On the other side, AM were divided into two subclusters, one presenting an upregulation of profibrotic markers such as *Lpl*, *Tgm2*, and *Il4ra* which align with an M2-like phenotype associated with tissue repair and fibrosis. Notably, this subpopulation was enriched several months post-radiation treatment (**Figure 30**). This shift was accompanied by morphological changes such as an increased volume of Ams. In another R1I murine model in response to high SBRT in small irradiated volumes, AMs displayed a metabolic shift over time post-radiation. This shift was towards lipid and cholesterol-associated metabolism²⁰¹. This metabolic shift was further confirmed by immunofluorescence and analysis revealed that it was accompanied by features of the senescence-associated secretory phenotype (SASP), suggesting a link between radiation-induced senescence and lipid metabolism changes in this subpopulation of AM.

In conclusion, thoracic irradiation triggers a complex and dynamic immune response in the lung, involving various immune cell populations, each contributing to the inflammatory and fibrotic processes. With this immune response as a foundation, we now shift our focus to the response of mesenchymal cells in the lung post-irradiation. These cells are essential in tissue repair and fibrosis, especially in the context of radiation-induced lung injury, where their activation and differentiation play a pivotal role in the progression of R1PF.

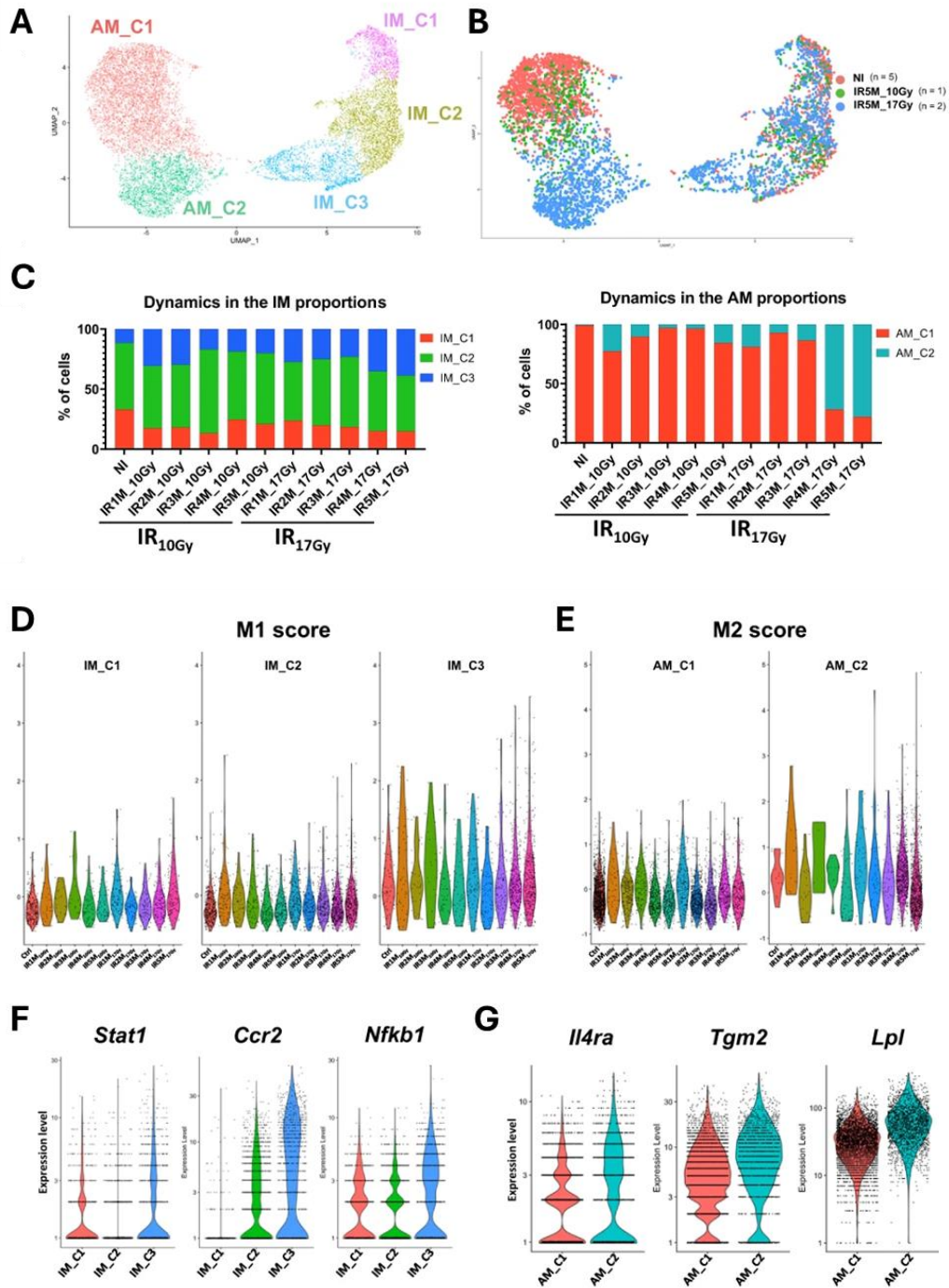


Figure 30. Proinflammatory and profibrotic profile of alveolar and interstitial macrophages after fibrogenic doses of IR from Curras-Alonso et al. 2023 (A) UMAP visualization of cells from the different IM and AM subpopulations annotated by cell type. (B) UMAP visualization of NI (n = 5), IR5M10Gy (n = 1) and IR5M17Gy (n = 2) IM and AM annotated by time point. (C) Dynamics in the proportion of the IM and AM subpopulations at the different time points after IR10Gy and IR17Gy. (D-E) Violin plot showing the single cell score calculated based on the M1 or M2 signature in the different AM and IM subpopulations. (F-G) Violin plots of M1 or M2 genes expression in the different IM and AM subpopulations.

b) Mesenchymal cells response to radiation in the lung

Myofibroblasts play a central role during the development of RIPF by abnormally synthesizing and secreting ECM. In response to TGF- β , myofibroblasts release collagen, fibronectin and proteoglycans, increasing the stiffness and thickness of the tissue. Myofibroblasts also secrete basic fibroblast growth factor (bFGF), which promotes EC proliferation and angiogenesis. Interestingly, in a mouse fibrogenic model, over months post-irradiation, an increase of the proportion of myofibroblasts in the lung has been reported suggesting a significant shift from matrix fibroblasts to myofibroblasts as fibrosis progressed. Additionally, they revealed a significant upregulation of genes involved in ECM deposition exclusively after high dose of radiation²⁰⁰. Furthermore, expanding damages, the excess of collagen reduces vascular density over time, which increases the susceptibility of fibrotic areas and ischemia¹⁶². A fibroblast cluster marked by CTHRC1 expression which is highly upregulated in fibrotic lungs was recently described^{134,202}. Furthermore, this cluster presents high migration and invasion capacity suggesting its role in fibrosis development. As this fibroblast population is almost exclusively present in fibrotic conditions, it may serve as a potential therapeutic target. Other notable populations include those expressing PDGFR α , Wnt5a, and other Wnt signaling-related genes, which are implicated in cellular communication with alveolar epithelial cells, further underscoring their regulatory influence in maintaining lung homeostasis and driving fibrosis progression^{134,202}. For RIPF, it has been confirmed that fibrogenic radiation in a murine model triggers a strong ECM genes response in fibroblasts populations. Indeed, through scRNA-seq analysis, three distinct subpopulations of lung fibroblasts were identified: two matrix fibroblasts, one Col13a1-positive (Col13a1+, Tcf21+), one Col14a1-positive (Col14a1+, Pi16+, Meg3+), and one subpopulation of myofibroblasts (Hhip+, Cdh11+, Pdgfrb+). Remarkably, month after fibrogenic irradiation, fibroblasts predominantly clustered with the myofibroblast population, representing over 80% of the total fibroblast population in these samples. Additionally, a small population of fibroblasts was found to co-express both Pdfgra and Hhip, with this dual expression increasing progressively after irradiation, from 0.4% in non-irradiated controls to 4.2% after fibrogenic radiation (**Figure 31**). This suggests that fibrogenic irradiation not only induces a shift toward myofibroblast dominance but also promotes a subset of fibroblasts with mixed characteristics, potentially contributing to the fibrosis observed in the lung.

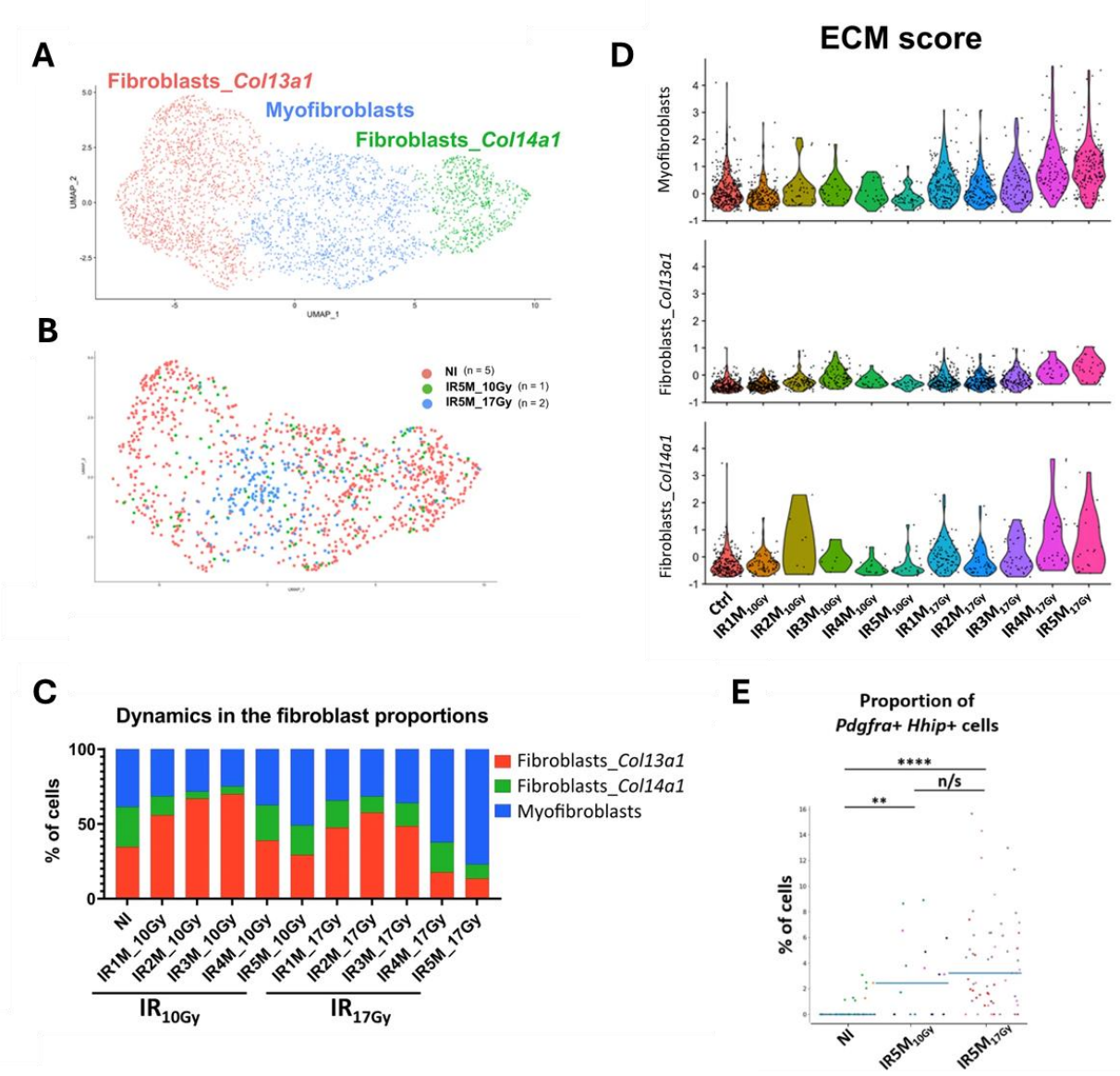


Figure 31. Myofibroblasts contribute to the ECM deposition after IR17Gy, adapted from Curras-Alonso et al. (A) UMAP visualization of cells from the different fibroblast subpopulations annotated by cell type. (B) UMAP visualization of NI (n = 5), IR5M_{10Gy} (n = 1) and IR5M_{17Gy} (n = 2) fibroblasts annotated by time point. (C) Dynamics in the proportion of the fibroblast subpopulations at the different time points after IR_{10Gy} and IR_{17Gy}. (D) Violin plot showing the single cell score calculated based on the ECM expressed genes in the myofibroblasts, fibroblasts Col13a1, and fibroblasts Col14a1. (E) Quantification of the Hhip+ cells in the NI, IR5M_{10Gy} and IR5M_{17Gy} lung tissue sections. To compare two groups, the P value was computed with the Mann–Whitney–Wilcoxon test (two-sided test) from scipy (n/s, adjusted p value >0.05; *, adjusted p value <0.05; **, adjusted p value <0.01; ***, adjusted p value <0.001; ****, adjusted p value <0.0001). Each dot represents one analyzed image. Each color per time point represents a different biological replicate (NI n = 3; IR5M_{10Gy} n = 3; IR5M_{17Gy} n = 5).

c) Epithelial cells response to radiation in the lung

After radiation, depending on the dose, AT2 can go through apoptosis. Whole thorax irradiation at 15 Gy of mice showed that AT1 and AT2 cells become apoptotic 6 weeks after irradiation²⁰³. Nevertheless, AT2 apoptosis alone is not enough to cause fibrosis, as equivalent AT2 apoptosis has been observed after non-fibrogenic and fibrogenic lung thorax irradiation. Moreover, AT2 cells achieved gradual recovery after non-fibrogenic doses, while they were not able to recover after fibrogenic doses, suggesting that the regenerative capacity of the AT2 cells is dose dependent¹⁷⁹. AT2 loss affects the effective alveolar repair, resulting in epithelial stress and fibroproliferation. In fact, targeted depletion of AT2 cells shows rapid progression of fibrosis²⁰⁴. Moreover, massive AT2 depletion stimulates macrophage influx and secretion of proinflammatory cytokines, leading to fibrosis. AT1 cells are also rapidly lost after radiation injury, which leads to rapid AT2 cell proliferation and transdifferentiation into AT1 cells to re-establish a functional alveolar epithelium¹⁵⁸. Recent studies show that the surviving AT2 cells exhibited significant changes in their transcriptional profile, especially in genes linked to EMT and transdifferentiation into AT1 cells. This study further identified a specific subpopulation of AT2 Krt8+ cells that demonstrated a high propensity for transdifferentiation towards AT1 cells, suggesting a distinct transitional stem cell state. Additionally, transcription factors such as Stat1 and Stat3 were upregulated, which have previously been implicated in idiopathic pulmonary fibrosis, underscoring a potential pathogenic pathway activated by high-dose of radiation²⁰⁰.

In AT1, thoracic irradiation on mice shows that aquaporin-5 was decreased after irradiation (12Gy and 30Gy), which impaired their function. In both epithelial populations, e-cadherin adhesion molecules were reduced, suggesting a loss in the maintenance of the epithelial barrier. Moreover, co-localization of pro-SP-c and α -SMA was observed in the alveoli after IR, suggesting that IR causes the transdifferentiating of AT2 cells into a mesenchymal-phenotype²⁰⁵. This EMT process has also been observed to be induced by the loss of Nrf2. Loss of this transcription factor expression has been related to the failure of AT2 cells recovery after lung irradiation, promoting a myofibroblast phenotype²⁰⁶.

d) Endothelial cells response to radiation in the lung

On the one hand, acute radiation effects on endothelium are triggered by EC apoptosis and appear in days to weeks after the IR. These can be mediated through the p53 pathway or the sphingomyelin ceramide pathway. Indeed, radiation induced DNA damage activates ataxia telangiectasia-mutated (ATM) gene and DNAdependent- kinase, which phosphorylates p53 and leads to cell cycle arrest. Then cells can either repair their DNA or initiate apoptotic cell death. Otherwise, irradiation can activate TNF, which hydrolyses sphingomyelin, generating ceramide. This ceramide activates MAPK, ERK SEK1 and c-Jun, which can modify the dynamics of the cell membrane and start a cascade of events that lead to EC apoptosis²⁰⁷.

On the other hand, chronic radiation effects result in EC senescence, that can take months to years to manifest. When EC cells become senescent, this leads to a senescence-associated secretory pathway, in which EC secrete several factors, such as cytokines and proteins, that cause dysfunction of the adjacent cells, leading to a chronic inflammatory state. The death or functional detriment of EC could trigger a chronic inflammatory state or acute capillary rarefaction and, therefore, the leak and disorder of the vascular networks that change the normal vascular homeostasis²⁰⁷. In (human umbilical vein endothelial cells) model, irradiation can decrease cell proliferation, change the morphology of the cells, increase the expression of SASP (insulin-like growth factor binding protein 5 (IGFBP5), CD44, plasminogen activator (PLAT), jagged 1 (JAG1), snail homolog 2 (SNAI2) and Sprout homolog 4 (SPRY4), as well as the expression of β -galactosidase²⁰⁸. Irradiation of pulmonary artery ECs with doses between 2 to 50 Gy leads to accelerated senescence and limited levels of apoptotic death²⁰⁹. In addition, IR can increase TNF α expression level, which can the promote inflammatory pathway trough endothelial senescence¹⁸¹ (Hansel, Jendrossek, and Klein 2020).

Apart from causing apoptosis and senescence, irradiation can lead to a phenomenon of endothelial activation. It implies changes in the normal vascular homeostasis and the appearance of a pro-inflammatory phenotype characterized by the expression of chemokines, cytokines and adhesion molecules that facilitate the recruitment and attachment of circulating leukocytes on the vascular wall²¹⁰. This inflammation after radiation is trigger via the NF κ B pathway, which can be activated through activation of ataxia telangiectasia mutated protein (ATM) in response to DSBs, or by oxidative stress or either by DAMPS released of stressed and dying cells. The resulting inflammation triggers the production and release of pro-inflammatory cytokines (IFN γ , TNF α , TGF β , IL-1, IL-6, IL-8 and CCL2) and the increase in the expression of cell adhesion molecules, such as PECAM-1 (CD31), ICAM-1 (CD54), VCAM-1, E-selectine and Pselectine, by irradiated ECs²¹¹. *In vitro* studies have shown that these cell

adhesion molecules are upregulated in irradiated ECs. Some other studies *in vivo* have shown that the expression of ICAM-1 is only increased in the pulmonary microvasculature in a dose- and time-dependent manner. Other changes also include deterioration in the vascular tone, altered coagulation status (decrease in thrombomodulin and increase in thrombin, platelet activation factor and circulating vWF), increase in reactive oxygen species (ROS) (superoxide and peroxynitrate), changes in the angiogenic pathways (increase in type II collagen, PAI-1 and SMA) and other metabolic pathways (increase in glycolysis, altered mitochondrial oxidation and lipid pathways), and increased immunologic alterations (increase in TLR and CXCL6)^{207,211}.

Recent studies have also shown a large deregulation of genes involved in the EndoMT), such as Col4a1 and Col4a2. This EndoMT signature was particularly present in gCap cells, suggesting a role in fibrotic processes and underscoring the heightened susceptibility of this EC subpopulation to fibrogenic radiation doses. It correlated with a progressive decrease of gCap cells population over months post-radiation, while aCap cells increased, indicating a shift within the EC populations unique to fibrogenic conditions²⁰⁰ (**Figure 32**).

Finally, research have highlighted the significant role of pro-angiogenic pathways in the lung's response to radiation. It has been showed that irradiation activated pro-angiogenic signaling pathways, notably the VEGFA-VEGFR2 axis, across various lung cell types, including immune cells, endothelial cells, and AT2 cells. The upregulation of VEGFA and VEGFB, along with their receptors FLT1/VEGFR1 and KDR/VEGFR2 indicated a robust response to radiation aimed at facilitating vascular repair. A particularly striking finding was the increase in pro-angiogenic activity in endothelial cells, especially in capillary subtypes, such as aCap and gCap. These gCap cells, characterized by KDR/VEGFR2 expression, exhibited a "tip-like" phenotype, which is associated with angiogenesis and cell motility. This shift was confirmed by an increased expression of motility-related genes such as CAV1 and ROBO4 in gCap cells after irradiation. This response suggests that these endothelial cells play an active role in vascular repair following radiation injury by acquiring characteristics that promote cell migration and vessel formation²¹².

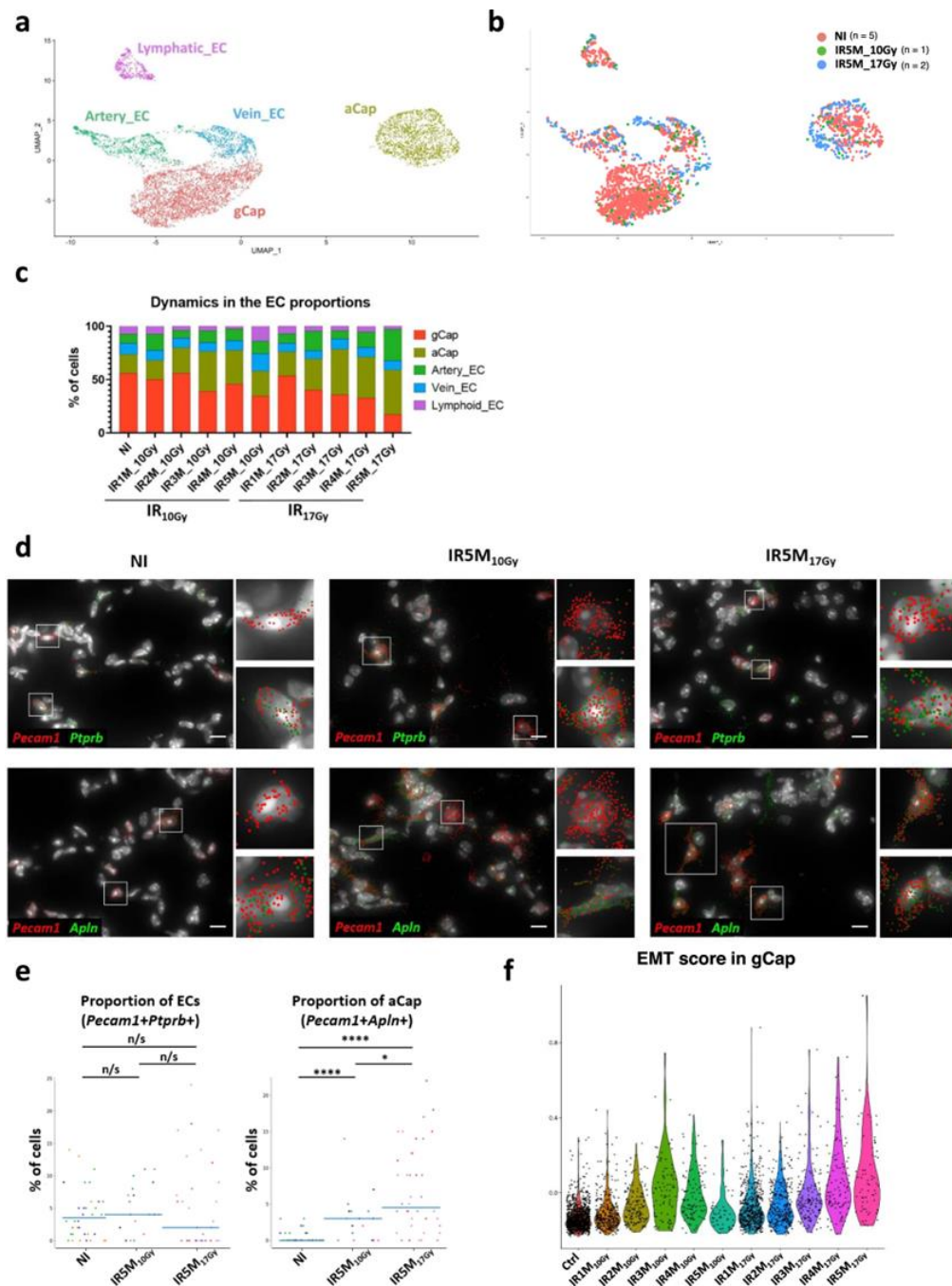


Figure 32. Characterization of the ECs after radiation injury from Curras-Alonso et al. (a-b) UMAP visualization of cells from the different EC subpopulations annotated by cell type or timepoint (c) Dynamics in the proportion of the EC subpopulations at the different time points after radiation. (d) Automatic *Pecam1* (red), *Ptprb* (green), and *Apln* (green) mRNA detection with sm-FISH in lung tissue sections. Scale bars, 10 μ m. (e) Quantification of the *Pecam1* + *Ptprb* + and *Pecam1* + *Apln* + cells in the NI, IR5M_{10Gy} and IR5M_{17Gy} lung tissue sections. (f) Violin plot showing the single cell score calculated based on the EMT signature from the GSEA in the gCap at the different time points after IR_{10Gy} and IR_{17Gy}.

2.3 Modeling radio-induced toxicities

Understanding how RILI occurs is crucial for advancing treatment strategies and mitigating side effects of radiation therapy. Modeling these toxicities allows to observe the biological response to radiation at the tissue, cellular, and molecular levels. Different models, ranging from murine to cell culture systems, organoids, organ on chips and organotypic slices could allow the study of RILI. Each model offers specific advantages and limitations, with varying degrees of translational relevance.

2.3.1 Murine model for modeling RILI

Murine models are classically used to study RILI due to their biological and genetic similarity to humans, relatively short life cycles, and well-characterized immune and pulmonary systems that respond similarly to radiation exposure. These models allow researchers to replicate complex tissue and organ responses to radiation, closely mimicking the progression of acute and chronic phases of RILI. Strains like C57BL/6 mice have been widely used to investigate the progression of fibrosis, with both early pneumonitis and late fibrotic stages that parallel human responses in RILI. The whole-thorax irradiation method, often at doses ranging from 13-20 Gy, provides a reliable framework for studying dose thresholds and markers of radiation injury¹⁹⁵. However, susceptibility to irradiation is also affected by the gender, as C57Bl/6 females are more sensitive to the development of PF than male²¹³. Even if this model requires long periods of time to observe lung fibrosis, it is, for now, the most accurate model to study the pathophysiology of the human RIPF over time. However, due to ethical pressures to reduce animal testing, alternative *in vitro* and *ex vivo* models are more and more being developed.

2.3.2 Development of ALI culture models and applications for RILI

Before the emergence of 3D tissue culture techniques, human primary cells or cell lines derived from healthy or tumor lung tissues were mostly used. These two-dimensional (2D) models are highly suited for high-throughput drug screening and can be derived from cell lines with specific histological and genetic alterations, allowing to simulate various clinical conditions. Despite their advantages, these models are limited by their lack of extracellular matrix components and inability to recreate the complex structure, architecture and microenvironment of lung tissue as well as interaction with surrounding organs. As a result, 2D models have limitations in fully replicating the multicellular and structural aspects of lung tissue responses, which are crucial for accurately studying RILI.

The Air-Liquid Interface (ALI) culture model emerged as *in vitro* system designed to more accurately replicate the *in vivo* conditions of the lung. Unlike conventional culture method in which cells are submerged and grown in a liquid medium on a flat surface, ALI culture utilizes a microporous membrane that supports the cells in three-dimensional (3D). Here, the apical side of the cell layer is exposed to air while only the basolateral side is submerged in culture medium^{214,215}. This setup enables the differentiation of epithelial cells into a mucociliary pseudostratified epithelium which replicates the architecture and function of the airway *in vivo*. ALI culture model can replicate the cellular arrangement and composition of this respiratory epithelium, which includes basal, ciliated, and mucus-producing goblet cells. The ALI model is advantageous for drug testing, as it allows to administer drugs in the form of aerosols or particles^{214,215}. Furthermore, this method avoids any structural changes or dilution effects that can occur when drugs are added to cells in submerged culture systems. As a result, the ALI model provides a more accurate representation of how drugs or cells will behave in the respiratory tract^{214,215}.

One of the main drawback concerning ALI is that many monoculture ALI systems do not fully recapitulate the complexity of the airway microenvironment^{214,215}. The cellular interaction between different cell types, including epithelial cells, immune cells, and endothelial cells are, as described earlier in the manuscript, crucial to maintain airway homeostasis and response to injury^{214,215}. Therefore, researchers have increasingly switched to coculture models, where multiple cell types are cultured together, improving the relevance of the model^{214,215}. Coculture systems enable the study of intercellular interactions, such as the communication between epithelial cells and immune cells, which could be used to understand inflammatory responses and tissue repair mechanisms in the lungs^{214,215}. Another limitation of ALI culture models is the use of primary cells, which can be challenging to obtain in large quantities and may show variability between donors. While immortalized cell lines are more readily available and offer greater standardization, they also often fail to exhibit the full range of characteristics seen in primary cells due to their transformation and clonality^{214,215}. For instance, certain immortalized bronchial cell lines, such as 16HBE14o- and Calu-3, which are commonly used in ALI models, fail to recapitulate polarization or formation tight junctions^{214,215}.

An interesting recent study conducted on both healthy and Chronic Obstructive Pulmonary Disease (COPD)-derived BSCs was utilizing ALI culture to examine the response to radiation therapy (**Figure 33**)²¹⁶. Both groups of cells were exposed to 2 and 4 Gy of radiation, then cultured them in ALI conditions to assess their differentiation potential into a stratified and polarized epithelium. It revealed that irradiated COPD BSCs exhibited a significant defect in

mucociliary differentiation compared to non-irradiated controls. Additionally, there was a decrease in survival and differentiation capacity of COPD BSCs. The study also explored the molecular mechanisms behind this increased sensitivity. Specifically, COPD BSCs showed higher levels of DNA damage markers and a decreased ability to repair DNA damage, leading to increased apoptosis. These results highlight the potential of ALI culture models in studying radiation responses in human airway stem cells and underscore the differences in sensitivity between healthy and diseased lung cells for radiation therapy treatment.

Overall, the ALI culture model represents valuable advancement *in vitro* lung research. Its ability to mimic some of the structure, function, and responses of the human airway system makes it a relevant model for studying respiratory diseases, drug delivery, toxicology or early radiation response.

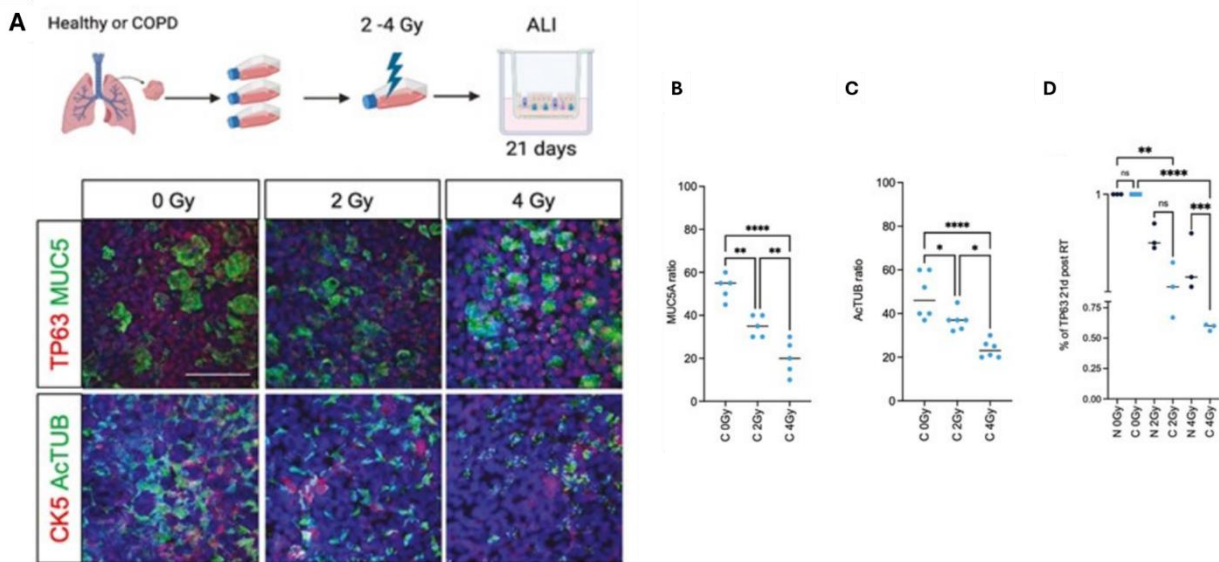


Figure 33. Differential sensitivity to COPD- and non-COPD PBEC irradiation in ALI culture Adapted from Giuranno et al. 2024. (A) Schematic representation of the treatment plan and representative examples of immunofluorescent staining of 3D ALI culture at day 21 ALI from COPD for TP63, CK5, MUC5AC, and Ac-TUB. (B) Quantification of MUC5AC and (C) ActTUB, and (D) TP63 in the non-COPD and COPD cultures upon irradiation (0-2-4 Gy) at 21 days in ALI expressed as ratio of total cells.

2.3.3 Pulmonary organoids: A promising tool for modeling RILI

Lung organoids are another 3D model in which the cells are able to self-organize into airway-like tissue forms, closely recapitulating some aspects of human lung tissue. These organoids could be generated from various sources of stem or progenitor cells, including adult stem cells (ASCs) (**Figure 34**), embryonic tissue, or induced pluripotent stem cells (iPSCs)^{214,215}. However, the stem cells source significantly influences the composition and complexity of the resulting lung organoids. Organoids derived from human pluripotent stem cells (hPSCs) typically express a more alveolar signature, featuring primarily AT1 and AT2 cells^{214,215}. In contrast, lung organoids derived from adult tissue, such as biopsies or bronchoalveolar lavage fluid, can contain more epithelial cell types, including basal, club, goblet, and ciliated cells^{214,215}.

The culture of lung organoids takes place in specialized 3D systems or matrices, such as Matrigel or the Celvivo system^{214,215}. These matrices provide a structural support for the organoids to form and maintain their shape. Organoids can be cultured either as submerged cultures or in air-liquid interface (ALI) conditions, which promote differentiation and simulate the natural lung environment^{214,215}. In ALI culture, the lung organoids can develop a mucociliary epithelium, featuring ciliated cells and mucus production. Proximal differentiation can be induced in alveolar organoids, which results in the development of ciliated cells^{214,215}.

Lung organoids are particularly valuable for high-throughput drug screening, as their 3D structure and cellular complexity make them more representative of human lung tissue compared to traditional 2D cultures^{214,215}. The organoids have also been used to model respiratory viral infections, such as those caused by respiratory syncytial virus (RSV) or influenza, providing insights into immune responses and pathogen-host interactions^{214,215}. Additionally, lung organoids can model both healthy and diseased lung states, enabling researchers to investigate COPD as well^{214,215}. The ability to generate donor-specific organoids for personalized medicine purpose is another innovative application. These organoids can be used to test how a patient's own lung tissue responds to various drugs or treatments which could be really interesting to measure sensitivity to radiation exposure^{214,215}. Finally, lung organoids are being used to study lung development and regeneration, providing valuable insights into the mechanisms behind lung growth and repair.

With all these characteristics, lung organoids would be an excellent model for studying RILI due to their ability to closely replicate the complex structure and cellular composition of human lung tissue. Their ability to self-organize into 3D structures and the possibility of adding immune

cells or endothelial cells into the culture make them ideal for modeling the inflammatory and vascular changes associated with RILI. They could offer a high level of control over radiation exposure, allowing researchers to study DNA damage, cellular hypertrophy, differentiation processes as well as regeneration and inflammation in response to various doses of radiation. Moreover, lung organoids are suitable for testing potential treatment combination with either radio-sensitizers, protectors, chemotherapy or immunotherapy. This makes lung organoids a promising tool for better understanding the mechanisms of RILI and developing new treatments.

Despite these promising applications, lung organoids, for now, have never been used in that purpose. They are also presenting several challenges. The complexity of the culture conditions required for their generation remains a major drawback, as it is essential to control the growth factors and matrix composition carefully^{214,215}. Additionally, achieving correct epithelial polarity and ensuring that proximal and distal cells develop in the appropriate proportions requires precise control over differentiation protocols^{214,215}.

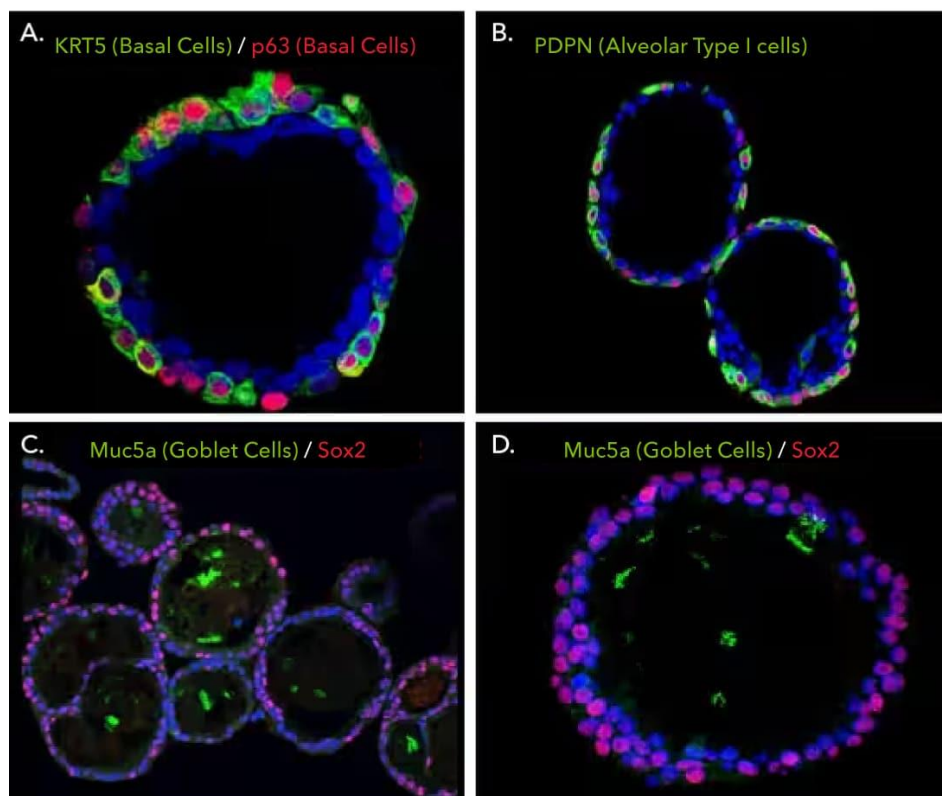


Figure 34. Characterization of Human Lung Organoids²¹⁷. *Adult stem cells isolated from human lung biopsy tissue were embedded in Cultrex UltiMatrix RGF Basement Membrane Extract and cultured in media for 20-60 days. Lung organoids were able to differentiate and exhibit markers for various cell types of the lung.*

2.3.4 Organ on chip : emergence of lung on chip to model acute RILI

Organ-on-chip technology represents a breakthrough in the development of *in vitro* models that replicate the complexities of organs. These are microfluidic devices that combine biological tissues and cells within a controlled, dynamic environment that mimics the physiological and mechanical conditions of the organ being studied. Organ-on-chip models enable the integration of multiple cell types, allowing for the simulation of organ functions such as fluid flow, mechanical stretching, and multi-cellular interactions that occur *in vivo*. For example, the gut-on-chip model integrates primary epithelial and stromal cells on a collagen scaffold to mimic the complex architecture of the intestinal wall. This system allows for the investigation of gut pathophysiology, including the effects of fluid shear stress on epithelial cell behavior, and provides insights into gastrointestinal diseases²¹⁸. Similarly, for the development of kidney-on-chip models, microfluidic devices that replicate nephron segments using small tubular channels coated with basement membrane components are used to study kidney diseases such as polycystic kidney disease. These devices have enabled to explore mechanotransduction and the interactions between kidney cells and their extracellular matrix, providing valuable data on nephropathies²¹⁹.

Building on these advances, lung-on-chip (LOC) could become an essential tool for modeling both healthy lung tissue and diseases that affect the lung, providing insights that *in vitro* and animal models cannot replicate. These systems were designed to simulate critical aspects of the lung, as they include a physiological flow, mechanical stretching forces, multi-compartment for co-cultures, and ECM interactions. Early LOC models began with simple 2D systems but have evolved into sophisticated multicellular and 3D models²²⁰. One of the most notable advances in LOC development was the creation of the alveolus-on-chip model, which integrates lung epithelial cells and endothelial cells. This model was further enhanced to include neutrophils to mimic infections and has been adapted for studying COVID-19. By using a micro-diaphragm to simulate the physical stretching of the lung tissue, researchers can now create environments that more closely mimic the mechanical properties of the lung during breathing²²⁰. Recent advancements have enabled the incorporation of primary human cells from healthy lung tissue into LOC platforms. However, the use of primary materials presents challenges due to their heterogeneity, which is being addressed by using type II alveolar epithelial cell organoids in LOC²²¹. These organoids help expand primary lung cells in hydrogels before integrating them into LOCs, improving the model's accuracy by better mimicking the human lung environment. In addition to modeling healthy lung tissue and common lung diseases, lung tumor-on-chip platforms has been used for studies on lung

cancer, particularly for understanding tumor-immune interactions and predicting patient-specific responses to immunotherapy. Recent advancements in lung tumor-on-chip technology have allowed for the creation of personalized tumor models, using patient-derived autologous cells from fresh tumor samples to evaluate individual responses to ICIs such as anti-PD-1²²².

LOC has been recently used to model acute RILI. In a model which consists of human lung alveolar epithelial cells cultured under ALI condition and interfaced with pulmonary endothelial cells, they create a model of alveolar-capillary barrier that was exposed to radiation (**Figure 35**)²²³. When exposed to 16 Gy radiation, the Lung alveolus chip recapitulates several hallmark features of acute RILI, including DNA damage, cellular hypertrophy, and inflammatory responses. Both the alveolar epithelium and the endothelial cells exhibit DSBs, as evidenced by the formation of 53bp1 foci, within just a few hours of radiation exposure. Moreover, exposure to radiation results in the disruption of tight junctions between cells, leading to increased barrier permeability which is a critical feature of RILI that was observed after 6 hours of radiation exposure at 16 Gy. The increase in permeability allows for the accumulation of edema fluid in the epithelial channel, which mimics the fluid accumulation seen in patients with RILI. The model also demonstrates the inflammatory response associated with RILI. In the presence of human peripheral blood mononuclear cells (PBMCs), radiation exposure triggers the upregulation of proinflammatory cytokines such as IL-6, IL-8, and TNF- α . The inflammation response is sustained over several days, further mimicking the clinical progression of RILI, which typically develops 1-3 weeks post-exposure²²³.

This Lung Alveolus Chip also offers an opportunity for drug testing against acute RILI. For example, the effects of lovastatin and prednisolone, two drugs commonly used to manage RILI, were evaluated using this model²²³. Lovastatin, which is known to upregulate HMOX1, an antioxidant enzyme involved in cellular protection against oxidative stress, significantly reduced DNA damage and cell hypertrophy. It also suppressed the inflammatory response by reducing the levels of IL-6 and TNF- α shortly after radiation exposure. Prednisolone is a glucocorticoid widely used in radiation therapy to manage inflammation, also showed protective effects by reducing DNA damage and cellular hypertrophy, but its effect on inflammatory cytokines was less pronounced compared to lovastatin. Interestingly, prolonged treatment with lovastatin led to elevated HMOX1 levels even after 7 days, suggesting that while HMOX1 can initially protect cells from radiation-induced damage, its prolonged upregulation may have a detrimental effect, possibly contributing to tissue dysfunction over time. This finding highlights the complexity of using HMOX1 as a therapeutic target, and the need for careful modulation of its activity²²³.

Ov

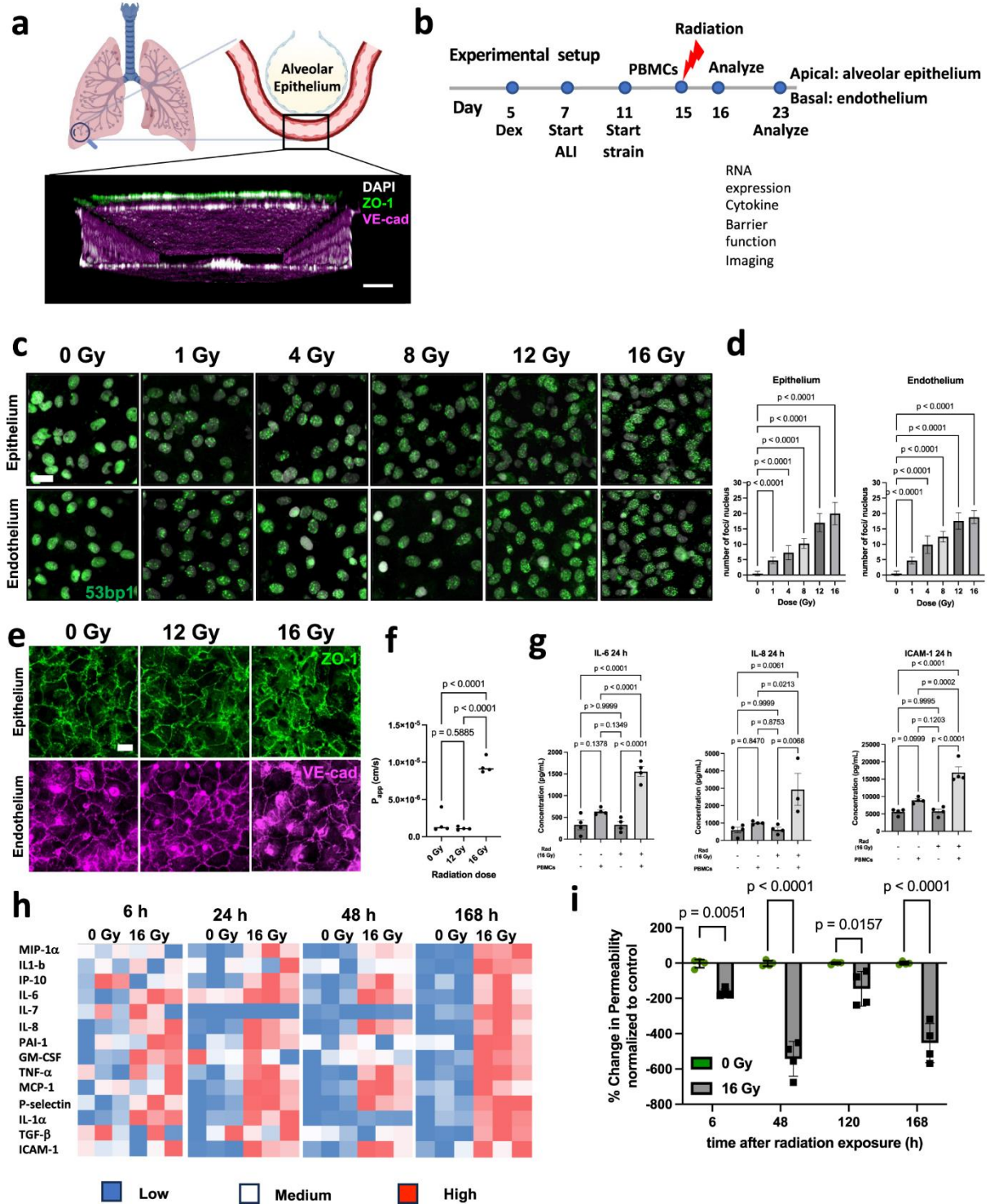


Figure 35. Human Lung Alveolus Chip recapitulates hallmark features of RILI. (a) Schematic of the alveolus-on chip model, showing the confocal z-stack illustrating endothelial tube formation. Scale bar = 100 μ m. (b) Experimental plan, Dex, dexamethasone; ALI, air-liquid

interface. (c) 53bp1 immunostaining (green) for double-stranded DNA breaks 2 h after radiation. DAPI counterstaining is shown in white. Scale bar = 20 μm . (d) Formation of 53BP1 foci was quantified per nucleus and showed a dose-dependent increase for both alveolar epithelial and endothelial cells. (e) Immunostaining with ZO-1 (epithelial cells; green) and VE-cadherin junctions (endothelial cells; magenta) post irradiation, showed that junction disruption required a minimum dosage of 16 Gy. Scale bar = 20 μm . (f) Barrier function assay showed a 7-fold increase in the apparent permeability co-efficient (P_{app}) at 6 h post radiation exposure to 16 Gy, but no difference in response to 12 Gy. (h) Heatmap showing cytokine response to radiation at 6 h, 24 h, 48 h and 7 d post radiation exposure, in the presence of PBMCs, $n = 3$ chips for each condition, $p < 0.05$. % change in barrier integrity normalized to 0 Gy control over 7 days post-radiation exposure, in the presence of PBMCs.

This kind of Lung Alveolus Chip model can offer a highly relevant, human-based alternative to animal models for studying RILI. Despite these advancements, several challenges remain. The scalability and cost of LOC systems are obstacles, although several startups are helping to address these issues by offering customizable chips that facilitate the use of LOC technology across research fields.

2.3.5 Organotypic slices model : focus on Precision Cut Lung Slices (PCLS) as an innovative tool for RILI

The Precision-Cut Lung Slices (PCLS) or organotypic lung slices model emerged in the 1990s as an innovative *ex vivo* model to study lung functions and pathologies²²⁴. The development of PCLS was made possible by advances in tissue preparation methods and specialized tools such as the microtome and vibratome, which allow precise slicing of tissues that preserve their structural integrity and cellular composition. Initially, PCLS were used for toxicological studies to evaluate cellular survival and the impact of environmental pollutants. Over time, it became evident that these slices could offer a more realistic representation of intact lung tissue, enabling more complex studies on chronic and acute lung diseases, such as pulmonary fibrosis, asthma, COPD, and could probably be relevant for acute RILI²²⁴.

The preparation of PCLS involves a rigorous method to preserve the functional and structural integrity of lung tissue. It begins by inflating the lungs with a low-melting-point agarose solution (0.75% to 3%), injected into the airways of animals or human lung explants^{221,224,225}. Once the agarose solidifies, the lungs are sliced into 100-500 µm-thick sections using vibratomes or rotary slicers, harvesting thin slices that retain the cell and ECM integrity^{221,224,225}. In some cases, the thickness of the slices may pose an issue, as the readouts can vary based on slice thickness^{221,224,225}. Additionally, the process of cutting and embedding lung tissue in agarose can activate repair and regenerative mechanisms, which might influence subsequent experiments^{221,224,225}. To minimize the impact of these processing steps, washing and resting steps before starting experiments can help reduce these effects. After slicing, the lung tissue slice are placed in culture with appropriate media and can be used for various experimental procedures^{221,224,225}. PCLS has been reported to be viable from 3 to 7 days in culture which remains short and limit analysis to acute response. However, engineered hydrogel biomaterials support has been recently developed to extend the *ex vivo* culture of PCLS (**Figure 36**)²²⁶. With this biomaterial, viability and architecture of PCLS is maintained up to 21 days in culture which is useful for long term analysis. Cryopreservation of PCLS is another way forward for maximizing the number of slices that can be used per lung. However, current protocols under development for cryopreservation need further improvement to enhance PCLS viability and functionality upon revival^{221,224,225}.

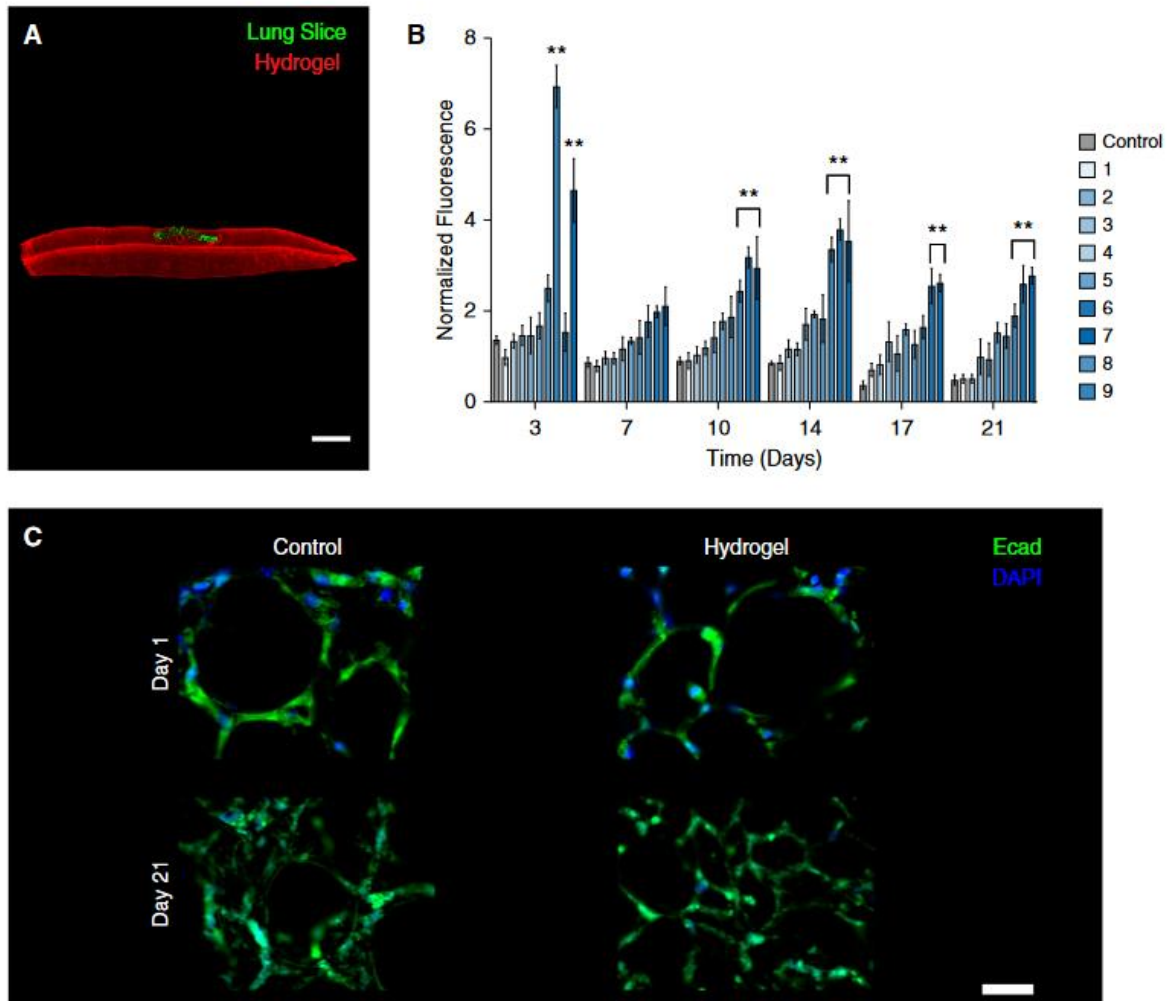


Figure 36. Embedding of Precision-Cut Lung Slices in Engineered Hydrogel Biomaterials Supports Extended Ex Vivo Culture from Bailey et al. (A) Representative images for PCLS (green) embedded within hydrogel (red) show that embedding by 3D printing led to more uniform hydrogel distribution around slices. Scale bar: 1 mm. (B) PCLS viability was monitored over 21 days using the PrestoBlue Cell Viability Reagent both in nonembedded PCLS controls and after embedding in nine different hydrogel conditions using 3D printing. Fluorescence intensities normalized to Day 1 show that some hydrogel conditions maintained significantly higher cellular metabolic activity over time than PCLS controls ($n = 5$). $**P < 0.05$ by ANOVA, Tukey test. (C) Representative immunofluorescent images in cross-section of nonembedded control and best-performing hydrogel samples stained for DAPI and E-cadherin (Ecad) show that hydrogels support maintenance of PCLS architecture over time. Scale bar: 10 μm .

Over the last decade, PCLS model has been well characterized. Indeed, PCLS maintain the native architecture of the lung, including airways, blood vessels, parenchyma and alveoli (**Figure 37A-B**)^{221,224,225,227,228}. This allows researchers to study cellular interactions within the context of the lung tissue. Various cell types, including epithelial cells (**Figure 37C**), smooth muscle cells, fibroblasts, and resident immune cells such as DC and macrophages (**Figure 37C**), are preserved, enabling comprehensive studies of inflammatory responses, tissue repair, and pulmonary function^{221,224,225,227,228}.

Advanced imaging techniques, such as high-resolution microscopy and cellular labeling, enable the real-time study of cellular activity and structural changes in the tissue, which is a major advantage of the PCLS model^{223,226,227}. PCLS generation specifically from human tissue has several other important advantages. Indeed, PCLS allows paired analysis of several treatments in the same patient. Also, they can be generated from different areas within the same lung to represent tissue heterogeneity and finally the generation of PCLS from tissue explants from healthy donors can be applied for *ex vivo* modeling of disease, or even radiation response. Thus, the model of PCLS has been used for various applications from studying lung physiology, chronic obstructive lung disease, lung cancer response and drug testing in the last years (**Figure 38**)^{223,226,227}.

More particularly, PCLS has been widely used to model lung IPF. IPF is a fibrotic disease of the lung tissue surrounding the alveoli that progressively stiffens the lung, making it difficult for the person to breathe which is close to the RIPF due to radiation treatment. Studies have utilized PCLS to identify the cell types that drive fibrosis signals^{229–231}. A number of pharmacologic inhibitors have been used as potential treatments for IPF^{232–236}, including current therapeutics that are being used in the clinics for the treatment of IPF, like nintedanib and pirfenidone^{237–239}. However, despite the major advantages and the relevance of the model, it has never been used to model the acute response to radiation in the lung in the same way as it has been used in the brain²⁴⁰.

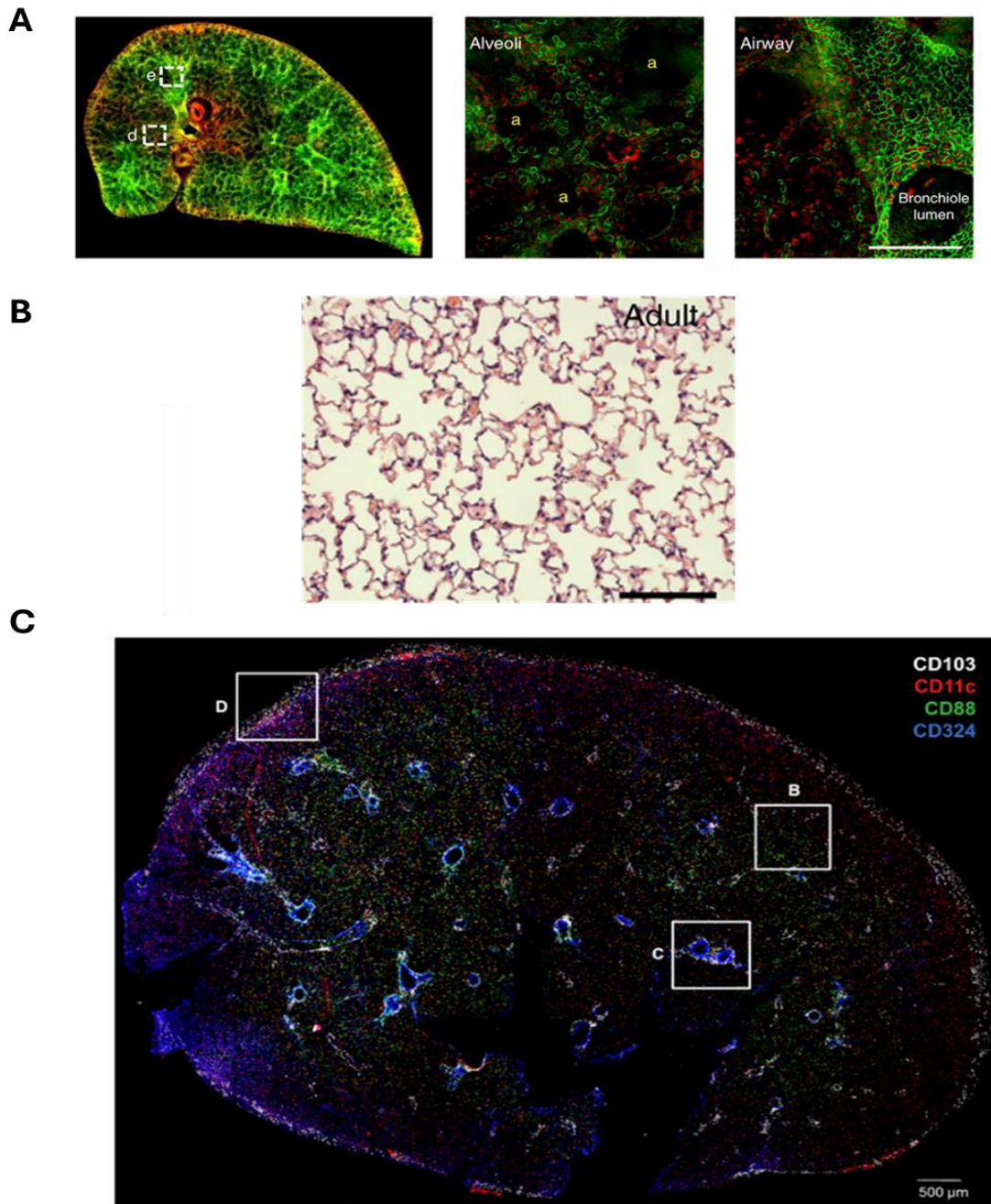


Figure 37. Characterization of PCLS structure and cellular microenvironment, Adapted from Akram et al. and Lyons-Cohen et al. (A) Deconvolved widefield, single plane z-stack image of PCLS. Epithelial cells were labelled EpCAM-FITC antibody (green) and cell nuclei were labelled with SiR-DNA (red). Boxed areas show EpCAM-FITC +ve cells in alveolar and airway epithelial cells. Scale bar = 50 μ m. (B) H&E staining of PCLS section in adult mice. (C) Whole PCLS from mouse lungs stained with various antibodies : CD103⁺ cDCs (CD103⁺CD11c⁺CD88⁻; white), CD11b^{hi} cDCs (CD11c⁺CD103⁻CD88⁻; red), macrophages (CD11c⁺CD88⁺; yellow), neutrophils (CD11c⁻CD88⁺; green) and airway epithelial cells (CD324⁺; blue).

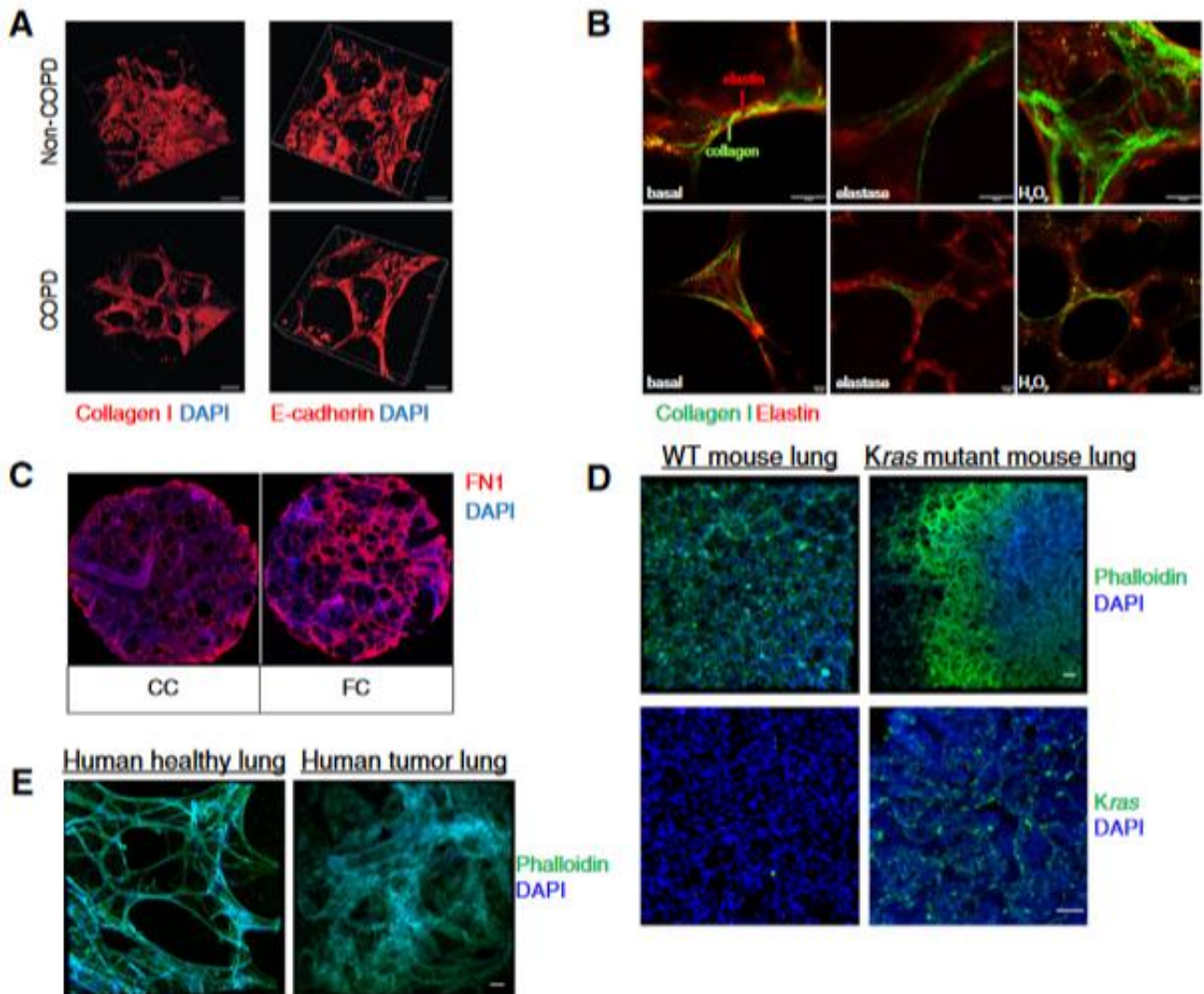


Figure 38. Various applications of PCLS for modeling COPD, IPF and lung cancer from Alsafadi et al. (A) Three-dimensional reconstruction of collagen I and E-cadherin staining on PCLS generated from healthy and COPD human explants. Scale bars: 100 μ m. (B) Collagen I and elastin fibers in an ex vivo elastase COPD disease model in mouse PCLS. Scale bars: 10 μ m. (C) Extracellular matrix deposition of fibronectin in PCLS treated with a fibrotic cocktail (FC) to model early fibrosis-like changes (48). Scale bar: 1 mm. (D) PCLS immunostained against phalloidin and Kras. PCLS were obtained from the mouse KRAS model. Scale bars: 50 μ m. (E) Structural differences between tumor and tumor-free regions of PCLS generated from human explants. Scale bars: 50 μ m. CC = control cocktail; FN1 = fibronectin; WT = wild-type.

However, despite many advantages, there are several drawbacks associated with PCLS. One of the main challenges is the limited viability of the slices in culture^{223,226,227}. While PCLS can be cultured for periods ranging from 1 to 28 days as reported in the literature, their viability decreases over time, which limits long-term studies^{223,226,227}. Additionally, although the slices preserve their lung architecture, the lack of circulatory flow may affect the delivery of nutrients and growth factors, which is crucial for long-term cell survival^{223,226,227}. Another limitation is the standardization of the PCLS preparation method^{223,226,227}. Variations in the slicing, culturing, and treatment protocols across different laboratories can introduce variability, making comparisons between studies difficult and potentially affecting the reproducibility of results^{223,226,227}.

In conclusion, PCLS is a highly relevant and physiologically accurate *ex vivo* model for studying a wide array of lung diseases, including IPF, lung cancer, and COPD. The model offers numerous advantages such as the preservation of the lung's native architecture, the retention of multiple cell types, and the ability to study cellular interactions in a controlled 3D environment. While PCLS has been widely used for studying long-term diseases and their progression, it also holds great potential for modeling acute responses in the lung, including RILI. The proximity of IPF and RILI in terms of fibrotic changes and the similarity in lung tissue damage associated with both conditions suggest that PCLS can be a useful platform for investigating the acute effects of radiation exposure. Overall, the ability to closely replicate the lung's complex tissue architecture and cellular interactions, combined with its versatility in disease modeling and drug testing, makes PCLS a valuable tool for studying RILI. It offers a unique opportunity to investigate acute lung responses to radiation exposure and to test therapeutic interventions in a more representative lung model, bridging the gap between traditional *in vitro* and animal models.

2.3.6 Conclusion : Which is the best model for acute RILI modeling ?

As described in previous section, RILI is a complex condition that can have both acute and chronic stages. Understanding the acute response to radiation exposure in lung tissue is critical for the development of effective treatment strategies. The choice of model used to study acute RILI significantly can influence the results, and various models offer distinct advantages and drawbacks in terms of complexity, scalability, and physiological relevance (**Figure 39**).

The classical 2D cultured epithelial lung cells are the simplest model in terms of handling. Despite they offer high throughput for testing drugs and radiation responses, this model lacks the complexity of the lung's 3D architecture and cannot fully replicate the interaction between different cell types, including immune cells, which play a crucial role in radiation responses. Additionally, the absence of gas exchange and cellular polarization limits the model's ability to mimic real-life lung functions and responses to radiation exposure.

In contrast, the ALI model allows for the exposure of cells to air, which supports differentiation and simulates *in vivo* conditions such as gas exchange. This model has been useful for understanding radiation impacts on airway cells. However, it is still limited by the lack of full lung complexity and the challenges of culturing primary cells, in which response can be variable between donors.

Then, lung organoids, being a 3D culture model, closely mimic the lung's cellular architecture and offer significant advantages over simpler models in studying RILI. They contain both proximal and distal lung cell types, which are essential for studying radiation-induced damage across different lung compartments. Furthermore, they can be used in co-culture systems with immune cells to better mimic the immune response to radiation. However, the complexity of their culture conditions and the difficulties in maintaining organoid functionality under various experimental setups pose challenges for high-throughput screening or comparison of radiation modalities.

More technologically advanced, LOC models represent another innovative approach for modeling RILI, offering a highly dynamic environment that replicates key aspects of lung physiology, such as mechanical stretching and fluid flow. The integration of epithelial cells and endothelial cells in a microfluidic chip setup simulates the alveolar-capillary barrier, which is crucial for studying radiation's impact on lung tissue integrity. Additionally, LOC models can incorporate immune cells, allowing for the study of the inflammatory cascade that follows radiation exposure. However, the main challenge for LOC systems lies in their complexity, as they require specialized equipment and technical expertise to establish and maintain.

Finally, PCLS stands out as an excellent model for studying acute RILI. The key advantage of PCLS is that they retain the native lung architecture, including airways, blood vessels, and alveoli, as well as various resident cell types, such as epithelial cells, fibroblasts, and immune cells. This allows for the study of radiation-induced tissue damage in a more physiologically relevant setting compared to simpler 2D models. PCLS can be cultured *ex vivo* and exposed to radiation while maintaining cellular interactions and structural integrity, making them particularly useful for modeling the acute inflammatory responses and early fibrotic changes associated with RILI. However, challenges such as limited tissue viability, the need for standardization, and the potential lack of full circulatory function can impact the reproducibility of results.


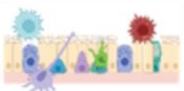
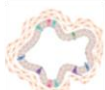

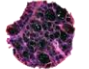
Model	Handling	Advantage	Disadvantage
2D cultured epithelial lung cells 	<ul style="list-style-type: none"> Easy system using primary cells, which can be used for many passages 	<ul style="list-style-type: none"> Fast, simple; common cell culture plastic; commercially available; high throughput testing 	<ul style="list-style-type: none"> No polarization, thus no ciliated and secretory cells no gas exchange; rarely reflects in vivo situation cell lines degenerated
Human airway epithelial cells in air-liquid interface (ALI) 	<ul style="list-style-type: none"> Primary cells cultivated on transwells; Use up to three passages (higher passages result in less differentiated epithelial cells) 	<ul style="list-style-type: none"> Differentiation to mucociliary pseudostratified epithelial culture Exposure to air allows gas exchange; commercially available 	<ul style="list-style-type: none"> More complex culture due to transwell use coated with hydrogel; Minimum culture time of 21 days to result in differentiated epithelium
Lung organoids 	<ul style="list-style-type: none"> Complex culture conditions; internally orientated ciliated apical surface; differentiation to proximal phenotype possible; culture for many passages 	<ul style="list-style-type: none"> Self-organizing 3D structure; coexistence of proximal and distal cell types; dependent on source of the stem cells, commercially available 	<ul style="list-style-type: none"> Sophisticated culture conditions; reversal of epithelial polarity in order to face apical surface outward
Lung-on-chip 	<ul style="list-style-type: none"> Complex 3D model system; addition of primary cells or cell lines possible 	<ul style="list-style-type: none"> Multicellular tissue combined with electronic sensors allow to monitor organ and tissue function in real time; possibility to couple it with microfluidic devices 	<ul style="list-style-type: none"> Very complicated system, which needs establishment and special equipment
Precision-cut lung slices (PCLS) 	<ul style="list-style-type: none"> Isolation from explanted human lung 	<ul style="list-style-type: none"> Contain all cell types and extracellular matrix; Complex architecture remains in the model; submerged and all culture possible; commercially available 	<ul style="list-style-type: none"> Preparation of fresh PCLS is challenging; Short duration of viability and changes in tissue architecture over time; Increased inflammatory markers due to tissue preparation

Figure 39. Comparative study on various lung model advantages and drawbacks.

My thesis will specifically concentrate on the molecular and cellular characterization of FLASH-RT mechanisms in the lung context. This modality gained significant attention for its potential to improve the therapeutic index by sparing the healthy tissue exposed to radiation while maintaining an antitumoral isoefficacy. Thus, in the next section of this manuscript, I will describe what is ultra-high dose rate radiotherapy and provide the first mechanistic insight for the FLASH sparing effect as well as the clue for clinical translation of this modality.

3. FLASH, A NEW WAY TO DELIVER RADIATION THERAPY

A study conducted by Favaudon et al. in 2014²⁴¹ challenged the conventional perspectives in radiobiology and introduced a new possibility for improving treatment outcomes using ultrahigh-dose rate radiotherapy (UHDR). While the concept of adjusting dose rate for therapeutic advantages wasn't completely novel, it had been ignored. Years ago, research on high-dose rate mainly examined immediate effects on skin, neglecting the impact on tumoral tissue^{242–244}. Previous studies indicated that some healthy tissues were less damaged at higher dose rates, suggesting that tumors could also benefit from this sparing effect, which could limit the usefulness of this approach in clinical practice.

Nevertheless, Favaudon et al. were the pioneers in presenting *in vivo* evidence of the so-called FLASH effect, showing both protection of normal tissue and a similar slowing of tumor growth at dose rate that were superior to 40 Gy/s (**Figure 40**). Indeed, from 24, and at 36 weeks post-treatment, lungs irradiated with a single dose of 17 Gy at dose rate of 0.03 Gy/s of conventional γ -rays exhibited fibrosis, interstitial thickening, and alveolar damage while lungs treated with FLASH showed less structural damage and a preserved lung architecture. These findings suggest that FLASH-RT can reduce long-term pulmonary toxicity compared to conventional irradiation²⁴¹. Xenograft tumor growth monitored using relative tumor volume over time, after CONV or FLASH-RT at 17 Gy was similar²⁴¹. It indicates that FLASH-RT maintains an isoefficient tumor control while delivering radiation at ultrahigh dose rates. Finally, the same was true for orthotopic lung tumor control of TC1-tumor bearing mice²⁴¹. This discovery unveiled new possibilities for enhancing the differential impact of radiotherapy on tumors and normal tissues.

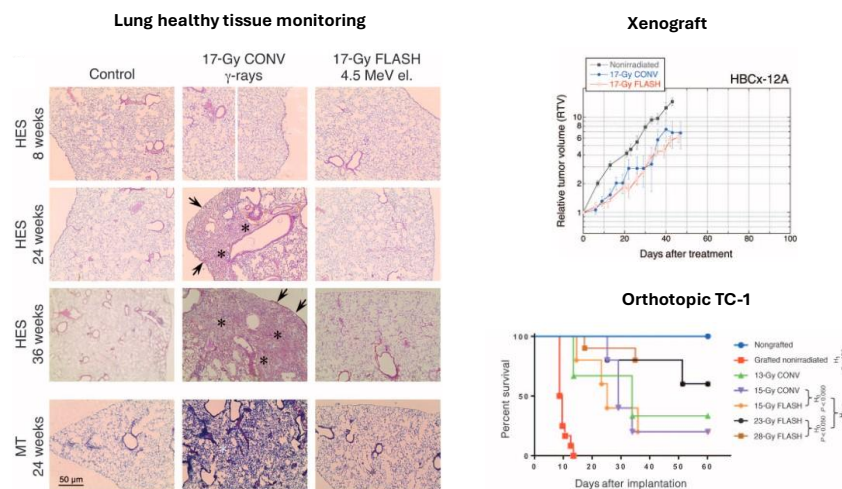


Figure 40. First Evidence of the FLASH Effect *in vivo*. Adapted from Favaudon et al. 2014.

3.1 The FLASH sparing effect in preclinical-murine models.

Following this work, the biological sparing effect of FLASH radiotherapy has been studied and observed across institutions and organs. Majority of studies were done in mouse preclinical models of radiation-induced toxicities. In the next subsection, we will discuss the various acute and late protective effects observed in murine models in the brain, gut, skin, heart and lungs, aiding describing the mechanisms of this sparing effect in various organs.

3.1.1 *FLASH-RT preserves cognitive function and reduces neuroinflammation*

Following the discovery of the protective effect of FLASH in the lungs, the next step was to assess whether this effect was organ-specific or could be generalized to multiple organs. The brain was an ideal choice to start this investigation because it is known to be highly sensitive to radiation due to its limited regenerative capacity and high susceptibility to late effects like cognitive decline and neuroinflammation. Conventional radiotherapy often leads to severe long-term side effects, including memory loss, neurogenesis impairment, and radiation-induced neurodegeneration²⁴⁵. Montay Gruel et al. first demonstrated that FLASH whole brain irradiation (WBI) at dose rate above 100 Gy/s preserved spatial memory and neurogenesis in mice comparing a single fraction of 10 Gy, contrasting with the cognitive impairment seen at conventional dose rates. Indeed, BrdU incorporation revealed significantly better preservation of hippocampal neurogenesis with FLASH WBI compared to CONV-RT (**Figure 41A**)²⁴⁶. Later, Montay Gruel et al. expanded these findings, showing that six months after irradiation, mice exposed to conventional dose rates experienced long-term neurocognitive deficits, while those exposed to FLASH retained memory function and showed no signs of anxiety or depression-like behaviors. Notably, the neuroprotective effects of FLASH were linked to reduced oxidative stress and neuroinflammation²⁴⁷. Furthering this research, they revealed that markers for astrogliosis and immune signaling (e.g., GFAP and TLR4) were expressed at lower levels following FLASH irradiation compared to conventional irradiation, while markers like C1q and C3 were elevated in both modalities. These findings underscore the distinctive protective effects of FLASH on brain tissue, particularly concerning neuroinflammation²⁴⁸. Limoli et al. contributed significantly to the understanding of the long-term protective effects of FLASH on synaptic plasticity. In their studies, they showed that FLASH-RT, when delivered in 3 × 10 Gy fractions, preserved cognitive performance and protected synaptic plasticity, maintaining synaptophysin levels and reducing neuroinflammation (marked by CD68+ microglia activation) in the hippocampus and prefrontal cortex. This preservation extended to the structural level, with no ultrastructural changes observed in presynaptic and postsynaptic bouton densities²⁴⁹. Their latest research corroborated these findings over a longer follow-up,

showing that FLASH irradiation maintained hippocampal neurogenesis, synaptic plasticity, and cerebrovascular structure, reducing neuroinflammation and preserving cognitive functions. These studies collectively underscore the neuroprotective potential of FLASH in the brain, offering a promising approach to mitigating radiation-induced cognitive decline due to radiotherapy treatment²⁵⁰.

3.1.2 FLASH-RT reduces gastrointestinal toxicity by preserving intestinal crypts

The intestines are particularly vulnerable during radiotherapy due to their highly proliferative crypt cells and susceptibility to gastrointestinal syndrome. Indeed, abdominal radiotherapy is limited by the radiosensitivity of the intestine, which significantly restricts the dose that can be safely administered to treat tumors near this organ²⁵¹. Levy et al. first demonstrated that total abdominal irradiation with FLASH reduced the occurrence of gastrointestinal syndrome, sparing crypt cells (**Figure 41B**), preserving epithelial integrity, and enhancing survival compared to CONV-RT²⁵². This key finding suggested potential to broaden the application of radiotherapy in abdominal cancers, particularly when addressing large tumor volumes or multiple metastatic sites while sparing healthy gut tissue. Subsequent studies focused on proton therapy, comparing FLASH proton radiotherapy (F-PRT) and conventional proton radiotherapy (S-PRT) using both the entrance and spread-out Bragg peak (SOBP) regions. Their results indicated that F-PRT preserved significantly more intestinal crypt cells and boosted regeneration post-irradiation compared to S-PRT²⁵³. In 2021, Ruan et al. further investigated the crypt-sparing effects of FLASH in the intestines. Their findings confirmed that FLASH delivered at dose rates above 280 Gy/s significantly increased crypt survival, especially in doses ranging from 7.5 Gy to 12.5 Gy. Notably, this protective effect diminished when irradiation time was extended, reinforcing the importance of the mean dose rate and pulse timing parameters in achieving the protective effects of FLASH as it will be further described later in this manuscript. Moreover, FLASH irradiation caused fewer alterations in the gut microbiome, suggesting additional benefits in minimizing long-term complications²⁵⁴. More recently, new studies provided insights into the underlying mechanisms of the intestinal FLASH effect. Using single cell transcriptomic analysis, they show that FLASH induce an accelerated differentiation of revival stem cells, a rare damage-induced cell population required for intestinal regeneration²⁵⁵. FLASH-induced better proliferation of these damage-induced progenitor cells, supported by immune responses such as macrophage-driven TGF- β signaling, leading to an improved tissue recovery. In summary, these preclinical studies collectively establish the protective effects of FLASH in the intestines, highlighting its capacity to spare sensitive crypt cells, reduce gastrointestinal toxicity, and promote recovery post-irradiation without compromising tumor control.

3.1.3 FLASH-RT preserves skin Integrity by reducing radiation-induced toxicities

Cutaneous tissue is one of the most radiosensitive tissues during cancer treatment, especially in head and neck, breast, or thoracic radiotherapy, where the skin is frequently exposed to radiation. Conventional radiotherapy often leads to severe acute and late skin toxicities, such as dermatitis, ulceration, fibrosis, and atrophy, significantly impacting patients' quality of life²⁵⁶. In an initial study conducted by Soto et al., the protective effect of FLASH was evaluated in murine models through hemithoracic irradiation at various doses from 20 to 40 Gy²⁵⁷. The results showed a significant reduction in the incidence and severity of skin ulceration at 30 and 40 Gy when using FLASH compared to CONV-RT²⁵⁷. The median survival was also notably higher with FLASH irradiation (superior at 180 days at both 30 and 40 Gy), compared to CONV-RT (100 and 52 days respectively at 30 and 40 Gy)²⁵⁷. Velapopoulo et al. extended these observations by examining the effects of FLASH-proton radiotherapy (F-PRT) compared to standard-proton radiotherapy (S-PRT) on skin, muscle, and bone tissues in murine hind legs²⁵⁸. Their study demonstrated that F-PRT significantly reduced severe toxicities, such as skin injury (**Figure 41C**), lymphedema, and inflammation, while mitigating late effects like hair follicle atrophy, epidermal hyperplasia, and myofiber atrophy²⁵⁸. These protective effects were not seen in S-PRT, which induced higher levels of pro-inflammatory markers and fibrosis-related pathways. RNA-seq analyses revealed that F-PRT spared pathways involved in apoptosis and keratinocyte differentiation, which were upregulated in S-PRT²⁵⁸. Together, these studies highlight the potential of FLASH to protect cutaneous tissue from radiation-induced damage, offering a significant advancement in the therapeutic index by allowing higher doses to tumors without increasing skin toxicities. This is particularly relevant for tumors located near sensitive tissues or in patients requiring high-dose regimens.

3.1.4 FLASH-RT preserves heart functions by reducing cardiac radio-induced toxicities

Recent studies on cardiac tissue have demonstrated that F-PRT offers significant cardioprotective benefits compared to S-PRT²⁵⁹. In experiments on mice, F-PRT minimized both acute and chronic cardiac toxicities, particularly in the heart's apex (**Figure 41D**)²⁵⁹. RNA-sequencing revealed that S-PRT activated inflammatory and fibrotic pathways, whereas F-PRT mainly influenced cellular processes like ATP synthesis and cytoplasmic translation. Notably, F-PRT reduced collagen deposition and preserved cardiac function, as measured through echocardiograms at 8 and 30 weeks post-treatment, illustrating its potential to enhance therapeutic outcomes while reducing cardiac damage²⁵⁹.

3.1.5 FLASH-RT preserves lung regenerative capacity while reducing DNA Damage

Following the initial work by Favaudon et al., further investigations into the FLASH effect in lung tissue have provided a more comprehensive understanding of its protective capabilities. One study by Fouillade et al. demonstrated that FLASH reduces DNA damage as well as preserved lung regenerative potential week after radiation therapy compared to CONV-RT response where an exhaustion of these progenitor was described (**Figure 41E**)²⁶⁰. Notably, *in vitro* studies also revealed lower levels of DNA damage and lethality under FLASH compared to conventional radiation²⁶⁰. Additionally, late-stage observations showed that FLASH resulted in fewer persistent DNA damage markers and senescent cells, suggesting that FLASH enhances tissue recovery and regeneration²⁶⁰.

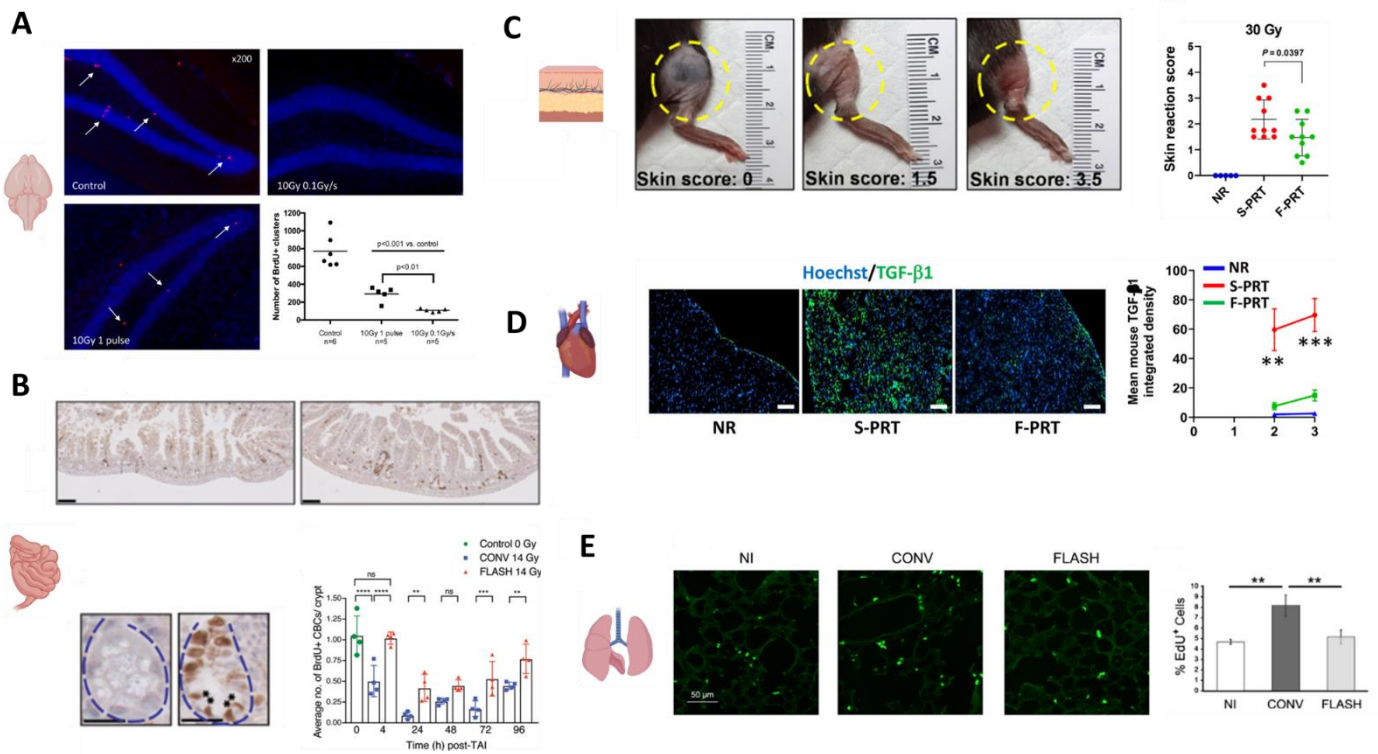


Figure 41. FLASH sparing effect on various healthy murine tissues. (A) FLASH-RT preserved hippocampal neurogenesis, as indicated by significantly higher BrdU-positive remaining clusters compared to CONV-RT. (B) FLASH-RT spared crypt cells in the intestines following total abdominal irradiation, maintaining higher levels of cell proliferation. (C) FLASH-RT significantly reduced skin toxicity compared to CONV-RT, as demonstrated by lower ulceration scores after hemithoracic irradiation. (D) FLASH-RT minimized cardiac fibrosis and inflammation, maintaining heart function better than standard proton RT. (E) FLASH-RT enhanced lung regenerative potential compared to CONV-RT.

The remarkable discovery of the FLASH sparing effect has opened new avenues for improving the therapeutic index of radiotherapy, specifically by reducing the toxicity to healthy tissues. The distinct biological benefits of FLASH radiotherapy have now been widely observed across various organs in preclinical murine models, with protective effects reported for both acute and late toxicities. In different organs, such as the brain, intestines, skin, and lungs, the findings provide compelling evidence that FLASH significantly mitigates the adverse effects typically induced by conventional radiotherapy.

3.1.6 Reproducibility of the FLASH sparing effect across institutions

While most pre-clinical studies investigating FLASH radiotherapy demonstrate a significant protective effect on normal tissues, a small subset of studies presents conflicting results. Over 85% of research, particularly in murine models, has consistently shown that FLASH reduces radiation-induced toxicities in organs such as the brain, lungs, intestines, and skin. This sparing effect has been observed at ultra-high dose rates, typically exceeding 40 Gy/s. However, in less than 15% of studies, the protective benefits of FLASH were either absent or less pronounced, often due to differences in dose rate thresholds, temporal structures of dose delivery, or variability in dosimetric practices²⁶¹. These discrepancies underscore the importance of standardizing experimental conditions and ensuring rigorous cross-institutional replication. For example, multi-institutional studies have recently been carried out on the replication of the FLASH effect and its characteristics in the brain on 2 different Linacs and the results are very encouraging²⁵⁰. Indeed, establishing reproducible results across various models and irradiation systems is crucial to fully validate the FLASH effect as it moves toward clinical application. However, the effectiveness of FLASH in sparing healthy tissues is not uniform across different organs, and understanding this variability is key to optimizing its application. One important metric to quantify this effect is the Dose Modifying Factor (DMF), which provides insights into the extent of protection FLASH offers relative to conventional radiotherapy.

3.1.7 How to quantify the FLASH sparing effect in various organs

The Dose Modifying Factor (DMF) is a critical measure in radiobiology used to quantify the ratio between doses needed to achieve the same biological effect under varying radiation conditions. For instance, if a study reports a DMF of 1.3, this indicates that FLASH-RT can reduce the radiation dose by 30% while achieving the same biological effect as conventional radiotherapy. This is particularly important for minimizing the adverse effects on healthy tissues during treatment. In murine models, the DMF varies across organs, reflecting the different

degrees of protection FLASH provides. The lungs, for example, show the most pronounced sparing effect, with DMF values ranging from 1.1 to as high as 1.8, particularly in early studies by Favaudon et al (**Figure 42**). This suggests that FLASH-RT can reduce the dose by up to 80% in certain instances while maintaining the same biological outcomes, significantly enhancing the therapeutic index. In contrast, the brain, intestines, and skin exhibit slightly lower DMF ranges, with values between 1.1 and 1.4 in the brain, 1.1 and 1.3 in the intestines, and 1.1 and 1.6 in the skin (**Figure 42**). Although these values are lower than those seen in the lungs, they still represent substantial protection against both early and late radiation-induced toxicities. The sparing effect of FLASH-RT is observed not only in acute toxicities, such as inflammation and DNA damage but also in late-stage outcomes, including fibrosis, cognitive decline, and regenerative capacity. For instance, the brain shows better cognitive outcomes and preserved synaptic plasticity, the intestines exhibit enhanced regeneration of crypt cells, the skin suffers fewer instances of fibrosis and ulceration, and the lungs maintain better functional recovery post-irradiation. Together, these findings demonstrate that FLASH has the potential to reduce early and late toxicities across various tissues, offering a distinct therapeutic advantage over conventional radiotherapy.

The promising results from these preclinical studies have laid a strong foundation for future clinical trials, but questions regarding the reproducibility of these effects across different irradiation systems and institutions remain and will be further described in next sections of this manuscript. Establishing consistency of the FLASH effect will be a critical step in translating these findings into clinical practice, ensuring that the sparing effect is robust and can be applied across different clinical settings. While the protective effects of FLASH radiotherapy on healthy tissues are well documented, a key concern for its clinical application is whether FLASH maintains the same tumor control efficacy as conventional radiotherapy. The next section will delve into studies exploring the antitumoral isoefficacy of FLASH, examining whether tumor response remains uncompromised when using this innovative high-dose-rate approach.

Organ	Dose Modifying Factor Range
Brain	[1.1-1.4]
Intestines	[1.1-1.3]
Lungs	[1.1-1.8]
Skin	[1.1-1.6]

Figure 42. Range of FLASH-RT dose modifying factors from preclinical mouse studies per organ.

3.2 Assessing the antitumoral isoefficacy of FLASH-RT in mouse pre-clinical studies

3.2.1 FLASH antitumoral control isoefficacy

FLASH-RT is being closely examined in clinical settings to determine if it can achieve the same level of tumor control as conventional dose-rate radiotherapy while also providing the described FLASH sparing effect (**section 3.1**). Numerous preclinical studies have investigated the effectiveness of FLASH-RT in controlling tumor growth across a wide range of tumor types, as indicated in **Figure 43**. A variety of models, including syngeneic murine tumors and xenografted human tumors have been used to study more than 20 tumor types. These tumor models span various types such as carcinomas, gliomas, and sarcomas and experiments have used both syngeneic and xenograft tumors, either implanted subcutaneously or orthotopically, and studied in immune-competent and immune-compromised mice. These studies have consistently shown that FLASH-RT is as effective as CONV-RT in controlling tumor growth for most tumor models. (**Figure 43**). For example, a study on mouse mammary carcinoma cells implanted in the feet of mice showed that both FLASH-RT and CONV-RT yielded similar TCD50 values²⁶². However, there are exceptions where FLASH-RT was found to be slightly more effective than CONV-RT in certain mouse models. Particularly, patient-derived xenografts of human T-cell acute lymphoblastic leukemia (T-ALL) were found to respond differently to the two modalities²⁶³. Indeed, two of the primary T-ALL cases showed an enhanced response to FLASH-RT, whereas the other one was more responsive to CONV-RT. While the precise mechanisms underlying these responses are under investigation, differences in expression of proteins in the GADD45, Wnt, metabolic, and p53 pathways have been found in the FLASH-sensitive primary T-ALL cancers²⁶³. The ability of FLASH-RT to kill tumors as effectively as CONV-RT seems to extend across different radiation beam modalities, with no significant differences in tumor response between FLASH and CONV. Despite promising findings, further research is needed to fully understand the factors influencing tumor response, especially in certain tumor types and irradiation setups. This has led several research teams to delve deeper into the mechanisms of antitumor response following FLASH or conventional irradiation, with a particular focus on the role of antitumor immune responses and the impact of hypoxia on the efficacy of both FLASH and conventional radiotherapy modalities.

References	Tumor types
Chabi et al. 2021 ²⁶³	Patient-derived xenograft (CD7+/CD45+ cells) human T-ALL
Montay-Gruel et al. 2021 ²⁶⁴	Orthotopic isogenic H454, human U87 glioblastoma
Favaudon et al. 2014 ²⁴¹	Xenograft HBCx-12A – human breast cancer
Sorensen et al. 2022 ²⁶²	Isogenic breast cancer
Gao et al. 2022 ²⁶⁵	Isogenic EMT6 breast cancer
Eggold et al. 2022 ²⁶⁶	Ovarian epithelial carcinoma
Cao et al. 2021 ²⁶⁷	Xenograft MDA-MB 231
Diffenderfer et al. 2020 / Kim et al. 2021 ^{253,268}	Isogenic flank pancreatic tumor MH641905
Cunningham et al. 2021 ²⁶⁹	Isogenic oral carcinoma cell line
Favaudon et al. 2014 ²⁴¹	Xenograft Hep-2 – human head and neck carcinoma
Favaudon et al. 2014 ²⁴¹	Orthotopic isogenic TC-1 – lung carcinoma
Y.E Kim et al. 2021 ²⁷⁰	Isogenic lewis lung carcinoma
Velalopoulou et al. 2021 ²⁵⁸	Isogenic orthotopic and subcutaneous fibrosarcoma
Levy et al. 2020 ²⁵²	Orthotopic isogenic ID8 ovarian cancer

Figure 43. Non-exhaustive list of tumor types used to demonstrate the isoefficacy of FLASH radiotherapy in murine models

3.2.2 FLASH isoeffective antitumoral immune response

In a recent study, it has been established that FLASH-RT could elicit a comparable antitumoral immune response to CONV-RT²⁷¹. In various tumor models, including subcutaneous and orthotopic grafts, FLASH and CONV demonstrated equivalent efficacy in delaying tumor growth across both immunocompetent and immunodeficient hosts²⁷¹. Specifically, tumor doubling time increased significantly after a 20 Gy dose of either FLASH or CONV, with both modalities exhibiting similar efficacy in moderately and severely immunodeficient models²⁷¹. Interestingly, FLASH maintained its antitumoral efficacy even in profoundly immunocompromised mice, suggesting that its mechanism of action may extend beyond immune modulation. In these immunocompromised settings, FLASH-RT led to significant tumor growth delay, reinforcing its potential utility in treating tumors where immune responses are typically suppressed (**Figure 44A**)²⁷¹. Further analysis of the tumor microenvironment (TME) revealed that both FLASH and CONV triggered similar immune profiles, with reductions in lymphoid cells and corresponding increases in myeloid cells few days post-radiation (**Figure 44B**)²⁷¹. This response was consistent across various tissue types, including lung tumors, with no significant differences in immune landscape remodeling between the two irradiation techniques. Four weeks after irradiation, the harvested lungs still showed a reduced tumor area following CONV or FLASH irradiation, which was correlated with an increased infiltration of CD3+ CD8+ T cells compared to the lungs of untreated mice, indicating that both modalities had an immunostimulatory effect on the tumor response (**Figure 44C**)²⁷¹. Additionally, both FLASH and CONV were found to generate a long-lasting immunologic memory, as demonstrated by successful tumor rejection upon rechallenge in murine models. This suggests that both irradiation modalities can function as effective in situ vaccines, promoting sustained immune surveillance and tumor control. Overall, these findings indicate that FLASH is equally effective as CONV in modulating antitumoral immune responses. FLASH retains its efficacy even in immunodeficient environments, positioning it as a viable option for treating immunologically "cold" tumors or patients with compromised immune systems. While further investigation is needed to explore specific mechanistic differences, these results suggest that the antitumoral effects of FLASH and CONV are largely dose-rate independent.

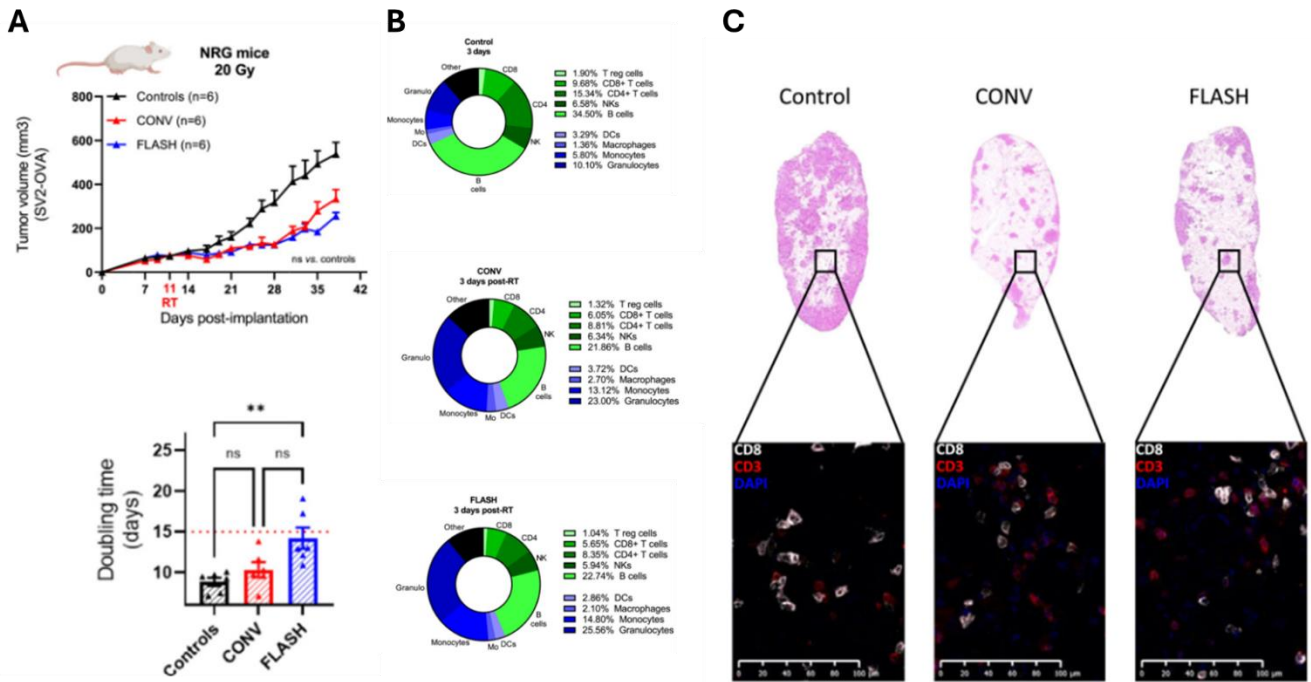


Figure 44. FLASH and CONV-RT antitumoral immune response. (A) Tumor growth over time in NRG mice implanted with tumors and treated with 20 Gy of either conventional (CONV) or FLASH radiotherapy. The graph illustrates reduced tumor volume following both CONV and FLASH treatments compared to controls, with a notable increase in tumor doubling time for the FLASH-treated group ($p < 0.01$). (B) Pie charts showing the immune cell composition of tumors 3 days post-radiation. (C) Representative images of lung bearing tumor sections stained for CD8+ T-cells (red), CD3 (white), and nuclei (DAPI, blue), showing enhanced infiltration of CD8+ T-cells in the irradiated groups. Adapted from Almeida et al. 2024.

3.2.3 Hypoxia and tumor sensitivity following FLASH-RT

Although no significant difference has been observed in terms of antitumoral immune modulation between FLASH and CONV irradiations, recent studies have indicated that FLASH could provide specific advantages in the treatment of hypoxic tumors²⁷². Typically, hypoxic tumors are known to be more resistant to conventional radiotherapy due to reduced oxygen levels. Induced tumors under hypoxia were treated with either FLASH or conventional radiotherapy and interestingly, the results showed that tumor response to FLASH was not significantly affected by acute hypoxia²⁷². Tumor growth control and overall response rates were comparable in both normoxic and hypoxic conditions for FLASH-RT. In contrast, conventional radiotherapy followed the expected pattern, with reduced sensitivity observed in hypoxic tumors, a well-known limitation of standard radiotherapy²⁷². Molecular analysis using RNAseq profiling uncovered a FLASH-specific profile in human GBM that involved cell-cycle arrest, decreased ribosomal biogenesis, and a switch from oxidative phosphorylation to glycolysis giving first insight into the mechanisms that could be involved²⁷². Consequently, FLASH-RT could offer a therapeutic advantage when treating tumors with varying oxygenation levels, particularly those more resistant to conventional radiotherapy due to hypoxia. This type of study indicates for the first time the necessity of conducting more molecular investigations into the response of various tumors to FLASH radiotherapy compared to conventional radiotherapy. While antitumoral efficacy appears similar in preclinical models, there seem to be differences in the mechanisms of action of FLASH radiotherapy within tumors.

Thus, now that we have described the FLASH effect, which entails a protective effect on healthy tissue at ultra-high dose rates while maintaining antitumoral isoefficacy compared to conventional radiotherapy, we will now delve into the mechanistic hypotheses that have been proposed to explain this duality between the response of healthy tissue and tumors to FLASH radiotherapy.

3.3 Underlying mechanisms of the FLASH effect

The unique promising ability of FLASH to balance therapeutic benefits without compromising efficacy has attracted significant attention in the field of radiation oncology. However, the precise mechanisms underlying the differential responses between normal and tumor tissues are still under investigation, but various hypotheses have emerged that provide insights into the potential actors at play. By comprehending these mechanisms, we may better understand the applications of FLASH to improve patient outcomes. In the following section, we will delve into key proposed mechanisms, including transient oxygen depletion, DNA damage responses, the protection of stem cell niches, vascular system impacts, immune modulation, lipid effects, and the role of mitochondrial metabolism.

3.3.1 Potential role of transient oxygen depletion in the FLASH effect

One of the most widespread hypotheses to explain the protective effect of FLASH on healthy tissue is that of transient oxygen depletion. According to this theory, the ultra-rapid dose rates used in FLASH-RT lead to rapid consumption of oxygen in irradiated tissue, creating a temporary hypoxic state. Since oxygen is a well-known sensitizer of the effects of radiation, its depletion would reduce the production of ROS, which are responsible for DNA damage, thus conferring protection on normal tissues⁴⁵. The oxygen enhancement ratio is a well-established measure that describes how the presence of oxygen increases the radiosensitivity of tissues²⁷³. The theory behind FLASH is that rapid dose delivery consumes oxygen faster than it can be replaced, inducing a radioprotective hypoxic state in normal tissues. This idea was supported by several theoretical models which suggested that FLASH irradiation could result in a temporary decrease in oxygen tension, sufficient to protect normal tissues^{274,275}. A series of experiments have confirmed this hypothesis, showing that the FLASH effect is attenuated when oxygen levels are artificially increased. For example, in a study by Montay-Gruel et al., inhalation of carbogen prior to irradiation eliminated the protective effect of FLASH in the brain²⁴⁷ (**Figure 45**). However, these experiments showed that oxygen levels were not reduced as significantly as expected, suggesting that oxygen depletion is not sufficient to fully explain the FLASH effect. More recent studies, using advanced techniques for measuring oxygen tension *in vivo*, have called into question the extent of this oxygen depletion. It has been shown that the reduction in oxygen levels was minimal during FLASH irradiation, suggesting that other mechanisms may also be involved in this protective effect^{267,276}. These data underline that, although transient oxygen depletion may play a role, it alone cannot explain the observed effects of FLASH on healthy tissue.

While the transient oxygen depletion hypothesis provides a compelling explanation for the radioprotective effect of FLASH, another significant theory focuses on the behavior of free radicals produced during irradiation. In particular, the rate at which these radicals recombine and diffuse through tissues may further explain why FLASH has a protective advantage over conventional radiotherapy.

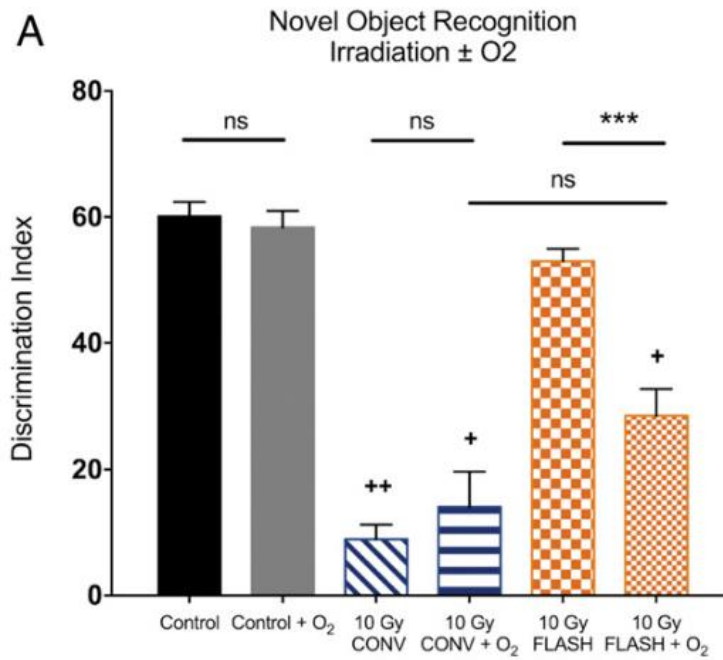


Figure 45. FLASH effect is influenced by the tissue's partial pressure of oxygen. *Wild-type mice, anesthetized under either normoxic conditions or while breathing carbogen (O₂-enriched air), were subjected to the object recognition test two months after irradiation. The increase in brain pO₂ due to carbogen inhalation before and during the irradiation reversed the neurocognitive protection provided by FLASH under normoxic conditions.*²⁴⁷

3.3.2 Free Radical Recombination and Diffusion hypothesis

Another popular theory to explain the protective effect of FLASH is the increased rates of recombination and diffusion of free radicals following FLASH-RT. During exposure to ionizing radiation, free radicals are generated in cells, causing damage to DNA and other cellular structures. According to this hypothesis, the extremely rapid dose rates used in FLASH-RT would produce a higher instantaneous density of free radicals, favoring their recombination before they could cause DNA damage. The fundamental principle of this theory is based on the physics of free radicals: at high densities, these radicals are more likely to interact with each other and recombine to form harmless molecules, such as water, rather than causing biological damage. This rapid recombination could reduce the production of deleterious ROS, which are normally responsible for most damage caused by conventional radiation. This hypothesis has been supported by several experimental studies. For example, a study by Montay-Gruel et al.²⁴⁷ showed that concentrations of hydrogen peroxide (H₂O₂), an indicator of free radical production, were significantly lower in water exposed to FLASH radiotherapy compared to CONV-RT. These results provide first evidence that free radical recombination may be faster under the ultra-high dose conditions of FLASH, thereby reducing ROS-induced biological damage. Others also suggested that FLASH irradiation conditions could alter the diffusion of free radicals in tissues, thereby reducing the extent of damage they can cause⁴⁴. These models indicate that the rapid increase in free radicals during FLASH irradiation limits their ability to diffuse through surrounding cells and tissues, thereby minimizing collateral damage in healthy tissues. However, although this theory presents a plausible mechanism to explain the protective effect of FLASH, it remains largely speculative and needs to be validated by further data. As pointed out by Alanazi et al.²⁷⁷ and Wardman²⁷⁸, theoretical models may be needed to fully understand how free radicals behave under ultra-high dose conditions and how this influences the underlying biological mechanisms. Current studies are continuing to explore this avenue, by using more precise measurements of radical recombination and diffusion to better understand their role in the protective effect of FLASH.

Although increased free radical recombination and diffusion may play a role in reducing oxidative damage, another important aspect to consider is how these changes translate into differences in DNA damage. Understanding the nature and extent of DNA lesions following FLASH compared to conventional radiotherapy offers deeper insights into how normal tissue might be spared while the tumor control is maintained.

3.3.3 Differential DNA Damage Response in FLASH

One of the main hypotheses to explain the protective effect of FLASH could be based on the nature of the DNA damage induced by this ultra-high dose rate irradiation. Ionizing radiation causes single and double strand breaks in DNA as described in section 1.3.5, activating cellular repair mechanisms. However, the ability of cells to repair these lesions may vary according to the dose rate, and it has been postulated that FLASH and conventional radiotherapy (CONV-RT) could induce different levels or types of DNA damage, resulting in better protection of healthy tissue while preserving anti-tumour efficacy. In the lungs, FLASH irradiation was shown to induce significantly less residual DNA damage than conventional radiotherapy (**Figure 46A**)²⁶⁰. Lung cells exposed to FLASH showed less apoptosis and senescence, indicating better DNA repair and increased regenerative potential²⁶⁰. Furthermore, studies on intestinal crypts demonstrated that FLASH irradiation preserved the crypts by causing less gamma H2AX foci than CONV-RT few hours post-treatment (**Figure 46B**)²⁵². In contrast, tumour cells do not benefit from this protective effect, as shown by experimental results using clonogenic assays^{279,280}. Consistently, no *in vivo* difference in residual DSBs was observed in ovarian tumors after exposure to FLASH-RT versus CONV-RT²⁵². Although this hypothesis is supported by several studies, it requires further investigation to better understand the molecular mechanisms underlying the protective effect of FLASH, particularly in normal cells compared with tumour cells.

Beyond DNA damage, the capacity of tissues to recover from radiation exposure is also influenced by the preservation of key cellular populations. Stem cells, critical for tissue regeneration, appear to be better protected by FLASH-RT. This preservation of stem cell niches in various tissues could be a significant factor in reducing long-term damage, adding another layer for understanding the protective effects of FLASH.

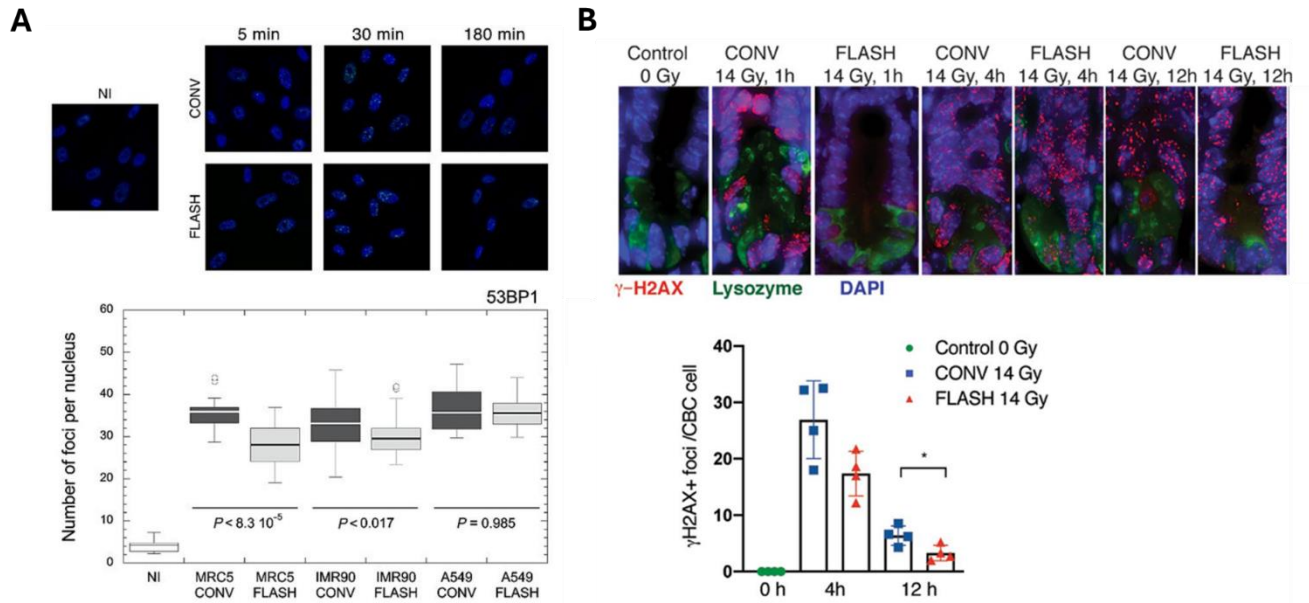


Figure 46. Comparative Analysis of DNA Damage and Repair Dynamics in CONV-RT and FLASH-RT. (A) Immunofluorescence analysis of 53BP1 foci in different cell lines (NI, MRC5, IMR90, A549) following conventional (CONV) and FLASH irradiation at various time points (5 min, 30 min, 180 min). The box plot below illustrates the number of 53BP1 foci per nucleus, showing a significant reduction in foci with FLASH-RT compared to CONV-RT, particularly in normal tissue cells (MRC5 and IMR90), indicating enhanced DNA repair efficiency after FLASH irradiation. (B) γ -H2AX foci staining in crypt base columnar (CBC) cells post-irradiation with CONV-RT and FLASH-RT (14 Gy) at different time points (1 h, 4 h, 12 h). The bar graph quantifies the γ -H2AX foci in CBC cells, highlighting significantly fewer DNA damage markers after FLASH-RT compared to CONV-RT, particularly at the 12-hour mark.

3.3.4 Stem cell preservation following FLASH-RT

The protection of stem cell niches is one of the central mechanisms put forward to explain the protective effect of FLASH-RT on healthy tissue. Stem cells, which are essential for tissue regeneration after damage, are particularly sensitive to irradiation. By preserving these niches, FLASH-RT enables better recovery of normal tissue than conventional radiotherapy. In the brain, it has been demonstrated that FLASH irradiation preserves neurogenic stem cells in the hippocampus²⁴⁶. These cells, responsible for neurogenesis, are crucial for the maintenance of cognitive function. In this study, an increase in proliferating cells (BrdU+), immature neurons (DCX+) and mature neurons (NeuN+) were observed in the hippocampus of mice irradiated with FLASH, compared with those treated with CONV-RT. This preservation could explain why cognitive functions are better preserved after FLASH irradiation, whereas they are often impaired with conventional radiotherapy²⁴⁶. Regarding the intestine, it has been shown that FLASH-RT preserves intestinal crypt stem cells better than conventional radiotherapy²⁵². Crypt stem cells play a fundamental role in the regeneration of intestinal epithelium after irradiation. By preserving these cells, FLASH-RT enables better recovery of intestinal tissues, thereby reducing the severity of gastrointestinal syndromes that are often associated with irreversible damage during conventional radiotherapy. This increased protection of the crypts could explain the significant reduction in gastrointestinal toxicities observed in preclinical studies of total abdominal irradiation using FLASH. Recent work by Tristan Lim et al. has provided further insight into how FLASH offers a protective effect intestinal crypt cell. Indeed, they demonstrated that FLASH accelerated the differentiation of revival stem cells, a rare stem cell population crucial for intestinal regeneration after radiation damage. This differentiation was supported by increased macrophage infiltration producing TGF- β , an essential cytokine for revSC induction, and enhanced IFN-I signaling in pericryptal fibroblasts, which stimulated the production of FGF growth factors that promote revSC proliferation. In contrast, under SR, IFN-I signaling had detrimental effects, promoting toxicity²⁵⁵. As for skin, studies have also demonstrated the protective effect of FLASH on cutaneous stem cell niches. In mouse models, FLASH-RT preserved Lgr6+ cutaneous stem cells, which are essential for the regeneration of the epidermis after irradiation²⁵⁸. This preservation of stem cells makes it possible to limit severe toxicities such as skin ulcerations, which are more frequent after high-dose conventional radiotherapy. In the lung, it has also demonstrated the preservation of regenerative potential in preclinical studies on mouse lung models. FLASH-RT enabled better preservation of lung dividing cells, which are essential for alveolar regeneration and tissue repair after irradiation. Comparing mice irradiated with FLASH and those irradiated with CONV-RT, the results an enhanced division level after CONV-RT versus FLASH that could lead to an

exhaustion of cell division potential and impaired regenerative functions²⁶⁰. In conclusion, the preservation of stem cell niches by FLASH-RT could be a key mechanism in explaining the reduction in acute toxicity in several normal tissues, including the brain, intestine, skin and lungs. However, for now, it only offers a reasonable explanation for the preservation of normal tissue function in the short term. It does not fully explain the long-term advantages, such as the sparing of neurocognitive abilities, which cannot be attributed solely to the preservation of hippocampal neurogenesis, reduction of lymphedema, or prevention of tissue fibrosis. The protection of stem cells alone cannot account for the comparable tumor-killing efficiency seen with FLASH-RT. While there has been much discussion in the literature about equating cancer stem cells to normal stem cells, their equivalence remains a contentious topic. Nevertheless, if cancer stem cells were also protected by FLASH-RT, this could raise concerns about the long-term clinical viability of this treatment approach.

While the protection of stem cell niches sheds light on tissue regeneration, another proposed mechanism involves the systemic effects of radiation. The fraction of blood volume irradiated during FLASH may influence inflammatory responses and further contribute to the reduced toxicity observed in healthy tissues. Investigating how the rapid delivery of FLASH minimizes systemic radiation effects is crucial to understanding its overall protective benefits.

3.3.5 Impact of the fraction of total blood irradiated

The fraction of total blood volume irradiated during FLASH radiotherapy has become a significant area of interest when considering potential mechanisms underlying its normal tissue-sparing effects. Unlike CONV-RT, which irradiates a larger fraction of the body's total blood volume over a prolonged period, FLASH-RT delivers radiation so rapidly that only a small portion of the blood circulating through the irradiated volume is exposed to radiation. This difference in blood irradiation has been hypothesized to play a role in the reduced normal tissue toxicity observed with FLASH. In CONV-RT, the total blood supply passing through the target area is exposed to radiation at a relatively low dose rate, leading to the irradiation of a larger fraction of the blood over the course of treatment. In contrast, FLASH-RT's ultra-high dose rate results in the irradiation of only a small fraction of the total blood volume, but at a much higher dose per pulse. This rapid delivery may reduce the systemic effects of radiotherapy, such as inflammation and fibrosis, that are typically mediated by circulating blood components. Several studies have explored the possibility that irradiating a smaller fraction of blood volume in FLASH could reduce the generation of radiolytic species or prevent the production of paracrine signaling molecules that typically contribute to radiation-induced

toxicities. For example, cytokines and other inflammatory mediators circulating in the blood are known to play a critical role in driving radiation-induced damage in normal tissues^{281,282}. By reducing the volume of blood irradiated, FLASH-RT may limit the generation of these harmful signals, thus mitigating the inflammatory response typically observed in normal tissues following conventional radiotherapy. Moreover, the reduction in inflammatory and fibrotic factors seen in normal tissues exposed to FLASH-RT has been linked to lower levels of pro-inflammatory cytokines (**Figure 47A-B**)^{241,258,283}. This could be explained, in part, by the smaller fraction of irradiated blood and a subsequent decrease in the systemic inflammatory response. Ongoing research is investigating these mechanisms more formally through experiments designed to assess the role of circulating blood components in radiation-induced toxicities, as well as the impact of FLASH on the blood's ability to mediate these effects.

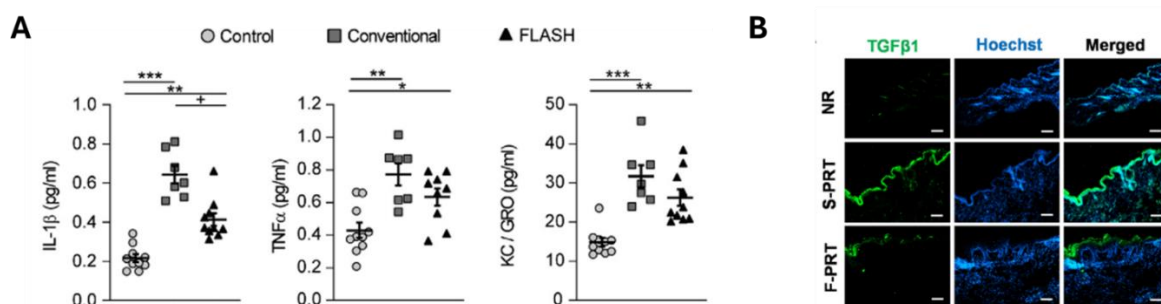


Figure 47. Inflammatory Cytokine Response and TGF-β1 Expression Following FLASH-RT and CONV-RT. (A) Quantification of pro-inflammatory cytokines ($IL-1\beta$, $TNF\alpha$, and KC/GRO) in the serum of mice post-irradiation with FLASH-RT, conventional radiotherapy (CONV-RT), and control (non-irradiated). The results show that FLASH-RT significantly reduces the levels of these cytokines compared to CONV-RT, indicating a lower systemic inflammatory response. (B) Immunofluorescence analysis of TGF-β1 expression in lung tissue sections from mice after no irradiation (NR), standard proton radiotherapy (S-PRT), and FLASH proton radiotherapy (F-PRT). TGF-β1 expression, associated with fibrosis and tissue damage, is notably reduced in the FLASH-RT group compared to the S-PRT group, suggesting a protective effect of FLASH-RT against fibrotic pathways.

Along with the fraction of blood irradiated, the integrity of the vascular system plays an essential role in maintaining tissue health post-irradiation. FLASH-RT's ability to preserve vascular function and reduce damage to blood vessels may complement the systemic benefits associated with lower blood irradiation, contributing to the overall reduction in normal tissue toxicities.

3.3.6 FLASH-RT and Vascular Integrity

Most of the studies examining the impact of FLASH radiotherapy on the vascular system have primarily focused on normal brain tissue, demonstrating a consistent preservation of vascular morphology in both adult and juvenile animal models. These studies have also shown a significant reduction in inflammation compared to conventional radiotherapy^{248,284,285}. The preserved vascular structure after FLASH irradiation was marked by reduced endothelial damage and maintenance of the blood-brain barrier integrity, as indicated by the lower expression of endothelial nitric oxide synthase (eNOS) and stable levels of tight junction proteins such as occludin and claudin-5. Because intratumoral vessels are primarily composed of stromal cells such as endothelial cells and pericytes, like normal tissue vasculature, these observations suggest that FLASH-RT might induce a similar response in tumor vessels. However, the specific effects of FLASH-RT on tumor vasculature are less studied and require further investigation to draw definitive conclusions. In preliminary investigations comparing high single doses of FLASH-RT versus CONV-RT from 10 to 25 Gy, acute and late time points (1 week and 1 month) were analyzed to determine vascular response. It was found that FLASH-RT led to a reduction in vascular dilation and decreased expression of endothelial NOS compared to CONV-RT. This suggests that the preservation of vascular function and reduced vascular damage could play a role in the differential tissue response between FLASH and conventional radiotherapy. Further studies are needed to elucidate whether these findings translate into a tangible therapeutic advantage for tumor vasculature, particularly in the context of preserving vascular function and reducing secondary damage to surrounding healthy tissues. Ultimately, understanding the role of the vascular system in mediating the FLASH effect is crucial, as the vasculature is a key component in radiation-induced damage and the subsequent repair processes. The potential to modulate the vascular response could significantly impact the therapeutic index of FLASH-RT, enhancing tumor control while preserving the function and integrity of normal tissue vasculature.

In addition to preserving vascular integrity, the immune response to radiotherapy is a critical factor in both normal tissue protection and tumor control. By examining how immune cell activation and infiltration are modulated by FLASH-RT, we gain a better understanding of its potential to maintain tumor control while sparing healthy tissues from the collateral damage typically caused by conventional radiotherapy.

3.3.7 Immune modulation in FLASH and Conventional Radiotherapy

The immune response, specifically the modulation of immune cell infiltration and activation, is proposed to play a key role in mediating radiation induced damages and tumor response. Studies have consistently demonstrated that both immunologically hot and cold tumors referring to those with or without significant CD8+ T cell infiltration could respond similarly to FLASH-RT and CONV-RT. For example, mouse oral carcinoma models (MOC1 and MOC2) showed no difference in tumor control between the two modalities, irrespective of their immune cell infiltration status²⁶⁹. This suggests that FLASH-RT maintains its antitumoral efficacy even in immunologically cold environments, where fewer immune cells are present to aid in tumor elimination. Further evidence comes from studies combining FLASH-RT with immune checkpoint inhibitors such as anti-PD1 therapy. In ID8 and UPK10 tumor models, both FLASH-RT and CONV-RT induced comparable adaptive immune responses, specifically the infiltration of CD8+ T cells, which are critical for antitumor immunity²⁶⁶. Interestingly, FLASH-RT slightly altered monocyte infiltration and macrophage polarity, suggesting a subtle but potentially significant modulation of innate immunity. However, this effect does not seem to extend to major immunosuppressive pathways, as FLASH-RT does not induce TGF β 1, a potent immunosuppressive cytokine known to promote fibrosis and hinder immune responses^{241,259}. Moreover, preliminary studies have indicated that the antitumor efficacy of FLASH-RT is independent of the host's immune status. Tumors grafted into immunocompromised mice, such as nude or immuno-competent mice, responded similarly to FLASH-RT and CONV-RT, further suggesting that the immune response is not the primary determinant of the observed isoefficacy between the two modalities²⁷¹. While the immune hypothesis remains a compelling explanation for the normal tissue sparing effects of FLASH-RT, evidence so far suggests that the immune response plays a relatively minor role in distinguishing between the effects of FLASH-RT and CONV-RT in tumors. This leads to the speculation that other factors, such as vascular and metabolic changes, might be more critical in mediating the differential effects observed between normal tissues and tumors under FLASH-RT. Further studies are necessary to elucidate these mechanisms, particularly focusing on the interactions between the immune system, tumor microenvironment, and vascular responses.

Although immune responses play a crucial role in radiation effects, other molecular processes, such as lipid peroxidation, may also contribute to the differential response between normal and tumor tissues. Lipid peroxidation is particularly relevant in tissues rich in polyunsaturated fatty acids, and FLASH-RT's ability to minimize this oxidative damage could further explain its protective effects on normal tissues.

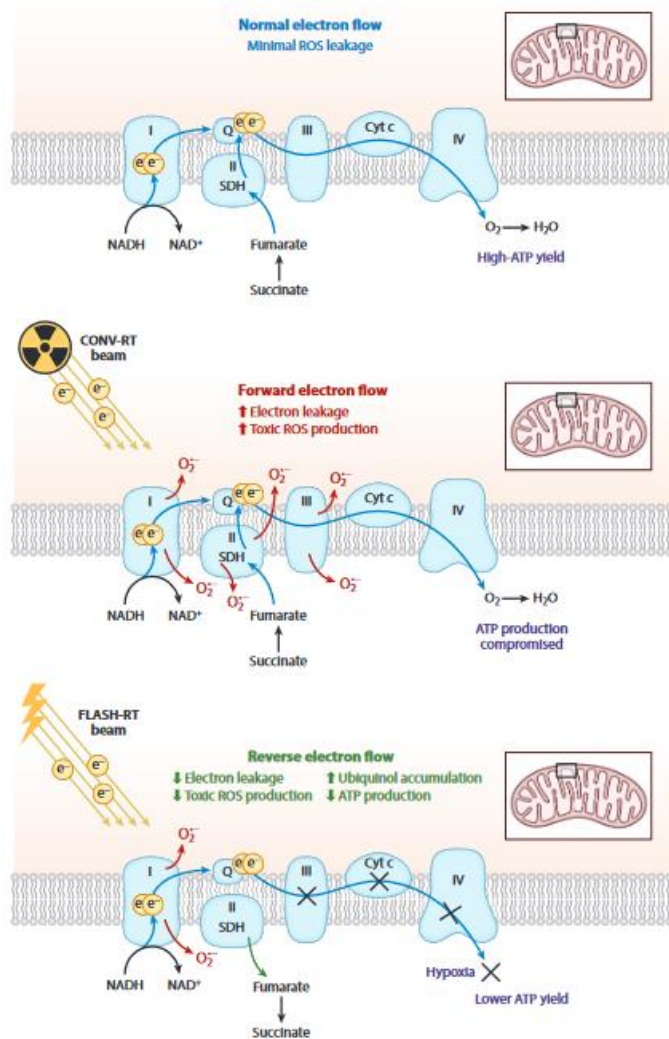
3.3.8 Differential Lipid Peroxidation in Normal and Tumor Cells Under FLASH-RT

Lipid peroxidation has been increasingly recognized as a potential factor in the differential response of normal tissues and tumors to FLASH versus conventional radiotherapy. Lipids, particularly polyunsaturated fatty acids in cell membranes, are sensitive to free radical damage, which propagates chain reactions and consumes oxygen. This process has been proposed as a key mechanism underlying the FLASH effect, particularly in lipid-rich tissues like the brain and endothelium^{44,275,286}. These chain reactions, involving organic hydroperoxides, are believed to be reduced in FLASH-RT, potentially sparing normal tissues from excessive oxidative damage. Froidevaux et al. demonstrated that lipid peroxidation yields increase linearly with CONV-RT doses, while they were conspicuously absent following FLASH-RT²⁸⁷. Additionally, lipidomic analyses of rodent brains irradiated with FLASH-RT revealed that, unlike CONV-RT, FLASH did not increase levels of lipid adducts such as 2-arachidonoylglycerol (2-AG) and palmitoylethanolamide (PEA), both of which are associated with neuroinflammation. A recent study by Portier et al. (2024) investigated the effects of FLASH and CONV irradiation on oxylipins, a class of bioactive lipid metabolites derived from omega-3 and omega-6 polyunsaturated fatty acids, in both normal and cancer cells. Using ultrahigh performance liquid chromatography coupled with tandem mass spectrometry (UPLC-MS/MS), 37 oxylipins were quantified in mouse lung tissues and human cell lines post-irradiation²⁸⁸. They found that in normal, normoxic cells, FLASH-RT resulted in a significant reduction in oxylipin levels compared to CONV-RT, with levels 20-50% lower at five minutes post-irradiation. This downregulation was specific to normal cells and was not observed in tumor cells, indicating a differential response between healthy and tumoral tissues. Notably, this reduction in oxylipins was transient, with near-complete recovery observed 24 hours post-irradiation, followed by further remodeling in the weeks and months after treatment²⁸⁸. These findings align with previous research showing that FLASH-RT minimizes lipid peroxidation compared to CONV-RT. Taken together, these studies suggest that FLASH-RT spares normal tissues by minimizing lipid peroxidation, particularly in oxygen-dependent reactions. This could explain the preservation of tissue functionality observed in FLASH-irradiated animals and supports the idea that lipids are critical targets in the FLASH effect. The distinct lipid response in normal versus tumor cells may further contribute to the therapeutic advantage of FLASH-RT in protecting healthy tissues while maintaining its efficacy in tumor control. Finally, the link between lipid peroxidation and mitochondrial metabolism highlights another critical aspect of the FLASH effect. Mitochondria, being key regulators of cellular energy and ROS production, may react differently to the ultra-high dose rates of FLASH compared to conventional irradiation, further influencing tissue preservation and tumor response.

3.3.9 Mitochondrial Metabolism and Reactive Oxygen Species after FLASH-RT

The role of mitochondrial metabolism in the FLASH effect has emerged as a novel area of investigation, given the significant impact of radiation on mitochondrial function and the production of ROS. Mitochondria, through oxidative phosphorylation, are responsible for most cellular ATP production. However, this process also generates superoxide radicals (O_2^-) as byproducts, which can lead to the formation of highly reactive molecules such as hydrogen peroxide (H_2O_2) and hydroxyl radicals ($OH\cdot$), especially under the oxidative stress induced by irradiation²⁸⁹. The electron transport chain, particularly complexes I, II, and III, are sensitive to radiation, and any disruption in electron flow through the ETC can elevate ROS levels, causing oxidative damage and contributing to genomic instability (**Figure 48**). Recent studies have begun to elucidate how FLASH-RT may differentially affect mitochondrial metabolism compared to CONV-RT. In tumor models, such as Lewis lung carcinoma, FLASH-RT has been shown to produce significantly higher ROS levels than CONV-RT, particularly at higher doses like 15 Gy²⁷⁰. This increase in ROS is thought to be associated with mitochondrial dysfunction and electron leakage from the ETC, specifically from complex II, which is involved in both the citric acid cycle and the ETC. Unlike in tumors, normal tissues may experience lower ROS yields following FLASH-RT due to a preservation of mitochondrial function, particularly in tissues like the brain, where mitochondrial complex I, II, and III activities were found to be more affected by FLASH than CONV irradiation²⁸⁶. One key hypothesis to explain this differential response involves reverse electron transport. Recent studies have proposed that the reverse electron flow process may be favored under the ultra-high dose rates of FLASH-RT, particularly in oxygen-depleted environments. In this scenario, FLASH-RT would minimize ROS production by reducing electron leakage and maintaining ATP production, albeit at lower levels than under normal conditions (**Figure 48**). This mechanism could explain the reduced oxidative damage and enhanced tissue preservation seen in normal tissues, while tumors, which have altered mitochondrial metabolism, may not benefit from the same protective effects.

Overall, the modulation of mitochondrial metabolism by FLASH-RT, particularly through mechanisms like reverse electron flow, presents an intriguing avenue for understanding how this radiation modality can selectively spare normal tissues while maintaining its antitumoral efficacy. Further research is needed to clarify how these processes operate in different tissues and tumor types.



(Caption appears on following page)

Figure 48. Reverse Electron Flow and the FLASH Effect on Mitochondrial Function. *In normal mitochondrial oxidative phosphorylation (OXPHOS), electrons are transferred through complexes I to IV in the electron transport chain (ETC), leading to high ATP production with minimal ROS leakage into the mitochondrial matrix and intermembrane space (Top). Conventional radiotherapy (CONV-RT) disrupts efficient electron transfer, causing reduced ATP production and elevated ROS levels, with oxygen acting as the primary electron acceptor (Middle). In contrast, FLASH-RT saturates cells with electrons, potentially promoting reverse electron flow, where fumarate serves as an alternative terminal electron acceptor from complex II. This results in reduced ATP production but also lowers ROS generation. Tissue hypoxia may further influence reverse electron flow, but its variation between normal tissues, tumors, and different FLASH modalities is yet to be fully understood. Figure from Limoli and Vozenin 2023²⁹⁰.*

In summary, the emerging evidence suggests that multiple mechanisms may work together to explain the tissue-sparing effects of FLASH radiotherapy while maintaining its antitumor efficacy. The transient oxygen depletion hypothesis offers a plausible explanation for reduced normal tissue toxicity by limiting reactive oxygen species production, although it does not fully account for all observed protective effects. Similarly, the theory of increased free radical recombination and diffusion adds another layer to the understanding of how FLASH might reduce oxidative stress in healthy tissues, further differentiating it from conventional radiotherapy. In addition to these biochemical processes, the differential DNA damage response between normal and tumor tissues, alongside the preservation of critical stem cell niches, provides insight into why normal tissues recover more efficiently after FLASH irradiation. Moreover, systemic factors such as the fraction of total blood volume irradiated, and the preservation of vascular integrity likely play important roles in reducing inflammation and fibrosis following FLASH exposure. Immune modulation appears to be relatively independent of the FLASH effect, as tumor control remains robust across both immunologically hot and cold tumor environments. However, the differential impact on lipid peroxidation and mitochondrial metabolism, particularly the ability of FLASH to minimize oxidative damage and maintain cellular energy homeostasis, highlights the complexity of these mechanisms and their interplay. In the end, further research is still necessary to fully elucidate the molecular and cellular processes at play and to explore how these mechanisms might be optimized to enhance therapeutic outcomes in clinical settings. The next section will address this crucial step, focusing on the challenges and advancements involved in transitioning FLASH from experimental research into clinical applications, and what this means for the future of radiotherapy.

3.4 Clinical translation of FLASH radiotherapy

The promising preclinical results of FLASH radiotherapy have generated widespread excitement within the radiation oncologist community due to its potential to drastically reduce normal tissue toxicity while preserving antitumoral efficacy. The observed "FLASH effect" has shown success across various organs in animal models, making it a revolutionary development in radiotherapy. However, the translation of these preclinical results into clinical practice is complex and full of challenges. Key obstacles include the need to develop a robust dosimetry technique for FLASH-RT quality control of dose deposits as well as identify the critical physical parameters governing FLASH's tissue-sparing capabilities. Furthermore, we will need accurate *vitro* models as well as large animals *in vivo* studies that can mimic the treatment conditions for patients and refine the clinical protocols for its safe and effective application. Clinical trials are currently underway to evaluate the feasibility of FLASH radiotherapy in cancer patients, but the road ahead requires robust research to establish its safety and therapeutic potential in a clinical setting.

3.4.1 Available pre-clinical and clinical irradiator for FLASH radiotherapy

The development of specialized irradiators for FLASH radiotherapy has played a critical role in advancing both pre-clinical studies and potential clinical applications. Among the various technologies, low-energy electron accelerators were the first to demonstrate the FLASH effect²⁴¹. Early studies used 4.5 MeV electron linear accelerators, which are technologically similar to those employed in conventional radiotherapy but adapted to deliver higher peak currents and radiofrequency power. These systems have since been optimized to deliver ultra-high dose rate ranging from hundreds of Gy/s with dose-per-pulse values from 1 to 10 Gy, enabling the exploration of the FLASH effect in preclinical settings. More recent advancements include the development of systems capable of delivering dose rates between 50 and 500 Gy/s using commercially available linear accelerators, albeit with limitations like reduced treatment distance^{291–293}. Notably, companies like Varian have created the FLEX extension, allowing non-clinical research with a 16 MeV electron beam that can achieve dose rates of 200 Gy/s²⁹⁴. Intraoperative electron radiation therapy (IOeRT) equipment has also been adapted for FLASH, with systems like the Mobetron (IntraOP Medical Corporation), the ElectronFLASH Linac (Sordina IORT Technologies) and FlashKnife (PMB-Alcen), delivering up to 300 Gy/s^{295,296}. Despite the advancements in electron beam technology, there are inherent limitations with low-to-medium energy electrons (5–20 MeV), such as their limited tissue penetration depth of only a few centimeters. These characteristics restrict their use to superficial tumors. Very High Energy Electrons (VHEE), with energies ranging from 100 to 250

MeV, have emerged as a particularly promising tool to tackle this issue, offering several advantages over low-energy electrons. VHEE's superior penetration depth and lateral precision make it well-suited for targeting deep-seated tumors, while being less affected by tissue heterogeneities²⁹⁷. In addition, VHEE's potential to deliver high doses per fraction in very limited time through electromagnetic scanning of particle beams could significantly enhance tumor control while reducing treatment times in FLASH context. Studies using numerical simulations have demonstrated the feasibility of VHEE to treat various tumor locations, showing minimal lateral scattering, especially when utilizing magnetic field-based beam focusing techniques²⁹⁷. Early experimental work, such as those conducted at CERN's CLEAR facility, has confirmed the ballistic advantages of VHEE in clinical contexts, making it an attractive candidate for further exploration in FLASH-RT applications²⁹⁸. Moreover, laser-plasma interactions have demonstrated the potential to accelerate electrons to VHEE levels, providing a compact and cost-effective approach to VHEE generation, although challenges related to energy dispersion and pulse structure remain²⁹⁹.

In contrast, proton beams have emerged as a strong candidate for FLASH radiotherapy due to their ability to penetrate deeper tissues, making them suitable for the treatment of larger tumors or those located in complex anatomical sites. Isochronous cyclotrons, which are already capable of achieving FLASH dose rates, require minimal modifications to meet the ultra-high dose requirements³⁰⁰. Systems like the IBA Proteus One and facilities such as the Paul Scherrer Institute have been pivotal in conducting FLASH proton experiments, showing promising results in both tumor control and the sparing of normal tissues³⁰¹. Proton systems are particularly advantageous due to their precision in targeting and minimizing radiation exposure to surrounding healthy tissues, positioning them as ideal candidates for clinical translation.

Photon-based FLASH systems, though less common, are also under active development. Traditional megavoltage (MV) X-ray machines are not inherently optimized for FLASH due to the inefficiency of electron-to-X-ray conversion, which results in significant energy loss through heat generation. Nonetheless, some experimental setups, such as synchrotron radiation facilities and novel X-ray machines with enhanced pulse repetition frequencies, have demonstrated the ability to go for ultra-high dose rates. For instance, the PHASER linear accelerator, developed by Stanford and SLAC, is designed to achieve average dose rates of 50 Gy/s with MV X-ray beams using a novel scanning system of electron sources. Similarly, preclinical platforms like PARTER at the Chengdu THz Free Electron Laser facility have achieved quasi-continuous dose rates of over 50 Gy/s, further expanding the potential for FLASH-RT in both research and future clinical applications. In summary, advancements in preclinical and clinical irradiators for FLASH radiotherapy span electron, proton, and photon

technologies. Each modality presents unique advantages for investigating the FLASH effect and its potential clinical applications. While electron systems remain the most developed due to their accessibility, proton and photon beams offer significant promise for treating deep-seated tumors. As this technology evolves, the challenge of accurate dose delivery and real-time monitoring becomes increasingly critical, which leads us to the next key aspect of FLASH radiotherapy: dosimetry.

3.4.2 Dosimetry of FLASH radiation therapy

Dosimetry for FLASH radiotherapy presents unique challenges due to the ultra-high dose rates required to achieve the FLASH effect, as well as the need for instantaneous dose measurements during patient treatments for quality control. The primary challenge arises from the high dose-rate, which introduces complexities in accurately reading and verifying the delivered dose. Traditional dosimeters, such as ionization chambers, solid-state detectors, and chemical dosimeters, often face issues like saturation or non-linearity when exposed to FLASH dose rates, due to charge recombination effects at high dose-per-pulse. Small volume ionization chambers, like the Advanced Markus Chamber, have been adapted for use in FLASH dosimetry, at the cost of important correction factors to account for ion recombination³⁰². A key consideration for effective use in FLASH radiotherapy is dose-rate independence of the detector. Luminescent detectors, such as scintillation and Cherenkov radiation-based systems, have emerged as promising tools due to their ability to provide high spatial and temporal resolution while maintaining dose-rate independence³⁰³. Scintillators, both organic and inorganic, offer nanosecond-level temporal resolution, which is crucial for real-time dose monitoring in FLASH setups. Systems that use Cherenkov radiation have demonstrated great potential for online dose monitoring, as they produce optical photons instantaneously upon interaction with electrons³⁰³. EPR-based alanine dosimeters have demonstrated remarkable stability across varying dose rates³⁰³, but they imply a complex readout apparatus, and a response delay a few days. The recent UHPulse European project (Metrology for advanced radiotherapy using pulsed particle beams with ultra-high dose rates) has led to the development of innovative, dose-rate-independent dosimeters, such as ultra-thin ion chamber³⁰⁴, silicon detectors³⁰⁵ and diamond semiconductors³⁰⁶. Another challenge is the accuracy of dose distribution measurements, especially in small field dosimetry, where precise spatial resolution is required. Detectors such as Gafchromic films have shown excellent dose-rate independence, even at the extreme dose rates of FLASH³⁰³. However, they are typically used for offline measurements few hours to days after radiation. To overcome this limitation, systems employing scintillating screens coupled with high-resolution cameras have been developed to allow real-time imaging of dose distribution. These systems can provide

near-instantaneous feedback on beam parameters, allowing for precise control over dose delivery during FLASH treatments³⁰³. Current research focuses on developing cost-effective detector arrays capable of enabling that would enable precise, real-time, dose measure over two-dimensional profiles. These developments underscore the need for continuous innovation in dosimetry techniques to ensure precise and reliable measurements in FLASH radiotherapy. In conclusion, the rapid development of dosimetric tools tailored for FLASH radiotherapy has significantly advanced our ability to measure and verify doses at ultra-high rates. Despite this progress, further refinement of detectors, particularly those capable of real-time dose verification, remains crucial to the clinical translation of FLASH treatments³⁰³.

3.4.3 Critical irradiation parameters for the FLASH sparing effect

In FLASH radiotherapy, the structure and timing of radiation delivery are critical to achieving the protective normal tissue sparing effect while maintaining the efficacy of tumor control. Clinical electron linear accelerators use pulsed radiation, where the dose is administered in short bursts lasting microseconds and delivered at hundreds of Herz (Pulse Repetition Frequency or PRF) (**Figure 49A**). Electron-based FLASH relies on a similar scheme but uses a very high dose-per-pulse and a limited number of pulses (typically 1 – 5), allowing the total dose to be administered in a matter of milliseconds. This rapid delivery is crucial for inducing the FLASH sparing effect. Proton-based FLASH, on the other hand, presents some differences in its temporal structure due to the physical nature of proton accelerators. In isochronous cyclotrons, the proton beam is quasi-continuous, with a pulse repetition frequency of about 10 MHz and nanosecond pulse durations. Current clinical cyclotrons can generally increase the dose rate over 40 Gy/s with minor improvements. However, the total irradiation time for proton-based FLASH is typically constrained by the process of energy-layer shifting, which is used to spread out the Bragg peak, and can extend the treatment time up to 1000 milliseconds. A key factor in both electron and proton-based FLASH is the intra-pulse dose rate. For the FLASH effect to occur, the radiation must be delivered with an ultra-high dose rate per pulse. In electron systems, each pulse carries several Grays of radiation, and the accumulation of these doses over a very short time is what creates the protective tissue-sparing response. In proton systems, while the dose per pulse may be lower, the near-continuous beam can still achieve the high overall dose rates needed for FLASH, provided that the irradiation is completed within a short time frame. The dose required to trigger the FLASH effect plays a crucial role in its clinical application. The FLASH effect, in preclinical settings, is generally observed at high doses exciding 10 Gy in acute and long-term toxic studies conducted *in vivo*. Nevertheless, this may be more related to the dose required to induce visible toxicities in comparative studies between conventional and FLASH-RT.

The mean dose rate is one of the most critical parameters in determining the effectiveness of FLASH radiotherapy. Mean dose-rate could be adjusted by changing the dose repetition frequency between pulses or by delivering the dose in less pulses. Research now suggests that a minimal dose rate of 100 Gy/s is required to observe an optimal FLASH sparing effect as it has been shown in the brain by Montay gruel et al²⁴⁷ (**Figure 49B**). Various studies suggest that this may be organ or endpoint specific, but most agree that the FLASH effect is maintained above 100 Gy/s. Additionally, for a given dose, achieving a dose rate of 100 Gy/s corresponds to a specific maximum irradiation duration. According to Montay gruel et al²⁴⁷, the most optimal total time for a 10-Gy irradiation appears to be below 100 ms. . However, if irradiations were conducted at a different dose, it remains unresolved whether the dose rate or the irradiation duration would be the determining factor.

In the context of pulsed electron irradiation, another important parameter may be the dose per pulse, or the number of pulses required to obtain a FLASH effect. For patients, for better quality control, it would be best to maintain the FLASH effect with a greater number of pulses, as irradiation with a single pulse remains too uncertain for patient safety. However, most studies have used single fractions of more than 10 Gy to characterize the effect *in vivo*. Thus, is it necessary to reduce the number of pulses to obtain a FLASH effect, and is this as important as the mean dose rate? Recent studies in the intestine by Ruan et al. suggest that the protective effect on the preservation of intestinal crypts is optimal when the dose of 11.2 Gy is delivered in a single pulse (**Figure 49C**)²⁵⁴. Further studies are therefore needed to really understand how the number of pulses or doses per pulse can influence the presence of the protective effect.

Concerning irradiation volume, the FLASH sparing effect was assessed using a mini-pig model. Two different irradiation field sizes of 3.5 × 4.5 cm and 8 × 8 cm were tested in a volume escalation study under FLASH irradiation conditions. The study showed that the FLASH sparing effect is influenced by the size of the irradiated area, with the larger field size (8 × 8 cm) leading to more significant late skin toxicity compared to the smaller field (3.5 × 4.5 cm)³⁰⁷. In the smaller irradiation field, late skin lesions evolved progressively, from erythema and ulceration to permanent hyperkeratosis and skin contracture at 6 to 8 months post-irradiation. However, for the larger field size, severe reactions such as telangiectasia occurred as early as 5 months, with full epithelial ulceration by 6 months and necrotic scabs developing by 7 to 9 months³⁰⁷. Although the lesions eventually healed by 11 months through wound contraction and reepithelialization, the larger irradiation volume induced more severe and persistent

damage. The findings suggest that the FLASH effect, which typically involves sparing of normal tissue, is more pronounced when irradiated volumes are smaller. These insights provide valuable information for refining FLASH radiotherapy protocols, especially when considering its application in clinical settings where larger treatment areas are often required for tumors.

The question of whether the FLASH effect is maintained under fractionated dosing regimens is critical for its application in clinical radiotherapy. While most early studies on FLASH radiotherapy focused on delivering a high dose in a single fraction, recent research has begun to explore whether not delivering the total dose over multiple sessions can still preserve its normal tissue-sparing effects. A recent study provided strong evidence that fractionation does not diminish the FLASH effect. In this study, 10 fractions of 3 Gy (30 Gy total) were delivered either with conventional radiotherapy or with FLASH RT to assess the impact on long-term potentiation (LTP), a measure of synaptic transmission in the brain (**Figure 49D**)³⁰⁸. Remarkably, the results from the 10x3 Gy FLASH regimen were identical to those from unirradiated controls, with both groups maintaining normal LTP function (**Figure 49D**)³⁰⁸. This finding suggests that FLASH RT can be fractionated without losing its protective effect on normal tissues, particularly in the context of cognitive function. The ability to maintain the FLASH effect with fractionated doses has significant implications for clinical practice as fractionation is a common strategy in conventional radiotherapy to balance efficacy and minimize toxicity. If the FLASH effect is preserved across multiple fractions, it opens the door for FLASH RT to be used more broadly in clinical settings, where delivering a single high dose may not always be feasible or desirable. Moreover, fractionation allows for greater flexibility in treatment planning, enabling clinicians to adapt the therapy to the specific needs of individual patients, such as those with large or complex tumors that may benefit from multiple treatment sessions. Maintaining the FLASH effect in a fractionated regimen provides an important tool for clinicians to reduce long-term side effects while still achieving the desired tumor control.

As more cancer patients are surviving their first treatments, an increasing number are requiring re-irradiation due to the occurrence of secondary cancers or recurrences. This presents a significant challenge in radiotherapy, as previously irradiated tissues are more susceptible to damage, leading to higher risks of long-term toxicities such as fibrosis, necrosis, and lymphedema. The potential for FLASH RT to minimize these risks during re-irradiation is an area of intense interest. A recent study explored the use of FLASH proton RT (F-PRT) in the re-irradiation setting, specifically comparing its effects with standard proton RT (S-PRT)³⁰⁹. The researchers investigated chronic toxicities in the intestine, skin, and bone using three murine models. In the intestine model, mice received an initial dose of 12 Gy S-PRT followed

by a second dose of either 12 Gy F-PRT or S-PRT. The study demonstrated that re-irradiation with F-PRT significantly reduced intestinal fibrosis and collagen deposition compared to S-PRT, leading to improved survival rates. These findings suggest that FLASH's tissue-sparing effects extend even to previously irradiated tissues, potentially offering a safer re-irradiation option for patients. In a separate experiment targeting skin and bone tissues, mice were first irradiated with 15 Gy S-PRT and then received hypofractionated re-irradiation (3 x 11 Gy) with either F-PRT or S-PRT. The results were similarly promising as F-PRT reduced the severity of skin toxicities such as dermatitis, which resolved completely post-treatment, while re-irradiation with S-PRT led to persistent and severe skin damage. Moreover, re-irradiation with F-PRT also significantly decreased the incidence of tibial fractures, with only 20% of mice developing fractures compared to 83.3% of those re-irradiated with S-PRT. These findings suggest that FLASH RT could offer a substantial advantage in the re-irradiation setting by reducing the risk of long-term complications in previously irradiated tissues. As re-irradiation becomes more common in cancer treatment protocols, the ability of FLASH RT to preserve normal tissue while maintaining tumor control could make it a highly valuable tool.

The transition of FLASH radiotherapy into clinical practice requires a deep understanding of the optimal parameters that govern the FLASH effect. Key parameters such as the temporal structure, dose per pulse, mean dose rate, and the number of pulses must be finely tuned to achieve the protective tissue-sparing effects without compromising tumor control. To fully transition FLASH RT into clinical practice, it is essential to conduct extensive studies on optimal parameters using a consistent and suitable model system. Although *in vitro* models would ideally be used to answer these questions due to their controlled environment and high-throughput capabilities, they present significant challenges when modeling the FLASH effect.

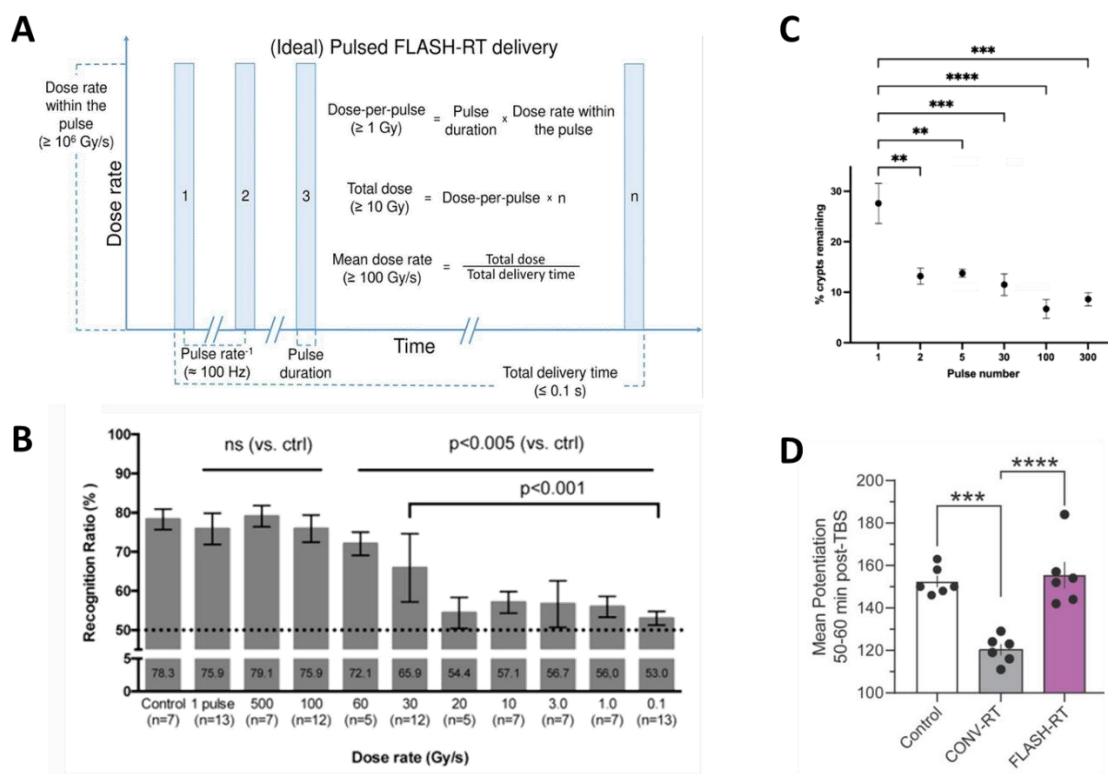


Figure 49. Optimal Irradiation Parameters in FLASH Radiotherapy (A) Schematic representation of the various parameters involved in pulsed electron FLASH radiotherapy. (B) Study on the impact of different mean dose rates on tissue sparing effects in the brain. (C) Analysis of the effect of pulse number on tissue sparing during FLASH irradiation. Increasing the number of pulses significantly reduces the sparing effect. (D) Early results from a study using a fractionated FLASH regimen (3 x 10 Gy), showing that the FLASH effect is maintained across fractionation.

3.4.4 *In vitro* modelling of the FLASH sparing effect for clinical translation

One of the foremost challenges in transitioning FLASH radiotherapy to clinical practice is the difficulty of modeling its effects accurately *in vitro*, which would be necessary to study the response in the context of patients or decipher the optimal parameters for FLASH radiation therapy. Conventional *in vitro* models, such as 2D cell cultures, fail to replicate the complexity of *in vivo* tissue structures, including the oxygen gradients, vascularization, and microenvironmental conditions that significantly influence the radiobiological response. As an example, it has been shown that clonogenic tests cannot distinguish between the two modalities at low doses³¹⁰, most results were inconsistent using this classical model for radiobiology. Reasons could be multiple as the strong influence of tissue oxygenation and ROS production for the FLASH sparing effect, both of which are difficult to simulate in standard *in vitro* conditions^{44,247}. Traditional 2D cultures are homogeneously oxygenated, whereas *in vivo* tissues exhibit a range of oxygen tensions, creating a significant limitation in replicating the protective effects of FLASH in an *in vitro* setting²⁷⁵. More advanced models, such as 3D organoids and microfluidic systems, have been developed to better mimic the architecture and microenvironment of tissues. These models are more capable of simulating the spatial distribution of oxygen and nutrients, offering a closer approximation to the physiological conditions seen in living organisms. Despite these advancements, there remains a lack of standardization in experimental setups, which complicates the replication and comparison of FLASH studies across different laboratories. This variability has led to inconsistent results in some preclinical studies, underscoring the need for a standardized approach to *in vitro* FLASH research²⁸⁶. The FLASH effect is a biological phenomenon primarily demonstrated *in vivo*, and validating a FLASH beam requires a precise combination of selected physical parameters and comprehensive biological testing. It has been postulated that *in vitro* experiments cannot replace *in vivo* validation as recent research indicates that radioprotection *in vitro* cannot be observed under atmospheric oxygen conditions (21%) for doses below 20 Gy. This is why alternative *in vivo* models have been used for radiobiological studies such as the zebrafish. As a vertebrate species, it shares considerable genetic similarity with humans. Zebrafish embryos are transparent, enabling real-time imaging and easy monitoring of radiation effects, such as tissue sparing. The model allows for high-throughput screening and controlled environmental conditions. Their use in studies like those involving proton irradiation continues to provide valuable insights into the optimization of FLASH RT for clinical applications³¹¹. These models are cost-effective, scalable, and enable dose-response analyses, making zebrafish a promising platform for preclinical FLASH research. Thus, to help the transition of FLASH to clinical practice and to better understand its underlying mechanisms, new and more complex models recapitulating the architecture of the tissue will need to be needed.

3.4.5 Large mammals' preclinical studies

The feasibility of FLASH radiotherapy for larger irradiation volumes has been investigated through a series of preclinical studies involving large mammals, such as mini pigs, cats, and dogs. These studies are essential for verifying the applicability of FLASH RT in clinical settings, given that larger animals with spontaneous tumors more closely mimic the complexity of human cancer treatments. The first set of studies was conducted on mini pigs and cats. These early trials aimed to evaluate the tolerability and therapeutic potential of single high-dose FLASH-RT in larger animal models. In mini pigs, doses ranging from 22 to 34 Gy were delivered using 4.5 MeV electron beams. Furthermore, a clinical, phase I, single-dose escalation trial (25-41 Gy) was performed in 6 cat patients with locally advanced T2/T3N0M0 squamous cell carcinoma of the nasal planum to determine the maximal tolerated dose and progression-free survival (PFS) of single-dose FLASH-RT³¹². Using, respectively, depilation and fibronecrosis as acute and late endpoints, a protective effect of FLASH-RT was observed ($\geq 20\%$ dose-equivalent difference vs. Conv-RT)³¹². Three cats experienced no acute toxicity, whereas 3 exhibited moderate/mild transient mucositis, and all cats had depilation. With a median follow-up of 13.5 months, the PFS at 16 months was 84% (**Figure 50A**)³¹². These early results highlighted the potential for FLASH RT to safely treat larger tumors in more complex anatomical settings³¹². Following these promising initial results, studies were expanded to dogs with both superficial tumors and microscopic residual disease³¹³. Ten canine cancer patients were included in this initial study including seven patients with nine solid superficial tumors and three patients with microscopic disease³¹³. The administered dose ranged from 15 to 35 Gy. Treatments were found to be feasible, with partial response, complete response or stable disease recorded in 11/13 irradiated tumors³¹³ (**Figure 50B**). Adverse events observed at follow-up ranging from 3-6 months were mild and consisted of local alopecia, leukotricia, dry desquamation, mild erythema or swelling³¹³. One patient receiving a 35 Gy dose to the nasal planum, had a grade 3 adverse skin event³¹³ (**Figure 50B**). The experience from this initial study was then used as a basis for a veterinary phase I/II clinical trial with more specific patient inclusion selection. A separate study on dogs with oral tumors revealed more significant challenges³¹⁴. Oral tumors present risks due to the sensitivity of the tissues and the involvement of bone in the treatment field. In this study, dogs received single fractions of ≥ 30 Gy FLASH-RT were subsequently followed for 12 months³¹⁴. Eleven dogs were enrolled in this prospective study. High grade adverse effects were common, especially if bone was included in the treatment field. Four out of six dogs, who had bone in their treatment field and lived at least 5 months after RT, developed osteoradionecrosis at 3-12 months post treatment³¹⁴ (**Figure 50C**). The treatment was overall effective with 8/11 complete clinical

responses and 3/11 partial responses³¹⁴. The study concluded that while single-fraction FLASH RT can be effective, the risk of osteoradionecrosis necessitates careful consideration of dose distribution and beam conformity when treating tumors near bone. Subsequently, another pre-clinical trial in cat patients confirmed the previous results concerning the importance of a robust clinical trial design for FLASH radiotherapy. Indeed, cats with T1-T2, N0 carcinomas of the nasal planum were randomly assigned to two arms of electron irradiation: arm 1 was the standard of care and used 10 × 4.8 Gy and arm 2 used 1 × 30 Gy FLASH³⁰⁷. In that case, the trial was prematurely interrupted due to maxillary bone necrosis, which occurred 9 to 15 months after radiotherapy in 3 of 7 cats treated with FLASH-radiotherapy (43%), as compared with 0 of 9 cats treated with conventional standard of care³⁰⁷ (**Figure 50D**). All cats were tumor-free at 1 year in both arms, with one cat progressing later in each arm³⁰⁷. The reported outcomes point to the caveats of translating single-high-dose FLASH-radiotherapy and emphasize the need for caution and further investigations before human clinical trials.

In conclusion, preclinical studies on large mammals such as mini pigs, cats, and dogs have provided valuable insights into the feasibility and safety of FLASH RT for treating larger tumors. These studies underscore the importance of careful dose planning and suggest that FLASH should be also fractionated to mitigate the risks of severe late toxicities, particularly when treating tumors in sensitive areas. The findings from these large animal models are critical for designing human clinical trials, guiding the development of optimized FLASH RT protocols that balance tumor control with minimal normal tissue toxicity.

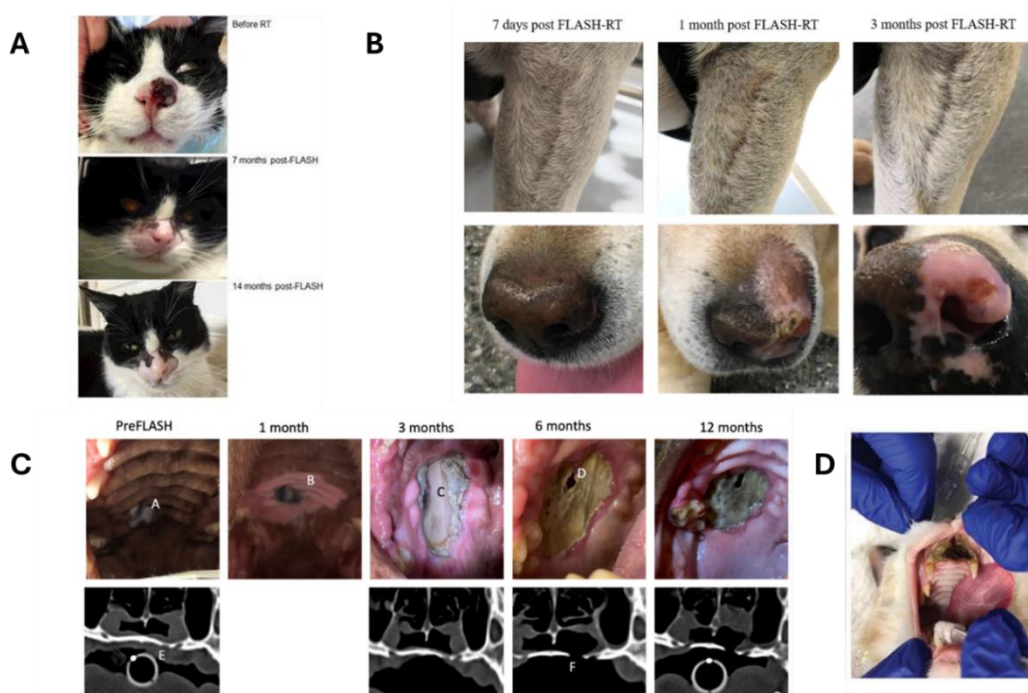


Figure 50. Large Mammal Studies of FLASH Radiotherapy.

3.4.6 Ongoing clinical trials

The transition of FLASH radiotherapy from preclinical studies to clinical applications is currently underway, with several pivotal trials aiming to assess its feasibility, safety, and efficacy. Below is a summary of the most notable ongoing and completed clinical trials involving FLASH RT. In 2018, a groundbreaking first-in-human treatment was conducted at Lausanne University Hospital (CHUV)³¹⁵. This pioneering study involved treating a patient with refractory skin lymphoma using electron-based FLASH RT. The treatment, which delivered radiation in milliseconds rather than minutes, was a world-first, showing that FLASH therapy could be safely administered to humans (**Figure 51A**). This trial laid the foundation for further clinical exploration of FLASH-RT's potential, demonstrating the feasibility of ultra-high dose rate delivery. Few years later, the FAST-01 trial, conducted at the Cincinnati Children's/University of Cincinnati Proton Therapy Center, marked the first-in-human study of proton-based FLASH RT. This trial, completed in 2022, focused on patients with painful extremity bone metastases (**Figure 51B**)³¹⁶. The primary goal was to assess the feasibility of delivering FLASH RT using protons at ultra-high dose rates. The study demonstrated that FLASH RT was not only feasible but also reduced pain without increasing side effects³¹⁶. Data from the FAST-01 trial has supported the development of additional clinical protocols and were considered a breakthrough in radiation oncology with FLASH-RT. Following the success of FAST-01, the FAST-02 trial was launched to further explore FLASH RT's capabilities. This trial focuses on treating bone metastases in the thorax and is designed to assess both the safety and efficacy of FLASH RT in a broader patient population³¹⁷. The goal is to evaluate pain relief and treatment-related side effects, particularly in the context of palliative care. FAST-02 is expected to build on the foundational knowledge gained from FAST-01 and further establish the clinical viability of FLASH-RT. In summary, the preliminary results from these clinical trials are highly encouraging, providing a strong basis for the continued development of FLASH RT. However, for now, none of these studies have been designed to assess the presence of a FLASH sparing effect in patients.

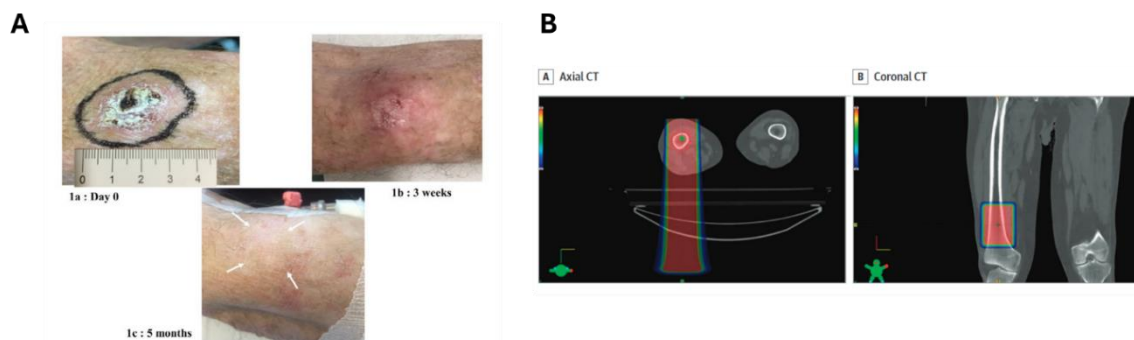


Figure 51. Ongoing clinical trials for FLASH-RT.

CHAPTER II : HYPOTHESIS AND MAIN OBJECTIVES

II- HYPOTHESIS AND MAIN OBJECTIVES

FLASH radiotherapy, characterized by ultra-high dose rates delivered in a fraction of a second, has shown great promise for improving the therapeutic index of radiotherapy. However, despite the growing interest in this novel treatment modality, there remain significant gaps in our understanding of its molecular mechanisms and its transition into clinical practice. Specifically, we lack a comprehensive **understanding of how FLASH spare healthy tissue**, particularly in the lung, and **how the optimal irradiation parameters can be tuned to maximize its therapeutic effects while minimizing collateral damage**. Furthermore, even if phase I clinical trials are ongoing, **for now, there is no evidence of a FLASH sparing effect in patients** which could greatly support its clinical transition.

Our laboratory's expertise in FLASH-RT, particularly in its pulmonary context^{241,260}, along with access to a preclinical FLASH electron irradiator³¹⁸ and expertise in ScRNA-seq for molecular analyses²⁶⁰, positions us well to address these gaps. Furthermore, our knowledge of the mechanisms underlying radiation-induced lung injury (RILI) after conventional radiation provides a solid foundation for investigating how FLASH may offer a protective effect for lung tissue²⁰⁰.

Thus, we propose to use a pulmonary *ex vivo* model to study the response of healthy lung tissue to FLASH radiotherapy, specifically focusing on the molecular and cellular changes that occur in response to this novel treatment compared to a conventional beam. By using a model that accurately replicates lung architecture and its microenvironment, we can effectively examine the mechanisms of the FLASH sparing effect, which is inherently an *in vivo* effect. My thesis is divided into two main objectives :

- 1) To support the clinical transition of FLASH, we need to **develop simple yet relevant lung models to demonstrate FLASH's protective effects**. In this context, **our first objective is to determine the optimal irradiation parameters for achieving the FLASH sparing effect**. We aim to study these parameters in an *ex vivo* lung model and **verify the presence of a FLASH effect in human tissue**. This data is currently lacking and is crucial for the clinical transition of FLASH. For this, we have chosen to **adapt PCLS as they recapitulate the lung's architecture and microenvironment**, which is essential for understanding the underlying mechanisms of FLASH.

- 2) In a second part, we aim to perform in-depth molecular analyses **to study the acute and late response of lung tissue to FLASH versus conventional radiotherapy**. Then, we will **focus on specific cell populations known to be spared by FLASH radiotherapy, such as cycling cells** in the lung. This will allow us to explore the molecular mechanisms behind FLASH's potential to reduce normal tissue damage, providing valuable insights into how FLASH could be leveraged for safer and more effective radiotherapy in clinical settings.

This work will primarily focus on understanding the response of healthy lung tissue to these two radiation modalities, providing crucial data for the clinical implementation of FLASH radiotherapy.

CHAPTER III to V : RESULTS

III- PART 1 – DEVELOPMENT OF AN EX VIVO MODEL FOR FLASH STUDIES

1. MODELING THE FLASH EFFECT *EX VIVO*

1.1 Introduction

In this first part of my thesis results, **our objective was to successfully model the FLASH sparing effect using a relevant *ex vivo* model.** The FLASH effect has been extensively demonstrated *in vivo*, but it seems very challenging to model it using functional classical tests such as the clonogenic survival assay. We chose to **adapt the PCLS model for short-term radiotoxicity studies in the pulmonary context.** Indeed, **PCLS recapitulates architecture, structure and cellular microenvironment of the lung,** parameters that appear to be major for modelling the FLASH sparing effect in healthy tissue²²⁴. Thus, in this first study, we present our protocol and characterization of the response of PCLS to conventional or FLASH-RT short term post-treatment.

In addition to what has been described in this article, numerous endpoints were tested using the PCLS model, including different methods to study viability, apoptosis, or DNA damage. For each endpoint, **our objective was initially to detect the relationship between the dose and the tested endpoint,** but most of the time, the thickness of the organotypic slice made this type of analysis irrelevant without very time-consuming optimization.

Surprisingly, this model **allowed us to demonstrate a FLASH protective effect on cycling pulmonary populations** in the short-term post-treatment, which was not the case using the viability assay we developed. We then **validated this effect *in vivo*,** further confirming the relevance of this model in studying the FLASH protective effect concerning the development of acute post-treatment toxicities in the lung. In addition, we also **explored,** as proof of concept, **the feasibility of studying the combination of radiotherapy and chemotherapy** treatments in the PCLS model, aiming to demonstrate its potential for broader applications in studying radiation-induced toxicities.

Article

Lung Organotypic Slices Enable Rapid Quantification of Acute Radiotherapy Induced Toxicity

Maxime Dubail ^{1,2}, Sophie Heinrich ^{1,2}, Lucie Portier ^{1,2}, Jessica Bastian ^{1,2}, Lucia Giuliano ³, Lilia Aggar ^{1,2}, Nathalie Berthault ^{1,2}, José-Arturo Londoño-Vallejo ^{1,2}, Marta Vilalta ⁴, Gael Boivin ⁴, Ricky A. Sharma ^{4,5}, Marie Dutreix ^{1,2} and Charles Fouillade ^{1,2,*}

¹ Institut Curie, Inserm U1021-CNRS UMR 3347, Paris Saclay University, Centre Universitaire, 91405 Orsay Cedex, France

² Institut Curie, PSL Research University, 75006 Paris, France

³ SBAI Department, Sapienza University of Rome, 00161 Rome, Italy

⁴ Global Translational Science, Varian, a Siemens Healthineers Company, Palo Alto, CA 94304, USA

⁵ UCL Cancer Institute, University College London, London WC1E 6DD, UK

* Correspondence: charles.fouillade@curie.fr; Tel.: +33-1-69-86-71-86

Abstract: To rapidly assess healthy tissue toxicities induced by new anti-cancer therapies (i.e., radiation alone or in combination with drugs), there is a critical need for relevant and easy-to-use models. Consistent with the ethical desire to reduce the use of animals in medical research, we propose to monitor lung toxicity using an ex vivo model. Briefly, freshly prepared organotypic lung slices from mice were irradiated, with or without being previously exposed to chemotherapy, and treatment toxicity was evaluated by analysis of cell division and viability of the slices. When exposed to different doses of radiation, this ex vivo model showed a dose-dependent decrease in cell division and viability. Interestingly, monitoring cell division was sensitive enough to detect a sparing effect induced by FLASH radiotherapy as well as the effect of combined treatment. Altogether, the organotypic lung slices can be used as a screening platform to rapidly determine in a quantitative manner the level of lung toxicity induced by different treatments alone or in combination with chemotherapy while drastically reducing the number of animals. Translated to human lung samples, this ex vivo assay could serve as an innovative method to investigate patients' sensitivity to radiation and drugs.

Keywords: radiation toxicity; FLASH radiotherapy; organotypic lung slices; ex vivo model; combined treatment



Citation: Dubail, M.; Heinrich, S.; Portier, L.; Bastian, J.; Giuliano, L.; Aggar, L.; Berthault, N.; Londoño-Vallejo, J.-A.; Vilalta, M.; Boivin, G.; et al. Lung Organotypic Slices Enable Rapid Quantification of Acute Radiotherapy Induced Toxicity. *Cells* **2023**, *12*, 2435. <https://doi.org/10.3390/cells12202435>

Academic Editor: Alexander Dietrich

Received: 13 September 2023

Revised: 3 October 2023

Accepted: 7 October 2023

Published: 11 October 2023



Copyright: © 2023 by the authors. Licensee MDPI, Basel, Switzerland. This article is an open access article distributed under the terms and conditions of the Creative Commons Attribution (CC BY) license (<https://creativecommons.org/licenses/by/4.0/>).

1. Introduction

In combination with chemotherapy and immunotherapy, radiotherapy remains one of the main therapeutic options in the fight against cancer [1]. To maximize the therapeutic index, radiation oncologists aim to deliver high doses to the tumor while preserving the surrounding organs at risk [2]. Several factors, such as the radiation protocol used, associated chemotherapies, or patient comorbidities, contribute to the development of radio-induced toxicities. To circumvent such toxicities, FLASH radiotherapy, an innovative radiation modality relying on ultra-high dose rates, has been recently described [3]. FLASH radiotherapy is an innovative method that delivers radiation at an ultra-high dose rate, inducing a sparing of healthy tissue from radio-induced toxicities while preserving the same anti-tumoral efficacy [3]. The so-called FLASH effect has been demonstrated in various organs, including the lung [3,4], the brain [5,6], the skin [7–9], and the intestine [10,11]. However, evaluation of the impact of different protocols of radiotherapy on the FLASH effect, as well as a combination with classical chemotherapies, is still needed to facilitate clinical translation of this technology. For this purpose, assays to rapidly quantify radiation toxicity of the different treatment combinations are promptly needed.

In the case of thoracic radiotherapy, radio-induced damages are characterized by pneumonitis that may evolve into lung fibrosis in the most severe cases [2]. Preclinical mouse models have been classically used to determine radiation-induced lung injury [12]. However, the number of animals required, as well as delays in fibrosis development, preclude the use of mouse models for screening purposes. Alternatively, *in vitro* lung models struggle to recreate the complex architecture and cellularity of lung tissue, thus lacking the cellular heterogeneity and interactions classically observed in the lung [13]. In recent years, organotypic slices have become a popular model for studying biological processes, including inflammatory responses, pathology modeling, infection, and new drug testing [14,15]. These thin tissue slices of 100 to 500 μm thickness can be obtained from murine models [16] as well as from patient samples [17,18]. In this model, cellular architecture is preserved, as shown by the characterization of epithelial cells [19,20], mesenchymal cells [21,22] (i.e., fibroblasts), endothelial cells [23], and immune populations [16,24]. Circulating immune cells are absent in organotypic lung slices, but co-culture systems have been developed to overcome this issue [25].

In the study of radiation effects, established and validated *ex vivo* models have been previously used in the brain [26], but, to our knowledge, it has never been applied to the lung. To evaluate the impact of different radiotherapy protocols and their association with drugs, we used lung organotypic slices to rapidly quantify radiation toxicity. First, we characterized the cell viability and cell division inside lung organotypic slices in culture. Then, a similar analysis performed 24 h after exposure to increased doses of radiation showed a dose-dependent decrease in cell viability and in the proportion of replicating cells, indicating that organotypic lung slices are a suitable model to monitor radiation toxicity *ex vivo*. When combined with standard chemotherapies, we showed that quantifying the proportion of replicating cells inside lung organotypic slices can be used to evaluate the toxicities of combined treatments. Interestingly, the analysis of cell replication was sensitive enough to detect a sparing effect induced by FLASH radiotherapy.

Altogether, this study demonstrates, for the first time, the usefulness of a lung *ex vivo* model to rapidly evaluate the toxicity of different radiation treatments (e.g., FLASH radiotherapy) while drastically reducing the number of animals required.

2. Materials and Methods

2.1. Mice and Ethics Statement

Studies were performed in accordance with the European Community recommendations (2010/63/EU) for the care and use of laboratory animals. The experimental procedures were specifically approved by the Ethics Committee of Institut Curie CEEA-IC #118 (authorization number APAFiS#32674-2021080916494690 given by the National Authority) in compliance with international guidelines. Females C57BL/6J mice purchased from Charles River Laboratories (Lyon, France) at 6 weeks of age were housed in the Institut Curie animal facilities.

2.2. Mouse Organotypic Lung Slices Obtention and Culture

Adult female C57BL/6J mice aged 6 to 10 weeks were anesthetized by intraperitoneal injection of ketamine/xylazine. Blood was then flushed through intracardiac injection of phosphate-buffered saline (PBS) and the trachea was exposed to inject 2 mL of 2.5% low-melting agarose (A9414-50G, Sigma-Aldrich, Saint-Louis, MI, USA) diluted in organotypic lung slices medium DMEM F12 (31331-028, Thermo Fisher Scientific, Waltham, MA, USA) supplemented with 1% SVF (CVFVSF00-0U, Thermo Fisher Scientific, Waltham, MA, USA), 1% penicillin/streptomycin (CABPES01-0U, Thermo Fisher Scientific, Waltham, MA, USA), 1% non-94 essential amino acids (11140035, Thermo Fisher Scientific, Waltham, MA, USA) and 1% L-glutamine (25030-024, Thermo Fisher Scientific, Waltham, MA, USA). Once the agarose was solidified, lungs were removed from the chest cavity, and 8 mm punches were made from each lobe individually. Tissue punches were embedded in 5% agarose, and 300 μm slices were made with a Vibratome (Leica VT1000S, Nanterre, France) as previously

described [14]. The whole procedure lasted less than 2 h. Around 50 slices were obtained from a lung and placed into a 24-well plate containing each 500 μ L of organotypic lung slice medium and cultured at 37 °C in 5% CO₂ for up to 72 h.

2.3. Lung Slices Irradiation

Lung slices were obtained from the same biological sample and randomly assigned to different groups for the different doses of radiation in each experiment. We used the electron linear accelerator (linac) ElectronFLASH (SIT S.p.A., R&D Dept., Roma, Italy) available at Institut Curie and previously described [27]. Lung slices were irradiated in culture plates with a vertical 7-MeV beam at a source distance of 1.1 m, allowing a dose homogeneity throughout the wells' positions better than 95%. The dosimetry was controlled by EBT-XD Gafchromic (Ashland, Bridgewater, NJ, USA) film measurements: films were cut into adapted pieces and placed at the position of the target (i.e., inside the culture wells with medium). For all conventional irradiations, we used these measurements to calibrate the monitoring ion chamber of the linac (0.007 Gy/MU at the target, which corresponds to \approx 0.5 Gy/s). The linac stopped automatically when the number of Monitor Units reached the prescribed value for any dose. In the case of FLASH irradiations, we set the dose per electron-pulse at 3 Gy/pulse (\pm 0.2 Gy) by adjusting the pulse duration, and we delivered 1, 2, and 3 pulses to achieve the target doses of 3, 6, and 9 Gy. All the beam parameters are summarized in Supplementary Table S1.

2.4. Whole Thorax Irradiation

Mice were exposed at the age of 10–12 weeks to a 9 or 13 Gy whole thorax irradiation with a horizontal 5-MeV beam at a Source Distance of 0.65 m, with a setup equivalent to the one previously described in [3]. Anesthesia was carried out with a nose cone using 2.5% isoflurane in the air without adjunction of oxygen. The dosimetry was controlled on an individual basis with Gafchromic films positioned on the mouse thorax surface at the center of the irradiation field. The dose rate was 0.1 Gy/s in the conventional modality and 3 Gy/pulse in the FLASH modality (Supplementary Table S1).

2.5. Drug Treatment

Freshly prepared organotypic lung slices were incubated at 37 °C in culture plates with concentrations of Docetaxel and Carboplatin ranging from 200 μ M to 10 μ M for each drug diluted in 500 μ L of organotypic lung slices medium. After one hour of incubation, slices were washed twice with a medium to remove the remaining drugs. Then, slices were irradiated, and cell division was measured as described below.

2.6. Cell Viability

To monitor the cell death induced after irradiation in the lung slices, we stained the organotypic lung slices with Hoechst and Ethidium-1 homodimer 24 h after exposure to doses ranging from 3 to 9 Gy. Organotypic lung slices were incubated in 500 μ L of culture medium containing 2 μ M Ethidium-1 homodimer. Then, organotypic lung slices were washed in PBS and incubated with the Hoechst nuclear dye for 2 h. For imaging, organotypic lung slices were transferred into a glass support adapted for microscopy (μ -Slide 4 Well Glass Bottom, Ibidi, Gräfelfing, Germany) and imaged on an inverted Nikon Spinning disk TIRF-FRAP using a 20 \times objective. Per slice, 3 to 5 fields of view were acquired, each containing 20 stacks spaced by 3 μ m. The proportion of EdU+ cells was quantified with a semi-automatic method combining 3D reconstruction and segmentation of the nuclei using IMARIS software version 9.3.1 (Bitplane, Belfast, UK).

2.7. Cell Replication

To estimate the proportion of cells that replicate after irradiation in the lung slices, we used a Click-IT chemistry protocol to monitor cell proliferation using 5-ethynyl-2'-deoxyuridine (EdU) incorporation (BCK-EdUPro-FC647). Irradiated slices were incubated

in 500 μL of culture medium containing 10 μM EdU. After the desired incubation time (i.e., 24, 48, or 72 h), they were treated according to the manufacturer's instructions. Then, organotypic lung slices were washed in PBS and incubated with a nuclear dye (e.g., DAPI). For imaging, organotypic lung slices were transferred into a glass support adapted for microscopy ($\mu\text{-Slide 4 Well Glass Bottom}$, Ibidi) and imaged on an inverted Nikon Spinning disk TIRF-FRAP using a 10 \times objective. Per slice, 3 to 5 fields of view were acquired, each containing 50 stacks spaced by 3 μm . The proportion of EdU+ cells was quantified with a semi-automatic method combining 3D reconstruction and segmentation of the nuclei using IMARIS software Bitplane.

2.8. Statistical Analysis

Statistical analyses were performed using the ggpubr package (<https://rpkgs.datanovia.com/ggpubr/> (accessed on 4 September 2023)) in R. For our EdU+ nuclei count data, we assumed samples are not independent (from the same biological sample), and our data do not follow a normal distribution. Comparisons of the means of these counts for the FLASH and CONV.

3. Results

3.1. Characterization of Lung Organotypic Slices

To counteract the limitations of current *in vitro* assays for radiation studies in the lung, we aimed to implement an *ex vivo* lung model to enable rapid and quantitative analysis of radiation toxicity. In order to preserve the complexity of the lung architecture and the distinct cell types, we adapted the lung *ex vivo* model, previously used for chemical toxicity study, to investigate radiation toxicities in healthy lungs. Briefly, mouse lungs were inflated with agarose and sliced at 300 μm . Once obtained, lung slices, maintained in a medium, were irradiated and analyzed in the days following their preparation (Figure 1A). To evaluate the preservation of lung architecture and, in particular, alveoli structure in the slices, we crossed the mouse transgenic line *Sftpc-CreERT2* [28] with the reporter line carrying the *R26-mTmG* allele [29] to label the AT2 cells with GFP upon tamoxifen treatment. This analysis showed that the lung structure is maintained in the slices and that AT2 cells are nicely preserved in the alveoli.

3.2. Analysis of Cell Viability and Cell Division in Organotypic Lung Slices

To characterize the lung *ex vivo* model, we aimed to evaluate the cell viability and cell division of organotypic slices for the first 3-days after obtention. For these purposes, we quantified, on the one hand, the proportion of dead cells stained by Ethidium (Figure 2A) and, on the other hand, the proportion of replicating cells that incorporate EdU for a period of 24, 48, or 72 h (Figure 2B). The analysis of cell viability showed that the proportion of Ethidium-positive cells increased over time from 14.9% after 24 h, 27.5% after 48 h, and 45.2% after 72 h (Figure 2C). On a similar trend, the proportion of replicating cells per field of view (FOV) increased steadily from 36 EdU+ cells after 24 h to 480 cells after 48 h and 818 cells after 72 h (Figure 2D).

Interestingly, the analysis of EdU incorporation in the lung by flow cytometry revealed that between 0.5 and 1% of cells are replicating *in vivo* for 24 h, suggesting that *ex vivo* analysis of EdU incorporation at 24 h reflects physiological conditions occurring *in vivo* (Supplementary Figure S1). For further analysis, we selected the 24 h time point to evaluate radiation toxicity in lung organotypic slices.

3.3. Radiation Induces a Dose-Dependent Decrease in Cell Viability and Cell Proliferation *Ex Vivo*

To characterize the effect of radiation in organotypic lung slices, we first monitored cell viability after exposure to different doses of radiation using Ethidium-1 staining (Figure 3A,C). Quantification of Ethidium-1 positive cells in organotypic lung slices 24 h after radiation exposure showed a dose-dependent increase in the proportion of Ethidium-1

positive cells ranging from 37.7% after 3 Gy to 44.8% after 6 Gy and 50.2% after 9 Gy. This result confirms that radiation induces *ex vivo* a dose-dependent decrease in viability.

Because it is well known that radiation triggers cell cycle arrest to enable cell repair [2], we hypothesized that radiation may impact the capacity of lung cells to replicate after irradiation. To test this hypothesis *ex vivo*, organotypic lung slices were exposed to conventional radiation at doses ranging from 3 Gy to 9 Gy and immediately incubated with EdU for 24 h. As expected, the proportion of EdU+ cells progressively decreased as the dose increased (Figure 3B,D). Quantification of the proportion of EdU+ cells after exposure to doses of 3 Gy, 6 Gy, and 9 Gy showed a decrease of 53%, 68%, and 80%, compared to the proportion of EdU+ cells observed in non-irradiated slices. To evaluate the robustness of the method, we estimated the variability in the proportion of EdU+ cells quantified after a dose of 9 Gy (i) between technical replicates by comparing four different organotypic slices obtained from the same mouse (Supplementary Figure S2A) and (ii) between biological replicates by analyzing organotypic slices obtained from three different mice (Supplementary Figure S2B). No significant difference was observed between the slices from the same mouse or between mice.

Altogether, these results indicate that radiation induces *ex vivo* a dose-dependent decrease in cell viability as well as cell replication 24 h after irradiation. Considering the robustness and reproducibility of the analysis of EdU incorporation in organotypic lung slices, these analyses appear to be suitable for comparison between different radiation modalities.

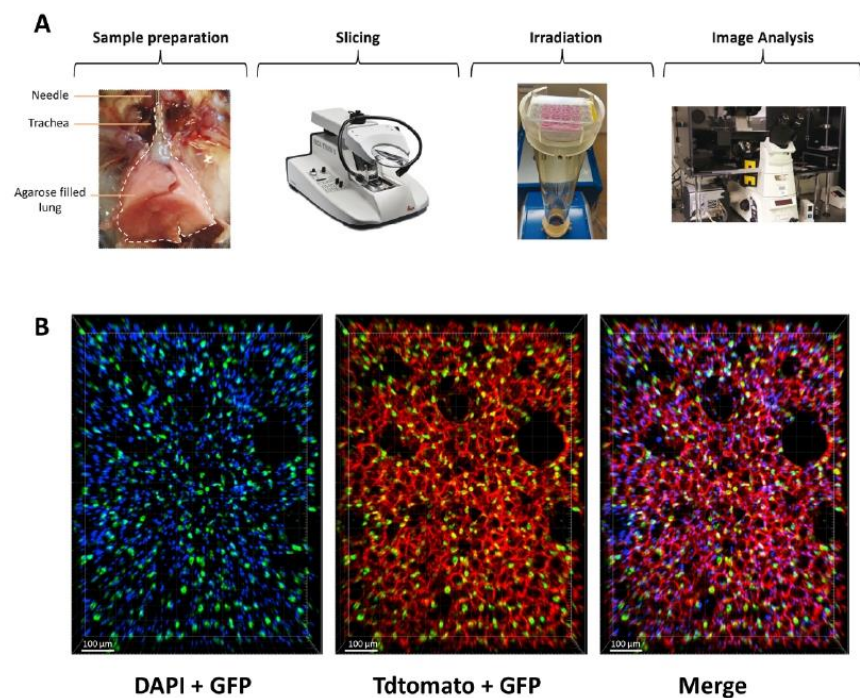


Figure 1. Structure and morphology of the lung are preserved *ex vivo*. (A) Scheme of the protocol to obtain and analyze radiation toxicity using lung organotypic slices. (B) Lung organotypic slices prepared from *Sftpc-CreERT2*; *R26-mTmG* mice in which all cells expressed TdTomato allowed to visualize the preserved structure of the lung and AT2 cells, labeled with GFP are present in the alveoli.

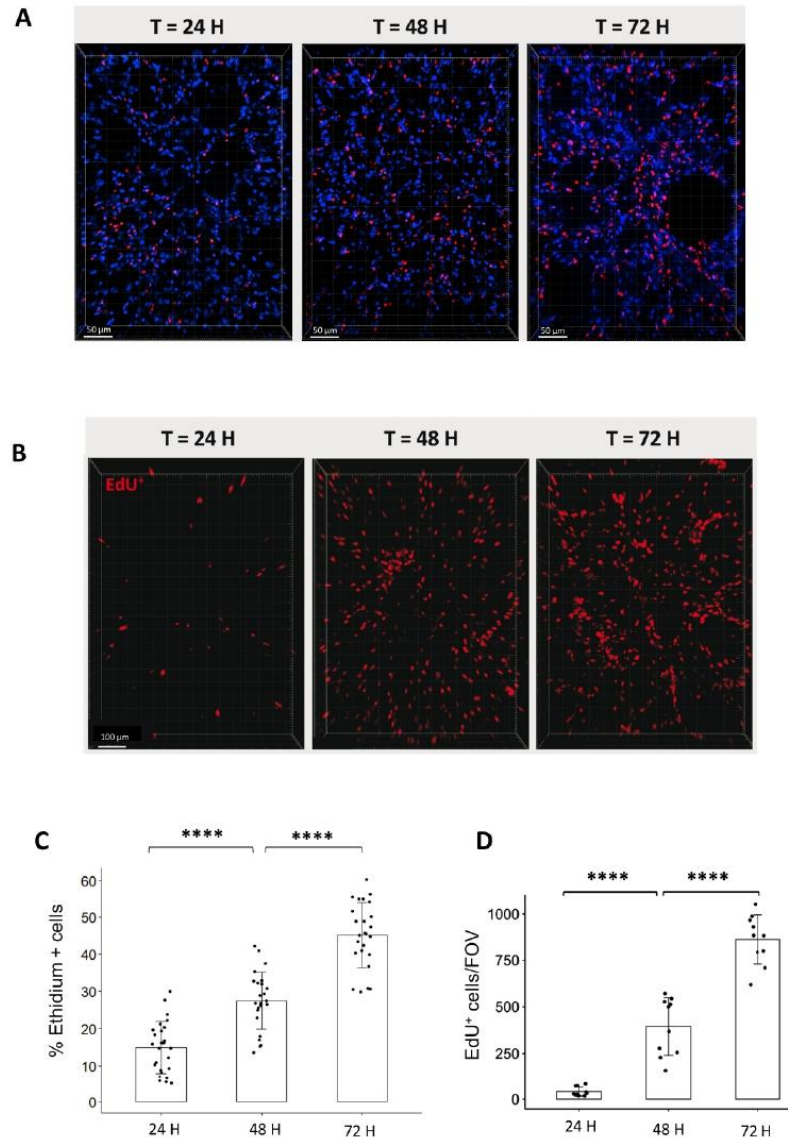


Figure 2. Analysis of cell viability and replication in organotypic lung slices in culture. **(A)** Representative 3D reconstruction of Ethidium incorporation in organotypic lung slices after 24, 48, and 72 h in culture. Images were acquired on a confocal microscope with a 20 \times objective. The scale bar represents 50 μ m. **(B)** Representative 3D reconstruction showing EdU+ cells after exposure to EdU for either 24, 48, or 72 h. Images were acquired on a confocal microscope with a 10 \times objective. The scale bar represents 100 μ m. **(C)** The quantification of the proportion of Ethidium positive cells per FOV (4 to 5 FOV for $n = 5$ slices) showed an increase in the proportion of dead cells from 24 to 72 h. Each dot represents the quantification for one field of view **(D)** Image analysis and quantification showed a steep increase in the number of EdU+ /FOV over time (min 4 FOV for $n = 3$ slices). Each dot represents the quantification for one field of view. **** p -value < 0.0001.

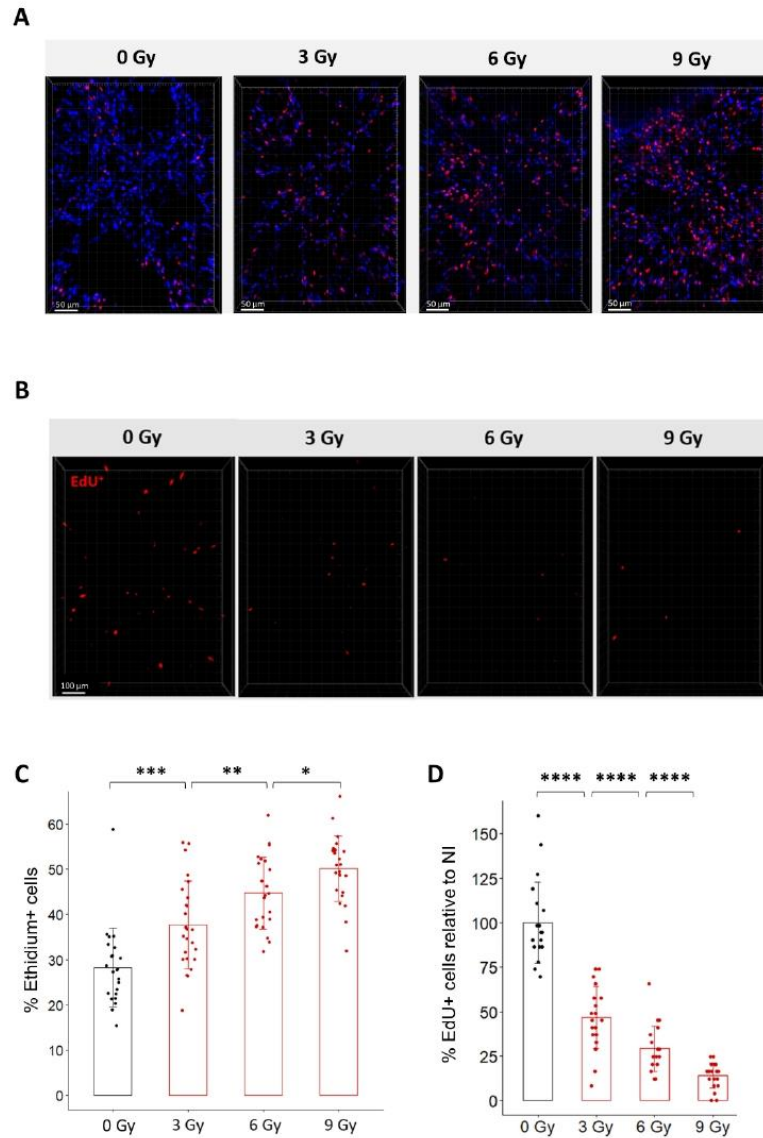


Figure 3. Dose-dependent effects of radiation on cell viability and cell replication in organotypic lung slices. **(A)** Representative 3D reconstruction of cell viability analysis in organotypic lung slices 24 h after exposure to different doses of radiation. Images were acquired on a confocal microscope with a 20 \times objective. The scale bar represents 50 μ m. **(B)** Representative 3D reconstruction showing EdU+ cells 24 h after exposure to doses from 3 to 9 Gy dose of radiation. Images were acquired on a confocal microscope with a 10 \times objective. The scale bar represents 100 μ m. **(C)** Quantification and image analysis revealed a dose-dependent increase in the proportion of Ethidium-positive cells per FOV ($n = 4$ to 5 FOV per slice for a total of 5 slices per condition) Each dot represents the quantification for one field of view. **(D)** Image analysis and quantification show a significant dose-dependent decrease in the proportion of EdU+ cells 24 h after radiation exposure ($n = 4$ to 5 FOV per slice for a total of 5 slices per condition) Each dot represents the quantification for one field of view. * p -value < 0.05; ** p -value < 0.01; *** p -value < 0.001; **** p -value < 0.0001.

3.4. Cell Replication Analysis Ex Vivo Allows to Discriminate between FLASH and CONV Irradiation

To determine if ex vivo analysis of cell replication is sufficient to discriminate between conventional (CONV) and FLASH modalities, we quantified the proportion of EdU+ cells in lung organotypic slices after exposure to different doses delivered either in CONV or FLASH conditions using the ElectronFLASH linear accelerator developed by SIT company (SIT S.p.A., R&D Dept., Roma, Italy). As a new FLASH device, we first confirmed that whole thorax FLASH irradiation using the ElectronFLASH linac triggers a sparing from radiation-induced lung fibrosis (Figure 4A,B). Then, we exposed the organotypic lung slices to doses of 3 Gy, 6 Gy, and 9 Gy delivered either in CONV (0.5 Gy/s) or FLASH (>100 Gy/s) modes and quantified the proportion of EdU+ cells 24 h after irradiation (Figure 4C,D and Supplementary Table S1). Interestingly, the proportion of replicating cells was higher after FLASH than CONV irradiation for the doses of 6 Gy and 9 Gy. These encouraging results indicate that analysis of EdU incorporation is suitable for detecting a FLASH-sparing effect on healthy tissue ex vivo.

To further validate the relevance of the cell replication potential to monitor the FLASH effect, we monitored in vivo the proportion of replicating cells 24 h after whole thorax exposure to a dose of 9 Gy delivered either in CONV or FLASH conditions (Figure 5). Despite some variability in the proportion of cycling cells between mice, FLASH thoracic irradiation induced a higher proportion of EdU+ cells than after CONV irradiation (Figure 5B,C), confirming the relevance of the measurement of cell replication to evaluate the FLASH effect ex vivo. Altogether, these results show that analyzing the proportion of cycling cells 24 h after irradiation is a rapid and efficient method to evaluate the FLASH effect on healthy lungs.

3.5. Organotypic Lung Slices Assay Can Evaluate Combined Treatment Toxicity

Most patients are treated by chemotherapies before radiation, and with the development of new drugs, there is a need to evaluate the toxicity of combined treatments on healthy organs. As a proof of concept for the treatment of lung cancer, we evaluated the combination of cytotoxic chemotherapies, such as Carboplatin and Docetaxel, with conventional radiotherapy. To determine the optimal concentration for each drug, we incubated the lung slices for 1 h with different doses of Carboplatin or Docetaxel, washed the drug, and incubated the slices with EdU. Quantification of the cycling cells 24 h after drug treatment confirmed, for both chemotherapeutic agents, a dose-dependent decrease in the proportion of EdU+ cells (Figure 6A,B).

Then, to evaluate radiation toxicity following drug treatment, we selected doses of Carboplatin and Docetaxel, inducing a slight decrease in the proportion of cycling cells, respectively 100 μ M and 50 μ M, and chose a conventional radiotherapy dose of 2 Gy to estimate the effect of a classical fraction of radiotherapy. Analysis of the proportion of replicating cells indicates that a single treatment of either 2 Gy or Carboplatin or Docetaxel alone induces a respective decrease of 31.2%, 29.9%, or 57.4% compared to non-treated samples. Interestingly, a combination of chemotherapies with radiation led to a more pronounced decrease in replicating cells, with 51.6% for Carboplatin-treated slices and 70.6% for Docetaxel-treated slices (Figure 6C,D). In conclusion, quantification of cell replication ex vivo using EdU incorporation allows us to rapidly evaluate the toxicity induced by a combination of cytotoxic drug treatments with radiation, potentially paving the way to preclinical investigations of a wide range of chemotherapies in association with radiotherapy.

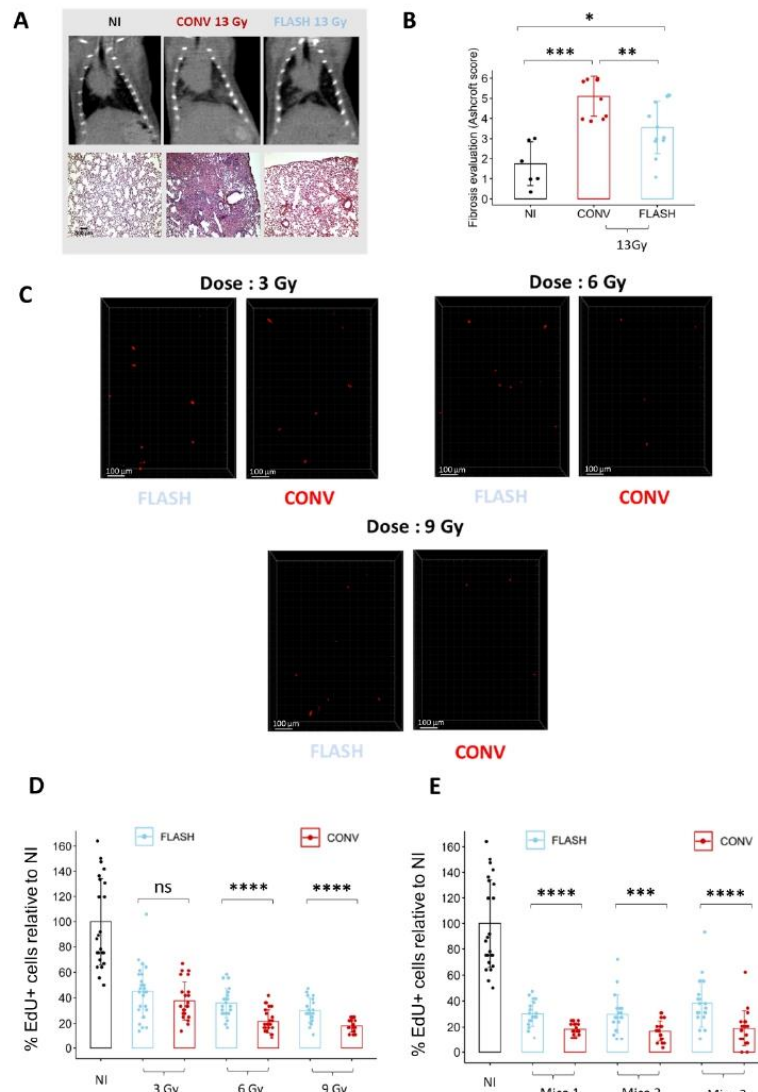


Figure 4. Ex vivo analysis of cell replication allows to discriminate between FLASH and CONV irradiation. (A) Representative CT-scan images from C57BL/6J mice 20 weeks after 13 Gy irradiation and hematoxylin/eosin/saffron staining (HES) of lung sections, resected 20 weeks after 13 Gy thoracic irradiation, showing thickening of alveolar septa, collagen deposition, and large fibrotic areas after CONV irradiation. Lung fibrosis development was reduced after FLASH. (B) Histopathological analysis of lung fibrosis using the Ashcroft score [30] revealed more severe fibrosis after CONV than FLASH irradiation. (C) Representative 3D reconstruction showing EdU+ cells 24 h after exposure to a range from 3 to 9 Gy dose of conventional or FLASH radiation. Images were acquired on a confocal microscope with a 10× objective. The scale bar represents 100 μm. (D) Cell division analysis using the EdU assay revealed a higher proportion of EdU+ cells after FLASH compared to CONV irradiation for doses of 6 Gy and 9 Gy (5 FOV for $n = 5$ slices) Each dot represents the quantification for one field of view. (E) Quantification of the proportion of EdU+ cells in three independent mice confirmed the robustness of cell division assay to detect a short-term FLASH effect. (5 FOV for $n = 5$ slices) Each dot represents the quantification for one field of view. ns, not significant; * p -value < 0.05; ** p -value < 0.01; *** p -value < 0.001; **** p -value < 0.0001.

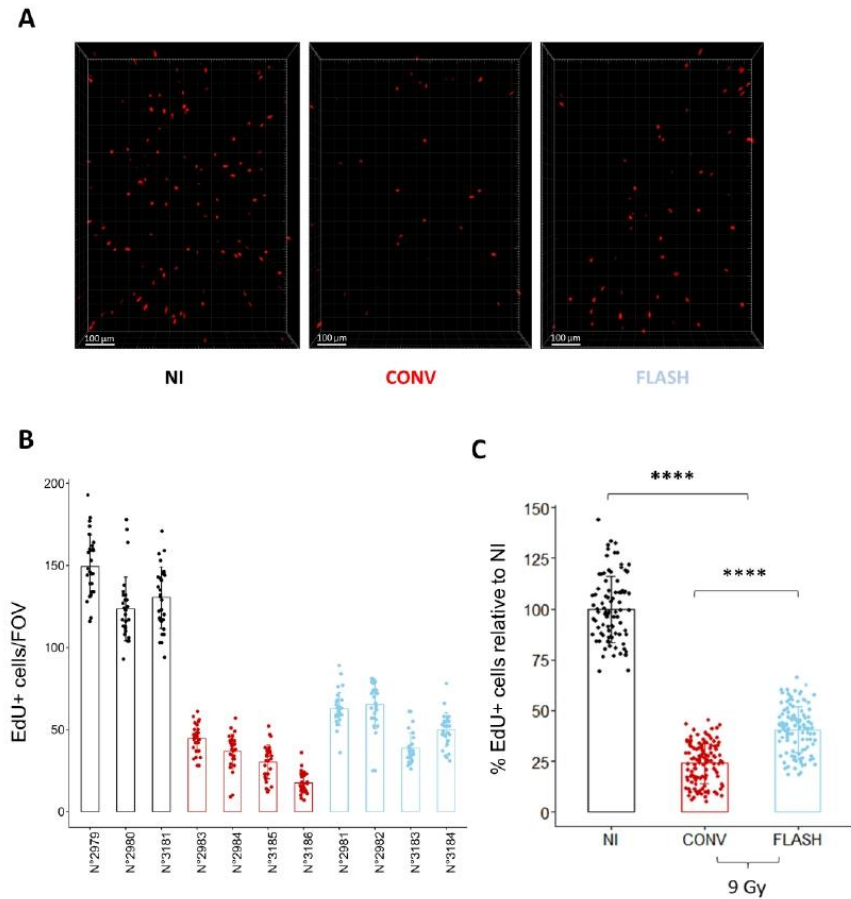


Figure 5. Cell replication analysis in vivo confirms the FLASH-sparing effect observed ex vivo. (A) Representative 3D reconstruction showing EdU+ cells 24 h after whole thorax irradiation at a dose of 9 Gy delivered either in CONV or FLASH modalities. Images were acquired on a confocal microscope with a 10× objective. The scale bar represents 100 μm. (B) Quantification of the number of EdU+ cells/FOV per mouse shows inter-individual variability of the proportion of replicating cells between mice. Each dot represents the quantification for one field of view (C) Grouped per condition and normalized to the proportion of replicating cells in the non-irradiated control, FLASH spared a significant proportion of replicating cells in vivo, confirming the results obtained ex vivo. (n = 3 to 4 mice per condition for n = 5 slices per mouse and 5 FOV per slice) Each dot represents the quantification for one field of view. **** p-value < 0.0001.

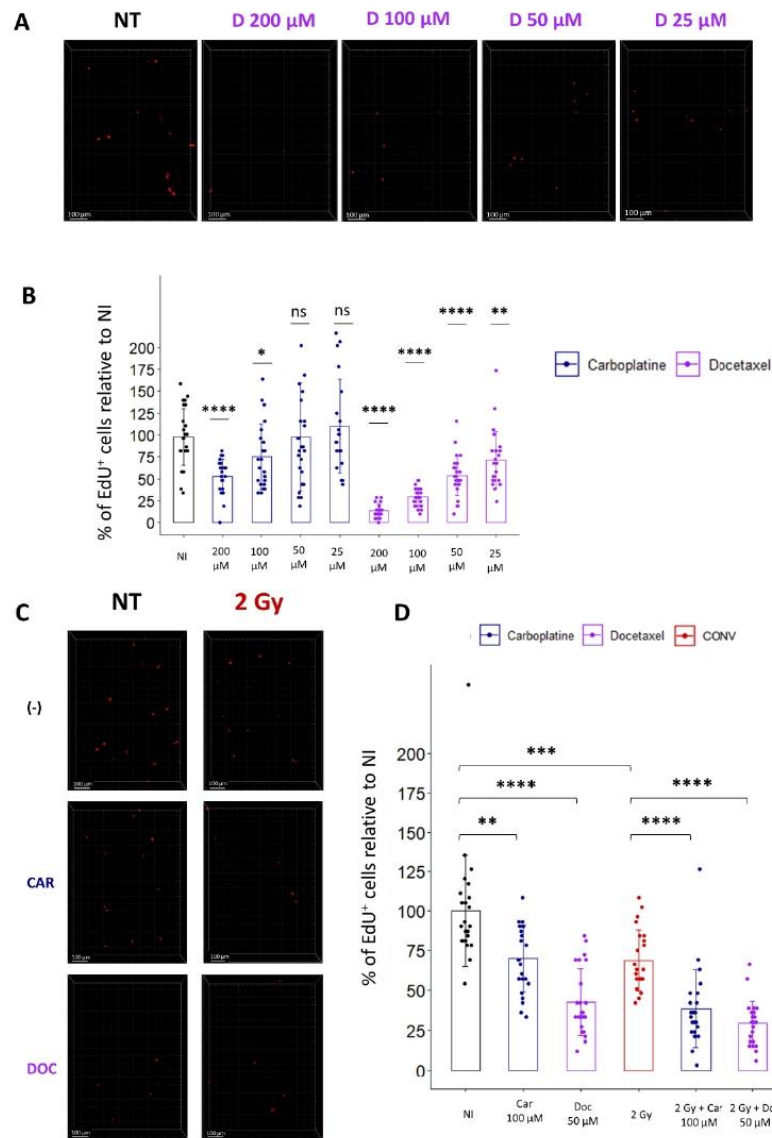


Figure 6. Ex vivo analysis of cell replication allows the evaluation of toxicity induced by chemotherapies alone or in combination with radiation. **(A)** Representative 3D reconstruction showing EdU+ cells 24 h after exposure to different concentrations of Docetaxel (from 25 μM to 200 μM). Images were acquired on a confocal microscope with a 10× objective. The scale bar represents 100 μm. **(B)** Image analysis and quantification show a significant decrease in the proportion of EdU+ cells 24 h after chemotherapy exposition (5 FOV for *n* = 5 slices) Each dot represents the quantification for one field of view. **(C)** Representative 3D reconstruction showing EdU+ cells 24 h after exposure to either a chemotherapeutic agent alone (i.e., Docetaxel 50 μM or Carboplatin 100 μM) or in combination with radiation (2 Gy). Images were acquired on a confocal microscope with a 10× objective. **(D)** Images quantification of the proportion of EdU+ cells reveals that chemotherapies alone induce a significant decrease in the proportion of replicating cells that is accentuated when chemotherapies are associated with radiation (5 FOV for *n* = 5 slices) Each dot represents the quantification for one field of view. ns, not significant; * *p*-value < 0.05; ** *p*-value < 0.01; *** *p*-value < 0.001; **** *p*-value < 0.0001.

4. Discussion

The aim of this study was to investigate *ex vivo* lung organotypic slices as a model to robustly and rapidly evaluate radiation toxicity in the lung. As a first step, we characterized the model showing that (i) the lung and alveolar structure is preserved in the slices, (ii) the optimal time point for analysis is 24 h after obtention when slice viability is the highest, and the percentage of replicating at 24 h post-irradiation is consistent with the proliferation rate observed *in vivo*. After exposure of the slices to increased doses of radiation, we observed a dose-dependent decrease in cell viability as well as in the proportion of cells able to incorporate EdU, in accordance with what is known of the effects of radiation on tissue. Importantly, quantification of the proportion of dividing cells into the slices after exposure to doses of 6 Gy or 9 Gy delivered either in conventional or FLASH modalities was sufficiently sensitive and robust to detect a FLASH-sparing effect (i.e., a higher proportion of replicating cells after FLASH compared to conventional irradiation). To potentiate the translational relevance of the findings, we demonstrated that the measurement of replicating cells in this *ex vivo* model can be used to assess the impact on healthy lungs of combined treatments such as the combination of chemotherapy with radiation. Preclinical studies of radiotherapy classically require large cohorts of animals, and the lung *ex vivo* model to analyze treatment toxicity is an interesting alternative to reduce the number of animals used in medical research.

Regarding the growing interest in FLASH radiotherapy in the community, the results obtained with the *ex vivo* lung model are in accordance with the known effects of FLASH irradiation on healthy tissue. Indeed, it has been previously shown in the brain and in the gut that FLASH radiotherapy spares the number of neuronal precursors in the dentate gyrus as well as the proportion of dividing stem cells from the intestinal crypts [5,10]. Previous studies in the lung reported a higher proportion of EdU+ cells 1-week after conventional compared to FLASH [4]. This discrepancy may be explained by the difference in EdU exposure (i.e., 24 h vs. daily injection during one week) and time of analysis after irradiation (i.e., 24 h vs. 1 week). One explanation could be that the present study investigates the cell cycle arrest induced 24 h after CONV and FLASH irradiation, while previous analysis integrates all the replicating cells in the week following irradiation, probably including the compensatory proliferation required to replace the damaged lung cells. More importantly, because of the rapid development of FLASH clinical trials, like the FAST-01 nonrandomized trial for the treatment of symptomatic bone metastases at the Children's Hospital in Cincinnati (USA) [31], clinical investigations are starting in different centers, and there are important needs to validate the FLASH capabilities of new irradiation devices as well as to determine the optimal biological parameters to observe the FLASH sparing effect. The robust analysis of dividing cells in lung organotypic slices can serve to rapidly assess if a new setup or new beam parameters are capable of inducing a FLASH-sparing effect in healthy tissue. In addition, this *ex vivo* model can reduce the cost of challenging FLASH studies while saving time in animal studies (i.e., results are obtained within days compared to several months when analyzing late toxicity, such as pulmonary fibrosis).

As a proof of concept, we have also shown that analysis of cell replication *ex vivo* can estimate lung toxicity induced by the association of radiation with drugs such as Carboplatin and Docetaxel, two drugs routinely used for the systemic treatment of lung cancer [32]. While lung organotypic slices have been previously used for the evaluation of respiratory toxicity induced by industrial compounds [33], it is the first time that a lung *ex vivo* model and, in particular, the count of EdU+ cells, is implemented as a preclinical tool for the assessment of toxicities induced by chemotherapies and radiation. Our encouraging results reported in this study pave the way to translational studies aiming at evaluating innovative radiation modalities alone or in combination with anti-cancer drugs to prevent lung toxicities (i.e., pneumonitis, interstitial fibrosis) affecting patients' quality of life [34].

This work provides an analysis of cell viability and replication after radiation, but this lung *ex vivo* model requires further characterization to integrate a more detailed

analysis of the multiple processes induced by radiotherapy. Indeed, radiation modality such as stereotactic radiotherapy using high doses per fraction for the treatment of early-stage lung tumors and metastasis triggers activation of a diverse set of compartments such as endothelial, mesenchymal, and immune cells. A deeper analysis of these specific populations will provide a more precise analysis of the acute effects of radiation in the lungs. More broadly, to provide a more comprehensive understanding of radiation injury in the lung, one could benefit from modern computational methods, like those used previously [35], to model the impact of radiation *ex vivo*.

We have shown that lung *ex vivo* models are suitable to rapidly analyze radiation toxicities, but alternative methods may also be considered. Indeed, future computational models of lung radiation injury can serve to predict responses to different treatments (i.e., radiotherapy alone or in combination with drugs). In addition, non-invasive imaging techniques (e.g., SPECT, CT scans) and the use of biomarkers to detect oxidative stress and endothelial cell death *in vivo* can provide early detection methods to estimate lung responses to radiotherapy [36].

Another limitation of this study is the use of organotypic slices prepared from mouse lungs. Alternatively, slices can be prepared from human lung resected from lobectomy [15,37], and future work will concentrate on the development of lung organotypic slices from patients to investigate treatment toxicities in humans. This will pave the way to more clinically relevant investigations on radiation toxicities, taking into account patients' intrinsic radiosensitivity.

Supplementary Materials: The following supporting information can be downloaded at: <https://www.mdpi.com/article/10.3390/cells12202435/s1>, Figure S1: 3D reconstruction and quantification of the proportion of EdU⁺ cells in organotypic lung slice; Figure S2: Evaluation of the variability of the proportion of EdU⁺ cells between slices and between mouse; Table S1: Beam parameters used for FLASH radiation of organotypic lung slices.

Author Contributions: Conceptualization, C.F. and M.D. (Marie Dutreix); methodology, M.D. (Maxime Dubail), S.H., L.P., J.B., L.G., L.A. and N.B.; validation, J.-A.L.-V., M.V., G.B., R.A.S., M.D. (Marie Dutreix) and C.F.; formal analysis, M.D. (Maxime Dubail), S.H. and C.F.; writing—original draft preparation, M.D. (Maxime Dubail) and C.F.; writing—review and editing, M.D. (Maxime Dubail), M.V., G.B., R.A.S., M.D. (Marie Dutreix) and C.F.; supervision, M.D. (Marie Dutreix) and C.F.; funding acquisition, M.D. (Marie Dutreix) and C.F. All authors have read and agreed to the published version of the manuscript.

Funding: This research was funded by INSERM (contract N°19CR057-00) as well as a grant from Varian, a Siemens Healthineers Company (contract N°CT9505), and the Centre National de Recherche Scientifique, Institut Curie and Paris Saclay University. The project has also received funding from the EMPIR program (18HLT04 UHDpulse), co-financed by the Participating States, and from the European Union's Horizon 2020 research and innovation program.

Institutional Review Board Statement: The animal study protocol was approved by the Ethics Committee of Institut Curie CEEA-IC #118 (protocol number APAFiS#32674-2021080916494690, authorized on the 10 of August 2021).

Data Availability Statement: All data generated and analyzed during this study are included in this published article (and its Supplementary Information Files). Raw data will be shared upon request to the corresponding author.

Acknowledgments: The authors are very grateful and want to thank Marco Marinelli and Gianluca Verona Rinati from Tor Vergata University for their fruitful interactions and their kind gift of the diamond detector. The authors greatly acknowledge Marie-Noëlle Soler and Laetitia Besse from the Multimodal Imaging Center-Light Microscopy Facility of the Institut Curie (CNRS UMS2016/InermUS43/Institut Curie/Université Paris-Saclay), as well as the Cell and Tissue Imaging Platform—PICT-IBiSA (member of France-Bioimaging—ANR-10-INBS-04) of the U934/UMR3215 of Institut Curie for help with light microscopy. The authors wish to thank Christophe Alberti, Elodie Belloir, Cédric Lantoiné, Pauline Dubreuil, and Virginie Dangles-Marie from the animal core facility of Institut Curie. Sophie Leboucher, head of the histology platform, Margaux Becerra, and the Pathex

platform are gratefully acknowledged. Thanks are due to the members of the Dutreix team for scientific exchanges and discussions.

Conflicts of Interest: Marie Dutreix and Charles Fouillade received funding from Varian, a Siemens Healthineers Company, and SIT companies. Gael Boivin, Marta Vilalta, and Ricky Sharma are employed by Varian, a Siemens Healthineers Company.

References

- Vinod, S.K.; Hau, E. Radiotherapy Treatment for Lung Cancer: Current Status and Future Directions. *Respirology* **2020**, *25*, 61–71. [[CrossRef](#)] [[PubMed](#)]
- De Ruysscher, D.; Niedermann, G.; Burnet, N.G.; Siva, S.; Lee, A.W.M.; Hegi-Johnson, F. Radiotherapy Toxicity. *Nat. Rev. Dis. Primers* **2019**, *5*, 13. [[CrossRef](#)] [[PubMed](#)]
- Favaudon, V.; Caplier, L.; Monceau, V.; Pouzoulet, F.; Sayarath, M.; Fouillade, C.; Poupon, M.-F.; Brito, I.; Hupé, P.; Bourhis, J.; et al. Ultrahigh Dose-Rate FLASH Irradiation Increases the Differential Response between Normal and Tumor Tissue in Mice. *Sci. Transl. Med.* **2014**, *6*, 245ra93. [[CrossRef](#)] [[PubMed](#)]
- Fouillade, C.; Curras-Alonso, S.; Giuranno, L.; Quelellenc, E.; Heinrich, S.; Bonnet-Boissinot, S.; Beddok, A.; Leboucher, S.; Karakurt, H.U.; Bohec, M.; et al. FLASH Irradiation Spares Lung Progenitor Cells and Limits the Incidence of Radio-Induced Senescence. *Clin. Cancer Res.* **2020**, *26*, 1497–1506. [[CrossRef](#)] [[PubMed](#)]
- Montay-Gruel, P.; Petersson, K.; Jaccard, M.; Boivin, G.; Germond, J.-F.; Petit, B.; Doenlen, R.; Favaudon, V.; Bochud, F.; Bailat, C.; et al. Irradiation in a Flash: Unique Sparing of Memory in Mice after Whole Brain Irradiation with Dose Rates above 100 Gy/s. *Radiother. Oncol.* **2017**, *124*, 365–369. [[CrossRef](#)] [[PubMed](#)]
- Montay-Gruel, P.; Acharya, M.M.; Petersson, K.; Alikhani, L.; Yakkala, C.; Allen, B.D.; Ollivier, J.; Petit, B.; Jorge, P.G.; Syage, A.R.; et al. Long-Term Neurocognitive Benefits of FLASH Radiotherapy Driven by Reduced Reactive Oxygen Species. *Proc. Natl. Acad. Sci. USA* **2019**, *116*, 10943–10951. [[CrossRef](#)] [[PubMed](#)]
- Soto, L.A.; Casey, K.M.; Wang, J.; Blaney, A.; Manjappa, R.; Breitzkreutz, D.; Skinner, L.; Dutt, S.; Ko, R.B.; Bush, K.; et al. FLASH Irradiation Results in Reduced Severe Skin Toxicity Compared to Conventional-Dose-Rate Irradiation. *Radiat. Res.* **2020**, *194*, 618–624. [[CrossRef](#)]
- Vozenin, M.-C.; De Fornel, P.; Petersson, K.; Favaudon, V.; Jaccard, M.; Germond, J.-F.; Petit, B.; Burki, M.; Ferrand, G.; Patin, D.; et al. The Advantage of FLASH Radiotherapy Confirmed in Mini-Pig and Cat-Cancer Patients. *Clin. Cancer Res.* **2019**, *25*, 35–42. [[CrossRef](#)]
- Cunningham, S.; McCauley, S.; Vairamani, K.; Speth, J.; Girdhani, S.; Abel, E.; Sharma, R.A.; Perentesis, J.P.; Wells, S.I.; Mascia, A.; et al. FLASH Proton Pencil Beam Scanning Irradiation Minimizes Radiation-Induced Leg Contracture and Skin Toxicity in Mice. *Cancers* **2021**, *13*, 1012. [[CrossRef](#)]
- Levy, K.; Natarajan, S.; Wang, J.; Chow, S.; Eggold, J.T.; Loo, P.E.; Manjappa, R.; Melemenidis, S.; Lartey, F.M.; Schüler, E.; et al. Abdominal FLASH Irradiation Reduces Radiation-Induced Gastrointestinal Toxicity for the Treatment of Ovarian Cancer in Mice. *Sci. Rep.* **2020**, *10*, 21600. [[CrossRef](#)]
- Ruan, J.-L.; Lee, C.; Wouters, S.; Tullis, I.D.C.; Verslegers, M.; Mysara, M.; Then, C.K.; Smart, S.C.; Hill, M.A.; Muschel, R.J.; et al. Irradiation at Ultra-High (FLASH) Dose Rates Reduces Acute Normal Tissue Toxicity in the Mouse Gastrointestinal System. *Int. J. Radiat. Oncol. Biol. Phys.* **2021**, *111*, 1250–1261. [[CrossRef](#)] [[PubMed](#)]
- Travis, E.L. The Sequence of Histological Changes in Mouse Lungs after Single Doses of X-rays. *Int. J. Radiat. Oncol. Biol. Phys.* **1980**, *6*, 345–347. [[CrossRef](#)] [[PubMed](#)]
- Zscheppang, K.; Berg, J.; Hedtrich, S.; Verheyen, L.; Wagner, D.E.; Suttrop, N.; Hippenstiel, S.; Hocke, A.C. Human Pulmonary 3D Models For Translational Research. *Biotechnol. J.* **2018**, *13*, 1700341. [[CrossRef](#)] [[PubMed](#)]
- Liu, G.; Betts, C.; Cunoosamy, D.M.; Åberg, P.M.; Hornberg, J.J.; Sivars, K.B.; Cohen, T.S. Use of Precision Cut Lung Slices as a Translational Model for the Study of Lung Biology. *Respir. Res.* **2019**, *20*, 162. [[CrossRef](#)]
- Alsafadi, H.N.; Uhl, F.E.; Pineda, R.H.; Bailey, K.E.; Rojas, M.; Wagner, D.E.; Königshoff, M. Applications and Approaches for Three-Dimensional Precision-Cut Lung Slices. Disease Modeling and Drug Discovery. *Am. J. Respir. Cell Mol. Biol.* **2020**, *62*, 681–691. [[CrossRef](#)] [[PubMed](#)]
- Lyons-Cohen, M.R.; Thomas, S.Y.; Cook, D.N.; Nakano, H. Precision-Cut Mouse Lung Slices to Visualize Live Pulmonary Dendritic Cells. *JoVE* **2017**, *122*, 55465. [[CrossRef](#)]
- Alsafadi, H.N.; Staab-Weijnitz, C.A.; Lehmann, M.; Lindner, M.; Peschel, B.; Königshoff, M.; Wagner, D.E. An Ex Vivo Model to Induce Early Fibrosis-like Changes in Human Precision-Cut Lung Slices. *Am. J. Physiol. Lung Cell. Mol. Physiol.* **2017**, *312*, L896–L902. [[CrossRef](#)]
- Gerckens, M.; Alsafadi, H.N.; Wagner, D.E.; Lindner, M.; Burgstaller, G.; Königshoff, M. Generation of Human 3D Lung Tissue Cultures (3D-LTCs) for Disease Modeling. *JoVE* **2019**, *144*, 58437. [[CrossRef](#)]
- Akram, K.M.; Yates, L.L.; Mongey, R.; Rothery, S.; Gaboriau, D.C.A.; Sanderson, J.; Hind, M.; Griffiths, M.; Dean, C.H. Live Imaging of Alveologenesis in Precision-Cut Lung Slices Reveals Dynamic Epithelial Cell Behaviour. *Nat. Commun.* **2019**, *10*, 1178. [[CrossRef](#)]

20. Lehmann, M. Differential Effects of Nintedanib and Pirfenidone on Lung Alveolar Epithelial Cell Function in Ex Vivo Murine and Human Lung Tissue Cultures of Pulmonary Fibrosis. *Respir. Res.* **2018**, *19*, 175. [[CrossRef](#)]
21. Burgstaller, G.; Sengupta, A.; Vierkotten, S.; Preissler, G.; Lindner, M.; Behr, J.; Königshoff, M.; Eickelberg, O. Distinct Niches within the Extracellular Matrix Dictate Fibroblast Function in (Cell Free) 3D Lung Tissue Cultures. *Am. J. Physiol. Lung Cell. Mol. Physiol.* **2018**, *314*, L708–L723. [[CrossRef](#)] [[PubMed](#)]
22. Li, G.; Cohen, J.A.; Martinez, C.; Ram-Mohan, S.; Brain, J.D.; Krishnan, R.; Ai, X.; Bai, Y. Preserving Airway Smooth Muscle Contraction in Precision-Cut Lung Slices. *Sci. Rep.* **2020**, *10*, 6480. [[CrossRef](#)] [[PubMed](#)]
23. Wright, J.L.; Churg, A. Short-Term Exposure to Cigarette Smoke Induces Endothelial Dysfunction in Small Intrapulmonary Arteries: Analysis Using Guinea Pig Precision Cut Lung Slices. *J. Appl. Physiol.* **2008**, *104*, 1462–1469. [[CrossRef](#)] [[PubMed](#)]
24. Temann, A.; Golovina, T.; Neuhaus, V.; Thompson, C.; Chichester, J.A.; Braun, A.; Yusibov, V. Evaluation of Inflammatory and Immune Responses in Long-Term Cultured Human Precision-Cut Lung Slices. *Hum. Vaccines Immunother.* **2017**, *13*, 351–358. [[CrossRef](#)] [[PubMed](#)]
25. Hofmann, F.; Bläsche, R.; Kasper, M.; Barth, K. A Co-Culture System with an Organotypic Lung Slice and an Immortal Alveolar Macrophage Cell Line to Quantify Silica-Induced Inflammation. *PLoS ONE* **2015**, *10*, e0117056. [[CrossRef](#)] [[PubMed](#)]
26. Suckert, T.; Rassamegevanon, T.; Müller, J.; Dietrich, A.; Graja, A.; Reiche, M.; Löck, S.; Krause, M.; Beyreuther, E.; von Neubeck, C. Applying Tissue Slice Culture in Cancer Research—Insights from Preclinical Proton Radiotherapy. *Cancers* **2020**, *12*, 1589. [[CrossRef](#)]
27. Giuliano, L.; Franciosini, G.; Palumbo, L.; Aggar, L.; Dutreix, M.; Faillace, L.; Favaudon, V.; Felici, G.; Galante, F.; Mostacci, A.; et al. Characterization of Ultra-High-Dose Rate Electron Beams with ElectronFlash Linac. *Appl. Sci.* **2023**, *13*, 631. [[CrossRef](#)]
28. Rock, J.R.; Barkauskas, C.E.; Cronce, M.J.; Xue, Y.; Harris, J.R.; Liang, J.; Noble, P.W.; Hogan, B.L.M. Multiple Stromal Populations Contribute to Pulmonary Fibrosis without Evidence for Epithelial to Mesenchymal Transition. *Proc. Natl. Acad. Sci. USA* **2011**, *108*, E1475–E1483. [[CrossRef](#)]
29. Muzumdar, M.D.; Tasic, B.; Miyamichi, K.; Li, L.; Luo, L. A Global Double-Fluorescent Cre Reporter Mouse. *Genesis* **2007**, *45*, 593–605. [[CrossRef](#)]
30. Hübner, R.-H.; Gitter, W.; Eddine El Mokhtari, N.; Mathiak, M.; Both, M.; Bolte, H.; Freitag-Wolf, S.; Bewig, B. Standardized Quantification of Pulmonary Fibrosis in Histological Samples. *BioTechniques* **2008**, *44*, 507–517. [[CrossRef](#)]
31. Mascia, A.E.; Daugherty, E.C.; Zhang, Y.; Lee, E.; Xiao, Z.; Sertorio, M.; Woo, J.; Backus, L.R.; McDonald, J.M.; McCann, C.; et al. Proton FLASH Radiotherapy for the Treatment of Symptomatic Bone Metastases: The FAST-01 Nonrandomized Trial. *JAMA Oncol.* **2023**, *9*, 62–69. [[CrossRef](#)]
32. Guen, Y.L.; Cesne, A.L. Docetaxel and Non-Small Cell Lung Cancer. *Bull. Cancer* **2004**, *91*, 263–270. [[PubMed](#)]
33. Hess, A.; Wang-Lauenstein, L.; Braun, A.; Kolle, S.N.; Landsiedel, R.; Liebsch, M.; Ma-Hock, L.; Pirow, R.; Schneider, X.; Steinfath, M.; et al. Prevalidation of the Ex-Vivo Model PCLS for Prediction of Respiratory Toxicity. *Toxicol. Vitro* **2016**, *32*, 347–361. [[CrossRef](#)] [[PubMed](#)]
34. Porcu, M.; De Silva, P.; Solinas, C.; Battaglia, A.; Schena, M.; Scartozzi, M.; Bron, D.; Suri, J.S.; Willard-Gallo, K.; Sangiolo, D.; et al. Immunotherapy Associated Pulmonary Toxicity: Biology Behind Clinical and Radiological Features. *Cancers* **2019**, *11*, 305. [[CrossRef](#)] [[PubMed](#)]
35. Zhang, X.; Dash, R.K.; Clough, A.V.; Xie, D.; Jacobs, E.R.; Audi, S.H. Integrated Computational Model of Lung Tissue Bioenergetics. *Front. Physiol.* **2019**, *10*, 560a–561a.
36. Audi, S.H.; Jacobs, E.R.; Zhang, X.; Camara, A.K.S.; Zhao, M.; Medhora, M.M.; Rizzo, B.; Clough, A.V. Protection by Inhaled Hydrogen Therapy in a Rat Model of Acute Lung Injury Can Be Tracked in Vivo Using Molecular Imaging. *Shock* **2017**, *48*, 467. [[CrossRef](#)] [[PubMed](#)]
37. Preuß, E.B.; Schubert, S.; Werlein, C.; Stark, H.; Braubach, P.; Höfer, A.; Plucinski, E.K.J.; Shah, H.R.; Geffers, R.; Sewald, K.; et al. The Challenge of Long-Term Cultivation of Human Precision-Cut Lung Slices. *Am. J. Pathol.* **2022**, *192*, 239–253. [[CrossRef](#)]

Disclaimer/Publisher’s Note: The statements, opinions and data contained in all publications are solely those of the individual author(s) and contributor(s) and not of MDPI and/or the editor(s). MDPI and/or the editor(s) disclaim responsibility for any injury to people or property resulting from any ideas, methods, instructions or products referred to in the content.

FLASH beam parameters			
Beam energy [MeV]	7		
Total absorbed dose [Gy]	3	6	9
Number of pulses	1	2	3
Pulse frequency [Hz]	100		
Mean dose rate [Gy/s]	7.5E+05	600	450
Instantaneous dose rate [Gy/s]	7.5E+05	7.5E+05	7.5E+05
Dose per pulse [Gy]	3		
Pulse width [μ s]	4		
Duration of exposure [ms]	0.004	10	20
Homogeneous field size _{v, 2%} [cm]	11		

Supplementary Table S1. Beam parameters used for FLASH radiation of organotypic lung slices.

1.3 Conclusion

In conclusion of the first part of the results, we **adapted the PCLS model to investigate acute lung toxicities** using **simple and rapid endpoints** such **viability and cell division**. Notably, the analysis of **cell division** within the slices **24 hours** post-treatment allowed us to **identify a FLASH sparing effect** in this population of interest. Following this, we utilized this model to conduct proof-of-concept experiments exploring its application in combination therapies with chemotherapy and radioprotectors (AsiDNA, CAPE, **see Annex 1**). Lastly, we demonstrated the feasibility of obtaining PCLS from lungs with orthotopic lung tumors, positioning it as an interesting and valuable model for future studies (**see Annex 1**).

2. OPTIMAL PARAMETERS FOR FLASH-RT IN THE LUNG

2.1 Introduction

After **establishing a relevant *ex vivo* model that demonstrates a protective effect of FLASH irradiation on cycling cells in the lung 24 hours after treatment**, we sought to apply this model to another major concern regarding the FLASH field which is **FLASH irradiation parameters**.

Indeed, by definition, the FLASH effect depends on irradiation parameters that allow for dose rates exceeding 100 Gy/s. However, during pulsed electron irradiation, several physical parameters can be adjusted to meet the FLASH definition, including the average dose rate, total irradiation time, and the temporal structure of the irradiation, which can be modified by adjusting the number of pulses and the dose per pulse. As described in the introduction of this manuscript, although it seems that the average dose rate is one of the key parameters needed to achieve the FLASH protective effect in healthy tissue²⁴⁷, other studies have shown the importance of the number of pulses during electron beam irradiation²⁵⁴. These studies have often been conducted on different organs, using varying irradiators, and with different endpoints.

Therefore, since we have demonstrated a robust and relevant protective effect *ex vivo* at 9 Gy in the PCLS model, we wanted to use our ElectronFLASH irradiator to **investigate the optimal parameters for FLASH irradiation in the lung**. Our irradiator allows us to adjust several parameters, such as repetition frequency (Hz), the number of pulses, and the dose per pulse. Thus, in the following sections of this manuscript, we will **use the PCLS model to define the optimal parameters required to achieve the optimal FLASH protective effect**. Some *in vivo* validations are still ongoing, and the manuscript will be submitted once they are completed, using the development of radiation-induced fibrosis as a late endpoint.

In addition to the optimal physical parameters identified for FLASH irradiation using PCLS, other conditions such as **oxygen concentration have been described as important to replicate the FLASH sparing effect**. Indeed, healthy lung tissue, under physioxia, exhibit 5% O₂ on average. Our pioneering experiments using the PCLS model were performed at 20% O₂ in culture, so we also wanted to determine the impact of this parameter on the presence of the FLASH effect. Specifically, we aimed to investigate the presence of a FLASH effect on cycling cells 24 hours post-irradiation in PCLS under hypoxic conditions.

Several studies have now shown that fractionation protocol maintains the FLASH sparing effect in healthy tissue. Fractionation is complex to implement for the PCLS model due to the viability related constraints of the model. However, **another major issue** that must be considered regarding the application of FLASH in the clinic is **re-irradiation**. Indeed, more and more patients are being treated for primary cancer, but they sometimes develop new tumors in the same organ or a nearby organ. In this context, these patients, who have already received a first dose of radiation, are more sensitive and sometimes experience secondary effects and toxicities. Thus, **in the context of lung tissue that has already been treated with conventional radiotherapy**, we wondered **whether we could still observe a protective FLASH effect**. To investigate this, a study combining *ex vivo* and *in vivo* analysis was conducted. The materials and methods, as well as the results obtained, will be described in this next section of additional results.

Finally, another innovative work regarding the validation of a VHEE laser plasma beam experimental setup has been carried out in collaboration between our team at Institut Curie and the Laboratoire d'optique appliquée (LOA). To preclinically validate this beam, dose escalation response experiments were performed on PCLS. In addition, first thoracic irradiation using this VHEE beam were carried out, with the aim of studying the development of radiation-induced fibrosis. This work is an integral part of another student's thesis and will also be submitted for publication soon. As VHEE could be one of promising applications for FLASH dose rate in clinics, this work, including PCLS, is highly relevant for future development in the FLASH field demonstrating once again the potential of the PCLS model for preclinical beam validation.

2.2 Material and methods

PCLS Preparation: Adult female C57BL/6J mice aged 6 to 10 weeks were anesthetized by intraperitoneal injection of ketamine/xylazine. Blood was then flushed through intracardiac injection of phosphate-buffered saline (PBS) and the trachea was exposed to inject 2 mL of 2.5% low-melting agarose (A9414-50G, Sigma-Aldrich, Saint-Louis, MI, USA) diluted in organotypic lung slices medium DMEM F12 (31331-028, Thermo Fisher Scientific, Waltham, MA, USA) supplemented with 1% SVF (CVFSVF00-0U, Thermo Fisher Scientific, Waltham, MA, USA), 1% penicillin/streptomycin (CABPES01-0U, Thermo Fisher Scientific, Waltham, MA, USA), 1% non-94 essential amino acids (11140035, Thermo Fisher Scientific, Waltham, MA, USA) and 1% L-glutamine (25030-024, Thermo Fisher Scientific, Waltham, MA, USA). Once the agarose was solidified, lungs were removed from the chest cavity, and 8 mm punches were made from each lobe individually. Tissue punches were embedded in 5% agarose, and 300 µm slices

were made with a Vibratome (Leica VT1000S, Nanterre, France) as previously described (**Article 1**). The whole procedure lasted less than 2 h. Around 50 slices were obtained from a lung and placed into a 24-well plate containing each 500 μ L of organotypic lung slice medium and cultured at 37 °C in 5% CO₂ for up to 72 h.

Mouse PCLS culture in Hypoxia : Culture medium for PCLS was equilibrated to a hypoxic oxygen concentration (2% O₂) or physioxic (5% O₂) in a hypoxia chamber (HypoxyLab, Oxford Optronix) the day before PCLS preparation. Subsequently, after obtaining the slices, they were transferred to the hypoxia chamber. Irradiation was performed in a sealed bag to maintain the oxygen concentration, and EdU incubation was conducted within the chamber. Finally, for each experiment, a subset of slices was cultured with the Image-iT™ Green Hypoxia probe (ThermoFisher) for 1 hour to estimate the oxygen concentration within the slices.

PCLS irradiation: PCLS were obtained from the same biological sample and randomly assigned to different groups for the different doses of radiation in each experiment. We used the electron linear accelerator (linac) ElectronFLASH (SIT S.p.A., R&D Dept., Roma, Italy) available at Institut Curie. Lung slices were irradiated in culture plates with a vertical 7-MeV beam at a source distance of 1.1 m, allowing a dose homogeneity throughout the wells' positions better than 95%. The dosimetry was controlled by EBT-XD Gafchromic (Ashland, Bridgewater, NJ, USA) film measurements: films were cut into adapted pieces and placed at the position of the target (i.e., inside the culture wells with medium). For all conventional irradiations, we used these measurements to calibrate the monitoring ion chamber of the linac (0.007 Gy/MU at the target, which corresponds to \approx 0.5 Gy/s). The linac stopped automatically when the number of Monitor Units reached the prescribed value for any dose. In the case of FLASH irradiations, we set the dose per electron-pulse at 3 Gy/pulse (\pm 0.2 Gy) by adjusting the pulse duration, and we delivered 1, 2, and 3 pulses to achieve the target doses of 3, 6, and 9 Gy. All the beam parameters that were adjusted will be summarized in Figures.

Dose and parameters measurements : PCLS were irradiated with a 7-MeV electron beam at the depth of maximum dose (7 mm of PMMA). The fine tuning of the parameters to achieve equivalent doses was done thanks to a FlashDiamond detector and verified by EBT-XD Gafchromic films at the bottom of the culture plates. Pulse length, time interval between pulses and total irradiation time were measured with the Teledyne WaveSurfer-4054HD oscilloscope.

Cell Division Analysis: To estimate the proportion of cells that replicate after irradiation in the lung slices, we used a Click-IT chemistry protocol to monitor cell proliferation using 5-ethynyl-2'-deoxyuridine (EdU) incorporation (BCK-EdUPro-FC647). Irradiated slices were incubated in 500 μ L of culture medium containing 10 μ M EdU. After the desired incubation time (i.e., 24, 48, or 72 h), they were treated according to the manufacturer's instructions. Then, organotypic lung slices were washed in PBS and incubated with a nuclear dye (e.g., DAPI). For imaging, organotypic lung slices were transferred into a glass support adapted for microscopy (μ -Slide 4 Well Glass Bottom, Ibidi) and imaged on an inverted Nikon Spinning disk TIRF-FRAP using a 10 \times objective. Per slice, 3 to 5 fields of view were acquired, each containing 50 stacks spaced by 3 μ m. The proportion of EdU+ cells was quantified with a semi-automatic method combining 3D reconstruction and segmentation of the nuclei using IMARIS software Bitplane.

Whole Thorax Irradiation : Mice were exposed at the age of 10–12 weeks to a 13 Gy whole thorax irradiation with a horizontal 5-MeV beam at a Source Distance of 0.65 m, with a setup equivalent to the one previously described in part I of results. Anesthesia was carried out with a nose cone using 2.5% isoflurane in the air without adjunction of oxygen. The dosimetry was controlled on an individual basis with Gafchromic films positioned on the mouse thorax surface at the center of the irradiation field. For FLASH-RT, 4 pulses of 3.3 Gy were administered at 100 Hz (430 Gy/s) or 10 Hz (43 Gy/s). The dose rate was 0.1 Gy/s in the conventional modality.

Mice re-irradiation : Mice were exposed at the age of 10–12 weeks to a 10 Gy whole thorax irradiation with a horizontal 7-MeV beam at a Source Distance of 0.65 m, with a setup equivalent in conventional. Then, 4 months post- prior thorax radiation, mice were re-exposed to 6, 9 or 12 Gy either at conventional or FLASH doses rates. The dose rate was 0.1 Gy/s in the conventional modality and 3 Gy/pulse in the FLASH modality

Statistical Analysis: Statistical analyses were performed using the ggpubr package (<https://rpkgs.datanovia.com/ggpubr/>) in R. For EdU+ nuclei count data, the Wilcoxon Mann-Whitney test was used to compare the means of these counts between conventional and FLASH conditions. For *in vivo* validation Kaplan Meir curve with LogRangtest were performed using the survival package in R.

2.3 Results

2.3.1 Impact of the mean dose rate on the FLASH sparing effect in lung tissue

Initially, although we demonstrated a FLASH effect using the PCLS model and EdU assay at a dose of 9 Gy, we were unsure whether the sensitivity of the developed test would be able to differentiate between different FLASH irradiation parameters. With this in mind, we aimed to replicate the initial experiments that highlighted a relationship between the presence of the FLASH protective effect and the mean dose rate/total irradiation time. First, we kept the same temporal structure of 3 Gy per pulse for a total irradiation dose of 9 Gy. Then, between these 3 pulses, we could adjust the repetition frequency (in Hz), which corresponds to the time between pulses (**Figure 52A**). By irradiating the PCLS at repetition frequencies ranging from 10, 25, 50, 75, 100, or 250 Hz, we could adjust the dose rates to 40, 110, 220, 340, 450, or 1120 Gy/s, respectively (**Figure 52A, B**). This corresponded to total irradiation times ranging from 200 ms to 8 ms (**Figure 52A**).

The proportion of EdU⁺ cells was quantified for each mean dose-rate and compared to the conventional dose-rate to assess the presence of the FLASH effect *ex vivo* (**Figure 54B**). Interestingly, a clear sparing effect on the proportion of EdU⁺ cells was observed over 310 Gy/s (**Figure 52B**). Dose-rates of 100 Gy/s or lower had similar toxicity than the conventional dose-rate (**Figure 52B**). In between, dose rate of 220 Gy/s, gave intermediate results with dividing cells slightly lower than at the dose-rates above 340 Gy/s, but still significantly different from the conventional (**Figure 52B**).

To test the relevance of these results obtained *ex vivo* 24 h post-irradiation in PCLS, we decided to validate *in vivo* that an irradiation at a 40 Gy/s in FLASH wasn't sufficient to protect mice from developing radio-induced fibrosis. For that purpose, mice were irradiated either in CONV, FLASH at dose rates upper than 300 Gy/s and in FLASH at low dose rates of 40 Gy/s for a total dose of 13 Gy sufficient to be fibrogenic. As it was done *ex vivo*, only the pulse repetition frequency was adjusted in FLASH from 10 Hz to 100 Hz. Then, the development of fibrosis was followed by CT-scan analysis, and we were able to trace the survival curve for over 1 year for the mice irradiated in different conditions (**Figure 52C**). Our results show that the survival of mice irradiated at both conventional and FLASH dose rates at 40 Gy/s is significantly reduced compared to mice irradiated in FLASH at dose rates above 300 Gy/s. The mice irradiated in CONV were all sacrificed after developing a high degree of pulmonary

fibrosis 250 days post-irradiation, the survival of mice irradiated in FLASH at 40 Gy/s is slightly higher, being sacrificed for a development of fibrosis 325 days post-irradiation (**Figure 52C**). At 1-year post-irradiation, only one mouse irradiated in FLASH was sacrificed for the development of a high degree of radiation-induced fibrosis (**Figure 52C**).

In conclusion, although depending on the endpoint monitored, whether for PCLS or radiation-induced fibrosis, it seems that the PCLS model has allowed us to identify the optimal conditions for healthy tissue sparing with FLASH in terms of the mean dose rate. **The mean dose rate must be higher than 100 Gy/s and total time of irradiation less than 80 ms in order to observe a FLASH effect in the lung** which is coherent with what was observed in the literature in other organs.

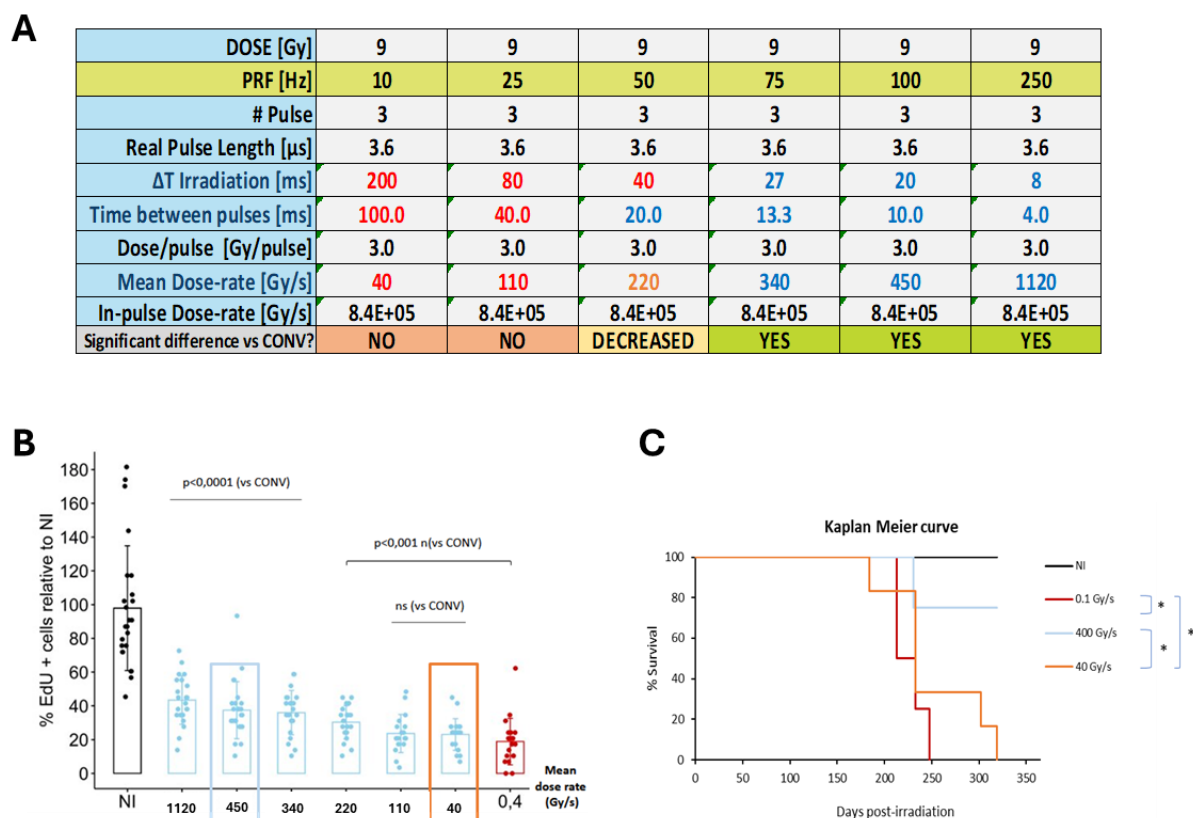


Figure 52. Impact of the mean dose rate on the FLASH protective effect. (A) List of parameters measurements for FLASH and CONV-RT in PCLS. (B) Quantification of the proportion of EdU^+ cells showed that a mean dose-rate over 100 Gy/s is required to observe a FLASH sparing effect (4 to 5 FOV for $n=5$ slices). (C) Kaplan Meir survival curves 1-year post-treatment showing that the FLASH irradiated mice survive better than the one irradiated in FLASH low-dose rate and CONV. A logRanktest was performed to compare the survival of each group. The p -value $< 0,05$ was considered significant. ($n= 6$ mice per condition).

2.3.2 Impact of the temporal structure of FLASH-RT on the sparing effect in lung tissue

Compared to the impact of the mean dose rate, the impact of the temporal structure of a FLASH electron irradiation has remained poorly studied due to technical limitations with LINAC that were used for FLASH. With the ElectronFLASH, we were able to discriminate the importance of the number of pulses and dose per pulse on the presence of a FLASH protective effect. Some studies suggest that the FLASH sparing effect is optimal when the dose is delivered in one single pulse. However, this raises several issues regarding the clinical application of FLASH, limiting any control over potential overdosing. Indeed, being able to irradiate in multiple pulses would, in theory, allow for stopping the irradiation during administration if the dose of a pulse measured is too high or low.

Therefore, we wanted to test this first hypothesis using PCLS model and cell division assay. For that purpose, we irradiated PCLS with either one single pulse of 9 Gy, two pulses of 4.5 Gy each or, our standard condition, three pulses of 3 Gy each (**Figure 53A**). The cell division analysis we performed reproduced the sparing effect we observed between FLASH and CONV but did not reveal any difference between a dose of 9 Gy delivered in one, two or three pulses (**Figure 55B**). This suggests that the upper 3 Gy/pulse and 300 Gy/s, the FLASH effect we observe *ex vivo* in lung PCLS remain the same even if we delivered the dose in one single pulse.

A

DOSE [Gy]	9	9	9
PRF [Hz]	100	100	100
# Pulse	1	2	3
Real Pulse Length [μ s]	3.2	1.6	1.0
Δ T Irradiation [ms]	0.003	10	20
Time between pulses [ms]	NA	10.0	10.0
Dose/pulse[Gy/pulse]	9.0	4.5	3.0
Mean Dose-rate [Gy/s]	2.9E+06	900	450
In-pulse Dose-rate [Gy/s]	2.86E+06	2.85E+06	3.00E+06
Significant difference vs CONV?	YES	YES	YES

B

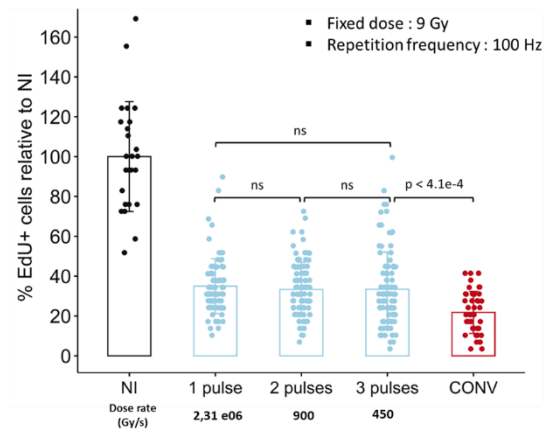


Figure 53. Impact of a single pulse FLASH irradiation on healthy tissue sparing effect. (A) List of parameters measured for FLASH and conventional radiotherapy (CONV-RT) in PCLS, with a fixed dose of 9 Gy and a repetition frequency of 100 Hz. (B) Quantification of the proportion of EdU+ cells following one, two or three pulses in FLASH-RT. ($n=5$ slices, 4-5 FOV per slice for a pool of independent experiments).

Similarly, the impact of increasing the number of pulses and therefore decreasing the dose per pulse on the presence of a FLASH effect hasn't been elucidated. Therefore, we tested the impact of increasing the number of pulses from 3 to 6 and then 9 pulses, corresponding respectively to a dose per pulse of 3 Gy, 1.5 Gy and 1 Gy per pulse (**Figure 54A**). By adjusting the number of pulses and the pulse repetition frequency, we made the total irradiation time the same, 27 ms, so that only the dose per pulse and the number of pulses, which are inseparable in our settings, vary (**Figure 54A**). We also added a 9-pulse control by decreasing the frequency so that the average dose rate was below 100 Gy/s for which we did not expect a FLASH effect in agreement with the previous data. Surprisingly, our results indicate that FLASH irradiation with a dose per pulse of 1 Gy and a pulse number of 9 is insufficient to achieve a protective effect in our ex vivo EdU assay using PCLS (**Figure 54B**). Only FLASH-RT with 6 pulses of 1.5 Gy is sufficient to trigger a sparing effect on cycling cells in PCLS compared to conventional irradiation (**Figure 54B**). These data suggest that **the average dose rate is not the only crucial parameter to trigger the sparing effect with FLASH irradiation in the lung**. These results, to be confirmed in vivo, show once again the sensitivity that our PCLS model and assay can bring for screening studies.

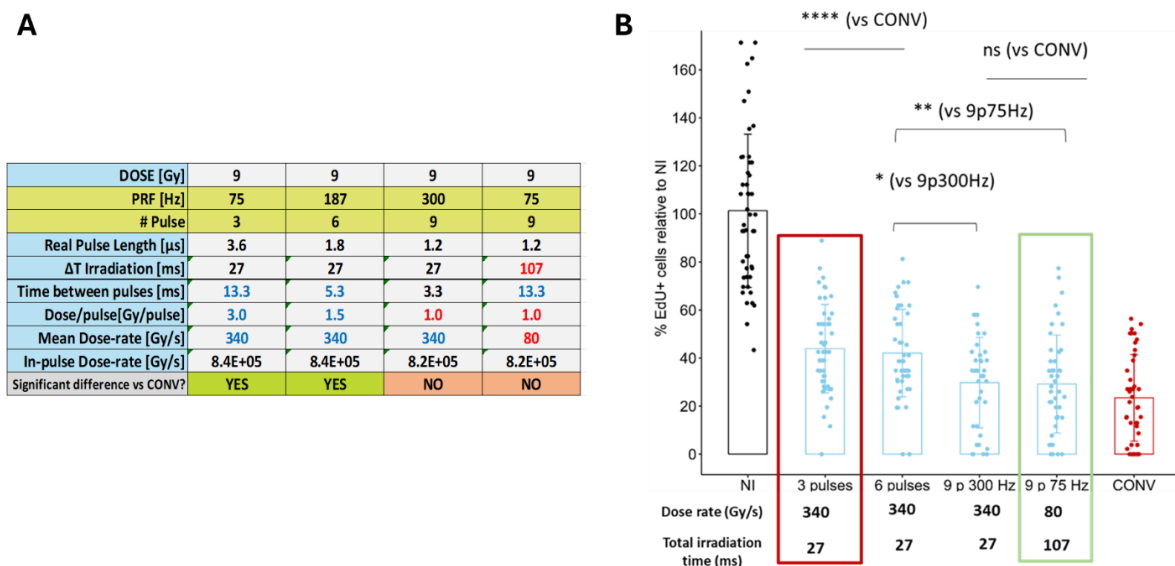


Figure 54. Minimal dose per pulse/Number of pulses to trigger a FLASH sparing effect in PCLS. (A) List of parameters measured for FLASH -RT in PCLS, with a fixed dose of 9 Gy and varying number of pulses while keeping same total irradiation time by adjusting PRF. (B) Quantification of the proportion of EdU+ cells following different pulse structures in FLASH irradiation. Statistical significance is indicated as follows: * $p < 0.05$, ** $p < 0.01$, **** $p < 0.0001$ ($n=5$ slices, 4-5 FOV per slice).

These results suggested, for the first time in the lung, that another parameter other than the mean dose rate or total irradiation time could influence the presence of the FLASH effect. However, with a fixed dose of 9 Gy, it was not possible to determine whether a pulse dose greater than 1 Gy or fewer than 6 pulses were required for FLASH-RT. To address this issue, we designed an experiment to independently compare these two parameters using two FLASH irradiation doses, 6 and 9 Gy. In the results presented in **above**, we showed that a protective effect was observed at both 6 and 9 Gy, concerning the sparing of cycling cells in PCLS 24 hours post-treatment. Therefore, we chose to compare FLASH irradiation modalities at 6 and 9 Gy to conventional irradiation at an equivalent dose (**Figure 55A**). At 6 Gy, we could adjust the number of pulses to 6 or 3, corresponding to dose per pulses of 1 Gy and 2 Gy respectively. At 9 Gy, we know that the effect is lost with 9 pulses of 1 Gy but conserved with 6 pulses of 1.5 Gy or 3 pulses of 3 Gy. Under these conditions, if we lose the FLASH effect at 6 Gy with 6 pulses of 1 Gy, it will indicate that the dose per pulse is the critical factor triggering the FLASH effect. If the effect is still preserved, it would suggest that it is a number of pulses greater than 6 that causes the loss of the FLASH sparing effect in PCLS. By analyzing the proportion of EdU+ cells after different temporal structures of FLASH irradiation at 6 and 9 Gy, our results indicate that the sparing effect on cell proliferation was lost for a dose per pulse inferior than 1.5 Gy per pulse independently of number of pulses (**Figure 55B**). Indeed, FLASH sparing effect was lost at 6 Gy with a dose per pulse of 1 Gy (**Figure 55B**).

A

DOSE [Gy]	6	9	6	9
PRF [Hz]	187	187	75	75
# Pulse	6	6	3	3
Real Pulse Length [μ s]	1.3	1.9	2.8	3.9
ΔT Irradiation [ms]	27	27	27	27
Time between pulses [ms]	5.3	5.3	13.3	13.3
Dose/pulse [Gy/pulse]	1.0	1.5	2.0	3.0
Mean Dose-rate [Gy/s]	220	340	220	340
In-pulse Dose-rate [Gy/s]	7.7E+05	7.9E+05	7.1E+05	7.7E+05
Significant difference vs CONV?	NO	YES	YES	YES

B

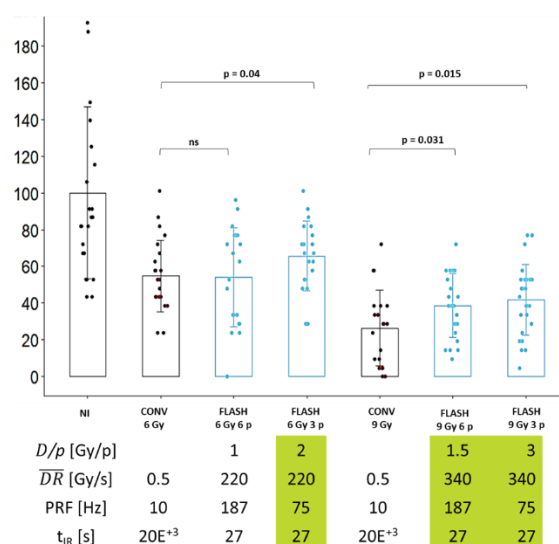


Figure 55. Importance of temporal structure of FLASH-RT. (A) Table summarizing the irradiation parameters for different experimental conditions (B) Quantification of EdU+ cells after irradiation, comparing conventional CONV and FLASH conditions at 6 Gy and 9 Gy, showing that FLASH irradiation with 6 pulses of 1.5 Gy (at 9 Gy) and a higher dose-rate (220 Gy/s) significantly preserves cell division as well as FLASH irradiation with 3 pulses at 6 Gy,

compared to conventional treatment, with significant differences (p -value < 0.05) observed. Statistical significance is indicated as follows: * p < 0.05, ** p < 0.01, **** p < 0.0001 ($n=5$ slices, 4-5 FOV per slice).

This suggests that a combination of optimal parameters is necessary for the presence of a FLASH sparing effect in the lung. Indeed, our studies indicate that the **mean dose rate must exceed 100 Gy/s** and **the dose per pulse must be greater than 1 Gy**. These results still need to be validated, and of course, it must be confirmed that this is not organ-dependent, as suggested by other studies which indicate that single-pulse irradiation optimizes the FLASH protective effect. However, this highlights other factors to consider when validating a new beam, not just irradiating at ultra-high dose rates, but ensuring that a FLASH sparing effect is induced. For this reason, the PCLS model and our cell division assay in PCLS seem to be sensitive enough to allow rapid analyses in order to address these issues.

2.3.3 Impact of the oxygen concentration in culture on the FLASH sparing effect in PCLS

Multiple studies have shown that the presence of a FLASH effect depends on the partial oxygen pressure within the tissue. Others have demonstrated that oxygen supplementation through anesthesia is sufficient to prevent a FLASH effect in the brain. The role of oxygen remains somewhat unclear, and although several studies suggest its limited role in the underlying mechanisms of FLASH, we wanted to investigate the impact of varying oxygen conditions on the observed FLASH effect within PCLS. Under physiological conditions, in the lung, oxygen concentration is typically around 5% (physioxia). Finally, we aimed to study the impact of hypoxic conditions on cell division in response to FLASH irradiation in PCLS. To this end, after obtaining the PCLS, they were incubated in balanced media at either 2% or 5% oxygen using a hypoxia chamber, both during the irradiation and for 24 hours post-treatment (**Figure 56A**). The oxygen concentration in the hypoxic conditions was validated using an iT Green probe, incubated for 1 hour with a batch of PCLS, which confirmed the presence of hypoxic regions in PCLS incubated at 2% oxygen (**Figure 56B**). Interestingly, at 2% oxygen, we were unable to reveal a response to irradiation (**Figure 56C**). Indeed, the level of cell division in non-irradiated slices incubated at 2% oxygen was significantly reduced (**Figure 56C**). It is known that hypoxic conditions can inhibit cell cycle entry, which prevents us from detecting a FLASH protective effect using this endpoint in PCLS (**Figure 56C**). However, it appears that the FLASH protective effect is preserved under physioxic conditions, suggesting that **we can detect a FLASH protective effect at oxygen concentrations between 5% and 20% in our PCLS model** by focusing on the entry of lung cells into the cell cycle (**Figure 56C**).

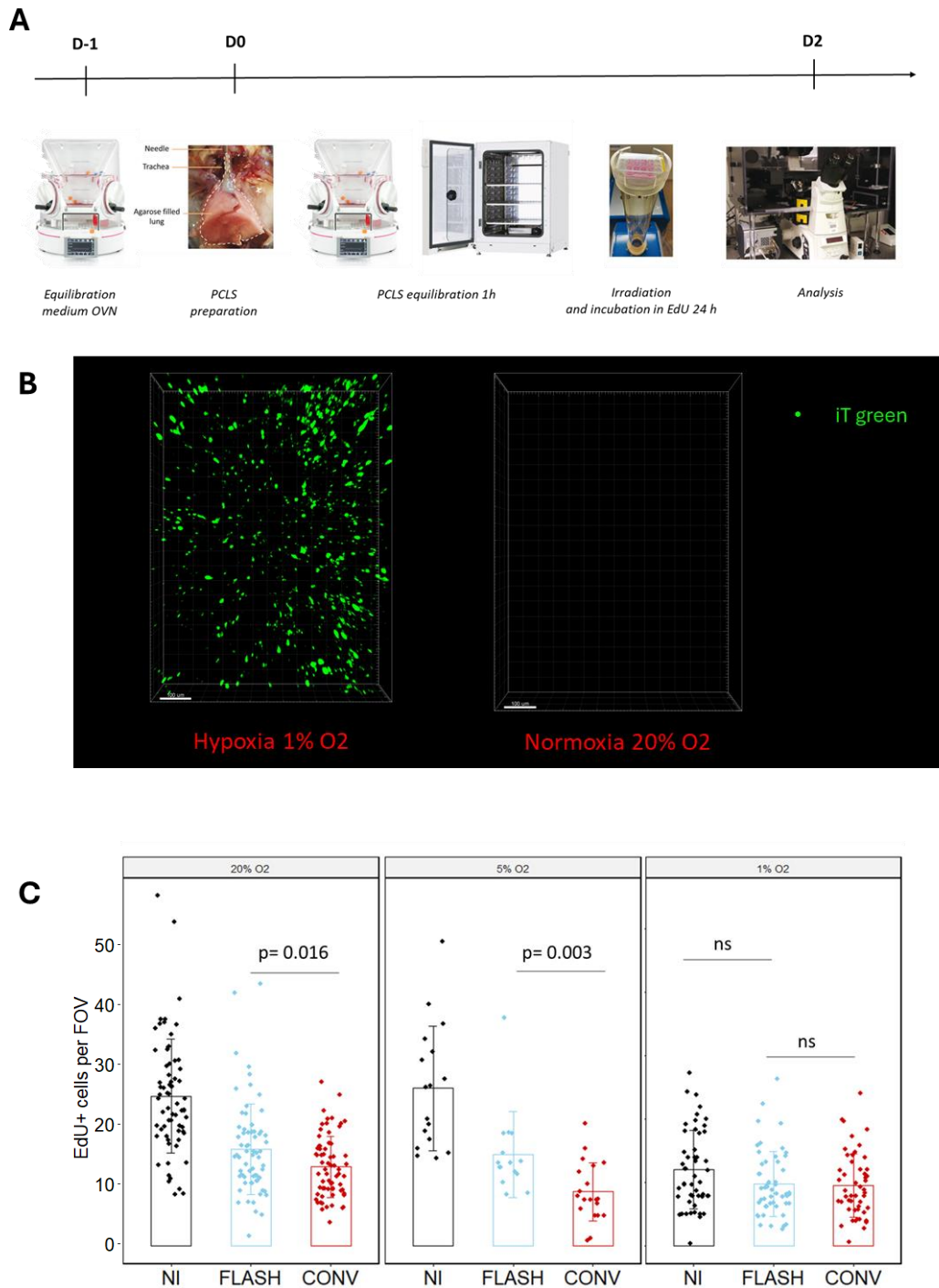


Figure 56. Impact of oxygen concentration on FLASH-RT sparing effect in PCLS. (A) Experimental workflow for PCLS irradiation under different oxygen conditions. (B) Representative images showing the presence of hypoxic (1% O₂, left) and normoxic (20% O₂, right) conditions in PCLS, with iT green hypoxia probe. (C) Quantification of EdU+ cells per field of view (FOV) in PCLS under different oxygen conditions (20%, 5%, and 1% O₂). FLASH radiotherapy significantly preserves cell division in both normoxic and physioxic conditions at 20% and 5% O₂, but not under 1% O₂. *p-value < 0.05, **p-value < 0.01, ns = not significant.

2.3.4 Conservation of the FLASH sparing effect in previously irradiated lung tissue

In clinical settings, many cancer patients receive multiple courses of radiotherapy, especially in cases of recurrent tumors or metastases. It is essential to investigate whether the FLASH effect can also be observed in previously irradiated tissues. This is particularly important in the context of re-irradiation, where tissue sensitivity may change due to prior radiation exposure, potentially modifying the response to subsequent treatments. Understanding whether FLASH radiotherapy retains its protective effects in re-irradiated tissues could help optimize treatment strategies for patients requiring re-irradiation, particularly in the lung.

To simulate a previous treatment scenario, mice were irradiated in the thoracic region with a dose of 10 Gy at conventional dose rate. Four months post-irradiation, we performed short-term studies using precision-cut lung slices (PCLS) to investigate acute responses to re-irradiation with a dose range comparing CONV and FLASH at dose of 3, 6 and 9 Gy. Additionally, long-term studies were conducted to evaluate development radiation-induced lung fibrosis, with another thoracic dose escalation experiments comparing conventional and FLASH-RT at doses of 6, 9, and 12 Gy.

In the acute response study, we first assessed the basal cell division rates in PCLS from mice that had been irradiated four months earlier at 10 Gy compared to non- previously irradiated mice (**Figure 59 A**). Surprisingly, no significant differences were observed in the division rates between the groups. Then, for the comparison between CONV and FLASH-RT 24 hours post-treatment, results were similar to those observed in non-re-irradiated mice, suggesting that the short-term FLASH sparing effect is preserved in previously irradiated lung tissue (**Figure 59B**). For the late toxicity analysis, we focused on the development of fibrosis in mice re-irradiated with either FLASH or conventional radiotherapy at a dose of 12, 9 or 6 Gy. Mice irradiated with FLASH at 12 Gy demonstrated improved survival in contrast to those irradiated with CONV-RT, indicating that the FLASH sparing effect looking at late radio-induced toxicities is still present even in tissues that have previously undergone irradiation. However, at lower doses of 6 and 9 Gy, although the mice developed some toxicity over time, no significant difference was observed between FLASH and conventional treatments.

These findings suggest that the FLASH sparing effect is conserved in lung tissue after re-irradiation, particularly at higher doses. However, at lower doses, no distinct advantage of FLASH over conventional radiotherapy was observed in terms of long-term toxicity. In conclusion, FLASH radiotherapy appears to retain its protective effect in previously irradiated lung tissue, but further studies with shorter intervals between irradiations are needed to explore how

the timing between treatments affects the presence of the FLASH effect on healthy lung tissue. This would help refine the optimal conditions for clinical applications of FLASH in re-irradiation scenarios.

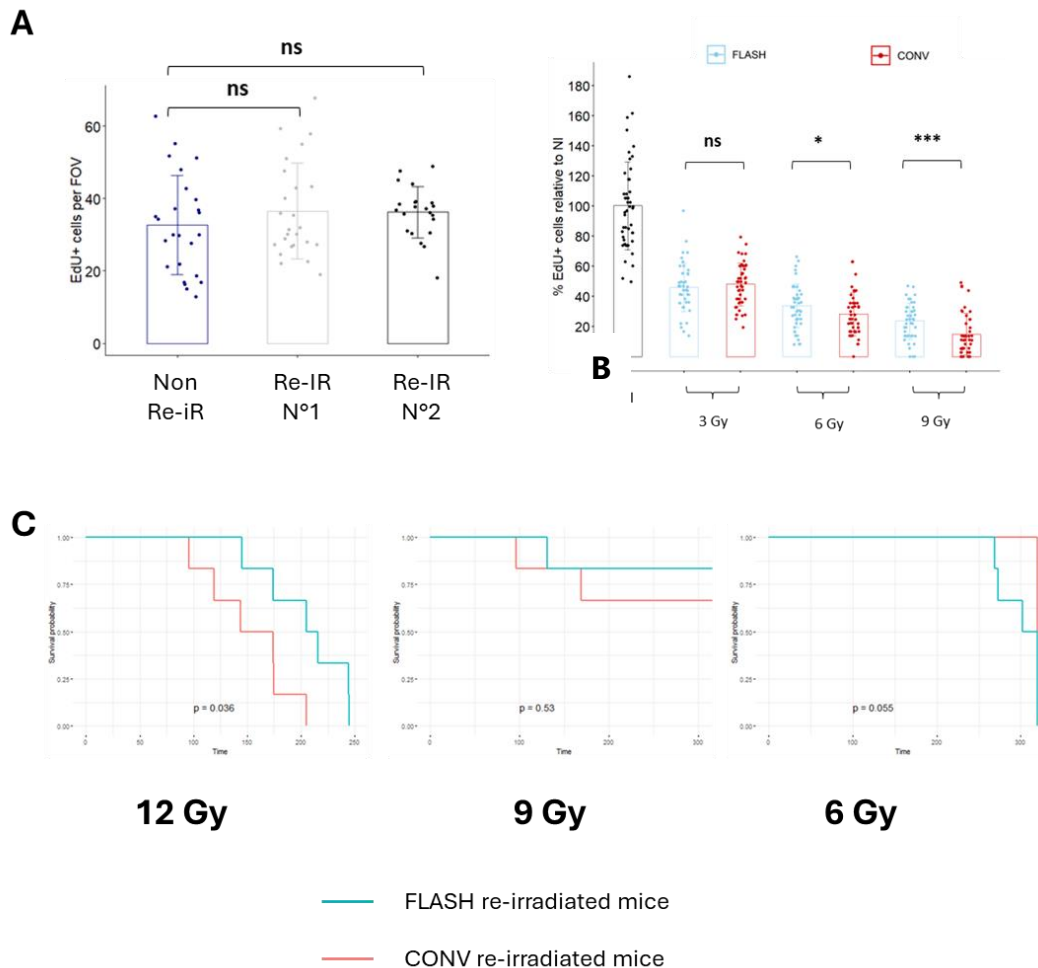


Figure 57. Conservation of the FLASH sparing effect in previously irradiated lung tissue. (A) Quantification of EdU+ cells per field of view (FOV) in non-re-irradiated and re-irradiated groups, showing no significant differences in the division rate. (B) Comparison of the percentage of EdU+ cells relative to non-irradiated (NI) control in lung tissue after conventional (CONV) or FLASH radiotherapy re-irradiation at doses of 3 Gy, 6 Gy, and 9 Gy. Significant differences were observed at 6 and 9 Gy between FLASH and CONV conditions. (C) Kaplan-Meier survival curves comparing FLASH and CONV re-irradiated mice at 12 Gy, 9 Gy, and 6 Gy. FLASH re-irradiated mice showed significantly better survival at 12 Gy compared to CONV re-irradiated mice. At 9 Gy and 6 Gy, no significant differences were observed.

2.4 Conclusion

In this second part, we applied this model and our tests **to investigate the irradiation parameters and optimal conditions needed to achieve the FLASH effect in the lung**. Regarding the parameters, we determined that the average dose rate and total irradiation time are critical factors, with the dose rate needing to exceed **100 Gy/s to achieve the optimal FLASH effect**, and more specifically, dose rates above 300 Gy/s. Additionally, we identified the dose per pulse as another crucial element for FLASH irradiation using an electron beam, where the dose per pulse **must exceed 1 Gy/pulse** in order to detect the FLASH protective effect in the PCLS model. Moreover, we demonstrated that **the FLASH protective effect in progenitor cells was preserved under both normoxic and pulmonary physioxic conditions**. Finally, we also showed that the **FLASH protective effect was maintained not only in the short term but also in the development of late toxicities in the context of re-irradiation**.

3. FLASH SPARING EFFECT IN PATIENTS

3.1 Introduction

After identifying the optimal FLASH irradiation parameters for a FLASH protective effect on healthy lung tissue in the murine PCLS model, we aimed to apply this model and assay to another major issue in the FLASH field.

Indeed, **although phase I clinical trials are ongoing**, currently, they are not designed to demonstrate the FLASH sparing effect in patients. For now, only a FLASH arm is being investigated, and the primary goal is often a feasibility study of clinical FLASH irradiation, along with all the dosimetric and safety constraints this entails. Therefore, even though the clinical transition of FLASH has begun, **we still have no proof of the FLASH protective effect on healthy tissue in patients**, and it will likely take many more years before this is demonstrated in a clinical trial specifically designed to address this objective.

One major advantage of the **PCLS model is that it can be derived from patient lung tissue**. Through collaboration with the Institut Mutualiste Montsouris, we have access to healthy distal lung resections from patients. Thus, we worked on **establishing a PCLS model derived from patients (PCLS-Hu)**. After establishing a protocol for obtaining PCLS-Hu, we **used this model to investigate the presence of the FLASH protective effect at a dose of 9 Gy**, under the optimal irradiation conditions in which this effect was observed in the murine model. This work was conducted on a cohort of 19 patients being treated for lung cancer at IMM, and it was carried out during my PhD.

After we characterized the response of dividing cells in PCLS-Hu short-term post-treatment, **we wanted to prospect some initial molecular insight into the underlying mechanisms of the FLASH sparing effect**. For that purpose, **we performed RNAseq analysis** on some lung samples from patients, comparing conventional irradiation and FLASH irradiation at a dose of 9 Gy after 24 hours of culture.

3.2 Material and method/Results – Article 2

Manuscript title : Potential of FLASH Radiotherapy Uncovered in Human Lung

Authors: Maxime Dubail¹, Chloé Lafouasse², Sophie Heinrich¹, Vincent Favaudon¹, Arturo Londoño-Vallejo¹, Marie Dutreix¹, Delphine Colin³, Jean-François Côté³, Jérôme Didier³, Christelle Pouliquen³, Abdelali Benali³, Pierre Verrelle⁴, Marine Lefèvre³, Nicolas Girard⁵, Agathe Seguin-Givelet^{2,6}, Gilles Créhange⁷, Charles Fouillade^{1#}.

¹Institut Curie, Inserm U1021-CNRS UMR 3347, University Paris-Saclay, PSL Research University, Centre Universitaire, 91405 Orsay Cedex, France.

²Institut Montsouris, Surgery Department, Institut du Thorax Curie Montsouris, Paris, France.

³Department of Pathology, Institut Mutualiste Montsouris, Paris, France.

⁴Institut Curie, Inserm U1196-CNRS UMR 9187, University Paris-Saclay, PSL Research University, Centre Universitaire CS 90030, Orsay, France.

⁵Institut du Thorax Curie Montsouris, Paris, France.

⁶Paris 13 University, Sorbonne Paris Cité, Faculty of Medicine SMBH, Bobigny, France.

⁷Institut Curie, PSL Research University, Radiation Oncology Department, Paris/Saint-Cloud/Orsay, France.

#Corresponding Author Information:

Charles Fouillade

Institut Curie – Centre de Recherche

INSERM U1021/CNRS UMR3347/Université Paris-Saclay

Centre Universitaire

Bâtiments 110-111-112

Rue Henri Becquerel

CS 90030

91401 Orsay Cedex

Email: charles.fouillade@curie.fr

Conflicts of Interest: Nicolas Girard received research grants/support from Abbvie, Amgen, AstraZeneca, Beigene, Boehringer Ingelheim, Bristol Myers Squibb, Daiichi-Sankyo, Gilead, Hoffmann-La Roche, Janssen, LeoPharma, Lilly, Merck Serono, Merck Sharp & Dohme, Novartis, Sanofi, Sivan, served as a consultant for Abbvie, Amgen, AstraZeneca, Beigene, Bristol Myers Squibb, Daiichi-Sankyo, Gilead, Ipsen Hoffmann-La Roche, Janssen, LeoPharma, Lilly, Merck Sharp & Dohme, Mirati, Novartis, Pfizer, Pierre Fabre, Sanofi, Sivan Takeda, and participated on a data safety monitoring board for Hoffmann-La Roche. One of his family members is employed by AstraZeneca.

Marie Dutreix is a member of the board of the Société Française du Cancer and Comité Stratégique de Filière, owns stock options, and serves as a consultant for ONXEO.

Agathe Seguin-Givelet received grants from Sivan, payments from AstraZeneca, Medtronic, General Electric, Bristol Myers Squibb, Ethicon, Medela, and participated on a data safety monitoring board for AstraZeneca.

Translational Relevance :

FLASH radiotherapy is an innovative method that spares normal tissue in animal models from radiation-induced toxicities while maintaining similar anti-tumoral efficacy, holding great promise for widening the therapeutic window of radiotherapy. While the first clinical trials have recently begun, the most pressing question for enhancing the clinical translation of this new modality is whether FLASH triggers a beneficial effect in humans. To address this question, we analyzed healthy lung tissues resected from cancer patients and demonstrated how FLASH spares cycling cells, while reducing the activation of pro-apoptotic, DNA damage, and oxidative stress pathways. For the first time in human tissue, the results from this study indicate that a beneficial effect of FLASH radiotherapy is observed in nearly all patients, paving the way for a broad application of this new radiation modality in the treatment of cancer patients.

Abstract :

Purpose: Although an increasing number of lung cancer patients are treated with radiotherapy, toxicities induced by radiation, such as pneumonitis and fibrosis, significantly affect patients' quality of life. Developed a decade ago, FLASH radiotherapy is an innovative method that, by delivering ultrafast treatment, reduces radiation toxicities on healthy tissue while preserving the anti-tumoral effect of radiotherapy. This FLASH effect has been described in different pre-clinical models but has not been observed in human patients yet. This study aims to determine if FLASH radiotherapy can induce a sparing effect in human healthy lung.

Patients and Methods: To address this question, precision-cut lung slices (Hu-PCLS) were prepared from healthy lung samples collected from 19 lung cancer patients undergoing lobectomy. After irradiation using ElectronFLASH operated either in conventional or FLASH mode, we monitored cell division for each patient and performed RNAseq analysis.

Results: Analysis of cell division 24 hours after treatment by conventional or FLASH radiotherapy showed a higher proportion of dividing cells after FLASH radiotherapy. Consistently, RNAseq analysis from irradiated lung samples confirmed an attenuated activation of cell cycle checkpoints, p53 pro-apoptotic genes, DNA damage, and anti-oxidant pathways after FLASH radiotherapy compared to conventional treatment. Interestingly, such transcriptional differences were not found in RNAseq analysis of tumoral tissue treated by conventional or FLASH radiotherapy.

Conclusions: Altogether, this study shows, for the first time in human tissue, that FLASH radiotherapy spares healthy lung cells from radiation damage, fostering future clinical applications to optimize radiotherapy for lung cancer patients.

Keywords: Radiation-induced lung injuries, FLASH effect, Quality of life, Hu-PCLS, RNAseq

Introduction :

Lung cancer affects over 2 million new patients worldwide every year. Patients with inoperable tumors are typically treated with a combination of chemotherapy, immunotherapy, and radiotherapy. While radiotherapy is effective in reducing tumors, it is often limited by the damage it causes to surrounding healthy tissues. In the lung, these radiation-induced damages are primarily characterized by acute pneumonitis, which occurs in 15-25% of patients and, in more severe cases, evolves into pulmonary fibrosis (1). As the number of cancer survivors and cases of lung re-irradiation increase, it is crucial to find ways to prevent radiation-induced lung toxicities, particularly given the few therapeutic options available and the potential decline in patients' quality of life (2,3).

Developed a decade ago, FLASH radiotherapy holds great promise in widening the therapeutic window for cancer patients. This novel method of radiation therapy delivers ultrafast treatment (<100 ms), reducing radiation-induced toxicities while maintaining an anti-tumoral efficacy comparable to conventional radiotherapy (4). The so-called "FLASH effect" has primarily been demonstrated in the lung and observed across various preclinical models, organs, and FLASH facilities at different institutions (5–8). Notably, the FLASH effect has been shown in large mammals such as mini-pigs and in cancer patients, including cats and dogs (9–11). To enhance the clinical implementation of FLASH radiotherapy, mechanistic studies are required to determine how to maximize its effect in human patients (12,13). In the lung, prior studies using preclinical mouse models of whole thorax irradiation have shown that FLASH radiotherapy spares lung progenitor cells, reduces persistent DNA damage, and limits the development of senescence and pulmonary fibrosis (14).

Recently, this novel method has generated significant enthusiasm in the radiation oncology and radiation biology communities. Clinical trials for FLASH radiotherapy have begun, with the first reports from patients treated with FLASH published recently. For instance, a patient with multiresistant T-cell cutaneous lymphoma was treated with a single FLASH dose to skin lesions at the CHUV (Centre Hospitalier Universitaire Vaudois) in Lausanne, Switzerland (15,16). The University of Cincinnati has completed the FAST-01 trial, treating 8 patients with limb bone metastases using proton FLASH (17,18), while the follow-up FAST-02 trial (<https://clinicaltrials.gov/study/NCT05524064>) is currently underway, focusing on thoracic bone metastases (19). So far, these studies have demonstrated the clinical feasibility of FLASH radiotherapy, showing no unexpected toxicities or reduced anti-tumoral efficacy compared to conventional radiotherapy. However, a sparing effect of FLASH radiotherapy in human tissues has yet to be demonstrated.

To address this gap and enhance the future clinical application of FLASH radiotherapy for treating thoracic malignancies, this study evaluates the differential effects of FLASH radiotherapy compared to conventional treatments in human lung tissue. For this, precision-cut lung slices (Hu-PCLS) were prepared from fresh lung samples collected from lobectomies, and exposed to either FLASH or conventional irradiation. Although the patients included in this study represented a heterogeneous population of lung cancer patients, analysis of cell division after irradiation showed a sparing effect of FLASH radiotherapy in nearly all patients (95%). Complementary RNAseq analysis of the human lung samples confirmed the preservation of cell cycle gene expression, accompanied by reduced activation of DNA damage, pro-apoptotic, and anti-oxidant pathways. By demonstrating a sparing effect of FLASH radiotherapy in human lung tissue, this study paves the way for improved treatments of lung cancer with minimal toxicities.

Material and Methods

Ethical Consent: All samples were collected from the Institut Mutualiste Montsouris under a dedicated protocol for lung cancer specimens approved by the French Ethics and Informatics Commission (EUdract 2017 - A03081-52). All patients in this study provided written informed consent for sample collection for research purposes.

Human PCLS Preparation: Tumor-free lung tissues were freshly recovered from distal lung samples to prepare precision-cut lung slices (Hu-PCLS) using a protocol adapted from previous publications (20,21). Briefly, lung tissues were cleaned twice in Phosphate Buffered Saline (PBS) to remove blood. Then, on ice, 2.5% low-melting agarose (A9414-50G) diluted in Hu-PCLS medium (DMEM F12 from Invitrogen (#31331-028) supplemented with 1% SVF (CVFVSF00-0U), 1% penicillin/streptomycin (CABPES01-0U), 1% non-essential amino acids (11140035), and 1% L-glutamine (25030-024) was injected slowly into small bronchi to inflate the lung resection. 8 mm punches were embedded in 5% agarose, and 500 μ m slices were made using a vibratome (Leica VT1000S). Hu-PCLS were placed into a 24-well plate containing 500 μ L of Hu-PCLS medium and cultured at 37°C in 5% CO₂ up to 24 hours. Between 15 to 25 Hu-PCLS were obtained per patient, and slices were randomly distributed among the different treatment conditions.

Irradiation: Hu-PCLS were irradiated in a 24-well plate using a vertical 7-MeV electron beam produced by the linear accelerator ElectronFLASH (SIT S.p.A., R&D Dept., Italy) at Institut Curie, capable of delivering both conventional (CONV) and FLASH radiotherapy. A total dose of 9 Gray (Gy) in a single fraction was delivered in both CONV and FLASH modalities. Dose measurements were performed using Gafchromic™ EBT-XD films (Ashland, NJ, USA) and a

flashDiamond Detector T60025 (PTW Freiburg, Germany), placed inside the wells at the position of the lung samples for planning and at the top of the plate for online monitoring. Irradiation duration was measured using a Bergoz in-flange Current Transformer mounted in the beam line and connected to a Teledyne Lecroy Wavesurfer 4054HD oscilloscope. The parameters used are summarized in the Supplementary Material. For each patient, a minimum of 5 Hu-PCLS slices were analyzed per condition.

Cell Division Analysis: To estimate the proportion of cells that replicate after irradiation in the Hu-PCLS, a Click-IT chemistry protocol was used to monitor cell proliferation via 5-ethynyl-2'-deoxyuridine (EdU) incorporation (BaseClick, #BCK-EdUPro-FC647). Hu-PCLS were incubated 1 hour after irradiation in 500 μ L of Hu-PCLS medium containing 10 μ M EdU. 24 hours post-irradiation, Hu-PCLS were fixed in 4% PFA, and EdU incorporation was revealed according to the manufacturer's instructions. Hu-PCLS were then washed in PBS and incubated with DAPI. The samples were transferred into a glass support adapted for microscopy (μ -Slide 4 Well Glass Bottom, Ibidi) and imaged on an inverted Nikon Spinning Disk TIRF-FRAP using a 10X objective. Four to five fields of view (FOV) were acquired per Hu-PCLS. Image post-processing and EdU quantification were performed using a semi-automatic method combining 3D reconstruction and segmentation of the nuclei with IMARIS software (Bitplane).

RNA Extraction: For transcriptional analysis induced by conventional and FLASH radiotherapy, lung resections were cut into small pieces of 2-3 mm, irradiated either in CONV or FLASH modes, and cultured at 37°C, 5% CO₂ for 24 hours. After a PBS wash, lung tissues were incubated in RNAprotect solution (Qiagen, Hilden, Germany) overnight at 4°C. Disruption and lysis of the lung tissue were performed in 600 μ L of RLT lysis buffer (Qiagen, Hilden, Germany) using a Tissue Ruptor II (Qiagen, Hilden, Germany). Lung homogenate was then processed according to manufacturer's instructions using an RNeasy Mini Kit. RNA integrity and concentration were estimated using the Agilent Bioanalyzer following the manufacturer's instructions (RNA 6000 Nano Kit #5067-1512).

RNAseq Analysis: All samples presented a RIN >7. Sequencing libraries were prepared from 500 ng of total RNA using the Illumina TrueSeq Stranded mRNA Library preparation kit, following the manufacturer's recommendations. 100 bp paired-end sequencing was performed with the Illumina NovaSeq 6000 instrument. Reads were mapped to the reference human genome (hg19/GRCh37) using STAR 2.7.6a (<https://github.com/alexdobin/STAR>). In the raw count matrix, background genes (expression <1) in most patient replicates were filtered out. For Gene Set Enrichment Analysis (GSEA) and heatmap generation, data were normalized using the DESeq2 package (<https://github.com/theovelab/DESeq2>). To explore the signaling pathways differentially impacted after FLASH versus conventional radiotherapy, GSEA was performed

comparing CONV vs. Non-Irradiated (NI), FLASH vs. NI, or CONV vs. FLASH. Significantly enriched pathways were selected based on p-value <0.05 and FDR q-value <0.25 with permutations (n = 1000, permutation type = gene set).

Statistical Analysis: Statistical analyses were performed using the `ggpubr` package (<https://rpkgs.datanovia.com/ggpubr/>) in R. For EdU+ nuclei count data, the Wilcoxon Mann-Whitney test was used to compare the means of these counts between conventional and FLASH conditions.

Data Availability Statement: RNAseq data from tumor-free human lung treated with either conventional or FLASH radiotherapy have been deposited in NCBI's Gene Expression Omnibus under the accession number GSE263484 (reviewer's token: cnypcgksflgnpef). All data and code are available upon request. The RNAseq dataset previously published (22) from xenografted human U-87 MG glioblastoma tumors exposed to conventional or FLASH radiotherapy is accessible through the accession number GSE223607.

Results

Hu-PCLS Prepared from a Cohort of Lung Cancer Patients

To analyze the effect of FLASH radiotherapy in human lung tissue, we established a cohort of 19 lung cancer patients, from whom healthy lung tissue was resected after surgery at the Institut Mutualiste Montsouris (Table 1). The cohort included 10 men and 9 women, with ages ranging from 48 to 86 years. The majority of patients were diagnosed with lung adenocarcinoma (13/19), with a smaller number presenting with squamous cell carcinoma (5/19) and large cell carcinoma (1/19). Notably, two patients had a history of breast cancer and had previously undergone radiotherapy and chemotherapy. Three patients received neoadjuvant therapy, including the anti-PD1 antibody (Nivolumab), prior to surgery. To assess the heterogeneity of the cohort, we first quantified the basal level of cell division in the lung. Hu-PCLS were prepared from fresh lung samples from each patient, and the proportion of dividing cells was measured 24 hours post-culture (Figure 1). As expected, the basal level of dividing cells varied between patients. Interestingly, Hu-PCLS from the three patients treated with neoadjuvant therapies exhibited a higher number of dividing EdU+ cells. While a positive correlation was observed between neoadjuvant therapy and increased cell division, statistical analysis did not show significant correlations between cell division and other clinical data such as sex or age (Supplementary Figure 1). Overall, this cohort represents a heterogeneous subset of lung cancer patients who may be exposed to FLASH radiotherapy in future studies.

Sample ID	Age (years)	Sex	Smoking status	Cancer	Neoadjuvant therapy	Previous thoracic radiotherapy	Lung comorbidities
Patient 1	72	M	35 PY	Squamous cell carcinoma	-	-	-
Patient 2	61	F	35 PY	Large cell carcinoma	-	-	Lung infection in childhood
Patient 3	72	M	60 PY	Adenocarcinoma	-	-	Stented ischemic heart disease
Patient 4	70	F	10 PY	Adenocarcinoma	-	-	-
Patient 5	76	M	56 PY	Adenocarcinoma	-	-	Sars-COV infection
Patient 6	86	M	0 PY	Adenocarcinoma	-	-	-
Patient 7	57	M	60 PY	Adenocarcinoma	-	-	Chronic bronchitis
Patient 8	56	F	40 PY	Adenocarcinoma	-	Breast cancer (2019)	-
Patient 9	67	M	40 PY	Squamous cell carcinoma	-	-	-
Patient 10	72	M	45 PY	Adenocarcinoma	-	-	-
Patient 11	66	F	20 PY	Adenocarcinoma	-	-	Sars-COV infection
Patient 12	60	F	60 PY	Adenocarcinoma	Cisplatin/ Pémétréxed/ Nivolumab	-	-
Patient 13	76	M	50 PY	Squamous cell carcinoma	Carboplatin/ Taxol/Nivolumab	-	-
Patient 14	48	M	30 PY	Adenocarcinoma	-	-	-
Patient 15*	67	F	45 PY	Squamous cell carcinoma	-	-	-
Patient 16*	64	F	20 PY	Squamous cell carcinoma	Carboplatin/ Pémétréxed/ Nivolumab	Breast cancers (1999, 2003)	-
Patient 17	72	M	55 PY	Adenocarcinoma	-	-	-
Patient 18	62	F	0 PY	Adenocarcinoma	-	-	-
Patient 19*	57	F	15 PY	Adenocarcinoma	-	-	-

Table 1. Patient information included in this study. M: Male; F: Female; PY: Number of Packs/Year; *Patients' samples selected for RNAseq analysis.

FLASH radiotherapy preserves cycling cells in Hu-PCLS.

A previous study in mouse models reported that compared to conventional radiotherapy (CONV), FLASH radiotherapy preserves the capacity of lung cells to divide 24 hours after whole thorax irradiation. To explore the differential effects of FLASH radiotherapy in human lung, Hu-PCLS were prepared from lung samples of 19 patients, irradiated with a dose of 9 Gy delivered in either CONV or FLASH mode, and the proportion of dividing cells was quantified 24 hours after irradiation. (A) As expected, conventional radiotherapy triggered a sharp decrease in the proportion of dividing cells, with EdU+ cells ranging from 9% to 33% in women and 18% to 42% in men. (B) In contrast, FLASH radiotherapy induced an attenuated response, with EdU+ cells ranging from 17% to 56% in women and 28% to 57% in men. FLASH radiotherapy preserved the proportion of cycling lung cells in 18 out of 19 patients. The relative strength of the FLASH sparing effect, defined as the ratio of EdU+ cells after FLASH radiotherapy to EdU+ cells after CONV radiotherapy, varied from 1.3 to 2.3. (C) One patient showed no significant difference between FLASH and CONV radiotherapy, with no obvious correlation to

clinical data. These results provide, for the first time, evidence of the sparing effect of FLASH radiotherapy in human lung, suggesting a potential broad application for lung cancer patients.

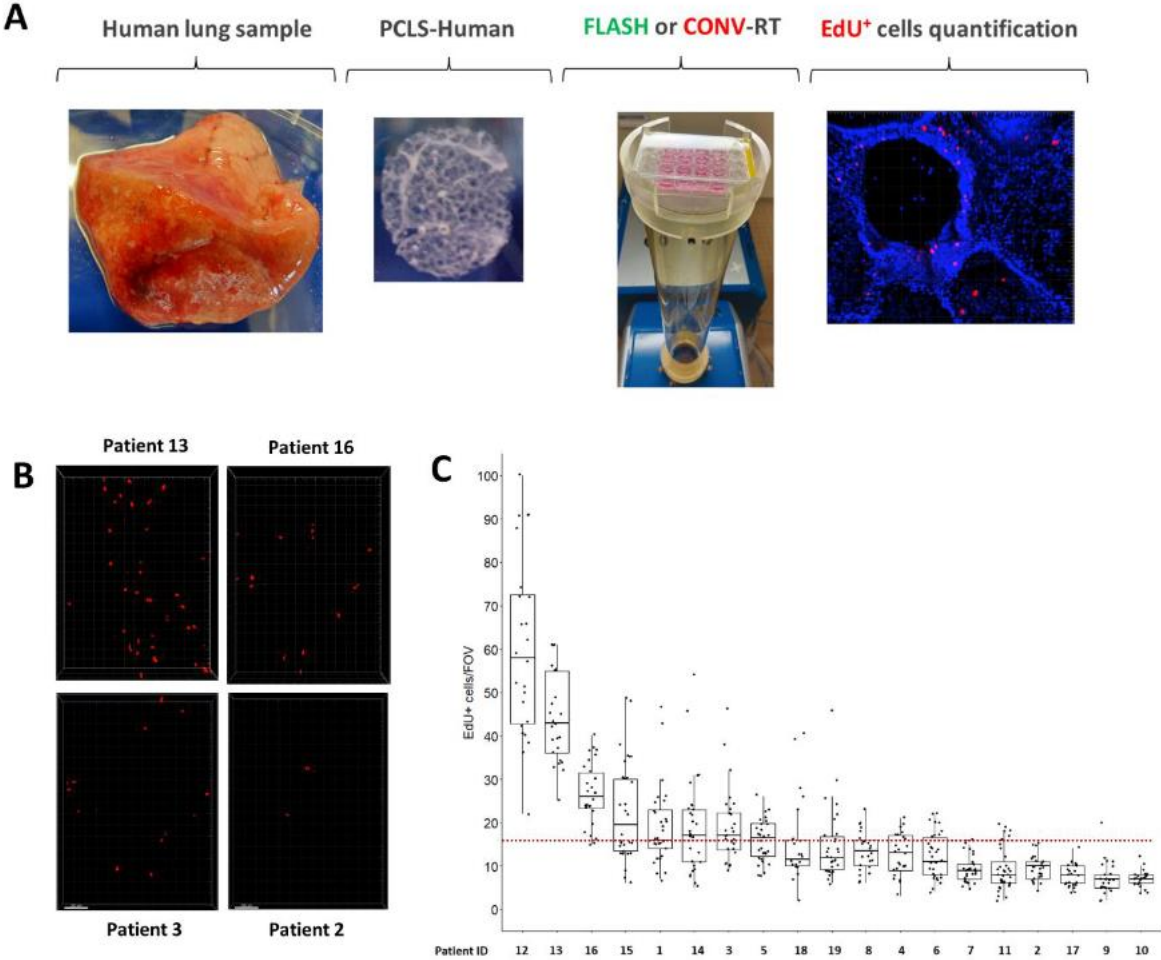


Figure 1. Analysis of EdU incorporation in Hu-PCLS reveals heterogeneous cell division rates across patients. (A) Schematic illustrating the workflow to obtain, process, and analyze Hu-PCLS. (B) Representative images showing the variation in the proportion of EdU⁺ cells across patients. Images were acquired on a confocal microscope with a 10× objective. The scale bar represents 200 μm. (C) Quantification of the number of EdU⁺ cells within Hu-PCLS 24 hours after slicing showed an average of 18 EdU⁺ cells per field of view (FOV). Notably, patients 12, 13, and 16, who received neoadjuvant immunotherapy, exhibited higher numbers of EdU⁺ cells, ranging from 27 to 61. (n = 4 to 5 FOV per slice for a total of 5–8 slices per patient). Each dot represents the quantification for one field of view.

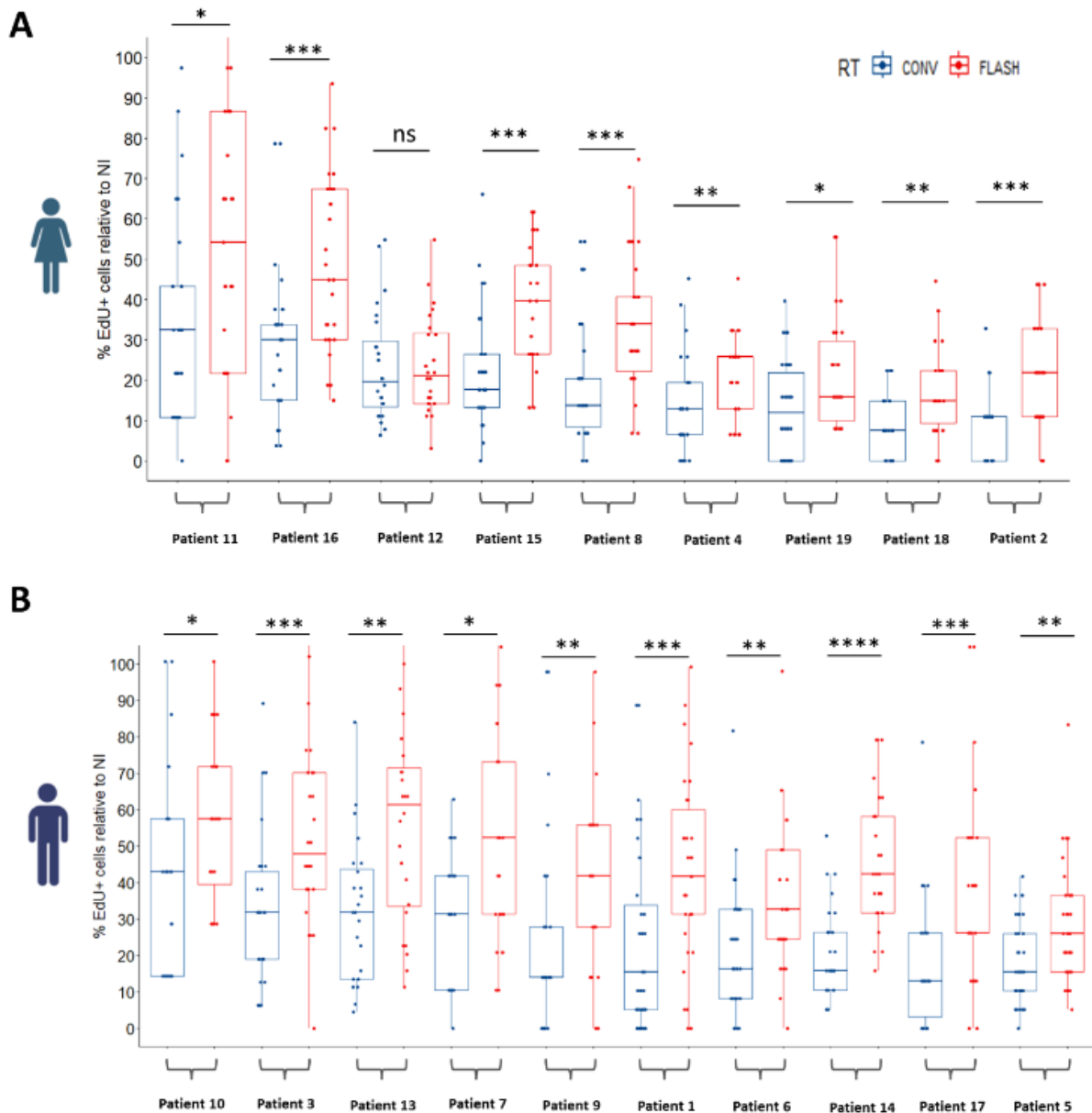


Figure 2. FLASH radiotherapy preserves a higher proportion of cycling cells in almost all patients. (A) Quantification of the proportion of EdU+ cells in Hu-PCLS prepared from female patients and analyzed 24 hours after conventional (CONV) or FLASH radiotherapy. Sorted by decreasing proportion after CONV treatment, analysis of cycling cells after irradiation shows that 8 out of 9 patients exhibit a higher proportion of EdU+ cells after FLASH compared to CONV. (B) A similar analysis performed on Hu-PCLS obtained from 10 male patients confirmed that FLASH radiotherapy spares the proportion of cycling cells in all male patients analyzed. ns = not significant; * p-value < 0.05; ** p-value < 0.01; *** p-value < 0.001; **** p-value < 0.0001.

RNAseq analysis confirms a differential effect of FLASH radiotherapy

To characterize the molecular characteristics of FLASH radiotherapy in the lung, RNAseq analysis was performed on lung samples collected 24 hours after exposure to either conventional or FLASH radiotherapy (Figure 3A). Computational analysis revealed that conventional radiotherapy triggered drastic transcriptional changes, with a large number of differentially expressed genes observed between CONV and Non-Irradiated (NI) samples (i.e., 2084 genes upregulated). However, similar analysis indicated that FLASH radiotherapy induced minor transcriptional changes, with only 55 genes found upregulated compared to NI (Figure 3B). Gene Set Enrichment Analysis (GSEA) revealed that conventional radiotherapy downregulates cell cycle-related genes such as TOP2A, MKI67, and CDK1, while FLASH radiotherapy attenuates this decrease, confirming the results obtained from the cell division analysis in patient Hu-PCLS (Figure 3C). Concomitantly, while conventional radiotherapy strongly upregulates p53 and DNA damage-related pathways, FLASH radiotherapy limits the activation of these genes, suggesting that FLASH radiotherapy reduces the level of stress and DNA damage induced by radiation. To determine if this sparing effect of FLASH radiotherapy is specific to healthy tissue, we analyzed previously published RNAseq data from xenografted human tumors resected 24 hours after treatment with either conventional or FLASH radiotherapy (22). Interestingly, in tumor tissue, FLASH radiotherapy activated cell cycle-related genes, DNA damage, and p53 pathways similarly to conventional radiotherapy (Figure 3D). Altogether, these RNAseq analyses confirm, at the transcriptional level, the presence of a FLASH effect, indicating a sparing of healthy tissue while having a comparable impact on tumor tissue.

FLASH radiotherapy limits activation of oxidative stress-related genes

To further investigate the mechanism of FLASH radiotherapy in human lung, we analyzed gene sets specifically enriched after conventional compared to FLASH radiotherapy. This analysis revealed that NRF2 signaling, a pathway playing a critical role in controlling stem cell self-renewal, proliferation, and differentiation (24), as well as genes involved in Reactive Oxygen Species (ROS) detoxification, were selectively upregulated after conventional radiotherapy (Figure 4A-4C). In particular, KEAP1, one of the key players of the NRF2 pathway (25), was found significantly upregulated in lung samples from three distinct patients exposed to conventional radiotherapy (Figure 4B). Activation of NRF2 transcriptional targets leads to an antioxidant response. Interestingly, conventional radiotherapy significantly increased the expression levels of many ROS detoxification genes, including NRF2 target genes such as PRDX1 and SOD1, as well as canonical thioredoxin reductase genes, TXNRD2 and TXNRD3 (Figure 4D). These transcriptional changes indicate that conventional radiotherapy triggers a burst of reactive species, subsequently activating an antioxidant program to counteract oxidative damage.

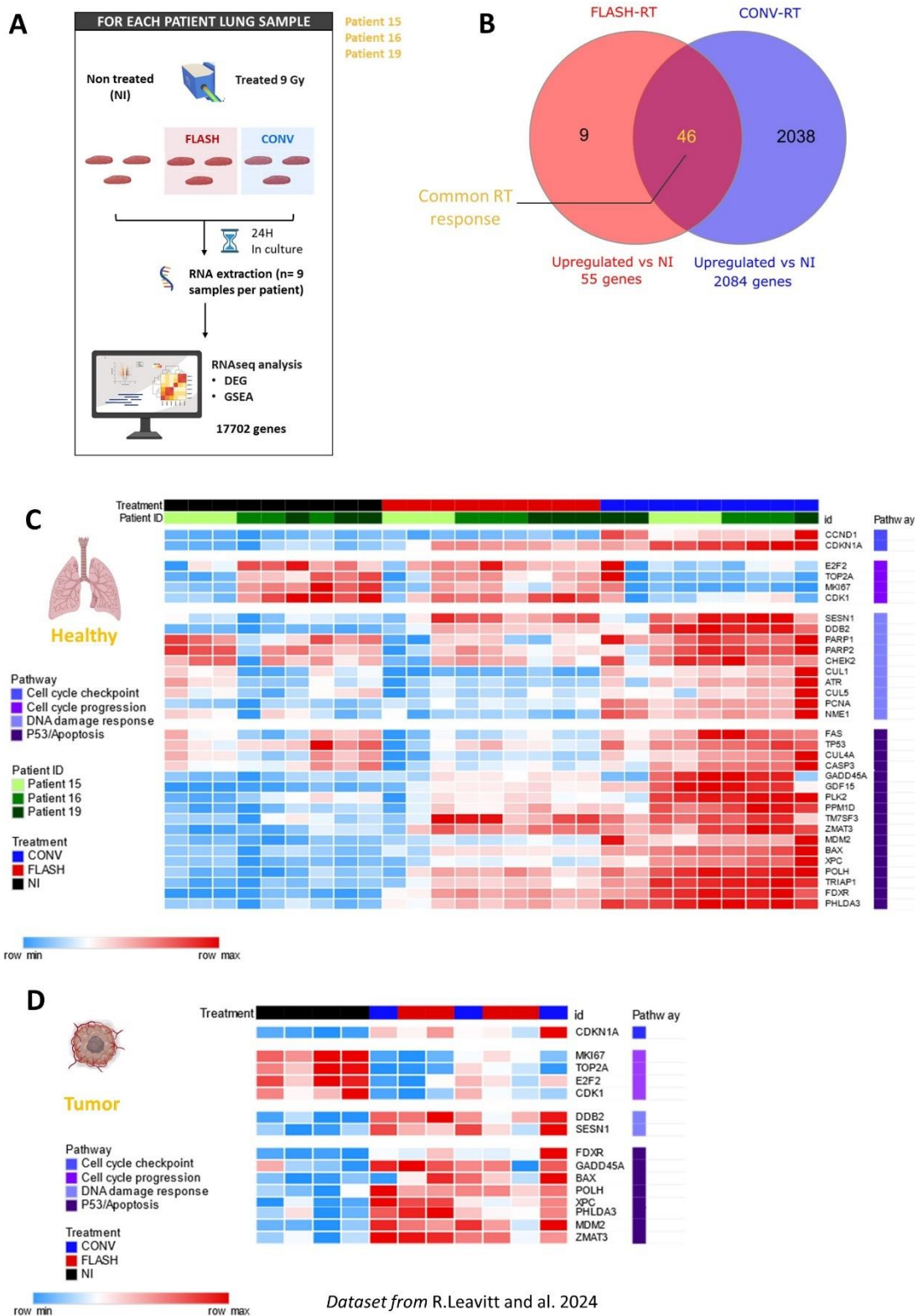


Figure 3. RNAseq analysis confirms FLASH radiotherapy induces specific transcriptional changes in human lung but not in tumor (A) Workflow for RNAseq processing and analysis from 3 selected patients. Each patient's sample was split across 3 conditions (NI, FLASH, CONV) with 3 replicates per condition. (B) Differentially expressed genes (DEG) analysis revealed that conventional radiotherapy (CONV) upregulates 40 times more genes than FLASH.

(C) Heatmap showing downregulation of cell cycle gene expression after conventional (CONV) radiotherapy compared to FLASH and non-irradiated (NI) conditions, as well as an attenuated activation of genes related to cell cycle checkpoints, p53 pro-apoptotic pathway, and DNA damage response. (D) Heatmap generated from RNAseq analysis of human tumor tissue treated with either conventional or FLASH radiotherapy, highlighting the absence of differences in the induction of cell cycle checkpoint, p53 pro-apoptotic pathway, and DNA damage-related genes between the two radiation modalities.

In contrast, FLASH radiotherapy did not elicit significant activation of antioxidant pathways, in line with previous results showing an attenuated induction of the p53 pathway. These results strongly suggest that, compared to conventional radiotherapy, FLASH induces fewer oxidative species, potentially preventing radiation-induced damage in healthy human lung tissue.

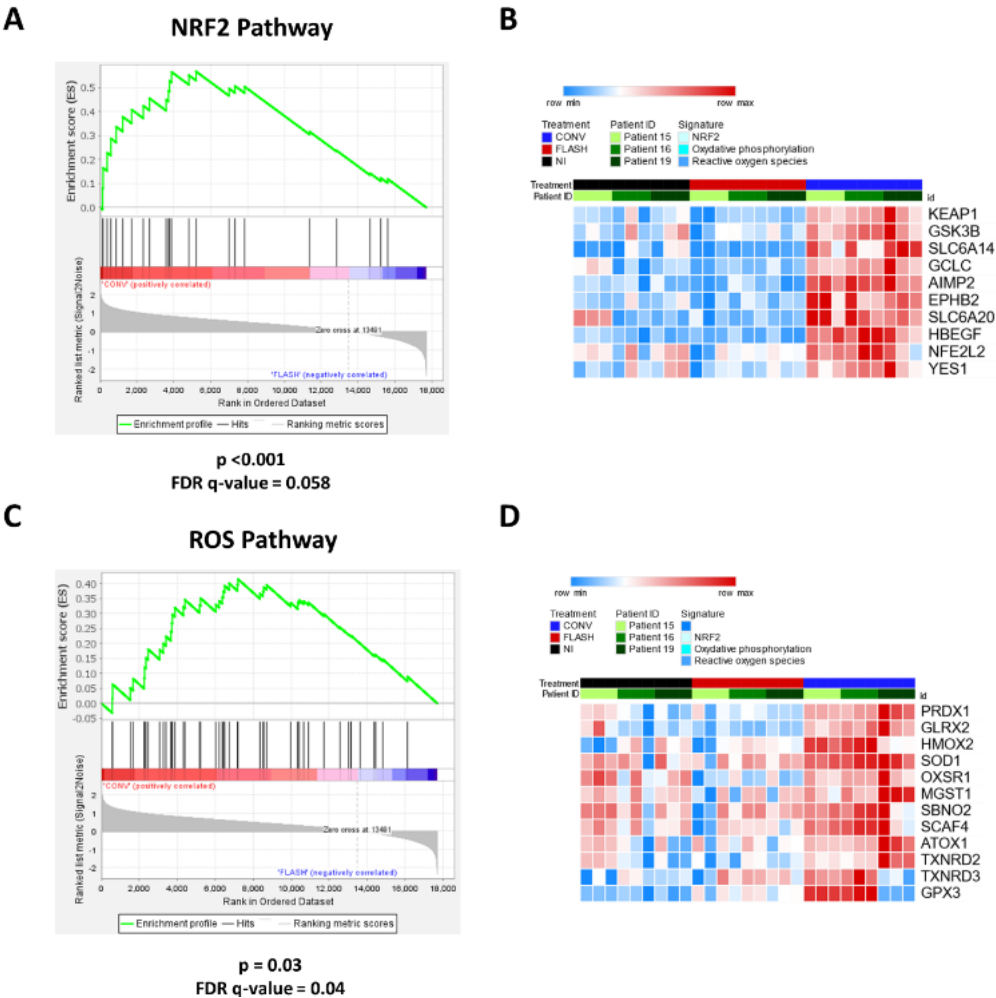


Figure 4. FLASH radiotherapy reduces induction of anti-oxidant program in human lung. (A) Gene Set Enrichment Analysis (GSEA) comparing differentially expressed genes after conventional (CONV) vs. FLASH radiotherapy revealed an enrichment of the NRF2 pathway specifically after CONV. (B) Heatmap representing the expression of NRF2-related genes, which

were strongly upregulated after conventional radiotherapy but not after FLASH radiotherapy. (C) Concomitantly, pathways involved in the management of Reactive Oxygen Species (ROS) are selectively enriched after conventional radiotherapy. (D) Heatmap illustrating the upregulation of genes responsible for ROS detoxification specifically after conventional radiotherapy.

Discussion

This study demonstrates that FLASH radiotherapy spares human lung tissue from radiation-induced toxicities. By analyzing a cohort of 19 lung cancer patients, we showed that compared to conventional radiotherapy, FLASH radiotherapy preserves the proportion of cycling cells in almost all patients (18/19). This beneficial effect was confirmed by RNAseq analysis 24 hours after treatment, showing the preservation of cell cycle-related genes (e.g., MKI67, TOP2A) after FLASH, compared to conventional radiotherapy. Additionally, the molecular analysis highlighted an attenuated upregulation of p53 pro-apoptotic transcriptional targets (e.g., BAX, GADD45A), as well as genes associated with DNA damage (e.g., ATR, PARP1, CHEK2). Importantly, this mitigation of radiation-induced transcriptional responses was observed specifically in healthy lung tissue, not in tumoral tissue, which fits the definition of a FLASH effect in human tissue: sparing healthy tissue while not affecting tumoral cells. Furthermore, FLASH radiotherapy triggered limited activation of oxidative stress-related pathways, suggesting a reduction in reactive species compared to conventional treatment. In the last decade, FLASH radiotherapy has shown great potential in widening the therapeutic window of radiation therapy. Preclinical studies have demonstrated that FLASH reduces toxicities in organs such as the lung, gut, brain, skin, and esophagus (4,7,26,27). Not only in mouse models, but also in larger mammals, including mini-pigs and pet cancer patients (9,10,28). To date, a few patients have been treated with FLASH radiotherapy for skin lesions or bone metastases (15–17), but clinical studies comparing FLASH with conventional radiotherapy in humans have not been reported. However, the results from this study, obtained from human lung resections, are the first to report a FLASH sparing effect observed in the vast majority of patients. This first study in human tissue holds great promise for the clinical translation of FLASH radiotherapy. Several studies investigating the molecular and cellular mechanisms underlying the sparing of healthy tissue induced by FLASH have reported the preservation of the cycling capabilities of stem/progenitor cells. In mouse brain models, FLASH radiotherapy preserved progenitor cell cycling, which correlated with attenuated astrogliosis and maintained neurocognitive function—effects typically impaired by conventional radiotherapy (27,29,30). Similarly, in mouse gut models, FLASH radiotherapy reduced intestinal damage, limited ferroptosis, and increased the proportion of intestinal stem cells capable of regenerating the crypts after radiation injury (26,31,32). Previous preclinical studies in mouse lung models showed that FLASH spares progenitor cells, reduces persistent DNA damage, reduces senescence, and limits radio-induced pulmonary

fibrosis (14). In this work, we observed similar preservation of cycling cells in lung tissue resected from patients, suggesting that the mechanism underlying the beneficial effect of FLASH radiotherapy is conserved across organs and species. Regarding the mechanism, RNAseq analysis of human lung tissue indicates that FLASH radiotherapy limits the transcriptional activation of genes involved in reactive oxygen species (ROS) detoxification, suggesting reduced ROS production after FLASH compared to conventional radiotherapy. Similar results were obtained in mouse brain models after FLASH radiotherapy (30). At the biochemical level, a recent study reported that FLASH irradiation induces less lipid peroxidation (33). In line with these previous studies and the mechanistic model of the FLASH effect (34), our study provides further evidence that FLASH radiotherapy produces fewer oxidative species, thus reducing oxidative damage. In conclusion, this study presents initial evidence of the beneficial effects of FLASH radiotherapy in human tissue, signaling a great potential for this innovative radiation modality to improve the therapeutic index of radiotherapy for lung cancer treatment.

Acknowledgements

This work was funded by INSERM (contract N°19CR057-00) and received support from La Ligue contre le Cancer. The contribution of the bioinformatics core facility at U900 Inserm-Institut Curie is gratefully acknowledged. High-throughput sequencing was performed by the ICGex NGS platform of the Institut Curie, supported by grants ANR-10-EQPX-03 (Equipex) and ANR-10-INBS-09-08 (France Génomique Consortium) from the Agence Nationale de la Recherche (“Investissements d’Avenir” program), by the ITMO-Cancer Aviesan (Plan Cancer III), and by the SiRIC-Curie program (SiRIC Grant INCa-DGOS-465 and INCa-DGOS-Inserm_12554). Data management, quality control, and primary analysis were performed by the Bioinformatics platform of the Institut Curie. The authors are grateful to Marie-Noëlle Soler and Laetitia Besse from the Multimodal Imaging Center-Light Microscopy Facility of the Institut Curie (CNRS UMS2016/InermUS43/Institut Curie/Université Paris-Saclay), as well as the Cell and Tissue Imaging Platform – PICT-IBiSA (member of France–Bioimaging – ANR-10-INBS-04) of the U934/UMR3215 of Institut Curie for their guidance with light microscopy. The authors wish to thank Sarah Lagha and Kheira Bouaziz from the Institut du Thorax Curie-Montsouris, as well as Simon Lefranc from the Centre de Ressources Biologiques of Institut Mutualiste Montsouris, for their help in providing patient samples. Thanks are also due to the members of the Londoño-Vallejo team for scientific exchanges and discussions.

References

1. De Ruyscher D, Niedermann G, Burnet NG, Siva S, Lee AWM, Hegi-Johnson F. Radiotherapy toxicity. *Nat Rev Dis Primers*. Nature Publishing Group; 2019;5:1–20.
2. Ran J, Wang J, Bi N, Jiang W, Zhou Z, Hui Z, et al. Health-related quality of life in long-term survivors of unresectable locally advanced non-small cell lung cancer. *Radiation Oncology*. 2017;12:195.
3. Farr KP, Khalil AA, Grau C. Patient-reported lung symptoms and quality of life before and after radiation therapy for non-small cell lung cancer: correlation with radiation pneumonitis and functional imaging. *Acta Oncologica*. Taylor & Francis; 2019;58:1523–7.
4. Favaudon V, Caplier L, Monceau V, Pouzoulet F, Sayarath M, Fouillade C, et al. Ultrahigh dose-rate FLASH irradiation increases the differential response between normal and tumor tissue in mice. *Science Translational Medicine*. 2014;6:245ra93-245ra93.
5. Montay-Gruel P, Bouchet A, Jaccard M, Patin D, Serduc R, Aim W, et al. X-rays can trigger the FLASH effect: Ultra-high dose-rate synchrotron light source prevents normal brain injury after whole brain irradiation in mice. *Radiotherapy and Oncology*. 2018;129:582–8.
6. Giannini N, Gadducci G, Fuentes T, Gonnelli A, Di Martino F, Puccini P, et al. Electron FLASH radiotherapy in vivo studies. A systematic review. *Front Oncol [Internet]*. Frontiers; 2024 [cited 2024 Aug 29];14. Available from: <https://www.frontiersin.org/journals/oncology/articles/10.3389/fonc.2024.1373453/full>
7. Ren W, Hou L, Zhang K, Chen H, Feng X, Jiang Z, et al. The sparing effect of ultra-high dose rate irradiation on the esophagus. *Front Oncol [Internet]*. Frontiers; 2024 [cited 2024 Jul 31];14. Available from: <https://www.frontiersin.org/journals/oncology/articles/10.3389/fonc.2024.1442627/full>
8. Montay-Gruel P, Corde S, Laissue JA, Bazalova-Carter M. FLASH radiotherapy with photon beams. *Medical Physics*. 2022;49:2055–67.
9. Vozenin M-C, De Fornel P, Petersson K, Favaudon V, Jaccard M, Germond J-F, et al. The Advantage of FLASH Radiotherapy Confirmed in Mini-pig and Cat-cancer Patients. *Clin Cancer Res*. 2019;25:35–42.
10. Gjaldbæk BW, Arendt ML, Konradsson E, Bastholm Jensen K, Bäck SÅJ, Munck af Rosenschöld P, et al. Long-term toxicity and efficacy of FLASH radiotherapy in dogs with superficial malignant tumors. *Front Oncol [Internet]*. Frontiers; 2024 [cited 2024 Jul 23];14. Available from: <https://www.frontiersin.org/journals/oncology/articles/10.3389/fonc.2024.1425240/full>

11. Rohrer Bley C, Wolf F, Gonçalves Jorge P, Grilj V, Petridis I, Petit B, et al. Dose- and Volume-Limiting Late Toxicity of FLASH Radiotherapy in Cats with Squamous Cell Carcinoma of the Nasal Planum and in Mini Pigs. *Clinical Cancer Research*. 2022;OF1–10.
12. Vozenin M-C, Bourhis J, Durante M. Towards clinical translation of FLASH radiotherapy. *Nat Rev Clin Oncol*. Nature Publishing Group; 2022;1–13.
13. Loo BW, Verginadis II, Sørensen BS, Mascia AE, Perentesis JP, Koong AC, et al. Navigating the Critical Translational Questions for Implementing FLASH in the Clinic. *Seminars in Radiation Oncology*. 2024;34:351–64.
14. Fouillade C, Curras-Alonso S, Giuranno L, Quelennec E, Heinrich S, Bonnet-Boissinot S, et al. FLASH Irradiation Spares Lung Progenitor Cells and Limits the Incidence of Radio-induced Senescence. *Clin Cancer Res*. American Association for Cancer Research; 2020;26:1497–506.
15. Bourhis J, Sozzi WJ, Jorge PG, Gaide O, Bailat C, Duclos F, et al. Treatment of a first patient with FLASH-radiotherapy. *Radiotherapy and Oncology*. 2019;139:18–22.
16. Gaide O, Herrera F, Sozzi WJ, Gonçalves Jorge P, Kinj R, Bailat C, et al. Comparison of ultra-high versus conventional dose rate radiotherapy in a patient with cutaneous lymphoma. *Radiotherapy and Oncology* [Internet]. 2022 [cited 2022 Feb 27]; Available from: <https://www.sciencedirect.com/science/article/pii/S0167814021090939>
17. Mascia AE, Daugherty EC, Zhang Y, Lee E, Xiao Z, Sertorio M, et al. Proton FLASH Radiotherapy for the Treatment of Symptomatic Bone Metastases: The FAST-01 Nonrandomized Trial. *JAMA Oncol*. 2023;9:62–9.
18. Daugherty EC, Mascia A, Zhang Y, Lee E, Xiao Z, Sertorio M, et al. FLASH Radiotherapy for the Treatment of Symptomatic Bone Metastases (FAST-01): Protocol for the First Prospective Feasibility Study. *JMIR Research Protocols*. 2023;12:e41812.
19. Daugherty E, Zhang Y, Xiao Z, Mascia A, Sertorio M, Woo J, et al. FLASH radiotherapy for the treatment of symptomatic bone metastases in the thorax (FAST-02): protocol for a prospective study of a novel radiotherapy approach. *Radiation Oncology*. 2024;19:34.
20. Alsafadi HN, Uhl FE, Pineda RH, Bailey KE, Rojas M, Wagner DE, et al. Applications and Approaches for Three-Dimensional Precision-Cut Lung Slices. *Disease Modeling and Drug Discovery*. *Am J Respir Cell Mol Biol*. American Thoracic Society - AJRCMB; 2020;62:681–91.
21. Gerckens M, Alsafadi HN, Wagner DE, Lindner M, Burgstaller G, Königshoff M. Generation of Human 3D Lung Tissue Cultures (3D-LTCs) for Disease Modeling. *JoVE*. 2019;58437.

22. Leavitt RJ, Almeida A, Grilj V, Montay-Gruel P, Godfroid C, Petit B, et al. Acute hypoxia does not alter tumor sensitivity to FLASH radiotherapy. *International Journal of Radiation Oncology*Biology*Physics* [Internet]. 2024 [cited 2024 Feb 26]; Available from: <https://www.sciencedirect.com/science/article/pii/S0360301624003201>
23. Dubail M, Heinrich S, Portier L, Bastian J, Giuliano L, Aggar L, et al. Lung Organotypic Slices Enable Rapid Quantification of Acute Radiotherapy Induced Toxicity. *Cells*. 2023;12:2435.
24. Dai X, Yan X, Wintergerst KA, Cai L, Keller BB, Tan Y. Nrf2: Redox and Metabolic Regulator of Stem Cell State and Function. *Trends in Molecular Medicine*. 2020;26:185–200.
25. Liu Q, Gao Y, Ci X. Role of Nrf2 and Its Activators in Respiratory Diseases. *Oxidative Medicine and Cellular Longevity*. 2019;2019:7090534.
26. Levy K, Natarajan S, Wang J, Chow S, Eggold JT, Loo PE, et al. Abdominal FLASH irradiation reduces radiation-induced gastrointestinal toxicity for the treatment of ovarian cancer in mice. *Scientific Reports*. Nature Publishing Group; 2020;10:21600.
27. Montay-Gruel P, Petersson K, Jaccard M, Boivin G, Germond J-F, Petit B, et al. Irradiation in a flash: Unique sparing of memory in mice after whole brain irradiation with dose rates above 100 Gy/s. *Radiotherapy and Oncology*. 2017;124:365–9.
28. Konradsson E, Arendt ML, Bastholm Jensen K, Børresen B, Hansen AE, Bäck S, et al. Establishment and Initial Experience of Clinical FLASH Radiotherapy in Canine Cancer Patients. *Front Oncol*. 2021;11:658004.
29. Montay-Gruel P, Markarian M, Allen BD, Baddour JD, Giedzinski E, Jorge PG, et al. Ultra-High-Dose-Rate FLASH Irradiation Limits Reactive Gliosis in the Brain. *Radiat Res*. 2020;
30. Montay-Gruel P, Acharya MM, Petersson K, Alikhani L, Yakkala C, Allen BD, et al. Long-term neurocognitive benefits of FLASH radiotherapy driven by reduced reactive oxygen species. *Proc Natl Acad Sci USA*. 2019;116:10943–51.
31. Ruan J-L, Lee C, Wouters S, Tullis IDC, Verslegers M, Mysara M, et al. Irradiation at Ultra-High (FLASH) Dose Rates Reduces Acute Normal Tissue Toxicity in the Mouse Gastrointestinal System. *International Journal of Radiation Oncology*Biology*Physics*. 2021;111:1250–61.
32. Shi X, Yang Y, Zhang W, Wang J, Xiao D, Ren H, et al. FLASH X-ray spares intestinal crypts from pyroptosis initiated by cGAS-STING activation upon radioimmunotherapy. *Proceedings of the National Academy of Sciences*. *Proceedings of the National Academy of Sciences*; 2022;119:e2208506119.

33. Froidevaux P, Grilj V, Bailat C, Geyer WR, Bochud F, Vozenin M-C. FLASH irradiation does not induce lipid peroxidation in lipids micelles and liposomes. *Radiation Physics and Chemistry*. 2023;205:110733.

34. Kacem H, Almeida A, Cherbuin N, Vozenin M-C. Understanding the FLASH effect to unravel the potential of ultra-high dose rate irradiation. *International Journal of Radiation Biology*. 2022;98:506–16.

Supplementary Material

MODALITY	CONV	FLASH
Dose [Gy]	9 ± 0.2	
Energy [MeV]	7	
Field size [mm]	Ø 120	
SSD [cm]	110	
Mean Dose-rate [Gy/s]	0.5	450
Treatment time [s]	~ 20	0.02
Pulse Repetition Frequency [Hz]	10	100
Pulse width [µs]	4	3.5 - 3.9
Number of pulses	~ 200	3
Dose-per-pulse [Gy/p]	~ 0.05	3
Dose/MU [Gy/MU]	0.007	NA
In-pulse Dose-rate [Gy/s]	~ 1E+04	8E+05

Supplementary Table 1. Beam parameters used for conventional (CONV) and FLASH irradiation of Hu-PCLS. In FLASH mode, the dose was monitored by adjusting the pulse width and the number of pulses. In CONV mode, the dose was controlled by adjusting the Monitor Units (MU) counted by a Monitor ionization Chamber. In this modality, the dose-per-pulse may slightly vary, and the number of pulses (and therefore the treatment time) is automatically adapted accordingly to achieve the set MU value. In each modality, the delivered dose was verified using films placed beneath the plate and a specific diamond-based detector, independent of dose-rate, above the plate. Across all irradiations, the difference between the CONV and FLASH doses never exceeded 0.2 Gy.

PATIENT DATA	CORRELATION COEFFICIENT
Gender	0,17
Previous cancer	0,09
Smoking status	0,29
Age	-0,04
Neoadjuvant therapy	0,84

Supplementary Figure 1. Correlation coefficient between patients data and basal division level in the cohort.

PATIENT DATA	CORRELATION COEFFICIENT
Steady state division level	-0,49
Decrease of cell division after CONV-RT	0,42
Previous cancer	-0,079
Smoking status	-0,19
Age	--0,21
Neoadjuvant therapy	0,09

Supplementary Figure 2. Correlation coefficient between patients data and FLASH vs CONV sparing ratio in the cohort.

3.3 Additional results – Article 2

In addition to the reported protective impact of FLASH on the ROS response and the expression of genes involved in their management pathways (Nrf2-Keap1) in comparison to conventional irradiation, **we have identified other changes that may be relevant** when comparing the molecular effects of conventional irradiation to FLASH. As discussed in the introduction of this manuscript, several underlying mechanisms have been proposed for the FLASH protective effect, including **the immune hypothesis** and **the mitochondrial impact hypothesis**. Thus, interestingly, we also identified **upregulation of genes involved in the electron transport chain and inflammatory upregulation after conventional irradiation compared to FLASH**.

The analysis of mitochondrial gene expression in human lung tissue after conventional and FLASH radiotherapy revealed significant differences in the activation of mitochondrial pathways (**Figure 58**). GO enrichment analysis highlighted the upregulation of mitochondrial RNA metabolic processes and mitochondrial gene expression in CONV-RT compared to FLASH treatment (**Figure 58A**). Further investigation through GSEA confirmed the preferential activation of genes involved in the mitochondrial electron transport chain (ETC) after CONV-RT, with a statistically significant enrichment observed (**Figure 58B**). Several ETC complexes were indeed upregulated after CONV-RT, including those related to mitochondrial ATP synthase and cytochrome oxidase complexes, as well as those implicated in mitochondrial complexes I, II and IV. These findings suggest that CONV-RT radiotherapy may induce higher alterations in mitochondrial function, potentially to the release of ROS which could explain the higher implication of ROS management pathway compared to FLASH.

RNAseq analysis revealed differential activation of inflammatory pathways following conventional CONV and FLASH radiotherapy in human lung tissues (**Figure 59**). Enrichment analysis of the IFN- α response pathway, IFN- γ response pathway as well as NF- κ B pathway showed a significant upregulation of genes associated with these inflammation processes following conventional radiotherapy compared to FLASH irradiation. This analysis underscores the reduced inflammatory activation following FLASH radiotherapy, which could contribute to its protective effects on healthy lung tissue.

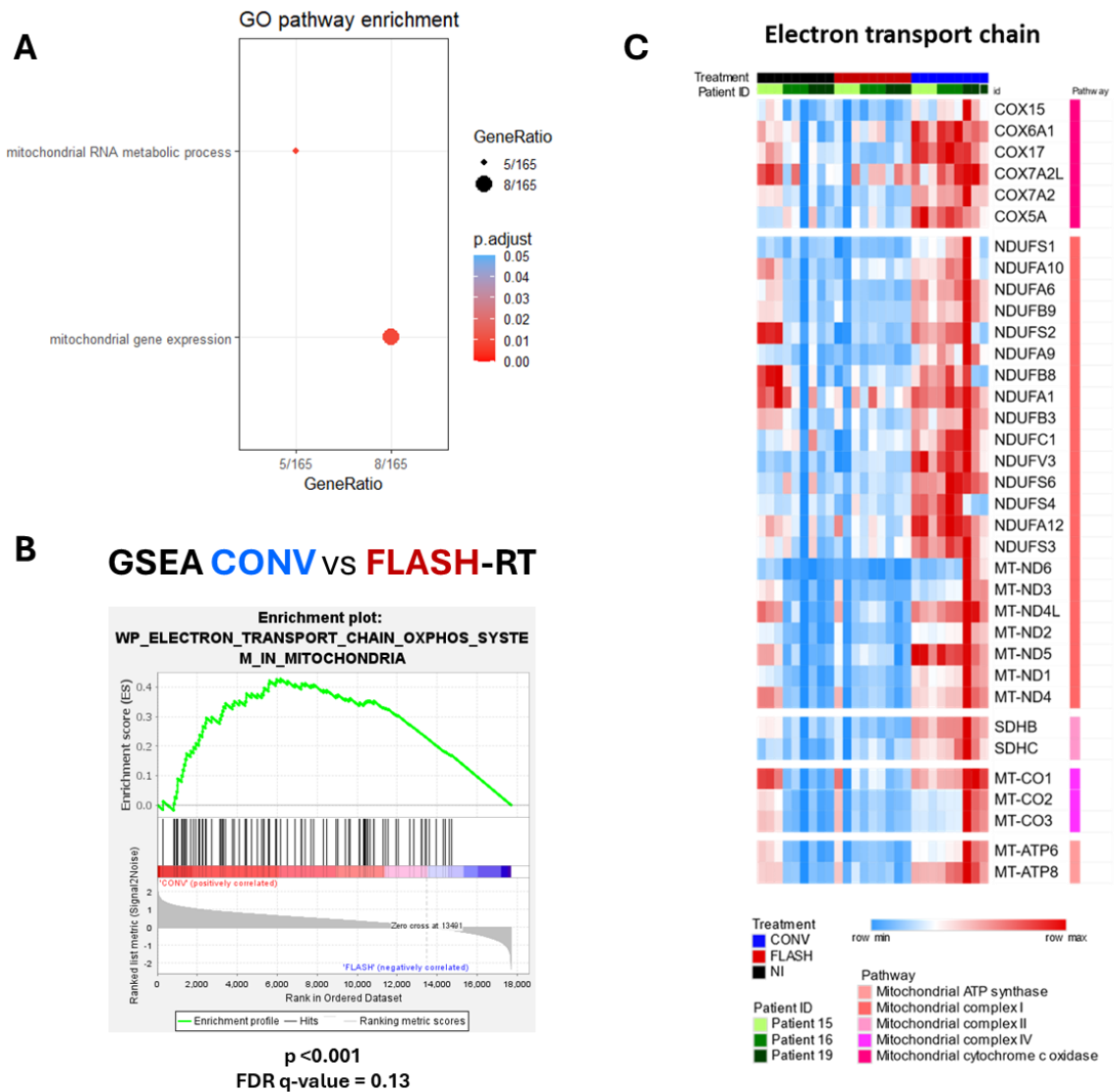


Figure 58. FLASH-RT reduced activation of electron transport chain system in patient lung samples. (A) Gene Ontology (GO) enrichment analysis showing mitochondrial gene expression enrichment after CONV-RT. (B) Gene Set Enrichment Analysis (GSEA) showing the enrichment of mitochondrial electron transport chain (ETC) genes in lung tissue after exposure to CONV versus FLASH radiotherapy. A clear differentiation in the enrichment of electron transport chain genes was observed ($p < 0.001$, FDR q-value = 0.13). (C) Heatmap representation of the expression of mitochondrial electron transport chain genes, showing the differential expression between the CONV and FLASH conditions across different patients.

Figure 59. FLASH reduces radio-induced acute inflammation in human lung compared to CONV-RT. (A) *Enrichment analysis of the interferon-alpha (IFN- α) response pathway following conventional (CONV) and FLASH radiotherapy in human lung samples.* (B) *Enrichment analysis of the TNF- α signaling via NF- κ B pathway in response to CONV and FLASH irradiation.* (C) *Enrichment analysis of the interferon-gamma (IFN- γ) response pathway after CONV and FLASH irradiation. Heatmaps show the relative expression levels of genes involved in each inflammatory pathway.*

4. CONCLUSION PART 1 – KEY INSIGHTS FROM EX VIVO PCLS MODEL ON FLASH-RT SPARING EFFECT IN THE LUNG

Thus, in conclusion of this first part of the results, we **adapted the PCLS model to study acute toxicities in the lung** by implementing **simple and rapid endpoints (viability and cell division)**. Interestingly, the study of cell division within the slices 24 hours post-treatment allowed us to **highlight a FLASH sparing effect** on this population of interest. Subsequently, we used this model and conducted proof-of-concept experiments for its use in combination therapies with chemotherapy and radioprotectors (AsiDNA, CAPE, **see Annex 1**). Finally, we demonstrated the possibility of obtaining PCLS from lungs containing orthotopic lung tumors, making it an interesting and relevant model for future studies (**See Annex 1**). Next, we aimed to apply this model and our test to several issues concerning FLASH radiotherapy: first, the **study of irradiation parameters and optimal conditions for achieving the FLASH effect** in the lung, and second, the **demonstration of a FLASH protective effect in human lung tissue**. Regarding the parameters, we identified the mean dose rate/total irradiation time as an important factor, **with the dose rate needing to exceed 100 Gy/s** for an optimal FLASH effect, which is achieved at dose rates above 300 Gy/s. Additionally, we were able to identify the dose per pulse as another important factor in FLASH irradiation with an electron beam, where **the dose per pulse must exceed 1 Gy/pulse to detect the FLASH protective effect** in the PCLS model. Finally, regarding our investigation into the presence of a FLASH protective effect in healthy lung resections from patients treated for their lung cancer, **the PCLS-Hu model enabled us to highlight a protective effect on cell division within the PCLS in nearly 94% of patients**. Although this is based on a short-term ex vivo endpoint, it supports the clinical transition of FLASH therapy. Thus, in the continuation of this manuscript and given the initial molecular insights provided by RNAseq analyses in patients, we aimed to study the **molecular changes occurring after FLASH or CONV irradiation** in the subcellular compartments in mice, **24 hours post-treatment** for acute phase and **several months** for the late.

IV- PART 2 – TRANSCRIPTIONAL ACUTE AND LATE CHANGES OCCURRING POST-FLASH OR CONV-RT IN MOUSE LUNG AT THE SINGLE CELL LEVEL

1. TRANSCRIPTIONAL CHARACTERIZATION OF THE FLASH SPARING EFFECT IN MOUSE WHOLE LUNG

1.1 Introduction

We decided to explore these **transcriptional changes more precisely in lung subpopulations**, using **scRNAseq**, to **provide initial insights into the underlying mechanisms of the FLASH effect in healthy tissue**. For this purpose, we irradiated the thorax of mice with a dose of 13 Gy, a fibrogenic dose, at conventional or FLASH dose rates. **24 hours** post-treatment, the lung was dissociated into a single-cell suspension, followed by scRNAseq using the 10X Genomics technology (

Figure 60). In addition to this short-term approach and for dynamic analyses of the transcriptional changes occurring after these irradiation modalities, we complemented this analysis with time points from **1 month up to 5 months post-treatment**, both for conventional and FLASH irradiation. Therefore, in the following part of this manuscript, we will first describe our dataset, and the specific responses that we were able to reveal in some subpopulations of

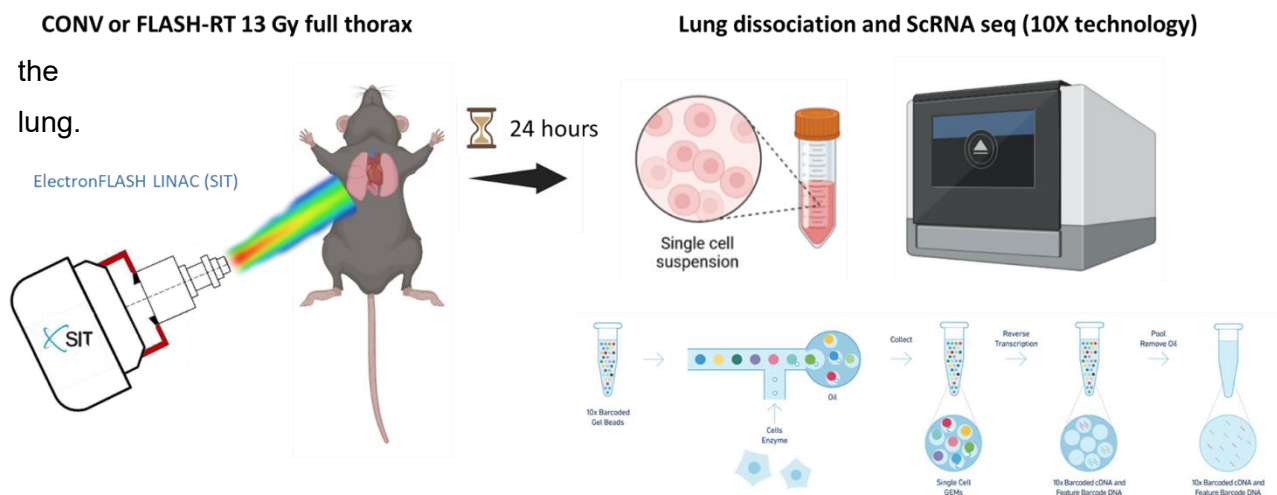


Figure 60. Scheme of experimental protocol for transcriptional analysis using ScRNAseq 24 hours after FLASH or CONV-RT at 13Gy.

1.2 Material and method

Mice and ethics statement : Studies were conducted in accordance with the European Community recommendations (2010/63/EU) for the care and use of laboratory animals. The experimental procedures were specifically approved by the Ethics Committee of Institut Curie (CEEA-IC #118) under authorization number APAFiS#32674-2021080916494690, granted by the National Authority, in compliance with international guidelines. Female C57BL/6J mice, purchased from Charles River Laboratories (Lyon, France) at 6 weeks of age, were housed in the Institut Curie animal facilities.

Mice irradiation : C57BL/6J female mice were used to study short term response to FLASH or CONV at 24 hours (24H), 1 months (1M), 2 months (2M), 3 months (3M), 4 months (4M) or 5 months (5M) post-treatment. Collimation, time-resolved fluence measurement, chemical dosimetry, depth-dose distribution, anesthesia, and immobilization procedures were performed as described in previous part of this thesis (**see results part 1**). Bilateral thoracic irradiation was performed using a 4.5-MeV linear electron accelerator facility (Electron-Flash 4000, Sordina IORT Technologies). CONV-RT and FLASH-RT dose rates were 0.4 Gy/s and > 300 Gy/s respectively, while both were administrated using a single dose of 13 Gy. Time points for lung tissue sampling were 24 hours (24h) after irradiation to account for early biomechanistic effects, a cinetics from 1 to 5 months after irradiation when pulmonary fibrosis was developing.

Lung dissociation for single cell suspension : For the preliminary preparation, Dispase (50 U/ml) was thawed from -20°C storage, with 2 ml used per mouse. A 1% agarose solution in PBS (low gelling) was prepared and maintained at 42°C before perfusion. Falcon tubes (50 ml) containing 3 ml of PBS (Mg^{2+}/Ca^{2+}) were prepared for each sample, and PBS with 10% FBS (PF10) was used for the dissociation steps. The centrifuge was set to 4°C. For lung extraction, mice were anesthetized with isoflurane followed by cervical dislocation. The ribcage was opened, the trachea was exposed, and then perfused with 2 ml of Dispase (50 U/ml) using a 20G needle, followed by 0.5 ml of 1% agarose to seal the trachea. Lungs were cooled on ice to solidify the agarose before being removed from the ribcage, cleaned of blood and heart tissue, and separated into lobes. The trachea and any remaining agarose were removed, and the lobes were finely minced and placed into the prepared Falcon tubes on ice. For lung dissociation, 320 µL of Elastase (25 U/ml) was added to the lung tissue, which was then further minced. The samples were homogenized and incubated at 37°C with shaking for 30 minutes. After homogenization with a pipette, the samples were incubated for additional periods and

filtered through a 100 µm filter. Mechanical dissociation was performed with a 10 ml syringe, followed by rinsing with PF10. DNase (37.5 µL at 10 mg/ml) was added, and the mixture was incubated on ice for 3 minutes before filtering again through a 40 µm filter. The cells were centrifuged at 150g for 6 minutes at 4°C, resuspended in RBC lysis buffer for 90 seconds, and the lysis was stopped with PF10. For FACS or scRNA-seq analysis, RBC lysis was performed in cycles as required. Finally, the cells were centrifuged again at 200g for 6 minutes at 4°C and resuspended in 1 ml of PBS 1% SVF 1% BSA.

GEM generation and barcoding for scRNAseq : Single-cell 3'-RNA-Seq samples were prepared using the Single Cell V reagent kit and loaded into the Chromium Controller according to the manufacturer's standard protocol (10x Genomics). Depending on the experiment, 6,000 to 10000 cells were captured for each mouse. Dissociated lung single cells were encapsulated in nanodroplets (GEMs) using a microfluidic device. These GEMs were created by combining barcoded single-cell 3' gel beads, a master mix containing reverse transcription (RT) reagents, single cells, and partitioning oil on the Chromium Next GEM Chip. Following cell lysis, the RNA was captured on gel beads coated with oligos containing an oligo-dTTT sequence, unique molecular identifiers (UMIs), and a specific barcode.

Reverse transcription and cDNA amplification : Incubation of the GEMs results in the production of barcoded, full-length cDNA from poly-A mRNA. Following reverse transcription, the GEMs are broken, and the cDNA is purified using silane magnetic beads. The purified cDNA is then PCR-amplified and washed before being analyzed for quality control using a Bioanalyzer (Agilent). The barcoded full-length cDNA is further amplified by PCR to produce sufficient material for library construction. After amplification, the cDNA is purified once more, and its quality is assessed via capillary electrophoresis on a Bioanalyzer (Agilent) prior to library preparation.

Library construction and sequencing : Finally, libraries were prepared using a fixed proportion of the total cDNA. Enzymatic fragmentation and size selection are performed to optimize the cDNA amplicon size. During GEM incubation, the read 1 primer sequence is added to the molecules. At this stage, the P5 and P7 sequences, a sample index, and the read 2 primer sequence are incorporated through End Repair, A-tailing, Adaptor Ligation, and PCR. This process ensures that the final libraries contain the P5 and P7 primers required for Illumina bridge amplification. The libraries were then sequenced using the NovaSeq sequencer (Illumina).

scRNA-seq Data Analysis : Single-cell suspensions were analyzed using the droplet-based single-cell RNA-seq method developed by 10x Genomics. Raw sequencing data were processed using the CellRanger pipeline version 3.1.0, 6.0.0, or 7.1.0 depending on the sample. Count matrices were analyzed using Seurat package version 5.0.1³¹⁹. For each sample, SoupX was employed to remove contamination by ambient RNA³²⁰, and quality controls were performed. The correct annotation of cell populations was validated using the expression of well-known markers. The SCTransform function was applied to the merged object, with cell cycle scores and the percentage of mitochondrial genes used as regressed variables. The samples from different patients were then separated and normalized individually. The 2000 most variable features were identified and used to set anchors for integration.

Transgenic mouse models – Sftpc Cre ERT2 Tdtomato GFP : To detect inducible Sftpc-positive alveolar type II (AT2) cells in the lung, we employed a transgenic mouse model combining two genetically modified strains. The Sftpc-CreERT2 knock-in mice (B6.129S-Sftpctm1(cre/ERT2)Blh/J, JAX Stock No. 028054) express a tamoxifen-inducible Cre recombinase under the control of the endogenous Sftpc promoter/enhancer elements. These mice were crossed with the B6.129(Cg)-Gt(ROSA)26Sortm4(ACTB-tdTomato,-EGFP)Luo/J strain (also known as mT/mG), which carries a loxP-flanked STOP cassette that prevents transcription of the CAG promoter-driven tdTomato fluorescent protein at the Gt(ROSA)26Sor locus. Upon tamoxifen administration, Cre-mediated re-combination in Sftpc expressing cells excises the STOP cassette, allowing for the expression of GFP (green fluorescence) specifically in the AT2 cells, while the tdTomato (red fluorescence) expression is lost.

Tamoxifen preparation and induction : For tamoxifen induction in Sftpc Cre ERT2 mice, a dosage of 10 μ L per gram of body weight was used, with each mouse weighing approximately 25 g, resulting in a 250 μ L injection per mouse. The injections were performed one time, just after treatment at a dose of 100 mg/kg. To prepare the solution, 1000 μ L was required per mouse (to account for potential pipetting losses), with 10 mg of tamoxifen added. For the induction, intraperitoneal (IP) injections were administered at 10 μ L per gram of mouse weight. The tamoxifen solution was prepared fresh each day and stored at 4°C if necessary. To aid in dissolution, the solution was heated at 37°C for 10-15 minutes with orbital shaking.

Sorting of Sftpc+ cells : Mice irradiation and lung tissue dissociation was done as described in prior steps. Dissociated cells were sorted with a BD FACSAria III sorter in order to isolate the AT2 cells with BD FACSDiva Software V8.0.3. Sftpc positive AT2 cells expressed a specific Cre recombinase induced by prior injection of 100 mg/kg tamoxifen which allowed the GFP protein expression, resulting in green fluorescence which in turn allowed specific cell sorting.

Lipidomic analysis on sorted Sftpc+ cells : Lipidomics analysis was performed on sorted Sftpc+ cells to identify lipid changes in response to different irradiation modalities (FLASH vs. conventional). A total of 200,000 cells were spiked with an internal lipid standard mixture and subjected to lipid extraction. The cells were dissolved in ammonium bicarbonate, followed by extraction with chloroform-methanol (10:1) and re-extracted with chloroform-methanol (2:1). The organic phases were collected, evaporated, and resuspended in an infusion mixture for mass spectrometry analysis. Samples were analyzed using a QExactive Plus mass spectrometer with a TriVersa NanoMate ion source. Direct infusion of 5 μ L of sample was performed under specified conditions. Lipid species, including DAG, TAG, CE, PC, PCO, Cer, GlcCer, LPC, LPCO, PG, PE, PEO, LPE, LPEO, LacCer, Gb3, Gb4, GM1, GM2, GM3, PA, PI, PS, LPA, and LPS, were detected in positive or negative ion mode, depending on the lipid type. The data were analyzed using LipidXplorer software, and post-processing and normalization were done manually.

1.3 Results

1.3.1 *ScRNAseq data visualization and identification of lung cells populations in 24 hours dataset*

To characterize the molecular and cellular changes that occur after FLASH or conventional irradiation at 24 hours post-irradiation, we generated single-cell suspensions from two non-irradiated (NI) mice, three mice irradiated with 13 Gy FLASH and three mice irradiated with 13 Gy CONV . This scRNA-seq analysis was performed using the 10X Genomics Chromium platform, as described in the associated materials and methods. All samples were merged into a single dataset using the Seurat package in R. A total of 49,202 cells were analyzed: 8,303 from the NI group, 22,094 from the FLASH group, and 18,805 from the CONV group, after quality control steps based on mitochondrial gene percentages and the number of detected expressed genes, as outlined in the materials and methods.

UMAP visualization based on condition shows the separation of the non-irradiated (NI), FLASH-irradiated and conventionally irradiated samples, indicating clear transcriptional shift from non-treated or irradiated samples (**Figure 61A**). Then, UMAP visualization based on the original identity highlights that certain clusters are specific to each individual sample, while others show an overlap between samples, suggesting that the clustering is not significantly affected by batch effects, and the differences observed are largely due to the condition of treatment (**Figure 61B**). The annotation of the clusters was based on the expression of canonical markers that were described by previous work on RILI development following conventional fibrogenic doses. This method enabled the identification of 17 lung cell types (**Figure 62A-B**). Based on the markers recently described in the literature, we identified AT0 cell clusters that appear to be specific to irradiated conditions (**Figure 62B**).

In the following section of results, we will attempt to define a global response of all pulmonary cell types to conventional or FLASH irradiation. Subsequently, I will describe the changes occurring in the distribution of different resident cell subpopulations at 24 hours post-irradiation.

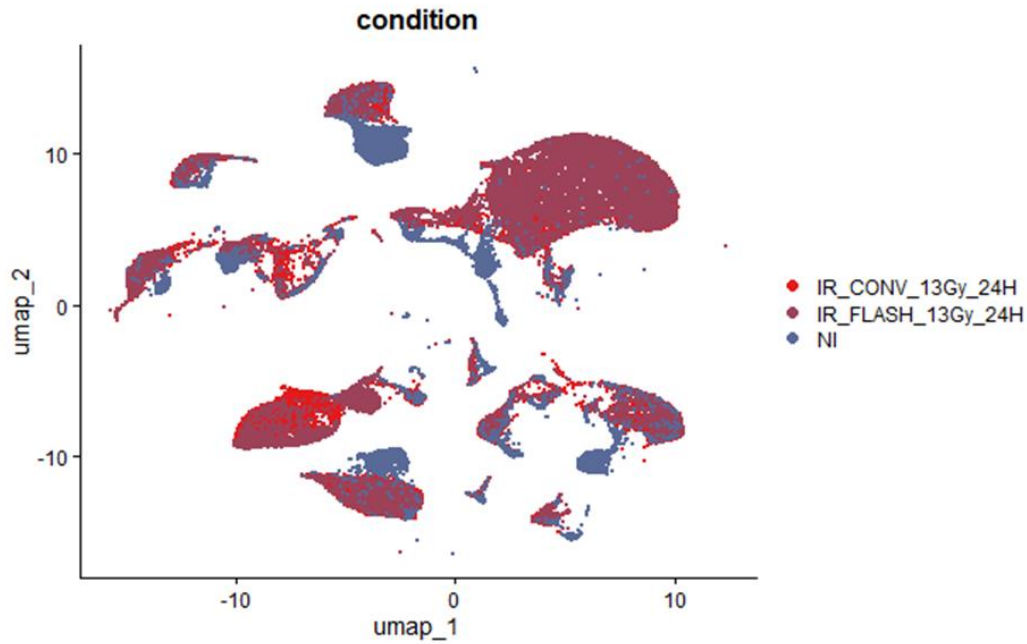
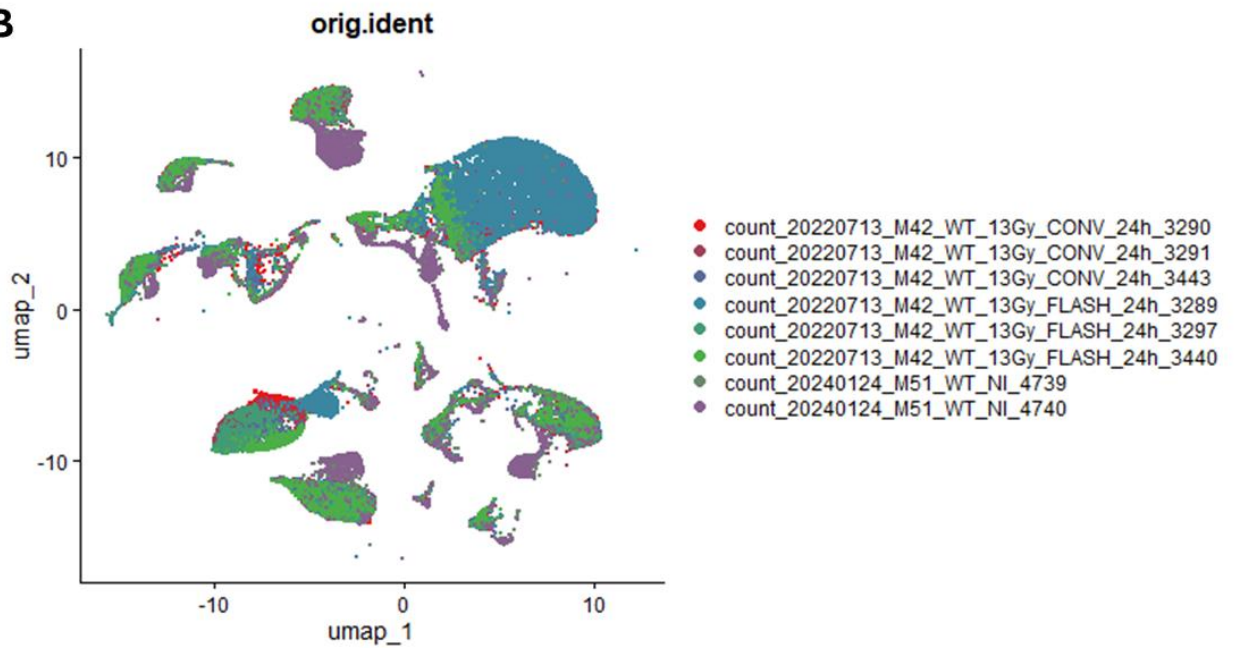
A**B**

Figure 61. Single-cell data visualization of the NI and irradiated lungs. *Uniform Manifold Approximation and Projection (UMAP)* from 49,202 cells from 2 NI, 3 IR_FLASH_13Gy_24H, and 3 IR_CONV_13Gy_24H samples annotated by (A) condition and (B) original identity (orig.ident).

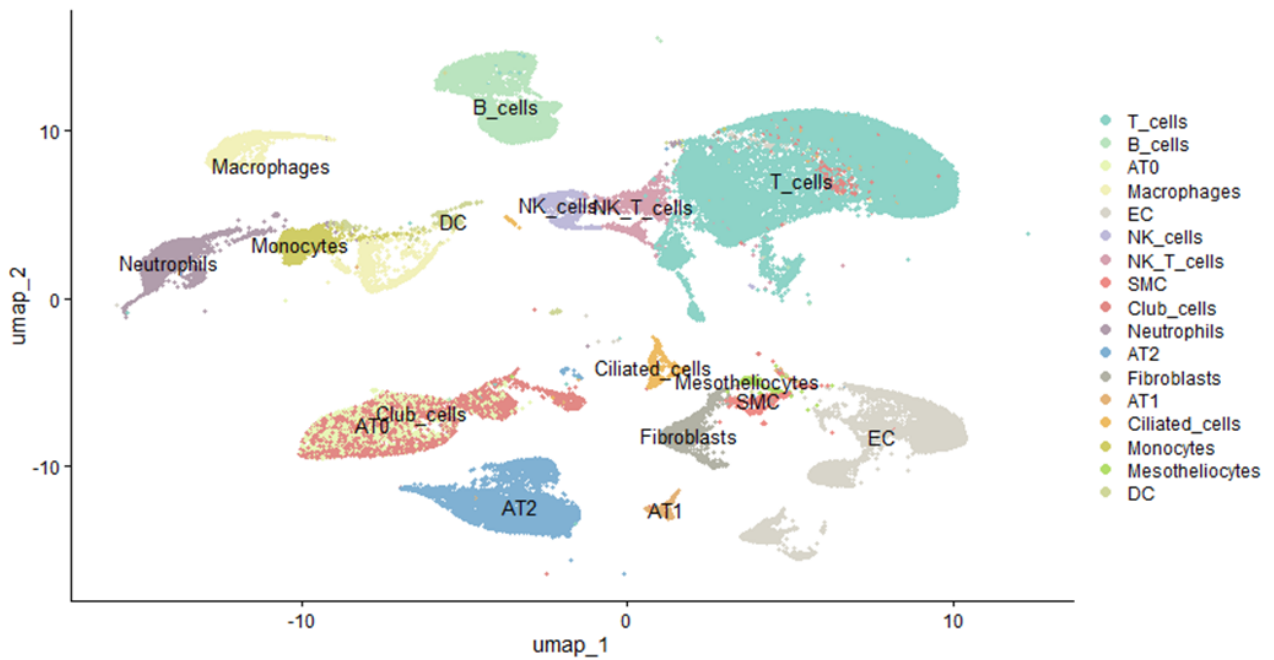
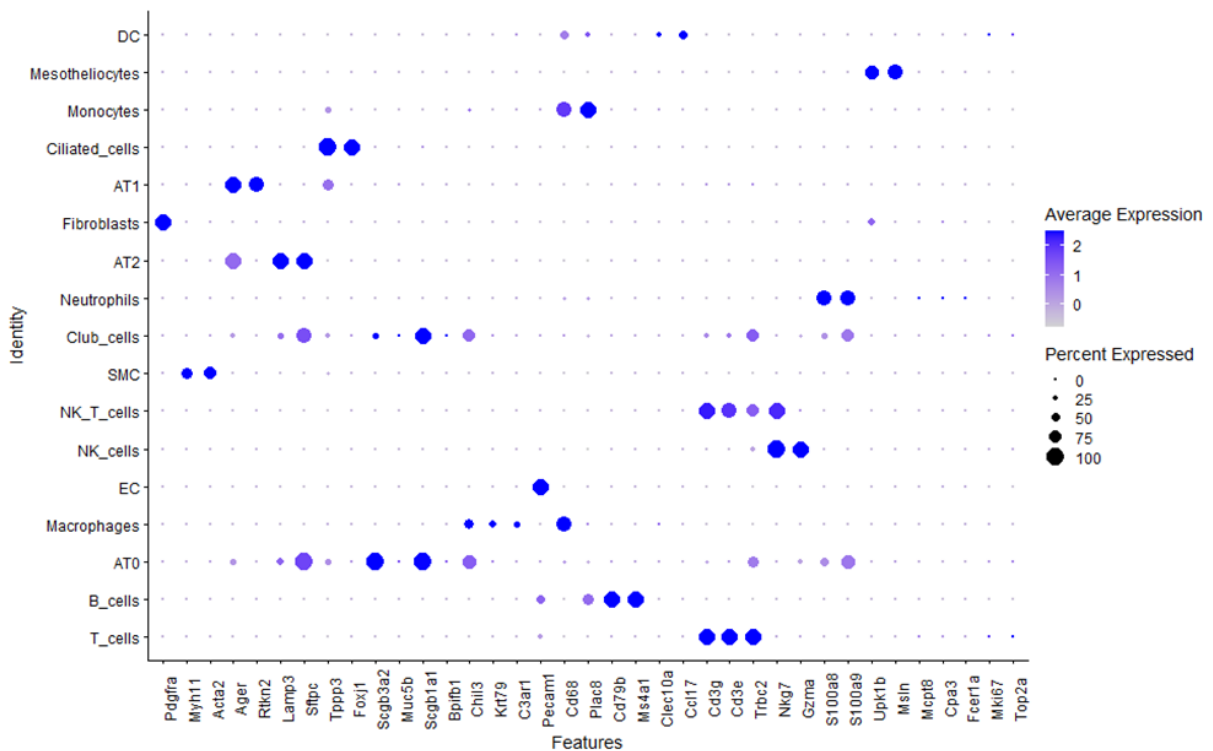
A**B**

Figure 62. Lung cell type identification and canonical marker expression. (A) *UMAP* visualization of the lung samples annotated by cell type. (B) Dot plot displaying the expression of canonical markers for cell type identification.

1.3.2 Common and specific response 24 hours post-FLASH or CONV-RT in the whole lung

At first, our goal was to identify a potential molecular signature specific to FLASH vs CONV-RT at the whole-lung level. Thus, we performed differentially expressed genes analysis (DEG) after FLASH or CONV irradiation compared to untreated cells across all lung cell subpopulations. A total of 514 genes were upregulated after FLASH irradiation compared to NI lung, while 635 genes were upregulated after CONV at 24 hours. Among these upregulated genes, 258 were identified as commonly upregulated after either FLASH or conventional irradiation across all pulmonary cell subtypes (**Figure 63A**). Based on this list, a GSEA overlap analysis of these genes with known pathways revealed that these commonly significantly upregulated genes were primarily involved in inflammatory response (IFN-g, IFN-a), cell cycle regulation (Myc target, G2M checkpoint), P53 and apoptosis pathways, as well as genes related to oxidative phosphorylation (**Figure 63A**). We then measured the average expression of these genes in our cells by irradiation condition, revealing only minor differences between CONV and FLASH irradiation modalities, indicating a common upregulation of these genes related to early radiation response (**Figure 63B**). Additional analyses of genes specifically upregulated after FLASH or CONV irradiation showed upregulations of genes related to the same identified pathways involved in the response to ionizing radiation which does not indicate a clear common response to FLASH vs CONV compared to non-treated lungs.

In the following part of this manuscript, we decided to focus on the resident lung populations that have been irradiated and not recruited because of the irradiation (**Figure 64**). Interestingly, the proportion of endothelial cells relative to the total number of resident lung cells decreased by approximately 21.5% after conventional irradiation and by 25.5% after FLASH irradiation. Similarly, the proportions of AT2, AT1, and fibroblasts followed the same trend. Regarding macrophages, an increase in their proportion was observed after conventional irradiation compared to FLASH, rising from 7% to 13.5%. Finally, there seems to be a drastic increase in the proportion of club cells after both FLASH and conventional irradiation, as well as the appearance of an AT0 cluster, representing cells in a transitional state after FLASH irradiation (8.3%) and conventional irradiation (18.8%).

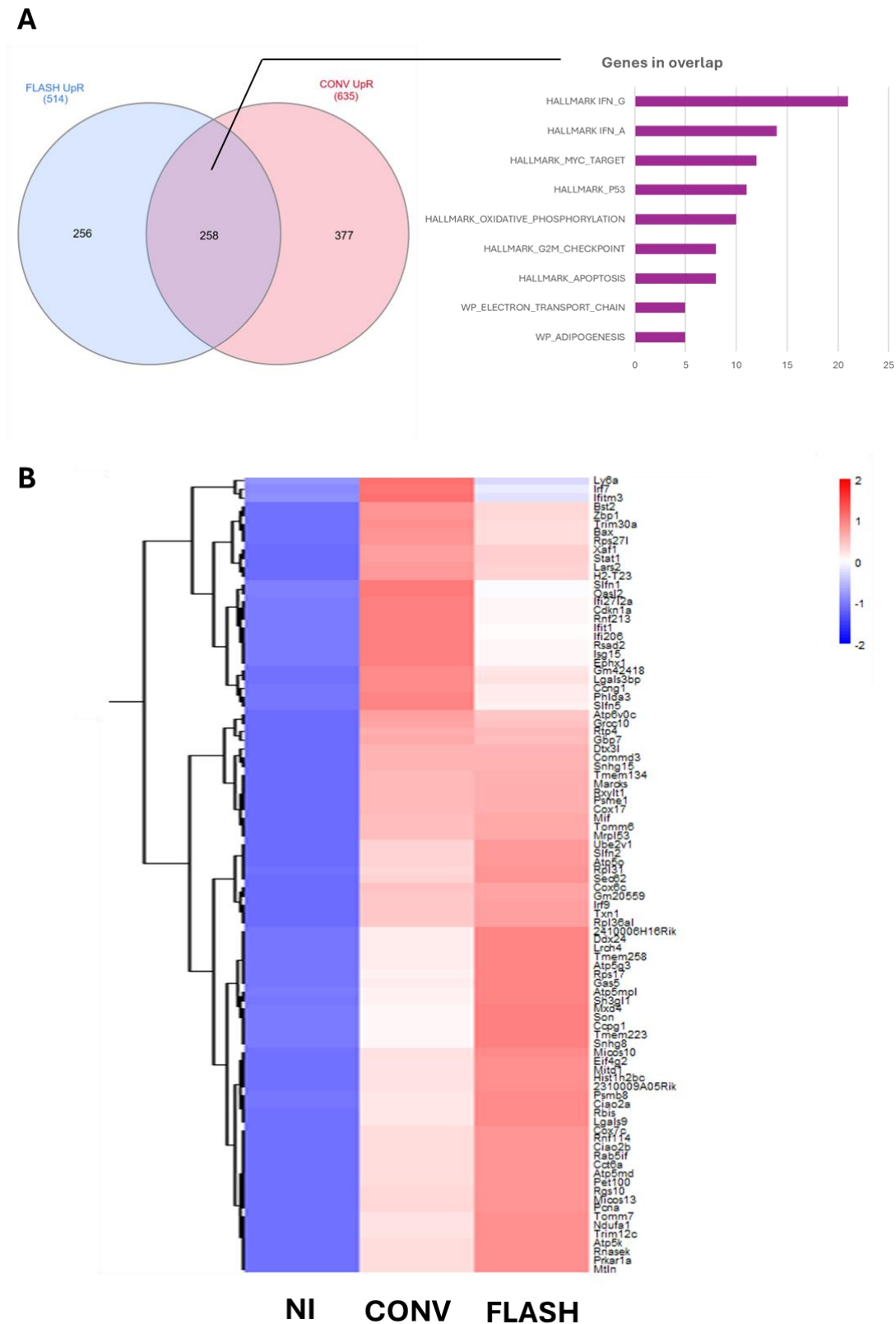


Figure 63. Common response 24 hours after FLASH and CONV-RT in the whole lung. (A) Venn diagram showing the overlap of upregulated genes (UpR) following FLASH irradiation and conventional irradiation. GSEA analysis on common upregulated genes revealed pathways associated to inflammation, apoptosis, cell cycle regulation. (B) Heatmap of

identified common upregulated genes after CONV and FLASH irradiation at 24 hours post-treatment. Genes are clustered according to their average expression per condition, with normalization across each row.

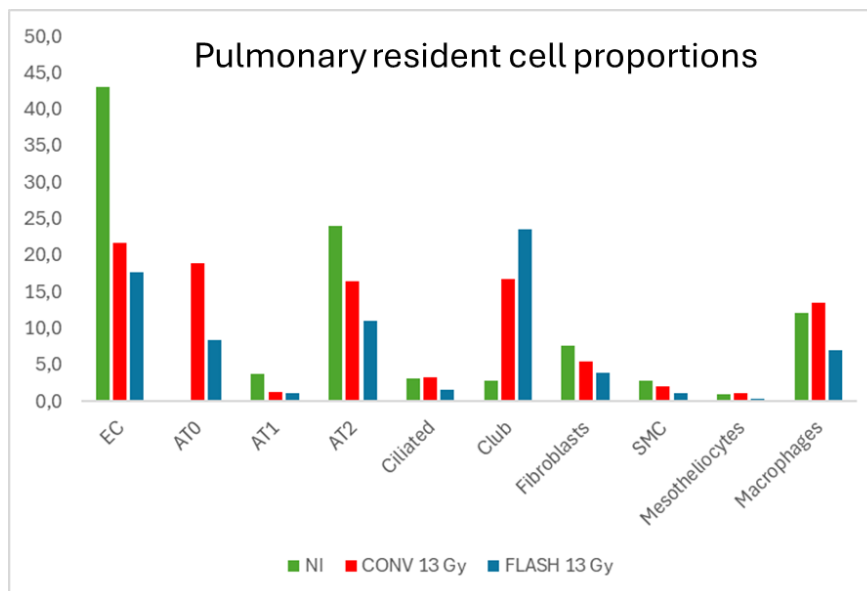


Figure 64. Distribution of lung cells subpopulations upon FLASH or CONV-RT. *Normalized proportion to the total of resident cells per condition.*

Thus, in the following part of this result section, we will focus on the response of two populations of interest, endothelial cells and AT2 cells. The other cell types, due to the low number of sequenced cells, did not reveal any major differences between these modalities. Furthermore, we decided to focus on innovative results showing a specific response to FLASH, rather than a response related to the delayed development of radiation-induced fibrosis. Indeed, we have identified an increase in the proportion of myofibroblasts during fibrosis development after CONV-RT that is not present in FLASH, as well as the inflammatory profiles of alveolar macrophages, which are also reduced after FLASH irradiation. In this manuscript, we decided to focus on early changes, detectable at different time points post-irradiation, which may be linked to underlying mechanisms of FLASH radiotherapy.

1.3.3 FLASH-RT spares lipid metabolism related pathway in AT2 cells at 24 hours

By subclustering the AT2 cell compartment, we identified two separate AT2 populations that differed by the expression of the *Lyz1* gene (**Figure 65A**). This population has already been described in the literature as a specific population in mice³²¹. Aside from the expression of *Lyz1*, these two populations did not show any other significant differences, so we decided to continue our analysis on the entire AT2 population. UMAP clustering per condition shows a transcriptional shift between non treated and irradiated AT2 cells (**Figure 65A**). Similar to what was identified in the whole lung and in the literature at short times post-irradiation, irradiation of AT2 cells induced inflammatory, apoptotic, and cell cycle arrest processes, as identified by DEG analysis.

DEG analysis between FLASH and CONV-RT revealed an upregulation of several genes associated with adipogenesis-related pathways following FLASH vs CONV-RT. These genes, linked to lipid metabolism, could be related to the primary function of AT2 cells to produce pulmonary surfactants (**Figure 65B**). Volcano plot analysis highlighted the gene *Apoe* as a top upregulated gene in FLASH compared to CONV-RT (\log_2 fold change = 2) (**Figure 65C**). The *Apoe* gene encodes a lipoprotein involved in plasma-to-cell lipid transport and pulmonary surfactant synthesis in AT2 cells³²².

Further examining the response of lipid metabolism related genes, we observed that irradiation impacts the expression of various genes involved in lipid metabolism pathways (**Figure 65D**). Interestingly, genes expression was preserved following FLASH irradiation for *Apoe*, *Plin2*, and *Mgll* compared to CONV-RT. Indeed, *Plin2*, which encodes a protein involved in the formation of intracellular lipid droplets³²³, as well as *Mgll*, which encodes a protein involved in lipid catabolism³²⁴, showed similar expression patterns to *Apoe* across the different conditions.

To functionally validate the transcriptional changes occurring at 24 hours post-irradiation in AT2 cells, we performed lipidomic analysis using mass spectrometry. To specifically isolate AT2 cells, we used a transgenic mouse model, *Sftpc-CreERT2* x *R26-mTmG* (**Figure 66A**). As described in the material and method section, upon tamoxifen injection in IP, the *Sftpc* expressing cells will become GFP+, allowing us to sort AT2 cells. For each condition, untreated or treated with a 13 Gy dose in either FLASH or CONV, we sorted 200,000 cells for analysis of lipid subpopulations (**Figure 66A**).

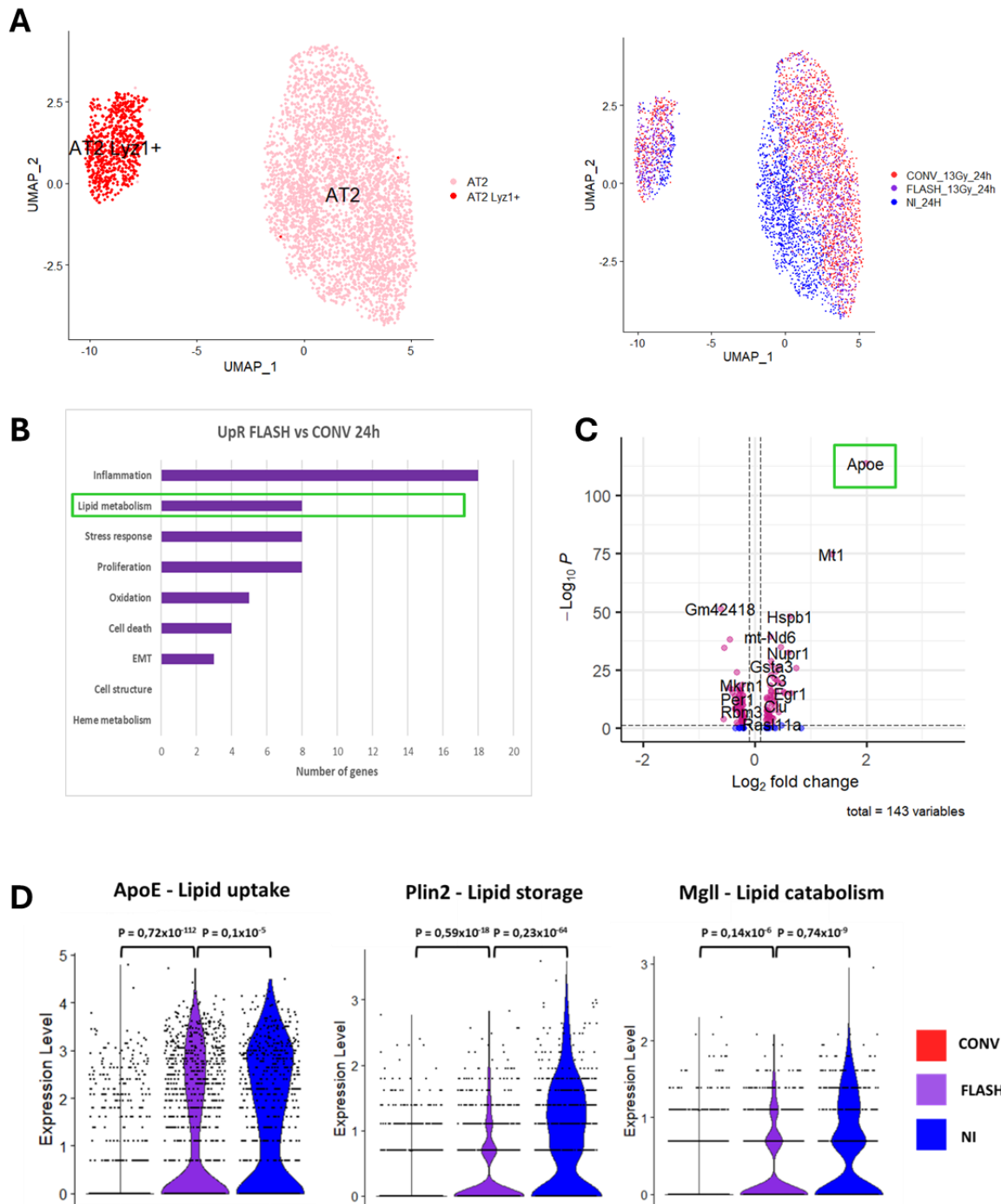


Figure 65. FLASH spares lipid metabolism pathway in AT2 cells at 24 hours post-treatment. (A) UMAP plots showing the clustering of AT2 cells based on the expression of the *Lyz1* gene (left) and by condition (right). (B) Gene ontology analysis (GSEA) of upregulated genes in FLASH compared to CONV irradiation at 24 hours. (C) Volcano plot of differential gene expression comparing FLASH to CONV irradiation at 24 hours. (D) Violin plots showing the expression levels of *Apoe* (lipid uptake), *Plin2* (lipid storage), and *Mgl1* (lipid catabolism) in CONV, FLASH, and NI conditions. Statistical significance is indicated by the *p*-values for each gene.

Preliminary validation allowed us to confirm the sensitivity and relevance of this lipidomic method, enabling the identification of major components of pulmonary surfactant in AT2 cells (**Figure 66B**). Specifically, the measurements suggested a high concentration of phosphatidylcholine (PC), reported as a major lipid component of pulmonary surfactant, along with other subspecies such as cholesterol and phosphatidylglycerol (PG)³²⁵ (**Figure 66B**).

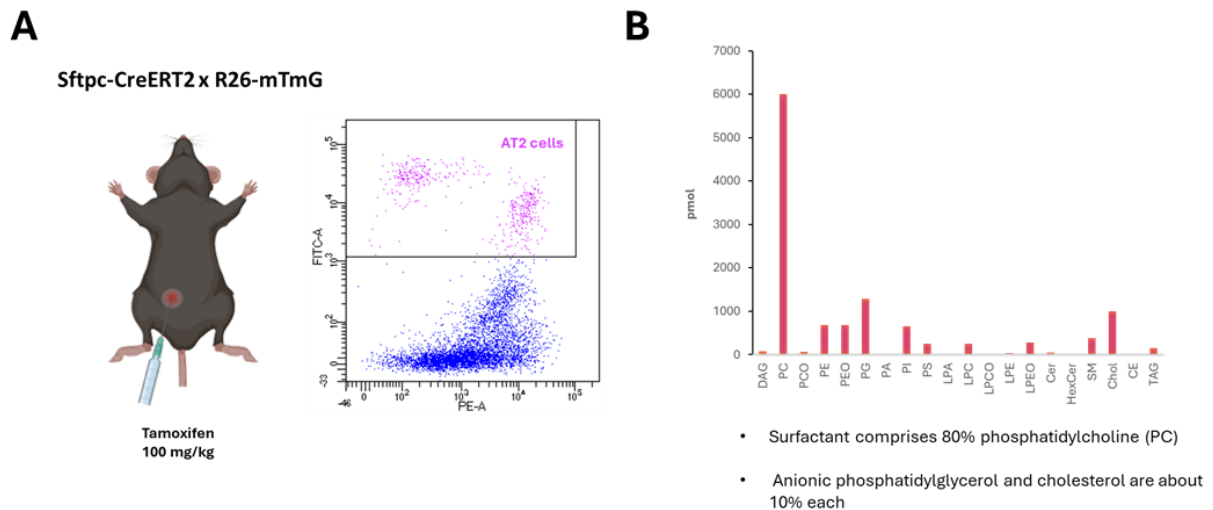


Figure 66. Experimental setup and relevance of lipidomic analysis for AT2 sorted cells. (A) *Experimental setup for sorting AT2 cells using the Sftpc-CreERT2 x R26-mTmG transgenic mouse model.* (B) *The bar graph shows the raw quantification of lipid species detected in AT2 non treated cells.*

Among the changes commonly induced by irradiation, we observed an increase in ceramide levels 24 hours post-treatment with both conventional and FLASH dose rates (**Figure 67A**). Notably, ceramides have been reported to be generated in ferroptosis processes, which can be induced by irradiation³²⁶. We were able to correlate this increase with an upregulation of genes involved in ferroptosis pathways following both FLASH and conventional irradiation in AT2 cells (**Figure 67B**). More specifically, most of these genes are commonly upregulated after either FLASH or conventional irradiation in AT2 cells, suggesting no difference in the induction of ferroptosis cell death between the two irradiation modalities (**Figure 67C**).

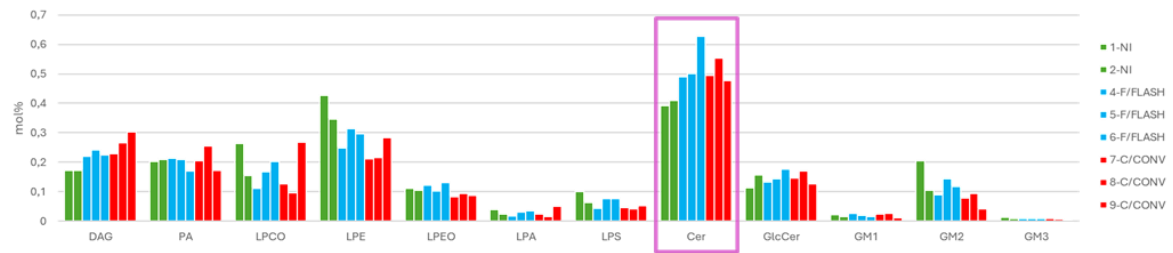
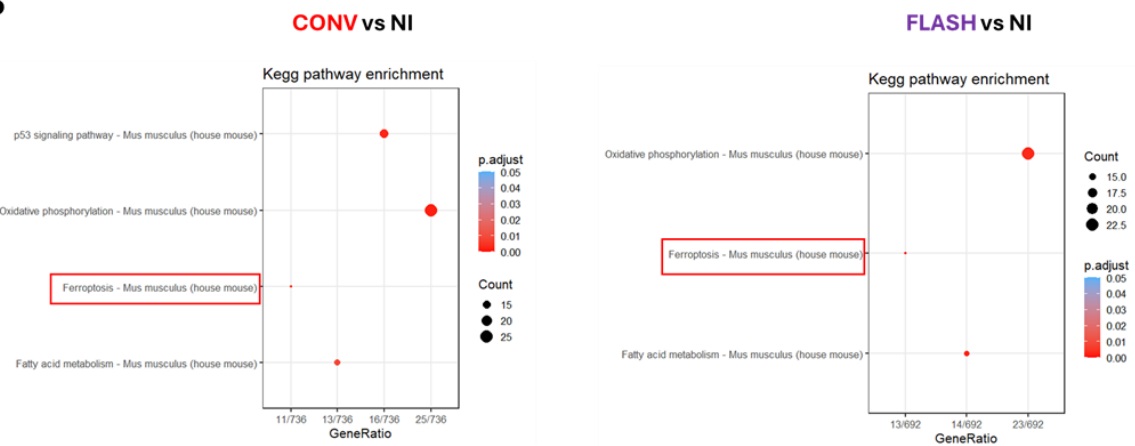
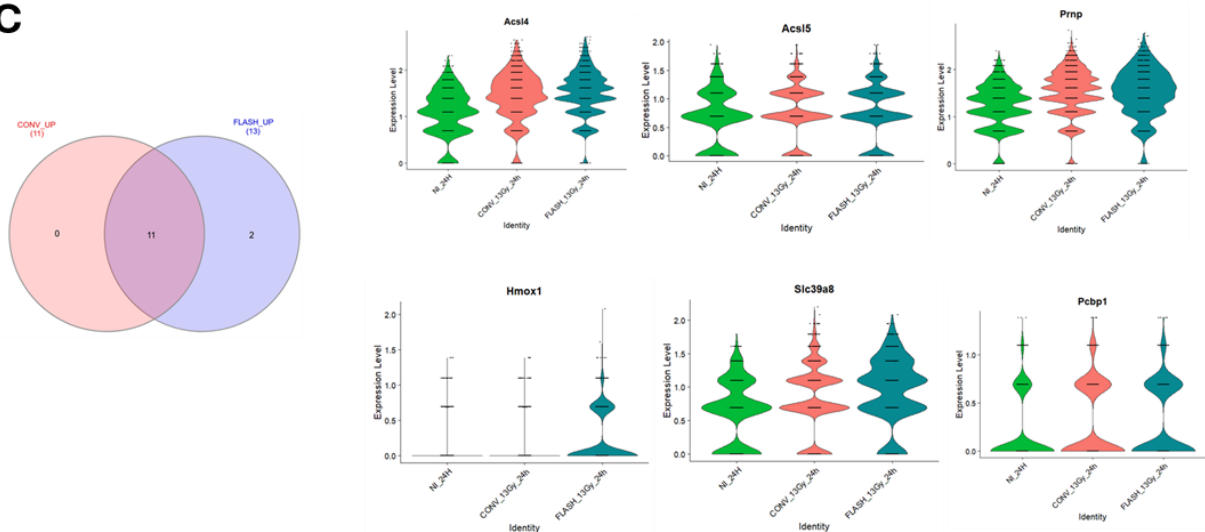
A**B****C**

Figure 67. Increased level of ceramide is correlated with a common upregulation of ferroptosis related genes following radiation in AT2 cells (A) Lipidomic analysis revealed an increase in ceramides levels post-radiation. (B) KEGG pathway enrichment analysis comparing CONV and FLASH-RT against NI highlight an enrichment in ferroptosis related genes after radiation. (C) Venn diagram illustrating the overlap of upregulated genes between CONV and FLASH irradiation conditions, with a focus on ferroptosis-related genes such as *Acs14*, *Acs15*, and *Prnp*.

More precisely, in regard to the FLASH-RT sparing effect on the expression of genes implicated in lipid intake and lipid storage, we found that FLASH-RT preserved cholesteryl ester levels compared to CONV-RT, which are implicated in lipid droplet formation³²⁷ (**Figure 68**). Indeed, cholesteryl esters function as a transport form of cholesterol in blood plasma and in cells in lipid droplets. In contrast, major lipidic components of pulmonary surfactants such as cholesterol, fatty acids and phospholipids were not affected by radiation.

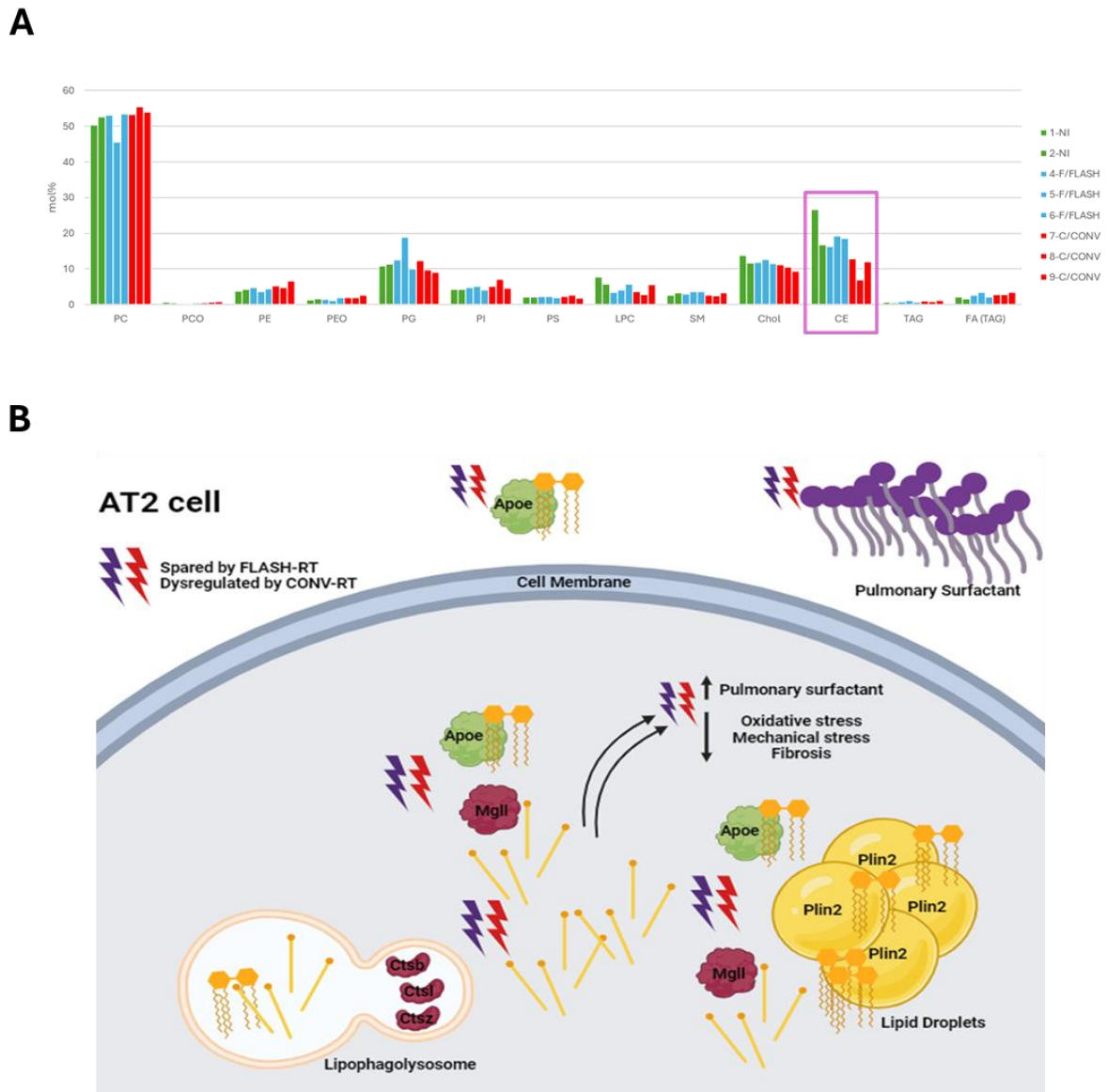


Figure 68. FLASH spares lipid droplet-related lipids level in AT2 cells compared to CONV-RT 24h after irradiation (A) Lipidomic analysis revealed a specific decrease in cholesteryl ester (CE) levels after CONV-RT. (B) Schematic representation of lipid metabolism response in AT2 cells 24 hours after FLASH or CONV irradiation.

1.3.4 Dynamic of AT2 lipid metabolism after FLASH or CONV-RT from 1 to 5 months post treatment

We then aimed to explore the dynamics of lipid metabolism changes occurring after FLASH or CONV-RT, focusing not only during the acute response in the lung but also during the development of later radiation-induced toxicities. Indeed, after a thoracic irradiation of 13 Gy at conventional dose rates, mice develop RIPF after 20 weeks, which is not observed following FLASH irradiation as described. To further investigate this, we conducted scRNA-seq analyses at different time points post-irradiation, from 1 to 5 months, to assess the dynamic changes in lipid-related transcriptional pathways after FLASH irradiation compared to conventional irradiation and determine whether these changes could serve as markers for later responses in the lung (**Figure 69A**). Interestingly, at 5 months post-conventional irradiation, the expression of *Apoe* appears lower in conventionally irradiated AT2 cell subclusters, highlighting potential differences in lipid metabolism between the two irradiation modalities at later timepoints (**Figure 69B**).

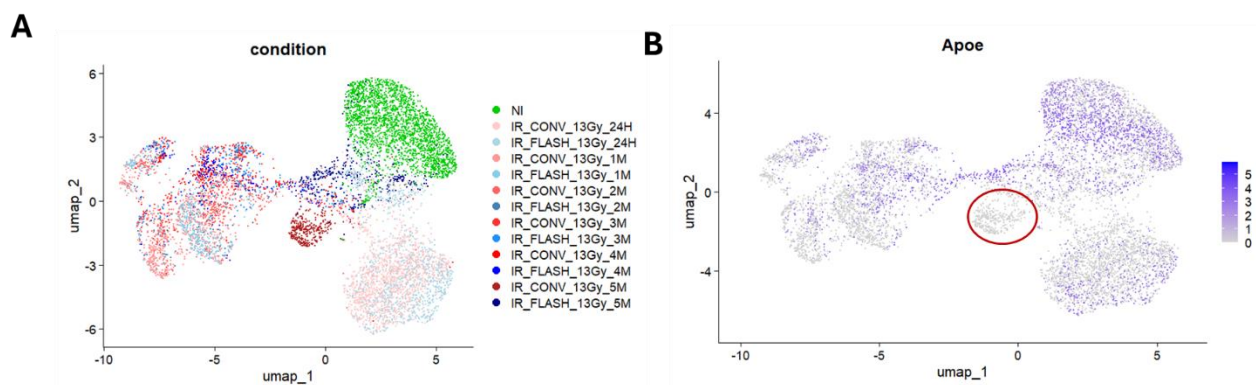


Figure 69. Characterization of AT2 cell clusters and *Apoe* expressions from 24 hours to 5 months post-irradiation. (A) UMAP visualization of AT2 cells by experimental condition (B) UMAP visualization of *Apoe* expression across the treatment conditions. The circled area highlights the cluster of AT2 irradiated cells at 5 months where *Apoe* expression appears decreased.

Interestingly, by quantifying the expression of *Apoe* over time following FLASH or conventional irradiation, it appears that from 24 hours and 1 month, which correspond to acute response phase, *Apoe* expression was decreased after both types of irradiations, with a less pronounced decrease following FLASH (**Figure 70**). From 2 to 4 months post-irradiation, *Apoe* expression in AT2 cells seems to stabilize regardless of the irradiation modality. However, at 5 months, when fibrosis develops after conventional irradiation but not after FLASH, a loss of *Apoe* expression is observed in AT2 cells, while FLASH irradiation preserves *Apoe* expression at stable levels (**Figure 70**).

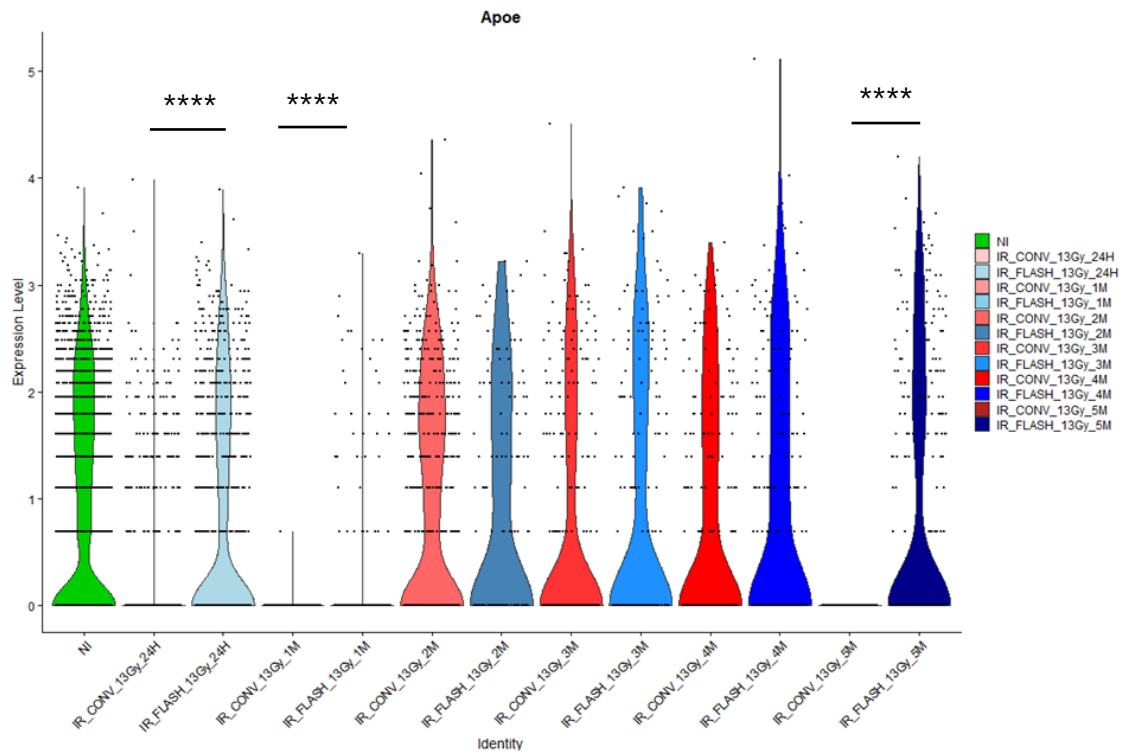


Figure 70. Dynamic of Apoe expression months following FLASH or CONV-RT.

Similarly, the expression of Plin2 follows a similar trajectory, suggesting a significant impact of irradiation on lipid uptake as well as storage processes in AT2 cells. This dysregulation of lipid metabolism in AT2 cells could serve as a potential marker for both acute responses and the later development of RILI, as well as a marker for the sparing effect of FLASH irradiation in the lung (**Figure 71**).

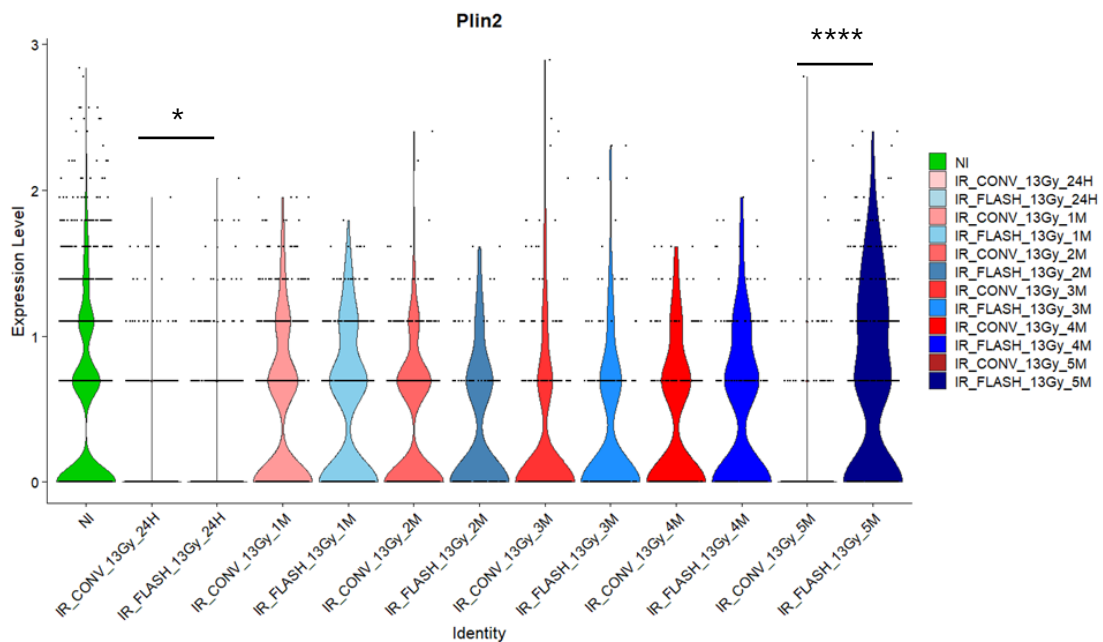


Figure 71. Dynamic of Plin2 expression months following FLASH or CONV-RT.

Thus, these changes suggest a significant sparing effect on several pathways involved in lipid metabolism and pathway implicated in the production, transport, and secretion of pulmonary surfactants, both in the acute and late phases in AT2 cells.

To conclude, through a scRNAseq analysis of murine **AT2 cells**, we unveiled that FLASH-RT **precociously and persistently spared the expression of genes related to lipid metabolism compared to CONV-RT**. Some of these first insights were validated by a lipidomics analysis on sorted AT2 cells which revealed a **preservation of cholesteryl ester levels** which are related to lipid droplet formation after FLASH-RT compared to CONV-RT. As one of primary functions of AT2 cells is pulmonary surfactant production, it seems that CONV-RT may impair this process. Indeed, a lipidomics analysis carried by mass spectrometry on macaque model lung parenchyma 6 months after whole-thorax irradiation found a notable decrease of phospholipids which are the main lipids constituting the pulmonary surfactant ^{328,329}. Lipid metabolism has also been associated with stress response and cellular senescence, as well as aging-related diseases³³⁰. It has also been demonstrated that *ApoE* knockout murine models have dysfunctional inflammation and oxidative stress response that may result to pulmonary fibrosis ³²⁹. In regard to *Plin2*, it has been shown that oxidative stress may lead to its overexpression and therefore to lipid droplet formation, resulting in a stress decrease ^{332,333}.

Our preliminary data suggests a **differential impact between FLASH and conventional radiotherapy on these complex lipids related metabolic processes in AT2 cells**, which present lipids and lipid metabolism pathways as an exciting new area of research that could help elucidate the underlying mechanisms of the FLASH effect. For now, several functional validation analyses of these initial lipidomic findings are currently ongoing.

1.3.5 *Characterization of endothelial subpopulations in acute and late radiation responses datasets*

Endothelial cells are among the most sensitive cell types to radiation. Once exposed, their essential protective functions are disrupted. The alteration of endothelial cells leads to their activation, which may eventually progress to senescence or cell death. These states can contribute to the development of chronic inflammation through the secretion of SASP (Senescence-Associated Secretory Phenotype) factors, pro-inflammatory cytokines, and chemokines. This is why we focused on studying the response of these populations to CONV or FLASH-RT from 24 hours to 5 months post-treatment (**Figure 72A**). The identification of the different endothelial clusters was based on the recently published single-cell atlas of endothelial cells¹⁴¹, which allowed us to classify five main clusters : artery endothelial cells (EC_artery), vein endothelial cells (EC_vein), lymphatic endothelial cells (EC_lymph), and two types of capillary endothelial cells which are general capillaries (gCap) and alveolar capillaries (aCap) (**Figure 72B**). Artery ECs were characterized by the expression of *Efnb2* and *Fbln5*, while vein ECs showed high levels of *Nr2f2* and *Vwf* (**Figure 72C**). Lymphatic ECs expressed *Ccl2a*, *Mmrn1*, and *Fgl2* (**Figure 72C**). The two types of capillaries exhibited distinct profiles: gCap was defined by the expression of *Ptprb* and *Gpihbp1*, and aCap was characterized by the expression of *Fibin*, *Car4*, *Apln*, *Tmcc2*, and *Prx* (**Figure 72C**).

Next, we examined the distribution of endothelial subpopulations following conventional or FLASH irradiation (**Figure 72D**). Starting from 3 months post-conventional irradiation, we observed a decrease in the proportion of gCap microvascular cells, coupled with an increase in the proportion of aCap, suggesting a possible differentiation of this population to replenish the aCap pool. At 5 months, in a fibrotic context, this decrease was even more pronounced, but we also observe a reduction in the proportion of aCap, the functional microvascular cells involved in gas exchange. This reduction may correlate with the progression of fibrosis, which aligns with previous studies conducted with higher doses²⁰⁰. After FLASH irradiation, a similar trend of gCap depletion is observed starting from 2 to 3 months post-irradiation. However, in contrast to conventional irradiation, the aCap pool remains elevated from this time onward, without any decrease even at 5 months post-irradiation, suggesting a preservation of alveolar gas exchange functions. These findings suggest a differential impact of FLASH irradiation over time on pulmonary microvascular populations, which may be correlated with the delayed development of radiation-induced fibrosis compared to conventional irradiation.

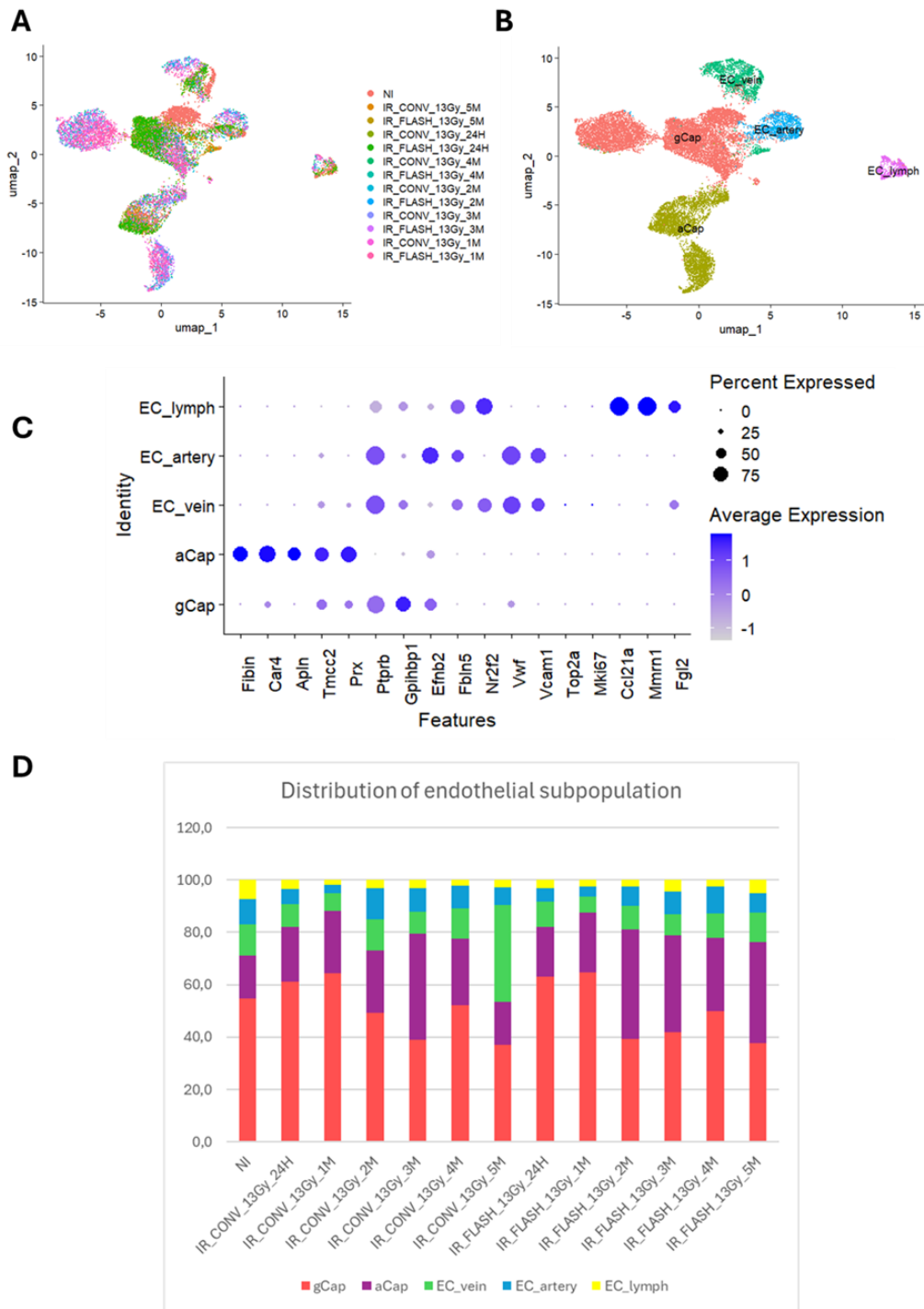


Figure 72. Identification of endothelial subpopulations and their distribution across irradiation conditions. (A) UMAP plot showing the distribution of endothelial cells across different conditions. (B) UMAP plot focusing on the identification of endothelial subpopulations. (C) Dot plot showing the expression of selected endothelial markers across endothelial subpopulations. (D) Stacked bar plot representing the relative proportions of different endothelial subpopulations across FLASH or CONV-RT from 24 hours to 5 months post-treatment.

1.3.6 FLASH-RT spares mitochondrial genes expression in endothelial subpopulations at 24 hours

Then, we focused on molecular analysis of DEG between FLASH and CONV-RT at 24 hours post-treatment in all EC populations. Among the top upregulated genes identified, we found a set of nine mitochondrial genes (**Figure 73A**). These genes encode proteins that are involved in the composition of various mitochondrial complexes. Specifically, this includes all the genes encoding the subunits of Complex I, which is involved in the transfer of electrons from NADH to ubiquinone, a crucial step in the mitochondrial respiratory chain for ATP production (**Figure 73B**). Similarly, all the genes encoding subunits of Complex IV, which plays a key role in the reduction of oxygen to water during oxidative phosphorylation, were upregulated following FLASH irradiation (**Figure 73B**). Finally, the ATP synthase subunit Atp6 was also upregulated after FLASH irradiation (**Figure 73B**). Interestingly, for most of these genes, we observed a slight reduction in their expression at 24 hours post-FLASH irradiation compared to non-treated conditions. However, this effect is more pronounced after conventional irradiation (**Figure 73C**). Moreover, this downregulation of expression was observed across almost all endothelial subpopulations, suggesting a common impact on the entire pulmonary endothelium.

Mitochondria has been reported to play a critical role in endothelial cell function, primarily through signaling mechanisms rather than energy production³³⁴. While energy demands in endothelial cells are lower compared to other cell types, mitochondria regulate essential processes like ROS production, calcium homeostasis, and cell death. Mitochondrial dynamics, including fusion and fission, are vital for maintaining endothelial function, especially under stress conditions such as oxidative stress. Thus, our results suggest, at the transcriptional level, a **sparing effect of FLASH on mitochondrial function** in endothelial cells that should be further explored with functional validation *in situ*.

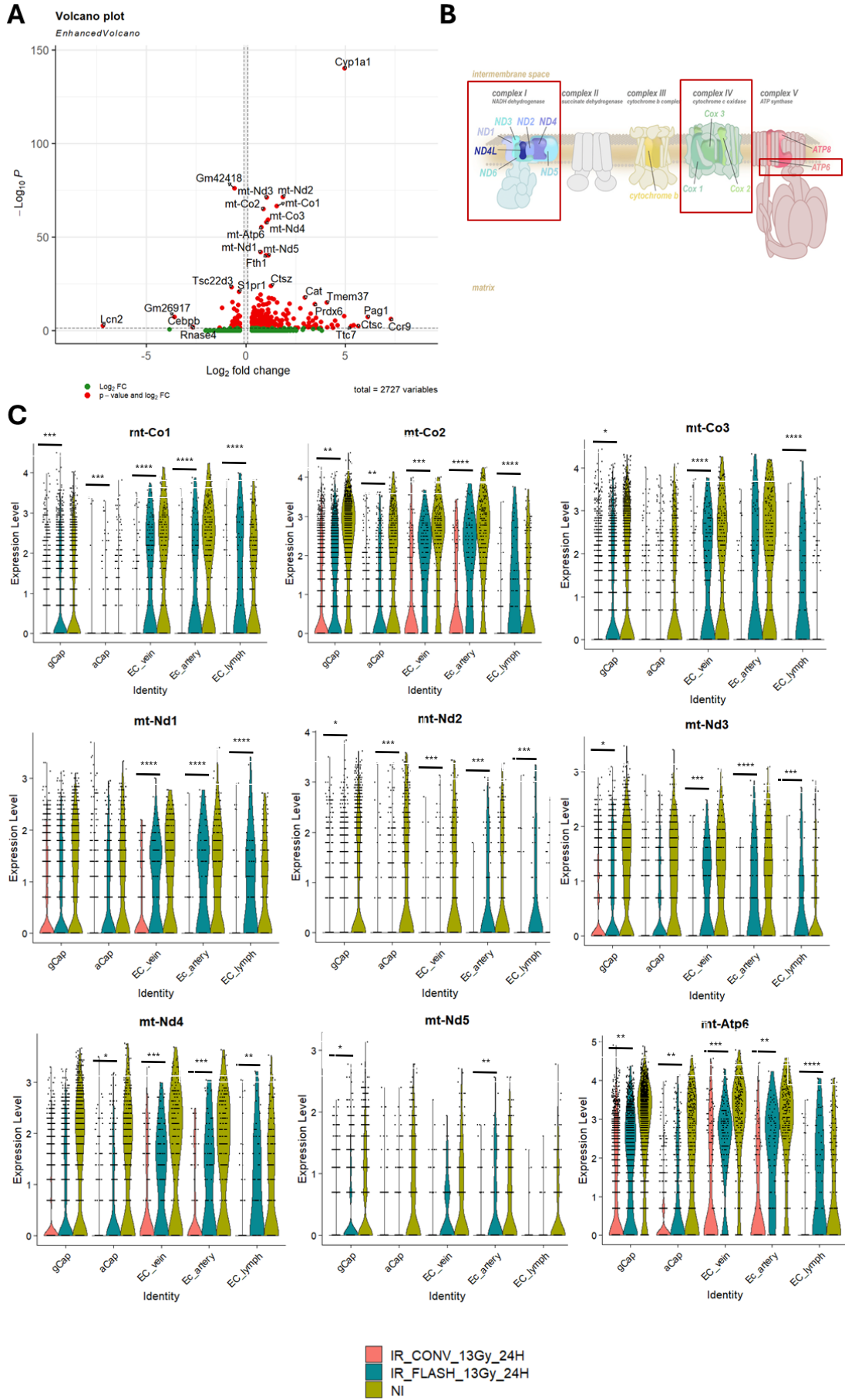


Figure 73. FLASH-RT spares mitochondrial genes expression in endothelial subpopulations. (A) Volcano plot displaying the differential gene expression between FLASH and conventional irradiation at 24 hours post-treatment. The plot highlights the most significant genes, with red points indicating upregulated genes ($\log_2FC > 0$, $p\text{-value} < 0.05$), and green points representing downregulated genes. (B) A schematic representation of the mitochondrial respiratory chain complexes. Each complex which is upregulated after FLASH is boxed and color-coded to show the position of mitochondrial subunits, highlighting genes from the mitochondrial genome involved in the complexes, including Complex I, Complex IV, and ATP synthase. (C) Violin plots showing the expression levels of mitochondrial genes (*mt-Co1*, *mt-Co2*, *mt-Co3*, *mt-Nd1*, *mt-Nd2*, *mt-Nd3*, *mt-Nd4*, *mt-Nd5*, *mt-Atp6*) across different endothelial subpopulations in both irradiation conditions compared to NI.

1.3.7 *Dynamic of EC mitochondrial genes expression after FLASH or CONV-RT from 1 to 5 months post treatment*

Subsequently, we wanted to understand how this response evolved over time following conventional and FLASH irradiation, from 1 month to 5 months post-irradiation. Given that we had shown that this response was common across endothelial subpopulations, this analysis was performed on the entire endothelial population. By conducting DEG analyses at each time point between CONV-RT and FLASH, we investigated whether there were commonly upregulated genes in at least 4 of the 6 conditions studied (**Figure 74A**). This approach allowed us to identify a list of 6 commonly upregulated genes, which included the mitochondrial genes previously identified (**Figure 74A**). Upon further examination of the dynamics of these mitochondrial genes over time after conventional or FLASH irradiation in endothelial cells, we found that all these genes followed a similar response pattern (**Figure 74B**). As demonstrated earlier, these genes are upregulated shortly after FLASH irradiation, but by 1-month post-treatment, their expression was downregulated compared to non-treated endothelial cells, with no significant differences between FLASH and conventional irradiation (**Figure 74B**). From 2 months onward, there was a marked upregulation of mitochondrial genes after FLASH irradiation compared to CONV. By 3 months post-treatment, the expression levels of mitochondrial genes stabilized, with no significant differences when compared to the untreated conditions (**Figure 74B**). Finally, at 4 and 5 months post-treatment, there was a significant decrease in the expression of these mitochondrial genes after conventional irradiation, which correlated with changes in the distribution of endothelial subpopulations and a reduction in the microvascular pools, an effect not observed after FLASH irradiation (**Figure 74B**).

Thus, the downregulation of mitochondrial genes could serve as an interesting marker for both early and late responses to FLASH compared to CONV-RT. Indeed, further exploration of molecular aspects could help to understand part of the underlying mechanisms of FLASH. Mechanistically, this could suggest that conventional irradiation may lead to a more significant accumulation of oxidative stress, as described. High oxidative stress is known to impair mitochondrial function, particularly by affecting the components of the mitochondrial respiratory chain. This stress could lead to more pronounced negative regulation of mitochondrial genes to limit ATP production and reduce the risk of excessive cellular damage. Irregularities in the mitochondrial respiratory chain and ATP production may also affect other metabolic pathways involved in mitochondrial gene regulation, which could explain the more pronounced downregulation of mitochondrial genes after conventional irradiation.

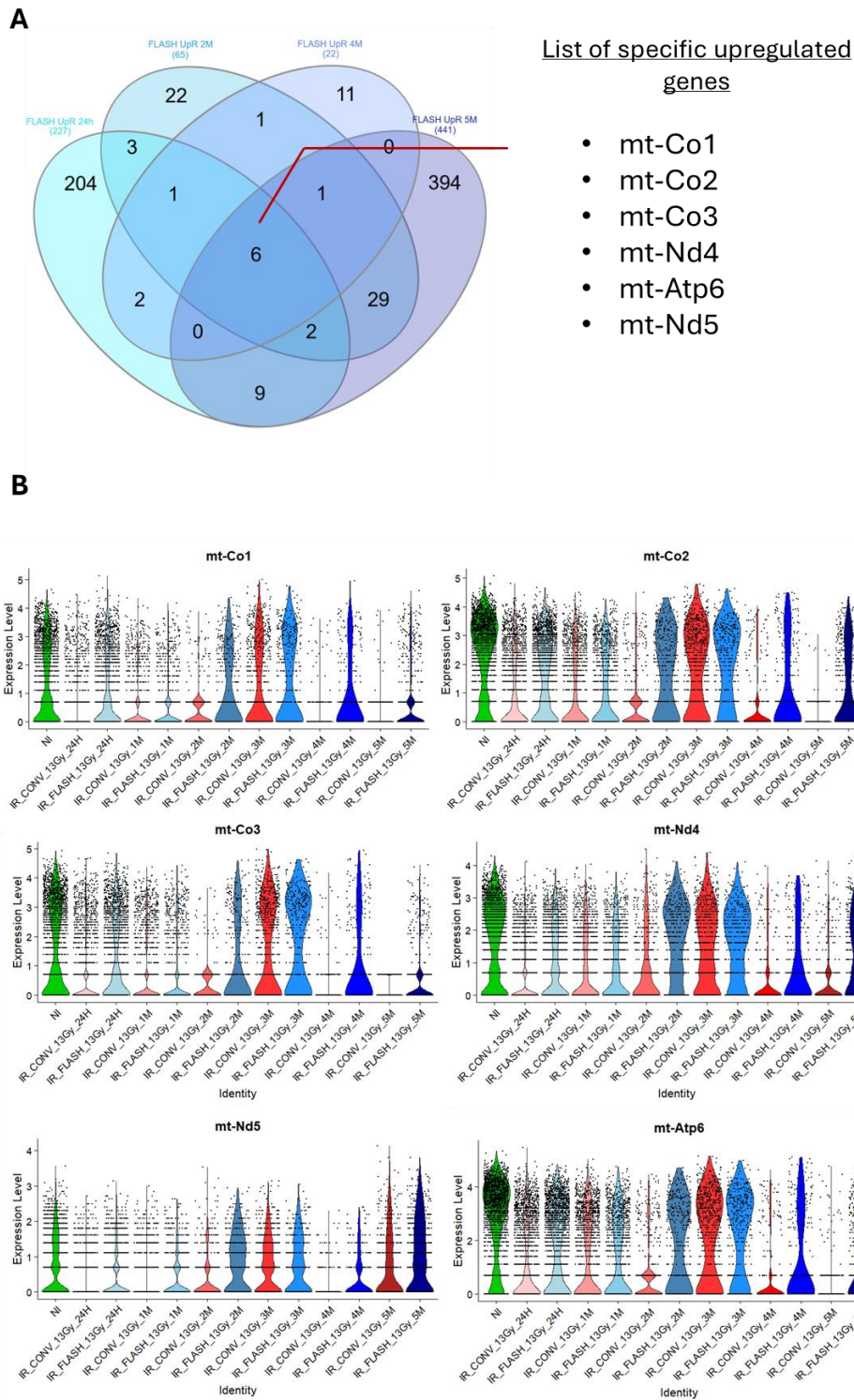


Figure 74. Upregulation of mitochondrial genes after FLASH is maintained across time post-radiation. (A) Venn diagram showing the overlap of specific upregulated mitochondrial genes (*mt-Co1*, *mt-Co2*, *mt-Co3*, *mt-Nd4*, *mt-Atp6*, *mt-Nd5*) across different time points after FLASH compared to conventional irradiation. (B) Violin plots displaying the expression levels of specific overlap upregulated mitochondrial genes.

1.3.8 *What happens in lung dividing cells 24 hours post-radiation ?*

As suggested by our studies at 24 hours post-irradiation in PCLS model, these rare populations of dividing cells in the lung appear to be differentially affected by conventional or FLASH irradiation. Therefore, in addition to the analyses performed on the entire AT2 and endothelial cell populations, **we aimed to characterize the response of subpopulations actively dividing in the lung**. To achieve this, we examined the proportion of cells expressing active division markers such as Mki67 (**Figure 75A**). However, less than 1% of the cells in the dataset actively express these markers, and although a few cells seem to be in the cell cycle across all subpopulations, most of the detected cells belong to a single cluster of T cells. We then checked the expression of this marker in the identified lung populations and, indeed, most of the cells expressing it were T cells, which may have been recruited following irradiation (**Figure 75**). Aside from a few AT0 cells undergoing transdifferentiation process, most of the dividing lung cells seem to be immune (**Figure 75B**). Due to the low number of selected cells in our dataset, we could not perform molecular analysis on this rare population.

Subsequently, in the following part, **we focused on lung dividing cells**, posing several questions. As a potential cellular biomarker of FLASH sparing effect, we sought to **identify the subpopulations of dividing cells in the lung** that are **spared at early time points post-irradiation**. We then aimed to **characterize the fate of these FLASH-spared irradiated cells at 24 hours post-treatment**. Finally, we wanted to **enrich this population of interest to perform a scRNA-seq analysis to identify potential molecular insights into the FLASH sparing effect on cycling cells in the lung**. To do so, during my PhD, **we developed a transgenic Mki67 Cre ERT2 x R26 mtmG mouse model** to characterize these progenitor subpopulations spared by FLASH radiotherapy.

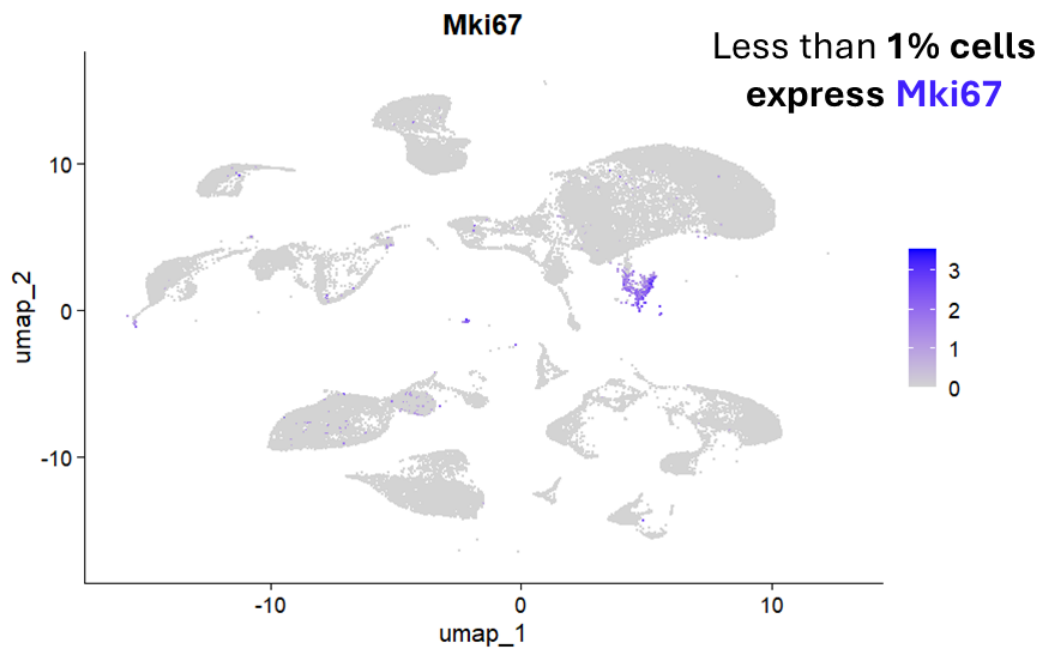
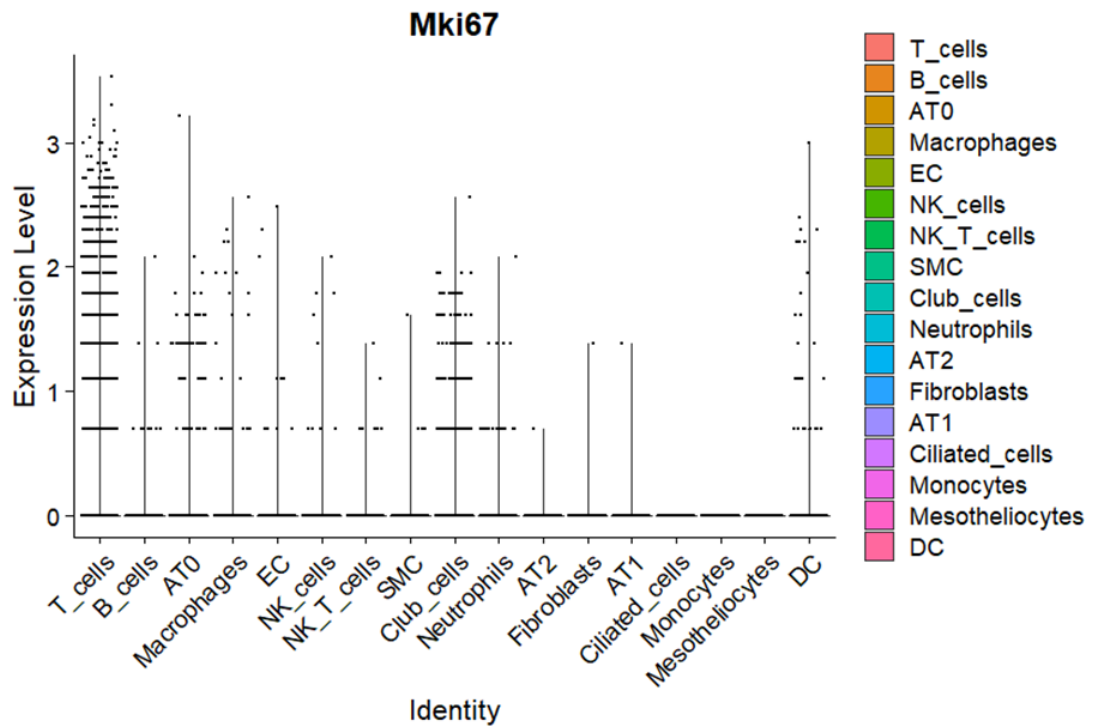
A**B**

Figure 75. Identification of dividing cells in lung dataset. (A) *UMAP* plot showing the expression of the proliferation marker *Mki67* across all lung cells in the dataset. (B) Violin plot showing the expression level of *Mki67* across different cell types.

V- PART 3 – CHARACTERIZATION OF THE FLASH SPARING EFFECT IN LUNG DIVIDING CELLS

1. DECIPHERING THE UNDERLYING MECHANISMS OF FLASH IN DIVIDING CELLS

1.1 Introduction

FLASH radiotherapy has been described as **protecting progenitor cell populations in the intestine, lung, and brain**^{246,254,260}. These cells, though relatively rare, play a crucial role in tissue repair and regeneration upon injury, making them highly significant in the context of radiation-induced damage. Due to their active division state, these cells are highly sensitive to irradiation, which can cause substantial DNA damage³³⁵. In the first part of the results of this manuscript, we demonstrated that cycling cell populations in PCLS are spared by FLASH compared to CONV-RT. This seemingly minor effect, which affects only a rare population of cells, can be crucial as these cells can initiate pulmonary regeneration following the inflicted damage.

In this final part of the results, we further investigated these cycling cell populations in the lung, which are differentially impacted by FLASH and conventional irradiation. Our objectives were as follows: 1) To **determine which cycling cell subpopulations are spared by FLASH** radiotherapy at **24 hours post-treatment** 2) To **assess the fate of these irradiated cells that are preserved by FLASH** radiotherapy 3) To **evaluate tissue regeneration dynamics or inflammatory responses in the weeks following either FLASH or conventional treatment** and finally 4) To **molecularly characterize the response of these cycling lung cell populations to both FLASH and conventional modalities**.

Several analyses were initially performed directly on PCLS with various antibody stainings or smFISH techniques. However, due to the thickness of the PCLS, optimization of these protocols was insufficient for reliably labeling all cells within the pulmonary epithelial, immune, endothelial, and mesenchymal subpopulations. To overcome this issue, we developed a transgenic Mki67 Cre ERT2 x R26 mtmG mouse model, which allows us to detect cells expressing or that have expressed Mki67 upon tamoxifen induction. In addition to generating and validating this model, we optimized our tamoxifen induction protocols based on the applications. Our primary method of analysis for this part was flow cytometry (FACS), and for molecular analyses, we performed scRNA-seq on sorted cells. Given that the results from this part are recent, they remain preliminary and require further validation, particularly by expanding our mouse groups for these analyses.

1.2 Material and method

Mice and ethics statement : Studies were conducted in accordance with the European Community recommendations (2010/63/EU) for the care and use of laboratory animals. The experimental procedures were specifically approved by the Ethics Committee of Institut Curie (CEEA-IC #118) under authorization number APAFiS#32674-2021080916494690, granted by the National Authority, in compliance with international guidelines. Female C57BL/6J mice, purchased from Charles River Laboratories (Lyon, France) at 6 weeks of age, were housed in the Institut Curie animal facilities.

Transgenic Mouse Model for Inducible Detection of Mki67-Expressing Cells : We utilized a transgenic mouse model expressing Cre recombinase under the control of the endogenous Mki67 promoter (B6.Cg-Mki67tm1.1(cre/ERT2)Mtz/J, JAX #029803). These mice were crossed with a Cre-responsive GFP reporter strain (B6.129(Cg)-Gt(ROSA)26Sortm6(CAG-ZsGreen1)Hze/J, JAX #007914), which carries a loxP-flanked STOP cassette preventing the expression of GFP. In the resultant offspring, administration of tamoxifen induces Cre-mediated excision of the STOP cassette, allowing GFP expression specifically in Mki67-expressing cells. This approach enabled the inducible and precise detection of proliferating cells expressing Mki67 through GFP fluorescence.

Tamoxifen preparation and induction : For tamoxifen induction in Mki67 Cre ERT2 mice, a dosage of 10 μ L per gram of body weight was used, with each mouse weighing approximately 25 g, resulting in a 250 μ L injection per mouse. The injections were performed one to three times a day, depending on readouts, before or after treatment at a dose of 100 mg/kg. To prepare the solution, 1000 μ L was required per mouse (to account for potential pipetting losses), with 10 mg of tamoxifen added. For the induction, intraperitoneal (IP) injections were administered at 10 μ L per gram of mouse weight. The tamoxifen solution was prepared fresh each day and stored at 4°C if necessary. To aid in dissolution, the solution was heated at 37°C for 10-15 minutes with orbital shaking.

Mice irradiation : Mki67 Cre ERT2 mtmG mice were used for several purposes including identification of FLASH spared lung dividing cells subpopulations, fate analysis and ScRNAseq. Collimation, time-resolved fluence measurement, chemical dosimetry, depth-dose distribution, anesthesia, and immobilization procedures were performed as described in previous part of

this thesis. Bilateral thoracic irradiation was performed using a 7-MeV linear electron accelerator facility (Electron-Flash 4000, Sordina IORT Technologies). CONV-RT and FLASH-RT dose rates were 0.4 Gy/s and > 300 Gy/s respectively, while both were administered using a single dose of 13 Gy.

Lung dissociation for single cell suspension : For the preliminary preparation, Dispase (50 U/ml) was thawed from -20°C storage, with 2 ml used per mouse. A 1% agarose solution in PBS (low gelling) was prepared and maintained at 42°C before perfusion. Falcon tubes (50 ml) containing 3 ml of PBS (Mg²⁺/Ca²⁺) were prepared for each sample, and PBS with 10% FBS (PF10) was used for the dissociation steps. The centrifuge was set to 4°C. For lung extraction, mice were anesthetized with isoflurane followed by cervical dislocation. The ribcage was opened, the trachea was exposed, and then perfused with 2 ml of Dispase (50 U/ml) using a 20G needle, followed by 0.5 ml of 1% agarose to seal the trachea. Lungs were cooled on ice to solidify the agarose before being removed from the ribcage, cleaned of blood and heart tissue, and separated into lobes. The trachea and any remaining agarose were removed, and the lobes were finely minced and placed into the prepared Falcon tubes on ice. For lung dissociation, 320 µL of Elastase (25 U/ml) was added to the lung tissue, which was then further minced. The samples were homogenized and incubated at 37°C with shaking for 30 minutes. After homogenization with a pipette, the samples were incubated for additional periods and filtered through a 100 µm filter. Mechanical dissociation was performed with a 10 ml syringe, followed by rinsing with PF10. DNase (37.5 µL at 10 mg/ml) was added, and the mixture was incubated on ice for 3 minutes before filtering again through a 40 µm filter. The cells were centrifuged at 150g for 6 minutes at 4°C, resuspended in RBC lysis buffer for 90 seconds, and the lysis was stopped with PF10. For FACS or scRNA-seq analysis, RBC lysis was performed in cycles as required. Finally, the cells were centrifuged again at 200g for 6 minutes at 4°C and resuspended in 1 ml of PBS 1% SVF 1% BSA.

Antibody panel for FACS analysis : Following dissociation, 5 million cells were incubated with a cocktail of antibodies in 500 µL of PBS containing 1% SVF and 1% BSA. The antibodies used for cell surface and intracellular markers were as follows: APC-conjugated anti-mouse CD31 (clone 390, 1/100), CD45 BUV395 (clone 104, 1/200), Alexa Fluor™ 700-conjugated CD117 (c-Kit) (ACK2, 1/100), PE/Cyanine7 anti-mouse CD34 (1/100). Additionally, Mki67+ cells were identified using GFP labeling, and all cells were labeled with Tdtomato (PE) as a marker for live cells. After incubation for 45 minutes at 4°C, cells were washed twice with PBS containing 1% SVF and 1% BSA to remove unbound antibodies.

FACS sorting of Mki67+ cells Mice irradiation and lung tissue dissociation was done as described in prior steps. Dissociated cells were sorted with a BD FACSAria III sorter in order to isolate the Mki67+ cells with BD FACSDiva Software V8.0.3. Mki67 positive cells expressed a specific Cre recombinase induced by prior injection of 100 mg/kg tamoxifen which allowed the GFP protein expression, resulting in green fluorescence which in turn allowed specific cell sorting. For scRNAseq analysis, an incubation for 45 minutes at 4°C with a CD45 BUV395 (clone 104, 1/200) antibody was done prior sorting. Only GFP+ (Mki67) Cd45- cells were sorted for scRNAseq.

GEM generation and barcoding for scRNAseq : Single-cell 3'-RNA-Seq samples were prepared using the Single Cell V reagent kit and loaded into the Chromium Controller according to the manufacturer's standard protocol (10x Genomics). Depending on the experiment, 10000 to 18000 cells were captured for each mouse. Dissociated lung single cells were encapsulated in nanodroplets (GEMs) using a microfluidic device. These GEMs were created by combining barcoded single-cell 3' gel beads, a master mix containing reverse transcription (RT) reagents, single cells, and partitioning oil on the Chromium Next GEM Chip. Following cell lysis, the RNA was captured on gel beads coated with oligos containing an oligo-dTTT sequence, unique molecular identifiers (UMIs), and a specific barcode.

Reverse transcription and cDNA amplification : Incubation of the GEMs results in the production of barcoded, full-length cDNA from poly-A mRNA. Following reverse transcription, the GEMs are broken, and the cDNA is purified using silane magnetic beads. The purified cDNA is then PCR-amplified and washed before being analyzed for quality control using a Bioanalyzer (Agilent). The barcoded full-length cDNA is further amplified by PCR to produce sufficient material for library construction. After amplification, the cDNA is purified once more, and its quality is assessed via capillary electrophoresis on a Bioanalyzer (Agilent) prior to library preparation.

Library construction and sequencing : Finally, libraries were prepared using a fixed proportion of the total cDNA. Enzymatic fragmentation and size selection are performed to optimize the cDNA amplicon size. During GEM incubation, the read 1 primer sequence is added to the molecules. At this stage, the P5 and P7 sequences, a sample index, and the read 2 primer sequence are incorporated through End Repair, A-tailing, Adaptor Ligation, and PCR. This process ensures that the final libraries contain the P5 and P7 primers required for Illumina bridge amplification. The libraries were then sequenced using the NovaSeq sequencer (Illumina).

scRNA-seq Data Analysis : Single-cell suspensions were analyzed using the droplet-based single-cell RNA-seq method developed by 10x Genomics. Raw sequencing data were processed using the CellRanger pipeline version 7.1.0. Count matrices were analyzed using Seurat package version 5.0.1320. For each sample, SoupX was employed to remove contamination by ambient RNA³²¹, and quality controls were performed. The correct annotation of cell populations was validated using the expression of well-known markers. The SCTransform function was applied to the merged object, with cell cycle scores and the percentage of mitochondrial genes used as regressed variables. The samples from different patients were then separated and normalized individually. The 2000 most variable features were identified and used to set anchors for integration.

Statistical analysis : statistical analyses were performed using the ggpubr package (<https://rpkgs.datanovia.com/ggpubr/>) (accessed on 4 September 2023) in R with a Wilcoxon test.

1.3 Results

1.3.1 Identification of lung dividing cells spared by FLASH-RT at 24 hours post-treatment

Initially, we aimed to identify which pulmonary subpopulations are spared by FLASH radiotherapy within 24 hours post-treatment. To this end, we irradiated the thoraxes of Mki67 Cre ERT2 x R26 mtmG mice with a dose of 9 Gy, using either conventional or FLASH irradiation modalities (**Figure 76**). This dose was chosen because it is the one for which the sparing effect has been detected both *ex vivo* and *in vivo*³³⁶. Subsequently, the mice were induced with three tamoxifen injections at 100 mg/kg during a day, in alignment with the three EdU injections performed in part I of the results (**Figure 76**). With that schedule, the goal was to induce all cells capable of entering the cell cycle within 24 hours post-treatment. After irradiation, pulmonary dissociations were performed for each condition, followed by antibody staining to identify the major pulmonary compartments, including endothelial (Cd31+Cd45-), immune (Cd31-Cd45+), and epithelial/mesenchymal (Cd31-/Cd45-). A subset of Cd31+Cd45+ cells were identified, which predominantly corresponded to B cells (**Figure 76**). Flow cytometry analysis was then conducted for each lung dissociation by condition, analyzing a total of 1 million lung cells (**Figure 76**). This strategy allowed us to analyze the proportion of Mki67+ cells, assess the distribution of Mki67+ cells across pulmonary subcompartments, and evaluate the proportion of cycling cells within each compartment.

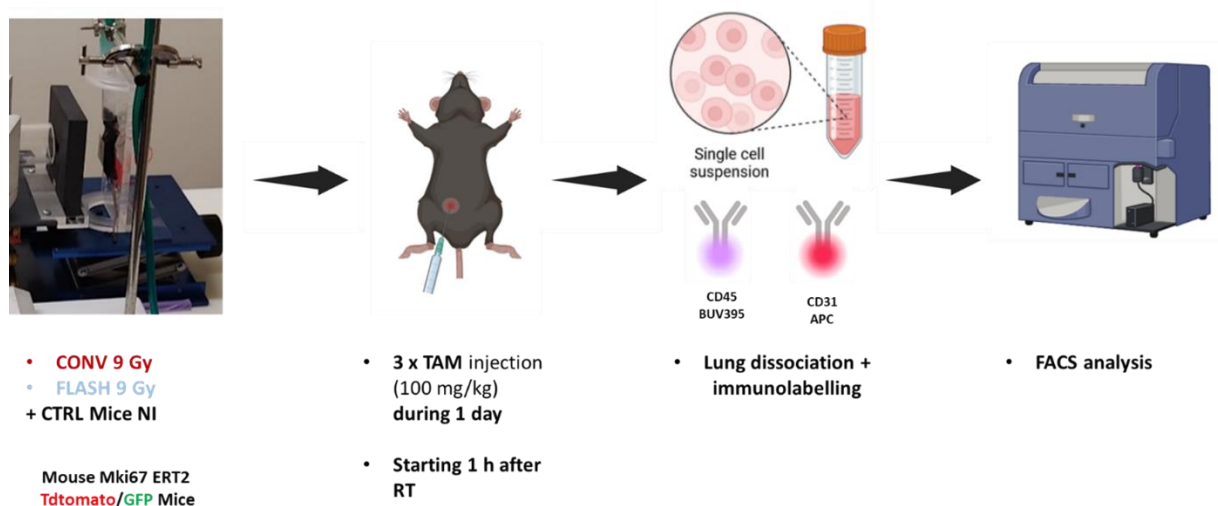


Figure 76. Experimental setup and protocol for the identification of Mki67+ cells and cell fate analysis.

For the FACS, we defined gates that were applied across all our conditions for the analysis presented in the following sections of this manuscript. Briefly, we eliminated cell doublets and focused on the proportion of GFP+ (Mki67+) cells in the entire lung dissociation (**Figure 77**). Subsequently, we assessed: 1) the distribution of Mki67+ cells across the four previously described pulmonary compartments and 2) the percentage of Mki67+ cells within a given population of interest (**Figure 77**). This allowed us to define the impact of irradiation on Mki67+ cells at 24 hours post-treatment.

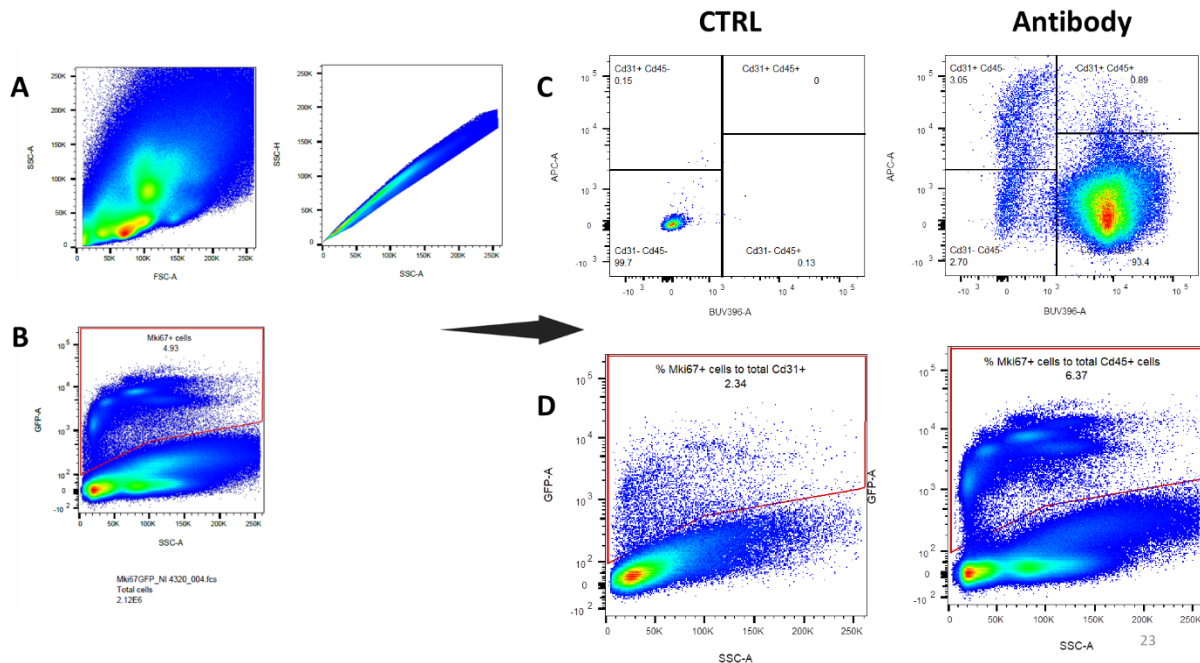


Figure 77. Gating procedure for FACS analysis with Mki67 Cre ERT2 x R26 mtmG mice. (A) Gating procedure on SSC-A and SSC-H to analyse singlet cells. (B) Gating procedure for Mki67+ cells for each condition. (C) Gating procedure for distribution of Mki67+ cells across immune, epithelial/mesenchymal and endothelial compartment. (D) Gating procedure to evaluate proportion of Mki67+ cells in the whole endothelial and immune compartment.

At 24 hours following irradiation, we observed a notable reduction in the proportion of Mki67+ cells, with conventional irradiation inducing a more significant decrease compared to FLASH (**Figure 78A**). Interestingly, the proportion of Mki67+ cells relative to the total cell count was slightly higher than that of EdU+ cells. This is likely due to the fact that Mki67 is an earlier marker expressed during the entry phases of the cell cycle, whereas EdU, a thymidine analog, integrates into DNA specifically during the replication phase. Using this model, we were able to confirm the FLASH effect described earlier in **results part 1**, with a 43% decrease in Mki67+

cells following FLASH irradiation, compared to a 69% reduction following conventional irradiation at 24 hours post-treatment (**Figure 78A**). Through double antibody staining for Cd31 and Cd45, we were able to investigate the distribution of Mki67+ cells across various pulmonary compartments, including epithelial/mesenchymal, immune, and endothelial populations. On average, the majority of Mki67+ cells were immune cells (approximately 90%), with a smaller proportion found in the epithelial/mesenchymal compartments (around 6%) and endothelial cells (2.3%) (**Figure 78B**). A few double-positive cells for Cd31 and Cd45 were identified, which, according to our scRNAseq data, are most likely B cells, representing a mere 0.15% of the total cells analyzed (**Figure 78B**). In examining the impact of the two irradiation modalities on the distribution of Mki67+ cells, no significant differences were observed (**Figure 78B**). While there was a slight increase in the epithelial/mesenchymal pool, no substantial variations were found between the FLASH and conventional irradiation conditions.

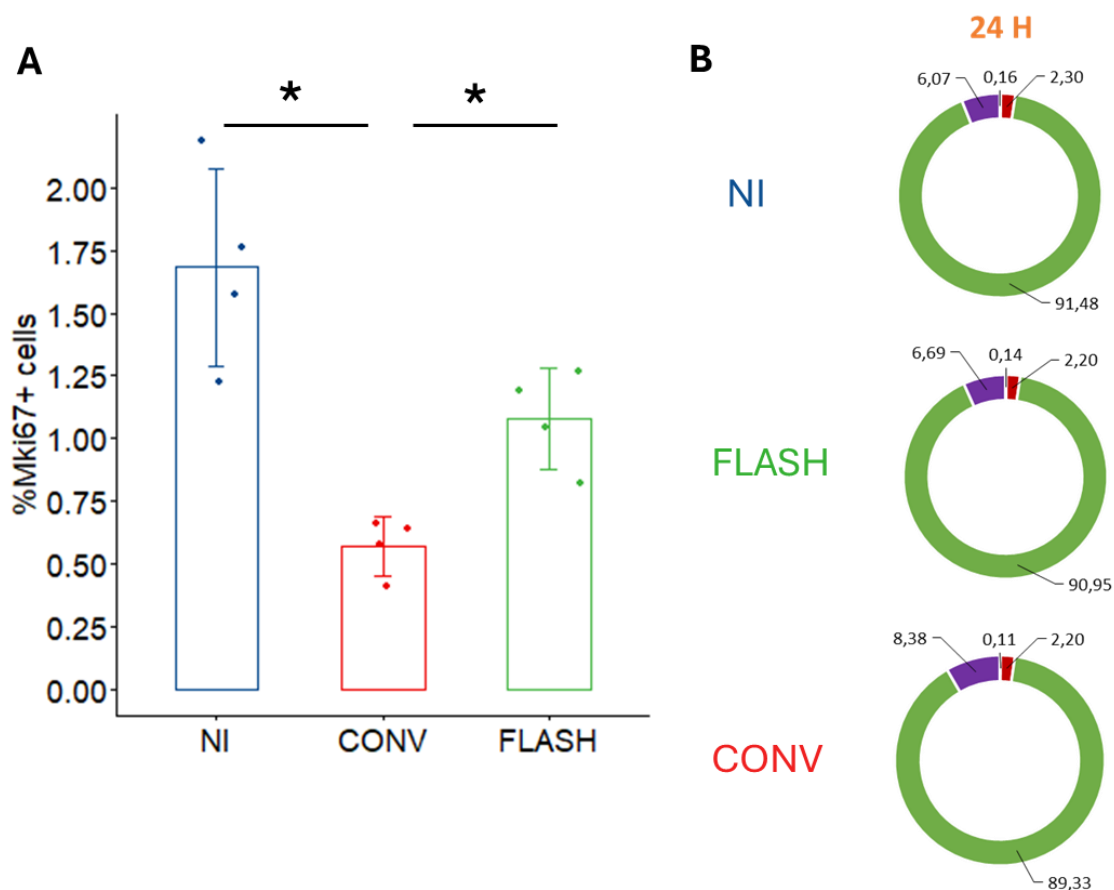


Figure 78. FLASH spares total Mki67+ cells 24 hours post-radiation but has no impact on Mki67+ cells distribution across lung compartments. (A) Barplot recapitulating FACS analysis on Mki67+ cells 24 hours results after a 9 Gy FLASH or CONV-RT in $n=4$ mice. (B) Distribution of Mki67+ cells across all lung subcompartments depending on condition. * p -value < 0.05.

Through this approach, we once again confirmed that FLASH irradiation preserves cycling cells 24 hours post-irradiation. However, using our labeling strategy, we further explored the individual impact of conventional versus FLASH irradiation on immune, endothelial, and epithelial/mesenchymal compartments (**Figure 79**). In the endothelial compartments, the number of Mki67+ cells decreased by half following FLASH irradiation and by 75% following conventional irradiation (**Figure 79**). Due to the rarity of these populations and the fact that it could be also influenced by dissociation biases, the results were more heterogeneous. Nevertheless, the trend still suggests a preservation effect of FLASH within the endothelial subpopulations (**Figure 79**). In the immune compartment, which accounts for about 90% of the total Mki67+ cells, the results closely resembled those observed for the entire lung that demonstrate the protective effect of FLASH on the dissociated lung populations (**Figure 79**). Lastly, like the endothelial compartments, there was a trend showing the preservation of Mki67+ cells in the epithelial/mesenchymal compartments under FLASH irradiation (**Figure 79**). While these data are still preliminary, they **suggest that the protective effect of FLASH on cycling cells in the lung extends across all epithelial, endothelial, mesenchymal, and immune subcompartments**, indicating a global protective effect on dividing cells in the lung after FLASH.

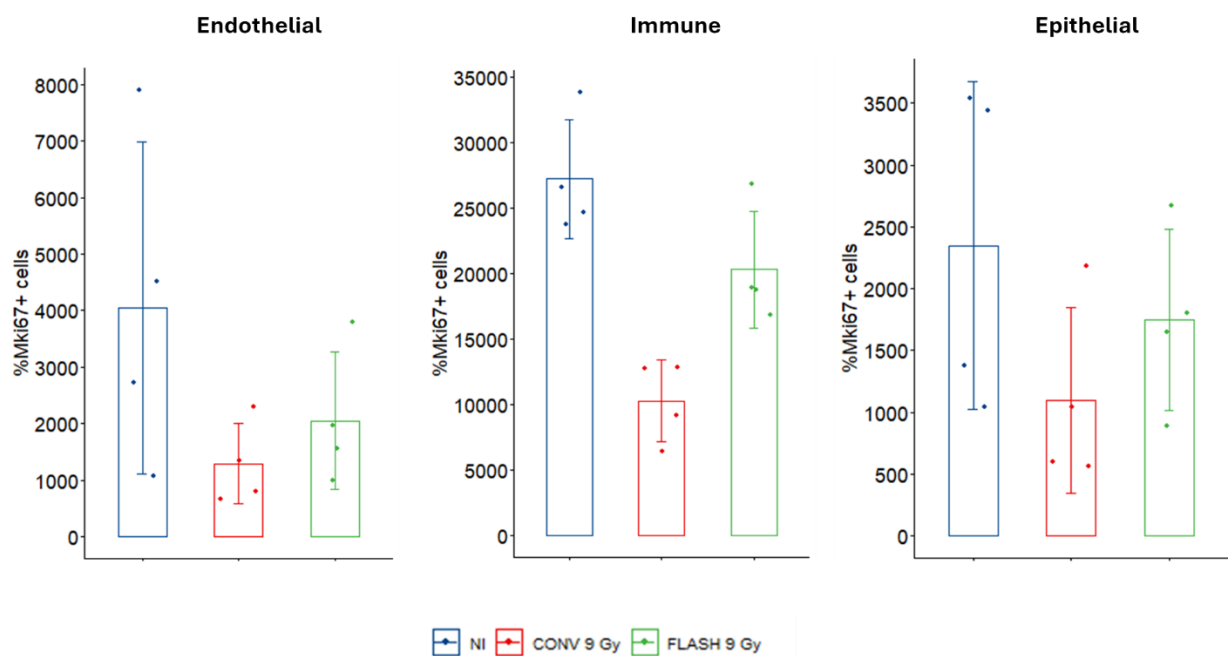


Figure 79. Preliminary results suggest that FLASH spares all lung dividing cells subpopulations at 24 hours post-radiation. *Barplots shows the counts of Mki67+ cells per million lung cells across endothelial, immune and epithelial/mesenchymal compartment depending on treatment condition.*

1.3.2 Monitoring of lung dividing cells spared by FLASH until 1-week post-treatment.

After demonstrating that FLASH-RT appeared to spare all pulmonary subpopulations that were actively cycling within 24 hours post-treatment, we next focused on the fate of these cells several days after exposure to both modalities (**Figure 80**). To investigate this, we repeated our schedule of three tamoxifen injections in the hours following irradiation. This schedule ensures that recombination only occurs in cells that express Mki67 during the 24-48 hours post-treatment, depending on the recombination timing and the stability of tamoxifen once injected. At 72 hours post-treatment, we observed a significant increase in the proportion of Mki67+ cells in our lung dissociations (around 14% on average in the NI, 9% in CONV-RT, and 12.5% in FLASH-RT) (**Figure 80**). This increase could be due to the active division of the cells marked within the first 24 hours following treatment or to the recombination and induction of cells by tamoxifen at slightly later point. Although the results remain preliminary and are more heterogeneous, we consistently observed a significantly higher proportion of Mki67+ cells after FLASH irradiation compared to conventional irradiation (**Figure 80**). At 7 days post-treatment, there was a decrease in the proportion of Mki67+ cells across all conditions, likely due to the replenishment of cycling cell populations. Since most of these cells are immune cells, which tend to have a faster turnover rate, this finding could be expected. Despite considerable heterogeneity, there is still a consistent trend toward the preservation of cycling populations that were irradiated and followed within the first 24 hours post-irradiation (**Figure 80**). **This kinetic pattern suggests that while these cells actively divide, they are still more persistently affected by conventional irradiation than by FLASH over time.**

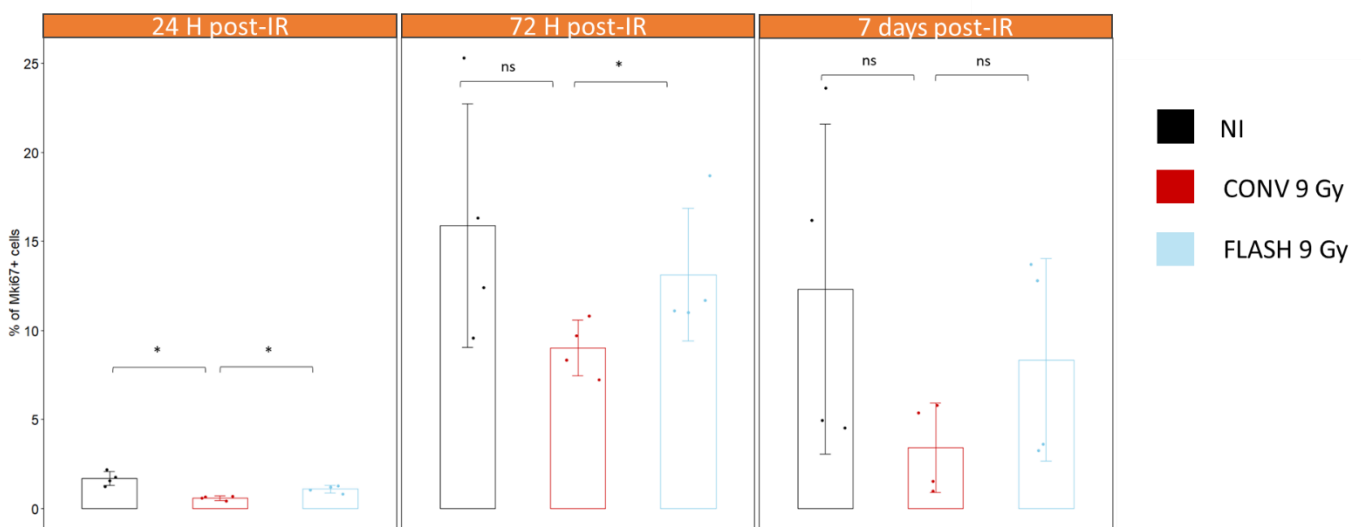


Figure 80. Monitoring of Mki67+ cells that divided in the lung within 24 hours post-irradiation.

1.3.3 Dynamic of cell division across lung subpopulations after CONV or FLASH-RT from 1 to 4 weeks post-treatment

In parallel with our studies on the short-term response to either conventional or FLASH irradiation at a dose of 9 Gy, which allowed us to identify and track the cycling cell populations in the lung that are spared by FLASH radiotherapy, we also focused on the dynamics of cell division for inflammatory response or tissue regeneration processes following irradiation at a higher dose of 13 Gy using the Mki67 Cre ERT2 x R26 mtmG mouse model. For this procedure, we examined the division rate of all Mki67+ cells, as well as zoomed in on the endothelial, immune, and epithelial/mesenchymal subpopulations in the weeks following treatment. To achieve this, we performed a series of tamoxifen injections in the week leading up to our analysis timing. These injections occurred five days a week, with the aim of encompassing and analyzing all cycling cells at one week, then two weeks, and continuing up to four weeks post-irradiation (**Figure 81**).

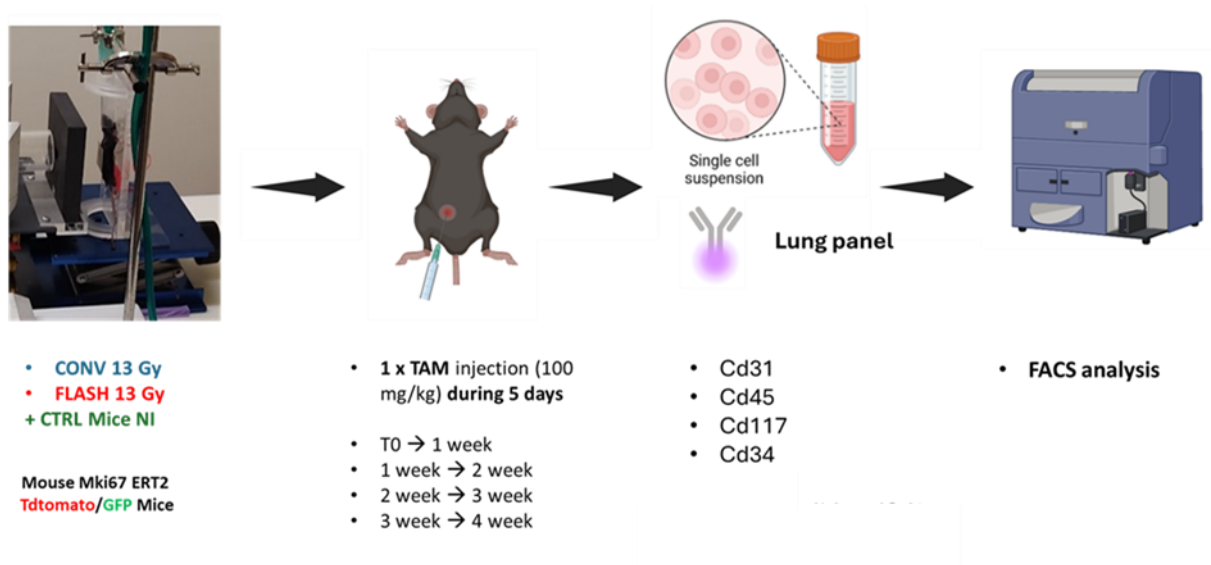


Figure 81. Experimental setup and protocol for studying cell division across lung subpopulations after CONV or FLASH-RT.

To study endothelial regeneration processes in more detail, we added antibodies for microvascular markers identified during our scRNA-seq analysis (**Figure 82**). This approach enabled us to identify gCap cells using c-Kit (Cd117) and aCap cells, which predominantly express Cd34 (**Figure 82**).

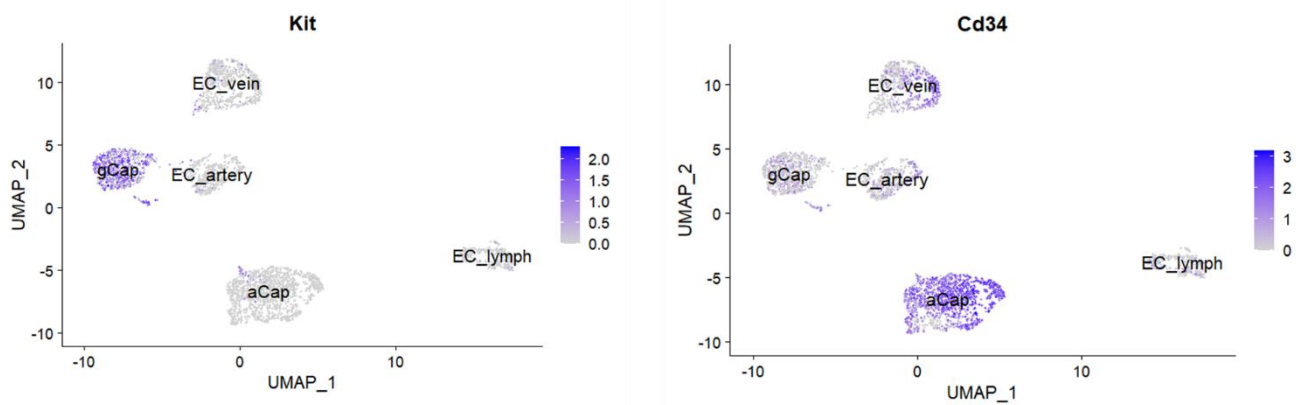


Figure 82. Selection of antibody panel for microvascular lung subpopulation identification in flow cytometry.

We first studied the proportion of cells that have expressed or are expressing Mki67 relative to the total number of dissociated lung cells according to the conditions at 1 week, 2 weeks, 3 weeks, or 4 weeks post-treatment (**Figure 83**). Interestingly, with this injection protocol, about 15% of the cells express or have expressed Mki67 in the non-treated conditions (**Figure 83**). At 1 week, no increase in this proportion was observed after FLASH irradiation. However, a drastic increase was observed, with approximately 33% of dissociated cells being Mki67+ one week after conventional irradiation (**Figure 83**). These results are similar to those obtained and published in the literature after one-week EdU injections into the lung following FLASH or CONV irradiation, again showing a dramatic increase in the proportion of cycling cells after conventional irradiation one-week post-treatment²⁶⁰. In the second week, a significant increase in the proportion of Mki67+ cells after FLASH irradiation was observed (26% of Mki67+ cells) (**Figure 83**). Compared to the first week, the proportion of Mki67+ cells after conventional irradiation decreased to 22%, suggesting slightly more cycling cells during the second week post-FLASH treatment (**Figure 83**). In the third week, this trend remains similar, with the proportion of Mki67+ cells increasing between the second and third weeks to 31% in FLASH and 27.5% in CONV (**Figure 83**). Finally, in the fourth week, a slight decrease was observed compared to the third week, with the proportion of Mki67+ cells around 24% after both FLASH and conventional irradiation (**Figure 83**). In conclusion, these results **suggest significantly different cell division dynamics in the lungs after 13 Gy irradiation between FLASH and conventional treatment**. Nevertheless, a trend of induced division over the weeks post-treatment is observed, which may reflect inflammatory or regenerative processes. For this reason, we then independently focused on each pulmonary sub-compartment. Examining the distribu-

tion of Mki67+ cells across the major sub-compartments identified, we observed that the majority of Mki67+ cells were still immune cells, with similar rates to those observed in other analyses at 24 hours post-treatment.

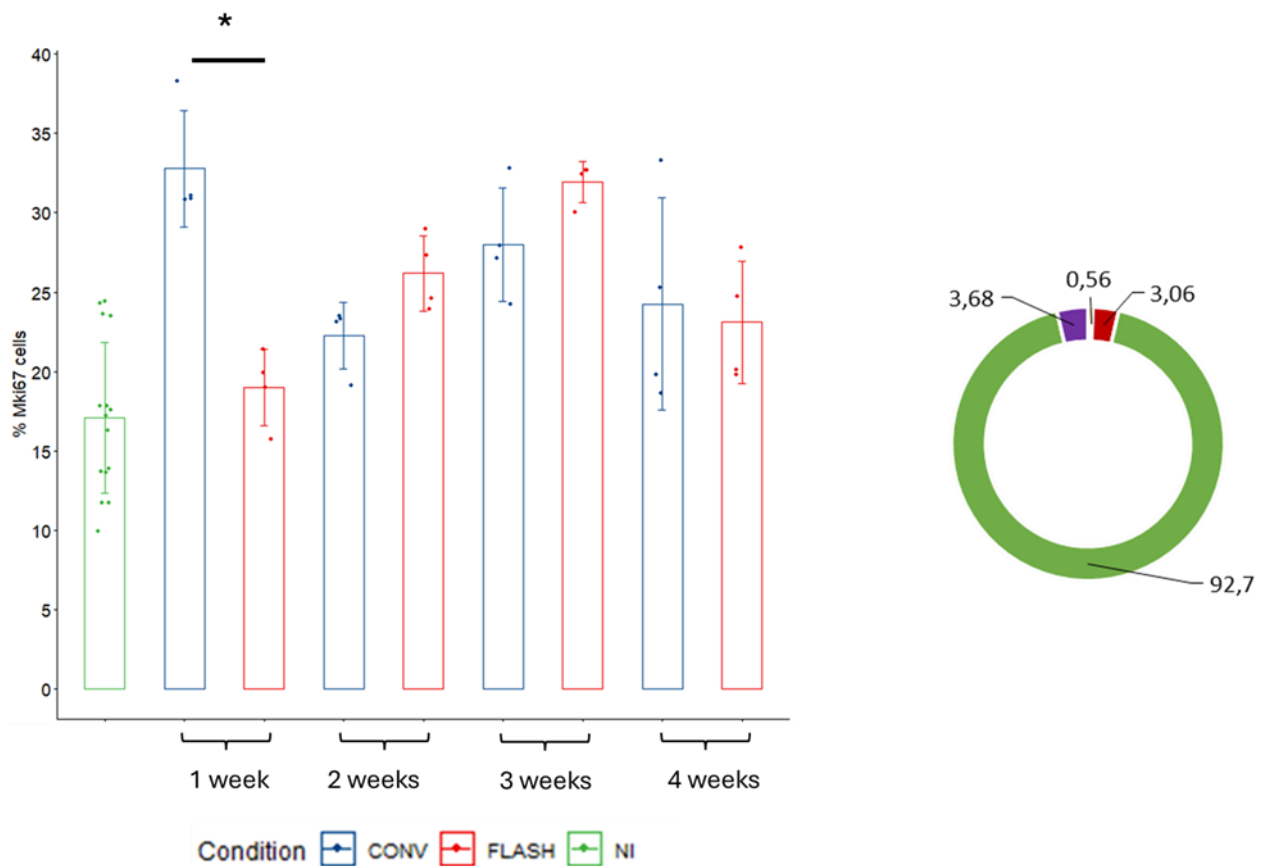


Figure 83. Dynamic of whole lung cell division after FLASH or CONV-RT at 13 Gy from 1 to 4 week post-treatment.

Using the Cd45 marker, we were able to further investigate the division dynamics of immune pulmonary cells. Following irradiation, inflammatory processes are triggered, inducing the division of T cells, alveolar macrophages, and other populations that can be recruited into the lung. These cells represent the majority of Mki67+ cells in the lung, and we observed a similar trend to that seen across all lung populations (**Figure 84**). At 1-week post-irradiation, the significant increase in the proportion of Mki67+ immune cells after conventional treatment compared to FLASH and NI conditions. This suggests the establishment of a significant inflammatory response following conventional irradiation. Subsequently, the proportion of Mki67+ immune cells seem to be higher after FLASH irradiation at 2 and 3 weeks post-treatment (**Figure 84**). Overall, these results suggest a potential differential dynamic of recruitment or division of immune cells in response to these two modalities, with a general trend of increased cycling cell proportions in the immune population.

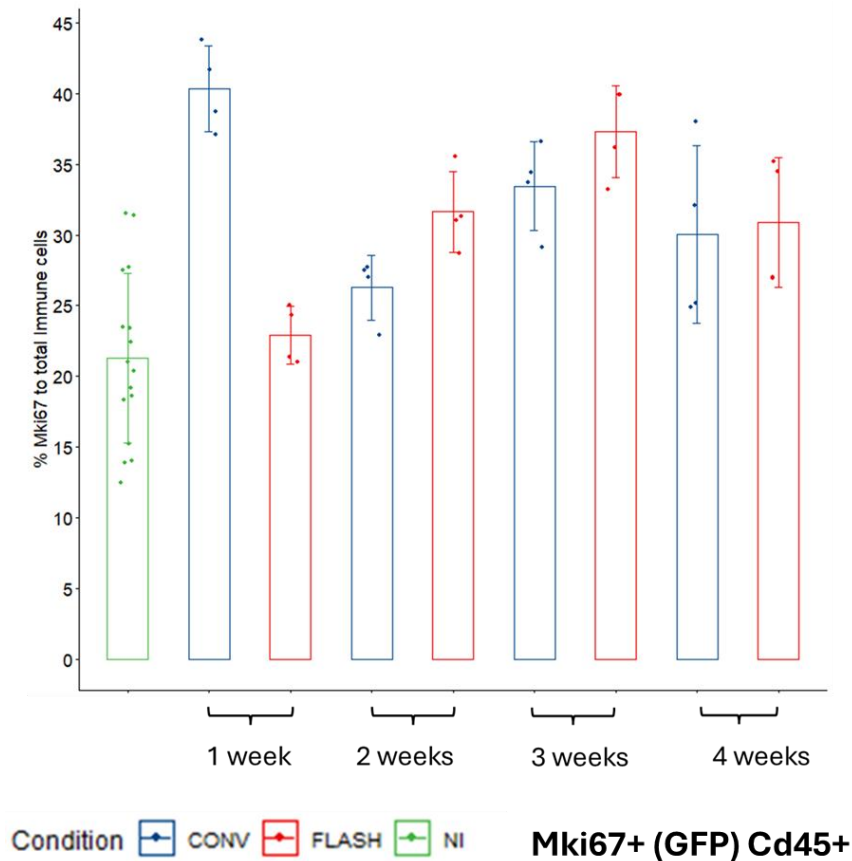


Figure 84. Dynamic of immune lung cells division after FLASH or CONV-RT at 13 Gy from 1 to 4-week post-treatment.

Then, we investigated Mki67+ cell division in the epithelial/mesenchymal compartment following irradiation. In the non-treated group (NI), a baseline proportion of around 2% of cells expressed or had expressed Mki67, several significant changes were observed post-irradiation. At 1 week post-irradiation, CONV-RT led to a moderate increase in the proportion of Mki67+ cells in the epithelial/mesenchymal compartment compared to NI and FLASH (**Figure 85**). The difference suggests a higher proportion of cycling cells in this compartment following conventional irradiation, which could be associated to early regeneration processes following radiation damages. By 2 weeks, the proportion of Mki67+ cells in the FLASH group showed a slight rise to 3%, like CONV group (**Figure 85**). In the third week, the trend continued with the proportion of Mki67+ cells reaching around 7% in the FLASH group and 9% in the CONV group, indicating sustained increased in cell cycling in the epithelial/mesenchymal compartment (**Figure 85**). At 4 weeks post-treatment, the proportion of Mki67+ cells in these compartments decreased to 2.5% after FLASH irradiation but remained higher after conventional irradiation at 4.8% (**Figure 85**). These results **suggest distinct regenerative**

dynamics between conventional and FLASH irradiation in the epithelial and mesenchymal compartments. This may indicate that conventional irradiation causes more significant short-term damage, but also results in a more persistent effect over time.

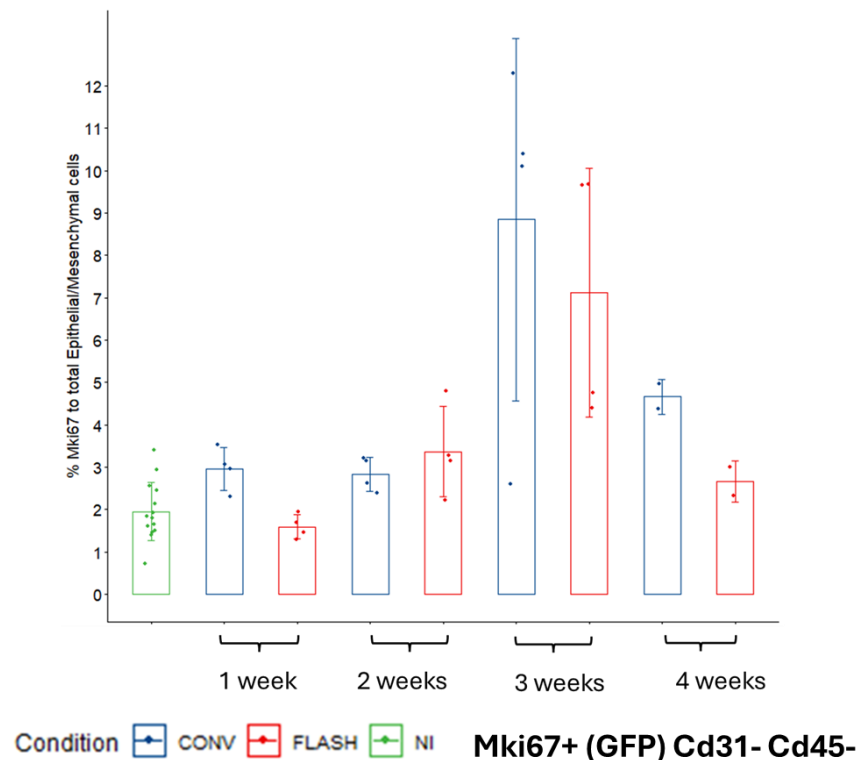


Figure 85. Dynamic of epithelial/mesenchymal cells division after FLASH or CONV-RT at 13 Gy from 1 to 4-week post-treatment.

Regarding the endothelial compartment, no increase in cell division was observed during the first week after FLASH or CONV-RT (**Figure 86**). A slight increase occurs after FLASH irradiation starting at 2 weeks, reaching 1.25% of total endothelial that are Mki67+ (**Figure 86**). At 3 weeks, despite significant heterogeneity, a major and drastic increase in the proportion of endothelial cells entering cell cycle is observed following both FLASH and conventional irradiation, with around 5% of endothelial cells being Mki67+ (**Figure 86**). Finally, at 4 weeks, this proportion is lower but still higher than in the untreated conditions, with a slightly higher rate after conventional irradiation (**Figure 86**). Overall, **these results do not suggest major differences in the regenerative dynamics and potential regeneration of endothelial cells following FLASH or conventional irradiation.** However, it is interesting to note a significant increase in endothelial cell division during the 3 weeks following treatment. To gain more insight into this peak of division, we decided to focus on the microvascular populations, which are known to be severely impacted by irradiation.

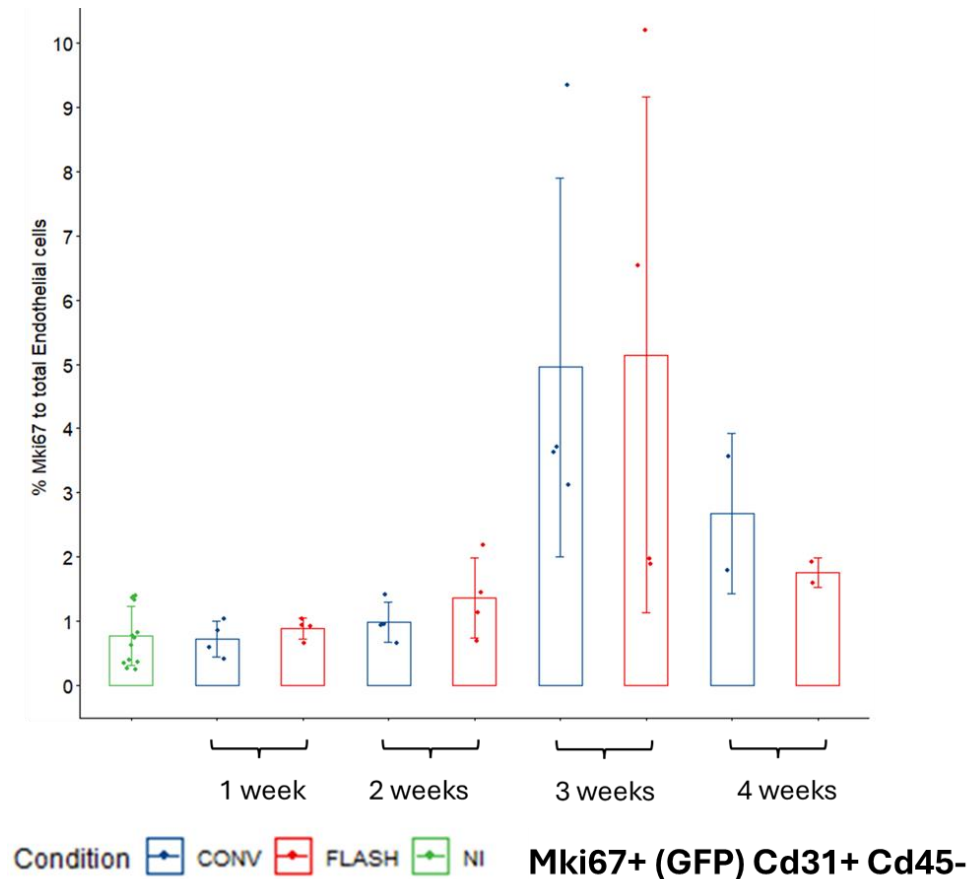


Figure 86. Dynamic of endothelial cells division after FLASH or CONV-RT at 13 Gy from 1 to 4-week post-treatment.

Using markers identified in our previous scRNAseq analyses, we were able to identify the microvascular populations of aCap and gCap within the endothelial compartment (**Figure 87**). To recap, aCap play a crucial role in facilitating gas exchange within the alveoli, while gCap are involved in tissue homeostasis and microvascular integrity. Notably, gCap are responsible for regenerating the pool of aCap after damage, indicating their role as progenitor cells for this population. Focusing on aCap, we observed a significant increase in the proportion of aCap expressing or having expressed Mki67 as early as 1- and 2-weeks post-irradiation (**Figure 87**). It is likely that these Mki67+ aCap originate from gCap that have divided and differentiated into aCap. This suggests that the proportion of Mki67+ aCap reflects capillary regeneration in response to irradiation-induced damage. As with all endothelial cells, we noticed a dramatic increase in the proportion of Mki67+ aCap, with a 4- to 5-fold rise at 3 weeks post-irradiation, indicating substantial regeneration of the aCap pool. When focusing on gCap, although the baseline proportion of Mki67+ cells is lower, a similar pattern is observed, with a slight increase in the first- and second-weeks post-irradiation, followed by a peak in division (**Figure 87**).

Interestingly, this peak appears more pronounced after conventional irradiation compared to FLASH, suggesting a greater need for regeneration in response to persistent microvascular damage caused by conventional irradiation (**Figure 87**). These data suggest a similar pattern of regenerative division, but with a more significant division of capillary progenitors at the critical 3-week time point in the lung. This process, although outside the scope of my thesis on FLASH mechanisms, is currently under investigation through scRNAseq analysis of these pulmonary vascular populations to unravel the dynamics and underlying mechanisms of this massive regeneration three weeks post-irradiation.

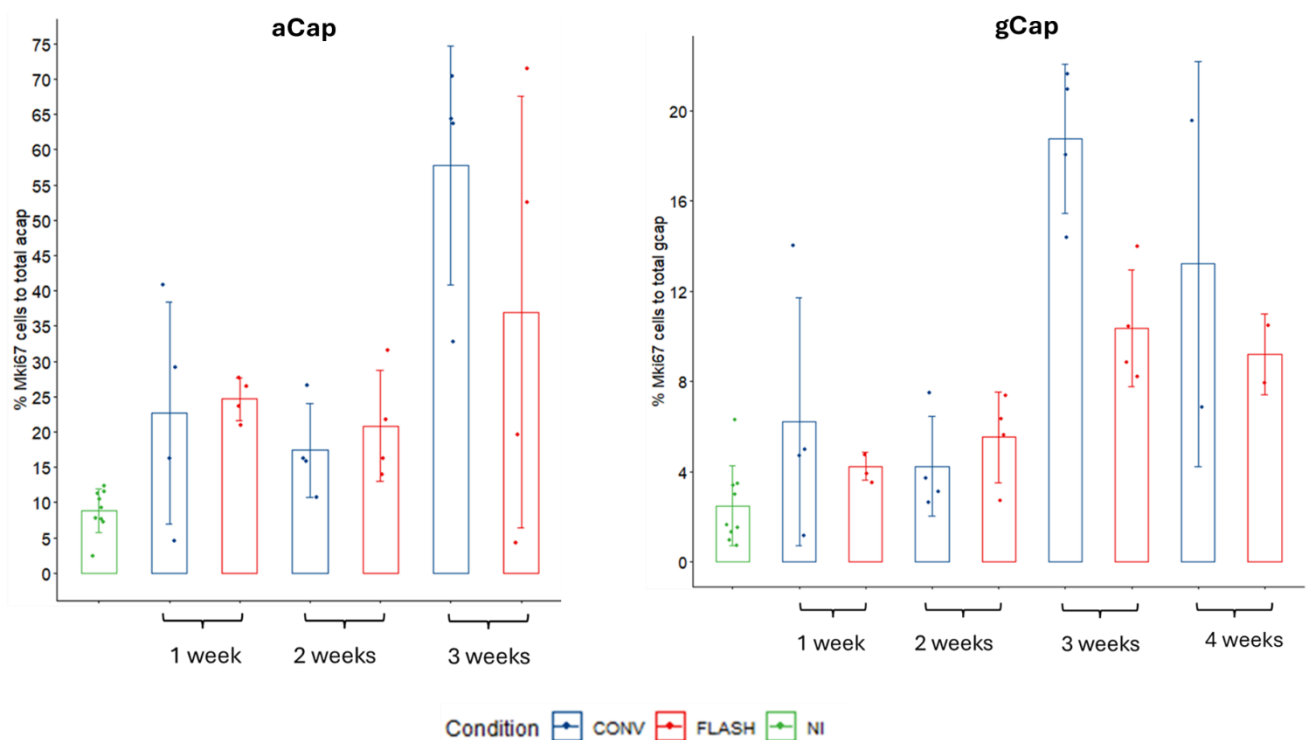


Figure 87. Dynamic of microvascular endothelial cells division after FLASH or CONV-RT at 13 Gy from 1 to 4-week post-treatment.

For the continuation of this project, we decided to **study the transcriptional changes that occur in cycling cell populations at very short-term post-treatment**, aiming to **investigate the underlying mechanisms of the FLASH effect in these populations**. However, an important challenge was to correctly determine the timing of induction and the post-irradiation analysis. Our goal was to examine the impact on cells that are actively cycling at the time of irradiation, not just those that remain and will enter the cell cycle later. To achieve this, **we chose to administer tamoxifen 24 hours prior to radiation treatment and to perform dissociation and scRNA-seq analysis 24 hours after irradiation**. In the following sections, I will present these preliminary results in detail, focusing on specific populations of interest.

1.3.4 Molecular insights of the FLASH sparing effect mechanisms in lung dividing cells

- a) Identification, characterization and distribution of Mki67+ cells after CONV or FLASH-RT in lung subpopulations.

To determine the molecular changes occurring in cells that are actively dividing or will divide following irradiation, we induced Mki67 Cre ERT2 x R26 mtmG mice 24 hours prior to treatment. The mice were then irradiated with a dose of 13 Gy, either by conventional or FLASH irradiation, while some mice remained untreated to serve as controls for our scRNA-seq analyses. After 24 hours post-treatment and 48 hours post-induction, we sorted the Mki67+ cells for scRNA-seq analysis (**Figure 88**). Interestingly, even with this induction protocol, we were able to detect an impact of irradiation on the proportion of cycling cells following both FLASH and conventional irradiation (**Figure 88**). Indeed, the proportion of Mki67+ cells went from 4% in non-treated mice to 2.2 in FLASH and 1.5% in CONV (**Figure 88**). These sorting results suggest that the FLASH effect is still preserved under these conditions (**Figure 88**). Due to the rarity of these populations, a pooled dissociation and sorting from three mice per condition was performed before proceeding with the analysis.

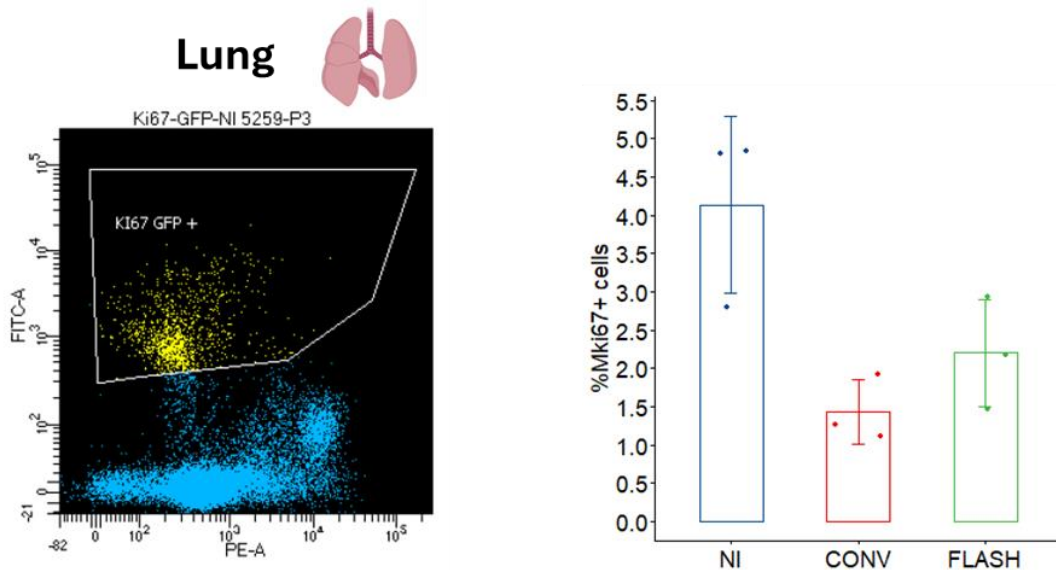


Figure 88. Sorting of Mki67+ cells for ScRNAseq at a dose of 13 Gy revealed a FLASH sparing effect.

Subsequently, we generated our analysis object in Seurat, which allowed us to differentiate the sorted cells based on their treatment condition (**Figure 89A**). We were able to identify the different subclusters using the markers we had previously defined (**Figure 89B**). Initially, we studied the distribution changes within our pulmonary subpopulations, including epithelial, immune (myeloid and lymphoid), mesenchymal, and endothelial populations (**Figure 89C-G**).

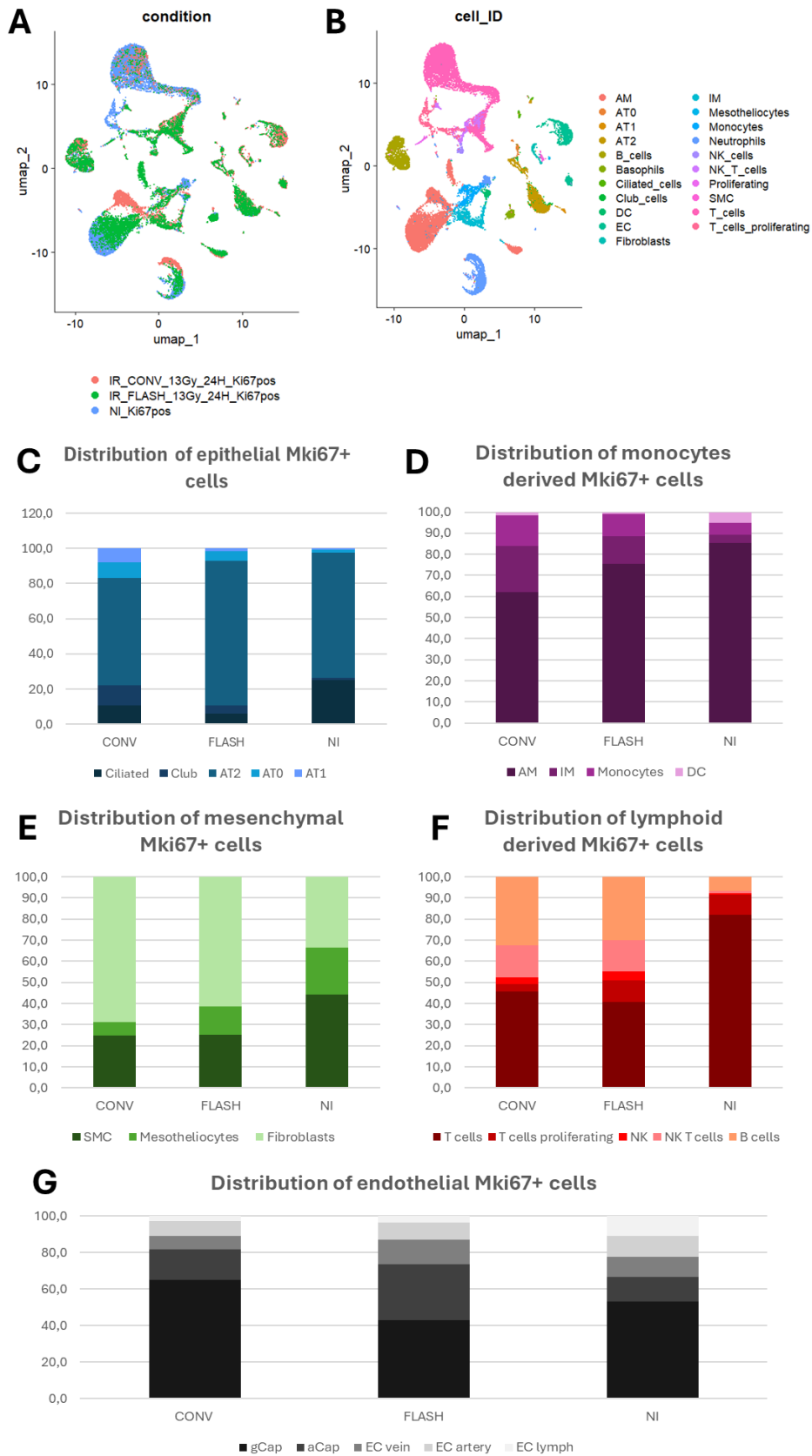


Figure 89. Identification and distribution of Mki67+ cells after CONV or FLASH-RT in lung subpopulations. (A) UMAP plot showing the distribution of Mki67+ cells across different

treatment conditions. (B) UMAP plot depicting the distribution of Mki67+ cells within the various lung subpopulations. (C) Bar plot showing the distribution of Mki67+ cells across epithelial subpopulations (Ciliated, Club, AT2, AT1). (D) Distribution of Mki67+ monocyte-derived cells such as AM, IM, Monocytes, and DCs. (E) Bar plot showing the distribution of Mki67+ mesenchymal-derived cells (SMC, Mesotheliocytes, and Fibroblasts) in each treatment condition. (F) Distribution of Mki67+ lymphoid-derived cells (T cells, Proliferating T cells, NK cells, B cells) across the different treatments. (G) Distribution of Mki67+ endothelial-derived cells (including capillary and artery endothelial subpopulations).

These results need to be correlated with the initial rates of dividing cells by condition. Indeed, the impact of irradiation significantly affects the proportion of Mki67+ cells, particularly the immune subpopulations, which consequently impacts the distribution in our scRNA-seq dataset. This is why the distribution analyses are done by sub-compartments, but it is important to keep in mind the initial rate of sorted Mki67+ cells and the fact that each dissociation may introduce a bias in the selection of certain populations. Therefore, this distribution analysis is primarily qualitative and requires further validation.

Concerning the distribution of epithelial cell populations, ciliated cells significantly decrease in both FLASH (5.9%) and CONV (10.5%) compared to NI (25.1%), indicating a potential impact of irradiation on these Mki67+ ciliated cells (**Figure 89C**). Club cells show an increase, with FLASH (5%) and CONV (11.8%) values higher than the NI condition (1.1%), highlighting a potential division of these cells or associated progenitors following radiation exposure (**Figure 89C**). AT2 cells show an increase in FLASH (82.2%) compared to CONV (60.7%) and NI (71.2%) (**Figure 89C**). This is associated with a clear increase in AT0 cells expressing Mki67 following both FLASH (5.5%) and CONV (9%) conditions compared to NI (1.9%), It could reflect how AT2 could divide, transition to AT0 state to regenerate alveoli, which could be more affected in CONV (**Figure 89C**). In the same manner, the proportion of AT1 cells expressing Mki67, which could be derived from AT2 cells division is significantly upper after CONV (8%) compared to NI (0.7%) and FLASH (1.4%) (**Figure 89C**). Overall, CONV seems to induce a greater loss of epithelial populations which could be associated with disrupted distribution of dividing cells indicating a clear transition from AT2 to AT0 and AT1 state compared to FLASH and non-treated conditions.

In terms of monocyte-derived populations, the distribution of Mki67+ cells varies significantly across the conditions. In the AM (alveolar macrophages) population, the proportion of Mki67+ cells is highest in non-irradiated conditions (NI), with about 85.3%, compared to 75.3% in the

FLASH condition and 62.2% in the CONV condition (**Figure 89D**). This suggests that the AM population is relatively preserved in terms of cell division after FLASH irradiation, though a slight decrease is observed with conventional irradiation (**Figure 89D**). In contrast, the IM (interstitial macrophages) population shows a notable increase after FLASH (13.2%) and CONV condition (21.9%) (**Figure 89D**). The IM population in non-irradiated conditions shows a much lower proportion of Mki67+ cells (3.9%), indicating that irradiation may induce recruitment and cell division of this subpopulation, especially after CONV-RT (**Figure 89D**). Monocytes also shows an increase in cell division in both irradiated conditions, with 14.3% Mki67+ cells in CONV, 10.5% in FLASH, and 5.5% in NI, further indicating a potential recruitment following radiation in the lung (**Figure 89D**). Lastly, the DC (dendritic cells) population that express Mki67 seems affected by irradiation with 5.3% in NI, 1.6% in CONV, and 0.9% in FLASH (**Figure 89D**). Overall, these results suggest that in the monocyte-derived populations expressing or having expressed Mki67, there is a decrease in the proportion of resident alveolar macrophages, accompanied by an increase in pulmonary monocyte and interstitial populations. This shift could reflect blood recruitment and an inflammatory response following irradiation of monocytes, with this effect appearing more pronounced after conventional irradiation compared to FLASH.

The mesenchymal Mki67+ populations represent only a small fraction of the cells identified in our dataset. However, after both FLASH and conventional irradiation, we observed an increase in the proportion of fibroblasts compared to other mesenchymal cells, possibly indicating cell division in response to irradiation (**Figure 89E**). This effect was slightly more pronounced after conventional irradiation than after FLASH.

In the lymphoid immune populations, post-irradiation, there was a significant decrease in the proportion of T cells, which represent 82% of these populations in the non-irradiated (NI) condition and drop to 40.7% and 45.5% after FLASH and conventional irradiation, respectively (**Figure 89F**). The proportion of T lymphocytes in active division, expressing markers such as Top2a and Mki67, was only decreased after conventional irradiation, dropping to 3.8% (**Figure 89F**). These results suggest a preservation of T cell populations in cycle after FLASH irradiation, but it also seems that irradiation significantly impacted the resident T lymphocyte populations in the lungs, regardless of the irradiation modality. Variations in other populations simply reflect the decrease in the proportion of T cells expressing or having expressed Mki67.

Finally, in the endothelial sub-compartments, we observed an increase in the proportion of aCap Mki67+ cells compared to other compartments after FLASH irradiation, representing 30.8% of the endothelial cells (**Figure 89G**). This may suggest a rapid division of gCap cells in response to FLASH irradiation compared to endothelial cells irradiated with conventional radiation.

Subsequently, we focused on the expression of the marker Mki67 in our sorted cell population. Indeed, although these cells were sorted based on GFP expression following recombination in the Mki67 Cre ERT2 Tdtomato/GFP model, these cells stably express GFP as soon as they start expressing this marker. Thus, when examining the expression of this marker in our population, we observed that very few cells actively express Mki67 (**Figure 90A**). Specifically, a cluster of T cells strongly expresses it, suggesting they are actively dividing, the same applies to some subpopulations of macrophages and monocytes (**Figure 90A**). Beyond this, the expression of this marker appears distributed across other subcompartments, making it difficult to isolate cells that are actively cycling. When performing differential analyses between our unsorted population at 24 hours (described in section II) and our Mki67-sorted population, we still observed an upregulation of genes involved in and associated with the cell cycle and its progression, confirming that these cells had been or were still cycling (**Figure 90B**). These findings suggest that after tamoxifen induction 24 hours before treatment, cycling cells that began expressing Mki67 already divided, and for the majority of them, they were likely no longer actively cycling at the time the scRNA-seq analysis was performed. Nevertheless, we checked the expression of Mki67 in these sorted cells, and interestingly, we observed a decrease in marker expression following both FLASH and conventional irradiation (**Figure 90C**). Furthermore, Mki67 was expressed at significantly lower levels after conventional irradiation compared to FLASH, once again suggesting and confirming an impact on cells capable of entering the cell cycle 24 hours post-treatment (**Figure 90C**).

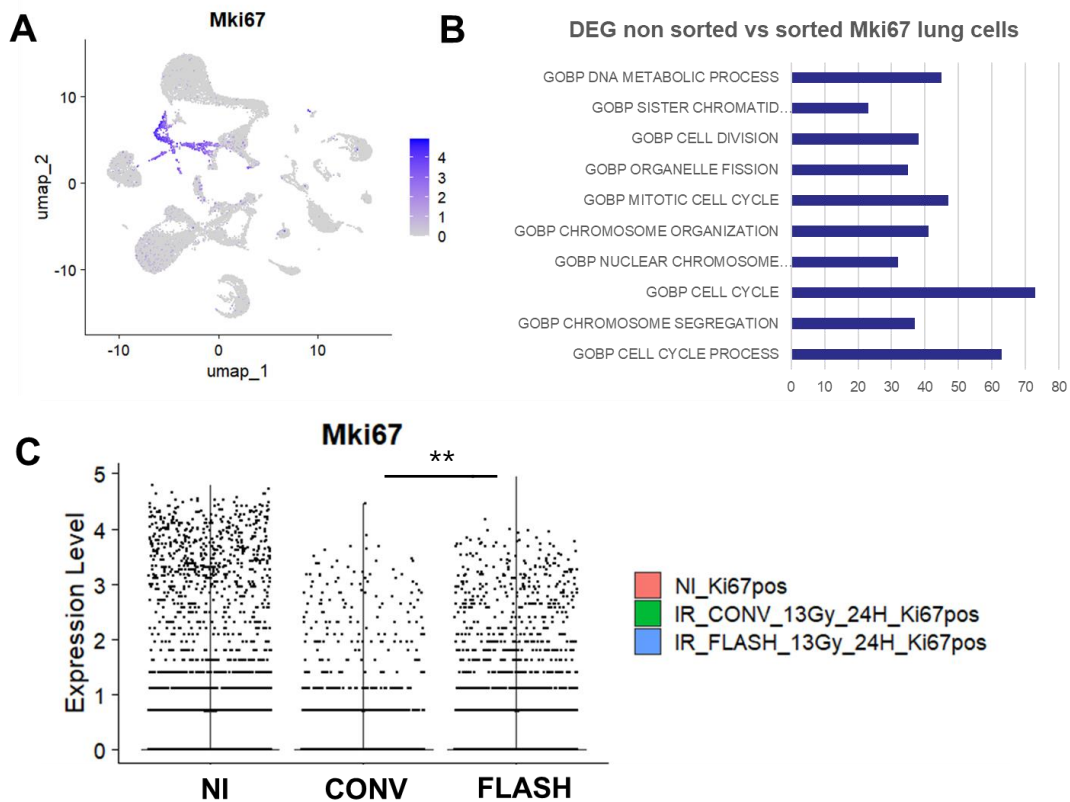


Figure 90. Characterization of cell division markers in Mki67 sorted populations across conditions. (A) UMAP showing Mki67 expression level across lung sorted dividing cells. (B) DEG between non sorted and sorted analysis shows upregulation of cell cycle pathways in lung sorted Mki67 cells. (C) Violin plot showing Mki67 expression across conditions in whole lung Mki67 dividing cells.

Subsequently, **we focused on the transcriptional changes occurring after conventional irradiation compared to FLASH in all pulmonary Mki67 subpopulations.** It is important to note that for certain populations, very few cells could be sorted, which limits the detection of transcriptional changes. This is the case for AT1 cells, club cells, ciliated cells, and the subpopulations of SMCs and mesotheliocytes as well. It should also be emphasized that this analysis was conducted using cells sorted as having expressed or currently expressing Mki67 in the lung within 24 hours before and after then 24 hours treatment. As previously identified, it turns out that only a small proportion of the sorted cells still actively express cell division markers like Mki67, which means that most of these cells were in the cell cycle prior to the scRNAseq analysis.

- b) FLASH-RT could enhance immune recruitment in endothelial Mki67+ cells compared to CONV-RT which favors endothelial cell division.

At very short times post-irradiation, endothelial cells are known to be strongly impacted, ionizing radiation can activate TNF, which hydrolyses sphingomyelin, generating ceramide. This ceramide activates MAPK, ERK, SEK1 and c-Jun, which can modify the dynamics of the cell membrane and start a cascade of events that lead to EC apoptosis²⁰⁷. When we investigated the differentially expressed genes between FLASH and CONV-RT in endothelial cell populations expressing Mki67 (**Figure 91A**), we identified an upregulation of genes associated to angiogenic processes, such as Vegfa³³⁷, a growth factor associated with endothelial cells, and Kit³³⁸, which promotes the division of microvascular cells (gCap) (**Figure 91B**). Thus, our data suggests a stronger induction of genes associated with pathways involved in endothelial regeneration after conventional irradiation compared to FLASH in sorted Mki67+ endothelial subpopulations. This could indicate a more significant impact of radiation on endothelial populations, leading to active regeneration in our sorted Mki67 endothelial cells. In the whole lung, in section II, we observed a downregulation of genes involved in mitochondrial functions in endothelial cells, which could be associated with a stronger impact on endothelium following CONV-RT. Indeed, mitochondrial endothelial cell function has been reported to be involved in several processes such as inflammatory activation following injury³³⁴.

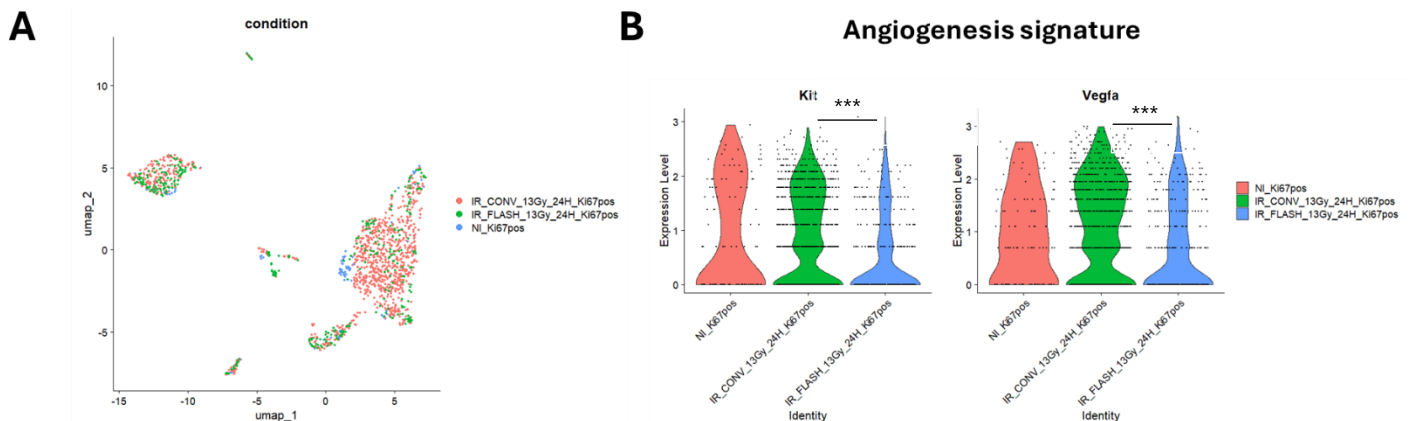


Figure 91. CONV-RT induces active endothelial regeneration related genes compared to FLASH-RT. (A) UMAP visualization of endothelial cells by experimental conditions. The different colors represent the following conditions (B) Violin plot representing the expression angiogenesis related genes (Kit and Vegfa) across experimental conditions in endothelial Mki67 cells.

In FLASH, within Mki67+ sorted endothelial cells, we identified the upregulation of about twenty genes involved in various inflammatory processes (**Figure 92A**). We observed that several were associated with the recruitment and activation of different immune cell populations, such as *Lgals3*, which is involved in innate immune responses and the modulation of T cell activity (**Figure 92B**). This was also associated with the upregulation of *Ly6e* expression, which regulates T cell proliferation, differentiation, and activation (**Figure 92B**). Additionally, a few cells seemed to express *Ccr2*, which is involved in the attraction of monocytes and macrophages and regulates T cell activation and differentiation as well (**Figure 92B**). These data suggest a stronger inflammatory activation profile in endothelial cells expressing Mki67 in the lung following FLASH-RT. This may be linked to immune cell recruitment and the regulation of several immune populations via endothelial cells. This was also associated with the upregulation of various mitochondrial genes, as noted earlier in section **part IV-1.3.6** of the results. These data suggest a greater endothelial inflammatory activation after FLASH irradiation, which could be associated with distinct immune recruitment and modulation. Consequently, we decided to focus on the differential impact of these two irradiation modalities on T lymphocytes, which are rapidly recruited after irradiation and are involved in the establishment of the acute immune response in the lung.

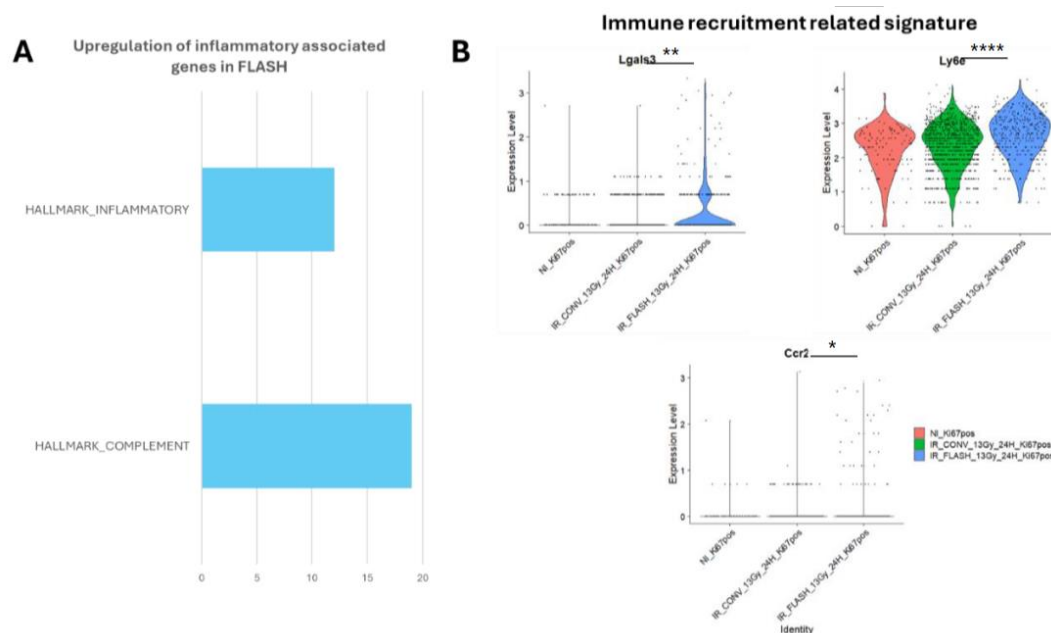


Figure 92. Endothelial cells exacerbate an inflammatory signature related to immune recruitment after FLASH-RT. (A) Boxplot showing the DEG upregulated signatures after FLASH vs CONV-RT in endothelial Mki67 cells. (B) Violin plots displaying the expression levels of immune recruitment-related genes, including *Lgals3*, *Ly6e*, and *Ccr2*, across different conditions in endothelial Mki67 cells.

c) FLASH-RT induces OXPHOS mitochondrial associated genes upregulation compared to CONV-RT in T-cells

We performed DEG analyses between our Mki67+ sorted T cells irradiated with CONV or FLASH in the lung, and interestingly, in addition to genes involved in classic radiation responses (such as P53) and T-cell division (MYC_target), we identified an upregulation of over 30 genes involved in mitochondrial function, particularly those encoding enzymes in the respiratory chain (**Figure 93A**). Upon closer inspection of the expression of some of these genes, we found a common upregulation in T-cells after irradiation, with a significantly stronger effect after FLASH irradiation (Figure 93B). This was the case for several genes encoding subunits of cytochrome c oxidase, components of complex I, and ATPase (**Figure 93B**). According to the literature, mitochondrial activity is strongly associated with activation and proliferation processes in T lymphocytes³³⁹. The overproduction of ROS through the mitochondrial pathway may play a role in T lymphocyte proliferation but may also determine the differentiation program of these cells³³⁹. Furthermore, it has been noted that T cell exhaustion can be reversed by upregulating mitochondrial functions³³⁹. These data suggest that after irradiation, there is an increase in mitochondrial function in T lymphocytes that expressed Mki67, with this effect being much more pronounced after FLASH irradiation. This could be associated with a more active division program after FLASH irradiation and may be linked to a distinct inflammatory response between the two modalities. Subsequently, we focused on the genes that were upregulated after conventional irradiation in T cells to investigate potential different mechanisms involved.

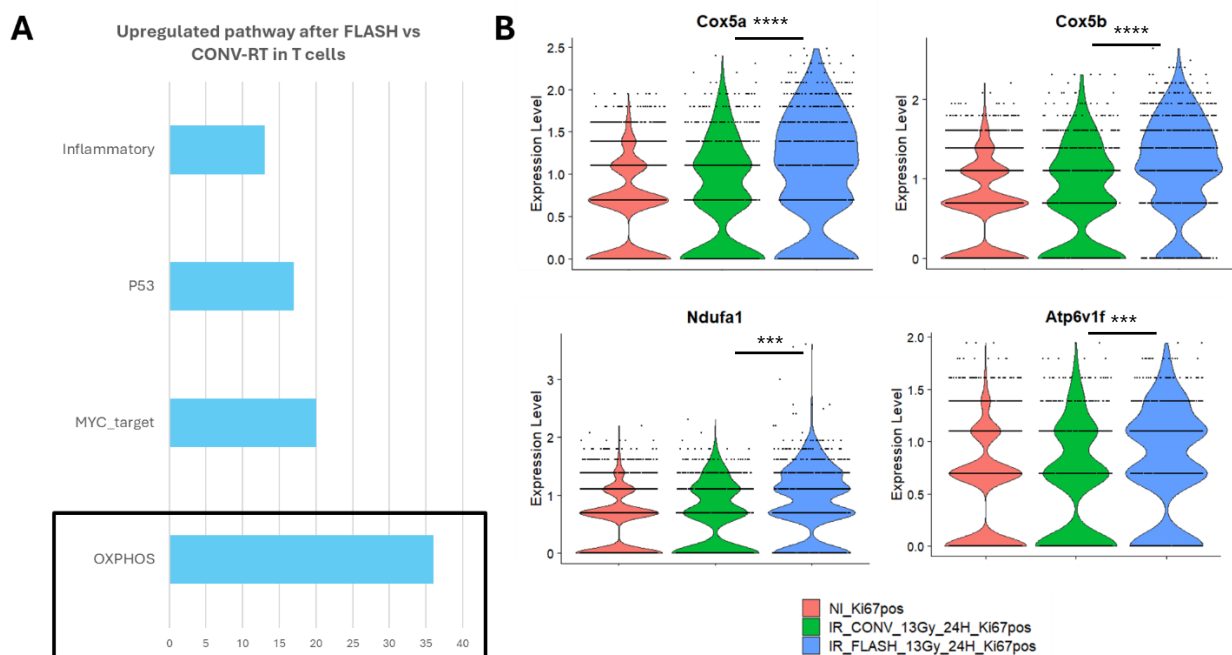


Figure 93. FLASH-RT induces an upregulation of mitochondrial associated OXPHOS chain genes compared to CONV-RT in T cells. (A) Bar plot showing the upregulated pathways in T cells after FLASH irradiation compared to CONV-RT, highlighting the OXPHOS pathway as the most significant. (B) Violin plots showing the expression levels of OXPHOS respiratory associated genes *Cox5a*, *Cox5b*, *Ndufa1*, and *Atp6v1f* across different conditions.

d) CONV-RT induces specific upregulation of TNF α via NFKB related genes in various immune lung Mki67+ cells

After conventional irradiation, we observed a stronger activation of genes associated with cell cycle arrest (G2M_checkpoint) and the classical irradiation response (P53, UV_response) (**Figure 94A**). Additionally, there was a significant upregulation of inflammatory genes, particularly those linked to the IFN α , IFN γ , and especially the TNF α via Nfkb pathway, which were notably elevated in T cells expressing Mki67 (**Figure 94A**). When we zoomed in on the genes upregulated within the Nfkb pathway, we identified a strong upregulation of transcription factors such as Junb, Fos, and Nfkb transcriptional activator (**Figure 94B**). The dimerization of c-Jun and Fos may be involved in the classical inflammatory response that is typically reported early after irradiation^{340–342}. This could trigger various inflammatory pathways but also exert anti or pro-apoptotic effects and regulate the cell cycle. The activation of the AP-1 transcription factor (the Fos/Jun complex) could also be linked to the regulation of Tgfb1 expression³⁴³. These data suggest a distinct inflammatory profile and response in T cells expressing Mki67 after conventional irradiation. Subsequently, we decided to focus on other immune compartments to explore whether similar changes could also be observed there.

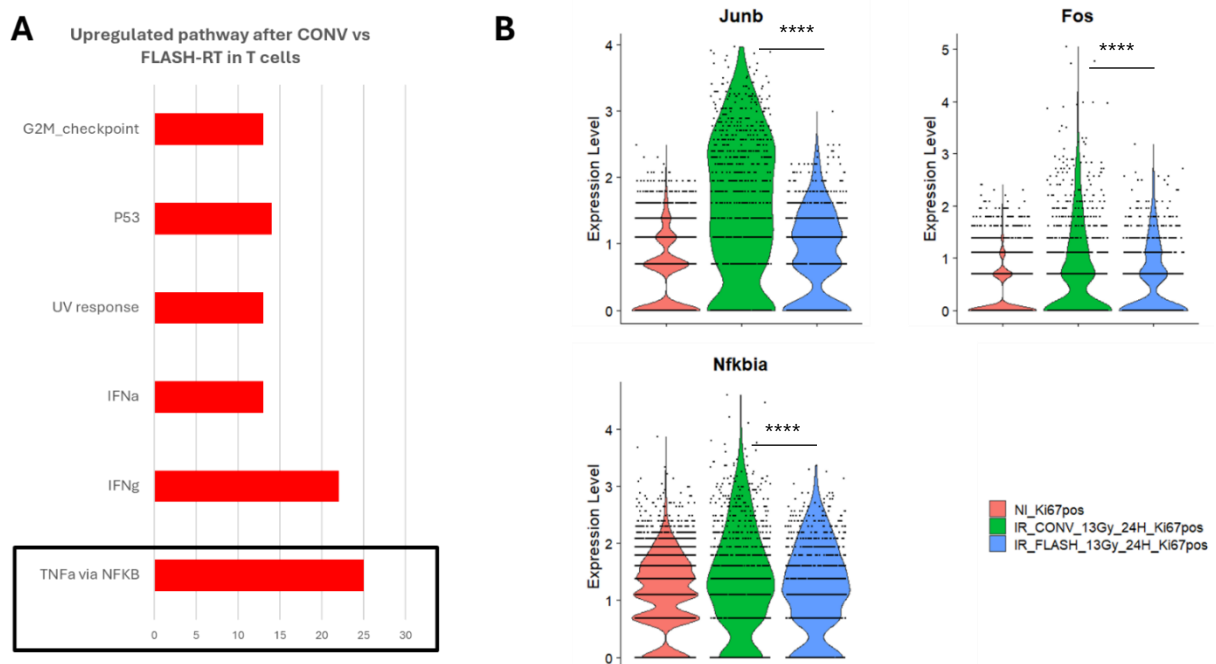


Figure 94. CONV-RT induce an upregulation of TNF α via NFKB related genes in T-cells compared to FLASH-RT. (A) Bar plot showing the upregulated pathways in T cells after conventional irradiation compared to FLASH-RT, highlighting the TNF α signaling via NFKB as the most upregulated pathway. B. Violin plots depicting the expression levels of key inflammatory genes (*Junb*, *Fos*, and *Nfkbia*) across the different conditions.

Through an in-depth analysis of differentially expressed genes after conventional irradiation compared to FLASH in the immune compartments of the lung (T cells, neutrophils, monocytes, DC, alveolar and interstitial macrophages), we also identified a significant common upregulation of genes associated with the TNF α via Nfkb pathway, with up to 64 genes upregulated in alveolar macrophages (**Figure 95A**). We then sought to determine if any of these genes were common across all immune subpopulations. As a result, we identified a list of 12 genes that were upregulated after conventional irradiation compared to FLASH in at least 5 of the 6 immune compartments analyzed (**Figure 95B**). Among these, we found *Btg1* and *Btg2*, which have been associated with the negative regulation of T cell division and apoptotic regulation^{344,345}. Additionally, we observed a common upregulation of genes associated with the transcription factors *Junb*, *Jun*, *Fos*, and *Fosb*, which together form the AP-1 transcription factor.

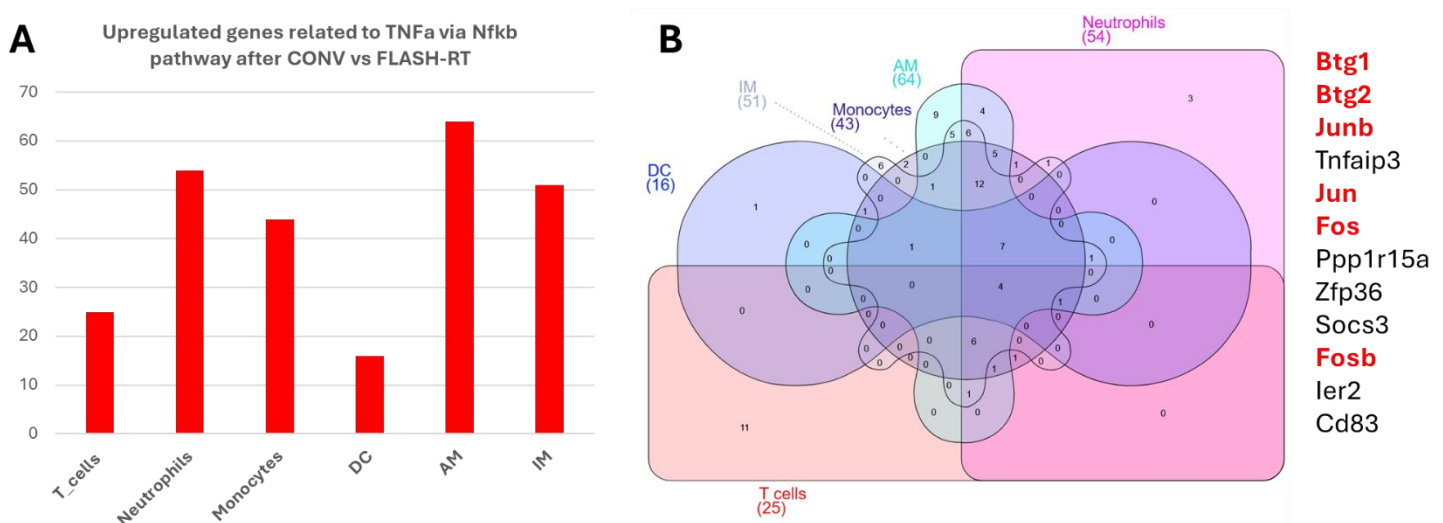


Figure 95. TNF α via NFKB related genes are commonly upregulated after CONV-RT in various immune cells populations. (A) Bar plot showing the number of upregulated genes related to the TNF α via NFKB pathway in T cells, macrophages (AM), monocytes, neutrophils, and dendritic cells (DC) after conventional vs FLASH-RT. (B) Venn diagram depicting the overlap of upregulated TNF α -related genes across the various immune cell populations. Common gene names of interest are highlighted in red (e.g., *Btg1*, *Junb*, *Fosb*).

Indeed, after FLASH-RT, across all immune sub-compartments, there is a slight, non-significant upregulation of these 4 genes compared to non-irradiated immune cells. However, after conventional irradiation, there was a major and common upregulation of Fos, Fosb, Jun, and Junb across all Mki67+ immune sub-populations (**Figure 96**). This effect is most pronounced in alveolar macrophages, which exhibited the highest upregulation of inflammatory signatures after conventional irradiation (**Figure 96**). These data suggest a potential shift towards an inflammatory response directed by the TNF α via NF κ b pathway, particularly through the genes encoding the AP-1 transcription factor, which is involved in numerous mechanisms ranging from the regulation and modulation of inflammation to the regulation of apoptosis.

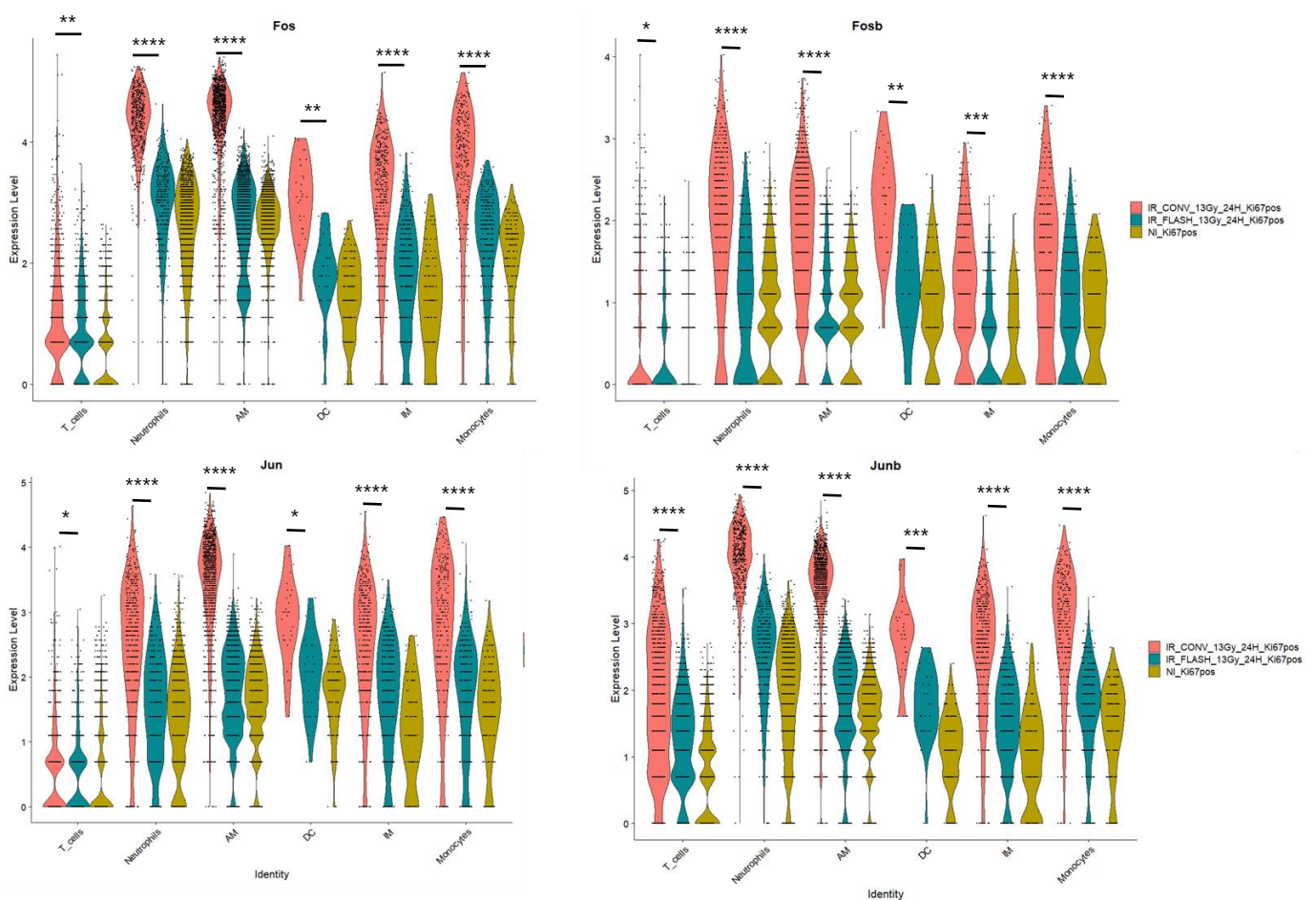


Figure 96. Common upregulation of AP-1 transcription factor related genes in immune Mki67 compartment after CONV-RT. *VinPlot* shows the expression of Fos, Fosb, Jun and Junb genes in T cells, neutrophils, AM, IM, DC and Monocytes across condition.

In some of these sub-compartments, particularly in neutrophils, we observe that the CONV-irradiated cluster is transcriptionally much farther away from both the FLASH-irradiated and non-treated neutrophils (**Figure 97A**). We characterized the markers associated with this cluster, and these are linked to the TNF α -mediated inflammatory response via NF κ b, as previously described, showing a major upregulation of genes such as Fos (**Figure 97B**).

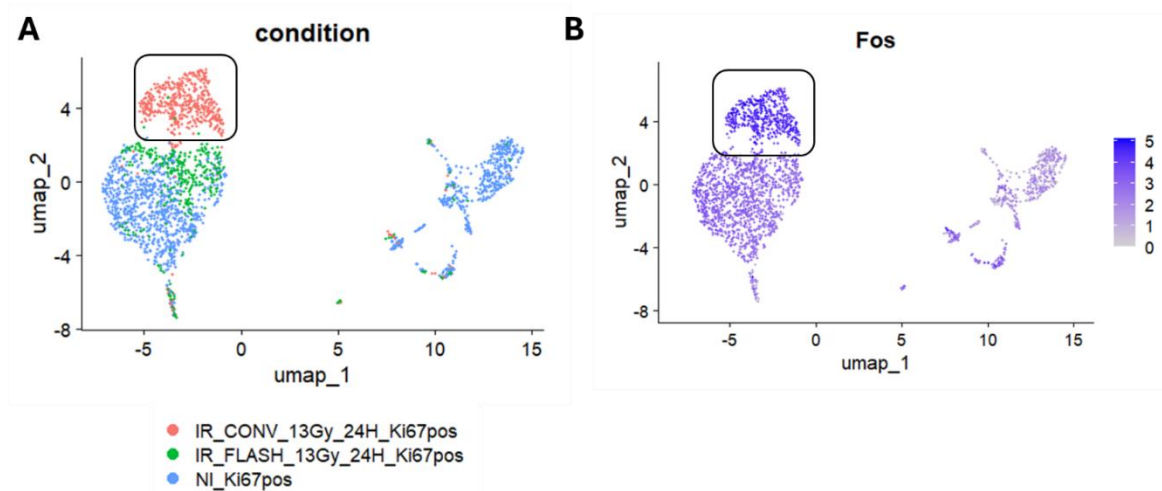


Figure 97. Identification of an inflammatory and AP-1 related cluster of Neutrophils after CONV-RT. (A) UMAP plot showing the distribution of Neutrophils MKi67 sorted cells across different conditions. (B) UMAP plot of Fos expression across Neutrophils MKi67 sorted cells showing an upregulation in CONV-RT associated cluster.

In monocyte populations, we also identified a cluster specific to conventional irradiation (**Figure 98A**). Similarly, this cluster was associated with an inflammatory response via upregulated NF κ b and exhibited higher expression levels of Fos as shown in the feature plot in **Figure 98B**.

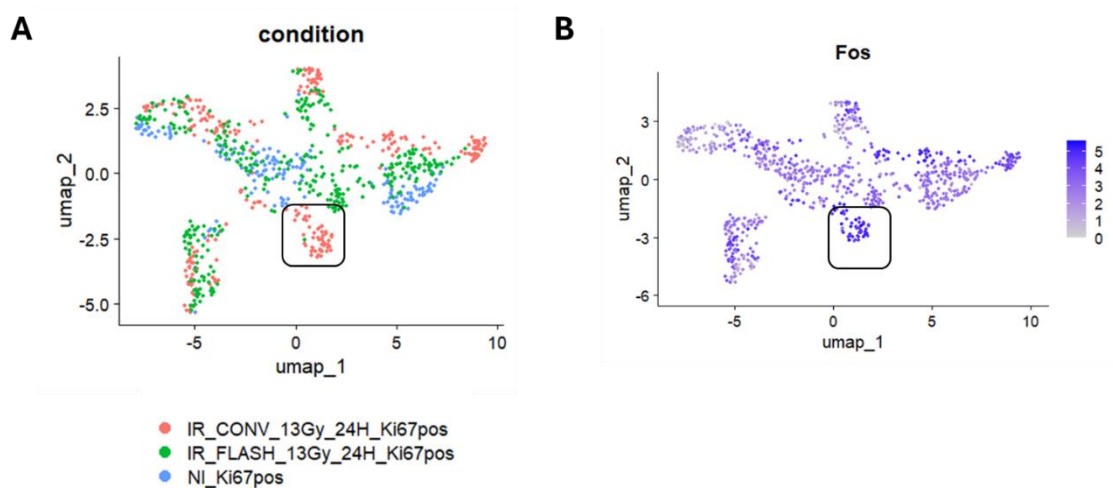


Figure 98. Identification of an inflammatory and AP-1 related cluster of Monocytes after CONV-RT. (A) UMAP plot showing the distribution of Monocytes MKi67 sorted cells across different conditions. (B) UMAP plot of Fos expression across Monocytes MKi67 sorted cells showing an upregulation in CONV-RT associated cluster.

Finally, in alveolar macrophages, we observe a distinct separation of several clusters irradiated with either conventional or FLASH treatment compared to the non-treated macrophages (**Figure 99A**). The specific cluster irradiated with conventional radiation is also associated with the expression of inflammatory genes linked to the TNF α pathway via NF κ b, and it shows an increased expression of the Fos gene (**Figure 99B**).

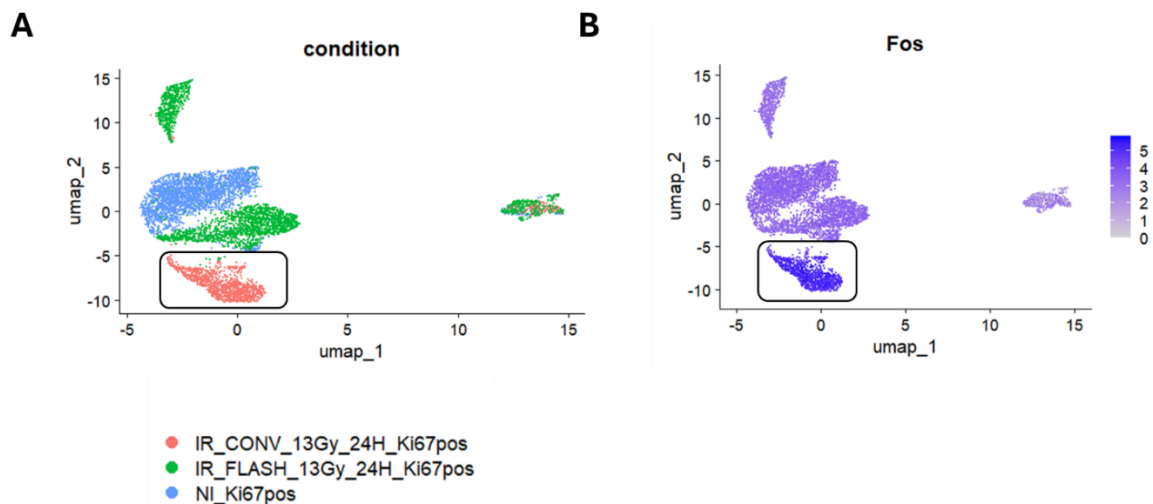


Figure 99. Identification of an inflammatory and AP-1 related cluster of AM after CONV-RT. (A) UMAP plot showing the distribution of AM MKi67 sorted cells across different conditions. (B) UMAP plot of Fos expression across AM MKi67 sorted cells showing an upregulation in CONV-RT associated cluster.

- e) CONV-RT induces an upregulation of anti-proliferative T cells factors Btg1 and Btg2 in various immune cell types

Regarding the two genes Btg1 and Btg2, which were identified as commonly upregulated across immune subpopulations after CONV-RT, we observe, similarly to Fos and Jun, a slight upregulation after FLASH irradiation compared to non-treated conditions (**Figure 100A**). However, in all immune subpopulations, including T cells, neutrophils, alveolar macrophages (AM), dendritic cells (DC), interstitial macrophages (IM), and monocytes, there was a significant and substantial upregulation of these two genes after CONV-RT (**Figure 100B**). As mentioned earlier, these genes have been associated with the modulation of T cell division. Given that these genes are upregulated across all pulmonary immune populations, we focused on the T cell subpopulations that actively express division markers like Mki67 (**Figure 100B**). Interestingly, we observed that the number of T cells actively dividing was lower after CONV vs FLASH-RT, suggesting a more pronounced impact on T cell division in the lung following conventional irradiation, which may correlate with the stronger expression of Btg1 and Btg2 in other immune compartment.

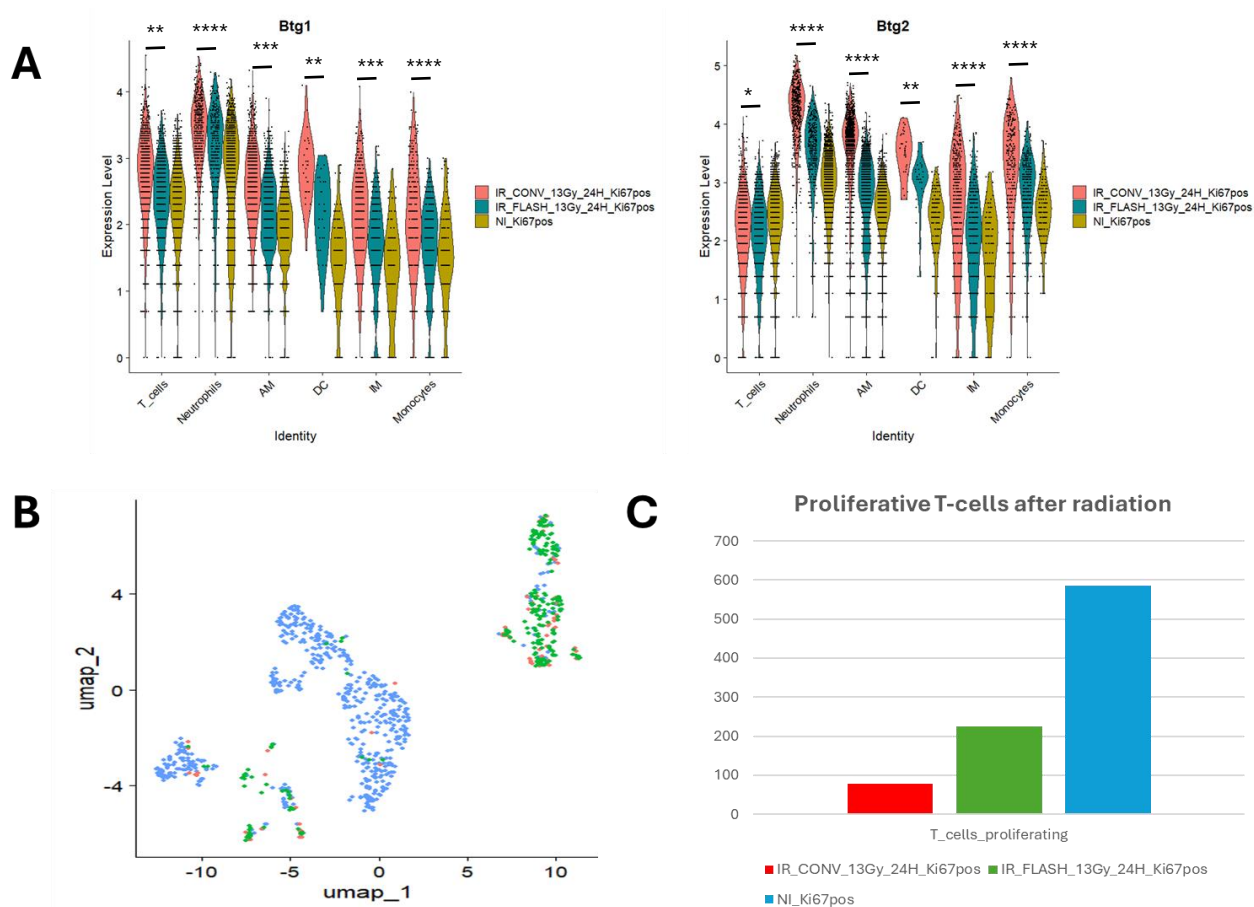


Figure 100. CONV-RT induces an upregulation of Btg1 and Btg2 in various immune Mki67 sorted cell types which is associated with a drop in active dividing T cells. (A) Violin plots showing the expression levels of Btg1 (left) and Btg2 (right) in different immune sorted Mki67 cells across the conditions (B) UMAP plot displaying the distribution of proliferating T-cells across conditions. (C) Bar plot showing the count of proliferating T-cells after radiation in different conditions.

f) FLASH-RT induces an upregulation of MIF factor expression in T cells

In addition to the observed differences in mitochondrial gene activation in T cells after FLASH versus conventional irradiation, we identified significant upregulation of the MIF gene. Firstly, after conventional irradiation, a slight upregulation of this factor was observed, which was even more pronounced following FLASH-RT (**Figure 101**). The MIF gene encodes a cytokine that promotes immune cell recruitment, but its functions extend beyond this and could

be link to epithelial regeneration in the lung^{346,347}. Its upregulation was correlated with the up-regulation of the gene coding for the CD74 receptor, which serves as the receptor for MIF. The interaction between MIF and CD74 has been shown to initiate survival and proliferation pathways associated with wound healing^{346,347}. CD74 expression has been observed to increase in response to inflammation, injury, or cancer and can be regulated by interferon gamma^{346,347}. Notably, in our dataset, the upregulation of MIF is specific to T cells expressing Mki67 in the lung after FLASH irradiation (**Figure 101**).

We then focused on the expression of its receptor, CD74, across various pulmonary subpopulations. Indeed, this pathway has been described in the lung in the context of acute injury from a variety of causes. These lung injuries lead to damage of the epithelium. Type I cells are more susceptible to damage and are largely destroyed during lung injury, while type II cells work to regenerate the alveolar epithelium, contributing to the repair process. Type II cells express are known to express CD74 on their surface, and during acute injury, cells could release macrophage migration inhibitory factor (MIF)^{346,347}. Extracellular MIF has been described to bind to CD74 on adjacent type II cells which promote cell proliferation and differentiation to restore the alveolar barrier^{346,347}.

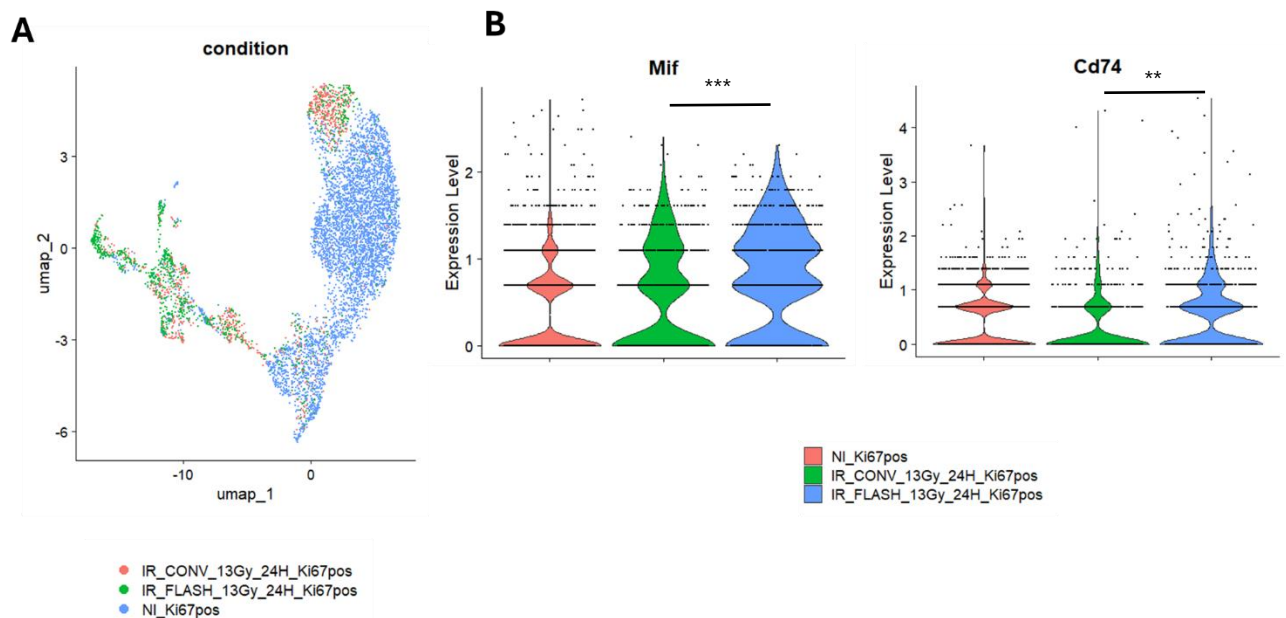


Figure 101. FLASH-RT induces a specific upregulation of Mif factor and Cd74 receptor in sorted Mki67 T cells. (A) UMAP plot showing the distribution of T cells across the conditions (B) Violin plots depicting the expression levels of Mif (left) and Cd74 (right) in T cells across conditions.

g) FLASH-RT induces an upregulation of Cd74 receptor of MIF in resident lung cells which could favorize epithelial regeneration upon injury

We focused on the expression of CD74 in various compartments within the alveolar space and its surrounding environment, including AT2 cells, AT0 transitional cells, alveolar macrophages (**Figure 102A**). Initially, after FLASH irradiation, we observed a significant upregulation of CD74 expression in the Mki67+ alveolar macrophage populations (**Figure 102B**). It appears that the expression of the receptor is downregulated after conventional irradiation compared to both the controls and the FLASH-treated cells in these subtypes (**Figure 102B**). CD74 expression was noted in alveolar macrophages and was associated with the accumulation of neutrophils induced by MIF in the lung during the acute response to damage³⁴⁸.

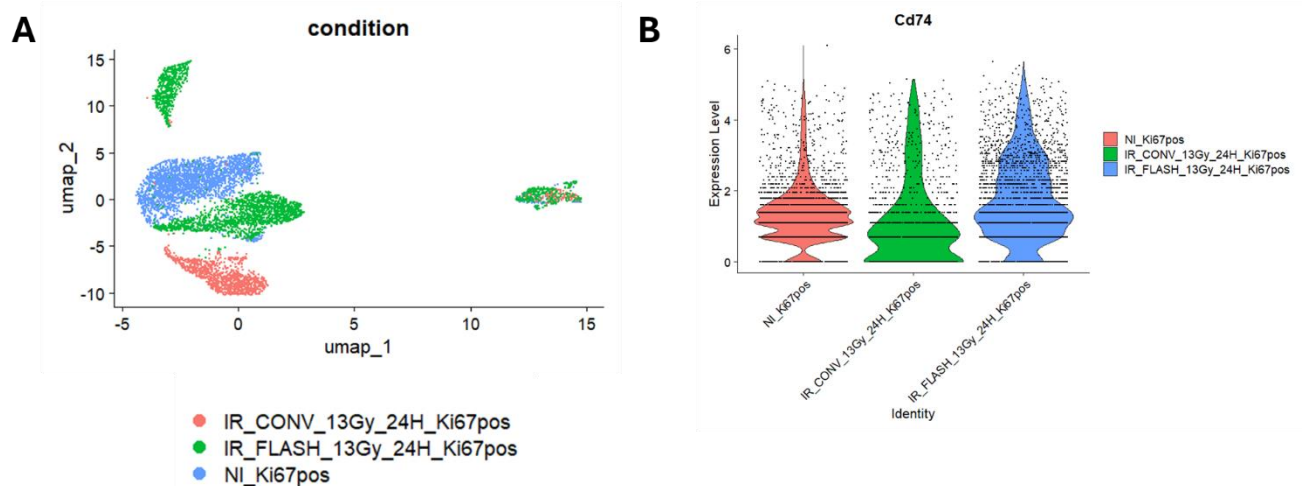


Figure 102. FLASH-RT induces an upregulation of Cd74 receptor expression in alveolar macrophages. (A) UMAP plot showing the distribution of AM cells across conditions (B) Violin plots depicting the expression levels of Cd74 in AM cells across conditions.

Similarly, in Mki67 sorted epithelial cells (**Figure 103A, C**), particularly in AT2 and AT0 cells, we observed the same trend of upregulation of CD74 expression after FLASH irradiation compared to CONV-RT (**Figure 103B, D**). After CONV-RT, the expression appears downregulated in relation to untreated cells (**Figure 103B, D**). This suggests a higher expression of the CD74 receptor in these epithelial populations, enabling an enhanced response to the MIF cytokine, which in turn promotes the transition and differentiation of AT2 cells into AT1 cells in the lung shortly after lung injury.

In global, these transcriptional data **suggest that FLASH irradiation triggers a response more oriented towards alveolar regeneration via the MIF/CD74 pathway** compared to Mki67+ sorted cells treated with conventional irradiation.

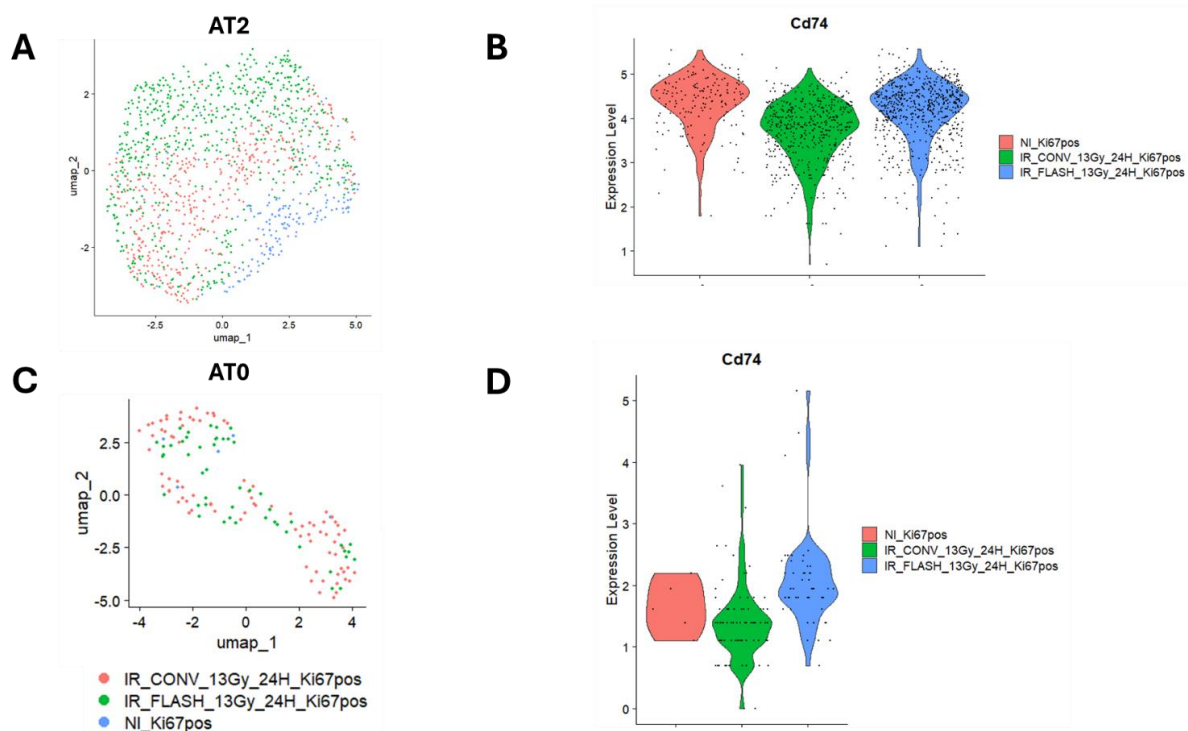


Figure 103. FLASH-RT induces an upregulation of Cd74 receptor expression in AT2 and AT0 Mki67 sorted cells. (A) UMAP plot showing the distribution of AT2 cells across conditions (B) Violin plots depicting the expression levels of Cd74 in AT2 cells across conditions. (C) UMAP plot showing the distribution of AT0 cells across the conditions (D) Violin plots depicting the expression levels of Cd74 in AT0 cells across conditions.

h) Proposed hypothesis and overview of FLASH vs CONV-RT response upon radiation in lung Mki67 cells

Based on the differential responses observed between FLASH and CONV-RT in lung Mki67+ sorted cells, we propose a hypothesis regarding the distinct mechanisms at play. We observed that FLASH irradiation may induce a more robust inflammatory response in endothelial Mki67 sorted cells compared to CONV-RT which could be associated with increased immune recruitment and modulation. On top of that, the MIF/Cd74 pathway was upregulated which could be also linked to enhanced immune recruitment but also to alveolar regeneration processes following injury. This is evidenced by the upregulation of key inflammatory markers such as MIF in T cells which present a more active phenotype after FLASH vs CONV-RT. Indeed, after CONV-RT, cell division of T cells could be modulated via the upregulation of Btg1

and Bgt2 in various immune subpopulations which have an inhibitory function on T cell division. Finally, macrophages and alveolar populations also present an upregulation of Cd74 that could promote regeneration in alveoli. This data suggests that, at the transcriptional level in Mki67 sorted cells, **FLASH treatment may trigger an increased regenerative response more focused on restoring the alveolar barrier via the MIF/Cd74 pathway.** Conversely, **CONV-RT was associated with an increased expression of genes related to TNF α via NF κ B pathway in immune subcompartments.** In T cells and other immune subtypes, **CONV-RT could induce upregulation of pro-inflammatory genes like Junb, Jun, Fos, Fosb, all linked to expression of the AP-1 transcription factor** that could be associated to many processes describe in literature such as inflammatory response linked to TGF β 1 or IL-6 as well as pro-apoptotic or anti-apoptotic response. These data still require experimental validation but provide an initial characterization and insights into the transcriptional mechanisms that vary in Mki67 sorted cells at 24 hours following FLASH or CONV treatment.

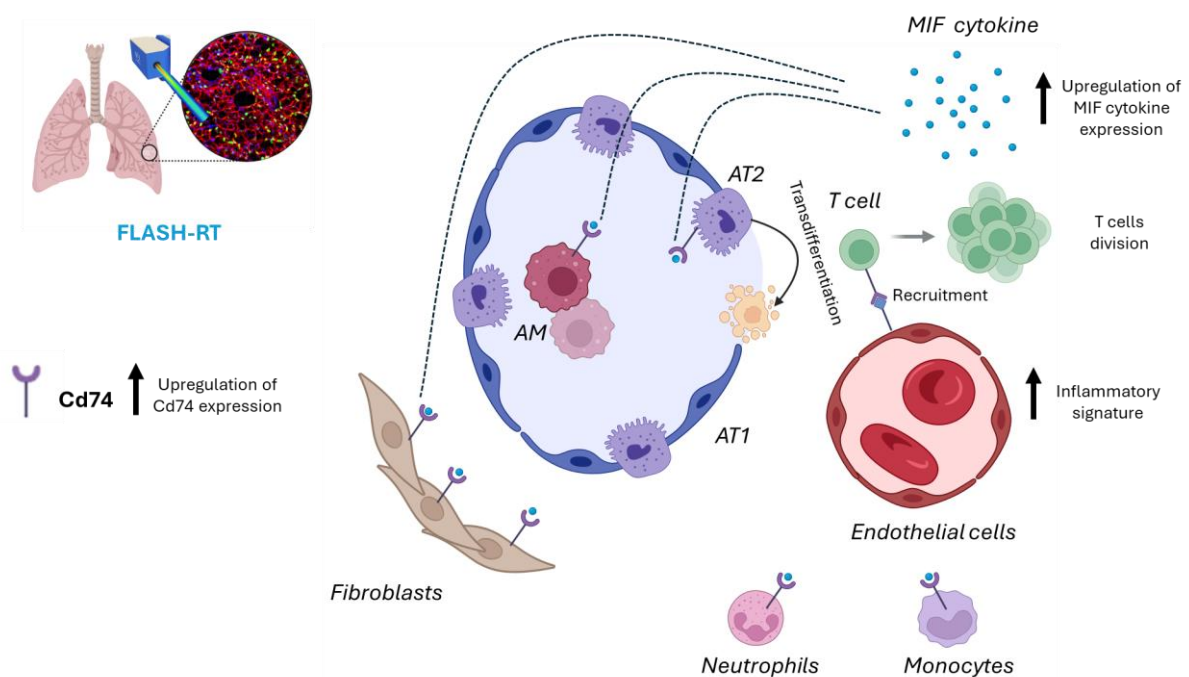


Figure 104. Overview and scheme of proposed differential mechanisms in Mki67 sorted lung cells subpopulations. After FLASH, endothelial Mki67 cells present an upregulation of inflammatory signatures linked to immune recruitment. T cells have an active phenotype link to expansion and immune activation in acute response. Furthermore, they express more MIF factor that could be released close to other alveoli cells types that all present an upregulation of Cd74 receptor expression. MIF/Cd74 could be linked to immune neutrophils recruitment at the site of injury as well as favorize epithelial regeneration in alveoli by inducing AT2 cell division and differentiation to AT1 cells.

1.3.5 Perspectives : Is there a common response in progenitors' cells after FLASH-RT ?

Finally, before conducting further experimental validations on the transcriptional changes occurring after FLASH or conventional irradiation in Mki67+ cells of the lung, we wondered whether a common response could be observed in these cycling cells across different organs. As described in the introduction of this manuscript, FLASH has been shown to protect cycling cells in the intestinal crypts, brain, and lung. To determine whether transcriptional changes are common across organs in these progenitor populations, we aimed to conduct a scRNAseq analysis 24 hours after FLASH or CONV irradiation treatment of the entire abdomen in Mki67 Cre ERT2 x R26 mtmG mice. Tamoxifen injections were administered in the same manner as for the lung, 24 hours before treatment. A 13 Gy dose was given either at a conventional rate or FLASH, with some mice serving as controls (non-irradiated). Subsequently, we performed a dissociation of the intestinal crypts followed by sorting of the GFP+ Mki67 populations in our model. Interestingly, we observed a more significant reduction in the proportion of cycling cells in the intestine 24 hours post-irradiation after conventional irradiation (**Figure 105A**). We then performed scRNAseq analysis, aiming to study, in a similar manner to the lung, the changes occurring specifically after FLASH or conventional irradiation (**Figure 105B**). We hope to potentially identify common responses. Of particular interest, the MIF/CD74 pathway has also been described as promoting epithelial repair in the intestine, encouraging crypt cell proliferation. The data were generated very recently, and since my thesis primarily focuses on the response in the lung, a detailed analysis will be carried out before my defense.

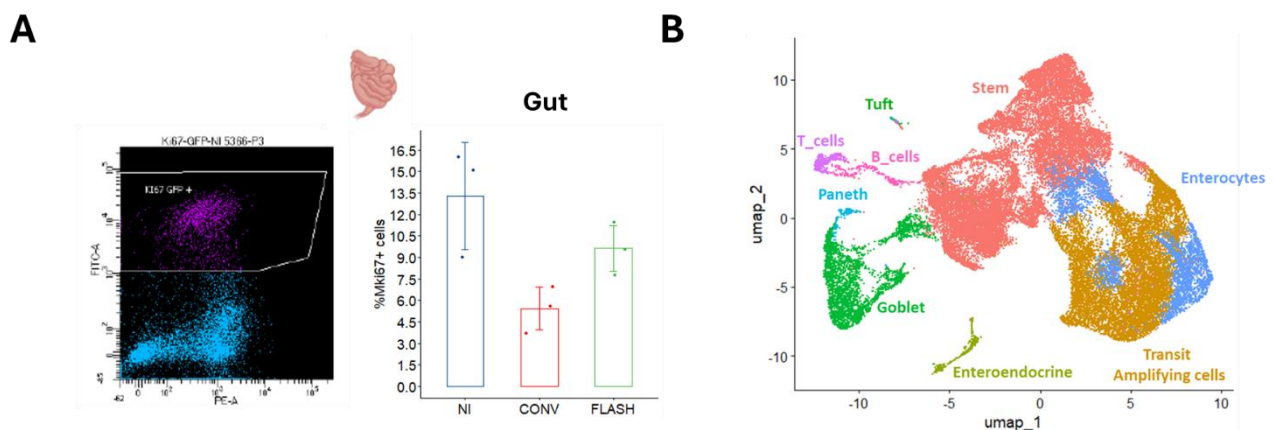


Figure 105. Sorting of FLASH, CONV and non-treated crypt Mki67+ cells following radiation for scRNAseq analysis 24 hours post-treatment. (A) FACS gate of Mki67 GFP+ cells in intestinal crypt dissociation and barplot quantifying the proportion of Mki67+ cells for each condition. (B) UMAP presenting the annotated intestinal crypt cells object 24 hours post-treatment.

CHAPTER VI : DISCUSSION

VI- DISCUSSION

Radiotherapy is a critical therapeutic option for approximately 50% of cancer patients. However, while it effectively targets tumor cells, ionizing radiation can also damage healthy tissue, leading to acute or chronic toxicities⁷³. In thoracic radiotherapy, radiation-induced damage typically manifests as pneumonitis, which may progress to lung fibrosis. To maximize the therapeutic index, radiation oncologists aim to deliver high doses to tumors while sparing surrounding tissues, a goal achieved through technologies like IMRT, SBRT, and proton therapy. However, certain tumors remain resistant to treatment, and highly radiosensitive organs remain at risk.

Recently, FLASH radiotherapy, a new modality delivering radiation dose at ultra-high dose rates, has been shown to spare healthy tissue while maintaining anti-tumor efficacy²⁴¹. This effect has been demonstrated in various organs, including the lung²⁶⁰, brain²⁴⁶, skin²⁵⁷, intestine²⁵², and heart²⁵⁹. Despite its promise, significant challenges remain before FLASH can be implemented in clinical settings. FLASH radiotherapy depends on specific irradiation parameters, and achieving the desired sparing effect may require more than just ultra-high dose rates³⁴⁹. It is crucial to identify the optimal parameters to induce a reproducible and effective FLASH effect. Furthermore, questions about common clinical practices remain, such as whether the FLASH effect persists when doses are fractionated or whether it can be preserved in cases of re-irradiation for recurrent tumors. Although many preclinical studies and phase I clinical trials have been initiated, solid evidence of the FLASH effect in humans is still lacking^{315,350}. Finally, the underlying mechanisms remain largely unknown, particularly why it spares healthy tissue while remaining effective against the tumor. Better understanding and characterizing the FLASH effect is essential to defining its clinical applications.

Our laboratory specializes in FLASH radiotherapy, especially in the context of healthy lung tissue, with access to a preclinical FLASH electron LINAC³¹⁸ and expertise in ScRNA sequencing²⁰⁰. While most lung studies focus on late radiation-induced toxicities such as fibrosis, these studies are time-consuming and not ideal for quickly screening irradiation parameters. Therefore, in my thesis, we developed an *ex vivo* PCLS model to explore these translational issues and perform acute transcriptional analyses to gain insights into the underlying mechanisms of the FLASH effect in the lung³³⁶.

1. PERTINENCE OF EX VIVO PCLS MODEL FOR ACUTE RADIATION INJURIES

The development of radiation-induced toxicities can vary depending on the organ, with some organs responding earlier than others. In the case of the lung, FLASH radiotherapy has been shown to protect against the development of radiation-induced fibrosis which occurs up to 5 months post-treatment in thoracic mouse irradiation models^{241,336}. However, in other organs such as the intestine, the FLASH sparing effect was observed very early, particularly in progenitor cells at the base of the crypts^{252,254,255,309}. In contrast, traditional *in vitro* studies and clonogenic assays have demonstrated limitations in showing an ultra-high dose rate dependent response. Nevertheless, *in vivo* studies come with their own drawbacks, and in the case of the lung, fibrosis is a very late and complex endpoint.

We hypothesized that the mechanisms of action of conventional and FLASH irradiation diverge in the very early post-irradiation time points, which can lead or not to the development of radiation-induced toxicities. This led us to develop a relevant *ex vivo* model to study acute healthy lung toxicities. PCLS model is particularly well-suited to recapitulate the lung architecture and microenvironment at a relatively low cost of development^{224,225}. Several studies have demonstrated the relevance of this model for studying lung physiology and the development of chronic obstructive diseases^{224,225}. We choose to develop simple and relevant tests for dose escalation, focusing on endpoints like cell viability and cell division. By comparing the response 24 hours post-irradiation, we were able to observe a protective effect of FLASH radiotherapy on dividing cells in the lung tissue in PCLS. This effect was then confirmed *in vivo*, demonstrating that this model is physiologically relevant for replicating the healthy tissue response to irradiation in the short-term post-treatment. Most importantly, this allowed us to highlight a sparing effect on the cycling populations in the lung post-treatment, similar to what has been observed in the brain and intestine. Thus, PCLS enabled us to robustly identify a FLASH sparing effect in the lung at very early post-treatment, which could be applied at larger scale for radiobiology purposes. Additionally, we also tested a proof-of-concept approach by combining therapeutic radiation doses with chemotherapy agents used in the treatment of lung cancer, successfully demonstrating combined effects on our cell cycle endpoints in lung tissue. This could make it relevant for drug toxicity screening in combination with various radiation protocols.

This model does have some limitations, as it only allows us to study the short-term response post-treatment. Additionally, several studies suggest that the preparation of PCLS induces a wound healing process that does not fully replicate pulmonary physiology^{224,225}. Furthermore,

in our study, we chose to focus on the response of healthy tissue, but for a more clinically relevant framework, particularly in the context of FLASH, could be to develop a model that includes the tumor microenvironment. This would mimic the environment surrounding the tumor and enable us to study the sparing effect between healthy tissue and the tumor more easily. Finally, other endpoints could also be investigated, such as DNA damage or the secretion of inflammatory cytokines, as has been done in the literature, which could be very interesting for the mechanistic study of FLASH^{224,225}.

On our side, we chose to use this model and the assay on lung cycling cells to address issues related to the clinical transition of FLASH, starting with the study of optimal irradiation parameters to trigger the effect in our model.

2. PCLS MODEL HELP TO CHARACTERIZE OPTIMAL FLASH IRRADIATION PARAMETERS IN THE LUNG

Since the re-discovery of the FLASH effect, several laboratories have published negative results regarding the sparing effect in certain organs²⁶¹. Despite being administered at high dose rates, it appears that multiple physical parameters are important to trigger the FLASH effect. To provide optimal irradiation parameters for the clinical transition of FLASH, several groups have investigated this question, particularly with electron beams. Initial studies began in the brain, where irradiations were performed at various dose rates using a preclinical LINAC²⁴⁷. These studies showed that the optimal dose rate for sparing cognitive and memory functions in mice was above 100 Gy/s, setting the threshold for the FLASH effect higher than what was described in initial lung studies²⁴¹. Similar results were observed in another model organism, the zebrafish³¹¹. In the intestine, a similar relationship was found between the mean dose rate and the presence of the FLASH effect, showing crypt sparing for dose rates of 280 Gy/s or higher²⁵⁴.

This raises the question: How can we explain this difference regarding the mean dose rate, and why was the FLASH effect described in the lung at a dose rate of 40 Gy/s? To address this, we used our PCLS model and acute radiation injury assay. The advantage was being able to use a unique model to investigate various irradiation parameters that we could modulate in our Electron FLASH Linac. Our studies showed that we needed to be strictly above 100 Gy/s to observe the effect, with an irradiation time shorter than 80 ms. Moreover, the sparing effect on cycling cells was optimal at a dose rate of 300 Gy/s, which is consistent with findings in the intestine²⁵⁴. To test whether these findings contradict what had been initially described in the

literature, we repeated a thoracic irradiation experiment comparing FLASH irradiation at a dose rate of 40 Gy/s to FLASH irradiation described as optimal at 300 Gy/s. Interestingly, we observed a sparing effect on the development of radiation-induced fibrosis at 40 Gy/s, but it was more pronounced at 300 Gy/s. These results suggest two things: 1) the irradiation parameters needed to achieve the FLASH effect still depend on the organ in question, and 2) the effect may depend on the endpoint being assessed, whether early or late. In fact, data in the intestine regarding crypt sparing suggests that higher dose rates are required for the FLASH effect, as seen in our PCLS model, but when looking at late-stage toxicity development, the threshold appears lower. However, it seems that data obtained from our PCLS model can provide valuable insights into other late endpoints. For example, we showed that FLASH irradiation at 300 Gy/s resulted in a longer delay in the onset of fibrosis compared to FLASH irradiation at 40 Gy/s. Although we cannot yet draw direct correlations between what happens in the short and long term in lung tissue, these data suggest that our PCLS model could be a relevant tool for studying FLASH irradiation parameters in the lung context.

Even though the mean dose rate appears to be the main parameter correlated with the FLASH effect, it seems, particularly with electron beams, that other parameters may also play a role, notably those related to the temporal structure of irradiation. All of this does not apply to other particles like protons, which have a different delivery system. A study by Ruan et al. in the intestine suggested that a dose delivered in a single pulse might induce a stronger preservation effect, particularly regarding crypt sparing. Subsequent teams have investigated this issue, and some have shown that the dose per pulse could also be a key factor in the presence of the FLASH effect²⁵⁴. Using our model, we examined this question and demonstrated that the FLASH effect on dividing cells in the lung was not enhanced by delivering the dose in a single pulse, suggesting that this might be specific to the intestine or endpoint. Additionally, we showed that regardless of the mean dose rate, a dose per pulse lower than 1 Gy did not spare cycling cells in the lung. We are now awaiting *in vivo* validation regarding the late endpoint of fibrosis based on these data. Other groups have also suggested an impact of dose per pulse independently of the mean dose rate, as demonstrated in a recent study by Liu et al³⁵¹. These could explain in part why some laboratories did not show a FLASH sparing effect and this is why an extent description of beam parameters should always accompanied the results obtained.

Finally, we used our model and *in vivo* analysis to study the presence of a FLASH effect in context of previously irradiated lung tissue. Using our experimental protocol, we separated an initial 10 Gy conventional dose from a FLASH dose escalation. We found the same short-term response post-irradiation in the PCLS. Regarding fibrosis development, we observed a sparing

effect at the higher dose of 12 Gy. These data suggest that the FLASH effect remains present in previously irradiated tissue even if the FLASH later response seems less important. In contrast, the sparing effect was totally conserved. This is not necessarily the case for all organs, a recent study showed that FLASH reirradiation significantly preserved the intestine, skin and bones compared with conventional reirradiation³⁰⁹. Between studies, treatment planning and doses used vary greatly, and the validation of a protective FLASH effect in reirradiation context must be verified in multiple settings and organs.

In conclusion, while we are getting closer to defining the irradiation parameters that induce the FLASH effect using electrons, it remains complex and requires further studies to ensure a successful clinical transition.

3. PCLS MODEL TO INVESTIGATE THE PRESENCE OF ACUTE FLASH SPARING EFFECT IN HEALTHY PATIENT SAMPLES

Regarding the clinical transition of FLASH-RT, although ongoing trials are ongoing, for now, the sparing effect has only been demonstrated in murine, zebrafish, dog or cat preclinical models. This is why we have chosen to apply the PCLS model to investigate the presence of an acute protective effect of FLASH radiotherapy in the human lung. At present, the PCLS model derived from human patient lung tissue is the only option that allows us to compare the response of healthy tissue to FLASH irradiation versus conventional irradiation. Although this model has its limitations, particularly regarding its relevance for anything beyond acute responses and the fact that we used only a cell division endpoint, our primary goal was to investigate the presence of a FLASH protective effect on cycling cells in human lung tissue. Interestingly, in the majority of the patient-derived tissue slices, we were able to observe a sparing effect on cycling cells 24 hours post-treatment with FLASH. Only one patient did not show any difference in this endpoint, which is particularly interesting because it suggests that there may be intrinsic or extrinsic differences (such as treatment protocols involving surgery) that the sparing response. Interestingly, the patients with the highest heterogeneity in basal division had undergone immunotherapy treatment prior to surgery. This is particularly true for the only patient who did not exhibit a protective FLASH effect. Future RNA sequencing studies on this type of patient will allow us to define and understand the differences between responders and non-responders 24 hours post-treatment. Although these data are limited to a single endpoint, a small cohort, and an *ex vivo* model, they support the clinical transition of FLASH. To gain further insight into the underlying mechanisms, we decided to conduct RNA sequencing on lung samples from three patients. Interestingly, we identified common

responses differential response involved. We validated the FLASH sparing effect in terms of gene expression associated with the cell cycle and even uncovered potential interesting differences related to genes involved in ROS generation and management. Interestingly, this has been proposed as one of the underlying mechanisms of the FLASH effect, particularly with the theory concerning the recombination and diffusion of free radicals following FLASH irradiation. This theory suggests that FLASH induces the generation of fewer ROS compared to conventional radiotherapy. These data remain very preliminary, and further research is needed to fully validate and understand the implications of this potential mechanism. One of major drawback of bulk sequencing is that we cannot define a signature associated with a specific cell subtype. For greater relevance and a deeper understanding of the underlying mechanisms of the FLASH protective effect at 24 hours post-treatment in the entire lung or within lung dividing cells, we conducted scRNAseq analysis on murine models irradiated with either FLASH or conventional dose rates.

4. ACUTE MOLECULAR CHARACTERIZATION OF THE FLASH SPARING EFFECT IN THE WHOLE LUNG AND LUNG CYCLING CELLS COMPARTMENT

Several hypotheses have been proposed regarding the mechanisms underlying the FLASH effect, including oxygen-related factors, protection of progenitor compartments, lipid peroxidation, and inflammatory dynamics. Our transcriptional data, along with experimental data generated by other laboratories, suggest that several of these mechanisms might be at play.

4.1 FLASH-RT spares lipid metabolism in AT2 cells compared to CONV-RT

Through a scRNAseq analysis of murine AT2 cells, we discovered that while both FLASH-RT and CONV-RT triggered the expression of genes involved in the early response to irradiation, FLASH-RT notably and persistently spared genes associated with lipid metabolism compared to CONV-RT. This mechanistic network was further confirmed by lipidomics analysis on sorted AT2 cells, which revealed an increase in ceramide levels, a marker of oxidative stress and cell death³⁵² processes following both FLASH-RT and CONV-RT. However, FLASH-RT preserved cholesteryl ester levels, which are linked to lipid droplet formation, in contrast to CONV-RT³²⁷. According to existing literature, CONV-RT is known to deplete AT2 cells and upregulate inflammatory and fibrosis-related factors. A recent study from our lab examining the long-term lung response to CONV-RT found that AT2 cells were progressively depleted over a period of 1 to 5 months after irradiation²⁰⁰. This depletion was associated with an increased transcriptional activity related to epithelial-mesenchymal transition and AT2-to-

AT1 transdifferentiation²⁰⁰. Additionally, a lipidomics study using mass spectrometry on macaque lung parenchyma 6 months post-whole-thorax irradiation observed a significant reduction in phospholipids, which are critical components of pulmonary surfactants³²⁹. Lipid metabolism is closely linked to stress response, cellular senescence, and aging-related diseases. Apoe knockout murine models have also demonstrated defective inflammatory and oxidative stress responses, leading to pulmonary fibrosis, atherosclerosis, and neurodegenerative diseases³⁵³. In the context of Plin2, oxidative stress has been shown to promote its overexpression, leading to lipid droplet formation and a reduction in cellular stress³⁵⁴. This suggests that one of the mechanisms underlying the FLASH sparing effect may be the alleviation of oxidative stress through the accumulation of lipids in lipid droplets, which could serve as valuable substrates for cellular processes. In line with this, our team demonstrated a reduction in oxylipin levels just 5 minutes after FLASH-RT compared to CONV-RT in normal cells and mouse lung tissue²⁸⁸. This was also shown in a model of liposome where FLASH does not induce lipid peroxidation compared to CONV-RT²⁸⁷. This reduction in lipid peroxidation products following FLASH-RT may be associated with a shift in redox-active metabolism. Thus, it seems that FLASH irradiation may have a differential impact on the lipid pools present in certain cell subtypes in AT2 cells, and it may also affect lipid metabolism, particularly vesicular transport pathways. Currently, validations are still underway to define an overview of the lipid changes associated with both modalities in the lung. However, the accumulation of lipid peroxides can be associated with various mechanisms of cell death, particularly ferroptosis, an iron-dependent form of cell death induced by the buildup of lipid peroxides which has been linked to both acute and chronic radiation-induced damage³⁵⁵. Interestingly, at the transcriptional level at least, the dynamics of these changes show that this sparing effect on Apoe or Plin2 expression was persistent at later stages, in cases where radiation-induced fibrosis develops after conventional irradiation but not after FLASH. In a way, these lipid alterations may only reflect the state of AT2 cells at short time points, in response to both irradiation modalities, or at later time points, where inflammatory mechanisms and EMT may occur, leading to a reduction in the AT2 pool in the lung.

4.2 Is there a FLASH sparing effect related to mitochondrial function in endothelial cells ?

After conventional irradiation, we observed a downregulation of several mitochondrial genes compared to FLASH, both at 24 hours and at later time points, such as 5 months post-treatment. These genes encode for the constituent proteins of the various subunits of the mitochondrial respiratory chain, which is essential for energy production in the form of ATP. However, this process also generates superoxide radicals (O_2^-) as byproducts, which can lead to the formation of highly reactive molecules, such as hydrogen peroxide (H_2O_2) and hydroxyl radicals ($OH\cdot$), especially under the oxidative stress induced by irradiation. The electron transport chain (ETC), particularly complexes I, II, and III, is sensitive to radiation, and any disruption in electron flow through the ETC can elevate ROS levels, leading to oxidative damage and contributing to genomic instability as well as DNA damage²⁹⁰. Recent studies have begun to explore how FLASH-RT may differentially affect mitochondrial metabolism compared to CONV-RT. Mitochondrial impairment has also been associated with apoptosis through cytochrome c release³⁵⁶. Thus, our data suggests differential impairment of mitochondrial gene expression in the subset of endothelial cells. Mitochondrial dynamics and autophagy/mitophagy are essential for the normal angiogenic and vasodilatory functions of endothelial cells³³⁴. Mitochondrial ROS are important for signaling physiological responses to nutrient status, hypoxia, and shear stress. Physiological ROS production in endothelial mitochondria also plays a crucial role in promoting inflammation³³⁴. But anormal level of ROS could also lead to mitophagy, mitochondrial fission and apoptosis³³⁴. In conclusion, our initial results suggest the importance of further investigating the impact of these two irradiation modalities on mitochondrial function. However, so far, only *in vitro* data from fibroblast cell lines have demonstrated the preservation of membrane potential, mtDNA copy number, and oxidative enzyme levels following FLASH irradiation compared to conventional irradiation³⁵⁷. This area shows promise for helping to better understand some of the mechanisms related to the sparing effect of FLASH. Further research is needed to clarify how these processes operate in different tissues and in tumor.

4.3 Characterization and proposed mechanisms of FLASH sparing effect in lung cycling cells

24 hours post-irradiation, we demonstrated that significantly more cells were cycling after FLASH irradiation than after conventional treatment. Unlike the intestine, where regeneration from the base of the crypts is a well-known process, very little is known about the populations of cells capable of regenerating the lung after injury. We confirmed that FLASH seemed to spare all compartments (immune, epithelial, endothelial) of cycling subpopulations at this timepoint. This is consistent with data from the literature showing similar sparing effects in the intestine and brain. These findings suggest a common mechanism of sparing cycling cells by FLASH irradiation, a mechanism that remains poorly understood at the molecular level, particularly in the lung.

Through an scRNAseq analysis on Mki67-sorted cells 24 hours post-irradiation, we identified a combination of changes occurring in lung Mki67 subcompartments, suggesting different mechanisms at play after FLASH versus conventional irradiation. On one hand, we observed that FLASH irradiation could induce an increase in alveolar regeneration via the MIF/Cd74 pathway. This pathway has been described in several organs, such as the lung and intestine, as promoting regeneration³⁴⁶. In the lung, it contributes to the division of AT2 cells and their differentiation into AT1 cells in response to damage such as that caused by lung infections or ischemia³⁵⁸. Strikingly, this phenomenon has never been observed in the context of the response to irradiation. This suggests the involvement of entirely different mechanisms following FLASH irradiation. In contrast, CONV-RT was associated with increased expression of genes related to TNF α through the NF- κ B pathway in immune subcompartments. In T cells and other immune cell types, CONV-RT appeared to induce the upregulation of pro-inflammatory genes such as *Junb*, *Jun*, *Fos*, and *Fosb*. These genes are associated with the expression of the AP-1 transcription factor and could be linked to inflammatory responses involving TGF β 1 or IL-6, as well as pro-apoptotic or anti-apoptotic responses. These findings can be linked to a recent study in the intestine, which suggested an acceleration of differentiation and regeneration of crypts from a stem cell population supported by the activation of an inflammatory pathway dependent on interferon signaling²⁵⁵. Interestingly, this was not observed after conventional irradiation. This suggests that in the lung, as in the intestine, complex signaling interactions and the establishment of a distinct inflammatory response might underlie the differences observed following FLASH irradiation. Since our study focuses solely on a 24-hour timeframe, we do not yet have a dynamic view of how this distinct inflammatory response evolves between conventional and FLASH irradiation. Nevertheless, preliminary scRNAseq data from sorted

Mki67 intestinal cells also suggest an upregulation of the MIF factor, which may be related to the observations made in the lung.

At this stage, these data represent only a preliminary transcriptional characterization of the differential response to FLASH compared to conventional irradiation in Mki67 sorted cell compartments. Further validations in tissue are required to experimentally validate the hypotheses we have defined regarding the induction of alveolar regeneration processes via the MIF/Cd74 pathway after FLASH. Additional protein-level validations will be necessary to confirm these transcriptional changes. However, referring to the data recently presented in the intestine or those generated during my thesis, it appears that regeneration processes associated with FLASH are complex and involve the establishment of very specific inflammatory and regeneration responses.

CHAPTER VII : PERSPECTIVES

VII- CONCLUSION AND PERSPECTIVES

The originality of this work resides in the association of an *ex vivo* approach and molecular scRNAseq analysis for an acute characterization of FLASH compared to CONV-RT in the lung. It aligns well with current challenges related to the clinical translation of FLASH radiotherapy. First, we developed a relevant *ex vivo* pulmonary model and highly sensitive assays capable of detecting the protective effects of FLASH at short post-treatment. Subsequently, we combined short-term approaches, using endpoints such as cell division in PCLS with late-response studies in the lung (RIPF development) to investigate and characterize the optimal parameters for FLASH irradiation in this organ. These efforts demonstrated that mean dose rate and dose per pulse are critical factors. Additionally, this model enabled us to show, in an initial cohort of patients, a short-term protective effect of FLASH radiotherapy in human lungs, supporting its clinical translation. Finally, we provided a first molecular analysis of the underlying mechanisms of this protective effect, ranging from 24 hours to 5 months in whole lung tissue or lung dividing cells, uncovering unseen responses in AT2, endothelial and cycling cells. We still do not fully understand how changes occurring short time after radiation, whether in cycling cells, AT2 cells, or endothelial cells, can influence later outcomes and correlate with data obtained several months post-treatment. A deeper understanding of the molecular dynamics following FLASH or conventional irradiation remains essential.

Our data suggests a differential impact of FLASH radiotherapy on lipids, particularly in AT2 cells. To validate this, we aim to sort AT2 to study lipid vesicle dynamics through microscopy analyses, using markers like Bodipy. Additionally, we plan to perform lipidomic analyses at earlier post-treatment time points, as changes in lipid pools occur much sooner than the transcriptional changes we have observed as suggested in some recent studies in kidney³⁵⁹. Finally, we propose to validate these changes spatially, using murine or patient tissues, through spatial lipidomics analysis³⁶⁰.

Regarding the mitochondrial impact of FLASH radiotherapy, we aim to better characterize this response through functional validation. Mitochondrial activity can be assessed in tissue sections either by measuring ATP levels or using mitochondrial markers to study mitochondrial function.

Finally, concerning cycling Mki67+ cells, scRNAseq analyses in intestinal progenitor cells are ongoing. We aim to explore potential shared sparing mechanisms in these two organs, particularly by investigating inflammatory processes, with a focus on the Mif/Cd74 pathway. For *in situ* functional validation of these findings, selected ligand/receptor pairs can be targeted on lung tissue sections using smFISH (or immunohistochemistry, if antibodies are available) to determine whether these processes can be directly detected in tissue. Additionally, specific gene knockdowns, such as for Cd74 or MIF, could be performed on tissue sections using lentiviral systems, followed by an analysis of the response in Mki67+ cells within the lung.

In conclusion, we are confident that this work has achieved two key objectives 1) Contributing to the clinical translation of FLASH radiotherapy by studying the optimal irradiation parameters for the lung and demonstrating the presence of a FLASH effect in patients and 2) Providing deeper molecular characterization of the pulmonary healthy tissue response to FLASH compared to conventional radiotherapy, suggesting potential mechanisms involved in the FLASH effect.

BIBLIOGRAPHY

1. Barton, M. B., Frommer, M. & Shafiq, J. Role of radiotherapy in cancer control in low-income and middle-income countries. *Lancet Oncol.* **7**, 584–595 (2006).
2. Barton, M. B. *et al.* Estimating the demand for radiotherapy from the evidence: A review of changes from 2003 to 2012. *Radiother. Oncol.* **112**, 140–144 (2014).
3. Tyldesley, S. *et al.* Estimating the Need for Radiotherapy for Patients With Prostate, Breast, and Lung Cancers: Verification of Model Estimates of Need With Radiotherapy Utilization Data From British Columbia. *Int. J. Radiat. Oncol. Biol. Phys.* **79**, 1507–1515 (2011).
4. Dunne-Daly, C. F. Principles of radiotherapy and radiobiology. *Radiat. Oncol.* **15**, 250–259 (1999).
5. Haussmann, J. *et al.* Recent advances in radiotherapy of breast cancer. *Radiat. Oncol.* **15**, 71 (2020).
6. Smart, D. Radiation Toxicity in the Central Nervous System: Mechanisms and Strategies for Injury Reduction. *Semin. Radiat. Oncol.* **27**, 332–339 (2017).
7. Rodrigues, G. *et al.* Definitive radiation therapy in locally advanced non-small cell lung cancer: Executive summary of an American Society for Radiation Oncology (ASTRO) evidence-based clinical practice guideline. *Pract. Radiat. Oncol.* **5**, 141–148 (2015).
8. Spinks, J. W. T. & Woods, R. J. *An Introduction to Radiation Chemistry*. (John Wiley and Sons Inc, United States, 1990).

9. Reisz, J. A., Bansal, N., Qian, J., Zhao, W. & Furdai, C. M. Effects of Ionizing Radiation on Biological Molecules—Mechanisms of Damage and Emerging Methods of Detection. *Antioxid. Redox Signal.* **21**, 260–292 (2014).
10. The International Commission on Radiation Units and Measurements. *J. ICRU* **11**, 5–6 (2011).
11. Baskar, R., Lee, K. A., Yeo, R. & Yeoh, K.-W. Cancer and Radiation Therapy: Current Advances and Future Directions. *Int. J. Med. Sci.* **9**, 193–199 (2012).
12. Baumann, M. *et al.* Radiation oncology in the era of precision medicine. *Nat. Rev. Cancer* **16**, 234–249 (2016).
13. Bentzen, S. M. Preventing or reducing late side effects of radiation therapy: radiobiology meets molecular pathology. *Nat. Rev. Cancer* **6**, 702–713 (2006).
14. Mackeprang, P.-H. *et al.* Consideration of image guidance in patterns of failure analyses of intensity-modulated radiotherapy for head and neck cancer: a systematic review. *Radiat. Oncol.* **19**, 30 (2024).
15. Storey, C. L., Hanna, G. G., Greystoke, A., & on behalf of AstraZeneca UK Limited. Practical implications to contemplate when considering radical therapy for stage III non-small-cell lung cancer. *Br. J. Cancer* **123**, 28–35 (2020).
16. Aupérin, A. *et al.* Meta-Analysis of Concomitant Versus Sequential Radiochemotherapy in Locally Advanced Non-Small-Cell Lung Cancer. *J. Clin. Oncol.* **28**, 2181–2190 (2010).
17. null null. Cisplatin-Based Adjuvant Chemotherapy in Patients with Completely Resected Non-Small-Cell Lung Cancer. *N. Engl. J. Med.* **350**, 351–360.

18. Vermorken Jan B. *et al.* Platinum-Based Chemotherapy plus Cetuximab in Head and Neck Cancer. *N. Engl. J. Med.* **359**, 1116–1127.
19. Bonner James A. *et al.* Radiotherapy plus Cetuximab for Squamous-Cell Carcinoma of the Head and Neck. *N. Engl. J. Med.* **354**, 567–578.
20. Blumenschein, G. R. *et al.* Phase II Study of Cetuximab in Combination With Chemoradiation in Patients With Stage IIIA/B Non–Small-Cell Lung Cancer: RTOG 0324. *J. Clin. Oncol.* **29**, 2312–2318 (2011).
21. Bradley, J. D. *et al.* Standard-dose versus high-dose conformal radiotherapy with concurrent and consolidation carboplatin plus paclitaxel with or without cetuximab for patients with stage IIIA or IIIB non-small-cell lung cancer (RTOG 0617): a randomised, two-by-two factorial phase 3 study. *Lancet Oncol.* **16**, 187–199 (2015).
22. Simone II, C. B., Burri, S. H. & Heinzerling, J. H. Novel radiotherapy approaches for lung cancer: combining radiation therapy with targeted and immunotherapies. *2015* **4**, 545–552 (2015).
23. Shaw, A. T. *et al.* First-Line Lorlatinib or Crizotinib in Advanced *ALK*-Positive Lung Cancer. *New England Journal of Medicine* vol. 383 2018–2029 (2020).
24. Xia, W.-Y. *et al.* Radiotherapy for non-small cell lung cancer in the immunotherapy era: the opportunity and challenge—a narrative review. *2020* **9**, 2120–2136 (2020).
25. Shaverdian, N. *et al.* Previous radiotherapy and the clinical activity and toxicity of pembrolizumab in the treatment of non-small-cell lung cancer: a secondary analysis of the KEYNOTE-001 phase 1 trial. *Lancet Oncol.* **18**, 895–903 (2017).

26. Gong, X. *et al.* Combined Radiotherapy and Anti-PD-L1 Antibody Synergistically Enhances Antitumor Effect in Non-Small Cell Lung Cancer. *J. Thorac. Oncol.* **12**, 1085–1097 (2017).
27. Antonia, S. J. *et al.* Durvalumab after Chemoradiotherapy in Stage III Non-Small-Cell Lung Cancer. *N. Engl. J. Med.* **377**, 1919–1929 (2017).
28. Theelen, W. S. M. E. *et al.* Effect of Pembrolizumab After Stereotactic Body Radiotherapy vs Pembrolizumab Alone on Tumor Response in Patients With Advanced Non-Small Cell Lung Cancer: Results of the PEMBRO-RT Phase 2 Randomized Clinical Trial. *JAMA Oncology* vol. 5 1276–1282 (2019).
29. Roussot, N. *et al.* A phase I study of the combination of atezolizumab, tiragolumab, and stereotactic body radiation therapy in patients with metastatic multiorgan cancer. *BMC Cancer* **23**, 1080 (2023).
30. Hwang, W. L., Pike, L. R. G., Royce, T. J., Mahal, B. A. & Loeffler, J. S. Safety of combining radiotherapy with immune-checkpoint inhibition. *Nat. Rev. Clin. Oncol.* **15**, 477–494 (2018).
31. Bray, F. *et al.* Global cancer statistics 2018: GLOBOCAN estimates of incidence and mortality worldwide for 36 cancers in 185 countries. *CA. Cancer J. Clin.* **68**, 394–424 (2018).
32. Siegel, R. L., Miller, K. D. & Jemal, A. Cancer statistics, 2020. *CA. Cancer J. Clin.* **70**, 7–30 (2020).
33. Prezzano, K. M. *et al.* Stereotactic body radiation therapy for non-small cell lung cancer: A review. *World J. Clin. Oncol.* **10**, 14–27 (2019).

34. Bradley, J. & Movsas, B. Radiation Pneumonitis and Esophagitis in Thoracic Irradiation. in *Radiation Toxicity: A Practical Guide* (eds. Small, W. & Woloschak, G. E.) 43–64 (Springer US, Boston, MA, 2006). doi:10.1007/0-387-25354-8_4.
35. Garon Edward B. *et al.* Pembrolizumab for the Treatment of Non–Small-Cell Lung Cancer. *N. Engl. J. Med.* **372**, 2018–2028.
36. Postow Michael A., Sidlow Robert, & Hellmann Matthew D. Immune-Related Adverse Events Associated with Immune Checkpoint Blockade. *N. Engl. J. Med.* **378**, 158–168 (2018).
37. Solassol, I., Pinguet, F. & Quantin, X. FDA- and EMA-Approved Tyrosine Kinase Inhibitors in Advanced EGFR-Mutated Non-Small Cell Lung Cancer: Safety, Tolerability, Plasma Concentration Monitoring, and Management. *Biomolecules* **9**, (2019).
38. Durante, M. & Loeffler, J. S. Charged particles in radiation oncology. *Nat. Rev. Clin. Oncol.* **7**, 37–43 (2010).
39. Hall, E. J. & Giaccia, A. J. *Radiobiology for the Radiologist*. (Lippincott Williams & Wilkins, 2006).
40. Goodhead, Dt. Spatial and temporal distribution of energy. *Health Phys.* **55**, 231–240 (1988).
41. Suit, H. *et al.* Proton vs carbon ion beams in the definitive radiation treatment of cancer patients. *Radiother. Oncol.* **95**, 3–22 (2010).
42. Whitmore, L., Mackay, R. I., van Herk, M., Jones, J. K. & Jones, R. M. Focused VHEE (very high energy electron) beams and dose delivery for radiotherapy applications.

- Sci. Rep.* **11**, 14013 (2021).
43. Le Caër, S. Water Radiolysis: Influence of Oxide Surfaces on H₂ Production under Ionizing Radiation. *Water* **3**, 235–253 (2011).
 44. Labarbe, R., Hotoiu, L., Barbier, J. & Favaudon, V. A physicochemical model of reaction kinetics supports peroxy radical recombination as the main determinant of the FLASH effect. *Radiother. Oncol.* **153**, 303–310 (2020).
 45. Kozlov, A. V., Javadov, S. & Sommer, N. Cellular ROS and Antioxidants: Physiological and Pathological Role. *Antioxidants* **13**, (2024).
 46. Spitz, D. R., Azzam, E. I., Jian Li, J. & Gius, D. Metabolic oxidation/reduction reactions and cellular responses to ionizing radiation: A unifying concept in stress response biology. *Cancer Metastasis Rev.* **23**, 311–322 (2004).
 47. Davies, M. J. Protein oxidation and peroxidation. *Biochem. J.* **473**, 805–825 (2016).
 48. Jeggo, P. A. & Löbrich, M. DNA double-strand breaks: their cellular and clinical impact? *Oncogene* **26**, 7717–7719 (2007).
 49. Azzam, E. I., Jay-Gerin, J.-P. & Pain, D. Ionizing radiation-induced metabolic oxidative stress and prolonged cell injury. *Cancer Lett.* **327**, 48–60 (2012).
 50. Ayala, A., Muñoz, M. F. & Argüelles, S. Lipid Peroxidation: Production, Metabolism, and Signaling Mechanisms of Malondialdehyde and 4-Hydroxy-2-Nonenal. *Oxid. Med. Cell. Longev.* **2014**, 1–31 (2014).
 51. Catalá, A. Lipid peroxidation of membrane phospholipids generates hydroxy-alkenals and oxidized phospholipids active in physiological and/or pathological conditions. *Chem. Phys. Lipids* **157**, 1–11 (2009).

52. Uchida, K. 4-Hydroxy-2-nonenal: a product and mediator of oxidative stress. *Prog. Lipid Res.* **42**, 318–343 (2003).
53. Dalle-Donne, I. *et al.* Protein carbonylation, cellular dysfunction, and disease progression. *J. Cell. Mol. Med.* **10**, 389–406 (2006).
54. Sies, H. Hydrogen peroxide as a central redox signaling molecule in physiological oxidative stress: Oxidative eustress. *Redox Biol.* **11**, 613–619 (2017).
55. Baird, L. & Yamamoto, M. The Molecular Mechanisms Regulating the KEAP1-NRF2 Pathway. *Mol. Cell. Biol.* **40**, e00099-20 (2020).
56. Jackson, S. P. & Bartek, J. The DNA-damage response in human biology and disease. *Nature* **461**, 1071–1078 (2009).
57. Krokan, H. E. & Bjoras, M. Base Excision Repair. *Cold Spring Harb. Perspect. Biol.* **5**, a012583–a012583 (2013).
58. Marteijn, J. A., Lans, H., Vermeulen, W. & Hoeijmakers, J. H. J. Understanding nucleotide excision repair and its roles in cancer and ageing. *Nat. Rev. Mol. Cell Biol.* **15**, 465–481 (2014).
59. Chapman, J. R., Taylor, M. R. G. & Boulton, S. J. Playing the End Game: DNA Double-Strand Break Repair Pathway Choice. *Mol. Cell* **47**, 497–510 (2012).
60. Li, G.-M. Mechanisms and functions of DNA mismatch repair. *Cell Res.* **18**, 85–98 (2008).
61. Morgan, M. A. & Lawrence, T. S. Molecular Pathways: Overcoming Radiation Resistance by Targeting DNA Damage Response Pathways. *Clin. Cancer Res.* **21**, 2898–2904 (2015).

62. Blackford, A. N. & Jackson, S. P. ATM, ATR, and DNA-PK: The Trinity at the Heart of the DNA Damage Response. *Mol. Cell* **66**, 801–817 (2017).
63. O’Driscoll, M. & Jeggo, P. A. The role of double-strand break repair — insights from human genetics. *Nat. Rev. Genet.* **7**, 45–54 (2006).
64. Kastan, M. B. & Bartek, J. Cell-cycle checkpoints and cancer. *Nature* **432**, 316–323 (2004).
65. Goldstein, M. & Kastan, M. B. The DNA Damage Response: Implications for Tumor Responses to Radiation and Chemotherapy. *Annu. Rev. Med.* **66**, 129–143 (2015).
66. Begg, A. C., Stewart, F. A. & Vens, C. Strategies to improve radiotherapy with targeted drugs. *Nat. Rev. Cancer* **11**, 239–253 (2011).
67. Nurse, P. A Long Twentieth Century of the Cell Cycle and Beyond. *Cell* **100**, 71–78 (2000).
68. Vousden, K. H. & Lane, D. P. p53 in health and disease. *Nat. Rev. Mol. Cell Biol.* **8**, 275–283 (2007).
69. Oren, M. & Rotter, V. Mutant p53 Gain-of-Function in Cancer. *Cold Spring Harb. Perspect. Biol.* **2**, a001107–a001107 (2010).
70. Flynn, R. L. & Zou, L. ATR: a master conductor of cellular responses to DNA replication stress. *Trends Biochem. Sci.* **36**, 133–140 (2011).
71. Reinhardt, H. C. & Yaffe, M. B. Kinases that control the cell cycle in response to DNA damage: Chk1, Chk2, and MK2. *Cell Regul.* **21**, 245–255 (2009).
72. Jaber, S., Toufektchan, E., Lejour, V., Bardot, B. & Toledo, F. p53 downregulates the Fanconi anaemia DNA repair pathway. *Nat. Commun.* **7**, 11091 (2016).

73. De Ruyscher, D. *et al.* Radiotherapy toxicity. *Nat. Rev. Dis. Primer* **5**, 13 (2019).
74. Marks, L. B. *et al.* Radiation Dose–Volume Effects in the Lung. *Int. J. Radiat. Oncol. Biol. Phys.* **76**, S70–S76 (2010).
75. Rodrigues, G., Lock, M., D’Souza, D., Yu, E. & Van Dyk, J. Prediction of radiation pneumonitis by dose–volume histogram parameters in lung cancer—a systematic review. *Radiother. Oncol.* **71**, 127–138 (2004).
76. Burnet, N. G. Defining the tumour and target volumes for radiotherapy. *Cancer Imaging* **4**, 153–161 (2004).
77. Bentzen, S. M. *et al.* Quantitative Analyses of Normal Tissue Effects in the Clinic (QUANTEC): An Introduction to the Scientific Issues. *Int. J. Radiat. Oncol.* **76**, S3–S9 (2010).
78. Wiedenmann, N. *et al.* The utility of multiparametric MRI to characterize hypoxic tumor subvolumes in comparison to FMISO PET/CT. Consequences for diagnosis and chemoradiation treatment planning in head and neck cancer. *Radiother. Oncol.* **150**, 128–135 (2020).
79. Bujold, A., Craig, T., Jaffray, D. & Dawson, L. A. Image-Guided Radiotherapy: Has It Influenced Patient Outcomes? *Qual. Technol. Outcomes Radiat. Oncol.* **22**, 50–61 (2012).
80. Macià I Garau, M. Radiobiology of stereotactic body radiation therapy (SBRT). *Rep. Pract. Oncol. Radiother.* **22**, 86–95 (2017).
81. Mohan, R. A review of proton therapy – Current status and future directions. *Precis. Radiat. Oncol.* **6**, 164–176 (2022).

82. Mirjolet, C. *et al.* Impact of proton therapy on antitumor immune response. *Sci. Rep.* **11**, 13444 (2021).
83. Prezado, Y. & Fois, G. R. Proton-minibeam radiation therapy: A proof of concept. *Med. Phys.* **40**, 031712 (2013).
84. Prezado, Y. *et al.* Tumor Control in RG2 Glioma-Bearing Rats: A Comparison Between Proton Minibeam Therapy and Standard Proton Therapy. *Int. J. Radiat. Oncol.* **104**, 266–271 (2019).
85. Bouchet, A., Serduc, R., Laissue, J. A. & Djonov, V. Effects of microbeam radiation therapy on normal and tumoral blood vessels. *Radiat. Ther. Synchrotron Radiat. Achiev. Chall.* **31**, 634–641 (2015).
86. Bertho, A. *et al.* Evaluation of the Role of the Immune System Response After Minibeam Radiation Therapy. *Int. J. Radiat. Oncol.* **115**, 426–439 (2023).
87. Schneider, T. *et al.* Combining FLASH and spatially fractionated radiation therapy: The best of both worlds. *Radiother. Oncol.* **175**, 169–177 (2022).
88. Mygind, N. & Dahl, R. Anatomy, physiology and function of the nasal cavities in health and disease. *Nasal Drug Deliv.* **29**, 3–12 (1998).
89. Bryche, B. *et al.* Massive transient damage of the olfactory epithelium associated with infection of sustentacular cells by SARS-CoV-2 in golden Syrian hamsters. *Brain. Behav. Immun.* **89**, 579–586 (2020).
90. Dalgorf, D. M. & Harvey, R. J. Sinonasal Anatomy and Function. *Am. J. Rhinol. Allergy* **27**, S3–S6 (2013).
91. Akgoz Karaosmanoglu, A. & Ozgen, B. Anatomy of the Pharynx and Cervical

- Esophagus. *Neuroimaging Anat. Part 2 Head Neck Spine* **32**, 791–807 (2022).
92. Noordzij, J. P. & Ossoff, R. H. Anatomy and Physiology of the Larynx. *Phonosurgery* **39**, 1–10 (2006).
 93. Hsia, C. C. W., Hyde, D. M. & Weibel, E. R. Lung Structure and the Intrinsic Challenges of Gas Exchange. *Compr. Physiol.* **6**, 827–895 (2016).
 94. Brand-Saberi, B. E. M. & Schäfer, T. Trachea: Anatomy and Physiology. *Thorac. Surg. Clin.* **24**, 1–5 (2014).
 95. Chen, F. & Fine, A. Stem Cells in Lung Injury and Repair. *Am. J. Pathol.* **186**, 2544–2550 (2016).
 96. Suarez, C. J., Dintzis, S. M. & Frevert, C. W. 9 - Respiratory. in *Comparative Anatomy and Histology* (eds. Treuting, P. M. & Dintzis, S. M.) 121–134 (Academic Press, San Diego, 2012). doi:10.1016/B978-0-12-381361-9.00009-3.
 97. Rock, J. R. *et al.* Basal cells as stem cells of the mouse trachea and human airway epithelium. *Proc. Natl. Acad. Sci.* **106**, 12771–12775 (2009).
 98. Rock, J. R., Randell, S. H. & Hogan, B. L. M. Airway basal stem cells: a perspective on their roles in epithelial homeostasis and remodeling. *Dis. Model. Mech.* **3**, 545–556 (2010).
 99. Schoch, K. G. *et al.* A subset of mouse tracheal epithelial basal cells generates large colonies in vitro. *Am. J. Physiol. Lung Cell. Mol. Physiol.* **286**, L631–642 (2004).
 100. Ghosh, M. *et al.* Context-dependent differentiation of multipotential keratin 14-expressing tracheal basal cells. *Am. J. Respir. Cell Mol. Biol.* **45**, 403–410 (2011).
 101. Carraro, G. *et al.* Single-Cell Reconstruction of Human Basal Cell Diversity in

- Normal and Idiopathic Pulmonary Fibrosis Lungs. *Am. J. Respir. Crit. Care Med.* **202**, 1540–1550 (2020).
102. Clara, M. Zur histobiologie des bronchialepithels. *Z Mikrosk Anat Forsch* **41**, 321–347 (1937).
103. Dierynck, I., Bernard, A., Roels, H. & De Ley, M. Potent inhibition of both human interferon-gamma production and biologic activity by the Clara cell protein CC16. *Am. J. Respir. Cell Mol. Biol.* **12**, 205–210 (1995).
104. Miele, L., Cordella-Miele, E., Facchiano, A. & Mukherjee, A. B. Novel anti-inflammatory peptides from the region of highest similarity between uteroglobin and lipocortin I. *Nature* **335**, 726–730 (1988).
105. Rawlins, E. L. *et al.* The role of Scgb1a1+ Clara cells in the long-term maintenance and repair of lung airway, but not alveolar, epithelium. *Cell Stem Cell* **4**, 525–534 (2009).
106. Kim, C. F. B. *et al.* Identification of bronchioalveolar stem cells in normal lung and lung cancer. *Cell* **121**, 823–835 (2005).
107. BOERS, J. E., AMBERGEN, A. W. & THUNNISSEN, F. B. J. M. Number and Proliferation of Clara Cells in Normal Human Airway Epithelium. *Am. J. Respir. Crit. Care Med.* **159**, 1585–1591 (1999).
108. Cutz, E. & Conen, P. E. Ultrastructure and Cytochemistry of Clara Cells. **62**, (1971).
109. Blackburn, J. B., Li, N. F., Bartlett, N. W. & Richmond, B. W. An update in club cell biology and its potential relevance to chronic obstructive pulmonary disease. *Am. J. Physiol. Lung Cell. Mol. Physiol.* **324**, L652–L665 (2023).

110. Basil, M. C. *et al.* Human distal airways contain a multipotent secretory cell that can regenerate alveoli. *Nature* **604**, 120–126 (2022).
111. Lafkas, D. *et al.* Therapeutic antibodies reveal Notch control of transdifferentiation in the adult lung. *Nature* **528**, 127–131 (2015).
112. Raman, T. *et al.* Quality control in microarray assessment of gene expression in human airway epithelium. *BMC Genomics* **10**, 493 (2009).
113. Tilley, A. E., Walters, M. S., Shaykhiev, R. & Crystal, R. G. Cilia Dysfunction in Lung Disease. *Annu. Rev. Physiol.* **77**, 379–406 (2015).
114. Knight, D. A. & Holgate, S. T. The airway epithelium: structural and functional properties in health and disease. *Respirol. Carlton Vic* **8**, 432–446 (2003).
115. Evans, M. J., Van Winkle, L. S., Fanucchi, M. V. & Plopper, C. G. Cellular and molecular characteristics of basal cells in airway epithelium. *Exp. Lung Res.* **27**, 401–415 (2001).
116. Heguy, A. *et al.* Responses of the human airway epithelium transcriptome to in vivo injury. *Physiol. Genomics* **29**, 139–148 (2007).
117. Chu, Q., Yao, C., Qi, X., Stripp, B. R. & Tang, N. STK11 is required for the normal program of ciliated cell differentiation in airways. *Cell Discov.* **5**, 36 (2019).
118. Ma, J., Rubin, B. K. & Voynow, J. A. Mucins, Mucus, and Goblet Cells. *CHEST* **154**, 169–176 (2018).
119. Kuo, C. S. & Krasnow, M. A. Formation of a neurosensory organ by epithelial cell slithering. *Cell* **163**, 394–405 (2015).
120. Brain, S. D., Williams, T. J., Tippins, J. R., Morris, H. R. & MacIntyre, I. Calcitonin

- gene-related peptide is a potent vasodilator. *Nature* **313**, 54–56 (1985).
121. Noguchi, M., Furukawa, K. T. & Morimoto, M. Pulmonary neuroendocrine cells: physiology, tissue homeostasis and disease. *Dis. Model. Mech.* **13**, (2020).
122. Haies, D. M., Gil, J. & Weibel, E. R. Morphometric study of rat lung cells: I. Numerical and dimensional characteristics of parenchymal cell population. *Am. Rev. Respir. Dis.* **123**, 533–541 (1981).
123. Wang, Y. *et al.* Pulmonary alveolar type I cell population consists of two distinct subtypes that differ in cell fate. *Proc. Natl. Acad. Sci. U. S. A.* **115**, 2407–2412 (2018).
124. Weibel, E. R. On the Tricks Alveolar Epithelial Cells Play to Make a Good Lung. *American Journal of Respiratory and Critical Care Medicine* vol. 191 504–513 (2015).
125. Beers, M. F. & Moodley, Y. When Is an Alveolar Type 2 Cell an Alveolar Type 2 Cell? A Conundrum for Lung Stem Cell Biology and Regenerative Medicine. *Am. J. Respir. Cell Mol. Biol.* **57**, 18–27 (2017).
126. Kadur Lakshminarasimha Murthy, P. *et al.* Human distal lung maps and lineage hierarchies reveal a bipotent progenitor. *Nature* **604**, 111–119 (2022).
127. Dominici, M. *et al.* Minimal criteria for defining multipotent mesenchymal stromal cells. The International Society for Cellular Therapy position statement. *Cytotherapy* **8**, 315–317 (2006).
128. Rolandsson, S. *et al.* Primary mesenchymal stem cells in human transplanted lungs are CD90/CD105 perivascularly located tissue-resident cells. *BMJ Open Respir. Res.* **1**, e000027 (2014).
129. Sveiven, S. N. & Nordgren, T. M. Lung-resident mesenchymal stromal cells are

- tissue-specific regulators of lung homeostasis. *Am. J. Physiol. Lung Cell. Mol. Physiol.* **319**, L197–L210 (2020).
130. Doherty, D. F., Roets, L. & Krasnodembskaya, A. D. The Role of Lung Resident Mesenchymal Stromal Cells in the Pathogenesis and Repair of Chronic Lung Disease. *Stem Cells Dayt. Ohio* **41**, 431–443 (2023).
131. Habel, D. M. & Hogaboam, C. M. Heterogeneity of Fibroblasts and Myofibroblasts in Pulmonary Fibrosis. *Curr. Pathobiol. Rep.* **5**, 101–110 (2017).
132. Derdak, S. *et al.* Differential collagen and fibronectin production by Thy 1+ and Thy 1- lung fibroblast subpopulations. *American Journal of Physiology-Lung Cellular and Molecular Physiology* vol. 263 L283–L290 (1992).
133. Racine-Samson, L., Rockey, D. C. & Bissell, D. M. The Role of $\alpha 1\beta 1$ Integrin in Wound Contraction. *J. Biol. Chem.* **272**, 30911–30917 (1997).
134. Tsukui, T. *et al.* Collagen-producing lung cell atlas identifies multiple subsets with distinct localization and relevance to fibrosis. *Nat. Commun.* **11**, 1920 (2020).
135. Barron, L., Gharib, S. A. & Duffield, J. S. Lung Pericytes and Resident Fibroblasts: Busy Multitaskers. *Am. J. Pathol.* **186**, 2519–2531 (2016).
136. Kramann, R. *et al.* Perivascular Gli1+ progenitors are key contributors to injury-induced organ fibrosis. *Cell Stem Cell* **16**, 51–66 (2015).
137. Marriott, S. *et al.* ABCG2pos lung mesenchymal stem cells are a novel pericyte subpopulation that contributes to fibrotic remodeling. *Am. J. Physiol. Cell Physiol.* **307**, C684–698 (2014).
138. Chen, L.-J. *et al.* Bleomycin induced epithelial–mesenchymal transition (EMT) in

- pleural mesothelial cells. *Toxicol. Appl. Pharmacol.* **283**, 75–82 (2015).
139. Joyce N. Gonzales & Alexander D. Verin. Pulmonary Vascular Endothelial Cells. in *Endothelial Dysfunction* (ed. Helena Lenasi) Ch. 12 (IntechOpen, Rijeka, 2018). doi:10.5772/intechopen.76995.
140. Niethamer, T. K. *et al.* Defining the role of pulmonary endothelial cell heterogeneity in the response to acute lung injury. *eLife* **9**, e53072 (2020).
141. Gillich, A. *et al.* Capillary cell-type specialization in the alveolus. *Nature* **586**, 785–789 (2020).
142. Schupp, J. C. *et al.* Integrated Single-Cell Atlas of Endothelial Cells of the Human Lung. *Circulation* **144**, 286–302 (2021).
143. Godoy, R. S. *et al.* Single-cell transcriptomic atlas of lung microvascular regeneration after targeted endothelial cell ablation. *eLife* **12**, e80900 (2023).
144. Ding, B.-S. *et al.* Endothelial-Derived Angiocrine Signals Induce and Sustain Regenerative Lung Alveolarization. *Cell* **147**, 539–553 (2011).
145. Lee, J.-H. *et al.* Lung Stem Cell Differentiation in Mice Directed by Endothelial Cells via a BMP4-NFATc1-Thrombospondin-1 Axis. *Cell* **156**, 440–455 (2014).
146. Dejana, E., Hirschi, K. K. & Simons, M. The molecular basis of endothelial cell plasticity. *Nat. Commun.* **8**, 14361 (2017).
147. Ardain, A., Marakalala, M. J. & Leslie, A. Tissue-resident innate immunity in the lung. *Immunology* **159**, 245–256 (2020).
148. Gibbings, S. L. *et al.* Three Unique Interstitial Macrophages in the Murine Lung at Steady State. *Am. J. Respir. Cell Mol. Biol.* **57**, 66–76 (2017).

149. Schyns, J. *et al.* Non-classical tissue monocytes and two functionally distinct populations of interstitial macrophages populate the mouse lung. *Nat. Commun.* **10**, 3964 (2019).
150. Gopallawa, I., Dehinwal, R., Bhatia, V., Gujar, V. & Chirmule, N. A four-part guide to lung immunology: Invasion, inflammation, immunity, and intervention. *Front. Immunol.* **14**, 1119564 (2023).
151. Plasschaert, L. W. *et al.* A single-cell atlas of the airway epithelium reveals the CFTR-rich pulmonary ionocyte. *Nature* **560**, 377–381 (2018).
152. Travaglini, K. J. *et al.* A molecular cell atlas of the human lung from single-cell RNA sequencing. *Nature* **587**, 619–625 (2020).
153. Schiller, H. B. *et al.* The Human Lung Cell Atlas: A High-Resolution Reference Map of the Human Lung in Health and Disease. *Am. J. Respir. Cell Mol. Biol.* **61**, 31–41 (2019).
154. Sikkema, L. *et al.* An integrated cell atlas of the lung in health and disease. *Nat. Med.* **29**, 1563–1577 (2023).
155. Deprez, M. *et al.* A Single-Cell Atlas of the Human Healthy Airways. *American Journal of Respiratory and Critical Care Medicine* vol. 202 1636–1645 (2020).
156. Basil, M. C. & Morrissey, E. E. Lung regeneration: a tale of mice and men. *Semin. Cell Dev. Biol.* **100**, 88–100 (2020).
157. Viana, F., O’Kane, C. & Schroeder, G. Precision-cut lung slices: A powerful ex vivo model to investigate respiratory infectious diseases. *Mol. Microbiol.* **117**, (2021).
158. Giuranno, L., Ient, J., De Ruyscher, D. & Vooijs, M. A. Radiation-Induced Lung

- Injury (RILI). *Front. Oncol.* **9**, 877 (2019).
159. Arroyo-Hernández, M. *et al.* Radiation-induced lung injury: current evidence. *BMC Pulm. Med.* **21**, 9 (2021).
160. Quan, T. E., Cowper, S. E. & Bucala, R. The role of circulating fibrocytes in fibrosis. *Curr. Rheumatol. Rep.* **8**, 145–150 (2006).
161. Perez, J. R. *et al.* A comparative analysis of longitudinal computed tomography and histopathology for evaluating the potential of mesenchymal stem cells in mitigating radiation-induced pulmonary fibrosis. *Sci. Rep.* **7**, 9056 (2017).
162. Straub, J. M. *et al.* Radiation-induced fibrosis: mechanisms and implications for therapy. *J. Cancer Res. Clin. Oncol.* **141**, 1985–1994 (2015).
163. Wynn, T. Cellular and molecular mechanisms of fibrosis. *J. Pathol.* **214**, 199–210 (2008).
164. Gieseck, R. L., Wilson, M. S. & Wynn, T. A. Type 2 immunity in tissue repair and fibrosis. *Nat. Rev. Immunol.* **18**, 62–76 (2018).
165. Chanda, D. *et al.* Developmental pathways in the pathogenesis of lung fibrosis. *Mol. Aspects Med.* **65**, 56–69 (2019).
166. Vacchelli, E. *et al.* Trial Watch: Immunostimulatory cytokines. *OncolImmunology* **1**, 493–506 (2012).
167. Lierova, A. *et al.* Cytokines and radiation-induced pulmonary injuries. *J. Radiat. Res. (Tokyo)* (2018) doi:10.1093/jrr/rry067.
168. Mukhopadhyay, S., Hoidal, J. R. & Mukherjee, T. K. Role of TNF α in pulmonary pathophysiology. *Respir. Res.* **7**, 125 (2006).

169. Wynn, T. A. & Ramalingam, T. R. Mechanisms of fibrosis: therapeutic translation for fibrotic disease. *Nat. Med.* **18**, 1028–1040 (2012).
170. Ryter, S. W. *et al.* Mechanisms of Cell Death in Oxidative Stress. *Antioxid. Redox Signal.* **9**, 49–89 (2007).
171. Wynn, T. & Barron, L. Macrophages: Master Regulators of Inflammation and Fibrosis. *Semin. Liver Dis.* **30**, 245–257 (2010).
172. Mezziani, L., Deutsch, E. & Mondini, M. Macrophages in radiation injury: a new therapeutic target. *Oncotmunology* **7**, e1494488 (2018).
173. Wynn, T. A. & Vannella, K. M. Macrophages in Tissue Repair, Regeneration, and Fibrosis. *Immunity* **44**, 450–462 (2016).
174. Pawlikowski, J. S., Adams, P. D. & Nelson, D. M. Senescence at a glance. *J. Cell Sci.* jcs.109728 (2013) doi:10.1242/jcs.109728.
175. Telgenhoff, D. & Shroot, B. Cellular senescence mechanisms in chronic wound healing. *Cell Death Differ.* **12**, 695–698 (2005).
176. Roger, L., Tomas, F. & Gire, V. Mechanisms and Regulation of Cellular Senescence. *Int. J. Mol. Sci.* **22**, 13173 (2021).
177. He, Y. *et al.* Cellular senescence and radiation-induced pulmonary fibrosis. *Transl. Res.* **209**, 14–21 (2019).
178. Soysouvanh, F. *et al.* Stereotactic Lung Irradiation in Mice Promotes Long-Term Senescence and Lung Injury. *Int. J. Radiat. Oncol. Biol. Phys.* **106**, 1017–1027 (2020).
179. Citrin, D. E. *et al.* Role of Type II Pneumocyte Senescence in Radiation-Induced Lung Fibrosis. *JNCI J. Natl. Cancer Inst.* **105**, 1474–1484 (2013).

180. Pan, J. *et al.* Inhibition of Bcl-2/xl With ABT-263 Selectively Kills Senescent Type II Pneumocytes and Reverses Persistent Pulmonary Fibrosis Induced by Ionizing Radiation in Mice. *Int. J. Radiat. Oncol.* **99**, 353–361 (2017).
181. Hansel, C., Jendrossek, V. & Klein, D. Cellular Senescence in the Lung: The Central Role of Senescent Epithelial Cells. *Int. J. Mol. Sci.* **21**, 3279 (2020).
182. Lafargue, A. *et al.* Ionizing radiation induces long-term senescence in endothelial cells through mitochondrial respiratory complex II dysfunction and superoxide generation. *Free Radic. Biol. Med.* **108**, 750–759 (2017).
183. Kalluri, R. & Weinberg, R. A. The basics of epithelial-mesenchymal transition. *J. Clin. Invest.* **119**, 1420–1428 (2009).
184. Jimenez, S. A. & Piera-Velazquez, S. Endothelial to mesenchymal transition (EndoMT) in the pathogenesis of Systemic Sclerosis-associated pulmonary fibrosis and pulmonary arterial hypertension. Myth or reality? *Matrix Biol.* **51**, 26–36 (2016).
185. Tanjore, H. *et al.* Contribution of Epithelial-derived Fibroblasts to Bleomycin-induced Lung Fibrosis. *Am. J. Respir. Crit. Care Med.* **180**, 657–665 (2009).
186. Kim, K. K. *et al.* Alveolar epithelial cell mesenchymal transition develops *in vivo* during pulmonary fibrosis and is regulated by the extracellular matrix. *Proc. Natl. Acad. Sci.* **103**, 13180–13185 (2006).
187. Hill, C., Jones, M., Davies, D. & Wang, Y. Epithelial-Mesenchymal Transition Contributes to Pulmonary Fibrosis via Aberrant Epithelial/Fibroblastic Cross-Talk. *J. Lung Health Dis.* **3**, 31–35 (2019).
188. Sunil Gowda, S. N. *et al.* Gallic acid-coated silver nanoparticle alters the expression

- of radiation-induced epithelial-mesenchymal transition in non-small lung cancer cells. *Toxicol. In Vitro* **52**, 170–177 (2018).
189. Jarzebska, N. *et al.* Scarred Lung. An Update on Radiation-Induced Pulmonary Fibrosis. *Front. Med.* **7**, 585756 (2021).
190. Yi, M. *et al.* Irradiated Human Umbilical Vein Endothelial Cells Undergo Endothelial-Mesenchymal Transition via the Snail/miR-199a-5p Axis to Promote the Differentiation of Fibroblasts into Myofibroblasts. *BioMed Res. Int.* **2018**, 4135806 (2018).
191. Choi, S.-H. *et al.* A Hypoxia-Induced Vascular Endothelial-to-Mesenchymal Transition in Development of Radiation-Induced Pulmonary Fibrosis. *Clin. Cancer Res.* **21**, 3716–3726 (2015).
192. Wirsdörfer, F. & Jendrossek, V. The Role of Lymphocytes in Radiotherapy-Induced Adverse Late Effects in the Lung. *Front. Immunol.* **7**, (2016).
193. Park, H.-R., Jo, S.-K. & Jung, U. Ionizing Radiation Promotes Epithelial-to-Mesenchymal Transition in Lung Epithelial Cells by TGF- β -producing M2 Macrophages. *In Vivo* **33**, 1773–1784 (2019).
194. Wirsdörfer, F. *et al.* Extracellular Adenosine Production by ecto-5'-Nucleotidase (CD73) Enhances Radiation-Induced Lung Fibrosis. *Cancer Res.* **76**, (2016).
195. de Leve, S. *et al.* Loss of CD73 prevents accumulation of alternatively activated macrophages and the formation of prefibrotic macrophage clusters in irradiated lungs. *FASEB J.* **31**, 2869–2880 (2017).
196. Reyfman, P. A. *et al.* Single-Cell Transcriptomic Analysis of Human Lung Provides

- Insights into the Pathobiology of Pulmonary Fibrosis. *Am. J. Respir. Crit. Care Med.* (2018) doi:10.1164/rccm.201712-2410OC.
197. Morse, C. *et al.* Proliferating SPP1/MERTK-expressing macrophages in idiopathic pulmonary fibrosis. *Eur. Respir. J.* **54**, 1802441 (2019).
198. Adams, T. S. *et al.* Single-cell RNA-seq reveals ectopic and aberrant lung-resident cell populations in idiopathic pulmonary fibrosis. *Sci. Adv.* **6**, eaba1983.
199. Ayaub, E. *et al.* Single Cell RNA-seq and Mass Cytometry Reveals a Novel and a Targetable Population of Macrophages in Idiopathic Pulmonary Fibrosis. Preprint at <https://doi.org/10.1101/2021.01.04.425268> (2021).
200. Curras-Alonso, S. *et al.* An interactive murine single-cell atlas of the lung responses to radiation injury. *Nat. Commun.* **14**, 2445 (2023).
201. Braga-Cohen, S. *et al.* Evidence of Alveolar Macrophage Metabolic Shift Following Stereotactic Body Radiation Therapy -Induced Lung Fibrosis in Mice. *Int. J. Radiat. Oncol.* S0360301624033911 (2024) doi:10.1016/j.ijrobp.2024.09.018.
202. Tsukui, T., Wolters, P. J. & Sheppard, D. Alveolar fibroblast lineage orchestrates lung inflammation and fibrosis. *Nature* **631**, 627–634 (2024).
203. Zhang, Y., Zhang, X., Rabbani, Z. N., Jackson, I. L. & Vujaskovic, Z. Oxidative Stress Mediates Radiation Lung Injury by Inducing Apoptosis. *Int. J. Radiat. Oncol.* **83**, 740–748 (2012).
204. Sisson, T. H. *et al.* Targeted Injury of Type II Alveolar Epithelial Cells Induces Pulmonary Fibrosis. *Am. J. Respir. Crit. Care Med.* **181**, 254–263 (2010).
205. Almeida, C. *et al.* The Role of Alveolar Epithelium in Radiation-Induced Lung Injury.

- PLoS ONE* **8**, e53628 (2013).
206. Traver, G. *et al.* Loss of Nrf2 promotes alveolar type 2 cell loss in irradiated, fibrotic lung. *Free Radic. Biol. Med.* **112**, 578–586 (2017).
207. Venkatesulu, B. P. *et al.* Radiation-Induced Endothelial Vascular Injury. *JACC Basic Transl. Sci.* **3**, 563–572 (2018).
208. Kim, K. S., Kim, J. E., Choi, K. J., Bae, S. & Kim, D. H. Characterization of DNA damage-induced cellular senescence by ionizing radiation in endothelial cells. *Int. J. Radiat. Biol.* **90**, 71–80 (2014).
209. Panganiban, R. A. M., Mungunsukh, O. & Day, R. M. X-irradiation induces ER stress, apoptosis, and senescence in pulmonary artery endothelial cells. *Int. J. Radiat. Biol.* **89**, 656–667 (2013).
210. Deanfield, J. E., Halcox, J. P. & Rabelink, T. J. Endothelial Function and Dysfunction. *Circulation* **115**, 1285–1295 (2007).
211. Baselet, B., Sonveaux, P., Baatout, S. & Aerts, A. Pathological effects of ionizing radiation: endothelial activation and dysfunction. *Cell. Mol. Life Sci.* **76**, 699–728 (2019).
212. Soulier, J. *et al.* Radiotherapy triggers pro-angiogenic signaling in human lung. Preprint at <https://doi.org/10.1101/2024.10.11.617840> (2024).
213. Haston, C. K. & Travis, E. L. Murine susceptibility to radiation-induced pulmonary fibrosis is influenced by a genetic factor implicated in susceptibility to bleomycin-induced pulmonary fibrosis. *Cancer Res.* **57**, 5286–5291 (1997).
214. Dichtl, S., Posch*, W. & Wilflingseder, D. The breathtaking world of human

- respiratory in vitro models: Investigating lung diseases and infections in 3D models, organoids, and lung-on-chip. *Eur. J. Immunol.* **54**, 2250356 (2024).
215. Baldassi, D., Gabold, B. & Merkel, O. M. Air–Liquid Interface Cultures of the Healthy and Diseased Human Respiratory Tract: Promises, Challenges, and Future Directions. *Adv. NanoBiomed Res.* **1**, 2000111 (2021).
216. Giuranno, L. *et al.* Enhanced radiation sensitivity, decreased DNA damage repair, and differentiation defects in airway stem cells derived from patients with chronic obstructive pulmonary disease. *Stem Cells Transl. Med.* **13**, 927–939 (2024).
217. https://resources.bio-techne.com/bio-techne-assets/docs/literature/pr-lung-organoid-culture-protocol-v7.pdf?_ga=2.69093330.296425874.1731598512-214171104.1731598510. https://resources.bio-techne.com/bio-techne-assets/docs/literature/pr-lung-organoid-culture-protocol-v7.pdf?_ga=2.69093330.296425874.1731598512-214171104.1731598510.
218. G er mie, L. *et al.* Evolution of a confluent gut epithelium under on-chip cyclic stretching. *Phys. Rev. Res.* **4**, 023032 (2022).
219. Lapin, B. *et al.* Construction of a Multitubular Perfusable Kidney-on-Chip for the Study of Renal Diseases. in *Kidney Research: Experimental Protocols* (eds. Hewitson, T. D., Toussaint, N. D. & Smith, E. R.) 85–106 (Springer US, New York, NY, 2023). doi:10.1007/978-1-0716-3179-9_7.
220. Innovative three-dimensional models for understanding mechanisms underlying lung diseases: powerful tools for translational research. *Eur. Respir. Rev.* **32**, 230042 (2023).

221. Nizamoglu, M. *et al.* Innovative three-dimensional models for understanding mechanisms underlying lung diseases: powerful tools for translational research. *Eur. Respir. Rev.* **32**, (2023).
222. Veith, I. *et al.* Assessing personalized responses to anti-PD-1 treatment using patient-derived lung tumor-on-chip. *Cell Rep. Med.* **5**, 101549 (2024).
223. Dasgupta, Q. *et al.* A human lung alveolus-on-a-chip model of acute radiation-induced lung injury. *Nat. Commun.* **14**, 6506 (2023).
224. Alsafadi, H. N. *et al.* Applications and Approaches for Three-Dimensional Precision-Cut Lung Slices. Disease Modeling and Drug Discovery. *Am. J. Respir. Cell Mol. Biol.* **62**, 681–691 (2020).
225. Koziol-White, C., GebSKI, E., Cao, G. & Panettieri, R. A. Precision cut lung slices: an integrated ex vivo model for studying lung physiology, pharmacology, disease pathogenesis and drug discovery. *Respir. Res.* **25**, 231 (2024).
226. Bailey, K. E. *et al.* Embedding of Precision-Cut Lung Slices in Engineered Hydrogel Biomaterials Supports Extended *Ex Vivo* Culture. *Am. J. Respir. Cell Mol. Biol.* **62**, 14–22 (2020).
227. Lyons-Cohen, M. R., Thomas, S. Y., Cook, D. N. & Nakano, H. Precision-cut Mouse Lung Slices to Visualize Live Pulmonary Dendritic Cells. *J. Vis. Exp.* 55465 (2017) doi:10.3791/55465.
228. Akram, K. M. *et al.* Live imaging of alveologenesis in precision-cut lung slices reveals dynamic epithelial cell behaviour. *Nat. Commun.* **10**, 1178 (2019).
229. Ahangari, F. *et al.* Saracatinib, a Selective Src Kinase Inhibitor, Blocks Fibrotic

- Responses in Preclinical Models of Pulmonary Fibrosis. *Am. J. Respir. Crit. Care Med.* **206**, 1463–1479 (2022).
230. Lang, N. J. *et al.* Ex vivo tissue perturbations coupled to single-cell RNA-seq reveal multilineage cell circuit dynamics in human lung fibrogenesis. *Sci. Transl. Med.* **15**, eadh0908.
231. Cedilak, M. *et al.* Precision-cut lung slices from bleomycin treated animals as a model for testing potential therapies for idiopathic pulmonary fibrosis. *Pulm. Pharmacol. Ther.* **55**, 75–83 (2019).
232. Koudelka, A. *et al.* Fatty acid nitroalkene reversal of established lung fibrosis. *Redox Biol.* **50**, 102226 (2022).
233. Tatler, A. L. *et al.* Caffeine inhibits TGF β activation in epithelial cells, interrupts fibroblast responses to TGF β , and reduces established fibrosis in *ex vivo* precision-cut lung slices. *Thorax* **71**, 565–567 (2016).
234. Hansen, N. U. B. *et al.* Tissue turnover of collagen type I, III and elastin is elevated in the PCLS model of IPF and can be restored back to vehicle levels using a phosphodiesterase inhibitor. *Respir. Res.* **17**, 76 (2016).
235. Löfdahl, A., Wenglén, C., Rydell-Törmänen, K., Westergren-Thorsson, G. & Larsson-Callerfelt, A.-K. Effects of 5-Hydroxytryptamine Class 2 Receptor Antagonists on Bronchoconstriction and Pulmonary Remodeling Processes. *Am. J. Pathol.* **188**, 1113–1119 (2018).
236. Mercer, P. F. *et al.* Exploration of a potent PI3 kinase/mTOR inhibitor as a novel anti-fibrotic agent in IPF. *Thorax* **71**, 701–711 (2016).

237. Hesse, C. *et al.* Nintedanib modulates type III collagen turnover in viable precision-cut lung slices from bleomycin-treated rats and patients with pulmonary fibrosis. *Respir. Res.* **23**, 201 (2022).
238. Lehmann, M. *et al.* Differential effects of Nintedanib and Pirfenidone on lung alveolar epithelial cell function in ex vivo murine and human lung tissue cultures of pulmonary fibrosis. *Respir. Res.* **19**, 175 (2018).
239. Maher, J. M. *et al.* Lung-restricted ALK5 inhibition avoids systemic toxicities associated with TGF β pathway inhibition. *Toxicol. Appl. Pharmacol.* **438**, 115905 (2022).
240. Savas, A., Warnke, P. C., Ginap, T., Feuerstein, T. J. & Ostertag, C. B. The effects of continuous and single-dose radiation on choline uptake in organotypic tissue slice cultures of rabbit hippocampus. *Neurol. Res.* **23**, 669–675 (2001).
241. Favaudon, V. *et al.* Ultrahigh dose-rate FLASH irradiation increases the differential response between normal and tumor tissue in mice. *Sci. Transl. Med.* **6**, 245ra93-245ra93 (2014).
242. Inada, T., Nishio, H., Amino, S., Abe, K. & Saito, K. High Dose-rate Dependence of Early Skin Reaction in Mouse. *Int. J. Radiat. Biol. Relat. Stud. Phys. Chem. Med.* **38**, 139–145 (1980).
243. Hendry, J. H., Moore, J. V., Hodgson, B. W. & Keene, J. P. The constant low oxygen concentration in all the target cells for mouse tail radionecrosis. *Radiat. Res.* **92**, 172–181 (1982).
244. Field, S. B. & Bewley, D. K. Effects of Dose-rate on the Radiation Response of Rat

- Skin. *Int. J. Radiat. Biol. Relat. Stud. Phys. Chem. Med.* **26**, 259–267 (1974).
245. Turnquist, C., Harris, B. T. & Harris, C. C. Radiation-induced brain injury: current concepts and therapeutic strategies targeting neuroinflammation. *Neuro-Oncol. Adv.* **2**, vdaa057 (2020).
246. Montay-Gruel, P. *et al.* Irradiation in a flash: Unique sparing of memory in mice after whole brain irradiation with dose rates above 100 Gy/s. *Radiother. Oncol.* **124**, 365–369 (2017).
247. Montay-Gruel, P. *et al.* Long-term neurocognitive benefits of FLASH radiotherapy driven by reduced reactive oxygen species. *Proc. Natl. Acad. Sci.* **116**, 10943–10951 (2019).
248. Montay-Gruel, P. *et al.* Ultra-High-Dose-Rate FLASH Irradiation Limits Reactive Gliosis in the Brain. *Radiat. Res.* (2020) doi:10.1667/RADE-20-00067.1.
249. Alaghband, Y. *et al.* Uncovering the Protective Neurologic Mechanisms of Hypofractionated FLASH Radiotherapy. *Cancer Res. Commun.* **3**, 725–737 (2023).
250. Drayson, O. G. G. *et al.* A multi-institutional study to investigate the sparing effect after whole brain electron FLASH in mice: Reproducibility and temporal evolution of functional, electrophysiological, and neurogenic endpoints. *Radiother. Oncol.* 110534 (2024) doi:10.1016/j.radonc.2024.110534.
251. Shadad, A. K. Gastrointestinal radiation injury: Symptoms, risk factors and mechanisms. *World J. Gastroenterol.* **19**, 185 (2013).
252. Levy, K. *et al.* Abdominal FLASH irradiation reduces radiation-induced gastrointestinal toxicity for the treatment of ovarian cancer in mice. *Sci. Rep.* **10**,

21600 (2020).

253. Kim, M. M. *et al.* Comparison of FLASH Proton Entrance and the Spread-Out Bragg Peak Dose Regions in the Spruing of Mouse Intestinal Crypts and in a Pancreatic Tumor Model. *Cancers* **13**, 4244 (2021).
254. Ruan, J.-L. *et al.* Irradiation at Ultra-High (FLASH) Dose Rates Reduces Acute Normal Tissue Toxicity in the Mouse Gastrointestinal System. *Int. J. Radiat. Oncol.* **111**, 1250–1261 (2021).
255. Lim, T. L. *et al.* Early Inflammation and Interferon Signaling Direct Enhanced Intestinal Crypt Regeneration after Proton FLASH Radiotherapy. Preprint at <https://doi.org/10.1101/2024.08.16.608284> (2024).
256. Dormand, E., Banwell, P. E. & Goodacre, T. E. Radiotherapy and wound healing. *Int. Wound J.* **2**, 112–127 (2005).
257. Soto, L. A. *et al.* FLASH Irradiation Results in Reduced Severe Skin Toxicity Compared to Conventional-Dose-Rate Irradiation. 7.
258. Velalopoulou, A. *et al.* FLASH Proton Radiotherapy Spares Normal Epithelial and Mesenchymal Tissues While Preserving Sarcoma Response. *Cancer Res.* **81**, 4808–4821 (2021).
259. Kim, K. *et al.* FLASH Proton Radiation Therapy Mitigates Inflammatory and Fibrotic Pathways and Preserves Cardiac Function in a Preclinical Mouse Model of Radiation-Induced Heart Disease. *Int. J. Radiat. Oncol.* **119**, 1234–1247 (2024).
260. Fouillade, C. *et al.* FLASH Irradiation Spares Lung Progenitor Cells and Limits the Incidence of Radio-induced Senescence. *Clin. Cancer Res.* **26**, 1497–1506 (2020).

261. Venkatesulu, B. P. *et al.* Ultra high dose rate (35 Gy/sec) radiation does not spare the normal tissue in cardiac and splenic models of lymphopenia and gastrointestinal syndrome. *Sci. Rep.* **9**, 17180 (2019).
262. Sørensen, B. S. *et al.* Pencil beam scanning proton FLASH maintains tumor control while normal tissue damage is reduced in a mouse model. *Radiother. Oncol.* **175**, 178–184 (2022).
263. Chabi, S. *et al.* Ultra-high-dose-rate FLASH and Conventional-Dose-Rate Irradiation Differentially Affect Human Acute Lymphoblastic Leukemia and Normal Hematopoiesis. *Int. J. Radiat. Oncol.* **109**, 819–829 (2021).
264. Montay-Gruel, P. *et al.* Hypofractionated FLASH-RT as an Effective Treatment against Glioblastoma that Reduces Neurocognitive Side Effects in Mice. *Clin. Cancer Res.* **27**, 775–784 (2021).
265. Gao, F. *et al.* First demonstration of the FLASH effect with ultrahigh dose rate high-energy X-rays. *Radiother. Oncol.* **166**, 44–50 (2022).
266. Eggold, J. T. *et al.* Abdominopelvic FLASH Irradiation Improves PD-1 Immune Checkpoint Inhibition in Preclinical Models of Ovarian Cancer. *Mol. Cancer Ther.* **21**, 371–381 (2022).
267. Cao, X. *et al.* Quantification of Oxygen Depletion During FLASH Irradiation In Vitro and In Vivo. *Int. J. Radiat. Oncol.* **111**, 240–248 (2021).
268. Diffenderfer, E. S. *et al.* Design, Implementation, and in Vivo Validation of a Novel Proton FLASH Radiation Therapy System. *Int. J. Radiat. Oncol.* **106**, 440–448 (2020).
269. Cunningham, S. *et al.* FLASH Proton Pencil Beam Scanning Irradiation Minimizes

- Radiation-Induced Leg Contracture and Skin Toxicity in Mice. *Cancers* **13**, 1012 (2021).
270. Kim, Y.-E. *et al.* Effects of Ultra-high dose rate FLASH Irradiation on the Tumor Microenvironment in Lewis Lung Carcinoma: Role of Myosin Light Chain. *Int. J. Radiat. Oncol.* **109**, 1440–1453 (2021).
271. Almeida, A. *et al.* Antitumor Effect by Either FLASH or Conventional Dose Rate Irradiation Involves Equivalent Immune Responses. *Int. J. Radiat. Oncol.* **118**, 1110–1122 (2024).
272. Leavitt, R. J. *et al.* Acute hypoxia does not alter tumor sensitivity to FLASH radiotherapy. *Int. J. Radiat. Oncol.* (2024) doi:10.1016/j.ijrobp.2024.02.015.
273. Freyer, J. P., Jarrett, K., Carpenter, S. & Raju, M. R. Oxygen enhancement ratio as a function of dose and cell cycle phase for radiation-resistant and sensitive CHO cells. *Radiat. Res.* **127**, 297–307 (1991).
274. Prax, G. & Kapp, D. S. A computational model of radiolytic oxygen depletion during FLASH irradiation and its effect on the oxygen enhancement ratio. *Phys. Med. Biol.* **64**, 185005 (2019).
275. Spitz, D. R. *et al.* An integrated physico-chemical approach for explaining the differential impact of FLASH versus conventional dose rate irradiation on cancer and normal tissue responses. *Radiother. Oncol.* **139**, 23–27 (2019).
276. Boscolo, D., Scifoni, E., Durante, M., Krämer, M. & Fuss, M. C. May oxygen depletion explain the FLASH effect? A chemical track structure analysis. *Radiother. Oncol.* **162**, 68–75 (2021).

277. Ahmed Alanazi, Jintana Meesungnoen, & Jean-Paul Jay-Gerin. A Computer Modeling Study of Water Radiolysis at High Dose Rates. Relevance to FLASH Radiotherapy. *Radiat. Res.* **195**, 149–162 (2020).
278. Peter Wardman. Radiotherapy Using High-Intensity Pulsed Radiation Beams (FLASH): A Radiation-Chemical Perspective. *Radiat. Res.* **194**, 607–617 (2020).
279. Adrian, G. *et al.* The FLASH effect depends on oxygen concentration. *Br. J. Radiol.* **93**, 20190702 (2020).
280. Schüler, E. *et al.* Ultra-high dose rate electron beams and the FLASH effect: From preclinical evidence to a new radiotherapy paradigm. *Med. Phys.* **49**, 2082–2095 (2022).
281. Leavitt, R. J., Limoli, C. L. & Baulch, J. E. miRNA-based therapeutic potential of stem cell-derived extracellular vesicles: a safe cell-free treatment to ameliorate radiation-induced brain injury. *Int. J. Radiat. Biol.* **95**, 427–435 (2019).
282. Chaudhuri, A. A., Binkley, M. S., Osmundson, E. C., Alizadeh, A. A. & Diehn, M. Predicting Radiotherapy Responses and Treatment Outcomes Through Analysis of Circulating Tumor DNA. *Semin. Radiat. Oncol.* **25**, 305–312 (2015).
283. Simmons, D. A. *et al.* Reduced cognitive deficits after FLASH irradiation of whole mouse brain are associated with less hippocampal dendritic spine loss and neuroinflammation. *Radiother. Oncol.* **139**, 4–10 (2019).
284. Alaghband, Y. *et al.* Neuroprotection of Radiosensitive Juvenile Mice by Ultra-High Dose Rate FLASH Irradiation. *Cancers* **12**, 1671 (2020).
285. Allen, B. D. *et al.* Maintenance of Tight Junction Integrity in the Absence of Vascular

- Dilation in the Brain of Mice Exposed to Ultra-High-Dose-Rate FLASH Irradiation. *Radiat. Res.* **194**, (2020).
286. Favaudon, V., Labarbe, R. & Limoli, C. L. Model studies of the role of oxygen in the FLASH effect. *Med. Phys.* **49**, 2068–2081 (2022).
287. Froidevaux, P. *et al.* FLASH irradiation does not induce lipid peroxidation in lipids micelles and liposomes. *Radiat. Phys. Chem.* **205**, 110733 (2023).
288. Portier, L. *et al.* Differential Remodeling of the Oxylipin Pool After FLASH Versus Conventional Dose-Rate Irradiation In Vitro and In Vivo. *Int. J. Radiat. Oncol.* **119**, 1481–1492 (2024).
289. Wardman, P. & Candeias, L. P. Fenton chemistry: an introduction. *Radiat. Res.* **145**, 523–531 (1996).
290. Limoli, C. L. & Vozenin, M.-C. Reinventing Radiobiology in the Light of FLASH Radiotherapy. *Annu. Rev. Cancer Biol.* **7**, 1–21 (2023).
291. Rahman, M. *et al.* Electron FLASH Delivery at Treatment Room Isocenter for Efficient Reversible Conversion of a Clinical LINAC. *Int. J. Radiat. Oncol.* **110**, 872–882 (2021).
292. Lempart, M. *et al.* Modifying a clinical linear accelerator for delivery of ultra-high dose rate irradiation. *FLASH Radiother. Int. Workshop* **139**, 40–45 (2019).
293. Schüller, E. *et al.* Experimental Platform for Ultra-high Dose Rate FLASH Irradiation of Small Animals Using a Clinical Linear Accelerator. *Int. J. Radiat. Oncol. Biol. Phys.* **97**, 195–203 (2017).
294. Oh, K. *et al.* Initial experience with an electron FLASH research extension (FLEX) for

- the Clinac system. *J. Appl. Clin. Med. Phys.* **25**, e14159 (2024).
295. Wu Y, No HJ, MBreitkreutz DY, Mascia AE, Moeckli R, Bourhis J, Schüler E, Maxim PG, Loo BW Jr. Technological Basis for Clinical Trials in FLASH Radiation Therapy: A Review. *Appl Radiat Oncol.* 2021;(2):6-14.
296. Moeckli, R. *et al.* Commissioning of an ultra-high dose rate pulsed electron beam medical LINAC for FLASH RT preclinical animal experiments and future clinical human protocols. *Med. Phys.* **48**, 3134–3142 (2021).
297. C DesRosiers, V Moskvin, A F Bielajew, & L Papiez. 150-250 MeV electron beams in radiation therapy. *Phys. Med. Biol.* **45**, 1781 (2000).
298. Kokurewicz, K. *et al.* An experimental study of focused very high energy electron beams for radiotherapy. *Commun. Phys.* **4**, 33 (2021).
299. Flacco, A. *et al.* Laser-FLASH: radiobiology at high dose, ultra-high dose-rate, single pulse laser-driven proton source. Preprint at <http://arxiv.org/abs/2410.05086> (2024).
300. Jolly, S., Owen, H., Schippers, M. & Welsch, C. Technical challenges for FLASH proton therapy. *Phys. Medica Eur. J. Med. Phys.* **78**, 71–82 (2020).
301. Myers, S., Degiovanni, A. & Farr, J. B. Future Prospects for Particle Therapy Accelerators. *Rev. Accel. Sci. Technol.* **10**, 49–92 (2019).
302. Petersson, K. *et al.* High dose-per-pulse electron beam dosimetry — A model to correct for the ion recombination in the Advanced Markus ionization chamber. *Med. Phys.* **44**, 1157–1167 (2017).
303. Siddique, S., Ruda, H. E. & Chow, J. C. L. FLASH Radiotherapy and the Use of

- Radiation Dosimeters. *Cancers* **15**, 3883 (2023).
304. Gómez, F. *et al.* Development of an ultra-thin parallel plate ionization chamber for dosimetry in FLASH radiotherapy. *Med. Phys.* **49**, 4705–4714 (2022).
305. Fleta, C. *et al.* State-of-the-art silicon carbide diode dosimeters for ultra-high dose-per-pulse radiation at FLASH radiotherapy. *Phys. Med. Biol.* **69**, 095013 (2024).
306. Marinelli, M. *et al.* Design, realization, and characterization of a novel diamond detector prototype for FLASH radiotherapy dosimetry. *Med. Phys.* mp.15473 (2022) doi:10.1002/mp.15473.
307. Rohrer Bley, C. *et al.* Dose- and Volume-Limiting Late Toxicity of FLASH Radiotherapy in Cats with Squamous Cell Carcinoma of the Nasal Planum and in Mini Pigs. *Clin. Cancer Res.* **28**, 3814–3823 (2022).
308. Limoli, C. L. *et al.* The sparing effect of FLASH-RT on synaptic plasticity is maintained in mice with standard fractionation. *Radiother. Oncol.* **186**, 109767 (2023).
309. Verginadis, I. I. *et al.* FLASH proton reirradiation, with or without hypofractionation, mitigates chronic toxicity in the normal murine intestine, skin, and bone. Preprint at <https://doi.org/10.1101/2024.07.08.602528> (2024).
310. TOWN, C. D. Effect of High Dose Rates on Survival of Mammalian Cells. *Nature* **215**, 847–848 (1967).
311. Beyreuther, E. *et al.* Feasibility of proton FLASH effect tested by zebrafish embryo irradiation. *Radiother. Oncol.* **139**, 46–50 (2019).

312. Vozenin, M.-C. *et al.* The Advantage of FLASH Radiotherapy Confirmed in Mini-pig and Cat-cancer Patients. *Clin. Cancer Res.* **25**, 35–42 (2019).
313. Konradsson, E. *et al.* Establishment and Initial Experience of Clinical FLASH Radiotherapy in Canine Cancer Patients. *Front. Oncol.* **11**, 658004 (2021).
314. Børresen, B. *et al.* Evaluation of single-fraction high dose FLASH radiotherapy in a cohort of canine oral cancer patients. *Front. Oncol.* **13**, 1256760 (2023).
315. Bourhis, J. *et al.* Treatment of a first patient with FLASH-radiotherapy. *Radiother. Oncol.* **139**, 18–22 (2019).
316. Mascia, A. E. *et al.* Proton FLASH Radiotherapy for the Treatment of Symptomatic Bone Metastases: The FAST-01 Nonrandomized Trial. *JAMA Oncol.* **9**, 62 (2023).
317. Daugherty, E. *et al.* FLASH radiotherapy for the treatment of symptomatic bone metastases in the thorax (FAST-02): protocol for a prospective study of a novel radiotherapy approach. *Radiat. Oncol.* **19**, 34 (2024).
318. Giuliano, L. *et al.* Characterization of Ultra-High-Dose Rate Electron Beams with ElectronFlash Linac. *Appl. Sci.* **13**, (2023).
319. Butler, A., Hoffman, P., Smibert, P., Papalexi, E. & Satija, R. Integrating single-cell transcriptomic data across different conditions, technologies, and species. *Nat. Biotechnol.* **36**, 411–420 (2018).
320. Young, M. D. & Behjati, S. SoupX removes ambient RNA contamination from droplet-based single-cell RNA sequencing data. *GigaScience* **9**, g1aa151 (2020).
321. Hurskainen, M. *et al.* Single cell transcriptomic analysis of murine lung development on hyperoxia-induced damage. *Nat. Commun.* **12**, 1565 (2021).

322. Yao, X., Gordon, E. M., Figueroa, D. M., Barochia, A. V. & Levine, S. J. Emerging Roles of Apolipoprotein E and Apolipoprotein A-I in the Pathogenesis and Treatment of Lung Disease. *Am. J. Respir. Cell Mol. Biol.* **55**, 159–169 (2016).
323. Zadoorian, A., Du, X. & Yang, H. Lipid droplet biogenesis and functions in health and disease. *Nat. Rev. Endocrinol.* **19**, 443–459 (2023).
324. Deng, H. & Li, W. Monoacylglycerol lipase inhibitors: modulators for lipid metabolism in cancer malignancy, neurological and metabolic disorders. *Acta Pharm. Sin. B* **10**, 582–602 (2020).
325. Bernhard, W. Lung surfactant: Function and composition in the context of development and respiratory physiology. *Ann. Anat. - Anat. Anz.* **208**, 146–150 (2016).
326. Thayyullathil, F. *et al.* Acid sphingomyelinase-dependent autophagic degradation of GPX4 is critical for the execution of ferroptosis. *Cell Death Dis.* **12**, 26 (2021).
327. Dumesnil, C. *et al.* Cholesterol esters form supercooled lipid droplets whose nucleation is facilitated by triacylglycerols. *Nat. Commun.* **14**, 915 (2023).
328. Tlatempa-Romero, B., Cázares-Ordoñez, V., Oyarzábal, L. F. & Vázquez-de-Lara, L. G. The Role of Pulmonary Surfactant Phospholipids in Fibrotic Lung Diseases. *Int. J. Mol. Sci.* **24**, 326 (2022).
329. Carter, C. L., Jones, J. W., Farese, A. M., MacVittie, T. J. & Kane, M. A. Lipidomic dysregulation within the lung parenchyma following whole-thorax lung irradiation: Markers of injury, inflammation and fibrosis detected by MALDI-MSI. *Sci. Rep.* **7**, 10343 (2017).

330. Roh, K. *et al.* Lysosomal control of senescence and inflammation through cholesterol partitioning. *Nat. Metab.* **5**, 398–413 (2023).
331. Yao, X., Gordon, E. M., Figueroa, D. M., Barochia, A. V. & Levine, S. J. Emerging Roles of Apolipoprotein E and Apolipoprotein A-I in the Pathogenesis and Treatment of Lung Disease. *Am. J. Respir. Cell Mol. Biol.* **55**, 159–169 (2016).
332. Jin, Y., Tan, Y., Chen, L., Liu, Y. & Ren, Z. Reactive Oxygen Species Induces Lipid Droplet Accumulation in HepG2 Cells by Increasing Perilipin 2 Expression. *Int. J. Mol. Sci.* **19**, 3445 (2018).
333. Lu, Y.-S. *et al.* UVA Induced Oxidative Stress Was Inhibited by Paeoniflorin/Nrf2 Signaling or PLIN2. *Front. Pharmacol.* **11**, 736 (2020).
334. Kluge, M. A., Fetterman, J. L. & Vita, J. A. Mitochondria and Endothelial Function. *Circ. Res.* **112**, 1171–1188 (2013).
335. Pawlik, T. M. & Keyomarsi, K. Role of cell cycle in mediating sensitivity to radiotherapy. *Int. J. Radiat. Oncol. Biol. Phys.* **59**, 928–942 (2004).
336. Dubail, M. *et al.* Lung Organotypic Slices Enable Rapid Quantification of Acute Radiotherapy Induced Toxicity. *Cells* **12**, 2435 (2023).
337. Abhinand, C. S., Raju, R., Soumya, S. J., Arya, P. S. & Sudhakaran, P. R. VEGF-A/VEGFR2 signaling network in endothelial cells relevant to angiogenesis. *J. Cell Commun. Signal.* **10**, 347–354 (2016).
338. Matsui, J., Wakabayashi, T., Asada, M., Yoshimatsu, K. & Okada, M. Stem Cell Factor/c-kit Signaling Promotes the Survival, Migration, and Capillary Tube Formation of Human Umbilical Vein Endothelial Cells. *J. Biol. Chem.* **279**, 18600–

18607 (2004).

339. Desdín-Micó, G., Soto-Heredero, G. & Mittelbrunn, M. Mitochondrial activity in T cells. *Mitochondria Innate Adapt. Immun.* **41**, 51–57 (2018).
340. Ferrer, I., Olivé, M., Blanco, R., Cinós, C. & Planas, A. M. Selective c-Jun overexpression is associated with ionizing radiation-induced apoptosis in the developing cerebellum of the rat. *Mol. Brain Res.* **38**, 91–100 (1996).
341. Sherman, M. L., Datta, R., Hallahan, D. E., Weichselbaum, R. R. & Kufe, D. W. Ionizing radiation regulates expression of the c-jun protooncogene. *Proc. Natl. Acad. Sci.* **87**, 5663–5666 (1990).
342. Lee, Y. J. *et al.* Effect of Ionizing Radiation on AP-1 Binding Activity and Basic Fibroblast Growth Factor Gene Expression in Drug-sensitive Human Breast Carcinoma MCF-7 and Multidrug-resistant MCF-7/ADR Cells *. *J. Biol. Chem.* **270**, 28790–28796 (1995).
343. Martin, M. *et al.* Coactivation of AP-1 activity and TGF- β 1 gene expression in the stress response of normal skin cells to ionizing radiation. *Oncogene* **15**, 981–989 (1997).
344. Hwang, S. S. *et al.* mRNA destabilization by BTG1 and BTG2 maintains T cell quiescence. *Science* vol. 367 1255–1260 (2020).
345. Kim, S. H., Jung, I. R. & Hwang, S. S. Emerging role of anti-proliferative protein BTG1 and BTG2. *BMB Rep.* **55**, 380–388 (2022).
346. Farr, L., Ghosh, S. & Moonah, S. Role of MIF Cytokine/CD74 Receptor Pathway in Protecting Against Injury and Promoting Repair. *Front. Immunol.* **11**, 1273 (2020).

347. Grieb, G., Merk, M., Bernhagen, J., & Bucala, R. Macrophage migration inhibitory factor (MIF): A promising biomarker. *Drug News Perspect.* **23**, 257 (2010).
348. Takahashi, K. *et al.* Macrophage CD74 contributes to MIF-induced pulmonary inflammation. *Respir. Res.* **10**, 33 (2009).
349. Vozenin, M.-C., Montay-Gruel, P., Limoli, C. & Germond, J.-F. All Irradiations that are Ultra-High Dose Rate may not be FLASH: The Critical Importance of Beam Parameter Characterization and In Vivo Validation of the FLASH Effect. 2.
350. Daugherty, E. C. *et al.* FAST-01: Results of the First-in-Human Study of Proton FLASH Radiotherapy. *Int. J. Radiat. Oncol.* **114**, S4 (2022).
351. Liu, K. *et al.* Redefining FLASH Radiation Therapy: The Impact of Mean Dose Rate and Dose Per Pulse in the Gastrointestinal Tract. *Int. J. Radiat. Oncol. Biol. Phys.* doi:10.1016/j.ijrobp.2024.10.009.
352. Vu, N. T., Kim, M., Stephenson, D. J., MacKnight, H. P. & Chalfant, C. E. Ceramide Kinase Inhibition Drives Ferroptosis and Sensitivity to Cisplatin in Mutant *KRAS* Lung Cancer by Dysregulating VDAC-Mediated Mitochondria Function. *Mol. Cancer Res.* **20**, 1429–1442 (2022).
353. Getz, G. S. & Reardon, C. A. ApoE knockout and knockin mice: the history of their contribution to the understanding of atherogenesis. *J. Lipid Res.* **57**, 758–766 (2016).
354. Zhang, S. *et al.* PLIN2 Mediates Neuroinflammation and Oxidative/Nitrosative Stress via Downregulating Phosphatidylethanolamine in the Rostral Ventrolateral Medulla of Stressed Hypertensive Rats. *J. Inflamm. Res.* **Volume 14**, 6331–6348

(2021).

355. Bartolacci, C., Andreani, C., El-Gammal, Y. & Scaglioni, P. P. Lipid Metabolism Regulates Oxidative Stress and Ferroptosis in RAS-Driven Cancers: A Perspective on Cancer Progression and Therapy. *Front. Mol. Biosci.* **8**, 706650 (2021).
356. Lv, J. *et al.* FLASH Irradiation Regulates IFN- β induction by mtDNA via Cytochrome c Leakage. 2024.04.10.588811 Preprint at <https://doi.org/10.1101/2024.04.10.588811> (2024).
357. Guo, Z., Buonanno, M., Harken, A., Zhou, G. & Hei, T. K. Mitochondrial Damage Response and Fate of Normal Cells Exposed to FLASH Irradiation with Protons. *Radiat. Res.* **197**, 569–582 (2022).
358. Marsh, L. M. *et al.* Surface expression of CD74 by type II alveolar epithelial cells: a potential mechanism for macrophage migration inhibitory factor-induced epithelial repair. *American Journal of Physiology-Lung Cellular and Molecular Physiology* vol. 296 L442–L452 (2009).
359. Li, W. *et al.* Lipid Polyunsaturated Fatty Acid Chains in Mouse Kidneys Were Increased within 5 min of a Single High Dose Whole Body Irradiation. *Int. J. Mol. Sci.* **24**, 12439 (2023).
360. Aramaki, S. *et al.* Lipidomics-based tissue heterogeneity in specimens of luminal breast cancer revealed by clustering analysis of mass spectrometry imaging: A preliminary study. *PLOS ONE* **18**, e0283155 (2023).
361. Sesink, A. *et al.* The AsiDNATM decoy mimicking DSBs protects the normal tissue from radiation toxicity through a DNA-PK/p53/p21-dependent G1/S arrest. *NAR*

Cancer **6**, zcae011 (2024).

362. Prades-Sagarra, E. *et al.* Caffeic Acid Phenethyl Ester (CAPE), a natural polyphenol to increase the therapeutic window for lung adenocarcinomas. *Radiother. Oncol.* **190**, 110021 (2024).

ANNEX I : Additional results and paper's part 1

ANNEX 1 – ADDITIONAL RESULTS AND PAPERS PART 1

In addition to the results presented in my this first published paper, through collaborations within our team or with other institutes, we have **used the PCLS model for several other applications related to testing radioprotectors for healthy tissue**, specifically the **AsiDNA**

molecule and the **CAPE compound**^{361,362}. On the one hand, AsiDNA is a cholesterol-coupled oligonucleotide that mimics double-stranded DNA breaks, hijacking the DNA damage response to sensitize tumor cells to radiation and chemotherapy. It triggers a G1/S cell cycle arrest in normal cells, offering protection to healthy tissues by preventing further damage³⁶¹. On the other hand, Caffeic Acid Phenethyl Ester (CAPE) has been shown to have anti-proliferative and pro-apoptotic effects in tumor cells, making it a potential therapeutic agent for cancer. In contrast, it exhibits radioprotective properties in normal tissues, with anti-inflammatory and antioxidant effects that help reduce radiation-induced damage³⁶². These studies allowed have confirmed the molecular and cellular effect of these compounds using an *ex vivo* model of PCLS. These studies have also been published and are part of the work I contributed to as a co-author, complementing this first section on the establishment of the PCLS model for various studies on radiotoxicities in the lung. As the materials and methods associated with these studies are present in the cited articles, I will not describe them further.

Another interesting perspective, whether for the response to radiotherapy in the lung tumoral context or for studying the FLASH effect, is the **establishment of a relevant model combining healthy tissue with tumoral tissue**. To this end, we explored several co-culture approaches that did not yield successful results with PCLS. However, by using an orthotopic tumor model generated by injecting LL2 tumor cells intravenously, we managed to generate a PCLS model with tumor cells. Although this work is an appendix to my thesis work, which focuses on the effects of FLASH radiotherapy on healthy lung tissue, the development of a robust protocol, along with the establishment of relevant endpoints with tumoral PCLS, could allow to consider the tumor response as well as the response of the surrounding healthy peritumoral tissue. This would be more relevant in the clinical context of patients undergoing treatment for lung cancer.

1. ADDITIONAL RESULTS

1.1 Complementary studies on radioprotector of healthy lung tissue to radiation

a) *AsiDNA (see associated article)*

To investigate the AsiDNA™-induced cell cycle arrest in the lung that protect the normal cells from radiation, PCLS were used. PCLS were then treated for 24 hours with AsiDNA™ or Nol8, and EdU (a marker of replicative cell division) was co-incubated for an additional 24 hours. Cell nuclei were subsequently stained for EdU incorporation. A significant loss of EdU-positive cells was observed following AsiDNA™ treatment compared to both untreated and Nol8-treated PCLS (Figure 52A), suggesting that AsiDNA™ similarly triggered cell cycle arrest *ex vivo*.

b) CAPE

To assess the radioprotective effects of CAPE in normal tissue in a 3D model, PCLS were used. The slices were treated with CAPE and radiation at dose of 4 Gy, then gene expression levels of several pro-inflammatory and antioxidant markers was evaluated. The expression of interleukins (IL-6, IL-1 α) and COX-2 was assessed, as they play an important role in the development of radiation pneumonitis and subsequently fibrosis. Radiation did not significantly change the expression of these markers. CAPE treatment prior to radiation decreased the expression of IL-6 ($p = 0.03$) in a dose-dependent manner, while the effect on the expression of COX-2 was less pronounced ($p = 0.11$).

1.2 Proof of concept of PCLS-tumor model obtention

Generation of orthotopic LL2-Luc mouse model and generation of PCLS : Briefly, orthotopic LL2-Luc tumors mice were generated by injecting 500000 low passage LL2-Luc cells at 70% confluency in IV by the tail of mice. These LL2 cells were modified to express constitutively luciferase, which in presence of luciferin, which was injected in IP at 150 mg/kg per mice, that can be detected by light emission and measured by IVIS. IVIS measurements were performed daily until tumors could be detected in the lungs. Then, once the lung were harvested, PCLS were performed according to the same method described in Article 1. The first proof of concept analysis of cell division was done using EdU assay as described in Article 1.

To generate a PCLS model containing tumor cells, LL2-Luc cells were intravenously injected into the tail vein of C57BL6/J WT mice. Subsequently, the luminescence emitted by tumor growth was measured daily using IVIS. Starting from day 28 post-injection, at least two tumor masses could be detected in the lungs of 20% of the injected mice. After lung harvest, macroscopic examination revealed 4 tumor masses distributed across the left, lower, and upper lobes. Despite technical challenges, some PCLS containing tumor tissue were successfully

generated, and as proof of concept, they were cultured in the presence of EdU for 24 hours. By visually examining the tumor localization in PCLS, we qualitatively analyzed the presence of EdU+ cells in the tumor, the peri-tumoral healthy region, and the healthy tissue. Interestingly, the proportion of EdU+ cells was higher in the peri-tumoral tissue, which could indicate immune recruitment or the presence of disseminated tumor cells. In the tumor mass, a large proportion of cells at its margins were EdU+, indicating they were in an active cell cycle phase, characteristic of tumor cells. Finally, EdU+ tumor cells were only found at the tumor margins, with no dividing cells at the center, a feature also commonly observed in solid tumors. In conclusion, this first generation of PCLS containing tumor cells allowed us to recapitulate several morphological and cellular aspects of the tumor as well as the peri-tumoral tissue, making it an interesting model for studying adiation responses in the future.

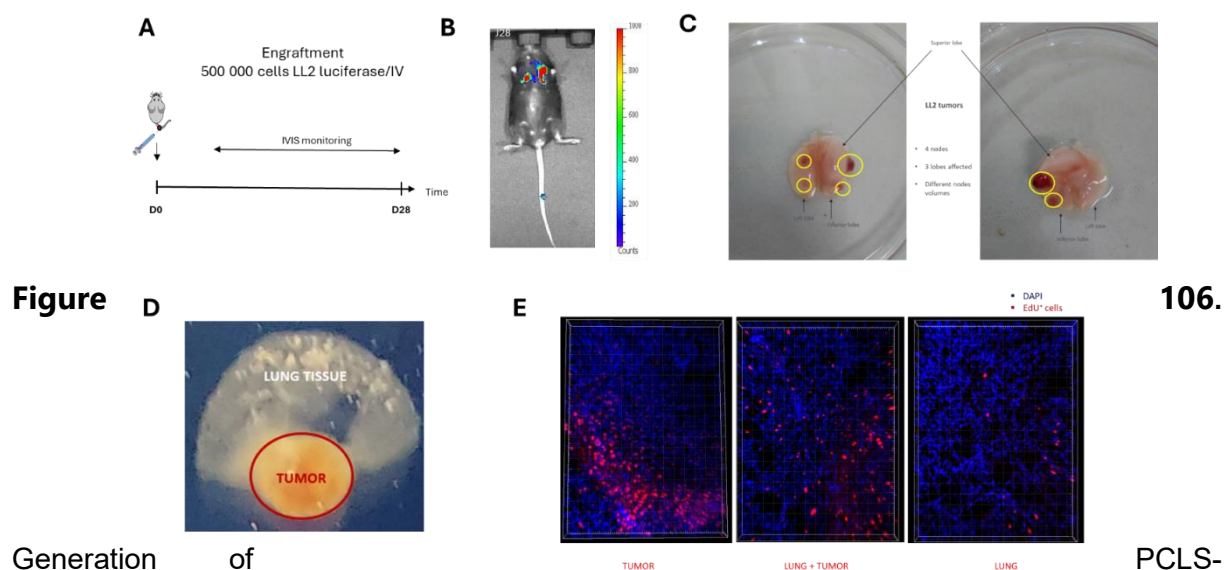


Figure 106. Generation of PCLS-tumor from orthotopic LL2-Luc tumor mouse model. (A) Schematic representation of the experimental procedure showing the engraftment of 500,000 LL2-Luc cells into the tail vein of mice. The cells express luciferase and, upon administration of luciferin (150 mg/kg, IP), can be detected through light emission measured by IVIS imaging. (B) IVIS imaging showing light emission corresponding to tumor growth in the lung, measured at d28 where tumors became visible. (C) Image of lung with tumors (circled in yellow) visible on macroscopic examination. (D) Image PCLS-tumor. (E) Representative 3D-reconstruction of images obtained after 24h incubation of PCLS-tumor in presence of EdU.

2. THE ASI DNA™ DECOY MIMICKING DSBs PROTECTS THE NORMAL TISSUE FROM RADIATION TOXICITY THROUGH A DNA-PK/P53/P21-DEPENDENT G1/S ARREST

NAR Cancer, 2024, 6, zcae011
<https://doi.org/10.1093/narcan/zcae011>
Advance access publication date: 12 March 2024
Nucleic Acid-Based Cancer Therapeutics

OXFORD

The AsiDNA™ decoy mimicking DSBs protects the normal tissue from radiation toxicity through a DNA-PK/p53/p21-dependent G1/S arrest

Anouk Sesink^{1,2}, Margaux Becerra^{1,2}, Jia-Ling Ruan³, Sophie Leboucher⁴, Maxime Dubail^{1,2}, Sophie Heinrich^{1,2}, Wael Jdey⁵, Kristoffer Petersson^{3,6}, Charles Fouillade^{1,2}, Nathalie Berthault^{1,2}, Marie Dutreix^{1,2} and Pierre-Marie Girard^{1,2,*}

¹Institut Curie, Université PSL, CNRS UMR3347, INSERM U1021, 91405 Orsay, France

²Université Paris-Saclay, CNRS UMR 3347, INSERM U1021, 91405 Orsay, France

³Oxford Institute for Radiation Oncology, Department of Oncology, University of Oxford, Old Road Campus Research Building, Roosevelt Drive, Oxford, UK

⁴Histology platform, Institut Curie, CNRS UMR3348, 91405 Orsay, France

⁵Valerio Therapeutics, 49 Bd du Général Martial Valin, 75015 Paris, France

⁶Radiation Physics, Department of Hematology, Oncology and Radiation Physics, Skåne University Hospital, Lund University, Lund, Sweden.

*To whom correspondence should be addressed. Tel: +33 1 69 86 31 31; Email: pierre-marie.girard@curie.fr

Present addresses:

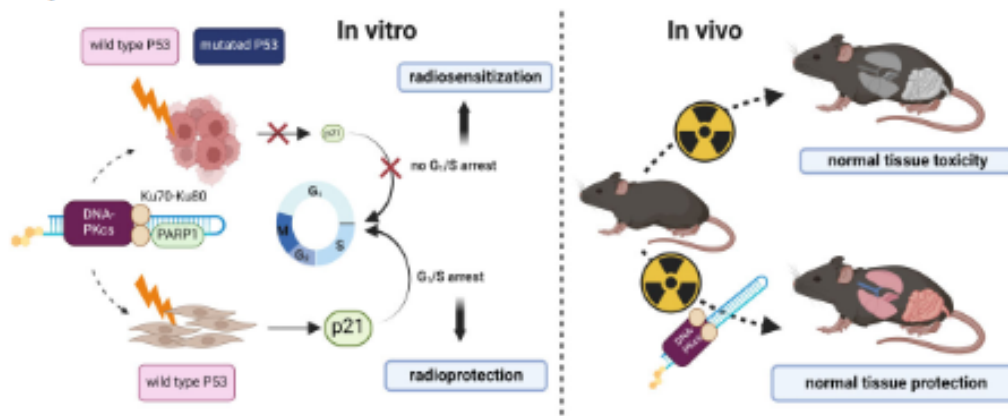
Anouk Sesink, Department of Radiation Oncology, Lausanne University Hospital and Lausanne University, Lausanne, Switzerland.

Margaux Becerra, Valerio Therapeutics, Paris, France.

Abstract

AsiDNA™, a cholesterol-coupled oligonucleotide mimicking double-stranded DNA breaks, was developed to sensitize tumour cells to radio- and chemotherapy. This drug acts as a decoy hijacking the DNA damage response. Previous studies have demonstrated that standalone AsiDNA™ administration is well tolerated with no additional adverse effects when combined with chemo- and/or radiotherapy. The lack of normal tissue complication encouraged further examination into the role of AsiDNA™ in normal cells. This research demonstrates the radioprotective properties of AsiDNA™. *In vitro*, AsiDNA™ induces a DNA-PK/p53/p21-dependent G1/S arrest in normal epithelial cells and fibroblasts that is absent in p53 deficient and proficient tumour cells. This cell cycle arrest improved survival after irradiation only in p53 proficient normal cells. Combined administration of AsiDNA™ with conventional radiotherapy in mouse models of late and early radiation toxicity resulted in decreased onset of lung fibrosis and increased intestinal crypt survival. Similar results were observed following FLASH radiotherapy in standalone or combined with AsiDNA™. Mechanisms comparable to those identified *in vitro* were detected both *in vivo*, in the intestine and *ex vivo*, in precision cut lung slices. Collectively, the results suggest that AsiDNA™ can partially protect healthy tissues from radiation toxicity by triggering a G1/S arrest in normal cells.

Graphical abstract



Received: August 10, 2023. Revised: February 1, 2024. Editorial Decision: February 26, 2024. Accepted: February 27, 2024

© The Author(s) 2024. Published by Oxford University Press on behalf of NAR Cancer.

This is an Open Access article distributed under the terms of the Creative Commons Attribution License (<http://creativecommons.org/licenses/by/4.0/>), which permits unrestricted reuse, distribution, and reproduction in any medium, provided the original work is properly cited.

Introduction

Radiotherapy and chemotherapy are customarily implemented in cancer treatments with curative intent; however, these therapies are often accompanied by the development of moderate to high levels of treatment-related toxicity. Radiotherapy frequently results in loss of epithelial integrity, tissue senescence, and cell death. Fibrosis formation, vascular damage with the potential development of secondary malignancies, and cardiac arrhythmia can all develop in the long term (1,2). Toxicities correlated to chemotherapy depend on the type of chemotherapeutic administered. These injuries range from anorexia, vomiting, and gastrointestinal toxicities to neurotoxicity (3). Consequently, treatment-induced toxicities often interfere with the completion of the initial treatment plan. To enhance treatment effect, it is crucial to alleviate treatment-related toxicities to both improve post-treatment outcomes and advance patients' welfare. This can be achieved by expanding the therapeutic index using sensitizers or protective treatment modalities to shift the normal tissue complication probability or the tumour control probability (4). The DNA repair inhibitor AsiDNA™ has previously been validated as a suitable treatment agent to enhance this index. The active part of the molecule consists of two complementary oligonucleotides of 32 bases stabilized at one blunt end by a hexaethyleneglycol linker (5). The functionalization of a cholesterol group at the other blunt-end of the molecule allows its cellular uptake via LDL receptors expressed at the cell membrane both *in vitro* and *in vivo*. (6,7). AsiDNA was designed to mimic double-stranded breaks, triggering deceptive signalling of DNA damage and impairing DNA repair of chromosomes damaged by radiation or chemical treatments (8,9). Indeed, AsiDNA™ binds both DNA-dependent protein kinase (DNA-PK) and PARP enzymes, activating their kinase and polymerase activity, and consequently leading to modification of numerous proteins in the cell [see (10) and references therein]. The characteristic substrates phosphorylated by AsiDNA™-dependent DNA-PK activation are histone H2AX and heat shock protein 90 (HSP90) (6,9,11,12).

Several preclinical studies have demonstrated an additive or synergistic tumour control effect of AsiDNA™ combined with radiotherapy or chemotherapy, without any added toxicity. (10,13–17). These observations are further supported by *in vitro* data, revealing no additional toxicity after continuous or cycling treatment of AsiDNA™ on normal cell models, while simultaneously increasing tumour cell sensitivity with no acquired resistance (7,8,18). In addition, human clinical trials have failed to show any dose-limiting toxicity, with none reaching the maximum-tolerated dose (19,20). Recently, AsiDNA™ treatment in combination with carboplatin +/- paclitaxel was tested in patients bearing solid tumours (21). These case reports showed no increased toxicity of combined carboplatin and AsiDNA™ treatment. Moreover, combined treatment allowed the dose delivery times of carboplatin to be exceeded before the occurrence of toxicities (21). Taken together, these pre-clinical and clinical studies suggest that AsiDNA™ can increase the therapeutic window by radio- or chemo-sensitizing tumour cells upon treatment, while minimizing normal tissue injuries. However, the mechanism of normal tissue resistance remains still poorly understood.

To address this knowledge gap, in the present study, we aimed to characterize the molecular mechanism underlying the potential normal tissue protection capacities of AsiDNA™ and to demonstrate its radioprotective potential *in vivo*. To

evaluate if the radioprotection property of AsiDNA™ is retained or enhanced with different modes of radiation, we combined AsiDNA™ treatment with conventional radiotherapy (CONV-RT) or FLASH radiotherapy (FLASH-RT). FLASH-RT is based on the delivery of dose rates over 1000 times higher (≥ 40 Gy/s) in comparison to CONV-RT (22). Numerous studies have demonstrated that FLASH-RT diminishes the severity of radiation-induced toxicities in normal tissues that remains present in CONV-RT, while maintaining an equivalent anti-tumour response (23–29).

Herein, we report that AsiDNA™ induces a DNA-PK/p53/p21-dependent G1/S arrest specifically in primary fibroblasts and immortalised epithelial cells, referred to as normal cells within this study, resulting in improved survival following ionizing radiation. This research provides evidence that this mechanism could account in mouse models for reduced early toxicity in the small intestine and reduced late toxicity in lung, demonstrating the potential benefit of the association of AsiDNA™ to standard radiotherapy in cancer treatment.

Materials and methods

Cell culture and transfection

Immortalized retinal pigment epithelial cell line hTERT (RPE-hTERT, kindly provided by A. Londono, Institut Curie, France), RPE-hTERT with shp53 (kindly provided by D. Fachinetti, Institut Curie, France), immortalized primary fibroblasts hTERT (VH10-hTERT, kindly provided by Aart G Jochemsen, and described in (30)), immortalized RPE-hTERT p21^{-/-} (kindly provided by R. G. Syljuåsen and described in (31)), primary human skin fibroblasts (BJ, ATCC CRL-2522), primary human lung fibroblasts (MRC-5, kindly provided by P. Jeggo, GDSC, Brighton, UK), and SV40-transformed MRC-5 fibroblasts (MRC-5v1, kindly provided by P. Jeggo, GDSC, Brighton, UK) were cultured in DMEM/F12 glutamax™ supplement medium (Thermo Fisher Scientific, France) supplemented with 10% fetal calf serum (FCS, Eurobio, France) and 100U/ml penicillin 100 µg/ml streptomycin (P/S, Thermo Fisher Scientific, France). A549 lung carcinoma cells (ATCC CCL-185), HCT116 colon carcinoma cells (ATCC CCL247), U2OS osteosarcoma cells (ATCC HTB-96), and DAOY medulloblastoma cells (ATCC HTB186) were cultured in DMEM/F12 glutamax™ supplement medium supplemented with 10% FCS, P/S and 1× Non-Essential Amino Acids (MEM NEAA 100X, Thermo Fisher Scientific, France). All cell lines were maintained in a humidified atmosphere at 37°C with 5% CO₂. The absence of Mycoplasma contamination was determined in-house by using LookOut Mycoplasma PCR (Sigma-Aldrich). Transfection of cell lines are described in the Supplementary Materials and Methods.

Molecules

AsiDNA™ (MW = 20931.4 g/mol) is a 64-nucleotide (nt) oligodeoxyribonucleotide consisting of two 32 nt strands of complementary sequence connected through a 1.19bis(phospho)-8-hydraza-2-hydroxy-4-oxa-9-oxononadecane linker with cholesterol at the 5'-end and three phosphorothioate internucleotide linkages at each of the 5' and the 3' ends. The sequence is: 5'-X GsCsTs GTG CCC ACA ACC CAG CAA ACA AGC CTA GA L-CL TC TAG GCT TGT TTG CTG GGT TGT GGG CAC sAsCsC-3',

where L is an amino linker, X a cholesteryl tetraethylene glycol, Cl a carboxylic (hydroxyundecanoic) acid linker, and s is a phosphorothioate linkage. AsiDNA™ was synthesized and purified by LGC (UK) and kindly provided by Wael Jdey (Valerio Therapeutics). The stock concentration of AsiDNA™ dissolved in water was at 40 mg/ml. Nol8 (MW = 6005.8 g/mol) has the same chemical structure as AsiDNA™ with the exception that it consists of two 8 nt strands of complementary sequence, and was synthesized and purified by Eurogentec (Belgium). The stock concentration of Nol8 dissolved in water was at 61 mg/ml.

In vitro treatments

Cell culture medium was supplemented with AsiDNA™ at concentrations of 20 or 40 μmol/l 24 or 48 h prior to IR treatment. In vitro irradiation was conducted using the ElectronFLASH (S.I.T., Vicenza, Italy) at a dose rate of 0.4 Gy/s.

Cell cycle analysis

Complete medium with total 10 μmol/l BrdU (Merck, France) was added to cells for a 40 min incubation either prior to- or post-AsiDNA™ treatment, under standard culture conditions. For drug treatment, cells were exposed to 1 μM Olaparib (AZD-2281, Roowin chemicals), 10 μM NU7026 (Merck, France), and 10 μM p21 inhibitor UC2288 (Merck, France) 1 h prior to AsiDNA™ treatment. Cells were harvested, fixed in cold 70% EtOH, and permeabilised in 1× PBS/0.5% BSA/0.1% Tween-20. BrdU detection was performed using FITC mouse anti-BrdU antibody (BD biosciences, France, #51-33284X). Following 1 h incubation, the cells were centrifuged and resuspended in 1× PBS containing 0.5% BSA, 10 μg/ml propidium iodide (Merck, France) and 0.2 mg/ml RNase A (Merck, France). The data acquisition was performed using the LSRFortessa™ X-20 Cell Analyzer (BD biosciences, France), and the quantification of cell cycle performed using FlowJo (BD biosciences, France).

Clonogenic survival after radiation

Cells were seeded at $1.5-3 \times 10^5$ cells per 25 cm² flasks and 20 μmol/l AsiDNA were added for 24 h, prior to irradiation with doses of 0, 2, 4 and 6 Gy using the electronFLASH irradiator at a dose rate of 0.4 Gy/s. Following a recovery period of 24 h, the cells were trypsinized, counted and seeded for clonogenic survival. Eight to twelve days post seeding, cells were fixed and stained in 80% Methanol, 4% formaldehyde, 2.5% crystal violet. Colonies exceeding 50 cells were counted, and the obtained data was analysed using GraphPad Prism.

Transfection

Prior to RNA interference, cells were attached overnight in 6-well plates for RPE-hTERT cells and in 60mm2 dishes for BJ cells. P53 siRNA; GAG UGG AAG GAA AUU UGC UGG A (20 nM, TP53HSS186390, Invitrogen), p21 siRNA; GAACU-UCGACUUUGUCACCGAGACA (CDKN1, 40 nM, CDKN1-AVHS40209, Invitrogen) or DNA-PK siRNA mix (PRKDC, 18 nM s773 GCGUUGGAGUGCUACAACATT, 18 nM s774 GCGCUUUUCUGGGUGAACUTT, ThermoFisher Scientific) were supplemented to the cells in Opti-MeM serum free medium (Gibco). RNA interference was performed following manufacturer's instructions for INTERFERin (Polyplus transfection) with medium replacement 7 h posttransfection. AsiD-

NA™ treatment on transfected cells was performed for 48 h starting at 24 h posttransfection.

Western blot analysis

Cell pellets were lysed in lysis buffer [10 mM HEPES, pH 7.5, 100 mM NaCl, 300 mM sucrose, 3 mM MgCl₂, 1 mM EGTA, 50 mM NaF, 20 mM β-glycerophosphate, 0.3% Triton X-100, 0.1 mM sodium orthovanadate, and complete mini EDTA-free protease inhibitors (Roche Diagnosis)] on ice for 5 min. Following centrifugation at 240 rcf 4°C, supernatants were transferred into 1.5 ml Eppendorf tubes and protein concentration determined using Bradford assay (Bio-Rad). Twenty to thirty micrograms of protein extracts were separated on 4–15% Mini-PROTEAN® TGX™ Precast Protein Gels (Bio-Rad) and transferred onto PROTRAN® nitrocellulose membrane (Whatman) using a Mini Trans-Blot Cell (Bio-Rad). Membranes were probed overnight at 4°C with the following primary antibodies diluted in Intercept blocking buffer (LI-COR Biosciences – GmbH): anti-p53 (R&D systems, AF1355-sp, dil. 1:500), anti-p21 (Waf/Cip (12D1), Cell Signaling Technologies, 2947s, dil. 1:1000), anti-hsp90-p (T5/7, Cell Signaling Technologies, 3488s, dil. 1:1000), anti-DNA-PK (Thr2609, Novus Biologicals, dil. 1:1000), and anti-β-actin (Sigma, A1978, dil. 1:2000). The membranes were probed with the appropriate secondary antibodies diluted in Intercept blocking buffer: IRDye 800CW goat anti rabbit (LI-COR 926-32211, dil. 1:15000), IRDye 680RD goat anti-mouse (LI-COR 926-32220, dil. 1:5000), IRDye 800CW goat anti mouse (LI-COR 926-32210, dil. 1:5000), IRDye 800CW donkey anti-goat (LICOR 926-32214, dil. 1:5000). Direct infrared fluorescence was detected on the Odyssey Infrared Imaging System (LI-COR Biosciences – GmbH).

Ex vivo and in vivo experimentation

Studies were performed in accordance with the recommendations of the European Community (2010/63/UE) or UK Home Office guideline for the care and use of laboratory animals. Experimental procedures were explicitly approved by the ethics committee of Institut Curie CREA-IC #118 (Authorization number APAFIS#5479-201605271 0291841 given by National Authority), or by the University of Oxford's Animal Welfare and Ethical Review Body (under project licenses PP8415318), in compliance with the international guidelines. All animals used within this research were acclimated for at least 1 week prior to experimentation. Mice were housed under pathogen-free conditions in cages containing sawdust with a maximum of six animals per cage, under a controlled 12 h light/dark cycle, a relative humidity of 55%, and a controlled temperature of 21°C. Food and sterile water were provided *ad libitum*. All experiments were conducted on C57BL/6J mice (Charles River, France) at 8–9 weeks of age, unless otherwise indicated in the corresponding materials and methods.

Precision-cut lung slices (PCLS)

PCLS were obtained from the lungs of female C57BL/6J mice (Charles River, France) or male and female C57BL/6J p53 Knock-out mice (Curie collection), at 4–6 months old, as recently described (32), and briefly presented in the Supplementary Materials and Methods. AsiDNA™ or Nol8 treatment of 5 μmol/l was performed for 48 h in 24-well plates, followed by a 24 h co-incubation with 10 μmol/l EdU. EdU positive cells were revealed using EdU DetectPro Imaging kit Imaging

(647 nm, BCK-EdUPro-IM647/BCK488-IV-IM-S, Baseclick), and visualized with the Inverted spinning disk-TIRF-FRAP (Nikon) with a 300 ms emission and 30% laser, DAPI (405 nm), 400 ms emission and 70% laser, 10× objective with 50 stacks of 3 μm. Data analysis was performed using IMARIS with spot function and PRISM software.

Animal irradiation and fibrosis analysis

The female C57BL/6/J mice model of radiation induced lung fibrosis was used (23,33). Mice were irradiated after 2 consecutive days of intraperitoneal AsiDNA™ injections (100 mg/kg), followed by a third day with intraperitoneal AsiDNA™ injection (200 mg/kg) and FLASH/CONV irradiation. Bilateral thorax irradiation of 13 Gy was performed using the ElectronFLASH (S.L.T., Vicenza, Italy), including a CONV dose rate of 0.4 Gy/s and a FLASH dose rate of >100 Gy/s (beam parameters are described in Supplementary data Table S1). Animals were immobilized under anaesthesia (2.5% Isoflurane in air) and positioned vertically with lead shielding designed to protect the entire body excluding the thorax. GAFchromic™ EBT-XD film (Ashland Inc., Wayne, NJ, USA) was used for the dosimetry of entrance and exit dose at each irradiation. Animals were examined for weight loss and respiratory distress daily post IR. High resolution Micro-CT imaging (Molecubes), 100 μm FDK reconstruction, was performed to examine lung fibrosis development each month from 4 months post irradiation. The 3D lung reconstruction and fibrosis classification (24) were performed using VivoQuant 2021 (VivoQuant) and ImageJ/FIJI (ImageJ) software. For the 3D lung reconstruction, connected Hounsfield Units (HU) (bottom panel of figure 5B) were detected. Air filled structures represent with HU around -600 and complete lung detection was set between -800 and -100 HU. Increased lung density was detected by the loss of connected HU between the set margins. Upon reaching the ethical endpoint, mice were anesthetized (2.5% Isoflurane in air) and underwent CT scanning prior to euthanasia by cervical dislocation. Lungs were isolated and histology was performed to detect areas of affected lung by pulmonary fibrosis. Note that mice that were still alive at day 200 (final endpoint) were euthanised.

Single cell RNA sequencing

Single cell RNA sequencing was performed on three controls provided by Curras *et al.* (34), 1 CONV, 1 CONV AsiDNA™ and 1 FLASH female C57BL/6/J mice 5 months post 13 Gy thorax irradiation. The protocol and data processing procedures were performed as previously described (34). In brief, following lung tissue dissociation, single cell samples for RNA sequencing were prepared using the droplet based scRNA-seq system (10x GENOMICS) followed by lysis of encapsulated single cells, RNA capturing, cDNA production, amplification, purification, library preparation, and sequencing. scRNA-seq data analysis was processed through the creation of a count matrix table suitable for R (4.0.5) and analysed using Seurat package (v4.0.1.).

Histology

For histological analysis, the lungs were removed, and gently inflated in 4% paraformaldehyde (PFA) under mild vacuum pressure (25 Torr, 1 h at room temperature). Lungs were fixed for 24 h at RT, after which they were embedded in paraffin and

cut into 7-mm thick slices. The preparations were stained with hematoxylin–eosin or Masson trichrome (R.A.L. Diagnostics, #361350).

Animal irradiation and intestine analysis

Female C57BL/6/J mice were irradiated and treated as previously described (29). Lower body irradiation of 10 Gy was performed using the linear accelerator described in Ruan *et al.*, including CONV dose rate of 0.1 Gy/min and FLASH dose rate of 3000 Gy/s with beam parameters described in Supplementary data Table S2. Animals were immobilized under anaesthesia in a cradle exposing the lower body. Brass shielding was used to protect the entire animal's body excluding the abdominal region. GAFchromic™ EBT-XD film was used for the dosimetry of the exit dose for each irradiation. Animals were examined for weight loss with the endpoint set at 4 days post IR. The jejunum of the small intestine was isolated using the swiss roll technique followed by intestine histology with haematoxylin and Eosin staining as previously described (35). The count of intestinal crypts was performed over a length of 3 mm for each sample and conducted twice by independent researchers.

In vivo detection of EdU, Ki67 and p21

Female C57BL/6/J mice received intraperitoneal AsiDNA™ injections (100 mg/kg) for 2 consecutive days, followed by a third day with intraperitoneal AsiDNA™ injection (200 mg/kg). EdU (100 mg/kg) was injected 4 h prior to euthanasia at 0, 24, 48 and 72 h post AsiDNA™ injection. The small intestine was isolated from 3 cm after the stomach, with a total length of 10 cm intestine isolated overall, using the swiss roll technique (36). Samples were fixed in 4% PFA for 36 h, embedded in paraffin, and cut into 4 μm thick slices. These slices were then deparaffinized and hydrated following a standard protocol. DAPI (0.5 μg/ml) staining and EdU detection were performed using BaseClick EdU IV Imaging kit 488 M in accordance with the manufacturer's protocol. EdU positive cells were detected using the 3D SIM Upright Widefield microscope (Leica), and quantified using a nuclear segmentation algorithm (Cellpose) and MIC-MAQ macro (supplementary Materials and methods), applied on nuclear DAPI signal and the individual EdU cell signal. Furthermore, standard immunofluorescence was conducted to detect Ki-67 (FISHER, MA5-14520, 1:200) and immunohistochemistry staining to detect p21 (Tebu-Bio, E-AB-70068, 1:200).

Statistical analysis

All statistical analyses were performed using GraphPad Prism (v 7.03). Statistical significance was set at * $P < 0.05$, ** $P < 0.01$, *** $P < 0.001$ and **** $P < 0.0001$. All statistical information is presented in the figures and figure legends.

Results

AsiDNA™ induces a G1/S arrest in normal proliferating epithelial cells and primary fibroblasts.

The adverse side effects induced by radio- and chemotherapies are derived from damage to dividing normal cells, resulting in cell death within the healthy tissue (37,38). Cell cycle arrest has previously been demonstrated to protect normal cells against cytotoxic radio- and chemo-therapies (39,40).

Consequently, in the present study, we assessed cell cycle progression in a panel of normal human cells treated with AsidDNA™. For this, primary skin fibroblasts (BJ), and immortalised normal epithelial cells (RPE-hTERT) were exposed to 20 and 40 μM of AsidDNA™ for 24 and 48 h, followed by cell cycle analysis using PI-BrdU bivariate flow cytometric dot plots (Figure 1A and B). The corresponding histograms showing cell cycle analysis (Figure 1C and D) allow quantification of the number of cells in each cell cycle phase (Figure 1E and F). Analysis of these results indicated significant cell cycle arrest at the G1/S boundary, which implies an accumulation of cells in G1 and an affiliated decrease of S-phase cells (Figure 1E and F). Similar results were obtained using MRC-5 (primary lung fibroblasts) and V110-hTERT (immortalised fibroblasts) (Supplementary Figure S1). It should be noted that AsidDNA™ treatment did not induce a G2/M arrest (absence of cell accumulation in G2/M) nor S phase arrest (absence of BrdU negative cells) following AsidDNA treatment (Figure 1 and Supplementary Figure S1).

A functional DNA-PK/p53/p21 pathway is required to promote AsidDNA™-induced G1/S arrest in normal proliferating epithelial cells and fibroblasts

Nbs8, which is structurally similar to AsidDNA™ but with an 8 bp instead of 32 bp nucleotide strand, showed no capacity to activate PARP and DNA-PK (Supplementary Figure S2A and B). Furthermore, although p21 was moderately induced at 48h following Nbs8 treatment, no significant G1/S arrest was observed (Supplementary Figure S2C–E). These results prompted us to investigate the role of PARP and DNA-PK in AsidDNA-induced cell cycle arrest. PARP and DNA-PKs activity were inhibited using olaparib (41), and NU7026 (42), respectively, and cell cycle progression was examined upon combined treatment with AsidDNA™. The inhibition of DNA-PK activity, but not of PARP, was able to prevent AsidDNA™-induced G1/S arrest in RPE-hTERT and BJ (Figure 2A and Supplementary Figure S3A). This dependency on DNA-PK activation was further confirmed using cells in which the expression of DNA-PK was down-regulated (Figure 2B and Supplementary Figure S3B). In support, previous research revealed that the p53–p21 axis is an important pathway controlling G1/S arrest upon activation of the DNA damage response (43). Therefore, the contribution of this axis to AsidDNA™-induced G1/S arrest was further examined. Cell lines with inactive p53 (MRC-sV1, Figure 2C) or with downregulated p53 expression (RPE-hTERT sip53, Figure 2B and RPE-hTERT shp53, Figure 2D), displayed no AsidDNA™-induced G1/S arrest. The results obtained following the downregulation of p21 expression (Figure 2B) or p21 inhibition (Supplementary Figure S3C) in RPE-hTERT cells revealed a leaky phenotype with a minor accumulation of cells at the G1/S transition, concomitantly with a minor decrease of S-phase cells following AsidDNA™ treatment. The efficient downregulation of DNA-PKs and p53 expression was confirmed with a partial inhibition of p21 expression using western blot analysis (Supplementary Figure S3D). To overcome this problem, RPE-hTERT cells with p21 gene knock-out were acquired (31). The result revealed a transient G1/S arrest at 24 h of treatment that is not sustained at 48 h (Figure 2E), demonstrating an essential role of p21 to establish a robust AsidDNA-induced G1/S arrest.

To further confirm the importance of the DNA-PK/p53/p21 axis to trigger AsidDNA™-induced G1/S arrest, the expression levels of p53 and p21 in response to 24h and 48h of AsidDNA™ treatment were examined by western blot in RPE-hTERT, RPE-hTERT shp53, RPE-hTERT p21^{-/-}, and RPE-hTERT cells treated with NU7026. The results revealed that AsidDNA™ exposure initiated p21 induction in RPE-hTERT cells that was absent in RPE-hTERT p21^{-/-} cells (Supplementary Figure S3E), in RPE-hTERT shp53 cells (Supplementary S3F), or in RPE-hTERT treated with DNA-PKs inhibitor NU7026 (Supplementary Figure S3G). Similarly, down-regulation of p53 expression in primary fibroblasts additionally resulted in the loss of the AsidDNA-induced G1/S arrest (Supplementary Figures S3B). Collectively, these results demonstrate that DNA-PK activity is required to promote the p53-dependent transcriptional activation of p21 which leads to the G1/S arrest induced by AsidDNA™. Furthermore, AsidDNA™-induced G1/S arrest was reversible. Following the removal of AsidDNA™ treatment, cells restarted their cell cycle and p21 expression returned to basal level (Supplementary Figure S4).

P53-proficient tumour cells show no G1/S arrest upon AsidDNA™ treatment

Standalone AsidDNA™ treatment has previously been demonstrated to cause toxicity in malignant cells, irrespective of their p53 status, and exerted no toxicity against normal cells (7,8,18,44). As such, we subsequently investigated AsidDNA™-induced cell cycle arrest in p53 proficient tumour cells (A549, HCT116 and U2OS). Among the three p53 proficient tumour cell lines, U2OS and HCT116 displayed no G1/S arrest after AsidDNA™ treatment. In A549 cells, a transient increase in G1 phase concomitantly with a transient decrease in S-phase was observed at 24 h that was absent at 48 h following AsidDNA™ treatment (Figure 3). Despite a functional p53, the lack of G1/S arrest was further confirmed by the absence of p21 induction upon AsidDNA™ treatment in the examined tumour cell lines (Supplementary Figure S5A). As expected, no G1/S arrest was observed following AsidDNA™ treatment in DAOY, a p53-deficient tumour cell line (Supplementary Figure S5B). Collectively, these results strongly suggested that AsidDNA-induced p53-dependent G1/S arrest is restricted to proliferating normal epithelial cells and fibroblasts. As previously observed following the impact of AsidDNA treatment on normal cell cycle progression, AsidDNA™ identically did not activate the G2/M checkpoint (Figure 3 and Supplementary Figure S5B) and the intra S-phase checkpoint (data not shown) in the examined tumour cell lines.

AsidDNA™-induced G1/S arrest promotes cell survival in response to ionizing radiation in normal epithelial cells and fibroblasts

The G1/S cell cycle checkpoint primarily prevents damaged DNA from being replicated during the S phase, which can be either mutagenic or lethal for the cells. It is therefore hypothesized that AsidDNA™-dependent G1/S arrest could protect healthy cells from radiation-induced toxicity. To test this hypothesis, normal human cell lines (BJ and RPE-hTERT) were treated with AsidDNA™ prior to irradiation. An increase in cell survival was observed in p53 proficient normal cells treated with AsidDNA compared to cells without

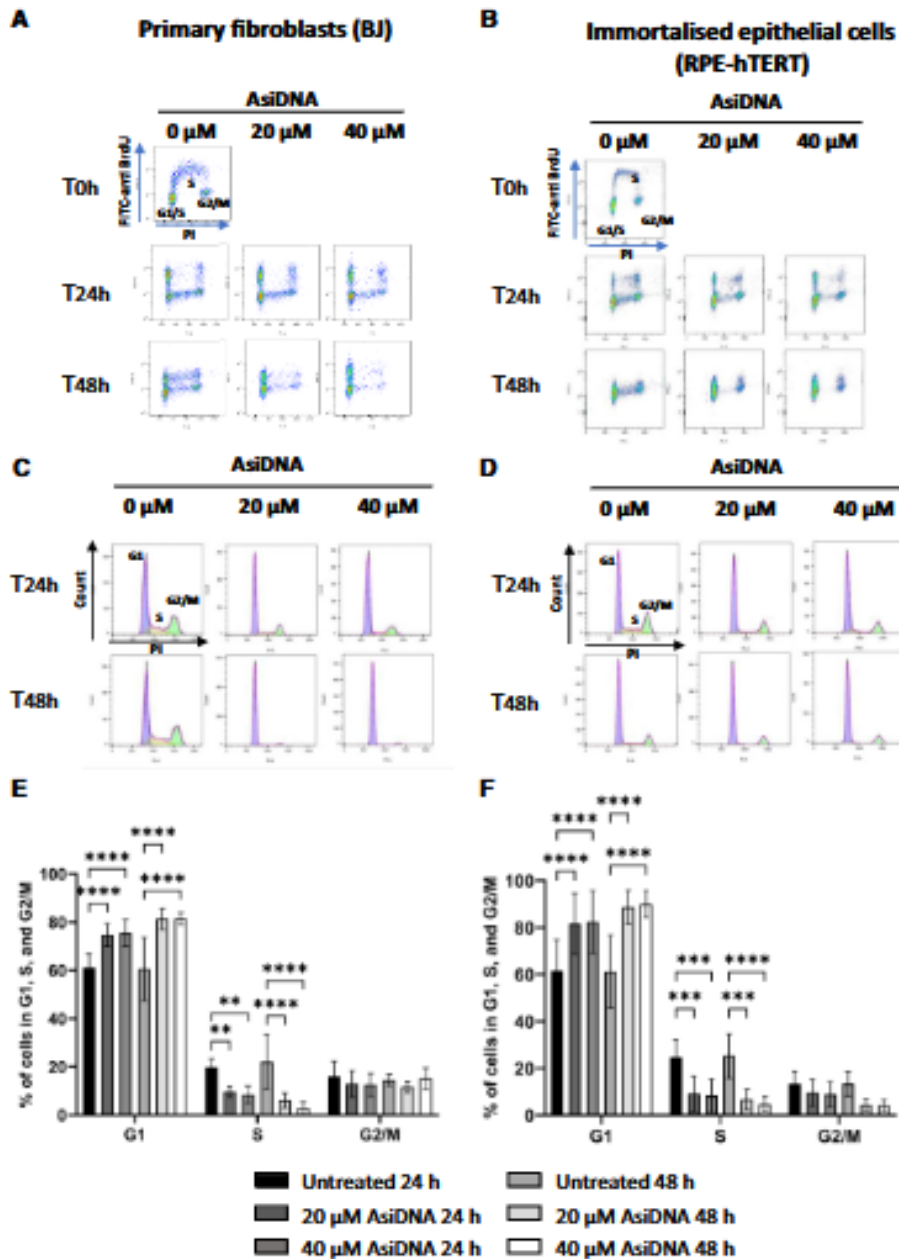


Figure 1. AsidDNA™ induces a G1/S arrest in healthy cells *in vitro*. Cells were pulse-labelled with BrdU following incubation with 20 and 40 μM of AsidDNA™ for 24 and 48 h. Representative images of the bivariate analysis by flow cytometry of BrdU incorporation versus DNA content (PI) in (A) BJ and (B) RPE-hTERT cells. The deconvolution of the cellular DNA content frequency histograms allows the identification of G1 phase (purple), S-phase (orange), and G2/M-phase (green) in (C) BJ, and (D) RPE-hTERT cells. The percentage of cells in G1, S, and G2/M is shown in (E) for BJ, and in (F) for RPE-hTERT cells. Data are expressed as mean \pm standard deviation ($n = 8-9$) with significance given by two-way ANOVA, Tukey's multiple comparison tests, and represented above the bar plots. Statistical significance was set at * P value < 0.05, ** P value < 0.01, *** P value < 0.001 and **** P value < 0.0001.

AsidDNA™ treatment (Figure 4A). Importantly, there was no protection from radiation induced toxicity in cells lacking the AsidDNA™-induced G1/S arrest as observed in RPE-hTERT shp53 cells (Figure 4B) and p53 proficient tumour cells (A549 and HCT116) (Figure 4C). It is worth noting that the extent of radioprotection or radiosensitivity is cell line dependent. Indeed, we observed that primary BJ fibroblasts displayed

a higher radioprotection by AsidDNA ($SF_{G1/S-AsidDNA} \approx 0.05$, $SF_{G1/S+AsidDNA} \approx 0.2$) compared to immortalized RPE-hTERT cells ($SF_{G1/S-AsidDNA} \approx 0.035$, $SF_{G1/S+AsidDNA} \approx 0.06$). Similarly, HCT116 cells displayed a higher radiosensitivity conferred by AsidDNA ($SF_{G1/S-AsidDNA} \approx 0.001$, $SF_{G1/S+AsidDNA} \approx 0.0002$) in comparison to the radioresistant A549 tumour cells ($SF_{G1/S-AsidDNA} \approx 0.1$; $SF_{G1/S+AsidDNA} \approx 0.07$). These *in vitro*

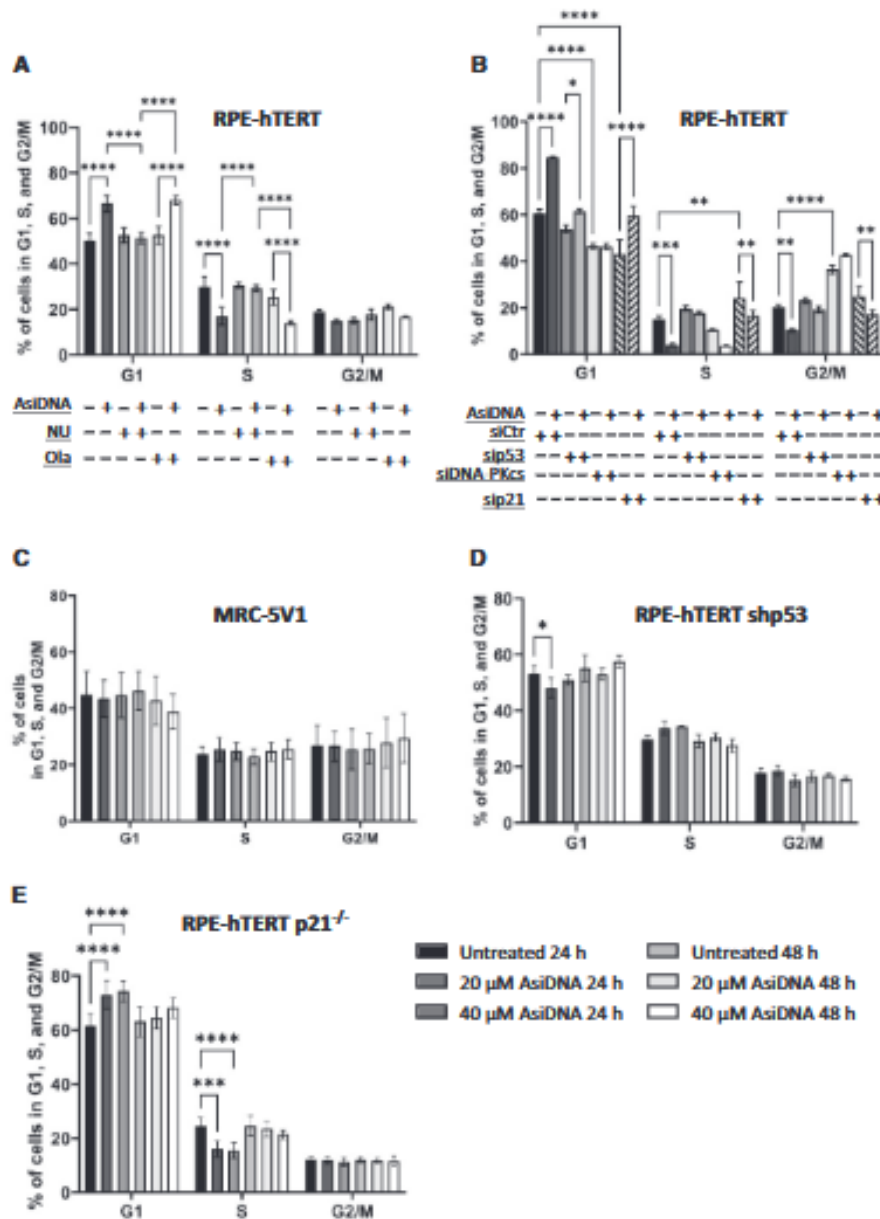


Figure 2. AsiDNA™-induced G1/S arrest *in vitro* is dependent on DNA-PK, p53, and p21. (A) RPE-hTERT cells were pre-treated with 1 μM olaparib (Ola) or 10 μM NU7026 (NU) for 1 h before addition of 20 μM AsiDNA™. The percentage of cells in G1, S and G2/M was analysed by flow cytometry 48 h post-AsiDNA™ treatment based on PI staining. (B) RPE-hTERT cells were transiently transfected with small inhibitory RNA (siRNA) silencing DNA-PKcs, p53, or p21 before being exposed to AsiDNA™ for 48 h. The percentage of cells in G1, S and G2/M was analysed by flow cytometry based on PI staining. (C) MRC-5V1, (D) RPE-hTERT shp53 and (E) RPE-hTERT p21^{-/-} cells were treated with 20 and 40 μM of AsiDNA™ for 24 and 48 h. The percentage of cells in G1, S and G2/M was analysed by flow cytometry at the end of AsiDNA™ treatment based on PI staining. All the data are expressed as mean ± standard deviation (n = 3–9) with significance given by two-way ANOVA, Tukey's multiple comparison tests, and represented above the bar plots. Statistical significance was set at * Pvalue < 0.05, ** Pvalue < 0.01, *** Pvalue < 0.001 and **** Pvalue < 0.0001.

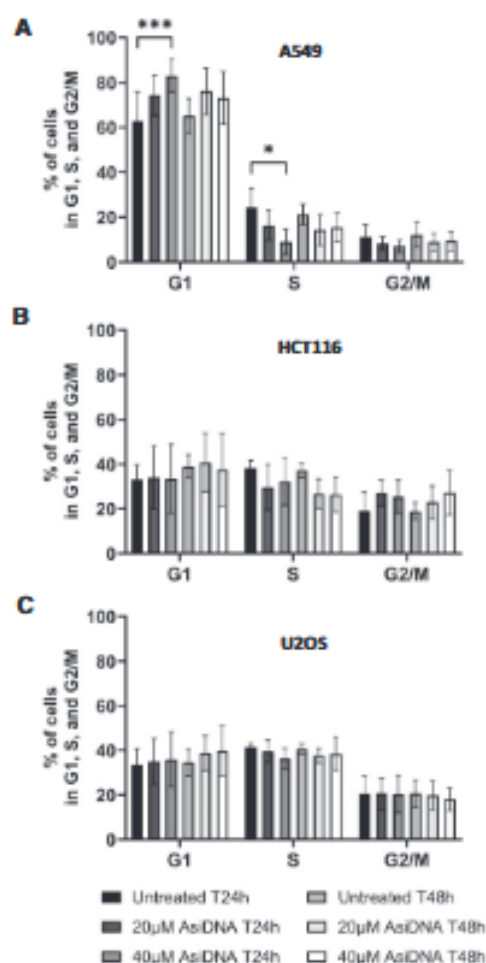


Figure 3. No effect of AsiDNA™ treatment on cell cycle progression in p53 proficient tumour cells *in vitro*. (A) A549, (B) HCT116 and (C) U2OS tumour cells were exposed to 20 and 40 µM of AsiDNA™ for 24 and 48 h. The percentage of cells in G1, S and G2/M was analysed by flow cytometry at the completion of AsiDNA™ treatment, based on PI staining. Data are expressed as mean ± standard deviation ($n = 5-7$) with significance given by two-way ANOVA, Tukey's multiple comparison tests, and represented above the bar plots. Statistical significance was set at *** P value < 0.001.

results demonstrate the essential role of the AsiDNA™-induced G1/S arrest in protecting explicitly normal cells, with a functional p53, against radiation-induced toxicity.

AsiDNA™ alleviates radiation-induced lung fibrosis in mice

To demonstrate that AsiDNA™ is similarly able to protect normal tissue against radiation-induced toxicity *in vivo*, radiation-induced lung fibrosis in C57BL/6J mice, a well-established model of late-responding radiation toxicity, was used (45). As FLASH-RT alleviates radiation-induced lung fibrosis in mice (23,24), we took advantage of hosting an electron accelerator that can perform radiotherapy modalities in both CONV-RT and FLASH-RT mode, enabling the examination of a possible gain of normal tissue protection following combined AsiDNA™ and FLASH-RT treatment. Mice were

divided into five groups ($n = 6-9$), sham-irradiated, exposed to 13 Gy CONV ± AsiDNA™ or 13 Gy FLASH ± AsiDNA™, through bilateral thorax irradiation. Lung fibrosis was evaluated using computed tomography (CT) from 4 months post-irradiation (Figure 5A). Each lobe of the lung was collected for histopathological analysis and single cell RNA sequencing, directly following euthanasia.

CT scans taken 5 months post irradiation revealed increased levels of fibrosis in the CONV-RT treated group, while fibrosis was absent in the mock-treated group and much less pronounced in the combined CONV-RT with AsiDNA™ treated group (Figure 5B). A strong reduction of fibrosis was also observed in the FLASH-RT treated group, which agrees with the previously reported results (23,24), and following combined treatment with FLASH-RT and AsiDNA™ (Figure 5B). Long-term follow-up of survival post irradiation demonstrated that AsiDNA™ delayed or even reduced the onset of lethal lung fibrosis when combined with CONV-RT (Figure 5C). Similar results were obtained with FLASH-RT, as previously reported (23), and with the combined treatment of FLASH-RT and AsiDNA™ (Figure 5C). It is to note that overall survival is similar between combined CONV-RT and AsiDNA™ treatment, FLASH-RT standalone, and combined FLASH-RT and AsiDNA™ treatment. These results suggest that, at the cellular level, the effect of AsiDNA™ combined with CONV-RT could mimic the effect of FLASH-RT on reduced normal tissue toxicities. Histopathological analyses of the lobes collected at the day of euthanasia, either by reaching the ethical endpoint or the final endpoint (day 200), confirmed the onset of lung fibrosis in all groups but in the non-irradiated controls (Supplementary Figure S6, and Supplementary data Table S3).

A decreased myofibroblast gene profile is observed in fibroblasts upon AsiDNA™ treatment

To characterize the similarity in cellular changes and expression signatures in lungs 5 months post CONV-RT, FLASH-RT, AsiDNA™ + CONV-RT or non-irradiated (Control) treatment, single cell suspensions were created and analysed using scRNA sequencing. By exploiting previously published single-cell datasets and known identifying markers (34), the identity of the various cell clusters was determined (Figure 6A). This analysis detected 21 distinct clusters: alveolar macrophages (AM), proliferating AM, AT1, AT2, B-cells, basophils, ciliated cells, ciliated club cells, club cells, dendritic cells (DC), endothelial cells (EC), fibroblasts, interstitial macrophages (IM), mesotheliocytes, monocytes, neutrophils, natural killer cells (NK cells), NK-T-cells, smooth muscle cells (SMC), T-cells and proliferating T-cells (Figure 6B-D). All cell types were identified independently of the received treatment modality but a radiation-induced cell proportion shift was detected in the AT2, B-cells, IM and NK-T cells (Figure 6D). Additionally, the AM, DC, Monocytes and NK-cells populations displayed altered cell proportions following CONV-RT compared to the other conditions (figure 6D). Recent findings by Curras *et al.* have identified a unique fibroblast subcluster exclusively present in irradiated mice lungs (34). In response to irradiation, fibroblasts can transition into myofibroblasts which are known to secrete and modify the extracellular matrix (ECM), including altering the collagen production, which in turn contributes to pulmonary fibrosis formation (46). To identify the contribution of fibroblasts in the development of,

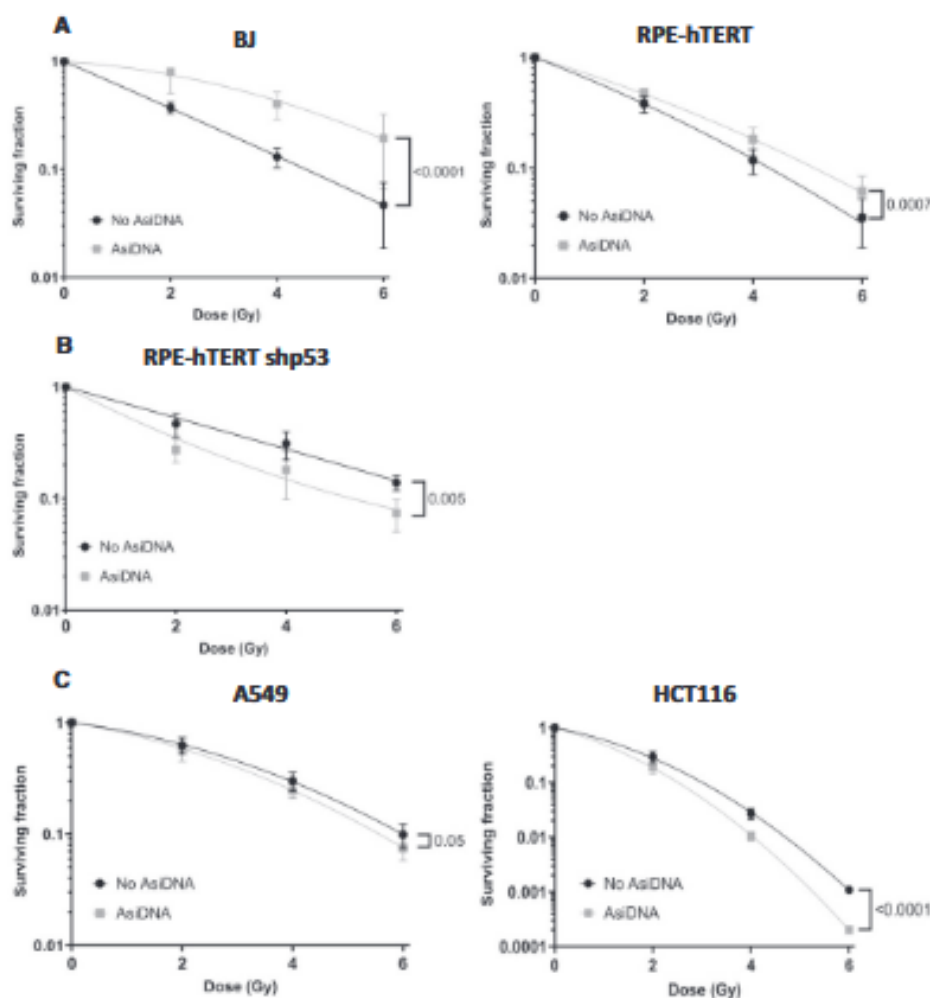


Figure 4. AsidDNA™ treatment protects p53-proficient normal cells, but not p53-proficient tumour cells, from radiation-induced toxicity *in vitro*. (A) p53 proficient normal cells (BJ and RPE-hTERT), (B) p53 deficient normal cells (RPE-hTERT shp53) and (C) p53 proficient tumour (HCT116 and A549) cells were pre-treated with AsidDNA™ 24 h before being co-exposed to increased doses of ionizing radiation (0–6 Gy). The survival fraction was determined 8–12 days post-treatment using a clonogenic survival assay. Data are expressed as mean \pm standard deviation ($n = 3$ for BJ, RPE-hTERT shp53, HCT116 and A549; $n = 4$ for RPE-hTERT), fitted to the linear-quadratic model as a function of dose with significance given by nonlinear fit using GraphPad Prism.

or the lack of, pulmonary fibrosis formation after CONV-RT, CONV AsidDNA™ treatment and FLASH-RT, myofibroblast markers expression, collagen homeostasis, fibroblast activation and EMC remodelling markers were examined within the fibroblast cell cluster. Clustering of the fibroblast resulted in the detection of a total of 891 cells, divided over the different treatment conditions (Figure 6E). Myofibroblast markers Hp and Pla1a, previously identified in Curras *et al.* (34), revealed to be substantially increased after CONV-RT standalone (Figure 6F–G). Remarkably, Nr1d1 gene expression, linked to healthy collagen homeostasis (47), was found to be significantly decreased in CONV-RT compared to the control, CONV AsidDNA™ or FLASH-RT (Figure 6H).

These results reveal an increase in fibroblast activation and myofibroblast transition together with an impact on the ECM, including collagen homeostasis, in the fibroblast cell cluster following CONV-RT standalone. This observed altered gene

expression in CONV-RT exposed fibroblast was decreased or absent in fibroblasts exposed to CONV AsidDNA™ or FLASH-RT, and supports the increased pathway activation known to play an essential role in the development of pulmonary fibrosis.

AsidDNA™ induces a cell cycle arrest in *ex vivo* precision cut lung slices involving DNA-PK and p53

To investigate the AsidDNA™-induced cell cycle arrest in the lung, *ex vivo* precision cut lung slices (PCLS) were used. Untreated C57BL/6/J mice were sacrificed, and agarose inflated lungs were isolated and cut. The PCLS were treated for 24 h with AsidDNA™ or Nol8, and EdU (a marker of replicative cell division) was co-incubated for an additional 24 h. Cell nuclei were then stained for EdU incorporation (Figure 7A). A significant loss of EdU positive cells was observed fol-

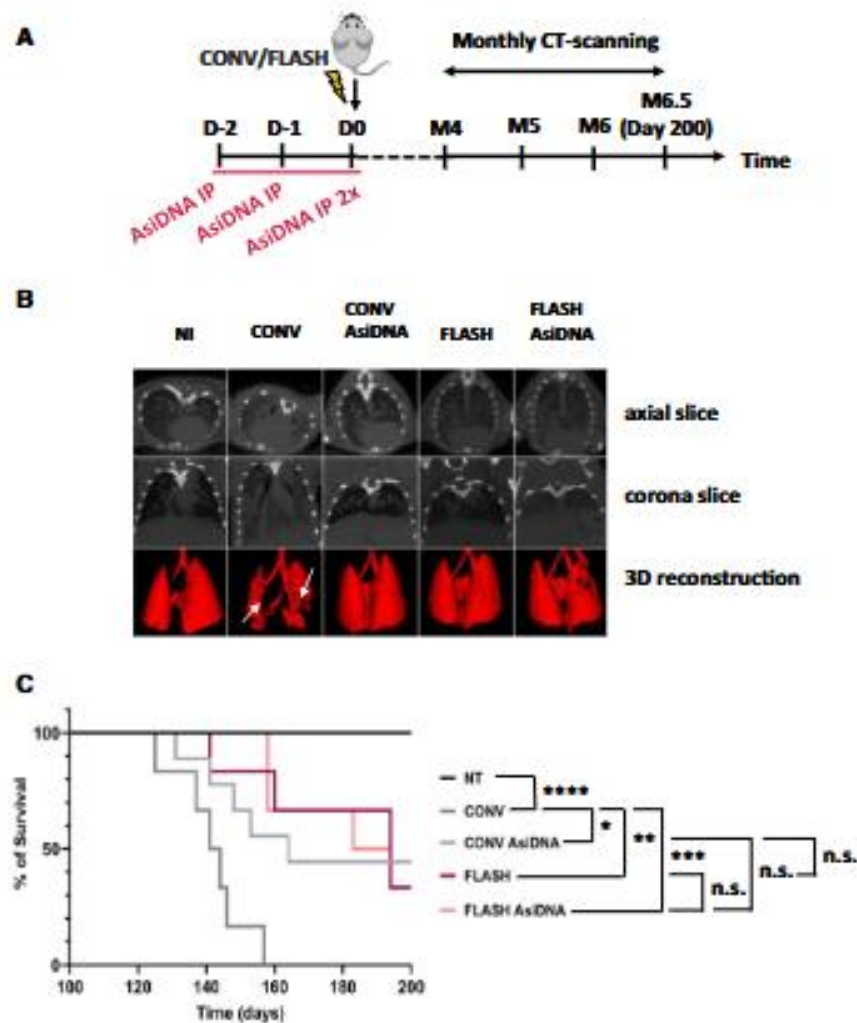


Figure 5. AsidDNA™ delayed the onset of radiation-induced pulmonary fibrosis in vivo. (A) Scheme of the experimental protocol. C57BL6/J mice were treated for 3 consecutive days with AsidDNA™ followed by 13 Gy CONV or FLASH irradiation of the thorax on the final day. Retro-orbital blood sampling was performed from 1 week up to 5 months post-treatment. CT scans were recorded from 4 to 6.5 months (sacrifice) post-treatment, and lobes of the lung were collected at the day of sacrifice (day 200) for histologic analysis. (B) Representative CT scans of lung from untreated mice (NI) or 5 months post-irradiation at 13 Gy CONV or FLASH radiotherapy alone or combined with AsidDNA™. Images are obtained using micro-CT imaging, high resolution, and 100 μ m reconstruction by Molecubes software (Molecubes, Belgium). Representative images are shown with the CT axial slice (top), CT coronal slice (middle) and 3D lung reconstruction of connected Hounsfield Units -800 to -100 (bottom). Images were obtained using VivoQuant software (Konica Minolta Company, Japan). (C) Kaplan-Meier representation of animal surviving fraction displayed in days post-treatment. Data are expressed with significance given by survival, curve comparison, and Logrank test. Significance: not significant, ns; * $P < 0.05$; ** $P < 0.01$; *** $P < 0.001$; **** $P < 0.0001$. The statistical analysis gave NT versus CONV is < 0.0001 , NT versus CONV AsidDNA is 0.003, NT versus FLASH 0.002, NT versus FLASH AsidDNA is 0.0015, CONV versus CONV AsidDNA 0.0178, CONV versus FLASH 0.0053 and FLASH versus FLASH AsidDNA is not significant.

lowing AsidDNA™ treatment compared to both untreated and N018 treated PCLS (Figure 7B), suggesting that DNA-PK activation by AsidDNA™ similarly triggered cell cycle arrest, likely at the G1/S border, in PCLS. To further support this conclusion, PCLS were derived from wild-type C57BL6/J mice and p53 knock-out (p53 $^{-/-}$) mice. Upon AsidDNA™ treatment in wild-type (WT) mice, a significant decrease in EdU positive cells was detected compared to the untreated conditions (Figures 7C and D). Additionally, the incorporated EdU positive cells of untreated PCLS in p53 WT and in p53 KO were similar. Strikingly, p53 KO PCLS treated with AsidDNA™ resulted in no significant decrease in the EdU incorporation (Figure 7D). Collectively, these results strongly support the activation

of G1/S arrest induced by AsidDNA™ treatment in PCLS requiring the activation of DNA-PK and p53.

AsidDNA™ alleviates radiation-induced intestine toxicity in mice

To study the capacity of AsidDNA™ to protect normal tissue from early responding radiation toxicity, a model of acute intestinal toxicity after whole abdominal irradiation in mice was used (29). The possible gain-of-protection by AsidDNA™ was examined in combination with CONV-RT and FLASH-RT (Figure 8A). For crypts analysis, the intestine was isolated at 4 days post treatment, and the jejunum was further processed

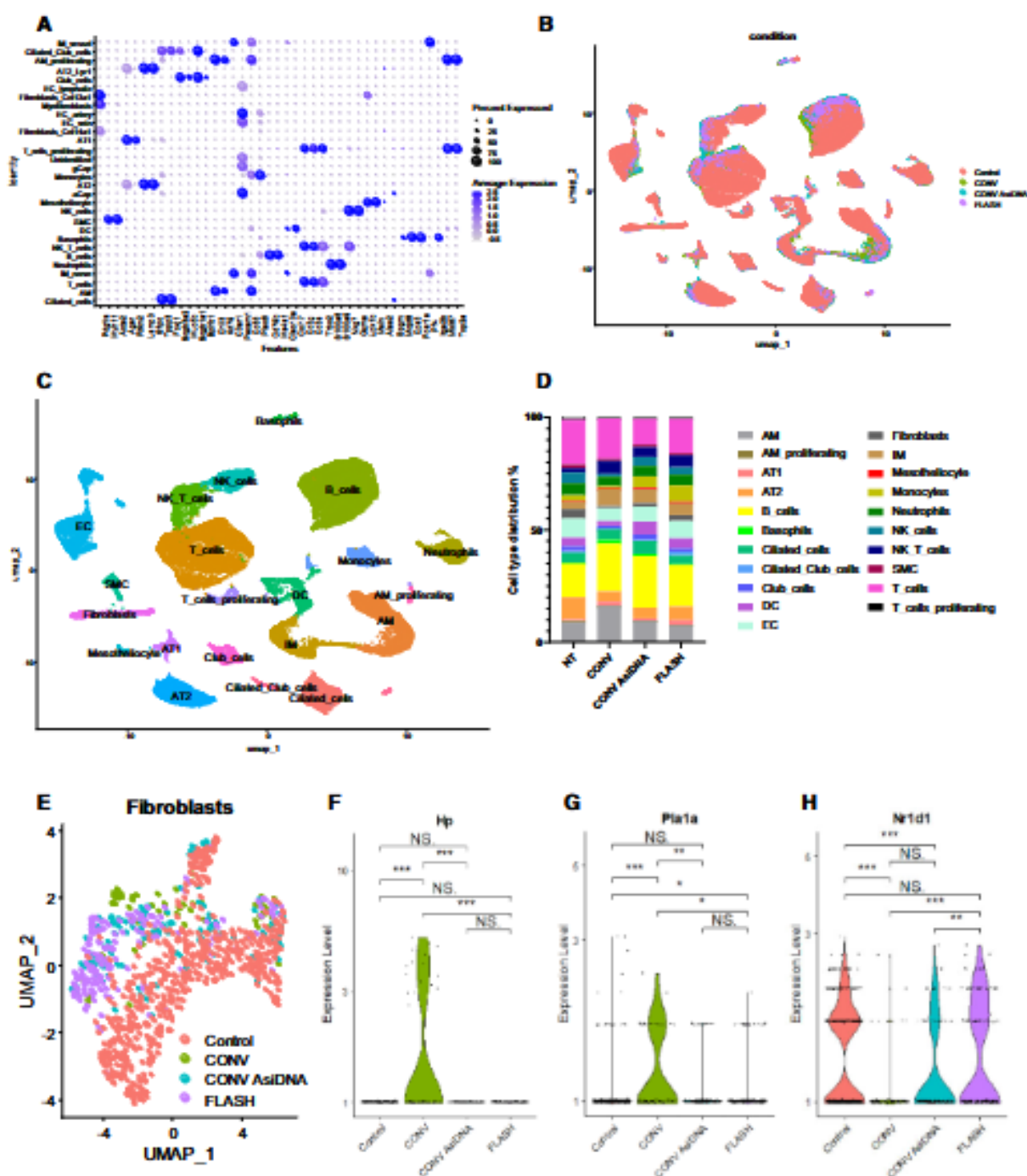


Figure 6. Single-cell RNA sequencing after irradiation and AsiDNA™ treatment. Identification of cell populations represented by (A) Dot plot of marker expression utilized for cell population identification. (B) UMAP visualizing the identified cell clusters separating representation of the Control (red), CONV (green), AsiDNA™ + CONV (blue), and FLASH (purple) treated samples. (C) UMAP visualizing the identified cell types in all samples. The individual dots signify single cells. Additionally, the created clusters are established on transcriptome resemblances. (D) Cell population proportions after Control, CONV, AsiDNA™ + CONV and FLASH treatment. Fibroblast populations represented by (E) UMAP visualizing the identified fibroblast cluster separating representation of the Control (red), CONV (green), AsiDNA™ CONV (blue) and FLASH (purple) treated samples. Pro-fibrotic markers were examined using Violin plots with myofibroblast signature genes *Hp* (F) and *Pla1a* (G), and healthy collagen homeostasis *Nr1d1* (H). CONV irradiation upregulates the expression of *Hp* and *Pla1a* and decreases the expression of *Nr1d1* compared to FLASH, CONV + AsiDNA™, and NI control, significance given by Wilcox test. (NS, *P*-value > 0.05; *, *P*-value < 0.05; **, *P*-value < 0.01; ***, *P*-value < 0.001; ****, *P*-value < 0.0001).

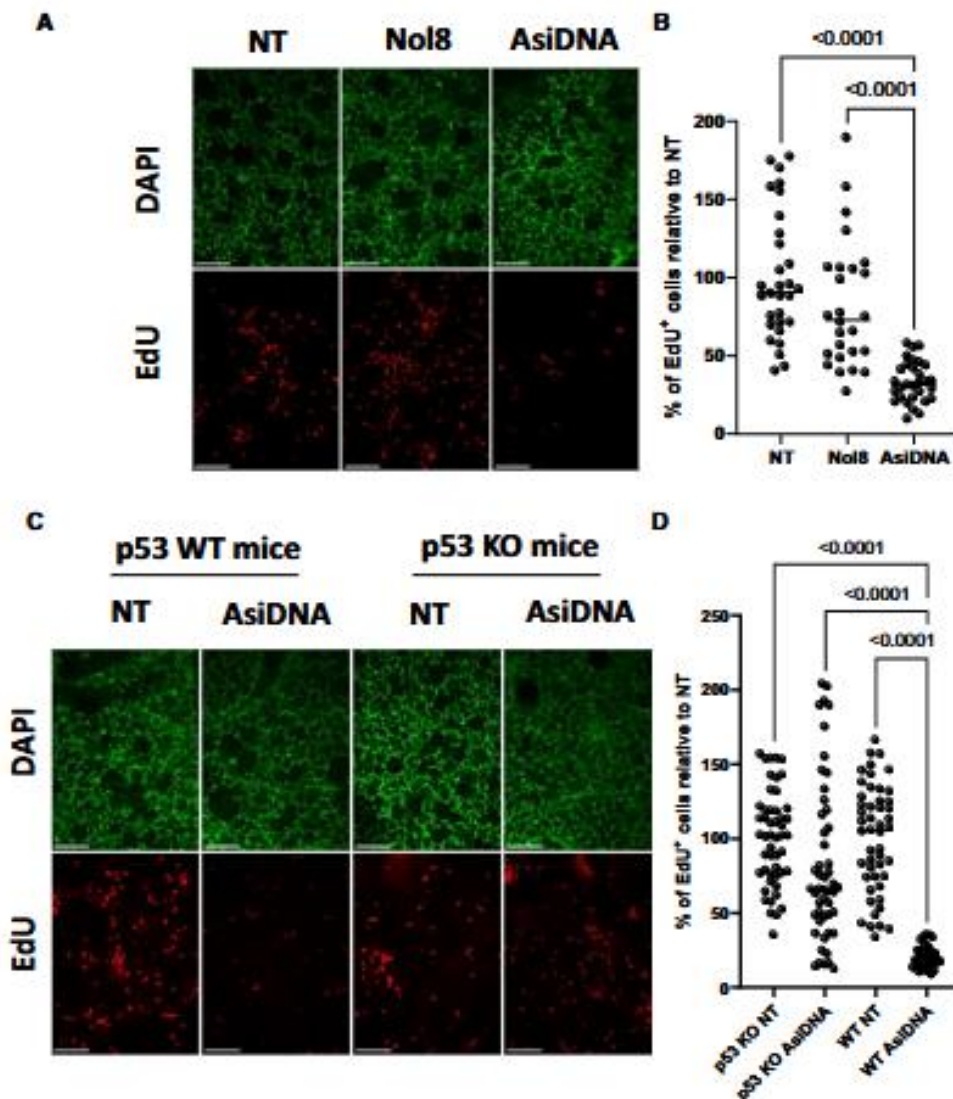


Figure 7. AsidDNA™ induces a DNA-PK and p53-dependent cell cycle arrest in the ex vivo model of precision cut lung slices. Precision cut lung slices (PCLS) were derived from C57BL6/J WT or p53 knock-out mice and treated with EdU upon 24 h of AsidDNA™ or Nol8 treatment. (A) Representative images of PCLS derived from WT mice ($N = 2$) with DAPI and EdU detection after AsidDNA™ or Nol8 treatment. (B) EdU positive cells detected after AsidDNA™ or Nol8 treatment ($N = 2$). EdU was detected in 6 slices per condition with 5 readouts per slice. (C) Representative images of PCLS derived from WT ($N = 2$) and p53 knock-out mice ($N = 2$) with DAPI and EdU detection after AsidDNA™ treatment. (D) EdU positive cells detected after AsidDNA™ or Nol8 treatment of two WT mice. EdU was detected in 8–10 slices per condition with 5 readouts per slice. Data are expressed as mean \pm standard deviation with significance given by two-way ANOVA, Tukey's multiple comparison test and represented above the bar plots. Scale bar = 100 μ m.

for histochemistry analyses (Figure 8B). The number of damaged crypts in each condition was normalized to the number of crypts present in the non-irradiated mice. More crypts remained after CONV-RT combined with AsidDNA™ treatment compared with CONV-RT standalone ($P < 0.0018$) (Figure 8C). Similarly, FLASH-RT resulted in less toxicity, preserving more of the intestinal crypts than CONV-RT ($P < 0.006$). Additionally, there was no difference detected in the percentage of remaining crypts between FLASH-RT standalone and FLASH-RT combined with AsidDNA™ treatment (Figure 8C). Collectively, these results showed a gain-of-protection for AsidDNA™ only when combined with CONV-RT.

AsidDNA™ induces a reversible cell cycle arrest *in vivo*

To demonstrate the capacity of AsidDNA™ treatment to arrest normal cell division *in vivo*, we used a well-established intestine model which exhibits a high rate of cell proliferation within the small intestinal crypts (48,49). EdU incorporation in intestine crypt cells of C57BL6/J mice was examined at 0, 24, 48 and 72h post AsidDNA™ treatment, and the small intestine was isolated for immunohistochemistry analyses 4 h after EdU incorporation (Figure 9A). A significant loss of EdU positive cells without any decrease in Ki67 was observed immediately following the final AsidDNA™ injection, compared

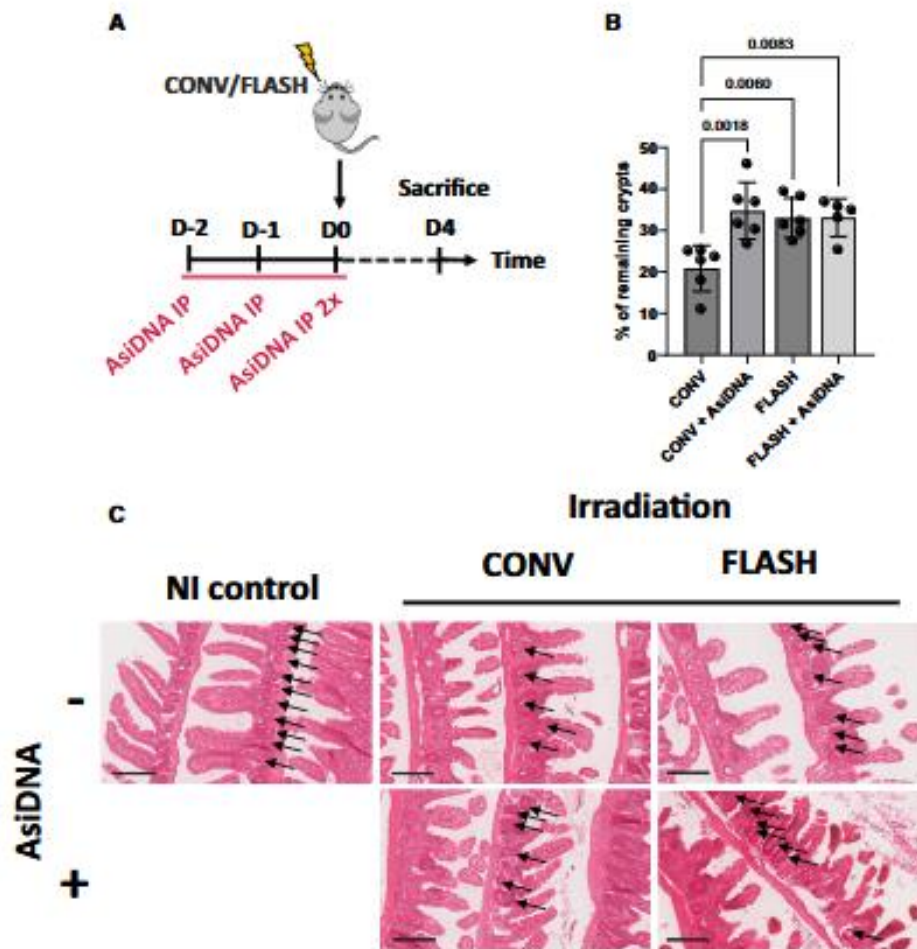


Figure 8. AsidDNA™ protects intestinal crypts from radiation toxicity. (A) Scheme of the experimental treatment timeline. C57BL6/J mice were treated for 3 consecutive days with AsidDNA™ followed by 10 Gy CONV or FLASH irradiation of the abdomen on the final day. (B) Small intestinal crypt survival of C57BL6/J mice 4 days after abdominal radiation, normalised to non-irradiated control mice. Data are expressed as mean ± standard deviation (n = 5-6) with significance given by one-way ANOVA, Tukey's multiple comparison test and represented above the bar plots. (C) Representative images of intestinal rolls stained with H&E from each treatment group. Arrows point to the intestinal crypts. Scale bar = 200 µm.

to the untreated group at time 0 h or 72 h (Figures 9B and C, Supplementary Figure S7). However, this reduction was only transient, as the level of EdU positive cells has recovered at 24, 48 and 72 h post AsidDNA™ treatment. Strikingly, this level exceeds that of the control groups suggesting a boost of cell proliferation upon release from AsidDNA™ (Figure 9C). As the reported *in vitro* G1/S arrest relies on p21 induction, p21 initiation in the small intestinal crypts in response to AsidDNA™ treatment was monitored. The number of p21 positive (p21⁺) cells was reduced in untreated groups (average of 8 and 13 p21⁺ cells per 100 cells at 0h and 72h, respectively) but significantly increased upon AsidDNA™ treatment (average of 64 p21⁺ cells per 100 cells, 0h post AsidDNA™) (Figures 9D and E). Most importantly, the number of p21 positive cells decreased rapidly at 24h post treatment (average of 20 p21⁺ cells per 100 cells, 24 h post AsidDNA™) reaching a basal level at 48 and 72 h post treatment (average of 13 p21⁺ cells per 100 cells, 48 and 72 h post AsidDNA™) (Figure 9D). Taken together, these results demonstrated that the loss of

DNA replication following AsidDNA™ treatment, as revealed by the decline of EdU incorporation, correlates with p21 induction, while recovery of EdU incorporation post-treatment correlates with a decrease in p21 initiation.

Discussion

The capacity of radiotherapy to damage and eradicate tumour cells comes at the expense of toxicity to the normal tissue, causing severe patient distress and leads to critical conditions in the treatment delivery. One approach to reduce or mitigate these toxic side-effects is to utilise chemical or biological agents as radioprotectors, administered in parallel to radiotherapy delivery (50). The ideal radioprotector exhibits low toxicity and exclusive protection of normal cells against the harmful effects of radiation, without compromising the cytotoxic effects on cancer cells. In recent years, our laboratory has developed a new class of drugs mimicking DNA DSBs that can disrupt the DNA repair machinery of cancer

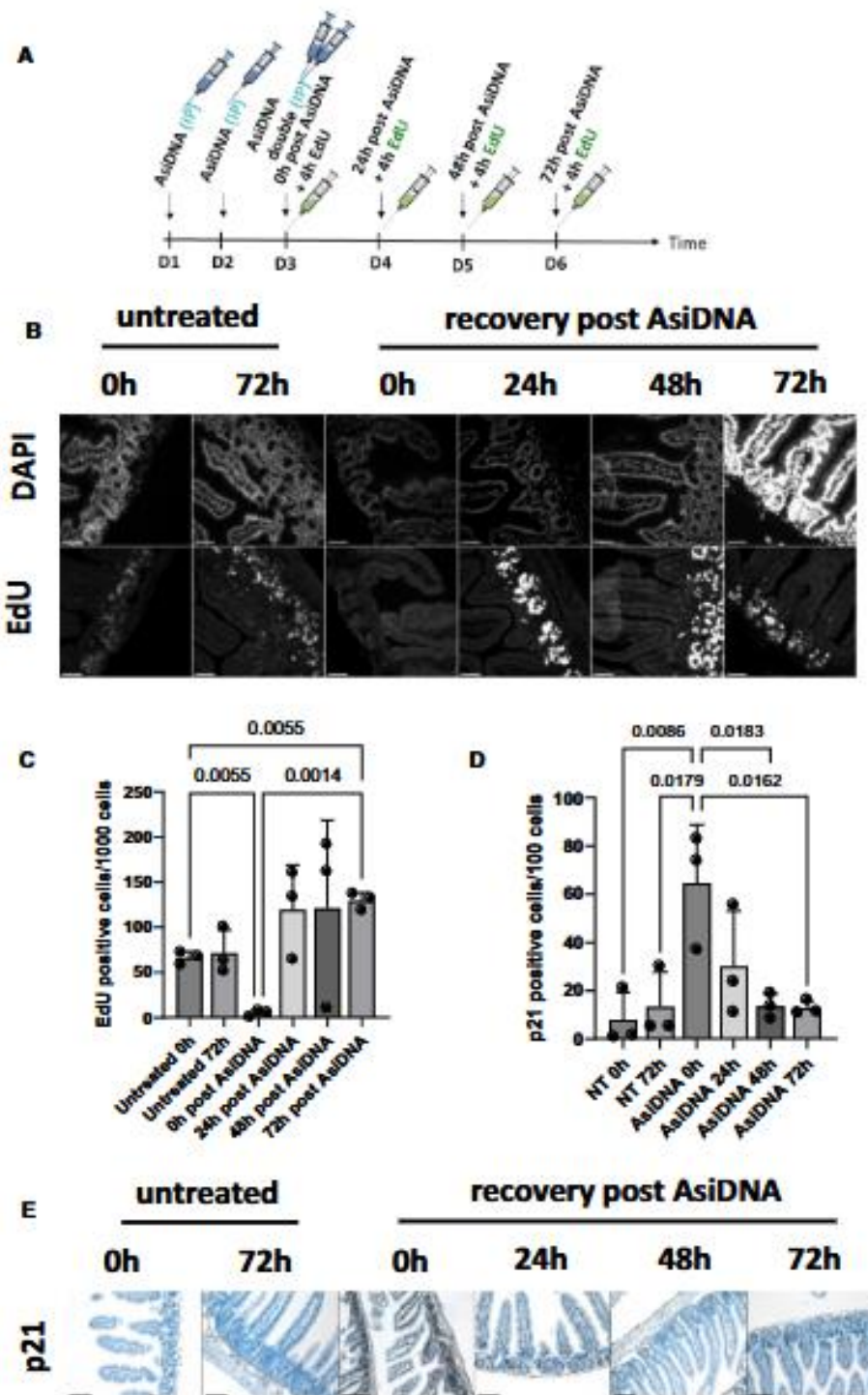


Figure 9. AsiDNA™ induced cell cycle arrest is reversible upon release of AsiDNA™ in intestinal normal tissue. (A) Scheme of the experimental treatment timeline. C57BL/6J mice were treated for 3 consecutive days with AsiDNA™ followed by 0–72 h of recovery. Thereafter, mice received EdU for 4 h prior to sacrifice. (B) Representative images of intestinal rolls stained with DAPI and Click-iT™ EdU AlexaFluor™ 488 for each treatment group. (C) EdU positive cells per 1000 detected cells in small intestinal crypts after AsiDNA™ treatment. A total number of 14 000–16 000 cells per mouse were scored. Data are expressed as mean ± standard deviation ($n = 3$) with significance given by one-way ANOVA, Brown-Forsythe and Welch tests. Scale bar = 50 μm . (D) p21 positive cells per 100 detected cells in small intestinal crypts after AsiDNA™ treatment. A total number of 6000–11 000 cells per mouse were scored. Data are expressed as mean ± standard deviation ($n = 3$) with significance given by one-way ANOVA, Tukey's multiple comparison test and represented above the bar plots. (E) Representative images of intestinal rolls stained by immunohistochemistry to detect p21 expression in each treatment group. Scale bar = 200 μm .

cells, thereby enhancing the antitumoral action of radiation (9,51). The leading molecule used in pre-clinical and clinical studies, termed AsiDNA™, is well tolerated, does not induce normal tissue toxicity, and allows increased treatment duration, (17,19–21) all indicating its suitability as a radioprotector. AsiDNA™ was designed based on its ability to bind and activate PARP and DNA-PK, with the aim of destabilizing the DNA repair machinery (9). Although activation of DNA-PK occurs in tumours as well as in normal cells, only tumour cells are sensitive to AsiDNA™ treatment (7,52).

The G1/S cell cycle checkpoint is responsible for ensuring that the optimum conditions are reached for a cell to undergo successful cell division, through the sensing of both mitogens and DNA damage (53). One of the key players of this checkpoint is the transcription factor p53 (54). p53 transactivates numerous target genes involved in the induction of the cell cycle arrest and/or apoptosis (55). In the present study, we demonstrated that in p53 proficient normal cells, AsiDNA™ treatment results in p53 activation, leading to p21 induction which, in turn, initiates a reversible G1/S cell cycle arrest. Normal cells deficient in either DNA-PK, p53, or p21 are unable to arrest at the G1/S boundary following AsiDNA™ treatment. Pull-down experiments with biotinylated AsiDNA™ have revealed that DNA-PK binds to AsiDNA™ in cellulo (M. Dutreix, unpublished results). Several studies have shown that structured DNA, single-stranded DNA, and damaged DNA promote the interaction of DNA-PK with p53 (56–58). We propose that AsiDNA™ can serve as a platform to connect DNA-PK and p53, resulting in p53 activation. In line with this assumption, our results revealed that MRC-5 primary cells can arrest at the G1/S boundary in response to AsiDNA™ treatment, while MRC-5V1 cells failed to do so. MRC-5V1 are SV40-transformed cells instigating p53 protein blockage by the SV40 large T antigen (59), which abrogates the DNA binding activity and transcriptional activity of p53. These results agree with a previous report showing the absence of p21 induction and G1/S arrest in MRC-5V1, that were present in MRC-5 primary cells, in response to ionizing radiation (60).

The p53 proficient tumour cell lines used within this study (A549, U-2 OS and HCT116) did not arrest at the G1/S boundary upon AsiDNA™ treatment, correlated with a lack of p21 induction. However, a p53- and p21-dependent G1/S arrest in tumour cells has been observed in response to DNA damaging agents such as chemical compounds (61–63) and ionizing radiation (64–66). Regardless, radiation-induced G1/S arrest is ATM/Chk2/p53/p21-dependent (67) whereas AsiDNA™-induced G1/S arrest, identified within this study, revealed its dependency on DNA-PK/p53/p21. Considering the two types of response, not only the DNA substrate differs, one being genomic DNA the other a synthetic DNA fragment, but most importantly, ATM has not been found associated to AsiDNA™ in pull-down experiments (Marie Dutreix, unpublished data), unlike DNA-PK. This also highlighted by the fact that immunofluorescence experiments failed to detect ATM phosphorylation in the nucleus upon AsiDNA treatment (9). As outlined in (68), in order for p53 to accumulate in cells and to transactivate target genes, the degradation of p53 must be inhibited, the p53 protein must accumulate in the nucleus and the sequence-specific binding activity must be induced. We have previously shown that DNA-PK is recruited, and consequently activated in response to AsiDNA™ in all normal and tumour cell lines examined so far, as revealed by phosphorylation of H2AX ((7,9), and unpublished

data). These results suggest that either the recruitment of p53 to DNA-PK/AsiDNA™ complex, and downstream transactivation of p21, is impaired in p53 proficient tumour cells, unlike p53 proficient normal cells or p53 is recruited but cannot exert properly its transcriptional activity. Normal and cancer cells differ by several phenotypic and genotypic modifications very well documented in ((69) and references therein). Among them, it is well describing that the metabolism of cancer cells differs from that of normal cells (70). We have previously demonstrated that PARP is another important protein that is activated by AsiDNA™ (9). High PARP activity leads to energy exhaustion in part due to NAD depletion (71). Notably, p53 is not only a key metabolic regulator, including NAD metabolism (72), but there is a cross-talk between p53, NAD homeostasis and PARP (73). Fischbach *et al.* revealed that p53 binds non-covalently to PARylated PARP-1, which in turn PARylates p53 (74). In another study, Wang *et al.* reported that the rapid recruitment of p53 (within seconds), to laser-induced sites of DNA damage, depends upon PARylation of p53 and closely mirrored the recruitment of PARP and Ku70 to the sites of damage (75). However, this rapid accumulation of p53 did not correlate with the presence of transcriptional activity. Most importantly, PARP inhibition delayed the recruitment of p53 but did not suppress the eventual recruitment of p53 at the sites of damage (75). Our research revealed that PARP and DNA-PK are activated upon binding to AsiDNA™ in normal and tumour cells, assessed by PARylation and phosphorylation of H2AX, respectively (this study, see also (9)). However, the inhibition of PARP by olaparib was unable to prevent AsiDNA™-induced G1/S arrest suggesting that PARP is not a key mediator in triggering p53 transcriptional activity. Taken together, we hypothesize that the lack of p53 transcriptional activity in AsiDNA™-treated p53 proficient tumour cells is likely due to the inability of p53 to connect to the AsiDNA™/DNA-PK complexes. A deeper understanding of the subcellular localization and mobility of p53 and AsiDNA™ in tumour and normal cells is required to validate or rule out our hypothesis.

In the present study, we confirmed the presence of the activated G1/S checkpoint in complex *ex vivo* and *in vivo* biological models. The *ex vivo* PCLS model retains comparable viability and tissue homeostasis during a cultivation period of 1 to 3 days (76), and can be used to monitor cell proliferation using EdU incorporation (32). AsiDNA™-treated PCLS derived from p53 WT mice revealed a severe decrease of EdU positive cells, while this decrease was absent in PCLS derived from p53 knock-out mice, or in PCLS p53 WT treated with Nol8, an AsiDNA™-like molecule unable to activate DNA-PK (5). This provides further evidence that AsiDNA™ treatment in PCLS results in DNA-PK/p53-dependent G1/S arrest. Additional conformation was observed *in vivo* where the capacity of AsiDNA™ to induce the G1/S arrest in the intestine was demonstrated with a severe decrease of EdU incorporation in the intestinal crypts of mice directly after AsiDNA™ treatment. It furthermore disclosed a full recovery of crypt division 24–48 h post-AsiDNA™ treatment, verifying the reversibility of the G1/S arrest. Remarkably, the decrease of EdU incorporation immediately after AsiDNA™ and its recovery post treatment, were both concomitantly associated with an increase of p21 expression, followed by its decrease. This provides further evidence that AsiDNA™ can activate a reversible G1/S checkpoint in PCLS. Moreover, the recovery of cell division in the crypts is associated to an excess in

EdU-positive dividing cells from 24 h post AsiDNA™ treatment. This boost in normal cell proliferation post drug treatment is a phenomenon that has been previously identified (77,78). As AsiDNA™ has widely been identified to not result in toxicity, this compensation occurrence might accompany the contribution to improved tissue recovery.

In response to DNA damaging agents, dividing cells stall or arrest their cell cycle progression to detect and repair DNA damage before they can resume the cell cycle (67). This contributes to the maintenance of both genome integrity, and overall survival. The results within this research revealed a significant increase of the survival of normal cells, *in vitro*, upon radiotherapy combined with AsiDNA™, compared to standalone treatment. This radioprotection was absent in tumour cells, independent of the p53 status, as well as in normal cells with a p53 deficient status. This confirms the necessity of an active and intact DNA-PK/p53/p21 cascade to exploit the radioprotection of normal tissue driven by AsiDNA™-induced G1/S arrest. More interestingly, this arrest overcomes the radiosensitizing activity of AsiDNA™ for which this molecule has been designed for (51).

The protective capacities of AsiDNA™ were similarly identified *in vivo* in the intestine crypt survival, as early model of radiation induced toxicity (29), and in the radiation-induced lung fibrosis, as late model of radiation induced toxicity (23). Combined CONV-RT with AsiDNA™ treatment resulted in an increase in crypt survival, compared to CONV-RT standalone, confirming the capacity of AsiDNA™ to protect against radiation induced toxicity *in vivo*. The intestinal epithelium regenerates itself through the proliferation and differentiation of stem cells (79). The intestine can therefore fully regenerate from any type of damage if the stem cells remain functional, revealing the capacity of AsiDNA™ to protect the stem cells in the crypts by acting at the G1/S transition. Remarkably, pharmacologic inhibition of the G1/S transition by CDK4/6 inhibitors prior to radiation (80), or by UCN-01 prior to chemotherapy (40) also protect the gastrointestinal epithelium in mice. The protective capacities of AsiDNA™ treatment were confirmed *in vivo*, with similar results obtained on the late radiotoxicity model of radiation-induced pulmonary fibrosis. Here, once again, AsiDNA™ combined with CONV-RT revealed increased protection of the lung to radiation toxicity presented by a delay in the onset of radiation induced fibrosis, compared to CONV-RT standalone.

Finally, the combination of AsiDNA™ with FLASH-RT, a RT modality that has been shown to alleviate radiation-induced toxicity (23,29), was explored. In one respect, FLASH-RT was shown to be less toxic, with decreased early (intestine model) and late (lung model) toxicity compared with CONV-RT, thereby reconfirming the FLASH effect. However, AsiDNA™ combined with CONV-RT did not result in the same delay in the onset of fibrosis compared to FLASH radiotherapy standalone, while combined AsiDNA™ CONV-RT treatment was as efficient as FLASH-RT standalone at protecting intestinal crypts. This may be explained by the possible limitations in the capacity of AsiDNA™ to interfere with the complex, and still relatively unknown, mechanism driving fibrosis in late responding tissues (81). Moreover, AsiDNA™ combined with FLASH-RT treatment did not result in any additive effect on the protection of toxicity in the intestinal crypts nor the lung, compared to FLASH-RT as standalone treatment. Interestingly, single cell RNA sequencing of irradiated lungs revealed a closer resemblance between

CONV AsiDNA™ and FLASH-RT in profibrotic gene signatures within the fibroblast population, in comparison to CONV-RT standalone. Similar results on profibrotic gene signatures were observed in the alveolar macrophages population (A. Sesink, and P.-M. Girard, unpublished results). Fouillade et al. (2020) revealed that FLASH irradiation tends to minimize DNA damage, compared to CONV irradiation, resulting in less induction of senescent cells and less proliferation of stem/progenitor cells to replace the damage tissue. The authors suggest that a full potential of replication, expectedly of the progenitor cell population, is required for the FLASH effect *in vivo*. On the other hand, AsiDNA does not affect the quantity of radiation-induced DNA damage (9). However, by enforcing dividing cells (e.g. stem/progenitor cells) into the G1-phase, it allows the cells to repair before entering into S-phase, increasing the survival of cells that will replace the damaged tissue. Collectively, our results indicate that the activity of AsiDNA™ and FLASH-RT could draw upon dissimilar mechanism interference to result in the same capacity to preserve the progenitor cell population within the targeted organ (i.e. lung, gut). Additional research is in progress to explore the spatio-temporal dynamics of mechanisms leading to radiation-induced pulmonary fibrosis (34).

In summary, we have identified an AsiDNA™-induced reversible G1/S-arrest dependent on the DNA-PK/p53/p21 activation cascade exclusively in healthy normal cells. The activation cascade can be exploited to protect the normal tissue against radiation induced toxicity while maintaining tumour control, thereby acting as a unique bilateral agent.

Data availability

The scRNA-seq datasets generated from non-irradiated control mice have been deposited in the Gene Expression Omnibus (GEO) repository, with the accession code GSE211713. The scRNA-seq datasets generated from irradiated mice including CONV-RT, AsiDNA CONV-RT and FLASH-RT have been deposited in the Gene Expression Omnibus (GEO) repository, with the code GSE240510.

Supplementary data

Supplementary Data are available at NAR Cancer Online.

Acknowledgements

AsiDNA™ molecules were kindly provided by Wael Jdey (Valerio Therapeutics). We would like to acknowledge L. Besse and M.-N. Soler for their helpful advice on image processing and the accessibility of the microscopy platform (Institut Curie, Orsay). We would further like to express our significant gratitude to V. Favaudon for his support throughout the work. We acknowledge L. Portier, and J. Soulier for their excellent technical support, and the Pathex platform (Institut Curie, Paris) for their aid in the assessment of pulmonary fibrosis in lung histology samples. The graphical abstract was created with Biorender.com.

Author contributions: Anouk Sesink and Pierre-Marie Girard designed and conceptualized the research; Anouk Sesink, Margaux Becerra, Nathalie Berthault, Jia-Ling Ruan, and Sophie Leboucher performed experiments and analyzed, validated, and visualized the results; Sophie Heinrich and Kristoffer Petersson analyzed and validated the results; Maxime

Dubail and Charles Fouillade developed ex vivo models; Anouk Sesink and Pierre-Marie Girard wrote the original manuscript draft. Marie Dutreix, and Pierre-Marie Girard supervised the work; Kristoffer Peterson, Wael Jdey, Marie Dutreix and Pierre-Marie Girard acquired the fundings. All authors critically revised, edited, and approved the final version of the manuscript.

Funding

The work was supported by grants to P.M.G. from European Union's Framework Program for Research and Innovation Horizon 2020 (ITN THERADNET) [under the Marie Skłodowska-Curie Grant Agreement no. 860245], and from Valerio Therapeutics (Paris, France) [CT10605]; the work was also supported by a grant to M.D. from S.I.T. Sordina IORT Technologies S.p.A.(Vicenza, Italy) [CT9792]; A.S. was the recipient of a PhD fellowship from ITN THERADNET [Grant Agreement no. 860245] and from Fondation pour la Recherche sur le Cancer (ARC, Villejuif, France); M.D. and P.M.G. wish to thank the Centre National de la Recherche Scientifique (CNRS), Institut Curie and Université Paris-Saclay for their financial and technical support.

Conflict of interest statement

Wael Jdey is employed by Valerio Therapeutics (former ONXEO). Valerio Therapeutics owns the patent for AsiDNA.

References

1. Barnett,C.C., West,C.M., Dunning,A.M., Elliott,R.M., Coles,C.E., Pharoah,P.D. and Burnet,N.G. (2009) Normal tissue reactions to radiotherapy: towards tailoring treatment dose by genotype. *Nat. Rev. Cancer*, 9, 134–142.
2. De Ruyscher,D., Niedermann,G., Burnet,N.G., Siva,S., Lee,A.W.M. and Hegi-Johnson,J. (2019) Radiotherapy toxicity. *Nat. Rev. Dis. Primers*, 5, 13.
3. Al-Mahayri,Z.N., Patrino,G.P. and Ali,B.R. (2020) Toxicity and pharmacogenomic biomarkers in breast cancer chemotherapy. *Front. Pharmacol.*, 11, 445.
4. Hellman,S. (1980) Improving the therapeutic index in breast cancer treatment: the Richard and Hinda Rosenthal Foundation Award lecture. *Cancer Res.*, 40, 4335–4342.
5. Quanz,M., Berthault,N., Roulin,C., Roy,M., Herbet,A., Agrario,C., Alberti,C., Jossierand,V., Coll,J.L., Sastre-Garau,X., et al. (2009) Small-molecule drugs mimicking DNA damage: a new strategy for sensitizing tumors to radiotherapy. *Clin. Cancer Res.*, 15, 1308–1316.
6. Berthault,N., Maury,B., Agrario,C., Herbet,A., Sun,J.S., Peyrieras,N. and Dutreix,M. (2011) Comparison of distribution and activity of nanoparticles with short interfering DNA (Dbait) in various living systems. *Cancer Gene Ther.*, 18, 695–706.
7. Thierry,S., Jdey,W., Alculumbre,S., Soumelis,V., Noguez-Hellin,P. and Dutreix,M. (2017) The DNA repair inhibitor dbait is specific for malignant hematologic cells in blood. *Mol. Cancer Ther.*, 16, 2817–2827.
8. Jdey,W., Thierry,S., Russo,C., Devun,F., Al Abo,M., Noguez-Hellin,P., Sun,J.S., Barillot,E., Zinovyev,A., Kuperstein,J., et al. (2017) Drug-driven synthetic lethality: bypassing tumor cell genetics with a combination of AsiDNA and PARP inhibitors. *Clin. Cancer Res.*, 23, 1001–1011.
9. Berthault,N., Bergam,P., Pereira,F., Girard,P.M. and Dutreix,M. (2022) Inhibition of DNA repair by inappropriate activation of ATM, PARP, and DNA-PK with the drug agonist AsiDNA. *Cells*, 11, 2149.

10. Herath,N.I., Berthault,N., Thierry,S., Jdey,W., Lienafa,M.C., Bono,F., Noguez-Hellin,P., Sun,J.S. and Dutreix,M. (2019) Preclinical studies comparing efficacy and toxicity of DNA repair inhibitors, olaparib, and AsiDNA, in the treatment of carboplatin-resistant tumors. *Front. Oncol.*, 9, 1097.
11. Quanz,M., Herbet,A., Sayarath,M., de Koning,I., Dubois,T., Sun,J.S. and Dutreix,M. (2012) Heat shock protein 90alpha (Hsp90alpha) is phosphorylated in response to DNA damage and accumulates in repair foci. *J. Biol. Chem.*, 287, 8803–8815.
12. Kotula,E., Faigle,W., Berthault,N., Dingli,F., Loew,D., Sun,J.S., Dutreix,M. and Quanz,M. (2013) DNA-PK target identification reveals novel links between DNA repair signaling and cytoskeletal regulation. *PLoS One*, 8, e80313.
13. Coquery,N., Pannetier,N., Farion,R., Herbet,A., Azurmendi,J., Clarencon,D., Baugé,S., Jossierand,V., Rome,C., Coll,J.L., et al. (2012) Distribution and radiosensitizing effect of cholesterol-coupled dbait molecule in rat model of glioblastoma. *PLoS One*, 7, e40567.
14. Bian,J., Devun,F., Jdey,W., Kotula,E., Quanz,M., Chautard,F., Sayarath,M., Sun,J.S., Verrelle,P. and Dutreix,M. (2014) A preclinical study combining the DNA repair inhibitor Dbait with radiotherapy for the treatment of melanoma. *Neoplasia*, 16, 835–844.
15. Herath,N.I., Devun,F., Lienafa,M.C., Herbet,A., Denys,A., Sun,J.S. and Dutreix,M. (2016) The DNA repair inhibitor DT01 as a novel therapeutic strategy for chemosensitization of colorectal liver metastasis. *Mol. Cancer Ther.*, 15, 15–22.
16. Herath,N.I., Devun,F., Herbet,A., Lienafa,M.C., Chouteau,P., Sun,J.S., Dutreix,M. and Denys,A. (2017) Potentiation of doxorubicin efficacy in hepatocellular carcinoma by the DNA repair inhibitor DT01 in preclinical models. *Eur. Radiol.*, 27, 4435–4444.
17. Ferreira,S., Foray,C., Gatto,A., Larcher,M., Heinrich,S., Lupu,M., Mispelter,J., Boussin,J.D., Pouppnot,C. and Dutreix,M. (2020) AsiDNA is a radiosensitizer with no added toxicity in medulloblastoma pediatric models. *Clin. Cancer Res.*, 26, 5735–5746.
18. Jdey,W., Kozlak,M., Alekseev,S., Thierry,S., Lascaux,P., Girard,P.M., Bono,F. and Dutreix,M. (2019) AsiDNA treatment induces cumulative antitumor efficacy with a low probability of acquired resistance. *Neoplasia*, 21, 863–871.
19. Le Tourneau,C., Dreno,B., Kirova,Y., Grob,J.J., Jouary,T., Dutriaux,C., Thomas,I., Lebbe,C., Mortier,J., Saiag,P., et al. (2016) First-in-human phase I study of the DNA-repair inhibitor DT01 in combination with radiotherapy in patients with skin metastases from melanoma. *Br. J. Cancer*, 114, 1199–1205.
20. Le Tourneau,C., Delord,J.P., Kotecki,N., Borcoman,F., Gomez-Roca,C., Hescot,S., Jungels,C., Vincent-Salomon,A., Cockenpot,V., Eberst,J., et al. (2020) A phase I dose-escalation study to evaluate safety, pharmacokinetics and pharmacodynamics of AsiDNA, a first-in-class DNA repair inhibitor, administered intravenously in patients with advanced solid tumours. *Br. J. Cancer*, 123, 1481–1489.
21. Kotecki,N., Jungels,C., Hoerner,F., Canon,J., Colinet,B. and De Beaumont,O. (2021) Long stabilization and disease control with AsiDNATM, a first-in-class DNA repair inhibitor in combination with carboplatin with or without paclitaxel in patients with advanced solid tumors: a case report. *Oncol. Cancer Case Rep.*, 07, 001–007.
22. Esplen,N., Mendonca,M.S. and Bazalova-Carter,M. (2020) Physics and biology of ultrahigh dose-rate (FLASH) radiotherapy: a topical review. *Phys. Med. Biol.*, 65, 23TR03.
23. Favaudon,V., Caplier,I., Monceau,V., Pouzoulet,F., Sayarath,M., Fouillade,C., Poupon,M.E., Brito,J., Hupe,P., Bourhis,J., et al. (2014) Ultrahigh dose-rate FLASH irradiation increases the differential response between normal and tumor tissue in mice. *Sci. Transl. Med.*, 6, 245ra293.
24. Fouillade,C., Carras-Alonso,S., Ciuranno,J., Queleuennec,F., Heinrich,S., Bonnet-Boissinot,S., Beddok,A., Leboucher,S.,

- Karakurt, I.I.U., Bohec, M., et al. (2020) FLASH irradiation spares lung progenitor cells and limits the incidence of radio-induced senescence. *Clin. Cancer Res.*, 26, 1497–1506.
25. Simmons, D.A., Lartey, F.M., Schuler, J., Rafat, M., King, G., Kim, A., Ko, R., Semaan, S., Gonzalez, S., Jenkins, M., et al. (2019) Reduced cognitive deficits after FLASH irradiation of whole mouse brain are associated with less hippocampal dendritic spine loss and neuroinflammation. *Radiother. Oncol.*, 139, 4–10.
 26. Velalopoulou, A., Karagounis, I.V., Verginadis, J.I., Goia, D., Kim, M., Shoniyozov, K., Cengel, K., Diffenderfer, E., Dong, L., Metz, J., et al. (2020) Proton FLASH radiation spares normal skin and soft tissues of the murine leg from radiation-induced damage while being equipotent with standard proton radiation in controlling sarcoma growth. *Cancer Res.*, 80, 5349.
 27. Velalopoulou, A., Karagounis, I.V., Cramer, G.M., Kim, M.M., Skoufos, G., Goia, D., Hagan, S., Verginadis, J.I., Shoniyozov, K., Chiango, J., et al. (2021) FLASH proton radiotherapy spares normal epithelial and mesenchymal tissues while preserving sarcoma response. *Cancer Res.*, 81, 4808–4821.
 28. Diffenderfer, E.S., Verginadis, J.I., Kim, M.M., Shoniyozov, K., Velalopoulou, A., Goia, D., Patt, M., Hagan, S., Avery, S., Teo, K., et al. (2020) Design, implementation, and in vivo validation of a novel proton FLASH radiation therapy system. *Int. J. Radiat. Oncol.*, 106, 440–448.
 29. Ruan, J.L., Lee, C., Wouters, S., Tullis, J.D.C., Verslegers, M., Mysara, M., Then, C.K., Smart, S.C., Hill, M.A., Muschel, R.J., et al. (2021) Irradiation at ultra-high (FLASH) dose rates reduces acute normal tissue toxicity in the mouse gastrointestinal system. *Int. J. Radiat. Oncol. Biol. Phys.*, 111, 1250–1261.
 30. Lenos, K., de Lange, J., Teunisse, A.F., Lodder, K., Verlaan-de Vries, M., Wiercinska, E., van der Burg, M.J., Szuhai, K., and Jochemsen, A.G. (2011) Oncogenic functions of hMDMX in in vitro transformation of primary human fibroblasts and embryonic retinoblasts. *Mol. Cancer*, 10, 111.
 31. Hauge, S., Macurek, J., and Syljuasen, R.C. (2019) p21 limits S phase DNA damage caused by the Wee1 inhibitor MK1775. *Cell Cycle*, 18, 834–847.
 32. Dubail, M., Heinrich, S., Portier, L., Bastian, J., Giuliano, L., Aggar, J., Berthault, N., Londono-Vallejo, J.A., Vilalta, M., Boivin, G., et al. (2023) Lung organotypic slices enable rapid quantification of acute radiotherapy induced toxicity. *Cells*, 12, 2435.
 33. Jin, J.L., Yoo, Y., Kim, Y., Kim, Y., Cho, J., and Lee, Y.S. (2020) Radiation-induced lung fibrosis: preclinical animal models and therapeutic strategies. *Cancers (Basel)*, 12, 1561.
 34. Curras-Alonso, S., Soulier, J., Defard, T., Weber, C., Heinrich, S., Laporte, J.L., Leboucher, S., Lameiras, S., Dutreix, M., Favaudon, V., et al. (2023) An interactive murine single-cell atlas of the lung responses to radiation injury. *Nat. Commun.*, 14, 2445.
 35. Grose, J.B., Ruan, J.L., Scott, J.L., Gorrill, J., Nicholson, J., Kelly, J., Anbalagan, S., Thompson, J., Stratford, M.R.L., Jevons, S.J., et al. (2018) Radiosensitization in vivo by histone deacetylase inhibition with No increase in early normal tissue radiation toxicity. *Mol. Cancer Ther.*, 17, 381–392.
 36. He, X.Y., Xiang, C., Zhang, C.X., Xie, Y.Y., Chen, J., Zhang, G.X., Lu, Y., and Liu, G. (2015) p53 in the myeloid lineage modulates an inflammatory microenvironment limiting initiation and invasion of intestinal tumors. *Cell Rep.*, 13, 888–897.
 37. Wang, K. and Tepper, J.E. (2021) Radiation therapy-associated toxicity: etiology, management, and prevention. *CA Cancer J. Clin.*, 71, 437–454.
 38. Prieto-Callejero, B., Rivera, J., Fagundo-Rivera, J., Romero, A., Romero-Martin, M., Gomez-Salgado, J. and Ruiz-Frutos, C. (2020) Relationship between chemotherapy-induced adverse reactions and health-related quality of life in patients with breast cancer. *Medicine (Baltimore)*, 99, e21695.
 39. Tian, J., Doi, J.I., Saar, M., Santos, J., Li, X., Peehl, D.M. and Knox, S.J. (2013) Radioprotection and cell cycle arrest of intestinal epithelial cells by darinapsin, a tumor radiosensitizer. *Int. J. Radiat. Oncol. Biol. Phys.*, 87, 1179–1185.
 40. Mull, B.B., Livingston, J.A., Patel, N., Bui, T., Hunt, K.K. and Keyomarsi, K. (2020) Specific, reversible G1 arrest by UCN-01 in vivo provides cytostatic protection of normal cells against cytotoxic chemotherapy in breast cancer. *Br. J. Cancer*, 122, 812–822.
 41. Gunderson, C.C. and Moore, K.N. (2015) Olaparib: an oral PARP-1 and PARP-2 inhibitor with promising activity in ovarian cancer. *Future Oncol.*, 11, 747–757.
 42. Veuger, S.J., Curtin, N.J., Richardson, C.J., Smith, G.C. and Durkacz, B.W. (2003) Radiosensitization and DNA repair inhibition by the combined use of novel inhibitors of DNA-dependent protein kinase and poly(ADP-ribose) polymerase-1. *Cancer Res.*, 63, 6008–6015.
 43. Bartek, J. and Lukas, J. (2001) Pathways governing G1/S transition and their response to DNA damage. *FEBS Lett.*, 490, 117–122.
 44. Ferreira, S. and Dutreix, M. (2019) DNA repair inhibitors to enhance radiotherapy: progresses and limitations. *Cancer Radiother.*, 23, 883–890.
 45. Jackson, J.L., Vujaskovic, Z. and Down, J.D. (2010) Revisiting strain-related differences in radiation sensitivity of the mouse lung: recognizing and avoiding the confounding effects of pleural effusions. *Radiat. Res.*, 173, 10–20.
 46. Crosby, J.M. and Waters, C.M. (2010) Epithelial repair mechanisms in the lung. *Am. J. Physiol. Lung Cell. Mol. Physiol.*, 298, L175–L1731.
 47. Chang, J., Garva, R., Pickard, A., Yeung, C.C., Mallikarjun, V., Swift, J., Holmes, D.E., Calverley, B., Lu, Y., Adamson, A., et al. (2020) Circadian control of the secretory pathway maintains collagen homeostasis. *Nat. Cell Biol.*, 22, 74–86.
 48. Marshman, E., Booth, C. and Potten, C.S. (2002) The intestinal epithelial stem cell. *Bioessays*, 24, 91–98.
 49. Parker, A., Maclaren, O.J., Fletcher, A.G., Muraro, D., Kreuzaler, P.A., Byrne, H.M., Maini, P.K., Watson, A.J. and Pin, C. (2017) Cell proliferation within small intestinal crypts is the principal driving force for cell migration on villi. *FASEB J.*, 31, 636–649.
 50. Checker, R., Patwardhan, R.S., Jayakumar, S., Maurya, D.K., Bandekar, M., Sharma, D. and Sandur, S.K. (2021) Chemical and biological basis for development of novel radioprotective drugs for cancer therapy. *Free Radic. Res.*, 55, 595–625.
 51. Biau, J., Chautard, E., Verrelle, P. and Dutreix, M. (2019) Altering DNA repair to improve radiation therapy: specific and multiple pathway targeting. *Front. Oncol.*, 9, 1009.
 52. Jdey, W., Thierry, S., Popova, T., Stern, M.H. and Dutreix, M. (2017) Micronuclei frequency in tumors is a predictive biomarker for genetic instability and sensitivity to the DNA repair inhibitor AsidNA. *Cancer Res.*, 77, 4207–4216.
 53. Hume, S., Dianov, G.I. and Ramadan, K. (2020) A unified model for the G1/S cell cycle transition. *Nucleic Acids Res.*, 48, 12483–12501.
 54. Engeland, K. (2022) Cell cycle regulation: p53-p21-RB signaling. *Cell Death Differ.*, 29, 946–960.
 55. Ozaki, T. and Nakagawa, A. (2011) Role of p53 in cell death and Human cancers. *Cancers (Basel)*, 3, 994–1013.
 56. Soubeyrand, S., Schild-Poulter, C. and Hache, R.J. (2004) Structured DNA promotes phosphorylation of p53 by DNA-dependent protein kinase at serine 9 and threonine 18. *Eur. J. Biochem.*, 271, 3776–3784.
 57. Achanta, G., Pelicano, J.I., Feng, J., Plunkett, W. and Huang, P. (2001) Interaction of p53 and DNA-PK in response to nucleoside analogues: potential role as a sensor complex for DNA damage. *Cancer Res.*, 61, 8723–8729.
 58. Shieh, S.Y., Ikeda, M., Taya, Y. and Prives, C. (1997) DNA damage-induced phosphorylation of p53 alleviates inhibition by MDM2. *Cell*, 91, 325–334.
 59. Ahuja, D., Saenz-Robles, M.T. and Pipas, J.M. (2005) SV40 large T antigen targets multiple cellular pathways to elicit cellular transformation. *Oncogene*, 24, 7729–7745.

60. Kohli, M. and Jorgensen, T.J. (1999) The influence of SV40 immortalization of human fibroblasts on p53-dependent radiation responses. *Biochem. Biophys. Res. Commun.*, 257, 168–176.
61. Shin, S.Y., Yoon, J.I., Ahn, S., Kim, D.W., Bae, D.H., Koh, D., Lee, Y.H. and Lim, Y. (2013) Structural properties of polyphenols causing cell cycle arrest at G1 phase in HCT116 human colorectal cancer cell lines. *Int. J. Mol. Sci.*, 14, 16970–16985.
62. Yun, J.I., Jeoung, D.J., Jin, S., Park, J.H., Lee, E.W., Lee, J.H., Choi, Y.H., Kim, B.W. and Kwon, J.H. (2022) Induction of cell cycle arrest, apoptosis, and reducing the expression of MDM proteins in human lung carcinoma A549 cells by Cedrol, isolated from *Juniperus chinensis*. *J. Microbiol. Biotechnol.*, 32, 918–926.
63. Liu, Z., Liu, Q., Xu, B., Wu, J., Guo, C., Zhu, F., Yang, Q., Gao, G., Gong, Y. and Shao, C. (2009) Berberine induces p53-dependent cell cycle arrest and apoptosis of human osteosarcoma cells by inflicting DNA damage. *Mutat. Res.*, 662, 75–83.
64. Wang, Z., Zhao, Z., Lu, J., Chen, Z., Mao, A., Teng, G. and Liu, F. (2015) A comparison of the biological effects of 125I seeds continuous low-dose-rate radiation and 60Co high-dose-rate gamma radiation on non-small cell lung cancer cells. *PLoS One*, 10, e0133728.
65. Halacli, S.O., Campinar, J.I., Cimen, E. and Sunguroglu, A. (2013) Effects of gamma irradiation on cell cycle, apoptosis and telomerase activity in p53 wild-type and deficient HCT116 colon cancer cell lines. *Oncol. Lett.*, 6, 807–810.
66. Shen, J.I. and Maki, C.C. (2010) p53 and p21(Waf1) are recruited to distinct PML-containing nuclear foci in irradiated and Nutlin-3a-treated U2OS cells. *J. Cell. Biochem.*, 111, 1280–1290.
67. Shaltiel, J.A., Krenning, J., Bruinsma, W. and Medema, R.H. (2015) The same, only different - DNA damage checkpoints and their reversal throughout the cell cycle. *J. Cell Sci.*, 128, 607–620.
68. Ljungman, M. (2000) Dial 9-1-1 for p53: mechanisms of p53 activation by cellular stress. *Neoplasia*, 2, 208–225.
69. Hanahan, D. (2022) Hallmarks of cancer: new dimensions. *Cancer Discov.*, 12, 31–46.
70. Amoedo, N.D., Valencia, J.P., Rodrigues, M.F., Galina, A. and Rumjanek, J.D. (2013) How does the metabolism of tumour cells differ from that of normal cells. *Biosci. Rep.*, 33, e00080.
71. Girard, P.M., Berthault, N., Kozlac, M., Ferreira, S., Jdey, W., Bhaskara, S., Alekseev, S., Thomas, F. and Dutreix, M. (2020) Evolution of tumor cells during AsidNA treatment results in energy exhaustion, decrease in responsiveness to signal, and higher sensitivity to the drug. *Evol. Appl.*, 13, 1673–1680.
72. Lacroix, M., Riscal, R., Arena, G., Linares, L.K. and Le Cam, J. (2020) Metabolic functions of the tumor suppressor p53: implications in normal physiology, metabolic disorders, and cancer. *Mol. Metab.*, 33, 2–22.
73. Pfister, N.T., Yoh, K.E. and Prives, C. (2014) p53, DNA damage, and NAD⁺ homeostasis. *Cell Cycle*, 13, 1661–1662.
74. Fischbach, A., Kruger, A., Hampp, S., Assmann, G., Rank, J., Hufnagel, M., Stockl, M.T., Fischer, J.M.F., Veith, S., Rossatti, P., et al. (2018) The C-terminal domain of p53 orchestrates the interplay between non-covalent and covalent poly(ADP-ribosylation) of p53 by PARP1. *Nucleic Acids Res.*, 46, 804–822.
75. Wang, Y.H., Ho, T.L.F., Hariharan, A., Goh, J.L.C., Wong, Y.L., Verkaik, N.S., Lee, M.Y., Tam, W.L., van Gent, D.C., Venkitaraman, A.R., et al. (2022) Rapid recruitment of p53 to DNA damage sites directs DNA repair choice and integrity. *Proc. Natl. Acad. Sci. U.S.A.*, 119, e2113233119.
76. Liu, G., Betts, C., Cunoosamy, D.M., Aberg, P.M., Hornberg, J.J., Sivas, K.B. and Cohen, T.S. (2019) Use of precision cut lung slices as a translational model for the study of lung biology. *Respir. Res.*, 20, 162.
77. Hietanen, K.E., Jarvinen, T.A., Huhtala, J.I., Tolonen, T.T., Kuokkanen, J.I.O. and Kaartinen, J.S. (2019) Treatment of keloid scars with intralesional triamcinolone and 5-fluorouracil injections - a randomized controlled trial. *J. Plast. Reconstr. Aesthet. Surg.*, 72, 4–11.
78. He, S., Roberts, P.J., Sorrentino, J.A., Bisi, J.F., Storrer-White, J.L., Tiessen, R.G., Makhuli, K.M., Wargin, W.A., Tadema, J.I., van Hoogdalem, E.J., et al. (2017) Transient CDK4/6 inhibition protects hematopoietic stem cells from chemotherapy-induced exhaustion. *Sci. Transl. Med.*, 9, eaa13986.
79. Noah, T.K., Donahue, B. and Shroyer, N.E. (2011) Intestinal development and differentiation. *Exp. Cell Res.*, 317, 2702–2710.
80. Wei, L., Leibowitz, B.J., Wang, X., Epperly, M., Greenberger, J., Zhang, L. and Yu, J. (2016) Inhibition of CDK4/6 protects against radiation-induced intestinal injury in mice. *J. Clin. Invest.*, 126, 4076–4087.
81. Arroyo-Hernandez, M., Maldonado, E., Lozano-Ruiz, F., Munoz-Montano, W., Nunez-Baez, M. and Arrieta, O. (2021) Radiation-induced lung injury: current evidence. *BMC Pulm. Med.*, 21, 9.

Received: August 10, 2023. Revised: February 1, 2024. Editorial Decision: February 26, 2024. Accepted: February 27, 2024

© The Author(s) 2024. Published by Oxford University Press on behalf of NAR Cancer.

This is an Open Access article distributed under the terms of the Creative Commons Attribution License (<http://creativecommons.org/licenses/by/4.0/>), which permits unrestricted reuse, distribution, and reproduction in any medium, provided the original work is properly cited.

Supplementary figures are accessible here :

<https://academic.oup.com/narcancer/article/6/1/zcae011/7626441#supplementary-data>

3. CAFFEIC ACID PHENETHYL ESTER (CAPE), A NATURAL POLYPHENOL TO INCREASE THE THERAPEUTIC WINDOW FOR LUNG ADENOCARCINOMAS

Radiotherapy and Oncology 190 (2024) 110021



Contents lists available at ScienceDirect

Radiotherapy and Oncology

journal homepage: www.thegreenjournal.com



Original Article

Caffeic Acid Phenethyl Ester (CAPE), a natural polyphenol to increase the therapeutic window for lung adenocarcinomas

E. Prades-Sagarra ^a, F. Laarakker ^a, J. Dissy ^a, N.G. Lieuwes ^a, R. Biemans ^a, M. Dubail ^b,
C. Fouillade ^b, A. Yaromina ^{a,1}, L.J. Dubois ^{a,1,*}

^a The M-Lab, Department of Precision Medicine, GROW - School for Oncology and Reproduction, Maastricht University, 6229 ER Maastricht, The Netherlands
^b Institut Curie, Inserm U1021-CNRS UMR 2247, University Paris-Saclay, PSL University, Centre Universitaire, 91405 Orsay Cedex, France

ARTICLE INFO

Keywords:
Lung cancer
Lung toxicity
Caffeic Acid Phenethyl Ester
Radiosensitization
Radiation-induced adverse effects

ABSTRACT

Background and purpose: Lung cancers are highly resistant to radiotherapy, necessitating the use of high doses, which leads to radiation toxicities such as radiation pneumonitis and fibrosis. Caffeic Acid Phenethyl Ester (CAPE) has been suggested to have anti-proliferative and pro-apoptotic effects in tumour cells, while radio-protective anti-inflammatory and anti-oxidant effects in the normal tissue. We investigated the radiosensitizing and radioprotective effects of CAPE in lung cancer cell lines and normal tissue *in vitro* and *ex vivo*, respectively. **Materials and methods:** The cytotoxic and radiosensitizing effects of CAPE in lung cancer were investigated using viability and clonogenic survival assays. The radioprotective effects of CAPE were assessed *in vitro* and *ex vivo* using precision cut lung slices (PCLS). Potential underlying molecular mechanisms of CAPE focusing on cell cycle, cell metabolism, mitochondrial function and pro-inflammatory markers were investigated.

Results: Treatment with CAPE decreased cell viability in a dose-dependent manner (IC₅₀ 57.6 ± 16.6 μM). Clonogenic survival assays showed significant radiosensitization by CAPE in lung adenocarcinoma lines ($p < 0.05$), while no differences were found in non-adenocarcinoma lines ($p \geq 0.13$). Cell cycle analysis showed an increased S-phase ($p < 0.05$) after incubation with CAPE in the majority of cell lines. Metabolic profiling showed that CAPE shifted cellular respiration towards glycolysis ($p < 0.01$), together with mitochondrial membrane depolarization ($p < 0.01$). CAPE induced a decrease in NF-κB activity in adenocarcinomas and decreased pro-inflammatory gene expression in PCLS.

Conclusion: The combination of CAPE and radiotherapy may be a potentially effective approach to increase the therapeutic window in lung cancer patients.

Introduction

Lung cancer is the most common cancer type in men, with an incidence of 1.5 million cases in 2020, and it is the third most frequent in women with over 0.7 million new diagnoses per year. With almost 1.8 million deaths in 2020, which accounts for 18 % of all cancer deaths, lung cancer is the first cause of cancer death worldwide [1,2]. Non-small cell lung cancer (NSCLC) accounts for 85 % of the cases and is the most commonly diagnosed type of lung cancer. NSCLC can be classified into different subtypes, being adenocarcinomas and squamous cell carcinomas the most frequent ones [3].

Radiotherapy, as monotherapy or in combination with other therapeutic options, is one of the standard treatments for lung cancer patients.

Lung tumours are often resistant to treatment, making high radiation doses necessary, which are inherently linked with high rates of radiation-induced lung toxicities (RILT) in the surrounding normal tissues [4,5]. Lung pneumonitis and fibrosis are the most frequent toxicities, affecting 5–25 % of lung cancer patients [6]. The normal lung tissue remains therefore a dose-limiting factor and narrows the therapeutic window, which is defined as the balance between tumour control and normal tissue complications [7]. One of the approaches to increase this therapeutic window is the use of pharmacological agents that sensitize the tumour to radiotherapy and, at the same time, protect the normal tissue against radiation-induced toxicities. Thus far, most attempts to use chemical protectors to prevent or reduce the radiation damage have failed, being amifostine the only FDA-approved

* Corresponding author at: Universiteitszingeel 50, Room H3.316, 6229 ER Maastricht, The Netherlands.

E-mail address: ludwig.dubois@maastrichtuniversity.nl (L.J. Dubois).

¹ These authors contributed equally to this work.

<https://doi.org/10.1016/j.radonc.2023.110021>

Received 13 June 2023; Received in revised form 16 October 2023; Accepted 15 November 2023

Available online 22 November 2023

0167-8140/© 2023 The Author(s). Published by Elsevier B.V. This is an open access article under the CC BY license (<http://creativecommons.org/licenses/by/4.0/>).

radioprotector agent. Amifostine has been suggested to protect the normal tissue by preventing DNA damage and oxidative stress [8,9]. However, its use in clinical trials has been questioned due to its heterogeneous effects, challenging administration and costs [8]. These limitations warrant further research into the development of new radioprotectors to increase the therapeutic window in lung cancer patients.

Polyphenols, naturally found in plants, have been proposed to have anti-oxidant and anti-inflammatory effects, which could reduce the radiation-induced toxicities, as well as cytotoxic and radiosensitizing effects in tumour cells [10]. Caffeic Acid Phenethyl Ester (CAPE), a natural phenolic compound, is the main active component of honeybee propolis. This polyphenol has been shown to have cytotoxic effects in several cancer types *in vitro* and *in vivo*, such as breast, colon, ovarian and prostate [11]. CAPE has also been proposed to decrease radiation toxicities in normal tissues, including liver and intestine, where it was able to inhibit the activation of the Nrf2 and NF- κ B pathways, as well as the expression of pro-inflammatory markers *in vitro* [12,13] and in rat models [14–16]. Only two studies have been conducted to evaluate the effects of CAPE in combination with radiation in lung models. CAPE was shown to have anti-proliferative and pro-apoptotic effects, and increased sensitivity to radiation [17]. In addition, CAPE was shown to protect the healthy lung tissue against radiation damage by NF- κ B inhibition and downregulation of pro-inflammatory cytokines *in vitro* and in mouse preclinical models [18]. However, to our knowledge, these studies investigated the effects of CAPE in only one lung cancer and one lung fibroblast cell line and warrant further investigation.

In the present study, we therefore assessed whether the radiosensitizing effects of CAPE are generalizable across multiple lung cancer cell lines from different origins and investigated the molecular mechanisms underlying these effects *in vitro*. Additionally, to understand its protective effects, we investigated if CAPE is able to protect normal lung tissue from radiation-induced toxicities both *in vitro* and, for the first time, *ex vivo* using precision cut lung slices (PCLS).

Material and methods

Cell lines and chemicals

Human NSCLC H1299, H1975, HCC827, H522, Calu-6 (adenocarcinomas, AD) and H520, HCC15, H292 lines (non-adenocarcinomas, non-AD), as well as human lung fibroblasts MRC-5 and WI-38 cell lines were cultured at 37 °C in a humidified incubator with 5 % CO₂ (Supplementary material). Cell lines were cultured in RPMI-1640, except for H1299 and Calu-6 (DMEM), and MRC-5 and WI-38 (EMEM), all supplemented with 10 % fetal bovine serum (FBS, Serana). CAPE (Sigma-Aldrich) was dissolved in DMSO to a 10 mM stock solution, and diluted further in culture media.

Cell viability assay

Cells were seeded in 96-well plates in optimized densities, allowed to attach overnight and treated with different concentrations of CAPE (2.5–180 μ M) for 24 h. Media was then refreshed, and cells were allowed to grow for another 48 h prior to endpoint measurement. Cell viability was determined using the alamarBlue Cell Viability Reagent (ThermoFisher) according to the manufacturer's protocol. Treatment response was quantified as IC₂₅ and IC₅₀ concentration, which is the concentration that causes a 25 % and 50 % reduction in cell viability, respectively.

Clonogenic survival assay

To assess whether CAPE increases radiosensitivity in tumour cells, cells were seeded at optimized densities in 60 mm dishes, allowed to grow overnight and treated with CAPE at IC₂₅ and IC₅₀ concentrations, or DMSO as control, for 24 h prior to irradiation. Cells were irradiated (1–6 Gy) using an XRAD 225CX (225 kV, 3.47 Gy/min; Precision X-ray

Inc.; H1299 and HCC15 lines) or an X-ray tube (225 kV, 0.81 Gy/min; Philips; all other cell lines). Cells were trypsinized immediately after irradiation, and seeded as single cells in 60 mm dishes in triplicate at optimized cellular density for clonogenic survival assay. Colonies were allowed to grow for 11 to 16 days depending on the cell line, and were fixed and stained with 0.4 % methylene blue in 70 % ethanol. Colonies with > 50 cells were manually counted and surviving fractions (SFs) were calculated based on plating efficiency. The SFs were fit to linear-quadratic model as a function of dose and the parameters of the clonogenic cell survival curves were compared between different treatments.

Cell cycle analysis

Cells were seeded in 6-well plates at optimized densities, allowed to attach overnight and treated with CAPE (IC₅₀) for 24 h. Cells were incubated with 10 μ M BrdU (Sigma-Aldrich) for 30 min (NSCLC) or 1 h (lung fibroblasts), and stained for BrdU and propidium iodide (PI) (Supplementary material). Fluorescence intensity was measured by flow cytometry (BD FACS Canto II), and data was analysed using FlowJo software (v10.8.1).

Metabolic profiling

Metabolic profiling was performed using Seahorse XF96 extracellular Flux analyser (Agilent). Cells were seeded at optimal seeding densities and incubated overnight to attach. Changes in oxygen consumption rate (OCR) and extracellular acidification rate (ECAR) were measured after addition of CAPE (IC₅₀ concentration) or DMSO as vehicle, according to the manufacturer's protocol (Supplementary material).

JC-10 mitochondrial membrane potential assay

Cells were seeded at optimized densities in 96-well plates, left to attach overnight and incubated with CAPE (IC₅₀) for 1 h. The JC-10 Mitochondrial Membrane Potential Assay Kit for microplate (Abcam) was performed according to the manufacturer's protocol.

NF- κ B activity

Cells were seeded at optimized densities in 96-well plates, allowed to attach overnight and transfected with the NF- κ B activity reporter plasmid pSI-Check2-hRluc-NF κ B-firefly (Supplementary material) using polyethylenimine (Polysciences, Inc.). Media was refreshed one day later and cells were incubated with CAPE (IC₅₀) or DMSO for 24 h. Cells were irradiated (6 Gy, XRAD 225CX) and collected after 30 min. The Dual-Luciferase Reporter Assay System (Promega) was used to measure the firefly and Renilla luciferase activity according to the manufacturer's protocol.

Precision-cut lung slices

PCLS were obtained from C57BL/6 mice (Supplementary Material). PCLS were treated with CAPE (20 or 40 μ M) for 24 h, irradiated (4 Gy, XRAD 225CX), and collected 24 h post-irradiation. Total RNA was isolated using the RNeasy mini kit (Qiagen) and reverse-transcribed into cDNA. qPCR was performed for Ptg2 (Cox-2), Il-6, Il-1 α and Sod1 genes, and Ct values were normalized to 18S gene. Primer sequences are provided in Supplementary Table 1.

Statistical analysis

GraphPad Prism software (v9.0) was used to perform statistical analyses. Mean values with standard deviations (SD) are reported. Two-sided (one- or two-sample) t-tests were used to assess statistical significance between the means of two experimental groups. One-way

ANOVA with Tukey's multiple comparison test was used to determine whether there are statistically significant differences between the means of more than two independent groups. *P*-values less or equal to 0.05 were considered statistically significant, *p*-values between 0.05 and 0.1 as indicative of a statistical trend.

Results

The cytotoxic effects of CAPE in human NSCLC and lung fibroblasts were determined using a cell viability assay. CAPE induced a decrease in cell viability in a dose dependent manner (Fig. 1) with IC_{50} values ranging between 32 and 88 μ M (Supplementary Table 2). The mean IC_{50} value was not significantly ($p = 0.36$) different between adenocarcinomas, non-adenocarcinomas and normal lung fibroblasts, with IC_{50} values of 65.3 ± 17.8 , 47.8 ± 14.4 and 53.2 ± 12.9 μ M, respectively.

To assess the radiosensitizing effect of CAPE in NSCLC cell lines, clonogenic survival assays were performed after treatment with CAPE for 24 h prior to radiation. CAPE, both at IC_{25} and IC_{50} (Supplementary Table 2), sensitized adenocarcinoma ($p < 0.05$), but not non-adenocarcinoma ($p > 0.13$) NSCLC cell lines to radiation (Fig. 2, Supplementary Fig. 1). The results could not be obtained due to too low plating efficiency for Calu-6 cells (4.29 ± 3.20 %) and lung fibroblasts (<1%).

To understand the mechanisms underlying the cytotoxic effects, cell cycle distribution was assessed after 24 h incubation with CAPE using BrdU/PI staining. In general, normal lung fibroblast cell lines resided mainly in G1 phase as compared to tumour cell lines. The number of cells in S-phase was significantly ($p < 0.05$) increased after treatment with CAPE in the majority of cell lines, accompanied with a decrease in

G1 phase (Fig. 3A, Supplementary Fig. 2).

To investigate the effects of CAPE on cell metabolism, changes in OCR and ECAR were measured after incubation with CAPE. Regarding mitochondrial respiration, CAPE induced a decrease in ATP production as well as spare respiratory capacity, while a significant ($p < 0.01$) increase in proton leak was observed in all cell lines (Fig. 3B, Supplementary Fig. 3A). With respect to the glucose metabolism, CAPE increased glycolysis ($p < 0.01$) and decreased the glycolytic reserve ($p < 0.01$) (Fig. 3C, Supplementary Fig. 3B). These findings suggest that CAPE inhibits oxidative phosphorylation and shifts the cell metabolism to glycolysis.

Interestingly, we observed that CAPE induces a massive mitochondrial proton leak (Fig. 3B, Supplementary Fig. 3A), indicative of mitochondrial membrane damage. To detect corresponding changes in mitochondrial membrane potential, we performed a JC-10 assay. Incubation with CAPE led to a significant ($p < 0.01$) decrease in mitochondrial membrane potential (Fig. 3D, Supplementary Fig. 4), as observed by an increase in the fluorescence ratio 525/590 nm. This depolarization was significantly ($p < 0.05$) more pronounced in tumour cell lines compared to normal lung fibroblasts (Fig. 3E).

Next, NF- κ B activity was assessed after treatment with CAPE and/or radiation. NF- κ B activity was not affected by CAPE alone in any of the cancer cell types (Fig. 4A, Supplementary Fig. 5). A statistical trend was observed when comparing NF- κ B activity in adenocarcinomas and non-adenocarcinoma lines upon pre-treatment with CAPE prior to radiation ($p = 0.0841$) (Fig. 4B, Supplementary Fig. 5). Furthermore, the combination of CAPE and radiation resulted in a significant decrease ($p = 0.0032$) in NF- κ B activity in normal lung fibroblasts (Fig. 4B, Supplementary Fig. 5), which supports CAPE anti-inflammatory effects in

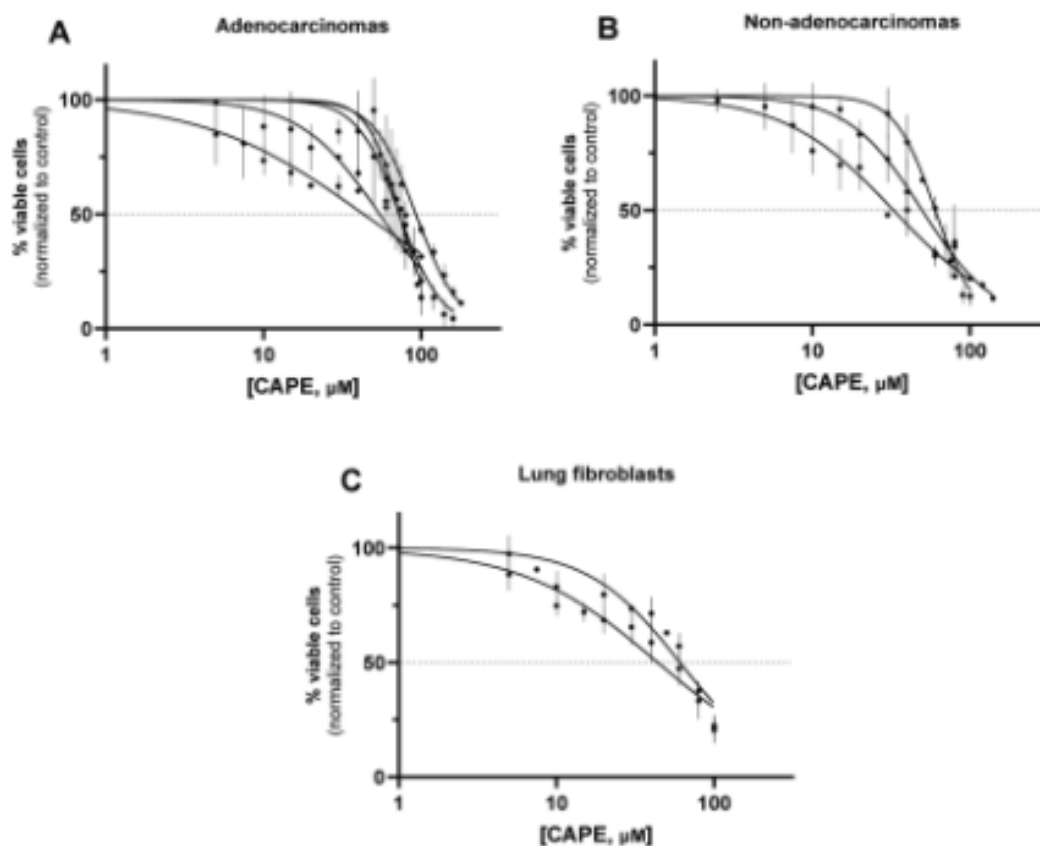


Fig. 1. CAPE induces a dose dependent decrease in cell viability in adenocarcinomas (A, 5 cell lines), non-adenocarcinomas (B, 3 cell lines) and lung fibroblasts (C, 2 cell lines). Data are represented as mean \pm SD of ≥ 3 independent experiments.

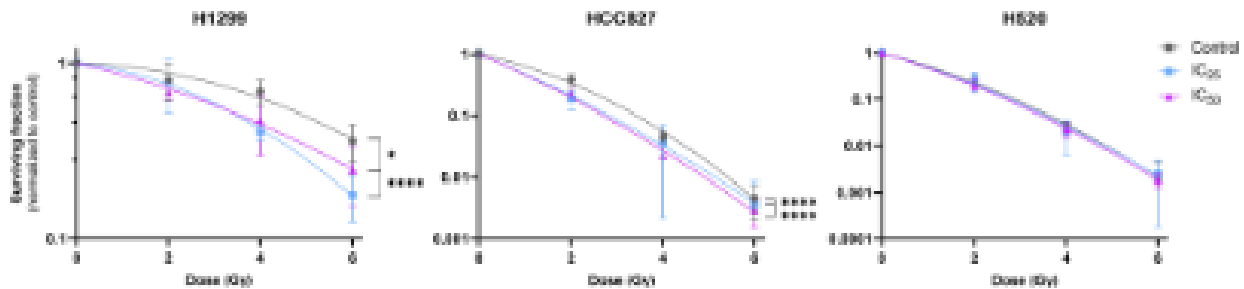


Fig. 2. CAPE sensitizes adenocarcinoma, but not non-adenocarcinoma cell lines to radiation. Representative example of the adenocarcinoma H1299 ($n = 4$) and HCC827 ($n = 4$), and the non-adenocarcinoma H820 ($n = 5$) cell lines. Data are shown as mean \pm SD. * $p < 0.05$, **** $p < 0.0001$ vs control.

normal tissue.

To assess the radioprotective effects of CAPE in normal tissue in a 2D model, PCLS were used. Slices were treated with CAPE and radiation, and gene expression levels of several pro-inflammatory and anti-oxidant markers were evaluated. The expression of interleukins (IL-6, IL-10) and COX-2 was assessed as they play an important role in the development of radiation pneumonitis and subsequently fibrosis [19,20]. Radiation did not significantly change the expression of these markers. CAPE treatment prior to radiation decreased the expression of IL-6 ($p = 0.03$) in a dose-dependent manner, while the effect on the expression of Cox-2 was less pronounced (Fig. 5, $p = 0.11$). CAPE did not affect the expression of IL-10 and Sodi (Supplementary Fig. 6).

Discussion

In the present study, we investigated the radiosensitizing and radioprotective effects of CAPE in lung cancer and in normal tissue, respectively. CAPE showed radiosensitizing effects only in adenocarcinoma cell lines, while this effect was not observed in non-adenocarcinoma cell lines. Additionally, to understand its protective effects, we investigated whether CAPE is able to protect normal lung tissue from radiation-induced toxicities. We showed that CAPE could decrease the expression of pro-inflammatory markers *in vivo*. Together, this supports that CAPE might increase the therapeutic window for lung cancer patients.

To explore potential mechanisms underlying the differential effects of CAPE radiosensitization in adenocarcinomas, non-adenocarcinomas and normal lung fibroblasts, the effect of CAPE on cell cycle distribution, cell metabolism, mitochondria function and expression of pro-inflammatory markers was investigated. CAPE induced anti-proliferative effects in the NSCLC cell lines tested in this study, which is in line with recently published papers testing the effects of CAPE in lung cancer cells [17] as well as in other cancer models [11]. We also observed that CAPE decreased cell viability in normal lung fibroblasts with a similar average IC₅₀ concentration. The effect of CAPE on cell cycle distribution has been previously described in lung and other cancer models [21–23] and is in line with our observations, namely that CAPE induces an S-phase delay. However, data on cell cycle distribution is heterogeneous as some previous studies indicated that CAPE induced a G1 arrest in tumour cells [17,24,25]. Further research on the effects of CAPE on cell cycle distribution and the underlying molecular mechanisms is therefore warranted.

Recent studies have suggested that CAPE plays a role in cell metabolism as well as mitochondrial function [26–28]. In the present study CAPE treatment resulted in a shift from oxidative phosphorylation towards glycolysis, similarly as reported in leukemic [26] and breast [27] cancer cells. CAPE also induced a massive increase in proton leak, which is indicative of mitochondrial membrane disruption. We therefore investigated the mitochondrial membrane potential after CAPE treatment, and observed that it induced a depolarization, in line with the results from a previous study in leukemic cells [28]. A balanced

potential is essential for the correct functioning of mitochondria, and depolarization could lead to an impaired ATP production [29], which was also observed in the present study. Furthermore, previous studies showed that CAPE, by causing loss of mitochondrial membrane potential, led to the release of pro-apoptotic proteins in the cytosol including cytochrome C [28]. This mechanism could explain the reported dose-dependent decreased viability as well as the pro-apoptotic effects of CAPE described in several cancer models [11]. Interestingly, we observed that CAPE treatment caused a higher depolarization in NSCLC cell lines compared to normal lung fibroblasts, supporting our hypothesis that CAPE could be a potential sensitizer in NSCLC cells, but a protector against radiation-induced toxicities in normal lung tissue.

Interestingly, a differential effect in radiosensitization by CAPE was found for adenocarcinoma compared to non-adenocarcinoma cell lines. Adenocarcinomas and non-adenocarcinomas (mainly squamous cell carcinomas) differ in histology and some molecular markers [30]. Despite both NSCLC types carry a high percentage of mutations, no differences in the mutation profile were found within adenocarcinoma nor non-adenocarcinoma cell lines, or between the cancer types upon review of the COSMIC and DepMap databases [31–32]. The differences in CAPE-induced radiosensitivity might be explained by the differential effects in NF- κ B activity in adenocarcinoma and non-adenocarcinoma cell lines. NF- κ B is a transcription factor involved in the regulation of pro-inflammatory genes as well as cell survival, proliferation and cell death [34]. We observed that CAPE slightly diminished NF- κ B activity in adenocarcinomas, while increased its activity in non-adenocarcinomas. Increased basal levels of NF- κ B activity have been reported in cancer cells as a mechanism of resistance to treatment via increased cell survival and decreased cell death, as well as promoting metastasis and de novo angiogenesis [25,36]. NF- κ B blocking has been linked to increased apoptosis and sensitivity to radiation, which is in line with our findings [25]. CAPE-mediated decrease in NF- κ B activity in adenocarcinomas could induce lower cell viability and proliferation together with increased cell death, leading therefore to increased sensitivity to treatment. In previous studies, CAPE has been proposed to block the NF- κ B pathway by preventing the binding of NF- κ B to the DNA [27]. CAPE has also been shown to decrease the protein expression levels of p50 and p65, both subunits of NF- κ B, as well as block its translocation to the nucleus [28].

In addition, we also showed a slight decrease in NF- κ B activity in normal lung fibroblasts, in line with previous published studies [18]. Literature supports that NF- κ B induces the expression of pro-inflammatory cytokines such as IL-1 and IL-6 [34], which play an important role in the development and progression of RILT [19,29]. Therefore, inhibition of NF- κ B in normal tissue could mitigate the radiation-induced inflammation and prevent RILT. In support of this hypothesis, our data on PCLS showed a decrease in the expression of some pro-inflammatory markers such as IL-6. Other studies confirmed this observation and showed that CAPE decreased the expression of pro-inflammatory genes, including Tnf- α , Tg β and IL-6 [26,28]. In addition, we have shown that CAPE may reduce Cox-2 gene expression in PCLS.

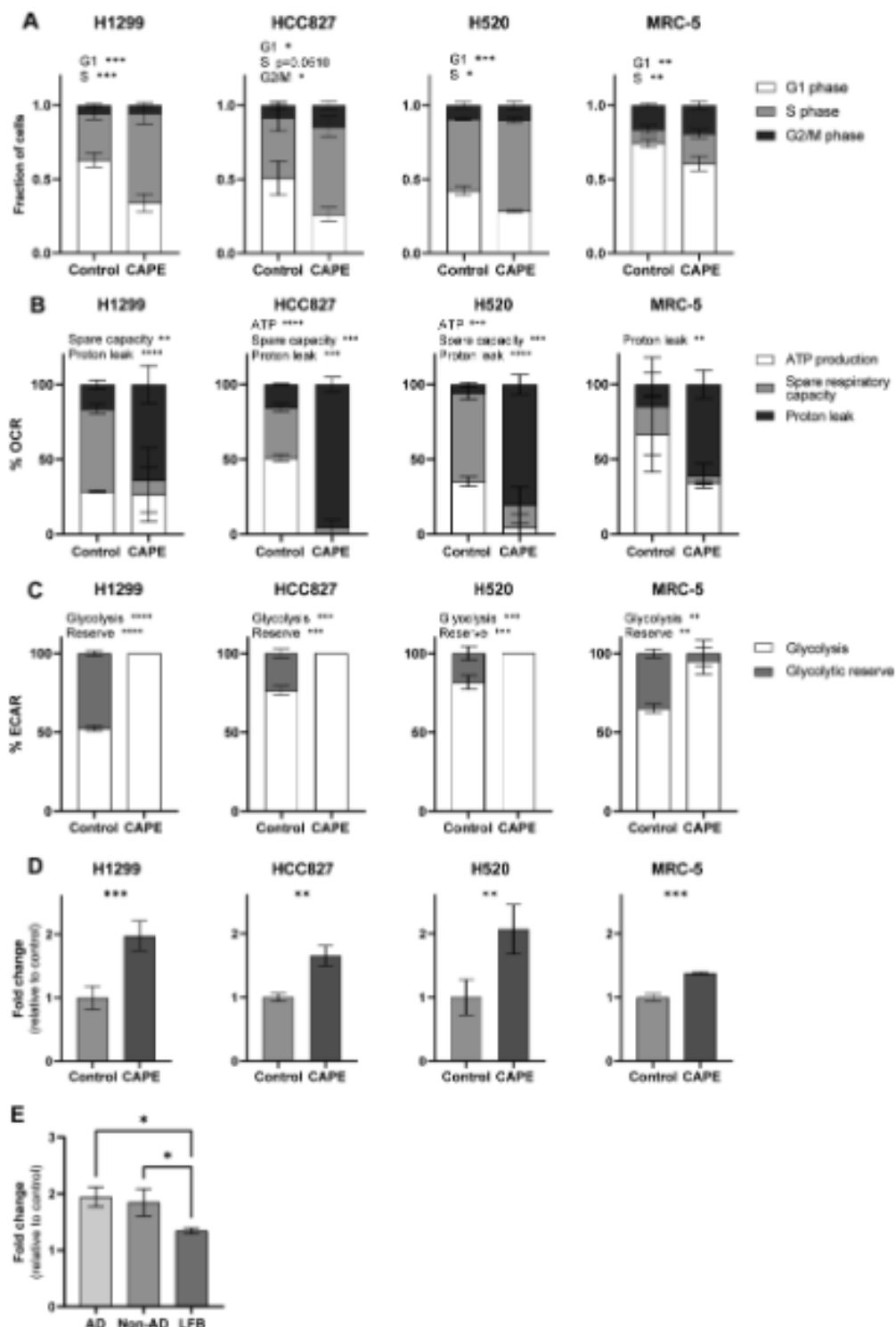


Fig. 3. CAPE alters cell cycle distribution, increases glycolysis and induces mitochondrial membrane depolarization in H1299, HCC827 (adenocarcinomas, AD), H520 (non-adenocarcinoma, non-AD) and MRC-5 (lung fibroblast, LFB). (A) Cell cycle analysis for H1299 (n = 4), HCC827 (n = 3), H520 (n = 3) and MRC-5 (n = 4). Mitochondrial respiration (B) and glycolysis stress (C) test for H1299 (n = 5), HCC827 (n = 3), H520 (n = 4) and MRC-5 (n = 3). (D) Mitochondrial membrane depolarization for H1299 (n = 4), HCC827 (n = 3), H520 (n = 4) and MRC-5 (n = 3). (E) Mitochondrial membrane depolarization for AD (5 cell lines), non-AD (3 cell lines) and LFB (2 cell lines). Data represent the mean ± SD. *p < 0.05, **p < 0.01, ***p < 0.001, ****p < 0.0001 vs control.

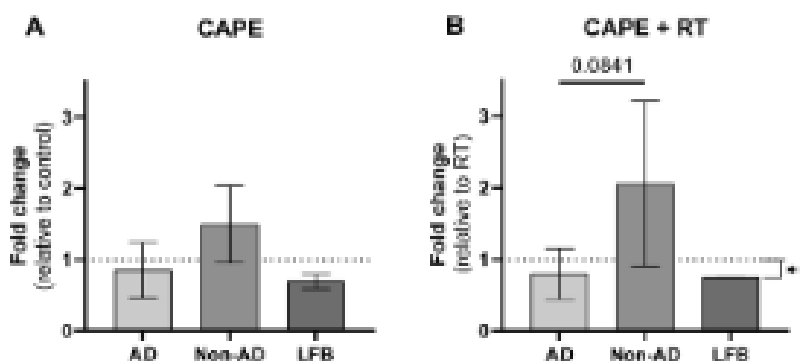


Fig. 4. Effect of CAPE (A) and CAPE combined with radiation (RT, B) on NF-κB activity for adenocarcinomas (AD, 5 cell lines), non-adenocarcinomas (non-AD, 2 cell lines) and lung fibroblasts (LFB, 2 cell lines). Data represent the mean ± SD. $p = 0.08$ for AD vs non-AD, $**p < 0.01$ for LFB RT vs RT + CAPE.

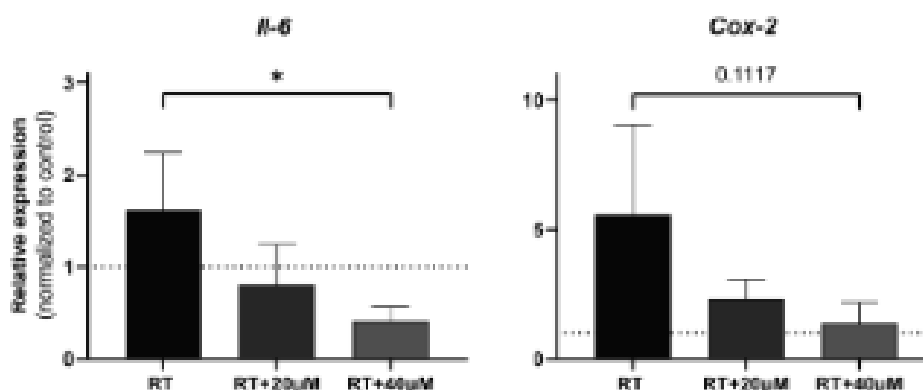


Fig. 5. Effect of CAPE combined with radiation (RT) on the expression of pro-inflammatory markers (IL-6, Cox-2) in PCLS ($n = 3$). Data represent the mean ± SD. $*p < 0.05$ vs RT.

COX-2 is an enzyme responsible for the synthesis of prostaglandins, which play a key role in inflammation. Previous *in vitro* and *in vivo* studies have proposed that CAPE reduces the expression and activity of COX-2, which supports its anti-inflammatory properties [40–42]. Overall, this supports that CAPE could protect the normal tissue against RIT, but also other normal tissue toxicities as previously observed in intestine and liver [14,15].

There are several limitations of the study that should be mentioned. The effects of CAPE in normal tissue were investigated in only two human normal lung fibroblast cell lines. Further research should be performed in multiple lung fibroblast cell lines to confirm these findings. In addition, these cell lines do not possess the ability to form colonies, which impedes testing the radioprotective effects of CAPE by means of the standard technique, clonogenic survival assays. The use of fractionated irradiation should be tested in combination with CAPE in order to add a more clinical relevance to the study, as fractionated radiotherapy is currently the most commonly used schedule in the clinic [43].

In conclusion, CAPE is a promising agent to widen the therapeutic window for lung cancer patients, especially for patients with adenocarcinoma, based on its radiosensitizing effects in tumour cells as well as its potential mechanisms against radiation-induced adverse effects. Further research should be performed to unravel the exact molecular mechanisms underlying these effects. In addition, studies in preclinical models should be carried out to confirm its properties and its future impact in the clinic.

Funding

E.P.S. has received funding from the European’s Union Horizon 2020 research and innovation program under the Marie Skłodowska-Curie grant agreement N°860245 (granted to L.J.D.), and from the European Union’s “EURATOM” research and innovation program under the 101061027 grant agreement (granted to E.P.S.).

Declaration of competing interest

L.J.D. has, outside of the submitted work, shares in the companies Conwert Pharmaceuticals and LivingMed Biotech, he is co-inventor of a non-issued, non-licensed patent on LSRT (N2024889). The other authors declare that they have no known competing financial interests or personal relationships that could have appeared to influence the work reported in this paper.

Appendix A. Supplementary material

Supplementary data to this article can be found online at <https://doi.org/10.1016/j.radonc.2023.110021>.

References

[1] Ferlay J, et al. Cancer statistics for the year 2020: An overview. *Int J Cancer* 2021.
 [2] Sung H, et al. Global Cancer Statistics 2020: GLOBOCAN Estimates of Incidence and Mortality Worldwide for 20 Cancer in 185 Countries. *CA Cancer J Clin* 2021; 71:209–48.

- [3] Herbst RS, Morgensztern D, Boshoff C. The biology and management of non-small cell lung cancer. *Nature* 2018;553:446–54.
- [4] De Ruyscher D, et al. Radiotherapy toxicity. *Nat Rev Dis Primers* 2019;5:13.
- [5] Granton PV, et al. A Longitudinal Evaluation of Partial Lung Irradiation in Mice by Using a Dedicated Image-Guided Small Animal Irradiator. *International Journal of Radiation Oncology*Biophysics* 2014;90:696–704.
- [6] Hanania AN, et al. Radiation-Induced Lung Injury: Assessment and Management. *Chest* 2019;156:150–62.
- [7] Montay-Grusel P, et al. Expanding the therapeutic index of radiation therapy by normal tissue protection. *Br J Radiol* 2019;92:20180008.
- [8] Devine A, Marignol L. Potential of Amifostine for Chemoradiotherapy and Radiotherapy-associated Toxicity Reduction in Advanced NSCLC: A Meta-Analysis. *Anticancer Res* 2016;36:5–12.
- [9] Belderbos J, et al. 42 - Acute and Late Toxicities of Thoracic Radiotherapy: Pulmonary, Esophagus, and Heart. In: Pass HI, Ball D, Scagliotti GV, editors. *IASLC Thoracic Oncology*. Second Edition. Philadelphia: Elsevier; 2018. 393–408.e4.
- [10] Prades-Sagarra E, Yaramina A, Dubois LJ. Polyphenols as Potential Protectors against Radiation-Induced Adverse Effects in Patients with Thoracic Cancer. *Cancers* 2023;15:2412.
- [11] Pandey P, et al. Therapeutic efficacy of caffeic acid phenethyl ester in cancer therapy: An updated review. *Chem Biol Drug Des* 2023. n/a/n/a.
- [12] Yang N, et al. Caffeic acid phenethyl ester up-regulates antioxidant levels in hepatic stellate cell line T6 via an Nrf2-mediated mitogen activated protein kinases pathway. *World J Gastroenterol* 2017;23:1203–14.
- [13] Lee Y, et al. Caffeic acid phenethyl ester-mediated Nrf2 activation and I κ B kinase inhibition are involved in NF κ B inhibitory effect: Structural analysis for NF κ B inhibition. *Eur J Pharmacol* 2010;643:21–8.
- [14] Chu J, et al. Protective effects of caffeic acid phenethyl ester against acute radiation-induced hepatic injury in rats. *Environ Toxicol Pharmacol* 2015;39: 683–9.
- [15] Jin LG, et al. Caffeic acid phenethyl ester attenuates ionize radiation-induced intestinal injury through modulation of oxidative stress, apoptosis and p38MAPK in rats. *Environ Toxicol Pharmacol* 2015;40:156–63.
- [16] Linard C, et al. Acute induction of inflammatory cytokine expression after gamma-irradiation in the rat: effect of an NF-kappaB inhibitor. *Int J Radiat Oncol Biol Phys* 2004;58:427–34.
- [17] Chen M-F, et al. Cell Killing and Radiosensitization by Caffeic Acid Phenethyl Ester (CAPE) in Lung Cancer Cells. *J Radiat Res* 2004;45:253–60.
- [18] Chen MF, et al. Caffeic acid phenethyl ester decreases acute pneumonitis after irradiation in vitro and in vivo. *BMC Cancer* 2005;5:158.
- [19] Giuranno L, et al. Radiation-Induced Lung Injury (RILI). *Front Oncol* 2019;9:877.
- [20] Hunter NR, et al. Mitigation and Treatment of Radiation-Induced Thoracic Injury With a Cyclooxygenase-2 Inhibitor, Celecoxib. *International Journal of Radiation Oncology*Biophysics* 2013;85:472–6.
- [21] Ren X, et al. Caffeic Acid Phenethyl Ester Inhibits the Proliferation of HEP2 Cells by Regulating Stat3/Pik1 Pathway and Inducing S Phase Arrest. *Biol Pharm Bull* 2019; 42:1689–93.
- [22] Kabata-Dzik A, et al. Comparison of Two Components of Propolis: Caffeic Acid (CA) and Caffeic Acid Phenethyl Ester (CAPE) Induce Apoptosis and Cell Cycle Arrest of Breast Cancer Cells MDA-MB-231. *Molecules* 2017;22.
- [23] Chiang K-C, et al. Caffeic Acid Phenethyl Ester Induces N-myc Downstream Regulated Gene 1 to Inhibit Cell Proliferation and Invasion of Human Nasopharyngeal Cancer Cells. *Int J Mol Sci* 2018;19:1397.
- [24] Tang H, et al. Anti-colon cancer effect of caffeic acid p-nitro-phenethyl ester in vitro and in vivo and detection of its metabolites. *Sci Rep* 2017;7:7399.
- [25] Liang Y, et al. Caffeic acid phenethyl ester suppressed growth and metastasis of nasopharyngeal carcinoma cells by inactivating the NF- κ B pathway. *Drug Des Devel Ther* 2019;13:1335–45.
- [26] Yucel B, Sonmez M. Repression of oxidative phosphorylation sensitizes leukemia cell lines to cytarabine. *Hematology* 2018;23:330–6.
- [27] Bonucelli G, et al. NADH autofluorescence, a new metabolic biomarker for cancer stem cells: Identification of Vitamin C and CAPE as natural products targeting "stemness". *Oncotarget* 2017;8.
- [28] Cavaliere V, et al. Caffeic acid phenethyl ester and MGI32, two novel nonconventional chemotherapeutic agents, induce apoptosis of human leukemic cells by disrupting mitochondrial function. *Target Oncol* 2014;9:25–42.
- [29] Zhou B, Tian R. Mitochondrial dysfunction in pathophysiology of heart failure. *J Clin Invest* 2018;128:3716–26.
- [30] Relli V, et al. Abandoning the Notion of Non-Small Cell Lung Cancer. *Trends Mol Med* 2019;25:585–94.
- [31] **The Catalogue of Somatic Mutations in Cancer (COSMIC).** [cited 2023 10 May]; Available from: <https://cancer.sanger.ac.uk/cosmic>.
- [32] Tate JG, et al. COSMIC: the Catalogue Of Somatic Mutations In Cancer. *Nucleic Acids Res* 2018;47:D941.
- [33] **The Cancer Dependency Map Project.** [cited 2023 10 May]; Available from: <https://depmap.org/portal/>.
- [34] Hoesel B, Schmid JA. The complexity of NF- κ B signaling in inflammation and cancer. *Mol Cancer* 2013;12:86.
- [35] Orlowski FZ, Baldwin AS. NF- κ B as a therapeutic target in cancer. *Trends Mol Med* 2002;8:385–9.
- [36] Mortezaei K, et al. NF- κ B targeting for overcoming tumor resistance and normal tissues toxicity. *J Cell Physiol* 2019;234:17187–204.
- [37] Natarajan K, et al. Caffeic acid phenethyl ester is a potent and specific inhibitor of activation of nuclear transcription factor NF-kappa B. *PNAS* 1996;93:9090–5.
- [38] Onori P, et al. Caffeic acid phenethyl ester decreases cholangiocarcinoma growth by inhibition of NF-kappaB and induction of apoptosis. *Int J Cancer* 2009;125: 565–76.
- [39] De Ruyscher D, et al. Nintedanib reduces radiation-induced microscopic lung fibrosis but this cannot be monitored by CT imaging: A preclinical study with a high precision image-guided irradiator. *Radiother Oncol* 2017;124:482–7.
- [40] Michaluart P, et al. Inhibitory Effects of Caffeic Acid Phenethyl Ester on the Activity and Expression of Cyclooxygenase-2 in Human Oral Epithelial Cells and in a Rat Model of Inflammation1. *Cancer Res* 1999;59:2347–52.
- [41] Lee KW, et al. Inhibition of Cyclooxygenase-2 Expression and Restoration of Gap Junction Intercellular Communication in H-ras-Transformed Rat Liver Epithelial Cells by Caffeic Acid Phenethyl Ester. *Ann N Y Acad Sci* 2004;1030:501–7.
- [42] Li L, et al. Caffeic acid phenethyl ester attenuates lipopolysaccharide-stimulated proinflammatory responses in human gingival fibroblasts via NF- κ B and PI3K/Akt signaling pathway. *Eur J Pharmacol* 2017;794:61–8.
- [43] Kapka L, Socha J. Dose and fractionation schedules in radiotherapy for non-small cell lung cancer. *Transl Lung Cancer Res* 2021;10:1969–82.

Supplementary materials are available here :

[https://www.thegreenjournal.com/article/S0167-8140\(23\)09328-3/fulltext](https://www.thegreenjournal.com/article/S0167-8140(23)09328-3/fulltext)

ANNEX II : Other co-author contributions

1. RADIOTHERAPY TRIGGERS PRO-ANGIOGENIC SIGNALING IN HUMAN LUNG

Radiotherapy triggers pro-angiogenic signaling in human lung

Juliette Soulier¹, Sandra Curras-Alonso¹, Maxime Dubail¹, Hugo Laporte^{1,2}, Ayan Mallick¹, Chloé Lafouasse³, Delphine Colin⁴, Jean-François Côté⁴, Jérôme Didier⁴, Christelle Pouliquen⁴, Abdelali Benali⁴, Marco Alifano⁵, Catherine Durdux⁶, Diane Damotte⁷, Marine Lefèvre⁴, Mylène Bohec^{8,9}, Kim Cao¹⁰, Gilles Créhange¹⁰, Pierre Verrelle¹¹, Nicolas Girard¹², Agathe Seguin-Givelet^{3,13}, Arturo Londoño-Vallejo¹, Charles Fouillade¹

¹Institut Curie, Inserm U1021-CNRS UMR 3347, University Paris-Saclay, PSL Research University, Centre Universitaire, 91405 Orsay Cedex, France.

²Institute of Cell Biology (Cancer Research), University Hospital Essen, Essen, Germany.

³Surgery Department, Institut Mutualiste Montsouris, Paris, France.

⁴Department of Pathology, Institut Mutualiste Montsouris, Paris, France.

⁵Thoracic Surgery Department, Paris Center University Hospitals, AP-HP, Paris, France; INSERM U1138, Integrative Cancer Immunology, University of Paris, 75006 Paris, France.

⁶Radiation Oncology Department, Georges Pompidou European Hospital, APHP, Paris, France.

⁷Pathology Department, Paris Center University Hospitals, AP-HP, Paris, France; INSERM U1138, Integrative Cancer Immunology, University of Paris, 75006 Paris, France.

⁸Institut Curie Genomics of Excellence (ICGex) Platform, Paris, France

⁹Institut Curie, PSL University, Single Cell Initiative, 75005 Paris, France.

¹⁰Institut Curie, PSL Research University, Radiation Oncology Department, Paris/Saint-Cloud/Orsay, France.

¹¹Institut Curie, Inserm U1196-CNRS UMR 9187, University Paris-Saclay, PSL Research University, Centre Universitaire CS 90030, Orsay, France.

¹²Institut du Thorax Curie Montsouris, Paris, France.

¹³Paris 13 University, Sorbonne Paris Cité, Faculty of Medicine SMBH, Bobigny, France.

Abstract

Radiotherapy is one of the main therapeutic options for the treatment of lung cancer. Although highly efficient, radiation cause severe damages to normal tissue and radio-induced toxicities vary from mild pneumonitis to pulmonary fibrosis. The mechanism leading to these toxicities remain unclear. To investigate the molecular responses of human lung to radiotherapy, we analyzed, by single cell RNAseq, lung tissue resected in the vicinity of the tumor (i.e. treated with radiation) and compared the transcriptional profiles of the distinct lung populations from the same patient removed at distance from the tumor (i.e. non-treated with radiation).

Analysis of six lung samples from patients suffering from Pancoast tumor, a rare lung malignancy that requires neo-adjuvant radiotherapy before surgery, revealed a strong induction of VEGF signaling after radiotherapy. Expression of VEGFA, one of the canonical pro-angiogenic ligands, was found upregulated in multiple cell populations in lung exposed to high doses of radiation. Irradiated capillaries, particularly gCap cells, expressing KDR/VEGFR2, present transcriptional profile similar to tip cells, characterized by sprouting and motility capacities. In addition, we identified a sub-population of alveolar macrophages expressing FLT1/VEGFR1, a receptor for VEGFA, in lung tissues treated by radiotherapy. Cell-Cell communication analysis revealed that FLT1/VEGFR1 positive macrophages interact with tip cells after radiotherapy through IL1B-IL1R signaling. Lastly, analysis of mouse single cell dataset confirmed the increase in the proportion of gCap cells presenting a tip-like phenotype after radiation injury.

Altogether, this study describes, at the single cell level, the pro-angiogenic responses of human lung after radiotherapy. These results will lead to a better understanding of the physiopathology of lung radiation injury and may pave the way to optimize treatments to improve patients' quality of life.

Introduction

Lung cancer is the leading cause of cancer-related death worldwide[1]. Most of the patients treated for this disease undergo radiation therapy. However, the lung is a sensitive organ to radiation[2], therefore the treatment is often limited by dose of irradiation that the lung can sustain. Radiation of healthy lungs induces damage, radio-induced lung injury (RILI), involving DNA damages[2] and oxidative stress[3], leading to inflammation and processes of wound healing in the lung tissues[4]. In some patients, this early toxicity can evolve into a chronic condition called radio-induced pulmonary fibrosis (RIPF)[5]. RIPF can develop after a RILI through the replacement of normal tissue by scar due to excessive deposition of extracellular matrix, proliferation of fibroblasts [6], disruption of the alveolar structure and vascular damages[7]. These changes prevent gas exchange and lung function, leading to respiratory failure and death[5]. There is for the moment no efficient treatment to cure or even stabilize RIPF[8]. Even if some of the molecular and cellular events that occur in RILI and that lead to RILF have been described[9], the detailed mechanisms and processes leading to fibrosis is not fully understood. Furthermore, most of what is known about RIPF comes from a model of total thoracic irradiation in the mouse[10], mostly because access to fresh human irradiated lung samples remain complex and challenging. In mouse models, it has been described that in reaction to irradiation, healthy tissue goes through processes of epithelial to mesenchymal transition, a switch of profile of the macrophages to either a pro-fibrotic or pro-inflammatory phenotype depending on the population, a transdifferentiation of the AT2 cells to AT1 cells and an increased extracellular matrix production by the myofibroblasts[11].

However, it is important to study the human lung response to irradiation in complement of these studies. Therefore, our goal in this study is to gain a better understanding of the cellular and molecular mechanisms of the human non tumoral lung response to irradiation. In that purpose, we collected samples from patients suffering from Pancoast tumor and who underwent radiotherapy previously to lobectomy[12]. Pancoast tumors are located at the apex of the lung and often invade the sternum [12, 13]. Due to this particularities, a combination of Platinum salts and radiotherapy is used to shrink the tumor prior to surgery[14]. Classically performed after surgery and chemotherapy, Pancoast tumors represent one of the rare cases of treatment with neoadjuvant radiotherapy, allowing us to access previously irradiated human lung. To perform this study, we used single cell RNA sequencing to analyze the molecular responses of human lung to radiotherapy and gain a better understanding of the cellular and molecular mechanisms involved.

After radiation injury, lung vessels are damaged, especially the capillaries. Pro-angiogenic signalling can be involved in the repair processes and angiogenesis. Formation of new vessels requires a complex signalling network involving the vascular endothelial growth factor (VEGF) signaling [15]. At the cellular level, angiogenesis has been shown to include the differentiation of the endothelial cells into two cell states: tip cells and stalk cells. Tip cells express the VEGF receptor KDR (also known as VEGFR2), and sense the VEGF secreted in the environment. Tip cells also develop filipodia, can migrate towards an extracellular gradient of VEGFA, occupying a leading position in angiogenesis. They are followed by the stalk cells that divide to allow elongation of the protruding new vessel [16]. Induction of VEGF signalling

in the tip cells triggers the expression of several genes including DLL4. DLL4 ligands then activate NOTCH receptor expressed by the stalk cells. In stalk cells, activation of NOTCH signalling inhibits KDR/VEGFR2 expression and activates FLT1/VEGFR1 expression, maintaining the stalk cell identity [9, 17, 18].

During this study, we will use a single cell RNA sequencing approach to study the cellular and molecular consequences of radiotherapy in human lung obtained from Pancoast patients, particularly the consequence on lung capillaries, a critical population for gas exchanges and lung function.

Material and methods

Human samples availability

Freshly resected lung human samples were obtained from six patients undergoing upper lobectomy of a Pancoast tumor who had previously received a neoadjuvant radiotherapy (40-45 Gy delivered by daily 2 Gy/fraction, considered sufficient to trigger pulmonary fibrosis) concomitant to a chemotherapy with platinum salts on the first and fourth weeks of radiotherapy treatment. Accessibility to the dosimetric computerized tomography (CT)-scans of the patients allowed us to determine a region in the lobe far away from the tumor that did not receive any radiation (NI) and a region next to the tumor that received the highest dose of radiation (IR). A sample of 2 cm³ from each of these regions was resected and immediately placed in cold 1x phosphate buffered saline and transported on ice directly to the research lab for single cell dissociation procedure (**fig. 1a**). Accessibility to human samples was achieved in collaboration with Institut Mutualiste Montsouris and Cochin Hospital. Informed consent was obtained from each patient before the surgery.

Lung tissue dissociation

Human lung samples were perfused with 1.5 ml of 50 U/ml dispase (Serlabo, WO-LS02100; Sigma Corning, DLW354235) using a 20G needle, followed by 0.5 ml of 1% agarose (Invitrogen, 15510-027) to block the exit of the dispase. Lungs were minced with a scalpel into small pieces and added into 3 ml of 1x DPBS MgCl₂+ and CaCl₂+ (Gibco, 14040-091). Then 320 µl of 25 U/ml elastase (Worthington, LS002292) were added and the suspension was homogenized and incubated for 45 min at 37°C with orbital shaking. Enzymatic activity was inhibited with 5 ml of PF10 (1x DPBS containing 10% fetal bovine serum (FBS)) and 20 µl of 0.5 M ethylenediaminetetraacetic acid (EDTA) pH 8 (Invitrogen, AM9260G). Cell suspension was filtered through 100 µm nylon cell strainer (Fisher Scientific, 22363549), which was rinsed with 5 ml of PF10. This was followed by 37.5 µl of 10 mg/ml DNase I (Sigma, D4527-40KU) treatment and incubation on ice for 3 min. Cell suspension was filtered again through a 40 µm nylon cell strainer (Fisher Scientific, 087711) and 5 ml of PF10 were added to rinse it. Samples were centrifuged for 6 min at 150 g and 4°C, pellet was resuspended in red blood cell (RBC) lysis buffer (Roche, 11814389001) and incubated for 90s at room temperature before stopping the lysis with 6 ml of PF10. Then, 500 µl of pure FBS were placed at the bottom of the sample, prior to a final centrifugation for 6 min at 150 g and 4°C. The pellet was resuspended in 1 ml of 1x DPBS containing 0.02% bovine serum albumin (BSA) (Sigma, D4527-40KU) and cell counting was done in a Malassez. Finally, concentration of the samples was adjusted to 1 million cells/ml in 1x DPBS containing 0.02% BSA.

Droplet based single cell RNA-seq and scRNA seq data analysis

Single cell suspensions were analyzed with the droplet based single cell RNA-seq method proposed by 10x Genomics using the protocol previously described[11]. Raw sequencing data were processed using the CellRanger pipeline (version 3.1.0, 6.0.0 or 7.1.0). Count matrices were analyzed using the Seurat package V5.0.1[19]. For each sample, SoupX[20] was used to remove contamination by ambient RNA and quality controls were

performed. The objects from individual patients were annotated using ScArches[21] and the Human Lung Cell Atlas as a reference[22] using a transfer learning method: the ScArches algorithm was trained on the Human Lung Cell Atlas, and the model was then applied to each of our sample individually. Correct annotation of cell populations was verified using the expression of well-known markers. As samples from the different patients presented batch effect when merged, we then integrated the Seurat objects of the different patients using the Seurat method (fig. 1b). In order to do that, we first merge all the samples together. The SCTransform function was run on the merged object, with the variables to regress set as the cell cycle score and the percentage of mitochondrial genes. Then the samples from different patients were separated and normalized individually. The 2000 most variable features were calculated and used to set anchors for integration. Finally, the different patient objects were integrated, and the resulting object was scaled.

Different tools and packages were used for the analysis. We used the UMAP method to visualize the data[23]. In order to perform the differentially expressed genes analysis (DEG), we used the MAST method[24] to compare two populations, with an adjusted p-value threshold of 0.05, and a logFC threshold of 0.1. Then the upregulated pathways were identified with GSEA and the WikiPathway database[25, 26]. The scoring of “tip” and “stalk” was computed with the AddModuleScore function from Seurat. The comparison between the scores was performed with a wilcox test, with a p-value threshold of 0.05. The intercellular interactions analysis was done with CellPhoneDB V5.0.0[27].

Results

The response of human lung to radiation is characterized by activation of pro-angiogenic pathways in several cell compartments.

Although most of the dose of irradiation is received by the tumor volume, the surrounding tissue is exposed to doses higher than 45 Gy. Thoracic radiotherapy induces RILI, that impinges cancer treatment possibilities and may evolve towards RIPF, a life-threatening complication of radiotherapy. In order to gain a better understanding of these radio-induced toxicities, we analyzed the response of non-tumoral lung to radiotherapy, by comparing, from the same patient, the transcriptional changes, at the single cell level, from lung tissue resected in the vicinity of the tumor with healthy tissue sampled from a non-irradiated distal part of the lung (**Fig 1a**). We used single cell RNA sequencing technology to determine the impact of irradiation to the different lung cell populations. Differential expression analysis between irradiated (IR) and non-irradiated (NI) areas identified genes upregulated in the lung exposed to high doses of radiotherapy (**Fig 1c**), in particular in immune cells (500 to 3.300 overexpressed genes), endothelial cells (EC) (1.500 genes) and type II epithelial (AT2) cells (2.800 genes). Strikingly, the most frequently upregulated pathway across the different cell populations was VEGFA-VEGFR2 signaling, known to be part of the vascular repair/regeneration pathway as well as the classic angiogenesis process[15]. Considering the fact that endothelial cells are a particularly radio-sensitive population[28], it is tempting to speculate that radiation activates the VEGFA-VEGFR2 signaling pathway to enhance vascular repair after radiation injury.

Indeed, blood vessels, in particular capillaries, are crucial for lung function, specifically the gas exchanges that take place in alveoli. To further dissect pro-angiogenic signaling in human lung, we looked in different cell compartments at the level of expression of major ligands (i.e. VEGFA and VEGFB) and their cognate receptors (i.e. FLT1/VEGFR1 and KDR/VEGFR2), in order to identify the sources and targets of this signaling. In the NI area, epithelial cells (mostly AT1), endothelial cells (EC), interstitial macrophages (IM) and mastocytes appeared as the main sources of VEGFA, while alveolar macrophages (AM), smooth muscle cells (SMC) and dendritic cells (DC) appeared to be the main sources of VEGFB (**fig. 2a**). Upon irradiation, the percentages of cells expressing VEGFA gene increased in AT1, IM, fibroblasts and SMC, while for VEGFB, the most important increases were seen in AM, B cells, fibroblasts and AT1 cells (**fig. 2b**). The expression of receptors KDR/VEGFR2 and FLT1/VEGFR1 was largely prevalent in the different types of ECs (**fig. 2c**), and their expression increased upon irradiation, especially in aCap (aerocytes) and gCap (general capillary cells) for KDR/VEGFR2 and in aCap and arterial ECs for FLT1/VEGFR1 (**fig. 2d**). A low percentage of dendritic cells, neutrophils and AM was also expressing FLT1/VEGFR1 and this percentage increased upon irradiation (**fig. 2c-d**). This observation is interesting, since a FLT1+ AM population has been shown to play an important role in some processes during angiogenesis[29]. Together, these results point to a stimulation of the pro-angiogenic signaling that target both lung capillary EC subsets, aCap and gCap. As the gCap have been described as the progenitor population of the endothelial capillary cells compartment[30], we focused subsequent analysis on this cell type.

Lung gCap ECs display gene expression patterns compatible with a tip phenotype.

To better apprehend the consequences of an increase in pro-angiogenic signaling pathway in response to radiotherapy, we further focused our analyses on the different subsets of EC (**Fig. 3a**) (**supplementary fig. 3a**). Since the expressions of either KDR/VEGFR2 or FLT1/VEGFR1 have been shown to be characteristic of two cell states involved in angiogenesis (tip and stalk cells, respectively), we defined two different scores, “tip” and “stalk”, using multiple markers described to be associated with either of these states[31]. The most characteristic marker of the tip cells is Kdr/Vegfr2, and, for the stalk cells, the Flt1/Vegfr1 receptor as well as Ackr1 receptor. However, the distinction of these cell states is subtle and the expression of all markers needs to be taken into account. Based on this analysis, we found a significant increase of the tip score in gCap cells, concomitantly to a significant decrease of the stalk score, in peri-tumoral lung regions exposed to radiotherapy, when compared to non-irradiated areas resected at distance of the Pancoast tumor. These results suggest that irradiated gCap cells respond to the increase in pro-angiogenic signaling by acquiring “tip”-like characteristics. To characterize the transcriptional state of tip cells in the lung after radiotherapy, we compared the transcriptional profiles of gCap cells KDR/VEGFR2 positive versus KDR/VEGFR2 negative. Interestingly, several genes associated with cell motility were upregulated in KDR/VEGFR2 positive tip cells (**fig. 3c**). Furthermore, there is in the IR area a correlation of expression of several motility related genes with the expression of KDR/VEGFR2. For instance, CAV1 promotes EC polarization and movement[32] and ROBO4 is involved in filopodia formation in EC[33] (**supplementary fig. 1a**). Together, these results support the idea that in response to radiation, lung gCap cells present “tip”-like phenotype that may play an active role in vascular repair process.

Alveolar macrophages (AM) present a pro-angiogenic signature in response to radiation.

When looking at the expression of angiogenic factors in the different cell populations, we identified a FLT1-positive population amongst resident macrophages. FLT1-positive macrophages have been shown to be crucial for efficient angiogenesis in the lungs[29]. It has been shown that the expression of FLT1/VEGFR1 by circulating monocytes is sufficient to attract them to sites of VEGFA expression and thus stimulate their migration in hypoxic tissue[29, 34]. Therefore, we investigated the presence of this population in human lungs after radiotherapy. Analysis of the dataset revealed an increase of FLT1/VEGFR1 expression specifically in alveolar macrophages (AM) in response to radiation (**fig. 4a-b**). Because FLT1-positive alveolar macrophages have been described to be recruited from circulating monocytes, we next examined the expression level of ITGAM, a specific marker of recruited AM [35]. This marker is expressed by most of the FLT1-positive AM macrophages (**supplementary fig. 2a**), suggesting that radiotherapy enhances the recruitment of monocytes-derived alveolar macrophages from the circulation. Since such macrophages are thought to interact with ECs and support angiogenesis [29, 36], we perform a cell-cell interaction analysis to identify potential signals received by gCap cells presenting a tip-like phenotype. This analysis revealed a potential IL-1b-mediated interaction between the FLT1-positive alveolar macrophages and

gCap cells. Indeed, we observed a significant increase of IL-1b expression after radiotherapy amongst the FLT1-positive AM, but not in the FLT1-negative AM (fig. 4c).

Sc RNA-seq analyses in a mouse model of RIFP reveal similar pro-angiogenic responses triggered by radiation.

Using previously published lung cell atlas after radiation injury [11], we aimed to characterize such vascular phenotypes dynamically in mouse lung. In this dataset, samples were analyzed every month after either a single fibrogenic (17Gy) or non-fibrogenic (10Gy) dose of radiation delivered to the whole thorax of the mice. After subsetting the endothelial cell populations[30] (fig. 5a), we identified in the mouse the same subpopulations identified in patients (supplementary fig. 3). In addition, in the mouse dataset, a subpopulation, characterized by high *Serpine2* expression, was found in lungs with strong fibrosis, 5 months after exposure to a fibrogenic dose of radiation. The proportion of KDR/VEGFR2 positive gCap cells increased from two months after irradiation (fig. 5b). Furthermore, this proportion decreased four months post 10Gy irradiation, while it kept increasing until five months post 17Gy irradiation. Concomitantly, irradiation with a dose of 10Gy triggered an increase of the stalk score at three months before returning to baseline at five months post irradiation. On the contrary, after a 17Gy irradiation, the stalk score increased progressively from three to five months post irradiation (fig. 5c).

In human, radiotherapy induced the expression of genes related to motility in KDR/VEGFR2 positive gCap cells, in agreement with their tip-like phenotype. To determine if radiation also triggered the expression of motility genes, we analyzed their expression in the mouse lung dataset. The comparison of gCap KDR-positive versus KDR-negative cells from 10Gy irradiated samples showed the upregulation of 31 motility-related genes, while the cells from 17Gy irradiated samples showed only 26 motility-related genes upregulated, like *Rab11a* [37] or *Cd34* [38]. These results confirm that radiation stimulates the expression of motility genes in gCap cells presenting a tip-like phenotype.

Discussion

Radiotherapy triggers microvasculature damage to the healthy tissues[39], and a functioning vasculature is crucial for the proper function of the lungs. This study aimed at investigating the effects of radiotherapy on human lung vasculature, particularly capillaries, at the single cell level. VEGF signaling is one of the canonical pathway implicated in angiogenesis through VEGFA-KDR interaction[40] and VEGFA-FLT1 and VEGFB-FLT1 interactions[34]. Our single cell RNAseq analysis from lungs resected from patients showed that radiotherapy increased VEGFA/B expression in multiple populations and this pro-angiogenic signal is mainly received by endothelial cells. Furthermore, we identified a subset of lung gCap (i.e. general capillaries) cells that expressed KDR/VEGFR2 and present a transcriptional profile similar to the tip cells, described as the leading endothelial phenotype during angiogenic sprouting[31]. In addition, the proportion of alveolar macrophages expressing FLT1 raised after radiotherapy. Cell-Cell Interaction (CCI) analysis predicted this subset of alveolar macrophages interact with the gCap cells, suggesting their implication in the response of lung vasculature to radiotherapy.

After radiotherapy, a high proportion of endothelial cells express FLT1/VEGFR1 but the functions of this receptor are complex. Indeed, FLT1/VEGFR1 has a ten times higher affinity for VEGFA than KDR/VEGFR2, but its kinase activity is ten times lower[41]. Therefore, it has been proposed that FLT1/VEGFR1 acts as a negative regulator of angiogenesis by trapping the VEGFA ligand[34]. However, *Flt1/Vegfr1* deficient mice present defects in the sprouting of new vessels [42], indicating that *Flt1/Vegfr1* is required for proper angiogenesis. These results suggest that the upregulation of FLT1/VEGFR1 in lung vasculature contributes to angiogenic response that occurs after radiotherapy.

The gCap have been shown to be capillary progenitor cells that are able to regenerate lung capillaries during homeostasis and after injury[30]. Our single cell RNAseq analysis indicated that the proportion of gCap cells expressing KDR/VEGFR2 is increased after radiotherapy. KDR/VEGFR2 has been identified as a marker of tip cells, an endothelial phenotype characterized by its sprouting[31]. Tip cells occupy a leading position in the new vessel formation and are followed by the stalk cells that divide to form the walls of the new vessel[16]. To explore the environment, the tip cells present a high number of filipodia and are able to migrate towards VEGFA gradient. In the tip cells, VEGFA signaling triggers the expression of several genes including DLL4. DLL4 then acts as a ligand for the NOTCH1 receptor expressed by the adjacent endothelial cells. Activation of the Notch pathway in these neighboring cells shifts their transcriptional profile towards a stalk phenotype, activating VEGF receptors expression, forming a VEGF-VEGFR-DLL4-NOTCH-VEGFR feedback loop[17, 31]. In line with this model of angiogenesis, our results suggest that radiotherapy upregulates the expression of VEGFA and that a subset of gCap cells, expressing its cognate receptor (i.e. KDR/VEGFR2), responding to this pro-angiogenic signal, differentiate into tip cells to promote the sprouting of new vessels.

Finally, we identified, in human lung, a population of alveolar macrophages that have been described to be crucial for angiogenesis[29]. After radiotherapy, this particular population may play an important role in the wound healing and repair processes. This subset of macrophages express FLT1/VEGFR1 receptor and are then able to capture VEGFA pro-angiogenic signaling. Interestingly, these macrophages express IL-1, a critical cytokine for angiogenesis. Indeed, it has been shown that supernatant of LPS-treated macrophages is sufficient to stimulate angiogenesis in Matrigel plug injected into mouse interscapular region [43]. The authors also demonstrated that inactivation of IL-1b with IL-1b blocking antibodies is enough to impair this angiogenesis in this model. Altogether, this suggests that radiotherapy increases, in human lung, the proportion of a subset of pro-angiogenic alveolar macrophages FLT1/VEGFR1 positive that secrete IL-1b and contribute to angiogenic responses post-radiotherapy.

Overall, we expect this work will contribute to advance our knowledges of lung responses to radiotherapy, especially its impact on vessels and capillaries. The deciphering of these mechanisms participates into the effort to gain a comprehensive understanding of the events involved in radiation induced lung injury and could contribute to the discovery of new therapeutic options to fight this side effect of radiotherapy.

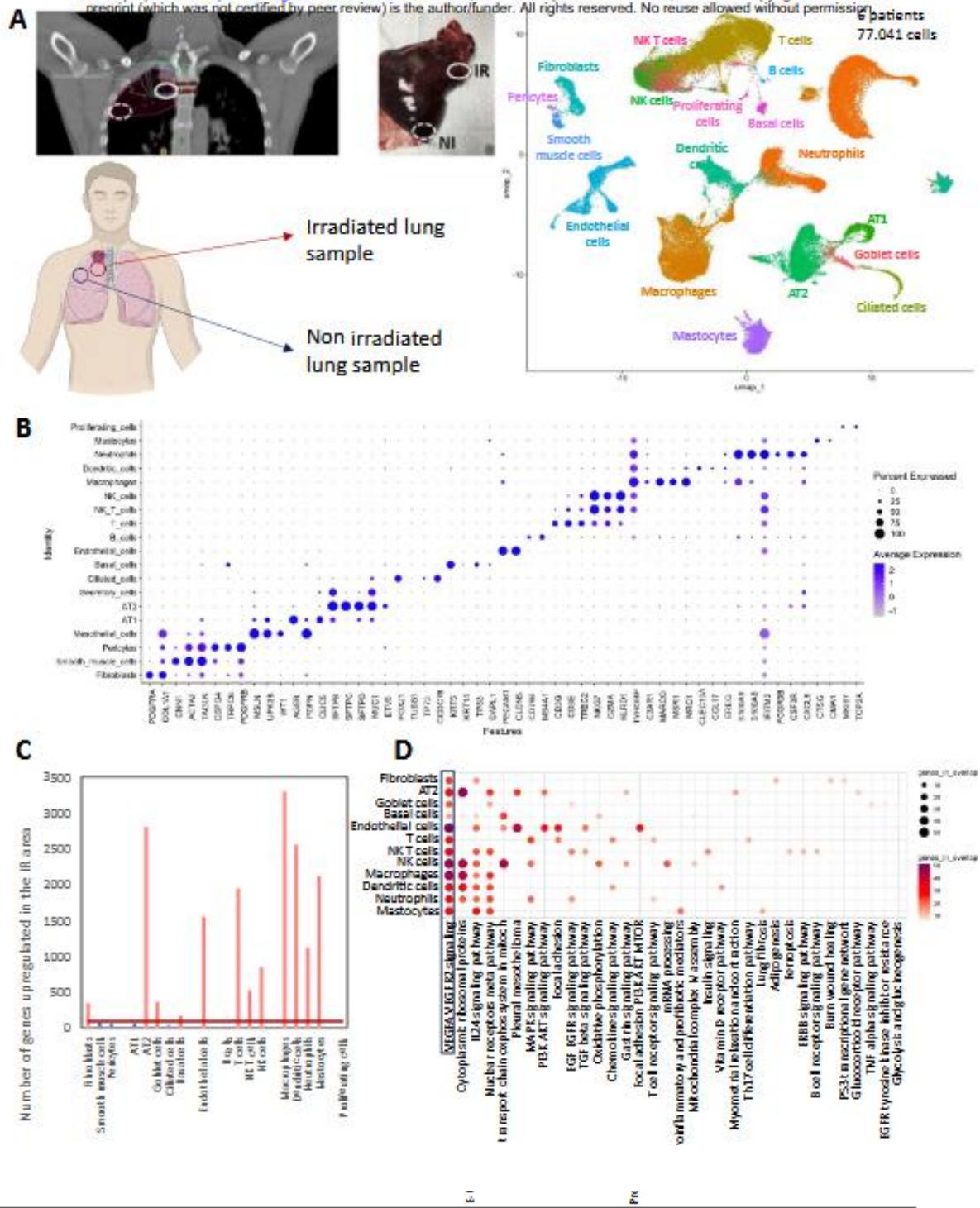


Figure 1. Angiogenesis signaling is upregulated in the irradiated human lung

A: dosimetric CT-scan of a patient who received radiation therapy at Institut Curie and surgery at IMM following a Pancoast tumor, surgical sample (6-8 weeks post radiotherapy), schematic representation of the location of the irradiated and non-irradiated non-tumoral samples from the Pancoast patients and UMAP visualization of 77.048 cells from six patients with 33.328 cells from the NI samples and 43.720 cells from the IR samples, annotated by cell type; **B:** DotPlot of the expression of characteristic markers of the different lung populations; **C:** number of genes significantly upregulated in the irradiated area of the lung compared to the non-irradiated in the different lung populations, the red line is placed at 100 pathways upregulated and the bars in blue represent the cell populations with less than 100 genes upregulated in the irradiated area; **D:** results of the gene set enrichment analysis of the upregulated genes in the IR area compared to the NI area for the cell populations presenting more than 100 genes upregulated. The pathways are from the WikiPathways database.

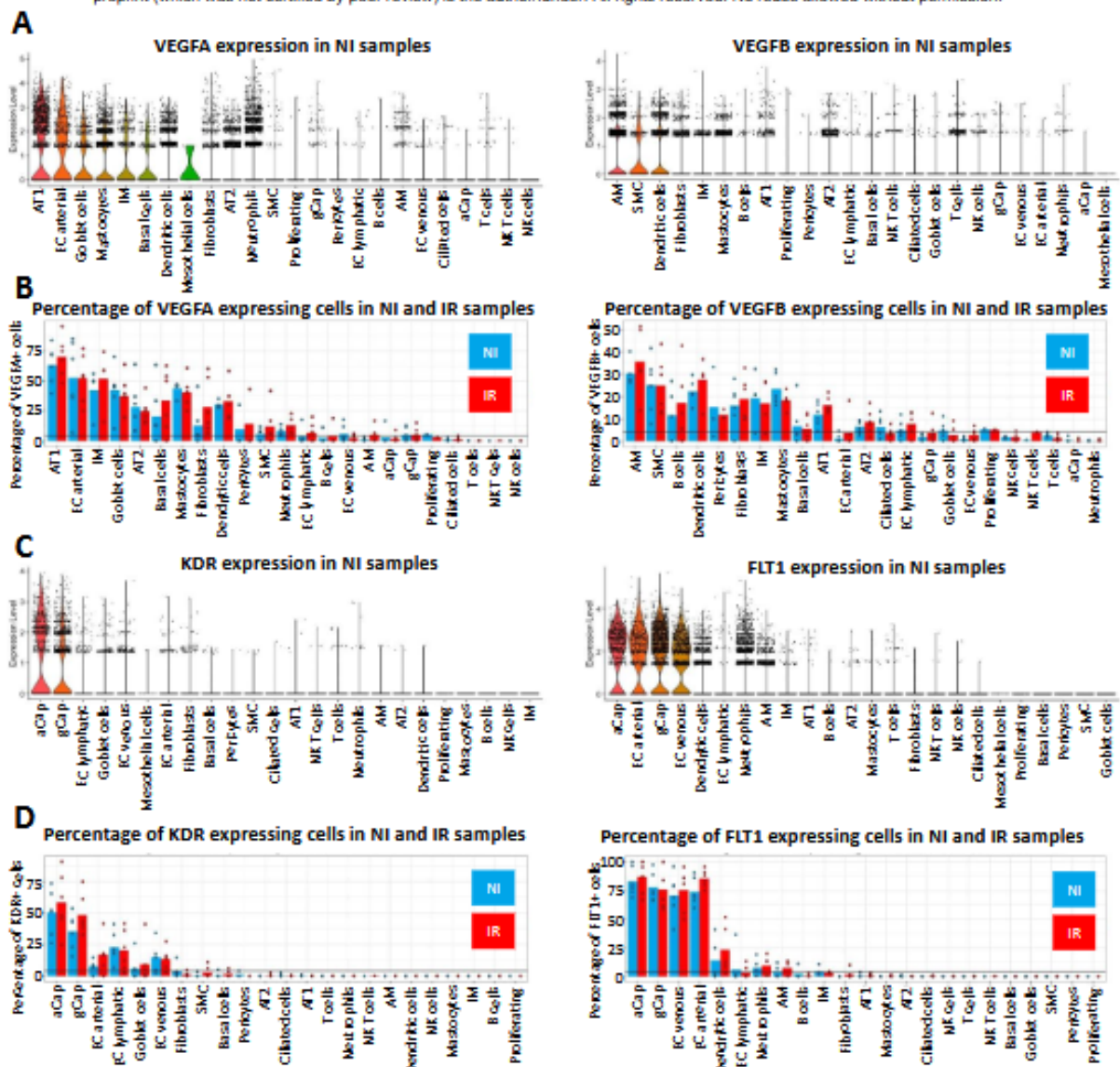


Figure 2. Angiogenic ligands and receptors show an increased expression after irradiation in different cell types.

A: violin plots of VEGFA (left panel) and VEGFB (right panel) expression in the non-irradiated area in the different lung populations, sorted by intensity of expression; B: percentage of cells expressing VEGFA (left panel) or VEGFB (right panel) in the irradiated or non-irradiated area, with each dot representing a patient; C: violin plots of KDR (left panel) and FLT1 (right panel) expression in the non-irradiated area in the different lung populations, sorted by intensity of expression; D: percentage of cells expressing KDR (left panel) or FLT1 (right panel) in the irradiated or non-irradiated area, with each dot representing a patient.

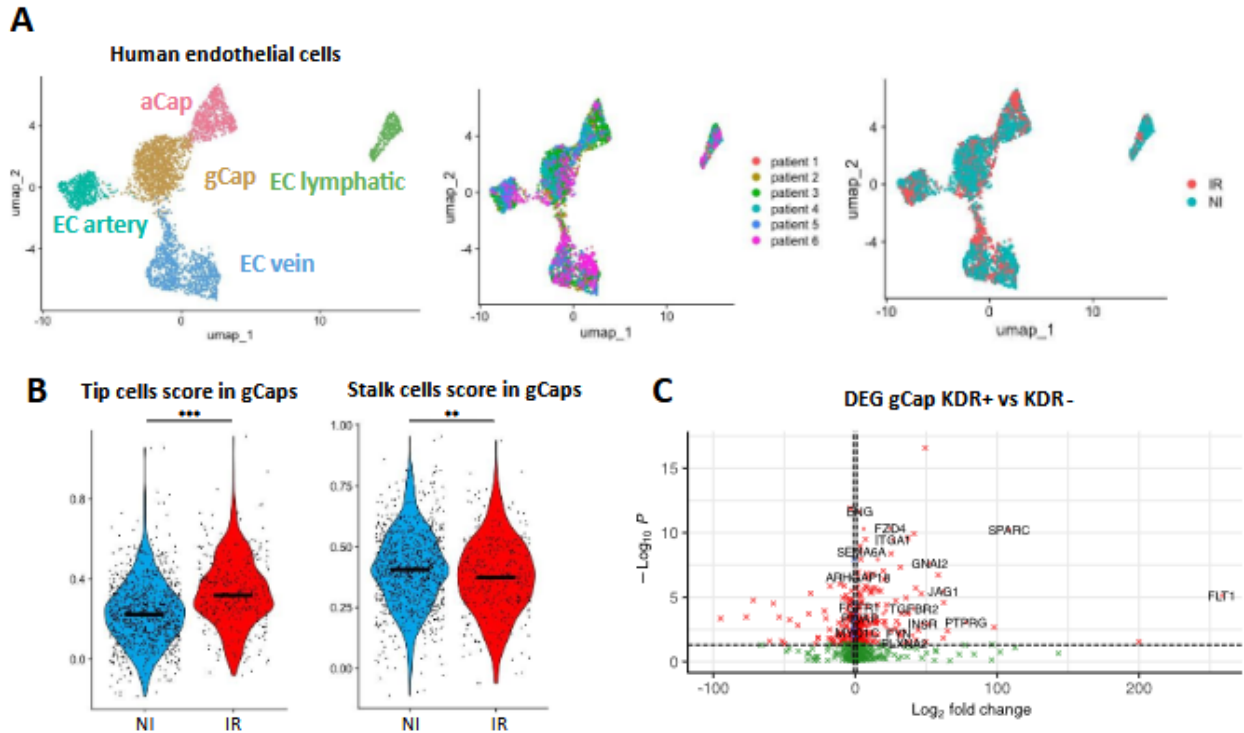


Figure 3. Irradiation induces pro-angiogenesis processes in gCap cells.

A: UMAP visualization of 3.648 cells from the different endothelial cell subpopulations annotated by sub cell type, by the patient of origin and by the area (irradiated or non-irradiated) of origin; B: violin plot of the stalk and tip cells scores calculated with the AddModuleScore function, based on the list of markers for these two cell states[31], the black line represents the median; C: volcano plot representation of the DEG analysis of gCap KDR positive versus the gCap KDR negative cells (i.e. genes overexpressed in the gCap KDR positive have a positive fold change). The genes named, and the genes identified with a dot are the genes related to cell motility (from the GOPB cell motility human gene list).

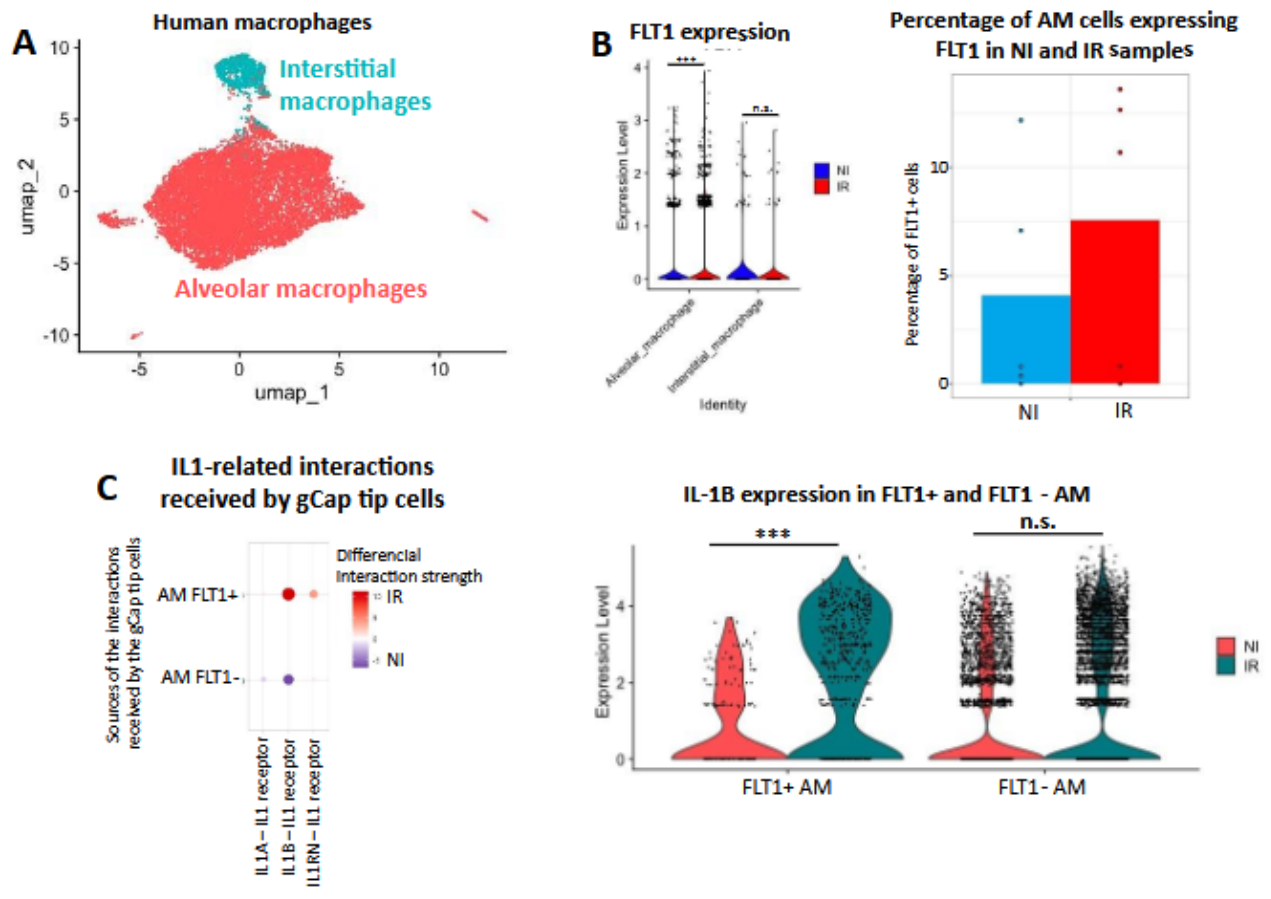


Figure 4. Alveolar macrophages receive and send VEGF signaling after irradiation

A: UMAP visualization of 14.168 cells from the different macrophage subpopulations annotated by sub cell type (4.159 cells from the NI area and 7.009 from the IR area); B: violin plots of FLT1 expression in the non-irradiated and irradiated area in the interstitial and alveolar macrophages and percentage of FLT1 positive alveolar macrophages in non-irradiated and irradiated area, each dot representing a patient; C: DotPlot of the IL-1 related intercellular interactions received by the gCap tip cells and sent by the alveolar macrophages FLT1 positive or negative and violin plots of IL-1 alpha expression in the non-irradiated and irradiated area in the FLT1 positive or FLT1 negative alveolar macrophages.

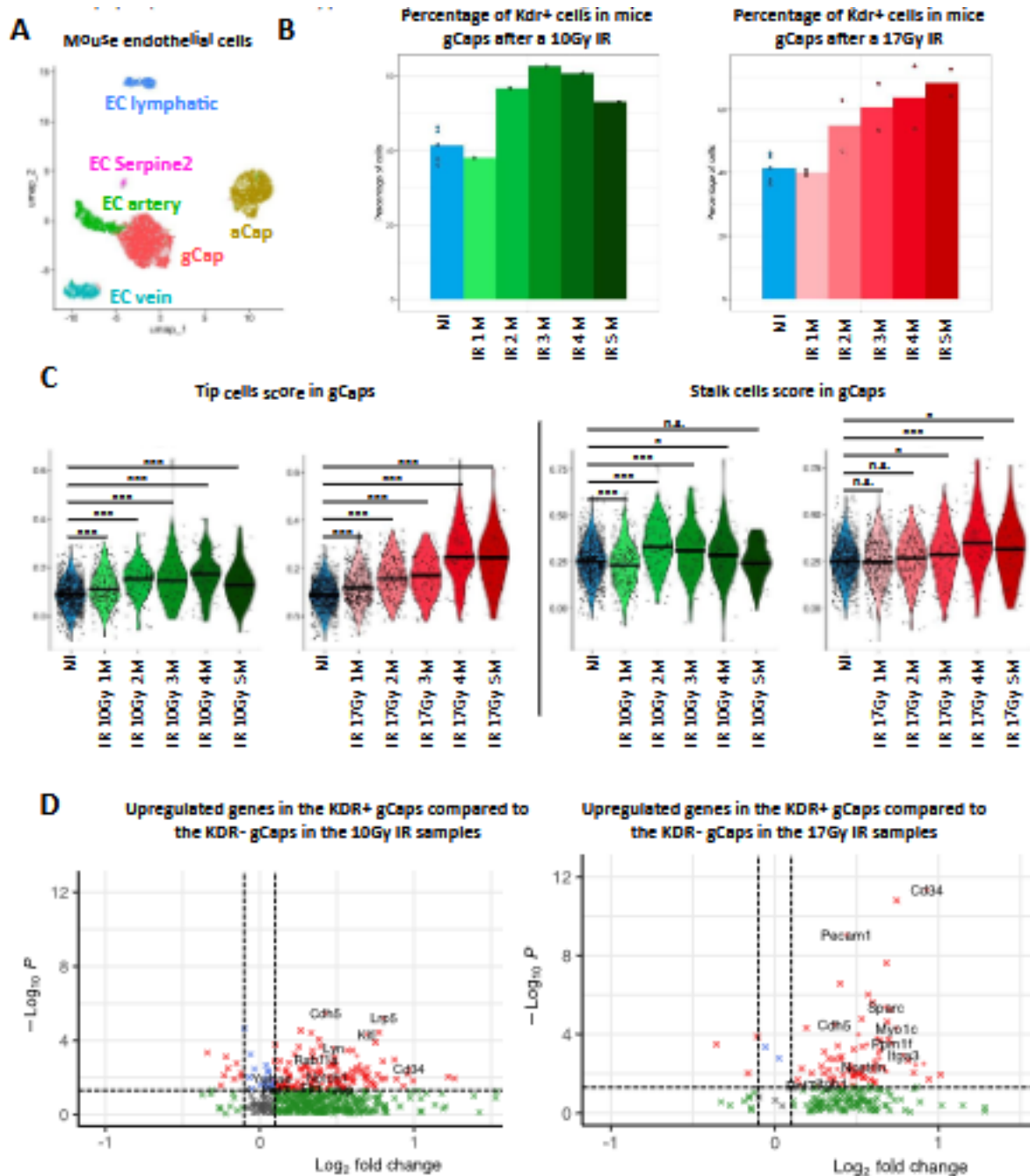
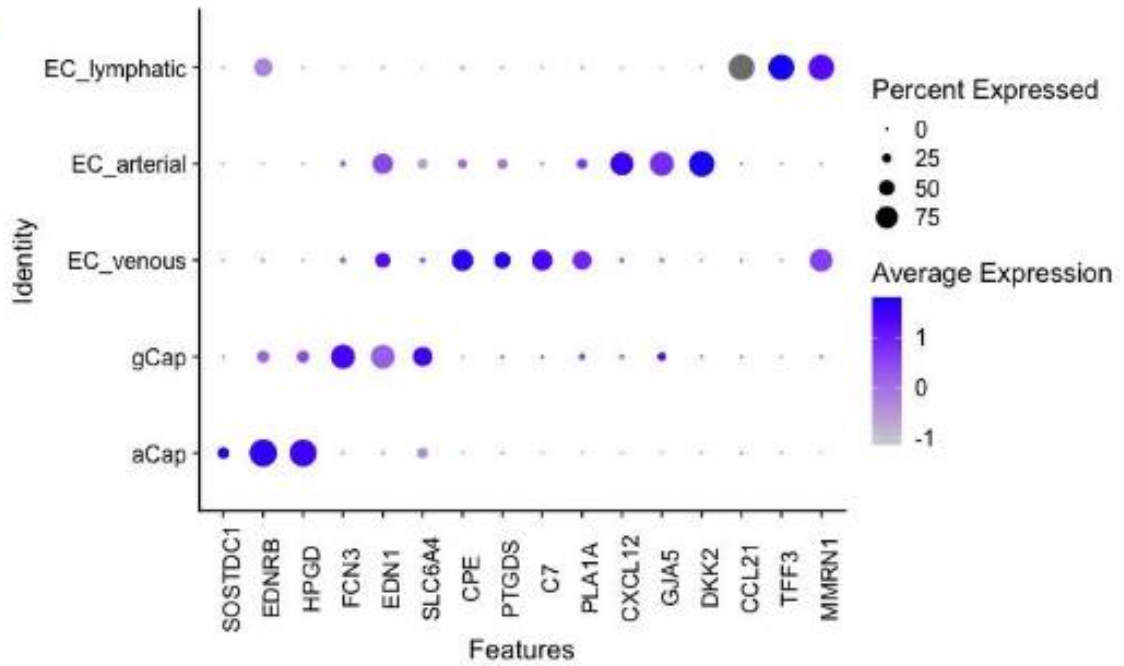
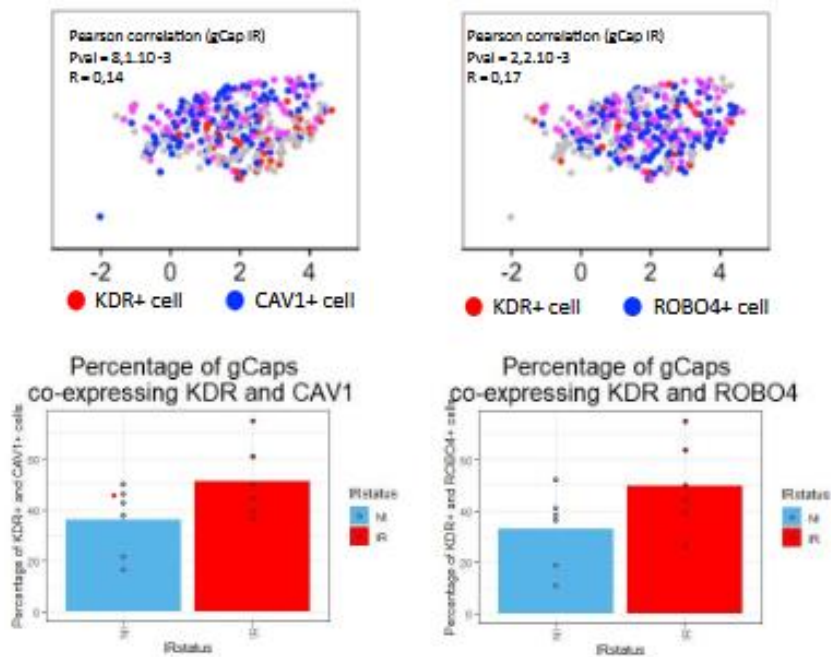
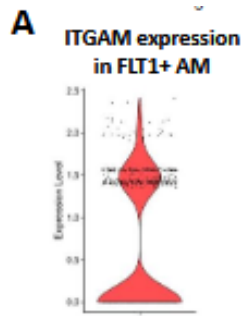


Figure 5. Angiogenesis processes evolve during the months post irradiation in mouse lungs

A: UMAP visualization of 4,958 cells from the different mouse endothelial cell subpopulations annotated by sub cell type; B: proportion KDR+ cells among the gCap cells, in the control mice or after a 10Gy or 17Gy irradiation; C: violin plot of the stalk and tip cells scores calculated based on the list of markers for these two cell states, the black line representing the median; D: volcano plot representation of the DEG analysis of the gCap KDR positive versus the gCap KDR negative cells (i.e. genes overexpressed in the gCap KDR positive cells have a positive fold change) in the 10Gy irradiated gCap cells (left panel) or the 17Gy irradiated gCap cells (right panel). The genes named are the genes related to cell motility (from the GOPB cell motility mouse gene list).

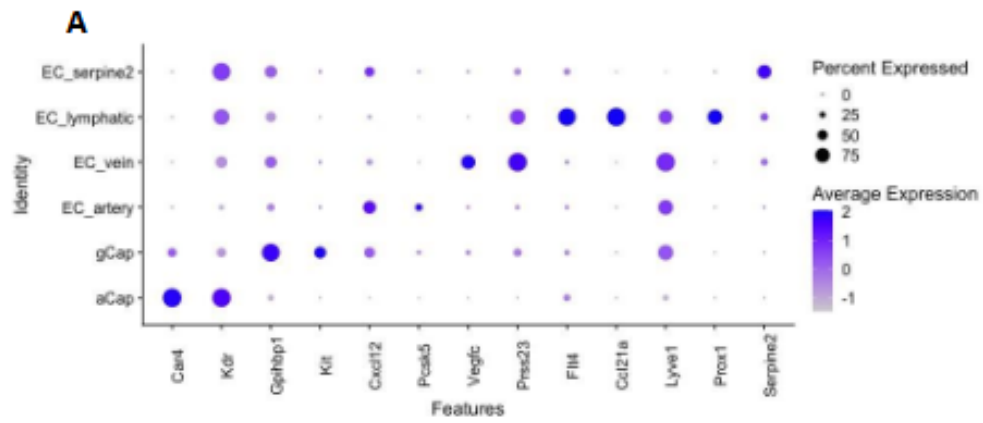
A**B****Supplementary Figure 1**

A: DotPlot of the expression of characteristic markers of the different endothelial cell sub populations in human; B: FeaturePlot representing the coexpression of KDR and CAV1 (left panel) or ROBO4 (right panel) in the gCap irradiated cells. Pink cells are coexpressing the genes and percentage of cells co-expressing KDR and CAV1 (left panel) or ROBO4 (right panel) in the non-irradiated or irradiated areas. The correlation and significance is calculated with a pearson test.



Supplementary Figure 2

A: violin plot of ITGAM expression in the FLT1 positive alveolar macrophages.



Supplementary Figure 3

A: DotPlot of the expression of characteristic markers of the different endothelial cell sub populations in mice.

Bibliography

- 1 GBD 2017 Disease and Injury Incidence and Prevalence Collaborators. Global, regional, and national incidence, prevalence, and years lived with disability for 354 diseases and injuries for 195 countries and territories, 1990–2017: a systematic analysis for the Global Burden of Disease Study 2017. *Lancet Lond Engl* 2018; 392: 1789–1858.
- 2 Giuranno L, Ient J, De Ruysscher D, *et al*. Radiation-Induced Lung Injury (RILI). *Front Oncol* [Internet] 2019 [cited 2024 Feb 27]; 9. Available from: <https://www.frontiersin.org/journals/oncology/articles/10.3389/fonc.2019.00877>.
- 3 Wei J, Wang B, Wang H, *et al*. Radiation-Induced Normal Tissue Damage: Oxidative Stress and Epigenetic Mechanisms. *Oxid Med Cell Longev Hindawi*; 2019; 2019: e3010342.
- 4 Zhao W, Robbins MEC. Inflammation and Chronic Oxidative Stress in Radiation-Induced Late Normal Tissue Injury: Therapeutic Implications. *Curr Med Chem* 2009; 16: 130–143.
- 5 Ding N-H, Jian Li J, Sun L-Q. Molecular Mechanisms and Treatment of Radiation-Induced Lung Fibrosis. *Curr Drug Targets* 2013; 14: 1347–1356.
- 6 Jarzebska N, Karetnikova ES, Markov AG, *et al*. Scarred Lung. An Update on Radiation-Induced Pulmonary Fibrosis. *Front Med* [Internet] Frontiers; 2021 [cited 2024 Apr 12]; 7. Available from: <https://www.frontiersin.org/articles/10.3389/fmed.2020.585756>.
- 7 Venkatesulu BP, Mahadevan LS, Aliru ML, *et al*. Radiation-Induced Endothelial Vascular Injury. *JACC Basic Transl Sci* American College of Cardiology Foundation; 2018; 3: 563–572.
- 8 Arroyo-Hernández M, Maldonado F, Lozano-Ruiz F, *et al*. Radiation-induced lung injury: current evidence. *BMC Pulm Med* 2021; 21: 9.
- 9 Chen Z, Wu Z, Ning W. Advances in Molecular Mechanisms and Treatment of Radiation-Induced Pulmonary Fibrosis. *Transl Oncol* 2019; 12: 162–169.
- 10 Wirsdörfer F, Jendrossek V. Modeling DNA damage-induced pneumopathy in mice: insight from danger signaling cascades. *Radiat Oncol* 2017; 12: 142.
- 11 Curras-Alonso S, Soulier J, Defard T, *et al*. An interactive murine single-cell atlas of the lung responses to radiation injury. *Nat Commun* Nature Publishing Group; 2023; 14: 2445.
- 12 PANCOAST HK. IMPORTANCE OF CAREFUL ROENTGEN-RAY INVESTIGATIONS OF APICAL CHEST TUMORS. *J Am Med Assoc* 1924; 83: 1407–1411.
- 13 Panagopoulos N, Leivaditis V, Koletsis E, *et al*. Pancoast tumors: characteristics and preoperative assessment. *J Thorac Dis* 2014; 6: S108–S115.

- 14 Kwong KF, Edelman MJ, Suntharalingam M, *et al.* High-dose radiotherapy in trimodality treatment of Pancoast tumors results in high pathologic complete response rates and excellent long-term survival. *J Thorac Cardiovasc Surg* 2005; 129: 1250–1257.
- 15 Abhinand CS, Raju R, Soumya SJ, *et al.* VEGF-A/VEGFR2 signaling network in endothelial cells relevant to angiogenesis. *J Cell Commun Signal* 2016; 10: 347–354.
- 16 Jakobsson L, Franco CA, Bentley K, *et al.* Endothelial cells dynamically compete for the tip cell position during angiogenic sprouting. *Nat Cell Biol* Nature Publishing Group; 2010; 12: 943–953.
- 17 Pasut A, Becker LM, Cuypers A, *et al.* Endothelial cell plasticity at the single-cell level. *Angiogenesis* 2021; 24: 311–326.
- 18 Hellström M, Phng L-K, Gerhardt H. VEGF and Notch Signaling. *Cell Adhes Migr* 2007; 1: 133–136.
- 19 Hao Y, Stuart T, Kowalski MH, *et al.* Dictionary learning for integrative, multimodal and scalable single-cell analysis. *Nat Biotechnol* Nature Publishing Group; 2024; 42: 293–304.
- 20 Young MD, Behjati S. SoupX removes ambient RNA contamination from droplet-based single-cell RNA sequencing data. *GigaScience* 2020; 9: g1aa151.
- 21 Lotfollahi M, Naghipourfar M, Luecken MD, *et al.* Mapping single-cell data to reference atlases by transfer learning. *Nat Biotechnol* Nature Publishing Group; 2022; 40: 121–130.
- 22 Sikkema L, Ramírez-Suástegui C, Strobl DC, *et al.* An integrated cell atlas of the lung in health and disease. *Nat Med* Nature Publishing Group; 2023; 29: 1563–1577.
- 23 McInnes L, Healy J, Melville J. UMAP: Uniform Manifold Approximation and Projection for Dimension Reduction [Internet]. arXiv; 2020 [cited 2024 Apr 13]. Available from: <http://arxiv.org/abs/1802.03426>.
- 24 Finak G, McDavid A, Yajima M, *et al.* MAST: a flexible statistical framework for assessing transcriptional changes and characterizing heterogeneity in single-cell RNA sequencing data. *Genome Biol* 2015; 16: 278.
- 25 Subramanian A, Tamayo P, Mootha VK, *et al.* Gene set enrichment analysis: A knowledge-based approach for interpreting genome-wide expression profiles. *Proc Natl Acad Sci* Proceedings of the National Academy of Sciences; 2005; 102: 15545–15550.
- 26 Mootha VK, Lindgren CM, Eriksson K-F, *et al.* PGC-1 α -responsive genes involved in oxidative phosphorylation are coordinately downregulated in human diabetes. *Nat Genet* Nature Publishing Group; 2003; 34: 267–273.
- 27 Troulé K, Petryszak R, Prete M, *et al.* CellPhoneDB v5: inferring cell-cell communication from single-cell multiomics data [Internet]. arXiv; 2023 [cited 2024 Mar 29]. Available from: <http://arxiv.org/abs/2311.04567>.

- 28 Langley RE, Bump EA, Quartuccio SG, *et al.* Radiation-induced apoptosis in microvascular endothelial cells. *Br J Cancer* Nature Publishing Group; 1997; 75: 666–672.
- 29 Murakami M, Zheng Y, Hirashima M, *et al.* VEGFR1 Tyrosine Kinase Signaling Promotes Lymphangiogenesis as Well as Angiogenesis Indirectly via Macrophage Recruitment. *Arterioscler Thromb Vasc Biol* American Heart Association; 2008; 28: 658–664.
- 30 Gillich A, Zhang F, Farmer CG, *et al.* Capillary cell-type specialization in the alveolus. *Nature* Nature Publishing Group; 2020; 586: 785–789.
- 31 Chen W, Xia P, Wang H, *et al.* The endothelial tip-stalk cell selection and shuffling during angiogenesis. *J Cell Commun Signal* 2019; 13: 291–301.
- 32 Beardsley A, Fang K, Mertz H, *et al.* Loss of Caveolin-1 Polarity Impedes Endothelial Cell Polarization and Directional Movement *. *J Biol Chem* Elsevier; 2005; 280: 3541–3547.
- 33 Sheldon H, Andre M, Legg JA, *et al.* Active involvement of Robo1 and Robo4 in filopodia formation and endothelial cell motility mediated via WASP and other actin nucleation-promoting factors. *FASEB J* 2009; 23: 513–522.
- 34 Shibuya M. Vascular endothelial growth factor receptor-1 (VEGFR-1/Flt-1): a dual regulator for angiogenesis. *Angiogenesis* 2006; 9: 225–230.
- 35 Wohnhaas CT, Baßler K, Watson CK, *et al.* Monocyte-derived alveolar macrophages are key drivers of smoke-induced lung inflammation and tissue remodeling. *Front Immunol* [Internet] Frontiers; 2024 [cited 2024 Apr 12]; 15. Available from: <https://www.frontiersin.org/journals/immunology/articles/10.3389/fimmu.2024.1325090/full>.
- 36 Sekiguchi K, Ito Y, Hattori K, *et al.* VEGF Receptor 1-Expressing Macrophages Recruited from Bone Marrow Enhances Angiogenesis in Endometrial Tissues. *Sci Rep* Nature Publishing Group; 2019; 9: 7037.
- 37 Palmieri D, Bouadis A, Ronchetti R, *et al.* Rab11a Differentially Modulates Epidermal Growth Factor-induced Proliferation and Motility in Immortal Breast Cells. *Breast Cancer Res Treat* 2006; 100: 127–137.
- 38 Alfaro LAS, Dick SA, Siegel AL, *et al.* CD34 Promotes Satellite Cell Motility and Entry into Proliferation to Facilitate Efficient Skeletal Muscle Regeneration. *Stem Cells* 2011; 29: 2030–2041.
- 39 Kim JH, Jenrow KA, Brown SL. Mechanisms of radiation-induced normal tissue toxicity and implications for future clinical trials. *Radiat Oncol J* 2014; 32: 103–115.
- 40 Eldridge L, Wagner EM. Angiogenesis in the lung. *J Physiol* 2019; 597: 1023–1032.
- 41 Shibuya M. Vascular endothelial growth factor and its receptor system: physiological functions in angiogenesis and pathological roles in various diseases. *J Biochem (Tokyo)* 2013; 153: 13–19.
- 42 Kearney JB, Kappas NC, Ellerstrom C, *et al.* The VEGF receptor flt-1 (VEGFR-1) is a positive modulator of vascular sprout formation and branching morphogenesis. *Blood* 2004; 103: 4527–4535.
- 43 Carmi Y, Voronov E, Dotan S, *et al.* The Role of Macrophage-Derived IL-1 in Induction and Maintenance of Angiogenesis1. *J Immunol* 2009; 183: 4705–4714.

2. LIPID POLYUNSATURATED FATTY ACID CHAINS IN MOUSE KIDNEYS WERE INCREASED WITHIN 5 MIN OF A SINGLE HIGH DOSE WHOLE BODY IRRADIATION



Article

Lipid Polyunsaturated Fatty Acid Chains in Mouse Kidneys Were Increased within 5 min of a Single High Dose Whole Body Irradiation

Wenxin Li ^{1,†}, Chi Zhang ^{2,3,†}, Shuhei Aramaki ^{1,2,4,*}, Lili Xu ², Shogo Tsuge ², Takumi Sakamoto ², Md. Al Mamun ², Ariful Islam ², Takamitsu Hayakawa ⁵, Yusuke Takanashi ⁵, Maxime Dubail ⁶, Kenta Konishi ¹, Tomohito Sato ^{2,4}, Tomoaki Kahyo ^{2,4}, Charles Fouillade ⁶, Katsumasa Nakamura ^{1,†} and Mitsutoshi Setou ^{2,3,4,†}

¹ Department of Radiation Oncology, Hamamatsu University School of Medicine, Handayama 1-20-1, Higashi-ku, Hamamatsu 431-3192, Shizuoka, Japan; d20101@hama-med.ac.jp (W.L.)

² Department of Cellular and Molecular Anatomy, Hamamatsu University School of Medicine, 1-20-1 Handayama, Higashi-ku, Hamamatsu 431-3192, Shizuoka, Japan; zhangchi07.pegasus@gmail.com (C.Z.); setou@hama-med.ac.jp (M.S.)

³ Department of Systems Molecular Anatomy, Institute for Medical Photonics Research, Preeminent Medical Photonics Education & Research Center Hamamatsu, Hamamatsu 431-3192, Shizuoka, Japan

⁴ International Mass Imaging Center, Hamamatsu University School of Medicine, 1-20-1 Handayama, Higashi-ku, Hamamatsu 431-3192, Shizuoka, Japan

⁵ First Department of Surgery, Hamamatsu University School of Medicine, 1-20-1 Handayama, Higashi-ku, Hamamatsu 431-3192, Shizuoka, Japan

⁶ Institut Curie, Centre de Recherche, INSERM U612, 91405 Orsay, France

* Correspondence: aramaki@hama-med.ac.jp; Tel.: +81 0534 345 282

† These authors contributed equally to this work.

‡ These authors should be considered co-last authors.



Citation: Li, W.; Zhang, C.; Aramaki, S.; Xu, L.; Tsuge, S.; Sakamoto, T.; Mamun, M.A.; Islam, A.; Hayakawa, T.; Takanashi, Y.; et al. Lipid Polyunsaturated Fatty Acid Chains in Mouse Kidneys Were Increased within 5 min of a Single High Dose Whole Body Irradiation. *Int. J. Mol. Sci.* **2023**, *24*, 12439. <https://doi.org/10.3390/ijms241512439>

Academic Editors: Igor Mantshalo and Aneta A. Tyrtyshnaia

Received: 15 July 2023

Revised: 30 July 2023

Accepted: 3 August 2023

Published: 4 August 2023



Copyright: © 2023 by the authors. Licensee MDPI, Basel, Switzerland. This article is an open access article distributed under the terms and conditions of the Creative Commons Attribution (CC BY) license (<https://creativecommons.org/licenses/by/4.0/>).

Abstract: To understand the ultra-early reaction of normal organ lipids during irradiation, we investigated the response of lipids, including polyunsaturated fatty acid (PUFA) chains, which are particularly susceptible to damage by ROS, in mice's kidneys, lungs, brains, and livers within 5 min of single high-dose irradiation. In this study, we set up three groups of C56BL/6 male mice and conducted whole-body irradiation with 0 Gy, 10 Gy, and 20 Gy single doses. Kidney, lung, brain, and liver tissues were collected within 5 min of irradiation. PUFA-targeted and whole lipidomic analyses were conducted using liquid chromatography–tandem mass spectrometry (LC-MS/MS). The results showed that PUFA chains of kidney phosphatidylcholine (PC), phosphatidylethanolamine (PE), and triacylglycerol (TG) significantly increased within 5 min of 10 Gy and 20 Gy irradiation. The main components of increased PUFA chains in PC and PE were C18:2, C20:4, and C22:6, and in TG the main component was C18:2. The kidney lipidomes also showed significant changes from the perspective of lipid species, mainly dominated by an increase in PC, PE, TG, and signal lipids, while lipidomes of the lung, brain, and liver were slightly changed. Our results revealed that acute PUFA chains increase and other lipidomic changes in the kidney upon whole-body irradiation within 5 min of irradiation. The significantly increased lipids also showed a consistent preference for possessing PUFA chains. The lipidomic changes varied from organ to organ, which indicates that the response upon irradiation within a short time is tissue-specific.

Keywords: polyunsaturated fatty acid; lipidomic; high dose radiation; kidney

1. Introduction

Radiotherapy is a standard treatment modality for cancer patients, aiming to destroy tumor tissue while minimizing damage to surrounding healthy tissue [1]. Fractionated external beam radiation therapy, delivering 1.8–2.0 Gy per fraction over several weeks, is

commonly employed. However, with advances in clinical radiation oncology techniques, stereotactic body radiation therapy (SBRT) has become widely used in clinical practice (8–30 Gy per fraction) [2]. It has been the standard treatment for early-stage lung cancer, and more and more experience has been gained in the treatment of primary pancreatic, liver, kidney, prostate and breast cancers. SBRT is particularly suitable for the treatment of limited metastatic tumors, especially brain, lung, liver and spinal metastases [3]. Although the irradiation target of these techniques is focused as much as possible on the tumor area, some normal tissue remains in the high-dose area. According to general principles, the small number of large dose fractions is more effective at killing healthy cells than tumor cells [4]. Ionizing radiation exerts its effects by generating reactive oxygen species (ROS) through energy transfer to water molecules, resulting in oxidative stress and direct ionization of DNA. With the rapid advances in mass spectrometry, the identification and quantitative assessment of lipids have been facilitated [5,6], and the effect of ROS on lipids has been revealed. Lipids play vital roles in cellular membranes and various cellular processes, and studies have demonstrated that ionizing radiation can modulate lipid profiles in several types of cancer [7].

Polyunsaturated fatty acids (PUFAs), a component of lipids, are particularly vulnerable to ROS-induced damage due to their high degree of double bonds, which can lead to lipid peroxidation [8]. Studies have shown that ROS seize hydrogen atoms from polyunsaturated and monounsaturated fatty acids tens to tens of thousands of times faster than that of saturated fatty acids [9]. Lipid peroxidation has been implicated in mediating inflammatory reactions and triggering programmed cell death, such as ferroptosis [10–12]. Previous investigations have revealed a decrease in PUFA chains within 72 h of irradiation [13]. It has been reported that the PUFA chains of phospholipids are relatively reduced in comparison to prostate cancer and its surrounding tissues. [14] Moreover, recent studies have emphasized the significance of phospholipids containing long PUFA chains in regulating cellular survival, particularly in driving cells toward ferroptosis [15]. However, existing research has primarily focused on lipid changes in the days to weeks following irradiation, with very little known about the ultra-early lipid changes in vivo post-irradiation.

Considering the rapid metabolism of lipids, our study aimed to investigate early-stage lipid changes. Based on previous findings, we hypothesized that PUFA chains may exhibit a decreasing trend immediately after irradiation. To explore this hypothesis, we conducted a comprehensive analysis of PUFA-targeted whole lipidomics using liquid chromatography–tandem mass spectrometry (LC-MS/MS) on kidney, lung, brain, and liver tissues obtained from mice within five minutes of single high-dose whole-body irradiation.

2. Results

2.1. Within 5 min of Irradiation, the PUFA Chain of Kidney Lipids Significantly Increased

Within 5 min of irradiation, we observed a significant increase in PUFA chains in kidney PC, PE, and TG. The proportion of PUFA chains in kidney PC increased by 5.33% and 5.39% after 10 and 20 Gy irradiation, respectively. Concurrently, the proportion of MUFA chains in kidney PC decreased by 1.61% and 1.59% under 10 and 20 Gy irradiation, respectively. Additionally, the proportion of SFA chains in kidney PC decreased by 3.72% and 3.79% under 10 Gy and 20 Gy irradiation, respectively (Figure 1A). While there were no significant changes observed in the total amount of FA chains, total SFA chains, and total MUFA chains within 5 min of irradiation in PC, the total PUFA chains increased significantly by 49.41% ($p = 0.023$) after 10 Gy irradiation and by 41.39% ($p = 0.088$) after 20 Gy irradiation (Figure 1B) (Table S2).

Similarly, the proportion of PUFA chains in kidney PE increased by 2.36% and 2.58% after 10 and 20 Gy irradiation, respectively. Conversely, the proportion of MUFA chains in kidney PE decreased by 0.09% and 0.16% under 10 Gy and 20 Gy irradiation, while the proportion of SFA chains in kidney PE decreased by 2.27% and 2.42% (Figure 1C). In terms of quantitative analysis, the total amount of FA chains in PE increased by 63.50% after 10 Gy irradiation ($p = 0.027$). Specifically, the amounts of total SFA chains, total MUFA

chains, and total PUFA chains in PE increased by 54.67% ($p = 0.044$), 62.84% ($p = 0.028$), and 74.21% ($p = 0.017$), respectively. Following 20 Gy irradiation, the amounts of total SFA chains, total MUFA chains, and total PUFA chains increased by 50.68% ($p = 0.145$), 58.72% ($p = 0.088$), and 71.34% ($p = 0.055$), respectively (Figure 1D) (Table S2).

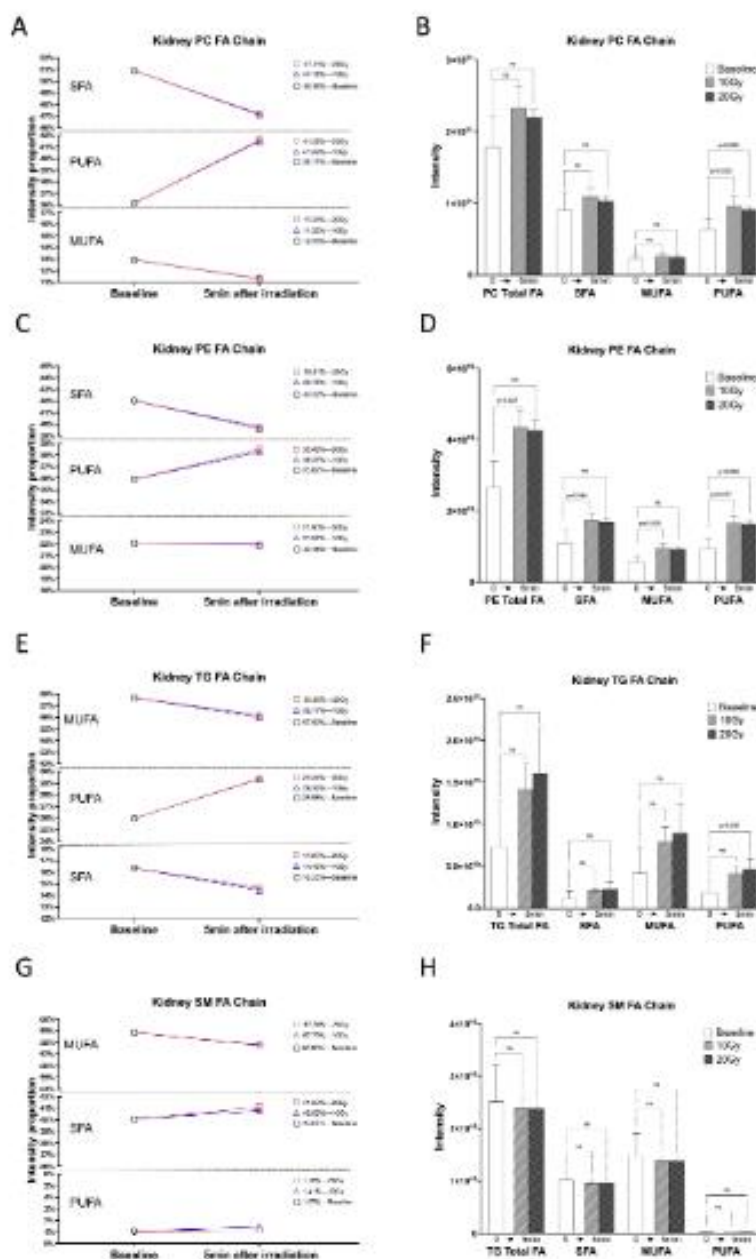


Figure 1. PUFA chains of kidney lipid increased within 5 min of 10 Gy and 20 Gy irradiation. (A,C,E,G) Proportional changes in SFA, MUFA, and PUFA chains intensities of kidney PC, PE, TG, and SM under 10 Gy and 20 Gy irradiation compared to 0 Gy. (B,D,F,H) Intensity histograms of total FA, SFA, MUFA, and PUFA chains in kidney PC, PE, TG, and SM under 0 Gy, 10 Gy, and 20 Gy irradiation. ns: no significant.

Regarding kidney TG, the proportion of PUFA chains increased by 3.41% and 3.38% after 10 and 20 Gy irradiation, respectively. Additionally, the proportion of MUFA chains in kidney TG decreased by 1.52% and 1.69%, and the proportion of SFA chains decreased by 1.89% and 1.69% under 10 Gy and 20 Gy irradiation, respectively (Figure 1E). Quantitatively, the total amount of FA chains, SFA chains, and MUFA chains did not exhibit significant changes. However, the total amount of PUFA chains increased significantly by 148.19% ($p = 0.031$) within 5 min of 20 Gy irradiation (Figure 1F).

We also examined the changes in FA chains in kidney sphingomyelin (SM) and found that the proportion of PUFA chains in kidney SM increased by 0.34% and 0.12% after 10 Gy and 20 Gy irradiation, respectively. The proportion of MUFA chains in kidney SM decreased by 1.07% and 1.1% under 10 Gy and 20 Gy irradiation, respectively. Moreover, the proportion of SFA chains in kidney TG increased by 0.1% and 1.01% at 10 Gy and 20 Gy irradiation, respectively (Figure 1G). However, there were no significant changes in the total amount of FA chains or the total amounts of PUFA, MUFA, and SFA chains in SM (Figure 1H) (Table S2).

Finally, we calculated the proportion of each lipid class in the whole lipids of the kidney and all four lipid classes—PC, PE, TG, and SM—each of which accounted for more than 5% of the total lipids in the kidney. We considered them as the major lipid classes (Figure S1). Based on the above results, it is evident that the major kidney lipid classes, including PC, PE, and TG, exhibit a significant increase in both the proportion and intensity of PUFA chains within 5 min of irradiation.

2.2. The C18:2, C20:4, and C22:6 FA Chains of Kidney Lipids Were Significantly Increased within 5 min of Irradiation

We examined the specific changes in PUFA chains within 5 min of radiation. Our findings revealed that the intensity of the C18:2, C20:4, and C22:6 FA chains accounted for a significant proportion of the total FA chains in kidney PC. Specifically, C18:2 chain intensity accounted for 35.96%, C20:4 chain intensity accounted for 19.46%, and C22:6 chain intensity accounted for 39.76% of the total FA chains in PC. In comparison, the number of these FA chains accounted for 22.45%, 19.39%, and 20.41% of the total amount of FA chains in PC without irradiation. Following 10 Gy and 20 Gy irradiation, the intensity of the C18:2 chain in PC increased by 31.21% ($p = 0.039$) and 26.9% ($p = 0.161$), the C20:4 chain increased by 38.40% ($p = 0.049$) and 31.52% ($p = 0.181$), and the C22:6 chain increased by 71.03% ($p = 0.016$) and 57.27% ($p = 0.051$) (Figure 2A).

In PE, we found that the intensity of C18:2, C20:4, and C22:6 accounted for 14.21%, 47.75%, and 26.34% of the total FA chains, and the number of these FA chains accounted for 24.11%, 22.32%, and 23.21% of the total amount of FA chains without irradiation. The intensity of the C18:2 chain in PE increased by 56.37% ($p = 0.024$) and 53.79% ($p = 0.033$), the C20:4 chain increased by 51.75% ($p = 0.042$) and 47.74% ($p = 0.158$), and the C22:6 chain increased by 118.72% ($p = 0.011$) and 118.08% ($p = 0.017$), respectively, within 5 min of 10 Gy and 20 Gy radiation (Figure 2B).

Interestingly, in TG, the intensity of the C18:2 FA chains accounted for 91.02% of the total FA chains of TG, while the amount of C18:2 chains accounted for 43.20% of the FA chains of TG without irradiation. The amount of C18:2 chains in TG increased by 121.18% ($p = 0.238$) and 125.01% ($p = 0.033$) within 5 min of 10 Gy and 20 Gy irradiation, respectively (Figure 2C).

2.3. Significant Increase in Kidney Lipidomes Within 5 min of Irradiation

We further investigated the overall changes in the kidney lipid profile within 5 min of irradiation. Using volcano plots based on lipidomic data, we identified significantly altered lipid species with p -values less than or equal to 0.05 and multiplicative changes higher than 2-fold (Table S1). Among the kidney lipid group, 9.85% of the lipids showed a significant increase. In comparison, 0.62% showed a significant decrease after 10 Gy irradiation (Figure 3A). Similarly, after 20 Gy irradiation, 15.54% of the lipids showed a

significant increase. In comparison, 0.31% showed a significant decrease (Figure 3B). These results indicate that the kidney lipidomes exhibited significant changes within a short time after radiation, primarily characterized by an increase in lipids, with less than 1% of the lipid species showing a decrease after irradiation at both doses.

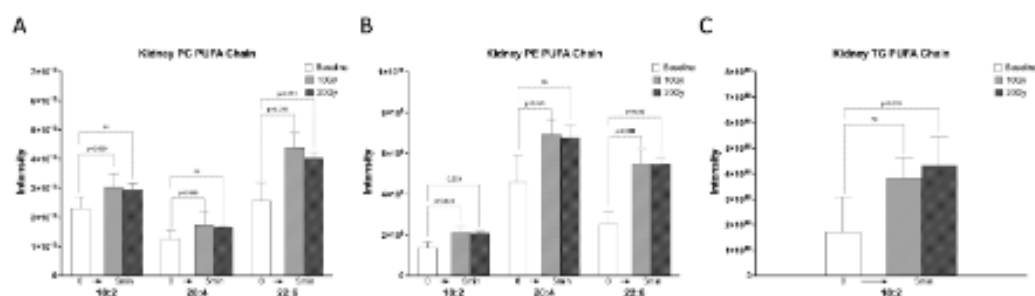


Figure 2. The 18:2, C20:4, and C22:6 chains as the main PUFA chains increased significantly within 5 min of irradiation. (A) Intensity histograms of PUFA chains (C18:2, C20:4, and C22:6) in kidney PC under 0 Gy, 10 Gy, and 20 Gy irradiation. (B) Intensity histograms of PUFA chains (C18:2, C20:4, and C22:6) in kidney PE under 0 Gy, 10 Gy, and 20 Gy irradiation. (C) Intensity histograms of PUFA chains (C18:2) in kidney TG under 0 Gy, 10 Gy, and 20 Gy irradiation. ns: no significant.

Furthermore, we classified the significantly changed lipid species into four categories: PC, PE, TG, and signaling lipids. Interestingly, all 15 changed PC species, 31 changed PE species, and 23 changed TG species exhibited significant increases (Figure 3C–E), consistent with the changes observed in PUFA chains. Among the altered signaling lipids, three species showed a significant decrease (Figure 3F). We also investigated the composition of FA chains in the significantly increased lipids. Among the 11 significantly changed PCs under 10 Gy irradiation, 20 chains were PUFA chains, and 2 were MUFA chains without any SFA chains. Similarly, among the 11 significantly changed PCs under 20 Gy irradiation, 21 chains were PUFA chains, and 1 was a MUFA chain, again without any SFA chains. Among the significantly changed PEs, 25 PEs with 50 FA chains showed significant changes after 10 Gy irradiation. Among these FA chains, 35 were PUFA chains, 10 were MUFA chains, and 5 were SFA chains. After 20 Gy irradiation, 27 PEs with 54 FA chains exhibited significant changes, including 37 PUFA chains, 11 MUFA chains, and 6 SFA chains. Regarding the TG species, 1 TG with significant changes after 10 Gy irradiation had 2 PUFA chains and 1 MUFA chain without any SFA chains. However, after 20 Gy irradiation, 23 TG species (containing 69 FA chains) showed significant changes, including 37 PUFA chains, 30 MUFA chains, and 2 SFA chains.

2.4. Lung, Brain, and Liver Showed Slight Lipidomic Alteration without Significant PUFA Change

We also examined the amount of PUFA chains in PC, PE, and TG in the lungs, brain, and liver within 5 min of irradiation and investigated the lipid changes in these organs. In the lung, the proportion of PUFA chains increased by 0.77% and 0.96% in PC, 0.35% and 0.27% in PE, and 1.10% and 2.19% in TG after 10 Gy and 20 Gy irradiation, respectively (Figure S2A,C,E). However, there were no significant changes in the intensity of total PUFA chains in lung PC, PE, and TG (Figure S2B,D,F).

Similarly, in the brain, the proportion of PUFA chains increased by 0.20% and 0.57% in PC, decreased by 0.22% and increased by 1.10% in PE, and decreased by 2.23% and 1.11% in TG under 10 Gy and 20 Gy irradiation within 5 min, respectively (Figure S3A,C,E). No significant changes were observed in the total PUFA chains in brain PC, PE, and TG (Figure S3B,D,F).

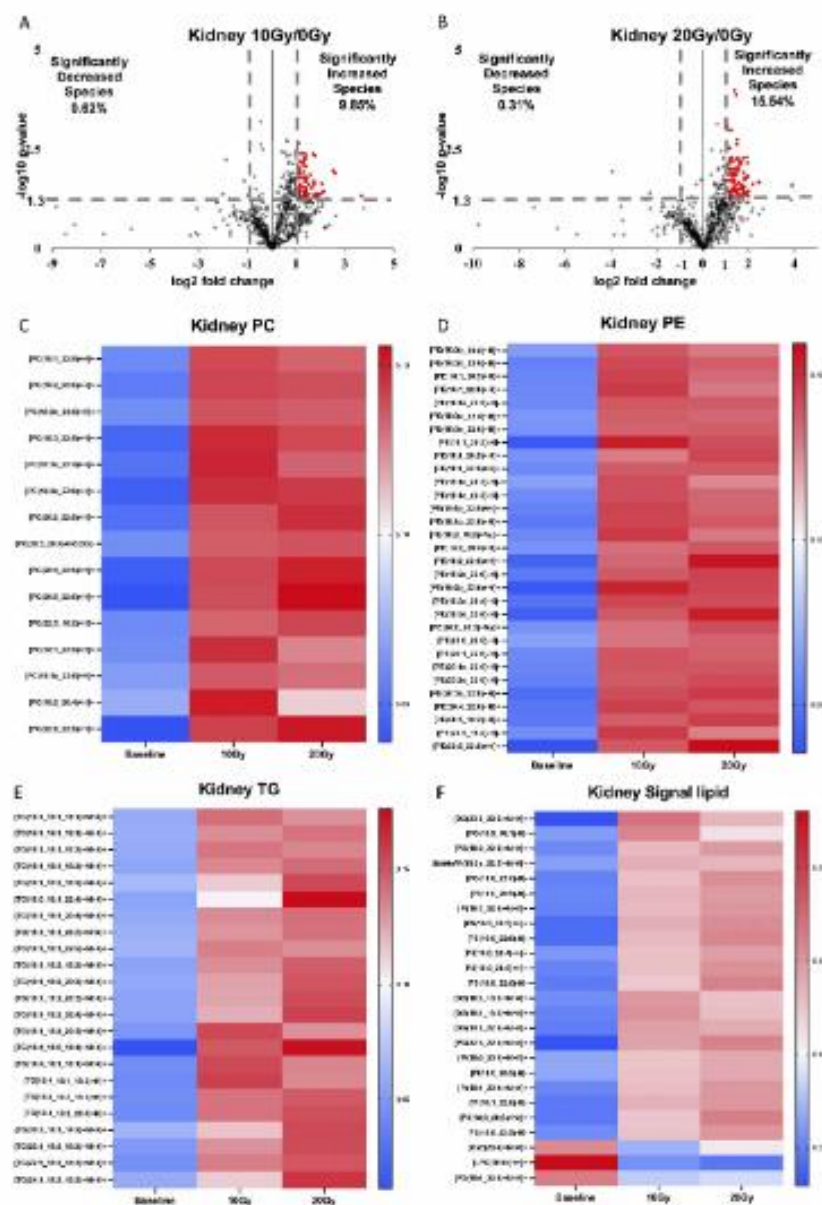


Figure 3. Kidney lipidome altered within 5 min of irradiation. (A) Volcano plot of lipid profile under comparison between 10 Gy and 0 Gy irradiation. (B) Volcano plot of lipid profile under comparison between 20 Gy and 0 Gy irradiation. (C) All significantly increased PC species upon 10 Gy and 20 Gy irradiation. (D) All significantly increased PE species upon 10 Gy and 20 Gy irradiation. (E) All significantly increased TG species upon 10 Gy and 20 Gy irradiation. (F) All other significantly increased lipid species upon 10 Gy and 20 Gy irradiation. The vertical line represents a change of more than 2-fold. The horizontal line represents p -value < 0.05 . Blue dots: significant decrease in lipid species ($FC < 0.5$, p -value < 0.05). Red dots: significant increase in lipid species ($FC > 2$, p -value < 0.05).

Regarding the liver, the percentage of PUFA chains in PC, PE, and TG decreased by 0.43% and increased by 0.25%, increased by 0.88% and 1.35%, and decreased by 2.30% and

1.75% (Figure S4A,C,E). However, there were no significant changes in the intensity of total PUFA chains in liver PC, PE, and TG (Figure S4B,D,F).

Furthermore, we examined the lipidomic changes in the lung, brain, and liver within 5 min of radiation using volcano plots. Among the lung lipid group, 0.00% of the lipids showed a significant change after 10 Gy irradiation (Figure 4A). After 20 Gy irradiation, 0.64% of the lipids showed a significant increase. In comparison, 0.16% showed a significant decrease (Figure 4B). In the brain lipid group, 0% of the lipids showed a significant increase. In comparison, 2.00% showed a significant decrease after 10 Gy irradiation (Figure 4C). After 20 Gy irradiation, 0.36% of the lipids showed a significant increase. In comparison, 0.55% showed a significant decrease (Figure 4D). Among the liver lipid group, 0.2% of the lipids showed a significant increase. In comparison, 0% showed a significant decrease after 10 Gy irradiation (Figure 4E). After 20 Gy irradiation, 0% of the lipids showed a significant increase, and 0.41% showed a significant decrease (Figure 4F).

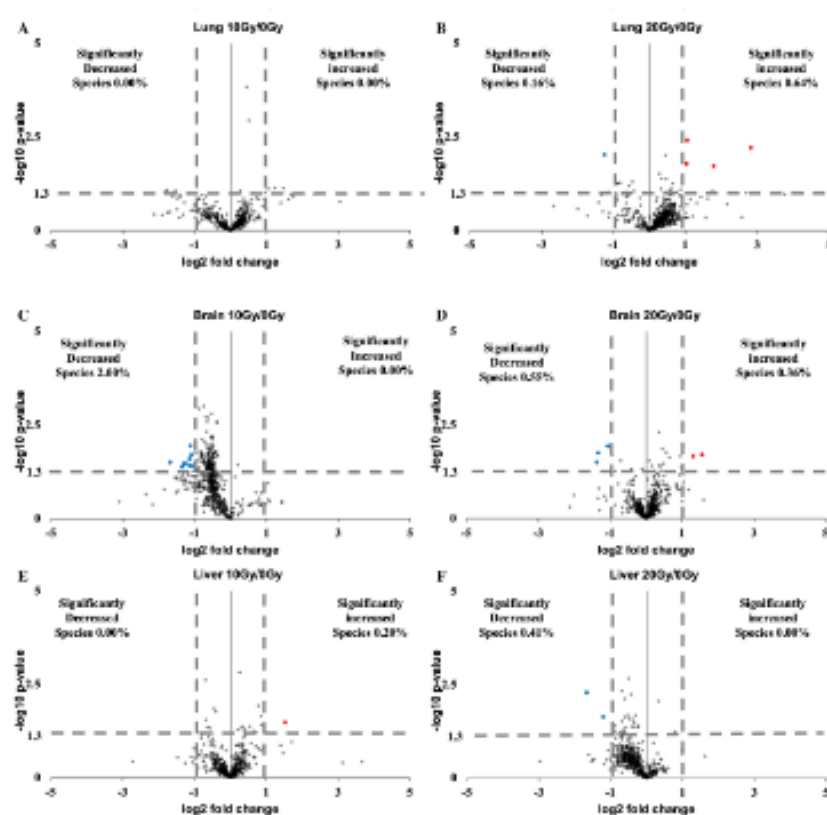


Figure 4. Lung, brain, and liver lipidomes within 5 min of irradiation. (A) Volcano plot of lipid profile under comparison between 10 Gy and 0 Gy irradiation in lung. (B) Volcano plot of lipid profile under comparison between 20 Gy and 0 Gy irradiation in lung. (C) Volcano plot of lipid profile under comparison between 10 Gy and 0 Gy irradiation in brain. (D) Volcano plot of lipid profile under comparison between 20 Gy and 0 Gy irradiation in brain. (E) Volcano plot of lipid profile under comparison between 10 Gy and 0 Gy irradiation in liver. (F) Volcano plot of lipid profile under comparison between 20 Gy and 0 Gy irradiation in liver.

3. Discussion

In this research article, we present a novel LC-MS/MS analysis of fatty acid (FA) chains in the major lipid classes of mice's multi-organ within a five-minute timeframe following irradiation. Our findings reveal a significant increase in PUFA chains of PC, PE, and TG

specifically in the kidney after exposure to high-dose radiation. This increase in PUFA chains was not only an increase in the amount of PC, PE, and TG containing PUFA chains alone (i.e., a change in the number of homogeneous lipids), but also an increase in the proportion of PC-, PE-, and TG-containing PUFA chains (i.e., the appearance of new lipids containing PUFA chains). In other words, this implies that within a short period following high-dose radiation, the SFA and MUFA chains in the major kidney lipids are replaced by PUFA chains. Furthermore, this turnover of fatty acid chains is particularly pronounced in the significantly altered lipids of the kidney. Notably, we observe substantial changes in the kidney lipid group within the five-minute window after high-dose radiation, primarily characterized by growth.

Moreover, the growing lipids predominantly comprise PC, PE, and TG, with the most significant increases occurring in lipids containing PUFA chains. These findings suggest that the rapid impact of high-dose radiation on the lipidome primarily affects the fatty acid chain composition rather than the head group. In contrast to previous studies indicating a decrease in PUFA chains in phospholipids 72 h after irradiation [13], our study demonstrates an increase in PUFA chains within minutes following exposure to 10 Gy of radiation. This preference for elevated PUFA-containing lipids establishes the groundwork for free radical oxidation/peroxidation.

Considering that *de novo* lipogenesis exceeds a five-minute timeframe [16], we hypothesize that the replacement of the fatty acid chains described above occurs via the Land cycle [17]. The Land cycle has the potential for rapid large-scale reactions. Previous reports have shown that phospholipase A2 releases substantial amounts of arachidonic acid and lysolecithin from phospholipids within seconds [18,19]. In our study, we also examine the levels of lysophospholipids in the kidneys after irradiation, which serve as a source for phospholipid synthesis via the Land cycle. We observe a decrease in the levels of LPC and LPE following irradiation (Figure S5), indicating that the new lipids containing PUFA chains that emerge after irradiation may be synthesized from lysolecithin and PUFA. Based on the short-term fluctuations in lipid PUFA chain levels, we propose the PUFA protection hypothesis. This hypothesis suggests that PUFAs contain more double-bonded structures, which are more susceptible to ROS attacks. The substantial rise in PUFA chains within major lipids shortly after radiation implies an overall increased susceptibility of lipids to ROS. This increased susceptibility helps lipids compete with proteins or nucleic acids for ROS, thereby protecting proteins and nucleic acids from ROS-induced damage. Although the increase in PUFA chains promotes ROS attack on the plasma membrane, it represents the optimal cellular response (sacrificing lipids to protect proteins and nucleic acids) in the face of an acute or massive ROS attack.

It is essential to note that we employed two radiation doses, namely 10 Gy and 20 Gy. The PUFA chains in kidney lipids did not exhibit significant differences between the two doses. We attribute these findings to the limitations of short-term PUFA chain increases. We selected the organs primarily due to the brain's and liver's high lipid content, the kidney's role as the main metabolic organ, and the lungs' susceptibility to radiation damage. Contrary to our expectations, the PUFA chains in brain, liver, and lung lipids did not display significant changes within the first five minutes of irradiation. Theoretically, even in as little as five minutes, radiation-induced physicochemical reactions would occur in the lipids of all organs. However, due to the complex material composition within different organs, the extent of the biological reaction of lipids over a five-minute time frame will be different. One possible explanation for the observed organ-specific differences is the relationship between the intensity of very early reactions and the radiosensitivity of organ tissues [20,21]. Generally, lipid reactions are not typically considered when evaluating radiosensitivity. Nonetheless, our research highlights the importance of considering phenomena beyond those accounted for by the traditional linear-quadratic (LQ) model during the application of hypofractionated irradiation. To gain a more comprehensive understanding of the ultra-early lipid response to radiation in normal and tumor tissues, we will design relevant tumor-bearing mice, increase the time points, and increase the sample size in subsequent

studies. These studies will help us to develop strategies to enhance the efficacy of tumor radiotherapy and mitigate the side effects of radiotherapy.

4. Materials and Methods

4.1. Animals Furthermore, X-ray Irradiation

Four-month-old C56BL/6 wild-type male mice (weight 26–28 g) were obtained from SLC Inc. (Hamamatsu, Japan). The mice were housed under a 12-h light/dark cycle for one week and provided unrestricted food and water access. Mice were randomly divided into three groups ($n = 3$ for each group). Group I mice were not irradiated and were used as the baseline group. Mice of groups II and III received whole-body irradiation with a single dose of 10 Gy and 20 Gy using an MX-160Labo X-ray machine (Medixtec, Nagoya, Japan), respectively. The dose rate was set to 1.5 Gy/min. After 5 min of X-ray radiation, all mice were dissected following cervical dislocation. Kidney, lung, brain, and liver tissue samples were collected rapidly and snap-frozen by dry ice. The frozen samples were then stored at -80°C until the lipid extraction.

4.2. Lipid Extraction

Lipids were extracted from kidney, lung, brain, and liver tissue by the modified Bligh and Dyer method [22]. The weight of the kidney was measured by a digital scale (PB3002-sdr, Mettler Toledo). Water was added at a rate of $8\ \mu\text{L}/\text{mg}$ by weight of individual kidney, lung, brain, and liver samples. Then, a digital homogenizer was used to homogenize the samples with water (HK-1, AS ONE Corporation, Osaka, Japan). After homogenization, chloroform and methanol were added to the lysate. The mixture was transferred to a glass tube, mixed very well, and left at room temperature. After 10 min, extra chloroform was added and mixed very well. Then, 0.28 M acetic acid was added, mixed well, and centrifuged at $110\ g\times$ for 15 min. The final ratio of water:methanol:chloroform:acetic acid was 1:2.5:2.5:1.25. An equal amount of the lower layer from each extract of a particular tissue was collected, followed by drying. The dried lipids were stored at -80°C until LC-MS/MS analysis.

4.3. LC-MS and LC-MS/MS of Kidney, Lung, Brain, and Liver Lipids

The lipid was dissolved in 100% methanol containing $1\ \text{ng}/\mu\text{L}$ PC (12:0/12:0) as internal standard. and transferred into a glass vial (Waters, New York, NY, USA) specified for LC-MS/MS with a glass insert (Systech, Scottsdale, AZ, USA) in it; a specific safe cap (Thermo Scientific, Lenexa, KS, USA) was screwed onto it for safe movement. Lipids were retrieved and analyzed by a Q Exactive™ Hybrid Quadrupole-Orbitrap™ mass spectrometer equipped with an electrospray ionization (ESI, Scottsdale, AZ, USA) source and attached to an Ultimate 3000 system (Thermo Scientific). The column and the sample temperature were maintained at 50°C and 10°C , respectively. A $10\ \mu\text{L}$ lipid sample was injected into the machine and isolated in an Acclaim 120 C18 column ($150\ \text{mm} \times 2.1\ \text{mm}$, $3\ \mu\text{m}$) (Thermo Scientific). The composition of the flow phase was depicted separately below by setting up the mobile phase as two parts, A and B. Part A consisted of water–acetonitrile–methanol (2:1:1 $v/v/v$), 5 mM ammonium formate, and 0.1% formic acid. Part B consisted of acetonitrile–isopropanol (1:9 v/v), 5 mM ammonium formate, and 0.1% formic acid. The elution flow rate was programmed at $300\ \mu\text{L}/\text{min}$ using a series of linear-gradient beginning with 20% solvent B, increasing linearly to 100% B within 50 min, sustaining 100% B for 60 min, then reducing linearly to 20% B between 60 min and 60.1 min, and terminating with 20% B within the final 10 min. The total operation time was 70 min, and conditions of the MS instruments were optimized as follows: probe heater temperature, 350°C ; S-lens RF level, 50; capillary temperature, 250°C ; auxiliary gas flow, 15 (au); sheath gas flow, 50 (au); sweep gas flow, 0 (au); spray voltage in positive mode, 3.5 kV, and negative mode, 2.5 kV. Data were acquired from 2.5 min to 60 min in both full MS and data-dependent MS/MS (dd-MS2) modes. The parameters of full MS mode were set as follows: automatic gain control (AGC) target, 1×10^6 ; mass resolving power, 70,000 (FWHM, at m/z 200);

recorded m/z range, 220–2000; and maximum injection time (IT), 100 ms. For dd-MS2, the following conditions were used: mass resolving power, 17,500 (FWHM, at m/z 200); AGC target, 1×10^5 ; maximum IT, 80 ms; loop count, 5; TopN, 5; isolation window, 2.0 m/z ; normalized collision energy (NCE), 30.0 eV; stepped NCE, 15.0% for positive mode and 35.0% for negative mode, and dynamic exclusion, 15.0 s.

4.4. Lipid Identification Furthermore, Quantification

We acquired the spectral data with the Xcalibur v3.0 Software (Thermo Scientific). The data was then subjected to LipidSearch™ software version 4.2.13 (Mitsui Knowledge Industry, Tokyo, Japan) for lipid identification and quantification [23–25]. The lipids were identified as lipid ions. We set the following parameters: database as HCD; retention time as 0.01 min; search type as product_QEX; precursor tolerance as 5.0 ppm; and product tolerance as 8.0 ppm. Identification quality filters of A, B, and C were applied. We used 0.01 m/z tolerance and −1.0 min to 2.0 min of the retention time range for the quantification. After identification, alignment was performed with a 0.25 retention time tolerance.

4.5. Data Processing

Lipid intensities recorded in the Xcalibur v3.0 software and area values of lipid species identified by LipidSearch™ software were divided by the area values of the internal standard PC(12:0_12:0) for normalization.

4.6. Data Analysis

After acquiring the annotated and quantitated data of lipidomic tissue, we separated them into different groups following the experimental conditions and managed to make comparisons to seek the variations between those groups. We used MS Excel to create pie charts and volcano plots with the normalized data. We divide the average of the various lipid intensities to obtain fold change. We then applied Student's *t*-test to examine the significance of the lipid alteration. We considered the lipids that showed an alteration with a fold change more significant than 2 and a *p*-value smaller than or equal to 0.05 as significantly altered. Then we used a scatter plot and set \log_2 fold change as X and $-\log_{10}$ *p*-value as Y to build the volcano plots.

We found that the lipids displayed significant statistical differences, and the accuracy of the auto-annotation of LipidSearch was confirmed using Xcalibur (Thermo fisher scientific) (Figure S6).

GraphPad produced the bar graphs (Prism version.8.0.2.263).

5. Conclusions

Our findings indicate that the kidneys of mice exhibit a significant increase in PUFA chains within 5 min of exposure to 10 Gy and 20 Gy radiation. However, no significant changes in PUFA chains were observed in the lung, brain, and liver lipids. In the kidney, PC's and PE's main PUFA chain components were C18:2, C20:4, and C22:6, which exhibited a significant increase. Similarly, the major PUFA chain component in kidney TG, C18:2, significantly rose. Additionally, we observed significant changes in the lipidome of the kidney within 5 min of radiation, characterized by an overall increase in lipids. These findings shed light on the acute biochemical response of multiple organs to high-dose radiation, as elucidated from a lipidomic perspective.

Supplementary Materials: The following supporting information can be downloaded at: <https://www.mdpi.com/article/10.3390/ijms241512439/s1>.

Author Contributions: Conceptualization, S.A.; methodology, L.X., S.T., T.S. (Takumi Sakamoto), M.A.M., A.L., T.H., K.K., T.S. (Tomohito Sato) and Y.T.; writing—original draft preparation, W.L. and C.Z.; writing—review and editing, T.K., M.D. and C.F.; supervision, K.N. and M.S.; funding acquisition, S.A. All authors have read and agreed to the published version of the manuscript.

Funding: This research was funded by Japan Society for the Promotion of Science(JSPS) OF FUNDER grant number JP21464465 and MEXT Project for promoting public utilization of advanced research infrastructure (Imaging Platform) OF FUNDER grant number JPMXS0410300220.

Institutional Review Board Statement: This study was approved by the Animal Care and Use Committee of the Hamamatsu University School of Medicine (ethical permission number: 2021002).

Data Availability Statement: All relevant data are within the paper and its Supporting Information files.

Acknowledgments: We would like to thank Masahiko Ikeda and Maki Hiroshima from Advance Research Facilities & Services and Promotion Center for Medical Collaboration & Intellectual Property at Hamamatsu university school of Medicine for their guidance and support of X-ray irradiation. We would like to thank Takuya Kitamoto and Minako Kondo, who belong to the Advanced Research Facilities and Services of HUSM, for experiment instructions about LC-MS.

Conflicts of Interest: The authors declare no conflict of interest.

References

1. Yap, M.L.; Zubizarreta, E.; Bray, F.; Ferlay, J.; Barton, M. Global Access to Radiotherapy Services: Have We Made Progress During the Past Decade? *J. Glob. Oncol.* **2016**, *2*, 207–215. [\[CrossRef\]](#) [\[PubMed\]](#)
2. Qiu, B.; Aili, A.; Xue, L.; Jiang, P.; Wang, J. Advances in Radiobiology of Stereotactic Ablative Radiotherapy. *Front. Oncol.* **2020**, *10*, 1165. [\[CrossRef\]](#) [\[PubMed\]](#)
3. Folkert, M.R.; Timmerman, R.D. Stereotactic ablative body radiosurgery (SABR) or Stereotactic body radiation therapy (SBRT). *Adv. Drug Deliv. Rev.* **2017**, *109*, 3–14. [\[CrossRef\]](#) [\[PubMed\]](#)
4. Nahum, A.E. The radiobiology of hypofractionation. *Clin. Oncol. (R. Coll. Radiol. (Great Br.))* **2015**, *27*, 260–269. [\[CrossRef\]](#) [\[PubMed\]](#)
5. Wenk, M.R. Lipidomics: New tools and applications. *Cell* **2010**, *143*, 888–895. [\[CrossRef\]](#)
6. Köfeler, H.C.; Fauland, A.; Rechberger, G.N.; Trötz Müller, M. Mass Spectrometry Based Lipidomics: An Overview of Technological 391 Platforms. *Metabolites* **2012**, *2*, 19–38. [\[CrossRef\]](#)
7. Liu, Q.; Luo, Q.; Halim, A.; Song, G. Targeting lipid metabolism of cancer cells: A promising therapeutic strategy for cancer. *Cancer Lett.* **2017**, *401*, 39–45. [\[CrossRef\]](#)
8. Yin, H.; Xu, L.; Porter, N.A. Free radical lipid peroxidation: Mechanisms and analysis. *Chem. Rev.* **2011**, *111*, 5944–5972. [\[CrossRef\]](#)
9. Niki, E. Lipid peroxidation: Physiological levels and dual biological effects. *Free Radic. Biol. Med.* **2009**, *47*, 469–484. [\[CrossRef\]](#)
10. Que, X.; Hung, M.Y.; Yeang, C.; Gonen, A.; Prohaska, T.A.; Sun, X.; Diehl, C.; Määttä, A.; Gaddis, D.E.; Bowden, K.; et al. Oxidized phospholipids are proinflammatory and proatherogenic in hypercholesterolaemic mice. *Nature* **2018**, *558*, 301–306. [\[CrossRef\]](#)
11. Nishizawa, H.; Matsumoto, M.; Chen, G.; Ishii, Y.; Tada, K.; Onodera, M.; Kato, H.; Muto, A.; Tanaka, K.; Igarashi, K. Lipid peroxidation and the subsequent cell death transmitting from ferroptotic cells to neighboring cells. *Cell Death Dis.* **2021**, *12*, 332. [\[CrossRef\]](#) [\[PubMed\]](#)
12. Wiernicki, B.; Dubois, H.; Tyurina, Y.Y.; Hassannia, B.; Bayir, H.; Kagan, V.E.; Vandenabeele, P.; Wullaert, A.; Berghe, T.V. Excessive phospholipid peroxidation distinguishes ferroptosis from other cell death modes including pyroptosis. *Cell Death Dis.* **2020**, *11*, 922. [\[CrossRef\]](#)
13. Benderitter, M.; Vincent-Genod, L.; Pouget, J.P.; Voisin, P. The cell membrane as a biosensor of oxidative stress induced by radiation exposure: A multiparameter investigation. *Radiat. Res.* **2003**, *159*, 471–483. [\[0471:tcmaab\]2.0.co;2](#). [\[CrossRef\]](#)
14. Li, J.; Ren, S.; Piao, H.L.; Wang, F.; Yin, P.; Xu, C.; Lu, X.; Ye, G.; Shao, Y.; Yan, M.; et al. Integration of lipidomics and transcriptomics unravels aberrant lipid metabolism and defines cholesteryl oleate as potential biomarker of prostate cancer. *Sci. Rep.* **2016**, *6*, 20984. [\[CrossRef\]](#)
15. Yuan, Z.H.; Liu, T.; Wang, H.; Xue, L.X.; Wang, J.J. Fatty Acids Metabolism: The Bridge Between Ferroptosis and Ionizing Radiation. *Front. Cell Dev. Biol.* **2021**, *9*, 1–15. [\[CrossRef\]](#)
16. Li, J.; Cheng, J.X. Direct Visualization of De novo Lipogenesis in Single Living Cells. *Sci. Rep.* **2014**, *4*, 6807. [\[CrossRef\]](#)
17. O'Donnell, V.B. New appreciation for an old pathway: The Lands Cycle moves into new arenas in health and disease. *Biochem. Soc. Trans.* **2022**, *50*, 1–11. [\[CrossRef\]](#)
18. Higgins, A.J.; Lees, P. The acute inflammatory process, arachidonic acid metabolism and the mode of action of anti-inflammatory drugs. *Equine Vet. J.* **1984**, *16*, 163–175. [\[CrossRef\]](#)
19. Takeda, R.; Islam, A.; Sato, T.; Kurita, H.; Kahyo, T.; Urano, T.; Setou, M. The stability of the metabolic turnover of arachidonic acid in human unruptured intracranial aneurysmal walls is sustained. *Clin. Neurol. Neurosurg.* **2021**, *208*, 106881. [\[CrossRef\]](#)
20. Kehwar, T. Analytical approach to estimate normal tissue complication probability using best fit of normal tissue tolerance doses into the NTCP equation of the linear quadratic model. *J. Cancer Res. Ther.* **2005**, *1*, 168. [\[CrossRef\]](#)
21. Scheenstra, A.E.; Rossi, M.M.; Belderbos, J.S.; Damen, E.M.; Lebesque, J.V.; Sonke, J.J. Alpha/Beta Ratio for Normal Lung Tissue as Estimated From Lung Cancer Patients Treated With Stereotactic Body and Conventionally Fractionated Radiation Therapy. *Int. J. Radiat. Oncol.* **2014**, *88*, 224–228. [\[CrossRef\]](#) [\[PubMed\]](#)

22. Bligh, E.G.; Dyer, W.J. A rapid method of total lipid extraction and purification. *Can. J. Biochem. Physiol.* **1959**, *37*, 911–917. [[CrossRef](#)] [[PubMed](#)]
23. Taguchi, R.; Ishikawa, M. Precise and global identification of phospholipid molecular species by an Orbitrap mass spectrometer and automated search engine Lipid Search. *J. Chromatogr. A* **2010**, *1217*, 4229–4239. [[CrossRef](#)]
24. Peake, D.; Kiyonami, R.; Yokoi, Y.; Fukamachi, Y.; Huang, Y. Processing of a Complex Lipid Dataset for the NIST Inter-laboratory Comparison Exercise for Lipidomics Measurements in Human Serum and Plasma. In Proceedings of the LIPID MAPS Annual Meeting Saint Louis, MO, USA, 31 May–4 June 2015; pp. 5–7.
25. Taguchi, R.; Nishijima, M.; Shimizu, T. Basic Analytical Systems for Lipidomics by Mass Spectrometry in Japan. *Methods Enzymol.* **2007**, *432*, 185–211. [[CrossRef](#)]

Disclaimer/Publisher's Note: The statements, opinions and data contained in all publications are solely those of the individual author(s) and contributor(s) and not of MDPI and/or the editor(s). MDPI and/or the editor(s) disclaim responsibility for any injury to people or property resulting from any ideas, methods, instructions or products referred to in the content.